Investigating the role of macrophages in gastric cancer

by

Yu-Kuan Huang (808053)

ORCID - 0000-0003-2262-7069

Submitted in total fulfilment of the requirement for the degree of Doctor of Philosophy

April 2020

Sir Peter MacCallum Department of Oncology

The University of Melbourne

Abstract

Gastric cancer (GC) is lethal, with standard treatments offering little benefit. The immune component of the tumour microenvironment has been shown to highly influence GC progression and response to immune checkpoint therapies (ICTs). Tumour-associated macrophages (TAMs), one of the most abundant immune infiltrates in GC, are known for their plasticity and multiplicity of function. An abundance of TAMs is commonly associated with poor survival of cancer patients. However, their influences on survival in the GC setting are inconsistent between studies possibly due to a range of activation states and phenotypes and require further investigation.

In this study, a human GC cohort was interrogated by multiplex immunohistochemistry and analysed using comprehensive bioinformatic spatial and transcriptomic techniques to investigate the spectrum of TAMs in GC. Their spatial distribution within the tumour and association with tumour-infiltrating T lymphocytes (TILs), GC microenvironment and clinical outcomes were determined. *In silico* and *in vivo* models were used to validate these findings.

Seven predominant TAM populations were identified in a complexed multi-dimensional spectrum model. Each TAM population exhibited a unique combination of cellular markers and correlated with a specific environmental signature resembling published characteristics of *in vitro*-polarised macrophages. The spatial distribution pattern of TAMs was highly-related to their distance to tumour cells but was independent of their overall densities. This distribution pattern was described as an overall decrease in CD206, and increases in IRF8, CD68 and CD163 as TAMs near the tumour cells.

The CD163+ TAMs expressing concurrent high CD68 (CD68++CD163+) were associated with improved patient prognosis. These TAMs co-existed with the CD3+CD8+ TILs within the same tumour. NOX2 and PD1 were identified as functional markers for these immune populations, respectively, and an upregulation of these markers on corresponding cells was observed when the cells were in proximity with each other. Inclusion of these functional markers

improved the survival predictive value of these immune populations compared to using overall cell density, and suggests that these immune cells may be functioning through the NOX2/PD1 axis. This may reflect the antigen-presentation ability and activation statues of the TAMs and TILs, respectively.

TAMs is commonly correlated with high programmed death ligand 1 (PDL1) expression, a current ICT target, in the literature. In this study, the CD68-only and CD206+ TAMs were identified as specific TAM populations that exhibit high PDL1. This indicates that these TAMs may be particularly associated with immunosuppression and may serve as a complementary biomarker for ICTs in addition to PDL1.

An *in vivo* macrophage depletion protocol was established in an immune-incompetent mouse model to further test this hypotheses on macrophage subtypes. Concentrations of different clodronate-liposome constructs were optimised for investigating tumour invasion and progression in the absence of overall and CD206+ macrophages.

In conclusion, this Thesis (i) establishes methods which allow investigation and reveal the spatial heterogeneity of TAMs in human GC, and (ii) identifies a specific TAM/TIL pair and PDL1+ TAM populations that may be utilised as potential therapeutic targets and biomarkers of patient survival and response to ICT.

Declaration

I declare that

1. the Thesis comprises only my original work towards the Doctor of Philosophy except where indicated in the preface;

2. due acknowledgement has been made in the text to all other material used; and

3. the Thesis is fewer than 100,000 words in length, exclusive of tables, maps, bibliographies and appendices.

Yu-Kuan Huang

April 2020

Preface

Chapter 3, 4 and 5 contain published data and figures modified from:

- "Macrophage Spatial Heterogeneity in Gastric Cancer Defined by Multiplex Immunohistochemistry" **Yu-Kuan Huang**, Minyu Wang, Yu Sun, Natasha Di Costanzo, Catherine Mitchell, Adrian Achuthan, John A. Hamilton, Rita Busuttil, Alex Boussioutas. 2019, *Nature Communications*.

All experiments and data analyses presented in this Thesis were performed by Yu-Kuan Huang. Except for the:

1. "The Intercellular Spatial Analysis Tool (ISAT)" 2018, CRAN. (https://cran.r-project.org/web/packages/ISAT/index.html), which was a joint development by Yu-Kuan Huang, Dr. Minyu Wang and Dr. Yu Sun, Sir Peter MacCallum Department of Oncology, Department of Medicine, The University of Melbourne.

2. Patient status of "inflammation score, tumour region of interest, and cancer histological/molecular subtype" was determined by a pathologist, Dr. Catherine Mitchell, Department of Pathology, Peter MacCallum Cancer Centre, Melbourne, Victoria 3000, Australia.

3. "Surgical procedures of the intra-gastric xenograft implantation" were performed by Yu-Kuan Huang, Dr. Rita Busuttil and Mrs. Natasha Di Costanzo, Sir Peter MacCallum Department of Oncology, Department of Medicine, The University of Melbourne.

Acknowledgements

Four years is not a short time but I am finally here; at the end of my candidateship and at the start of the endless pursuit for truth. Along the way I have many people to thank for their inspiring supervision, kind advices and timely technical supports.

Many thanks to my supervisors: Prof. Alex Boussioutas, Dr. Rita Busuttil and Prof. John Hamilton. To Alex, thank you for taking me into the lab and to work on a challenging project. With your creative and thorough thought, you helped me to gain confidence and to establish the foundation of the study step by step. To Rita, thank you for being always available to answer my every query, science and non-science related. You are skilful and passionate in your work and a very good trainer in animal handling. To John, thank you for your tremendous support on the myeloid side of the project. I benefited greatly from your writing, and more importantly, your attitude on being critical on my own data which is what science is all about.

Many thanks to my mentors from different programmes during my PhD study: Dr. Paul Beavis, Dr. Simon Keam and Mr. Alun Needham. To Paul, my PhD mentor, thank you for your support and feedback whenever I needed them. Thank you also on giving me advice on the adaptive immunity which was not at the beginning, but later become a substantial part of my project. To Simon, my mentor from the PeterMac mentoring programme, thank you for your timely advice on Thesis writing and experiences sharing on my career planning. To Alun, my mentor from the Industry Mentoring Network in STEM (IMNIS) programme in Victoria, thank you for introducing me to a brand new industrial side of biotechnology in Australia and to other experts in the field. Thanks also for your commitment that I had more meetings with you than most of the other participants in the programme.

Many thanks to my lab mates from the Gastric Group and the Hamilton Lab for your support at all stages of my PhD. To Natasha Di Costanzo and Todd Waugh, thank you for helping me section tissue blocks, preparing materials for

experiments and brainstorming for words to more precisely express my thoughts. To Dr. Minyu Wang, a super big thanks to you for introducing me to many of the experimental techniques and helping me to settle when I first came to Australia. It was truly an intellectual challenging but satisfying time working with you to develop something new. To Dr. Sharon Pattison, thank you for your fantastic PhD work which allowed my analyses on the patient cohort you established. To Dr. Andrew Buckle, thank you for revising my writing. To Dr. Kunning (Helen) Wang, Athanasios Koulis and Dr. Wenwen Sun, thank you for your helpful advices from different points of view on my project. To Dr. Adrian Achuthan, thank you for your help on selecting macrophage markers and further optimisation of different *in vitro* experiments. To Dr. Ming-Chin (Kevin) Lee, thank you for your help on designing mouse flow panel. To Dr. Andrew Fleetwood and Dr. Andrew Cook, thank you for your helpful advices on my project and on showing me to operate instruments and acquiring cytokines. To Tanya Lupancu, thank you for preparing blood monocytes for me and I hope all goes well with your PhD.

Many thanks to my PhD Committee: Prof. Marc Achen, Dr. Karen Sheppard, Dr. Ewa Michalak, Dr. Conor Kearney, Dr. Jason Li, Dr. Amit Kumar, Dr Francesca Froldi, thank you for your brilliant comments, suggestions and supports throughout these years.

Many thanks to Dr. Catherine Mitchell from Pathology for helping us with the characterisation of patient status for the use of my analyses. Many thanks to people in the Immunology meeting group: To A/Prof. Paul Neeson and Heloise Halse, thank you for your help on establishing multiplex IHC platform. To Dr. Angela Pizzolla, thank you for the helpful discussions on the NOX2 complex, introducing me to other people working on similar topics and planning future experiments. To Dr. Junyun Lai, thank you for your help on designing mouse flow panel. Many thanks to the people in the Gastrointestinal (GI) research program: the Ramsay Lab, Phillips Lab and the Clemons Lab, for their insightful comments throughout these years.

Many thanks to the Core facilities at the Peter MacCallum Cancer Centre for helping me to collect and process data. To A/Prof. Sarah Ellis, Prinsloo Marne, Dr. Jill Danne, Dhanya Menon and Dr. Metta Jana of the Centre for Advanced Histology and Microscopy: thank you for the resources and the help on setting up the multiplex IHC platform and training me to using other microscopes. To Dr. Maria Doyle, Richard Lupat and Lucy Liu of the Bioinformatics Core Facility: thank you for hosting R workshops and helping me solve programming problems. To Ralph Rossi, Viki Milovac and Sophie Curcio of the Flow Cytometry Core Facility: thanks for your help on designing flow panels and acquiring and analysing data. To Michael Durrant and Danni Norman of the Animal Core Facility: thanks for your assistance in maintaining animals and showing me the correct ways of animal handling. To Dr. Caroline Owen, Niranga Nawagamuwa, and Dr. Erika Cretney of the Research Education Administration: thank you for your help on managing my candidateship, getting reimbursements for travels and hosting student retreats and symposiums.

Many thanks to my collaborators. Dr. Yu Sun: thank you for teaching I on R programming and helping me solve different coding problems. Dr. Na Li and Dr. Joseph Sia: thanks for the discussions on my data which led to further development of my project. Elhadi Iich: thanks for your helpful advice and the information on single-cell RNA sequencing. Dr. Joe Kong: thanks for your advice on clinical statistics. Dr. You-Fang Zhang: thank you for the kind advice on doing PhD. Dr. Andrew Lim and Nicholas Wong: thank you greatly for your help on designing flow panels.

I am grateful for the funding sources for my PhD: the Melbourne International Research Scholarship and the Taiwanese Government Scholarship to Study Abroad. I would like to thank and pay my respect to the patients, their families and the mice who provided their tissues and information for research.

Many thanks to my former supervisors and mentors for their guidance and previous support when applying for PhD positions. To Prof. Chi-Shiun Chiang: my supervisor from my bachelor and master research programme, thank you for the training in your lab that influenced me hugely. Dr. Wen-Jiun Peng: my

supervisor in the company, thank you for the different tasks you had for me which allowed me to acquire different skills outside the academic field. Dr. Charles Sia: my mentor in the company, thank you for the advice on my career planning and decision making.

Many thanks to my family: my dad, my mom and my brother. Thank you for your guidance when I was young which shaped my personality and your continuous support on my career and my decision to study abroad. Many thanks to Hsun: my partner, thank you for sharing your life with me and for accompanying and supporting me in Australia.

Lastly, I would like to thank the past me who restlessly pursued the truth and being always wanting to know. I would like to dedicate this work to my grandfather who is now looking down on me from heaven. I have fulfilled our promises and I will do my best to remain humble and curious in my future career.

Publications, awards and presentations

Publications:

1. "Macrophage Spatial Heterogeneity in Gastric Cancer Defined by Multiplex Immunohistochemistry" **Yu-Kuan Huang**, Minyu Wang, Yu Sun, Natasha Di Costanzo, Catherine Mitchell, Adrian Achuthan, John A. Hamilton, Rita Busuttil, Alex Boussioutas. 2019, *Nature Communications*.

2. "ISAT: Extract Cell Density and Nearest Distance Based on PerkinElmer InForm Software Output" Minyu Wang, Yu Sun, **Yu-Kuan Huang**. 2018, CRAN. (https://cran.r-project.org/web/packages/ISAT/index.html)

3. "High-dimensional analyses reveal distinct role of T cell subsets in the immune microenvironment of gastric cancer" Minyu Wang, **Yu-Kuan Huang**, Joe Kong, Yu Sun, Heloise Halse, Natasha Di Costanzo, Ian R. Gorden, Catherine Mitchell, Rita A. Busuttil, Paul J. Neeson, Alex Boussioutas. 2020, *Clinical & Translational Immunology.*

4. "SPIAT: An R package for the Spatial Image Analysis of Cells in Tissues" Tianpei Yang, Volkan Ozcoban, Anu Pasam, Nikolce Kocovski, Angela Pizzolla, **Yu-Kuan Huang**, Greg Bass, Simon P. Keam, Paul J. Neeson, Shahneen K. Sandhu, David L. Goode, Anna S. Trigos. 2020, bioRxiv.

5. "SFRP4 drives invasion in gastric cancer and is an early predictor of recurrence" Rita A. Busuttil, Joshy George, Colin House, Stephen Lade, Catherine Mitchell, Natasha Di Costanzo, Sharon Pattison, **Yu-Kuan Huang**, Patrick Tan, Jae-Ho Cheong, Sun Young Rha & Alex Boussioutas. *Submitted*

6. "Tumor Infiltrating Lymphocyte Function Predicts Response to Neoadjuvant Chemoradiotherapy in Locally Advanced Rectal Cancer." *Joseph Cherng Huei Kong, *Glen Robert Guerra, *Rosemary Magdalena Millen, Sara Roth, Huiling Xu, Paul John Neeson, Philip Kevin Darcy, Michael Henry Kershaw, Shienny Sampurno, Jordane Malaterre, David Shi Hao Liu, Toan Duc Pham, Vignesh Narasimhan, Minyu Wang, **Yu-Kuan Huang**, Kumar

Visvanathan, Jacob McCormick, Andrew Craig Lynch, Satish Warrier, Michael Michael, Jayesh Desai, William Murray, Catherine Mitchell, Samuel Ngan, Wayne Allen Phillips, ^Alexander Graham Heriot and ^Robert George Ramsay. 2018, *Journal of Clinical Oncology*.

Awards:

1. Melbourne International Research Scholarship (MIRS): 2016 – 2020
2. Government Scholarship to Study Abroad (GSSA, Taiwan Ministry of Education): 2018 – 2020
3. Industry Mentoring Network in STEM (IMNIS) programme participant: 2018-2019
4. Graham Brown Student Publication Prize Best Publication Award, 2019

Presentations:

Oral:

1. 2019 48th Annual Scientific Meeting of the Australian and New Zealand Society for Immunology
2. 2018 VCCC Student Symposium

Poster:

1. 2019 48th Annual Scientific Meeting of the Australian and New Zealand Society for Immunology
2. 2018 5th European Congress of Immunology
3. 2017 Fluorescence Microscopy Symposium
4. 2017 VCCC Student Symposium
5. 2017 CTx Symposium Cancer Therapeutics CRC

List of abbreviations

Acronym	Word
AJCC	American Joint Committee on Cancer
APC	Antigen-presenting cell
BMI	Body mass index
CCL	Chemokine C-C motif ligand
CCR	Chemokine C-C motif receptor
CD	Cluster of differentiation
CI	Confidence interval
CIN	Chromosomal instability
CPS	Combined positive score
CSF	Colony-stimulating factor
CTLA-4	Cytotoxic T-lymphocyte-associated protein 4
CXCL	Chemokine C-X-C motif ligand
CXCR	Chemokine C-X-C motif receptor
CYTOF	Cytometry by time-of-flight
DC	Dendritic cell
EBV	Epstein-Barr virus
ECM	Extracellular matrix
EMT	Epithelial–mesenchymal transition
FFPE	Formalin-fixed paraffin-embedded
FOXP3	Forkhead box p3
GC	Gastric cancer
GM-CSF	Granulocyte-macrophage colony-stimulating factor
GS	Genomically stable
H&E	Haematoxylin and eosin
H. pylori	Helicobacter pylori
HMGB1	High mobility group box 1
HR	Hazard ratio
ICT	Immune checkpoint therapy
IDO	Indoleamine 2,3-dioxygenase
IFN	Interferon
IL	Interleukin
IRF	Interferon regulatory factor
ISAT	Intercellular spatial analysis tool
LPS	Lipopolysaccharide
MAUGIC	Molecular analysis of upper gastrointestinal cancer
M-CSF	Macrophage colony stimulating factor

MDSC	Myeloid-derived suppressor cell
MIHC	Multiplex immunohistochemistry
MSI	Microsatellite instability high
Mϕ	Macrophage
NADPH	Nicotinamide adenine dinucleotide phosphate H
NC	Nearest cell
NF-KB	Nuclear factor kappa B
NK	Natural killer
NOX2	NADPH oxidase 2
OR	Odds ratio
OS	Overall survival
OXPHOS	Oxidative phosphorylation
p.d.i.	Post-drug injection
p.x.i.	Post-xenograft implantation
PBMC	Peripheral blood mononuclear cells
PCA	Principal component analysis
PD1	Programmed cell death protein 1
PDL1	Programmed death-ligand 1
PFS	Progression-free survival
RC	Reference cell
RFS	Relapse-free survival
RNA-seq	RNA sequencing
ROI	Region of interest
STAT	Signal transducer and activator of transcription
TAM	Tumour-associated macrophage
TCGA	The Cancer Genome Atlas
TCR	T cell receptor
TGF	Transforming growth factor
TH	Helper t cells
TIL	Tumour-infiltrating lymphocyte
TME	Tumour microenvironment
TNF	Tumour-necrosis factor
TSA	Tyramide signal amplification
VEGF	Vascular endothelial growth factor

Table of Contents

Abstract I

Declaration III

Preface IV

Acknowledgements V

Publications, awards and presentations IX

List of abbreviations XI

Table of Contents XIII

List of Figures XIX

List of Tables XXVI

List of Appendices XXVII

Chapter 1 : Literature review 1

1.1 GASTRIC CANCER 1

1.1.1 Incidence and mortality *1*

1.1.2 Cancer classification *3*

1.1.3 Risk factors and aetiology *8*

1.1.4 Cancer diagnosis and staging *10*

1.1.5 Treatments for gastric cancer *11*

1.2 TUMOUR MICROENVIRONMENT 19

1.2.1 The immune system *19*

1.2.2 The three "Es" of cancer immunoediting *20*

1.2.3 Cancer-Immune cycle *22*

1.3 MACROPHAGES 23

1.3.1 Bipolar classification of macrophages *23*

1.3.2 Tumour-associated macrophages *25*

1.3.3 Tumour-associated macrophages in gastric cancer *25*

1.3.4 Tumour-associated macrophages as therapeutic targets *26*

1.4 MACROPHAGE DIVERSITY AND HETEROGENEITY 37

1.4.1 Spectrum model of macrophage activation *37*

1.4.2 Tissue macrophages of dual origins *39*
1.4.3 Spatial and metabolic reprogramming of macrophages *42*
1.4.4 Macrophages in non-infectious immunity and interaction with and other cells *45*
1.4.5 Macrophage markers: Too similar and too different *47*
1.5 Remaining challenges and Thesis aims 49
Chapter 2 : Materials and methods 50
2.1 MAUGIC cohort 50
2.1.1 OPAL study cohort *50*
2.1.2 MAUGIC-Affy cohort *50*
2.1.3 OPAL-Affy cohort *50*
2.1.4 Patient exclusion criteria for survival analysis *51*
2.1.5 Classifications of cancer subtype and inflammation status *51*
2.1.6 Cancer staging *52*
2.2 Multiplex immunohistochemistry 52
2.2.1 Staining *52*
2.2.2 Tissue imaging and image processing *54*
2.2.3 Cell phenotyping *55*
2.3 Cell culture 56
2.4 In vivo experiment design 56
2.4.1 Mice *56*
2.4.2 Macrophage depletion *56*
2.4.3 Xenograft inoculation *57*
2.4.4 Immunohistochemistry *57*
2.4.5 Invasion score *58*
2.5 Flow cytometry 58
2.5.1 Mouse peripheral blood mononuclear cell *58*
2.5.2 Tumour samples *60*
2.5.3 Mouse spleen *61*
2.6 Analysis 61
2.6.1 Software and statistics *61*
2.6.2 Distance analysis *62*

2.6.3 R packages 62

Chapter 3 : Establishing a model for the analysis of cellular phenotype and spatial interaction using multiplex immunohistochemistry 63

3.1 Introduction 63

3.1.1 Tumour-associated macrophages 63

3.1.2 Multiplex immunohistochemistry 63

3.1.3 Regions of interest 64

3.1.4 Spatial analysis 65

3.1.5 Selection of immunohistochemical markers 65

3.2 Aims 66

3.3 Results 67

3.3.1 Cohort selection 67

3.3.2 Multiplex immunohistochemistry panel optimisation 68

3.3.3 Cell phenotyping 71

3.3.4 Validation of cell phenotyping 75

3.3.5 Distance analysis criteria and model setup 78

3.4 Discussion and Conclusions 84

3.4.1 Summary 84

Chapter 4 : Spatial mapping of tumour-associated macrophages 85

4.1 Introduction 85

4.2 Aims 86

4.3 Results 86

4.3.1 Distribution of TAMs across different tumour regions 86

4.3.2 Distribution of TAMs in proximity to tumour cells 90

4.3.3 Association of TAM populations and patient clinical outcomes 93

4.3.4 Co-localisation of TAM populations 95

4.3.5 PDL1 expression on multiplex IHC-characterised TAMs 97

4.3.6 PDL1 expression on fresh sample-isolated TAMs 104

4.3.7 Marker expression on TAMs between the tumour-nest and stroma 106

4.3.8 PDL1-positive cell density-stratified patient overall survival 112

4.3.9 Combined positive score of PDL1 119

4.4 Discussion and Conclusions 122

4.4.1 Limitations *125*
4.4.2 Summary *125*

Chapter 5 : Transcriptomic landscape of tumour-associated macrophage **126**

5.1 Introduction 126
5.1.1 Resources *127*
5.2 Aims 127
5.3 Results 128
5.3.1 Definitions of gene/density correlation groups *128*
5.3.2 Gene signatures between mIHC-characterised TAMs *130*
5.3.3 Characterisation of TME with in vitro-polarised macrophage gene signature *146*
5.3.4 Expression of phospho-STAT6 on TAM populations *153*
5.4 Discussion and Conclusions 157
5.4.1 Gene signatures between mIHC-characterised TAMs *157*
5.4.2 Characterisation of TME with in vitro-polarised macrophage gene signature and pSTAT6 staining *160*
5.4.3 Summary *161*

Chapter 6 : Interactions between tumour-associated macrophages and tumour-infiltrating T lymphocytes **162**

6.1 Introduction 162
6.2 Aims 163
6.3 Results 164
6.3.1 Multiplex TIL panel staining and cell phenotyping *164*
6.3.2 Density correlations between the TAMs and TILs *168*
6.3.3 Spatial TIL distribution relative to tumour cells *171*
6.3.4 Spatial relationship between TAMs and TILs *171*
6.3.5 TIL environmental gene signature and survival *178*
6.3.6 Combined TAM/TIL-associated gene signature and patient survival *181*
6.4 Discussion and Conclusions 186
6.4.1 Spatial and transcriptomic relationship between the TAMs and TILs *186*

6.4.2 Influence of TAMs and TILs on patient survival relevance 188
6.4.3 Summary 189

Chapter 7 : Evaluation of interactions between the CD68++CD163+ TAMs and CD8+ TILs 190

7.1 Introduction 190
7.2 Aims 191
7.3 Results 191
7.3.1 Identification of NOX2 as a potential functional marker for TAMs ... 191
7.3.2 Validation between multiplex TAM, TIL and NOX2 panels 197
7.3.3 Distribution of multiplex NOX2 panel-characterised cells 197
7.3.4 Refining CD68++CD163+ TAMs with NOX2 intensities 202
7.3.5 NOX2 intensity-refined TAM density correlation 204
7.3.6 Functional marker expression on TAMs and TILs in proximity 206
7.3.7 Survival relevance of individual TAM and TIL densities..... 210
7.3.8 Survival relevance of TAM and TIL combined densities 213
7.3.9 Survival relevance of the Immune/Tumour Trio density..... 219
7.4 Discussion and Conclusions..... 225
7.4.1 NOX2 as a possible functional marker for CD68++CD163+ TAMs . 225
7.4.2 NOX2+ TAMs co-localise with PD1+ TILs 226
7.4.3 NOX2 and PD1 status on TAMs and TILs improves their survival prediction..... 228
7.4.4 Proximity of immune cells to tumour cells outweighs the proximity between immune cells for survival analysis..... 229
7.4.5 Limitations 230
7.5 Summary..... 234

Chapter 8 : Investigating the Influence of macrophages on tumour invasion in a mouse model..... 235

8.1 Introduction..... 235
8.2 Aims 236
8.3 Results 236
8.3.1 Optimisation of in vivo macrophage depletion system..... 236
8.3.2 Xenograft tumour implantation 242

8.3.3 Effect of macrophage depletion on tumour progression 245
8.4 Discussion and Conclusions 259
8.4.1 Summary 263
Chapter 9 : Discussion, Future directions and Conclusions 264
9.1 Discussion 265
9.1.1 Spectrum model of macrophage activation 265
9.1.2 Multiplicity in TAM origin 271
9.1.3 Spatial and metabolic reprogramming of macrophages 272
9.1.4 Interaction of macrophages with other cells 275
9.1.5 Macrophage markers: Too similar and too different 280
9.1.6 The roles of macrophages in gastric cancer 280
9.2 Limitations 283
9.2.1 Subjective phenotyping and criterion setting 283
9.2.2 Correlation is not causation 283
9.3 Remaining challenges and future directions 285
9.4 Concluding remarks 287
Appendices 288
References 328

List of Figures

Figure 1.1.1 Worldwide gastric cancer incidence rates (2018) 1
Figure 1.1.2 Age-standardised rates in Australia from 1995-2014 2
Figure 1.1.3 Anatomical features of human stomach 3
Figure 1.1.4 Histological GC subtypes by Laurén classification 4
Figure 1.1.5 Molecular GC subtypes by TCGA 7
Figure 1.1.6 Standard treatment algorithm for gastric cancer in Japan 12
Figure 1.1.7 Immune checkpoint targets 16
Figure 1.2.1 The three Es of cancer immunoediting 21
Figure 1.2.2 Cancer-Immune cycle 22
Figure 1.3.1 Metabolic switch between M1/M2 macrophages 24
Figure 1.4.1 Polarisation spectrum of human macrophages 38
Figure 1.4.2 Tissue macrophages and their origins 39
Figure 1.4.3 The dual origins of tissue macrophages 40
Figure 1.4.4 Opposed effects of macrophages on cancer progression 41
Figure 1.4.5 Metabolic reprogramming of M1/M2 macrophages 43
Figure 1.4.6 Metabolic reprogramming of macrophages in situ 44
Figure 1.4.7 Sterile immune response 46
Figure 3.1.1 Defining regions of interest 64
Figure 3.3.1 Consort diagram of OPAL study cohort 67
Figure 3.3.2 Optimisation of multiplex TAM panel 69
Figure 3.3.3 Optimised multiplex TAM panel 70
Figure 3.3.4 Definition of tumour-nest and stromal areas 71
Figure 3.3.5 Seven predominant TAM populations in gastric cancer 72
Figure 3.3.6 Representative images of cell populations defined with the multiplex TAM panel 73
Figure 3.3.7 Distinguishing CD163+ (CD206-) M2-like TAM populations 74
Figure 3.3.8 Three-dimensional distribution of macrophage markers 74
Figure 3.3.9 Validation of cell phenotyping robustness 77
Figure 3.3.10 Pearson correlations between TAM populations 78
Figure 3.3.11 Diagram of the spatial distribution analysis 79
Figure 3.3.12 Reference and nearest cell population selection 80

Figure 3.3.13 Correlation of cell density and minimum distance 81
Figure 3.3.14 Schematic relationship of increased cell density with median distance between RC/NC 82
Figure 3.3.15 Defining direct contact distance criterion between cells 83
Figure 4.3.1 Distribution of overall macrophage across regions of interest 87
Figure 4.3.2 Distribution of TAMs between tumour areas across ROIs 88
Figure 4.3.3 Density of TAM populations of different cancer subtypes 89
Figure 4.3.4 Schematic illustration of the spatial distance analysis 90
Figure 4.3.5 Median distance of TAMs to tumour cell in regions of interest 91
Figure 4.3.6 Effective percentage of TAM populations in the Core 92
Figure 4.3.7 OS and RFS based on CD68++CD163+ TAM density 94
Figure 4.3.8 Density correlations of TAMs in the tumour Core 96
Figure 4.3.9 Principal component analyses of TAM density in the Core 96
Figure 4.3.10 PDL1-expression in GC tissue and on TAM populations 98
Figure 4.3.11 Definitions of different PDL1 intensity criteria 99
Figure 4.3.12 TAM PDL1 status defined at single-cell level 100
Figure 4.3.13 Relevance of PDL1-high TAMs between GC subtypes 102
Figure 4.3.14 TAM PDL1-intensity-stratified patient overall survival 103
Figure 4.3.15 Analysing macrophages using flow cytometry 105
Figure 4.3.16 PDL1 median intensity on CD163/CD206 TAMs 106
Figure 4.3.17 Schematic model of marker intensities between the tumour-nest and stroma 107
Figure 4.3.18 Change in PDL1 expression with distance from the TS interface 108
Figure 4.3.19 PDL1 expression on TAMs at the TS interface 109
Figure 4.3.20 Change in macrophage marker expression with distance from the TS interface 111
Figure 4.3.21 Overall survival based on TAM density (PDL1; Mean) 113
Figure 4.3.22 Overall survival based on TAM density (PDL1; Top 10%) 114
Figure 4.3.23 Overall survival based on TAM density (PDL1; Top 1%) 114
Figure 4.3.24 Cellular source of PDL1 in gastric cancer patients 117
Figure 4.3.25 Survival based on PDL1 cellular source 118
Figure 4.3.26 Combined positive scores between GC subtypes 120

Figure 4.3.27 Overall survival based on different combined positive scores .. 121
Figure 4.3.28 Tumour cell density between different GC subtypes 122
Figure 4.4.1 TAM density and intensity distribution between tumour locations 123
Figure 5.1.1 Defining different resource cohorts..... 127
Figure 5.3.1 Definitions of gene/density correlation groups..... 129
Figure 5.3.2 M1-like macrophages 131
Figure 5.3.3 CD163+ (CD206-) macrophages..... 132
Figure 5.3.4 CD206+ (CD163-) macrophages..... 133
Figure 5.3.5 Differential CD163/CD206 expression at the Margin..... 134
Figure 5.3.6 All CD163+ macrophages 136
Figure 5.3.7 All CD206+ macrophages 137
Figure 5.3.8 Inversely correlated TAMs: CD68+CD163+/CD68+CD206+..... 139
Figure 5.3.9 Inversely correlated TAMs: CD68+IRF8+/ CD68+CD163+CD206+ 140
Figure 5.3.10 Unsupervised clustering of MAUGIC-Affy cohort with CD68++CD163+ TAM gene signature..... 141
Figure 5.3.11 Patients in the MAUGIC-Affy cohort grouped using a refined CD68++CD163+ TAM signature 142
Figure 5.3.12 Validation of patient overall survival classified by the refined CD68++CD163+ TAM signature 143
Figure 5.3.13 Gene comparisons between the High-Low patient groups 144
Figure 5.3.14 Unsupervised clustering of TAM-associated environmental signatures and associated pathways..... 145
Figure 5.3.15 Interrogation of MAUGIC-Affy cohort with in vitro macrophage gene signature..... 147
Figure 5.3.16 A refined in vitro macrophage gene signature..... 148
Figure 5.3.17 Gene-gene correlations of the refined macrophage signature . 149
Figure 5.3.18 Stratification of the MAUGIC-Affy cohort with the refined in vitro macrophage signature..... 150
Figure 5.3.19 Cancer subtype between patient groups 151
Figure 5.3.20 Immune related genes between patient groups 151

Figure 5.3.21 Survival and significant clinical relevance between patient groups 152
Figure 5.3.22 Non-significant clinical relevance between patient groups 152
Figure 5.3.23 Phospho-STAT6 staining in GC specimen 154
Figure 5.3.24 pSTAT6 staining on TAM populations within the tumour Core . 155
Figure 5.3.25 pSTAT6 staining at the tertiary lymphoid structure in GC tissue 156
Figure 5.4.1 Schematic model of spatial macrophage polarisation in situ 157
Figure 6.1.1 Inverse locations of TAMs and TILs within gastric cancer 163
Figure 6.3.1 Cell populations identified with the multiplex TIL panel 165
Figure 6.3.2 Representative images of the multiplex TIL panel 166
Figure 6.3.3 CD68-IRF8+ cells located in tertiary lymphoid structures 167
Figure 6.3.4 High PDL1 expression on CD68-IRF8+ cells 168
Figure 6.3.5 Association between TAMs and TILs in the Core 169
Figure 6.3.6 Density correlation of TAMs and TILs in the tumour Core 170
Figure 6.3.7 Median distance of T cell populations to tumour cells 171
Figure 6.3.8 Median distance defined tumour microenvironment 172
Figure 6.3.9 Distribution of immune cell populations with distance defined TME 173
Figure 6.3.10 Correlation of TAMs and TILs in tumour areas 174
Figure 6.3.11 Immune cell distance to tumour cells by GC subtypes 175
Figure 6.3.12 Immune cell densities between different GC subtypes 176
Figure 6.3.13 T cell density-derived environmental signatures 179
Figure 6.3.14 Overall and relapse-free survival based on TIL density 180
Figure 6.3.15 Stratification of patients with TAM and TIL combined density and ratio 181
Figure 6.3.16 Environmental gene signatures of CD68++CD163+ TAM and CD3+CD8+ TILs 182
Figure 6.3.17 PCA of TAMs and TILs with population gene signatures 183
Figure 6.3.18 Association of immune populations to pathway categories 185
Figure 6.4.1 Tumour-immune cell distribution pattern 187
Figure 7.3.1 Inverse gene signatures between the CD68++CD163+ and CD68+IRF8+ TAM 192

Figure 7.3.2 Survival relevance NOX2 (CYBB) on GC overall survival 192
Figure 7.3.3 Subunits of the NADPH oxidase complex 193
Figure 7.3.4 Representative images of the multiplex NOX2 panel 195
Figure 7.3.5 Marker signatures and representative images of cell types identified with the multiplex NOX2 panel 196
Figure 7.3.6 Characteristics of TAMs and TILs in the tumour Core 198
Figure 7.3.7 NOX2 and PD1 expression on TAMs/ TILs between tumour-nest and stroma 199
Figure 7.3.8 Cell density correlations of the multiplex NOX2 panel 201
Figure 7.3.9 NOX2-expression refined CD68++CD163+ TAM 203
Figure 7.3.10 Density correlations of NOX2-refined CD68++CD163+ TAMs . 205
Figure 7.3.11 Proximity of NOX2-expressing TAMs and PD1-expressing TILs 207
Figure 7.3.12 Functional marker expression on TAMs and TILs in proximity . 209
Figure 7.3.13 Overall survival based on overall cell density 210
Figure 7.3.14 Overall survival based on effective density (0-10 µm) 211
Figure 7.3.15 Survival based on NOX2-refined CD68++CD163+ TAM density 213
Figure 7.3.16 Survival based on TAM / TIL combined density 214
Figure 7.3.17 Overall survival based on NOX2-refined TAM / TIL combined density 215
Figure 7.3.18 Overall survival based on TAM/TIL (RC/NC) pairing proximity. 216
Figure 7.3.19 Overall survival based on TAM/TIL (NC/RC) pairing proximity. 217
Figure 7.3.20 Possible cell distribution patterns in the shared microenvironment 218
Figure 7.3.21 Immune/Tumour trio densities with different distance thresholds between cells..... 220
Figure 7.3.22 Immune/Tumour trio percentage in each cell type..... 221
Figure 7.3.23 Correlations of trio density with percentage in each cell type ... 222
Figure 7.3.24 Overall survival based on Immune/Tumour trio density..... 224
Figure 7.4.1 Schematic role of NOX2 in macrophage polarisation 226
Figure 7.4.2 Schematic model of NOX2/PD1 expression on TAMs and TILs in proximity to each other 228

Figure 7.4.3 Putative functions of the CD68++CD163+ TAM 232
Figure 7.4.4 Marker and cytokine profile of CD8+ TILs with different PD1 positivity 233
Figure 8.1.1 Schematic graph of macrophage depletion design..... 236
Figure 8.3.1 Design of toxicity/safety study 237
Figure 8.3.2 Mouse body weight change in safety study 238
Figure 8.3.3 Flow gating strategy of mouse PBMC and depletion efficacy – safety study 239
Figure 8.3.4 Mouse liver morphology and representative images of liver macrophage – safety study 240
Figure 8.3.5 Quantification of mouse liver macrophage depletion efficacy – safety study 241
Figure 8.3.6 Baseline control of mice in experiment pre-clodronate treatment242
Figure 8.3.7 Experimental design of macrophage depletion in tumour-bearing mice..... 243
Figure 8.3.8 Definitions of gastric cancer invasion 244
Figure 8.3.9 Mouse body weight change in tumour study 246
Figure 8.3.10 Mouse PBMC depletion efficacy – tumour study 248
Figure 8.3.11 Mouse PBMC depletion efficacies of tumour and non-tumour-bearing mice..... 249
Figure 8.3.12 Gating strategy and depletion efficacy of mouse splenic macrophages..... 250
Figure 8.3.13 Depletion efficacy of splenic macrophages in tumour and non-tumour-bearing mice 251
Figure 8.3.14 Depletion efficacy of liver macrophages in tumour and non-tumour-bearing mice 252
Figure 8.3.15 Representative images of liver and lung macrophages..... 253
Figure 8.3.16 Depletion efficacy of lung macrophages in tumour and non-tumour-bearing mice 254
Figure 8.3.17 Depletion efficacy of gastric tumour-associated macrophages 255
Figure 8.3.18 Quantitation of CD206 expression on different gastric macrophage populations 256
Figure 8.3.19 Representative images of human mucosal macrophages..... 257

Figure 8.3.20 Representative images of mouse gastric tumour macrophage populations 258
Figure 8.3.21 Invasion scores and tumour- formation 259
Figure 9.1.1 Schematic spatial and transcriptomic model of TAMs in GC 266
Figure 9.1.2 Schematic spatial and transcriptomic model of the TAMs and TILs within tumour Core 277
Figure 9.1.3 Multi-function and plasticity of macrophages in gastric cancer ... 282

List of Tables

Table 1.1.1 Cancer age-standardised rates (ASR) in Australia, 2018 2
Table 1.1.2 AJCC 6th gastric cancer staging 11
Table 1.1.3 Targeted therapy trials for gastric cancer 14
Table 1.1.4 Immune checkpoint therapy trials for gastric cancer..... 18
Table 1.3.1 Clinical trials focusing on TAM depletion 28
Table 1.3.2 Clinical trials focusing on TAM repolarisation 33
Table 1.3.3 Clinical trials focusing on restoration of macrophage function 34
Table 2.2.1 Multiplex tumour-associated macrophage (TAM) panel 53
Table 2.2.2 Multiplex tumour-infiltrating T lymphocyte (TIL) panel 53
Table 2.2.3 Multiplex NOX2 panel..... 54
Table 2.2.4 Mouse multiplex TAM panel 54
Table 2.2.5 Number of images per region of interest per patient sample 55
Table 2.5.1 Mouse flow panel..... 60
Table 2.5.2 Human flow panel..... 60
Table 3.3.1 Clinical and pathological characteristics of the OPAL study cohort 68
Table 3.3.2 Median distance between cell populations of the multiplex TAM panel 79
Table 4.3.1 Multivariate analysis of clinical parameters and CD68++CD163+ TAM density 95
Table 4.3.2 Clinical parameters of TAM PDL1-intensity-stratified patients..... 103
Table 4.3.3 Clinical parameters of patients grouped with PDL1+ cells..... 115
Table 4.3.4 Clinical parameters of patients grouped with PDL1 cellular source 118
Table 4.3.5 Combined Positive Score (CPS) for PDL1-positivity..... 119
Table 4.3.6 Percentage of PDL1-positive cases in cohort defined with different combined positive scores 121
Table 6.3.1 Clinical parameters associated immune distance to tumour..... 175
Table 6.3.2 Immune cell densities between different GC subtypes 176
Table 7.3.1 Correlations of the subunits of the NADPH oxidase complex..... 193
Table 8.3.1 Number of mice between experimental groups 245
Table 8.4.1 Summary of macrophage depletion at different organs 260

List of Appendices

Appendix 1 Macrophage spatial heterogeneity in gastric cancer defined by multiplex immunohistochemistry, Nature Communications, 2019 (Main and Supplementary data) 288
Appendix 2 Identification and characterisation of TAM populations 312
Appendix 3 in vitro-polarised macrophage genes..... 314
Appendix 4 Phosphorylated-STAT6 staining in GC in different ROIs..... 316
Appendix 5 Unsupervised clustering of TAM and TIL-associated pathways .. 317
Appendix 6 Characterisation of immune gene signatures with pathway categories..... 318
Appendix 7 Overall survival with inversely correlated genes between the CD68++CD163+ and CD68+IRF8+ TAMs 320
Appendix 8 Validation of cell phenotyping between multiplex IHC panels..... 321
Appendix 9 Functional marker expressions on immune cells in proximity..... 323
Appendix 10 Density between TAM/TIL stratified patient groups 324
Appendix 11 Immune/Tumour trio density and percentage among GC subtypes 325
Appendix 12 Full timeline of in vivo macrophage depletion safety study..... 326

Chapter 1 : Literature review

1.1 Gastric cancer

1.1.1 Incidence and mortality

Gastric cancer (GC) is a significant threat to public health worldwide. With over one million new diagnoses annually, it ranked 5th in incidence and 3rd in cancer-related mortality in 2018[1]. The incidence of GC is distributed unevenly across global geographic regions. Eastern Asia, Central and Eastern Europe, and South America have the most GC cases reported each year. In contrast, GC occurs with low incidence in Africa, Northern America and Northern Europe[1, 2] (Figure 1.1.1). The Republic of Korea and Japan have the highest incidence, however, due to the implementation of screening programs for early-detection[3, 4], their survival rates are significantly higher than the other countries where GC is normally diagnosed at more advance stages.

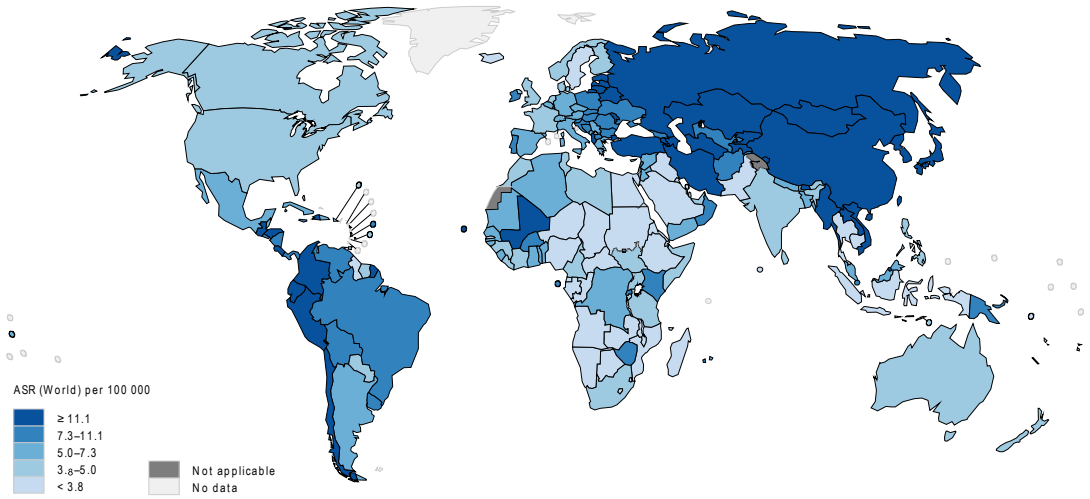


Figure 1.1.1 Worldwide gastric cancer incidence rates (2018)

ASR: Age-standardised rate. Rate including both genders and all ages. Image[1] adapted from http://globocan.iarc.fr/

In Australia, GC is relatively rare compared to other cancers[1] (Figure 1.1.1 and Table 1.1.1). However, despite a gradual decrease in incidence and mortality for the past two decades (Figure 1.1.2A, B and C), the 5-year survival (30%) only increased by 5%, demonstrating the urgent need for improved diagnostics and treatments for GC (Figure 1.1.2D)[1, 2].

Table 1.1.1 Cancer age-standardised rates (ASR) in Australia, 2018

Cancer type	Incidence		Mortality	
	ASR per 10^5	Rank	ASR per 10^5	Rank
Stomach	**4.6**	**20**	**2.3**	**14**
Lung	26.2	5	16.8	1
Melanoma of skin	33.6	4	3.2	10
Colon / rectum	36.9	3	10.9	3
Prostate	85.6	2	10	4
Breast	94.5	1	12.3	2
Data from http://globocan.iarc.fr/				

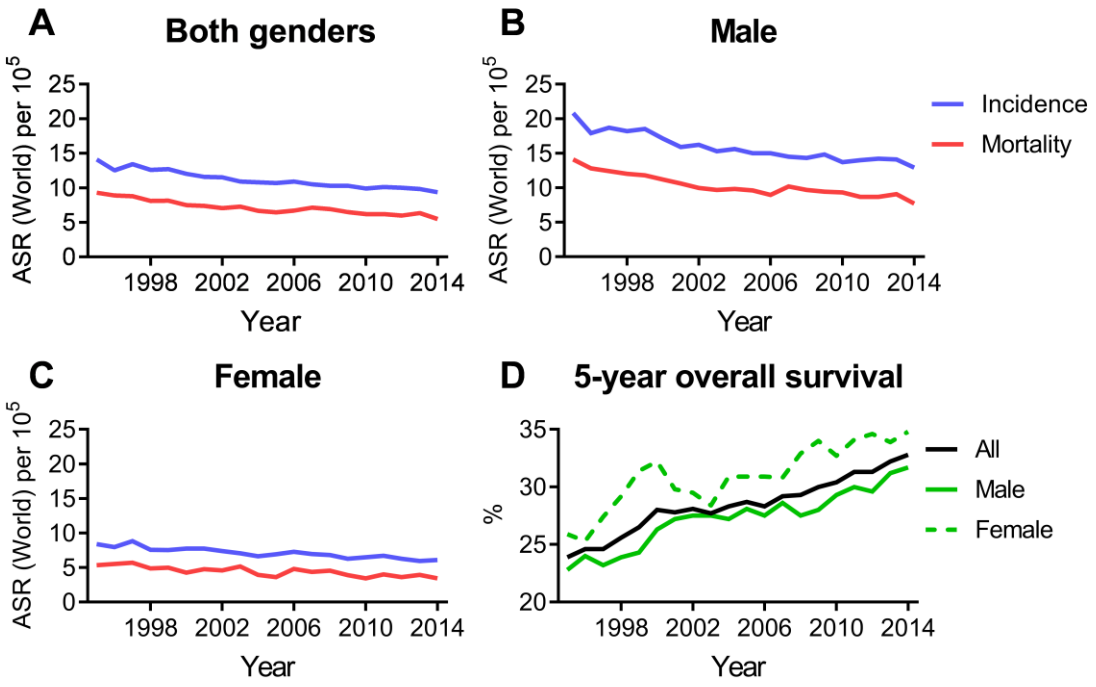


Figure 1.1.2 Age-standardised rates in Australia from 1995-2014

GC incidence and mortality of (A) both gender, (B) male and (C) female. (D) 5-year overall survival. ASR: Age-standardised rate. Rate including all ages. Data[2] from http://globocan.iarc.fr/

1.1.2 Cancer classification

1.1.2.1 Gastric cancer at anatomic regions of the stomach

The human stomach can be divided into five different regions based on their functions and anatomy; the cardia, fundus, body, antrum and pylorus (Figure 1.1.3A). The cardia is connected to the oesophagus, forming the gastro-oesophageal junction (GOJ)[5]. The cardia, fundus and produce acid and pepsin for digestion, whilst food is mixed with gastric juice and digested in the antrum and pylorus, and then emptied into the small intestine. In general, GCs located at the antrum are associated with a smaller tumour size, less invasion and metastasis, and with longer patient survival compared to tumours at the cardia, fundus and body[6].

The stomach wall is composed of four major layers; innermost mucosa, submucosa, muscularis propria and serosa (Figure 1.1.3B and C). GC generally initiates at the mucosal surface and invades outward through the serosa into the peritoneum as the disease advances[7] (further introduced in §1.1.4.1).

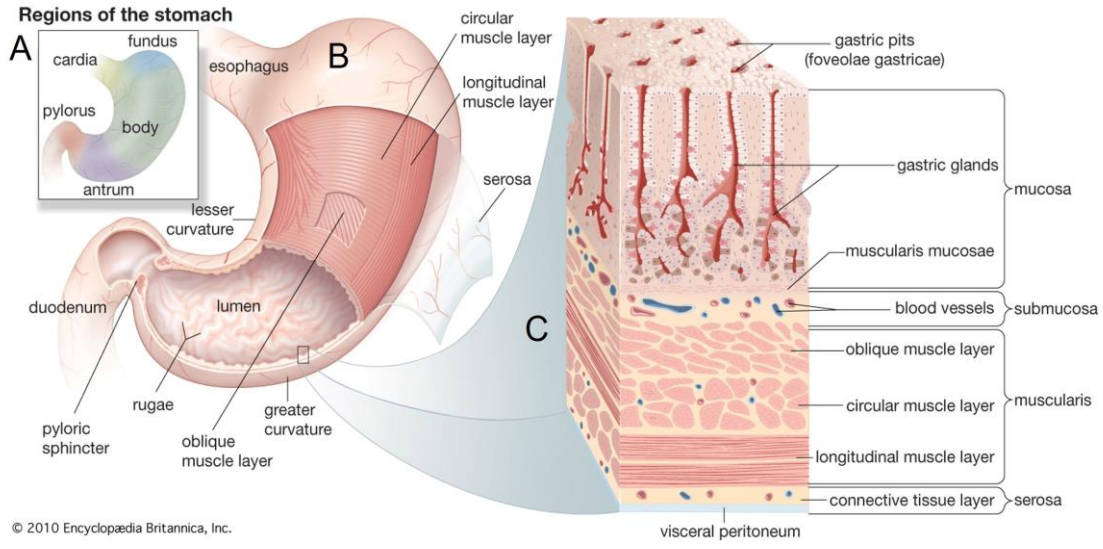


Figure 1.1.3 Anatomical features of human stomach

(A) Regions of the stomach. Cardia: part of stomach connected to the oesophagus. Fundus: upper part of the stomach adjacent to the cardia. Body (corpus): main part of the stomach. Antrum: for the mixing of food and gastric juice. Pylorus: part of the stomach connected to the small intestine. (B and C) Major layers of the stomach wall. Image modified from the Encyclopaedia Britannica: https://www.britannica.com/science/gastric-gland

1.1.2.2 Histological classification

GC is a heterogeneous disease with the majority of cases (>95%) classified as adenocarcinomas[8]. Over the past half century, Laurén's criteria[9] has been used to describe GC based on its histological appearance (Figure 1.1.4). It characterises GC tumours into intestinal (54%), diffuse (32%) and mixed subtypes (14%; mixture of intestinal and diffuse). Intestinal GC is characterised as well-differentiated and with gland-like structures, compared to the poorly differentiated and randomly scattered tumour cell morphology of the diffuse GC[9]. These GC subtypes exhibit differences in aetiology, response to therapy and survival[10, 11]. Recently, a change in trend has been observed with an increasing percentage of diffuse and decreasing intestinal types[12-14].

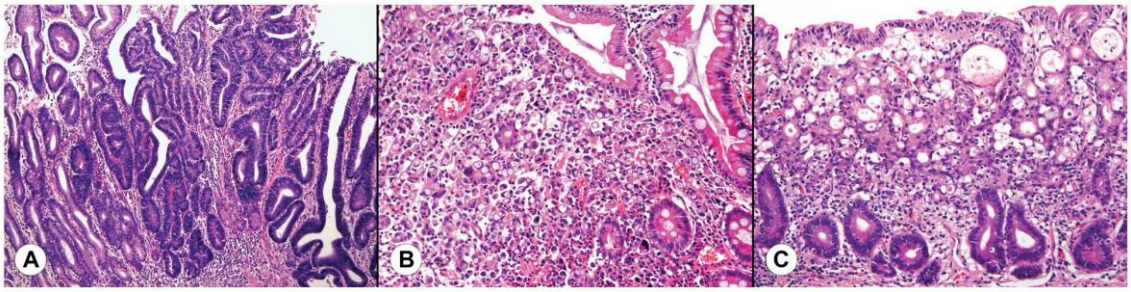


Figure 1.1.4 Histological GC subtypes by Laurén classification

Representative H&E stains of (A) Intestinal (B) Diffuse and (C) Mixed subtype. Image[15] from Chong *et al., Oncology Reports*, 2014.

Intestinal GC is thought to arise through chronic inflammation driving a step wise process[16] known as the Correa cascade[16, 17], This progresses from normal gastric mucosa, through atrophic gastritis, small intestinal metaplasia (acquired CDX2), dysplasia and ultimately GC. Intestinal GC occurs more often in elderly males and is associated with longer survival[18], *Helicobacter pylori* infection (*H. pylori*; further introduced in §1.1.3.2)[19] and expression of the small intestine marker, Caudal type homeobox 2 (CDX2)[20].

Diffuse GC more commonly affects younger females, is resistant to conventional chemotherapy[21] and has a much poorer survival[18]. Diffuse GC can be either sporadic or related to inherited pathogenic mutations in the cadherin-1

(*CDH1*) gene[22]. Germline mutations in *CDH1* give rise to the syndrome Hereditary Diffuse Gastric Cancer (HDGC) which is characterised by familial clusters of diffuse GC and lobular breast cancer[23]. HDGC accounts for 1-3% of all GC[24] with a cumulative GC incidence of 70% and 56% by 80 years of age in men and women, respectively[22]. Pathogenic *CDH1* mutations alter tumour cell biology resulting in aggressive tumour invasion[25] and lymph node metastasis[26].

Another classification system developed by the World Health Organization (WHO) classifies four major histological subtypes of GCs, including tubular, papillary, mucinous and poorly cohesive (inclusive of signet ring cell carcinoma), and rare variants[27]. The WHO tubular and papillary carcinomas correspond to the Laurén intestinal subtype, whilst the signet-ring cell and other poorly cohesive carcinomas resemble the diffuse GC[11]. Compared to Laurén's classification, the WHO classification is predominantly histologically driven, irrespective of their aetiology and clinical relevance[11]. However, it is more descriptive of all different GC subtypes, compared to only gastric adenocarcinomas (95%) in Laurén's classifications[7].

1.1.2.3 Molecular classification

A study by Boussioutas *et al.* was the first to use mRNA gene expression profiling to characterise GC (n=65) and adjacent pre-malignant lesions (n=59)[28]. In this study, intestinal GC was characterised by high expression of cell proliferation markers whereas diffuse GC exhibited a more active extracellular matrix (ECM) production and remodelling phenotype[28]. These characteristics of diffuse GC were in keeping with the epithelial-mesenchymal transition (EMT) process that the epithelial cells lose their polarity and gain migratory properties[29]. Importantly, similar molecular signatures were observed in tumour specimens irrespectively of ethnic background[28] (further introduced in §1.1.3.1), suggesting the existence of universal molecular carcinogenic events irrespective of aetiology.

In 2011, the gene expression profiles of 37 human GC cell lines were analysed and two intrinsic GC subtypes (defined as G-INT and G-DIF) were described by Tan, *et al.*[30]. Theses intrinsic GC subtypes were further validated in primary human GC tumour samples (n=521) that a concordance of 64% was observed

with the G-INT and G-DIF corresponding to Laurén's intestinal and diffuse GC. The G-INT patients exhibited an improved prognosis (hazard ratio [HR] =1.79; 95% confidence interval [CI], 1.28-2.51; p-value<0.001) and response to chemotherapy compared to G-DIF. G-INT cell lines were more sensitive to 5-fluorouracil and oxaliplatin whilst the G-DIF cell lines were more sensitive to cisplatin[30].

In 2014, the Cancer Genome Atlas (TCGA) program performed a large-scale-integrated multi-platform analysis of 295 primary gastric adenocarcinomas combining the data generated from (1) somatic copy number analysis, (2) whole-exome sequencing, (3) array-based DNA methylation profiling, (4) messenger RNA sequencing, (5) microRNA sequencing and (6) reverse-phase protein array. This comprehensive characterisation of GC revealed four distinct molecular subgroups (Figure 1.1.5): Epstein-Barr virus (EBV)-positive (9%), microsatellite instable (MSI; 22%), chromosomal instability (CIN, 50%), and genomically stable (GS, 20%) subtypes[31]. The four subtypes exhibited different molecular signatures indicating different tumour microenvironments (TME) and suggesting different possible treatment options[32].

The EBV-positive subtype was associated with a high frequency of PIK3CA mutations (80%), extreme DNA hypermethylation, overexpression of programmed death-ligand 1 (PDL1) and PDL2, and a higher degree of immune cell signalling due to chronic infection[31]. The MSI subtype was associated with elevated mutation rate caused by impaired DNA mismatch repair activity and common alterations in beta-2 microglobulin (B2M) and human leukocyte antigen B (HLA-B) genes of the major histocompatibility complex class I (MHC I) molecules[31]. The subsequently generated neo-antigens within MSI tumours could therefore enhance host immunity[33] and respond to treatment with immunotherapy inhibitors (further introduced in §1.1.5.4).

Around 78% of the GS tumours were classified as diffuse subtype and were associated with EMT and angiogenesis-related pathways[32]. CIN tumours consisted about 50% of all GC cases and approximately 50% were of intestinal GC subtype[31]. Increased tumour protein 53 (TP53) mutations, receptor tyrosine kinases (RTKs) and RAS activation genes, such as the human epidermal

growth factor receptor 2 (HER2), vascular endothelial growth factor A (VEGFA), epidermal growth factor receptor (EGFR), were commonly found in these tumours[31].

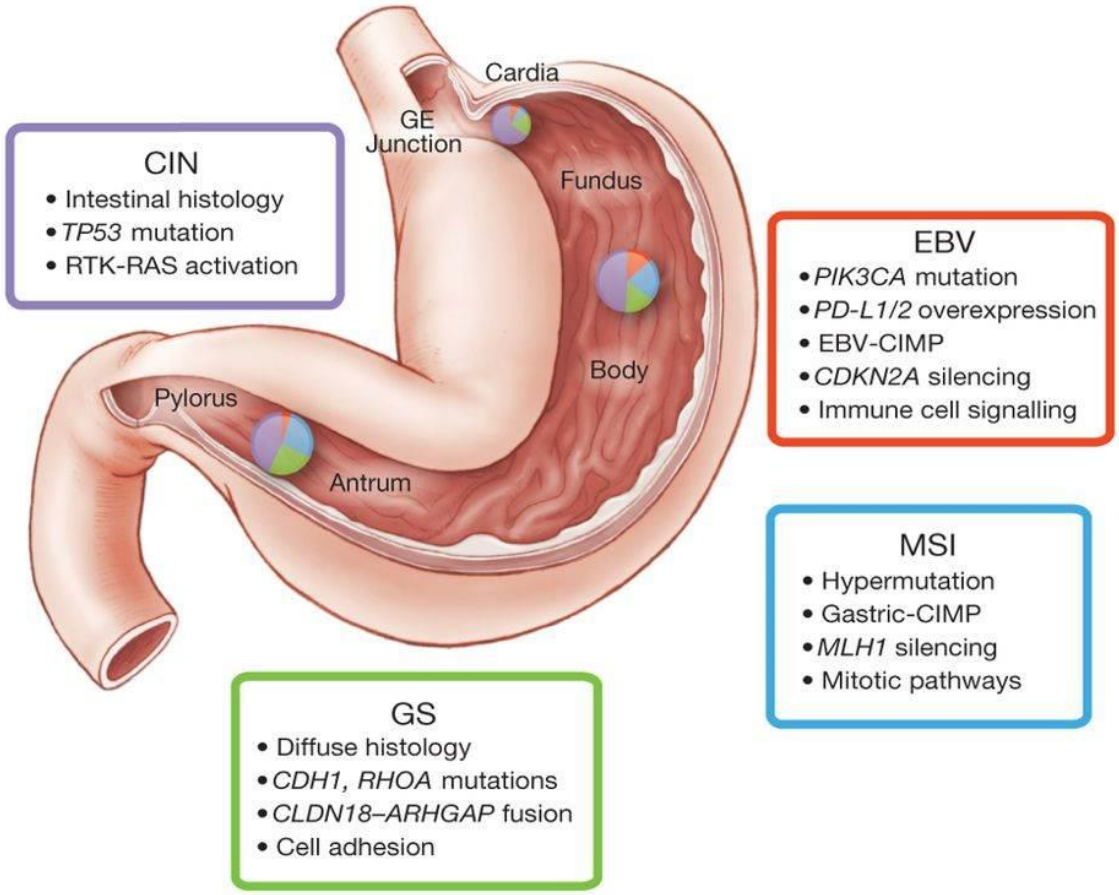


Figure 1.1.5 Molecular GC subtypes by TCGA

ARHGAP: Rho GTPase-activating protein 8. CLDN18: Claudin 18. CDH1: cadherin-1. CDKN2A: cyclin-dependent kinase Inhibitor 2A. CIMP: CpG island methylator phenotype. CIN: chromosomal instability. EBV: Epstein-Barr virus-positive. GS: genomically stable. MSI: microsatellite instability-high. MLH1: MutL homolog 1. PIK3CA: phosphatidylinositol-4, 5-bisphosphate 3-kinase catalytic subunit alpha. RAS: rat sarcoma viral oncogene. RHOA: Ras homolog family member A. RTK: receptor tyrosine kinase. Image[31] from the Cancer Genome Atlas, *Nature,* 2014.

1.1.3 Risk factors and aetiology

The development of GC is associated with a combination of factors including (i) gender, ethnicity and age, (ii) infection, and (iii) diet and lifestyle[34].

1.1.3.1 Gender, ethnicity and age

In general, males have a 2-fold higher incidence and mortality rate of GC than females[1], making it the 4th most common and 3rd most lethal cancer type for men worldwide (7th and 5th for women, respectively).

Ethnicity has been associated with the risk of GC and correlates by age, incidence, mortality rate, hereditary and genetic disorders[35-37] and tumour formation at different anatomic-subregions of a stomach[38]. In the United States, Asian, Hispanic, and African American had increased GC risk compared with the non-Hispanic white population between the ages of 60-64[39]. Non-Hispanic white people were 50% less likely to develop GC than Asians in both genders, however, had the worst 5-year survival among all races[39]. Cardia GC was associated with non-Hispanic white people[38], which may be one reason for their poorer survival[6], while non-cardia GC was found more commonly in other ethnicities and with lower social economics status[38].

1.1.3.2 Infection

Chronic inflammation caused by bacterial and viral infection is highly associated with GC[40]. Helicobacter pylori (*H. pylori*) is a bacterium that colonises the stomach and infects around 45% of the global population[41]. It has been shown to correlate with the increased incidence of non-cardia GC (89% infection rates compared to 17.8% of cardia GC), especially in the patients with early age of infection prior to cancer diagnosis[42]. Infection with *H. pylori* is thought to trigger the Correa cascade of intestinal GC development[16] (§1.1.2.2), however, only 1-2% of the *H. pylori*-infected population would eventually developed GC[43]. The global distribution patterns of *H. pylori* infection and GC incidence are dissimilar[44] which is partly due to different *H. pylori* strains[45, 46] and in combination with other factors (e.g. diet and lifestyle; §1.1.3.3). Individuals infected with cytotoxin-associated gene A-positive ($CagA^+$) *H. pylori,* but not $CagA^-$ *H. pylori*, have been shown to exhibit 5.8 fold greater risk of developing

GC compared to uninfected individuals (95% CI: 2.6-13.0)[45]. East Asian CagA$^+$ *H. pylori*, compared to Western CagA$^+$ *H. pylori*, have been shown to be more oncogenic and correlate with the elevated GC incidence in East Asian countries[47, 48].

Another source of infection is Epstein-Barr virus (EBV) that accounts for approximately 9% of global GC cases[31] (§1.1.2.3). It has similar prevalence in Asia (8.3%), Europe (9.2%), and the US (9.9%)[31, 49]. EBV infection is more common in males (11%) than females (5%) and with GC located at the cardia (14%) than the antrum (5%)[49]. EBV has been shown to alter host immunity[50] and a co-infection of EBV with *H. pylori* may increase the risk of GC[51]. However, the roles of this virus in GC development and progression remain to be determined.

1.1.3.3 Diet and lifestyle

GC is associated with high-salt[52], and salt-preserved food[53] correlating with an increased risk of GC by 2-folds compared to a low-salt diet. Consumption of salt has been shown to (i) enhance gastritis and the carcinogenic effects of N-nitroso compounds in rats[53], and (ii) persistent *H. pylori* infection at the damaged mucosa in mouse[54]. A starch/meat/fat-enriched diet was also shown to increase GC risk by 2-fold compared to a fruit, vegetable, and vitamin C-enriched diet[53, 55], with no impact of the anatomical location and the histological GC type[56]. This may be related to the modulation of enzyme functions or antioxidant activities in these foods[55].

Smoking has been shown to be a risk factor for GC in a large scale multi-epidemiological study[57]. Current cigarette smokers were identified as having higher risk of developing GC with an odds ratio (OR) of 1.25 (95% CI: 1.11-1.40) compared to never smokers. Former, and ever smokers showed an OR of 1.12 (95% CI: 0.99-1.27) and 1.20 (95% CI: 1.09-1.32), respectively, compared to people who never smoked. Similarly, alcohol drinkers were found to increase the risk of GC compared to non-drinkers (OR: 1.39, 95% CI: 1.20-1.61)[58]. Lastly, obesity (body mass index [BMI]>30) has been shown to be a risk factor for GC (OR: 1.13, 95% CI: 1.03-1.24), especially with cardia GC (OR: 1.61, 95% CI:

1.15-2.24), in men (OR: 1.27, 95% CI: 1.09-1.48) and in non-Asians (OR: 1.14, 95% CI: 1.02-1.28)[59, 60].

The influence of diet and lifestyle may outweigh the effects of genetic and hereditary factors[1, 37, 61, 62]. Decreased GC incidence in descendants of immigrants from countries with high GC incidence was observed when relocating to lower incidence countries (e.g. Asian/Japanese immigrants to the US). However, these first generations of immigrants retained their original risk profiles suggesting that the development of GC may be due to accumulations of early events in life.

1.1.4 Cancer diagnosis and staging

Diagnosis of GC primarily depends on endoscopy-collected biopsies[63]. Endoscopic ultrasonography has been shown to assist in staging through discriminating superficial (T1-T2) compared to more advance GC (T3-T4; introduced in the following section)[64] but this is not used routinely. Computed tomography (CT) and magnetic resonance imaging (MRI) are used for locally advanced GC as well as detecting liver and lymph node metastasis[63]. Fluorodeoxyglucose-positron emission tomography (FDG-PET) is useful for the detection of lymph node and bone metastasis[63, 65].

1.1.4.1 Cancer AJCC staging

After histological diagnosis, GC is characterised into different cancer stages to inform the progression of the disease and for determining appropriate treatment. The American Joint Committee on Cancer (AJCC) staging system incorporates features of cancer, including (i) the depth of tumour invasion (T), (ii) the extent of spread of tumour cells to regional lymph nodes (N) and (iii) the presence of distant metastases (M; TNM)[66, 67] (Table 1.1.2; related to Figure 1.1.3C). For this study, AJCC 6th edition is used for classifying patient samples as this was the edition in use at the time of patient enrolment (from 1999-2009)[68]. The AJCC manual is constantly updated and the most recent version is the 8th edition[69], which is more characteristic of later stages of GC compared to the 6th.

Table 1.1.2 AJCC 6th gastric cancer staging

Modified[67] from Hsu *et al., Annals of Thoracic Surgery,* 2010.

Staging		Definitions
Depth of tumour invasion (T)	TX	Primary tumour cannot be assessed.
	T0	No evidence of primary tumour.
	Tis	Carcinoma *in situ,* without invasion into lamina propria. Represent the "**early stage**" of GC.
	T1	Invasion of tumours through the inner mucosa layers (mucosa and submucosa; related to Figure 1.1.3B and C) but not yet reached the muscularis layer of the stomach (muscularis propria).
	T2	Invasion of tumours through the muscularis layers or the serosa.
	T3	Penetration of tumours through the stomach wall locally.
	T4	Invasion of tumours to nearby organs*. Represent the "**most advance stage**" of GC.
Lymph node metastasis (N)	N0	No regional lymph node metastasis
	N1	1–6 regional lymph nodes
	N2	7–15 regional lymph nodes
	N3	15 or more regional lymph nodes
Distant metastasis (M)	MX	Distant metastasis cannot be assessed
	M0	No distant metastasis
	M1	With distant metastasis
*: Organs including the spleen, liver, pancreas, kidney, small intestine, colon, and retroperitoneum etc.		

1.1.5 Treatments for gastric cancer

1.1.5.1 Endoscopic resection and surgery

Endoscopic treatment options for GC are often limited due to late onset of diagnosis[70]. However, countries with high GC incidence, such as Japan[71] and Korea[72], have established guidelines which describe for tumours that can be resected endoscopically or by surgery (Figure 1.1.6).

Currently, the only curative methods are endoscopic resection and surgical removal of early stage GC. Endoscopic resection includes endoscopic mucosal resection (EMR) and endoscopic submucosal dissection (ESD) that are applicable for mucosal localised (≤ 2 cm), non-ulcerous, and well differentiated GC cases with no nodal metastases (N0; Figure 1.1.6)[70]. EMR refers to the removal of GC lesion as well as the mucosa surrounding the lesion aided by

fluid injected into the submucosal layer underneath the tumour[73]. ESD operates with a similar approach as EMR but involves the removal of submucosa from the muscle layer. This technique provides a more precise control on the depth of tissue dissection and is capable of removing larger size of the lesions (>25mm) at the fluid-expanded submucosal space[74]. For GC with more advanced stages but with no distant metastasis (M0; Figure 1.1.6), gastrectomy and lymph node dissection can be performed.

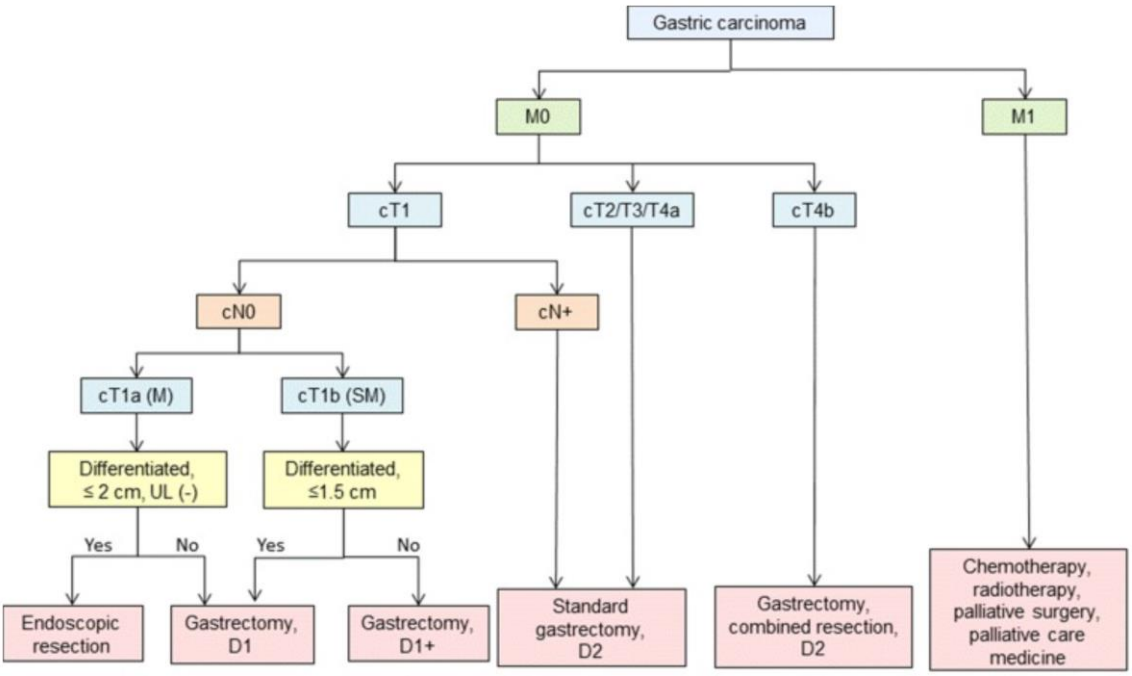


Figure 1.1.6 Standard treatment algorithm for gastric cancer in Japan

Modified[71] from Japanese Gastric Cancer, *Gastric Cancer,* 2017. M: mucosal. SM: submucosal. UL: ulcer.

1.1.5.2 Neoadjuvant and adjuvant therapy

Interventions applied prior or post primary treatment of cancer are referred as neoadjuvant or adjuvant therapies, respectively. These procedures, including chemo-, radio- and chemoradio-therapies, are aimed to either shrink a tumour before surgery, or to maximise the effectiveness of the primary treatments and to minimise the risk of cancer recurrence[75].

There is no international consensus on which method should be applied; adjuvant chemoradiotherapy (US and Australia), perioperative chemotherapy (Europe), and adjuvant chemotherapy (Japan, South Korea and Australia) are listed as standard treatments in different global regions[75]. 5-fluorouracil (5-FU)[76], cisplatin[77] and oxaliplatin[78] are common chemotherapy regimens for GC and some success has been reported for both neoadjuvant[79] and adjuvant[80] settings on progression-free and overall survival (PFS and OS, respectively) compared to surgery alone. Adjuvant and neoadjuvant radiatiotherapy[81] and chemoradiotherapies[82] may be beneficial for GC patients over surgery alone in some clinical trials. However, the efficacy and timing of these interventions requires further study given that therapeutic effectiveness has not been observed across all trials[83-85].

1.1.5.3 Targeted therapy

Targeted therapies have been introduced in patients with advanced GC based on specific characteristics of individual tumours. HER2 is overexpressed in around 18% of GC[86], is associated with intestinal and CIN GC subtypes, enhanced tumour progression and serosal invasion and metastasis[86]. Clinical trials examining the combination of trastuzumab (anti-HER2 antibody) with chemotherapy agents showed significantly improved OS compared to chemotherapy alone in advanced or cardia GC (HR: 0.74; 95% CI: 0.60-0.91; p=0.005)[87]. Therefore, it is now considered as the first line therapy of patients with HER2-positive advanced GC[70].

VEGF, a critical tumour angiogenesis pathway molecule, is elevated in the serum of GC patients[88] and is associated with poor survival[89]. GC patients receiving ramucirumab, an anti-VEGFR antibody, had improvement in OS (HR: 0.776, 95% CI: 0.60-0.99; p=0.047) compared to the placebo group[90]. Antibodies targeting HER1 (EGFR)[91], other angiogenic antibodies[92, 93] and other tumour/microenvironment targets are being examined[94] (Table 1.1.3).

Table 1.1.3 Targeted therapy trials for gastric cancer

Data from www.clinicaltrials.gov. Table[94] modified from Kiyozumi *et al. J Cancer Metastasis Treat* 2018.

Target	Trial/ registry No.	Year	Regimen	Phase	n	Median OS			Median PFS		
						Months	HR / 95%CI	p-value	Months	HR / 95%CI	p-value
HER2	ToGA	2010	FP/XP	3	594	11.1	HR: 0.74	0.0046	5.5	HR: 0.71	0.0002
			FP/XP + tratuzumab			13.8	0.60-0.91		6.7	0.59-0.85	
	LOGiC	2016	CapeOx + placebo	3	545	10.5	HR: 0.91	0.3492	5.4	HR: 0.82	0.0381
			CapeOx + lapatinib			12.2	0.73-1.12		6	0.68-1.00	
EGFR	REAL-3	2013	EOC	3	553	11.3	HR: 1.37	0.013	7.4	HR: 1.22	0.068
			EOC + panitumumab			8.8	1.07-1.76		6	0.98-1.52	
VEGF	AVAGAST	2011	XP + placebo	3	774	10.1	HR: 0.87	0.1002	5.3	HR: 0.80	0.0037
			XP + bevacizumab			12.1	0.73-1.03		6.7	0.68-0.93	
VEGFR2	REGARD	2014	Placebo	3	355	3.8	HR: 0.776	0.047	1.3	HR: 0.483	<0.0001
			Ramucirumab			5.2	0.60-1.00		2.1	0.38-0.62	
	RAINBOW	2014	Paclitaxel + placebo	3	665	7.36	HR: 0.807	0.0169	2.86	HR: 0.635	<0.0001
			Paclitaxel + ramucirmab			9.63	0.68-0.96		4.4	0.54-0.75	
VEGFR, RET, RAF	INTEGRATE	2016	Placebo	2	147	4.5	HR: 0.74	0.147	0.9	HR: 0.40	<0.001
			Regorafenib			5.3	0.51-1.08		2.6	0.28-0.59	
HGF	RILOMET-1	2017	ECX + placebo	3	609	10.7	HR: 1.34	0.003	6·0	HR: 1·26	0.016
			ECX + rilotumumab			8.8	1.10-1.63		5·6	1.04-1.51	
mTOR	GRANITE-1	2013	Placebo	3	656	4.34	HR: 0.90	0.1244	1.41	HR: 0.66	<0.0001
			Everolimus			5.39	0.75-1.08		1.68	0.56-0.78	

OS: overall survival; PFS: progression-free survival; HR: hazard ratio; CI: confidence interval; FP: 5-fluorouracil and cisplatin; XP: capecitabine and cisplatin; CapeOx: capecitabin + oxaliplatin; EOC: epirubicin + oxaliplatin + capecitabine; ECX: epirubicin + cisplatin + capecitabine

1.1.5.4 Immunotherapy for gastric cancer

In 2006, Galon *et al.* established a positive correlation between increased T cell densities with improved survival in colorectal cancer patients[95]. In 2018, Dr. James P. Allison and Dr. Tasuku Honjo were awarded the Nobel prize in Physiology or Medicine for their discoveries in immune checkpoint targets, cytotoxic T-lymphocyte-associated protein 4[96] (CTLA-4) and programmed cell death protein 1[97] (PD1). Antibodies to these targets were approved by the FDA in 2011[98] and 2014[99], respectively, and have revolutionised treatments for immunogenic cancers[100, 101].

CTLA4 (CD152) is an inhibitory T cell receptor which competes with the T cell co-stimulatory protein, CD28, when binding to CD80/CD86 on antigen-presenting cells[102] (Figure 1.1.7). The activation of CTLA4 inhibits T helper cells but enhances regulatory T cells (Treg) activities contributing to an overall immune suppressive outcome[103]. PD1 (CD279) is an inhibitory receptor expressed on multiple cell types of both lymphoid[104, 105] and myeloid[106-109] compartments. Binding of PD1 on T cells with both PDL1 (CD274) and PDL2 (CD273) on antigen-presenting cells or tumour cells[110, 111], results in a dephosphorylation of CD28 which inhibits downstream T cell activation[112]. These inhibitory signalling pathways are designed for maintaining self-homeostasis[113], and dysfunction of which leads to an increased risk of autoimmune diseases[114, 115]; however, are being deployed by tumour cells to evade immune surveillance[116].

To date, multiple immune checkpoint targets have been identified (Figure 1.1.7). Treatment approaches that aim at restoring T cell functions through removing these immune-suppressive cells in different cancer models are being examined[116-118]. Among these targets, anti-CTLA4 and anti-PD1/PDL1 are the most promising[117, 119], already finding utility in treating multiple different cancer types[120, 121] and may be useful in GC[122-124].

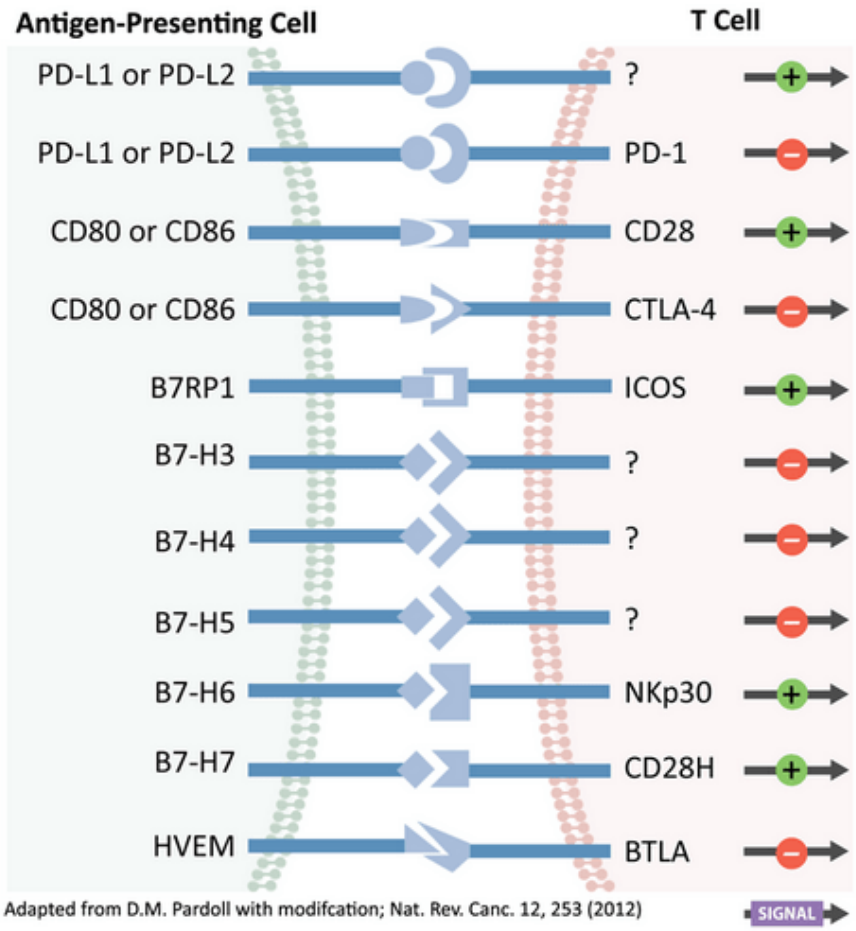


Figure 1.1.7 Immune checkpoint targets

+/-: stimulatory or inhibitory signal. CTLA-4: cytotoxic T-lymphocyte-associated protein 4. B7RP1: B7-related protein-1. BTLA: B- and T-lymphocyte attenuator. ICOS: inducible T cell co-stimulator. HVEM: Herpesvirus entry mediator. NKp30: Natural cytotoxicity triggering receptor 3, CD337. PD-1: programmed cell death protein 1. PD-L1: programmed death-ligand 1. Image from https://www.prosci-inc.com

Multiple clinical trials examining the efficacy of immunotherapy in GC are in progress, primarily targeting the PD1/PDL1 axis[125, 126] (Table 1.1.4). Patients with EBV-positive and MSI GC are assumed to be more likely to benefit from immunotherapies due to their high immune active profiles[31] (§1.1.2.3). These criteria, as well as PDL1 expression, are used for patient selection when evaluating the efficacy of immunotherapies in patients with metastatic GC[126]. In this study, the majority of the patients with EBV/MSI GC subtype (92%) or PDL1-positivity (80%) responded to checkpoint inhibitors. However, a small

proportion of patients with GS/CIN GC (9%) and PDL1-negativity (29%) were also responsive[126], suggesting a need for more precise biomarkers and a better understanding of immune function[126, 127]. In addition to cancer subtype, distinct tumour immunity signatures have been shown to distinguish between Asian and non-Asian GCs in another study[128]. Asian GC tumours had lower immune activity and higher immune suppression[128], suggesting differential immunotherapy responses may be expected.

Collectively, current evidence suggests that a better understanding of the tumour microenvironment is crucial which includes (i) defining a more accurate threshold for PDL1-positivity[129, 130], (ii) exploring how the tumour microenvironment respond to these checkpoint inhibitions[131] and (iii) identifying the source of PD1/PDL1 within the tissue[132]. PDL1 expression was reported in approximately 40% of GC cases[123], with a unevenly distributed pattern across the tumour specimen. High PDL1 has been shown to be profoundly located at the tumour/stroma interface, expressed by both tumour and immune cells[133], and highly correlated with the stromal infiltration of macrophages within the tumour microenvironment[134].

Table 1.1.4 Immune checkpoint therapy trials for gastric cancer

Data from www.clinicaltrials.gov. Table[135] updated from Kiyozumi *et al. J Cancer Metastasis Treat* 2018.

Target	Registry No	Year	Trial/ authors	Regimen	Phase	n	Median OS			Median PFS		
							Months	HR / 95%CI	p-value	Months	HR / 95%CI	p-value
PD1	NCT02267343	2016	ONO-4538-12	Placebo	3	493	4.14	HR: 0.63	<0.0001	1.45	HR: 0.60	<0.0001
				Nivolumab alone			5.32	0.50-0.78		1.61	0.49-0.75	
	NCT02335411	2020	KEYNOTE-059	Pembrolizumab (previously treated)	2	259	Ongoing. Complete responses in 2.3% of patients (6/259); Median response was 8.4 (1.6-17.3) months.					
				Pembrolizumab (previously untreated)								
				Pembrolizumab + 5-FU + cisplatin or capecitabine								
	NCT02370498	2020	KEYNOTE-061	Pembrolizumab	3	395	9.1	HR: 0.83	0.042	1.5	HR: 1.27	- -
				Paclitaxel			8.3	0.66-1.03		4.1	1.03-1.57	
	NCT02494583	2020	KEYNOTE-062	Pembrolizumab + cisplatin + 5-FU or capecitabine	3	257	12.5	HR: 0.85	0.046	6.9	HR: 0.84	0.039
				Placebo + cisplatin + 5-FU or capecitabine		250	11.1	0.70-1.03		6.4	0.70-1.02	
				Pembrolizumab alone	3	256	10.6	HR: 0.91	- -	2.0	HR: 1.66	- -
				Placebo + cisplatin + 5-FU or capecitabine		250	11.1	0.74-1.10		6.4	1.37-2.01	
PD1/ CTLA-4	NCT02872116	2022	CheckMate649	5-FU + oxaliplatin	3	2005	Ongoing. No unexpected side effects in chemotherapy arms					
				Nivolumab + 5-FU + oxaliplation								
				Nivolumab + ipilimumab								
PDL1	NCT02625623	2019	JAVELIN Gastric 300	Avelutinib	3	371	4.6	HR: 1.10	0.81	1.4	HR: 1.73	>0.99
				Paclitaxel or ilinotecan			5.0	0.90-1.40		2.7	1.40-2.20	
PDL1/ CTLA-4	NCT02340975	2019	Kelly *et al.*	Durvalumab	1/2	114	Ongoing. Combination of checkpoint inhibition has a manageable safety profile.					
				Tremelimumab								
				Durvalumab + tremelimumab								

1.2 Tumour microenvironment

The tumour microenvironment is comprised of tumour cells and stromal components[136] (e.g. immune cells, fibroblasts and endothelial cells). The interaction between these cell types and the extracellular matrix, vascular distribution, oxygen (hypoxia), nutrients and chemokines further complicates the tumour milieu[137]. These factors all contribute to the progression and metastasis of cancer[138-140], therefore, therapies that direct killing of the tumour cell as well as influencing the tumour microenvironment are being explored[141, 142]. Examples of this include targeting angiogenesis[143, 144] (Table 1.1.3) and immunotherapy[145] (Table 1.1.4). Understanding the tumour microenvironment not only informs current immune status of the disease, but could provide clues for future therapies and inform how the tumour might have been established through interaction with the immune system[146, 147].

1.2.1 The immune system

The immune system is comprised of different biological and cellular processes that protects the host from diseases and maintains body homeostasis[148]. The human immune system has two major lines of defence: the innate and the adaptive immune system. The innate immunity (e.g. the complement system, neutrophils, macrophages, dendritic cells, natural killer cells) represents the first line of defence and rapid response (within hours) to foreign substances[149]. This is an antigen-independent process compared to the antigen-dependent activation of the adaptive immunity[150] (e.g. T and B lymphocytes). Whilst the adaptive immune system generally exhibits a delay in activation, it ultimately provides a specific and prolonged clearance of insults, and a rapid and efficient immune memory response upon future re-exposures. These two lines of defence are cooperative through the antigen presentation process[151] and their cytokine/chemokine crosstalks[152]. Overactivity of immunity could results in allergy, inflammatory diseases and autoimmunity, whilst defects in either system could render the host vulnerability to infection and possibly cancer[148].

1.2.2 The three “Es” of cancer immunoediting

The relationship between the immune system and the development of cancer was first described by Dr. Rudolph Virchow over 150 years ago[153]. To date, the establishment of tumours is described as undergoing three major chronological immunoediting phases through the immune system: **Elimination**, **Equilibrium** and **Escape** (referred to as “the three Es”; Figure 1.2.1)[154-156].

This **Elimination** process is an extrinsic tumour suppressing mechanism. It starts with the collaboration of both innate and adaptive immune systems to remove newly developed malignant cells derived from DNA mutations[157], inflammation[158] or virus infection[159]. Effector molecules (e.g., IFN-α, β and γ), as well as recognising molecules (e.g., NKG2D) have been shown to be important in this process[160, 161]. If this phase is successful, no disease will progress. However, tumour cell clones which survive immune surveillance will enter the next dynamic equilibrium stage. The **Equilibrium** stage is where the growth of tumour cells is kept in control by the immune system. Opposing roles of IL-12 (anti-tumour) and IL-23 (pro-tumour) in maintaining cancer cells in this immune-mediated dormancy have been proposed[162]. The **Equilibrium** stage is thought to be the longest phases of the three Es, allowing tumour cells to increase heterogeneity and genetic instability through multiple different mechanisms[155], including MSI and CIN. If further genetic and epigenetic changes occur in these tumour cells which lead to their **Escape** from immune detection, this dynamic equilibrium will be unstable resulting in tumour outgrowth and clinically detectable disease. This stage is often characterised by a reduced immune recognition and an increased immune suppression[163].

In summary, understanding the mechanisms of cancer immunoediting provide a biological strategy for immune-based therapies. While current cancer research primarily focuses on the therapy post the **Escape** phase when clinical symptoms become more detectable, additional prevention points exist in the earlier elimination and equilibration stages. However challenges remain in providing early detections and identifying reliable biomarkers[163, 164].

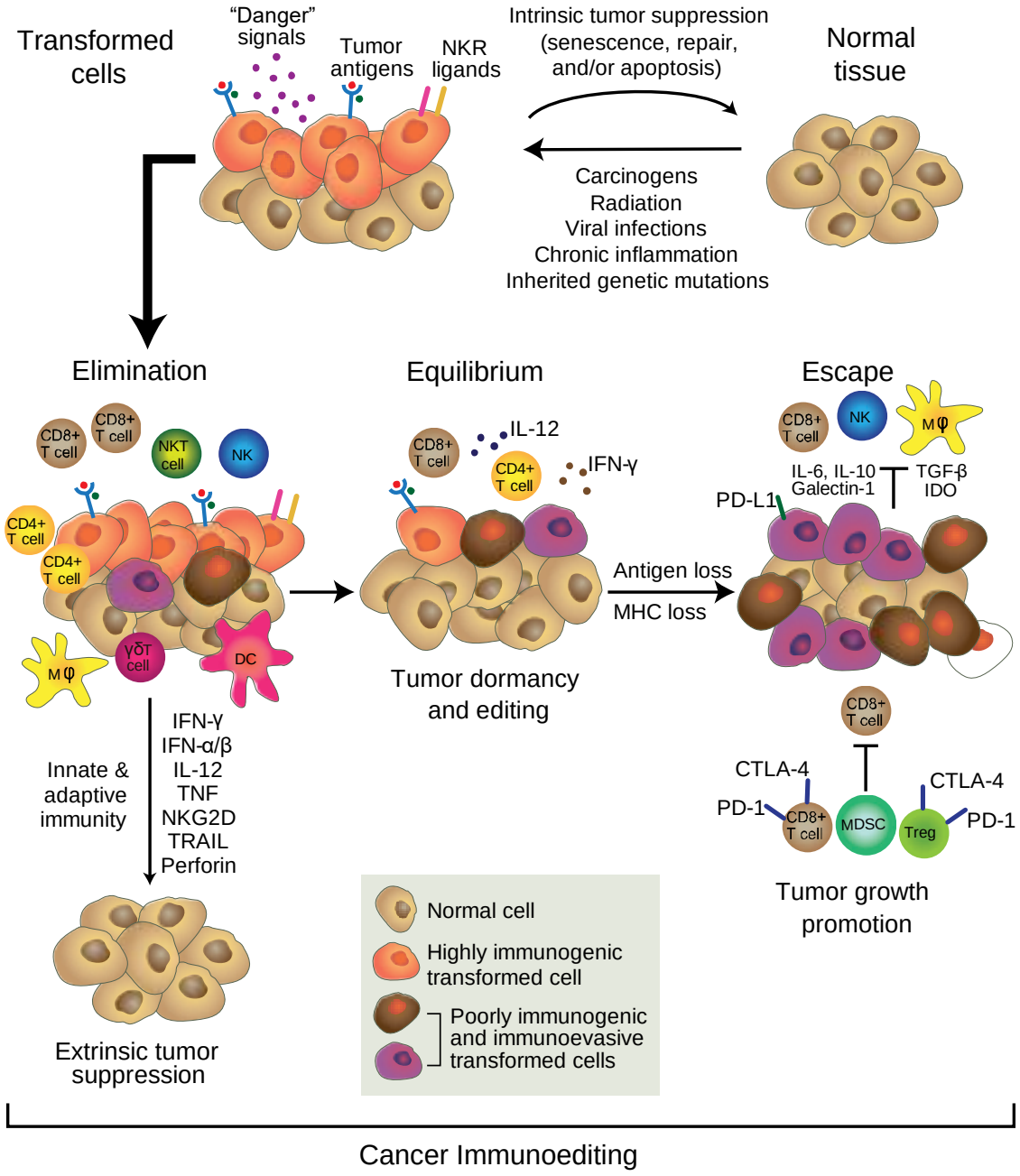


Figure 1.2.1 The three Es of cancer immunoediting

Newly derived malignant cells that have undergone carcinogenesis are detected and eliminated by the immune system in the Elimination stage. Tumour cells escaping the surveillance, will enter a dynamic Equilibrium stage. At the final Escape stage, the tumour cells not only outgrow the anti-tumour capacity of immunity but also employ specific immune cells to assist their progression. CTLA-4: cytotoxic T-lymphocyte-associated protein 4. DC: dendritic cell. IDO: indoleamine-2, 3-dioxygenase. IFN: interferon. MDSC: myeloid-derived suppressor cell. Mϕ: macrophage. NK: natural killer. NKG2D: natural killer group 2D. NKR: natural killer receptor. MHC: major histocompatibility complex. PD-1: programmed cell death protein 1. TGF: transforming growth factor. TNF: tumour-necrosis factor. TRAIL: TNF-related apoptosis-inducing ligand. Treg: regulatory T cell. Image[154] from Schreiber, *et al., Science,* 2011.

1.2.3 Cancer-Immune cycle

The Cancer-Immune cycle[165], which describes how immune cells recognise and interact between tumour cells and immune cells in the microenvironment, forms the bases of modern immune checkpoint therapy[165]. In this model, the cycle starts with neo-antigens released into the microenvironment post cancer cell death. These antigens are taken up by antigen-presenting cells (APCs; e.g. macrophages and dendritic cells) and are presented to the adaptive immune system to acquire specific recognitions of tumour cells. Activated T cells then migrate to the tumour site where they eliminate the tumour cells expressing these neo-antigens (Figure 1.2.2). However, in a tumour which has undergone immune **Escape**, this process is often disrupted or hijacked by the cancer cells at multiple different points within the cycle. Therefore, approaches that aim to restore an effective Cancer-Immune cycle are being investigated and are referred to as immune checkpoints.

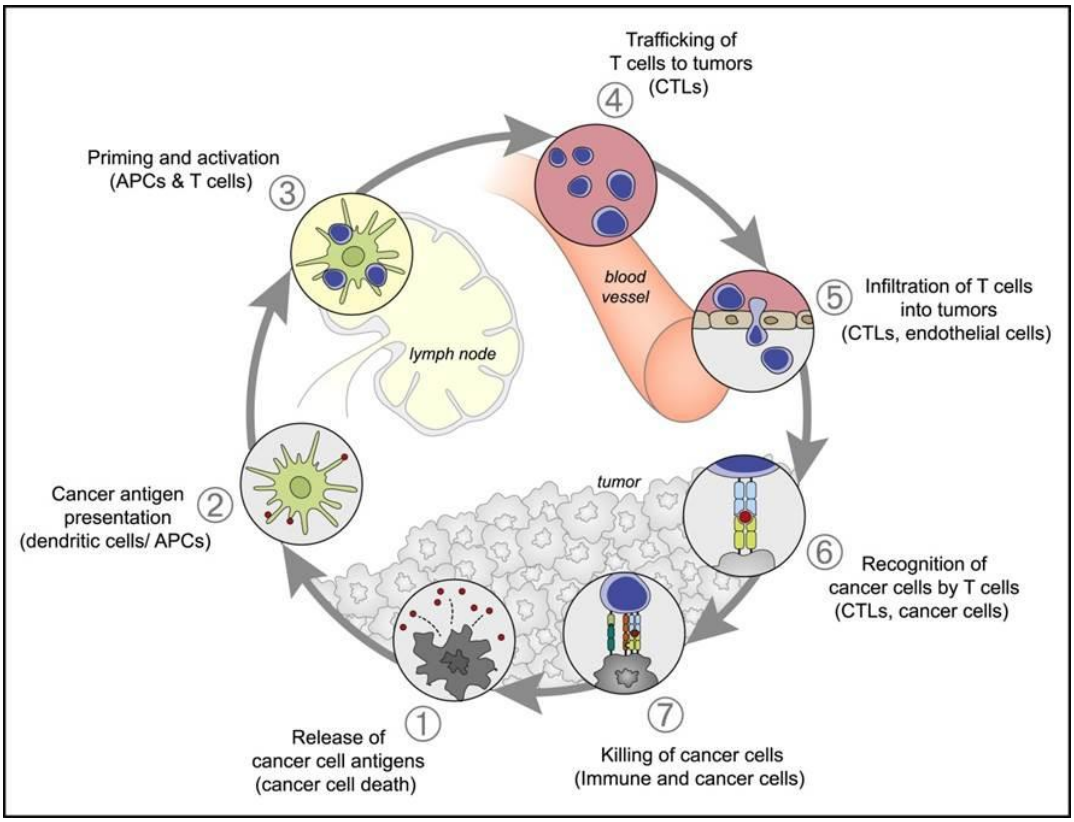


Figure 1.2.2 Cancer-Immune cycle

APC: antigen-presenting cell. CTL: cytotoxic T lymphocyte. Image[165] from Chen and Mellman, *Immunity*, 2013.

1.3 Macrophages

Macrophages, first discovered by Dr. Élie Metchnikoff in 1883, are one of the long-studied immune cells of the innate immune system[166]. They were first described as having the ability to actively clear up foreign particles and microbes, where it acquired its name as the "big (macro-) eater (-phage)"[167]. Significant inroads into understanding this cell type has been made in the past 150 years, particularly in the last two decades, and macrophages are now recognised by the hallmark of multi-functionality and plasticity[168].

1.3.1 Bipolar classification of macrophages

A commonly used method classifying macrophages is the M1/M2 bipolar system described based on the T helper 1 (Th1) / T helper 2 (Th2) cytokine inductions in mouse models[169]. This *in vitro* polarising M1/M2 system describes an intrinsic kill/repair, and the pro-/anti-inflammatory abilities of macrophages[170, 171].

The M1 phenotype, or "classically-activated" macrophages, are induced by interferon gamma (IFN-γ), lipopolysaccharide (LPS), tumour necrosis factor alpha (TNF-α), and is associated with the enhanced production of pro-inflammatory cytokines[169] (e.g. interleukin [IL]-1β, IL-6, IL-12, IFN-β), chemokines (e.g. chemokine C-C motif ligand 2 [CCL2], , chemokine C-X-C motif ligand 9 [CXCL9], CXCL10 and CXCL11[172]), as well as antigen presentation/co-stimulatory molecules (e.g. MHC I[173], II[174] and CD80/CD86[175]). M1 macrophages function through inducible nitric oxide synthase (iNOS; *NOS2*)[168] imparting a direct anti-tumour effect of nitric oxide (NO)[176] via inhibition of mitochondrial electron transport[177]. In addition, M1 macrophages function in the clearance of viruses, bacteria and pathogens[178]. Granulocyte macrophage colony-stimulating factor (GM-CSF), or CSF-2, has been shown to differentiate/polarise macrophages from blood monocytes towards the M1 pro-inflammatory status through an interferon regulatory factor 5 (IRF5) and nuclear factor kappa B (NF-κB) associated pathway[171, 179]. However, notably, these polarisation effects were more pronounced in a Th1- (C57BL/6, B10D2) compared to a Th2-type (BALB/c, DBA/2) mouse strains[180, 181].

The M2 phenotype, or “alternatively-activated” macrophages”, are polarised by IL-4 or IL-13[182]. These macrophages have high production of angiogenic and extracellular matrix (ECM) remodelling factors (e.g. VEGF, transforming growth factor beta [TGF-β], and matrix metalloproteinases [MMPs])[183] and exhibit enhanced phagocytosis capacity associated with the defence against pathogens and the clearance of apoptotic cells[169, 170]. Macrophage colony-stimulating factor (M-CSF), or CSF-1, is critical for the survival and maturation of these macrophages[171, 184]. M2 macrophages have an elevated expression of arginase-I (ARG1)[185], which competes with the iNOS over L-arginine and serves as a metabolic switch between macrophage phenotypes[186, 187] (Figure 1.3.1). Elevated L-arginine has been shown to promote the generation of a memory-like T cell phenotype, enhancing their survival capacity and anti-tumour potential[188]. Therefore, by removing L-arginine from the microenvironment, along with their tissue-remodelling characteristics, the M2 macrophages have been described as experts in resolving inflammation, promoting wound healing and suppressing active T cell activities[189].

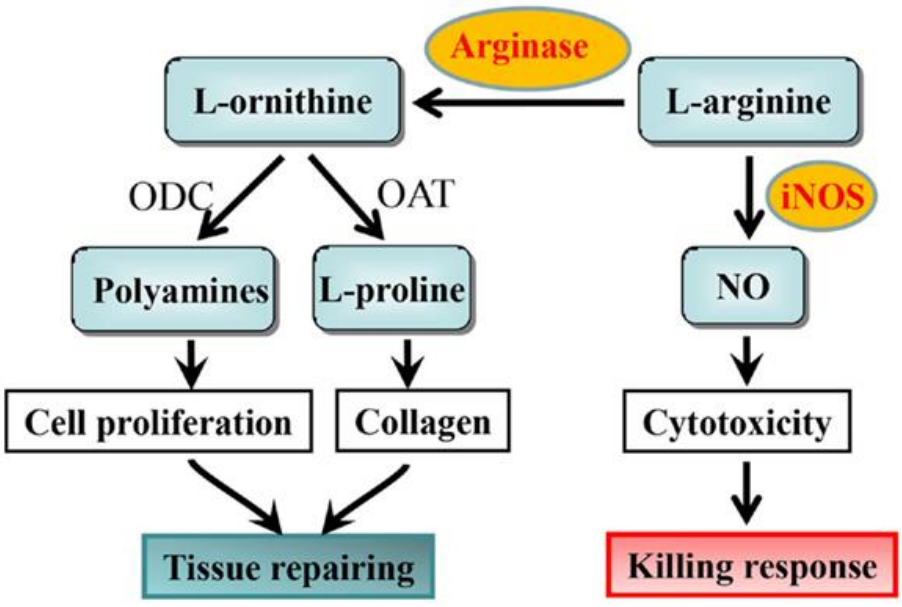


Figure 1.3.1 Metabolic switch between M1/M2 macrophages

iNOS: inducible nitric oxide synthase. NO: nitric oxide. OAT: ornithine aminotransferase. ODC: ornithine decarboxylase. Image[186] from Yang and Ming, *Frontiers in Immunology,* 2014.

1.3.2 Tumour-associated macrophages

Macrophages are one of the most abundant cell types recruited into the tumour microenvironment[190, 191], via tumour-derived M-CSF, CCL2[140] and stromal cell-derived factor 1 (SDF-1, or CXCL12)[192]. It has been shown that the degree of macrophage infiltration can be as high as 50% of the tumour mass in breast cancer[193] and between 5-30% in GC[194, 195]. These macrophages, referred as tumour-associated macrophages (TAMs) are in general, more close to the M2-like phenotype and are associated with tumour development, progression and metastasis[196, 197].

TAMs can shape the tumour microenvironment in a number of ways[198, 199]. Angiopoietin-2 release by tumour cells attracts monocytes into the microenvironment[200] which can further differentiation into TAMs. TAMs have been shown to migrate deep into tumour hypoxic regions[201] where they can stimulate angiogenesis and tumour cell proliferation through enhanced VEGFA production[202, 203] and support tumour cell migration and invasion via the release of MMP-2, MMP-7 and MMP-9[201, 204]. TAMs have also been shown to suppress T cell cytotoxic effects with their upregulated arginase-I, prostaglandin E_2 (PGE2), and TGF-β production and support the expansion of regulatory T cells[205, 206]. In addition, TAMs protect tumour cells by decreasing the efficacy of chemotherapy through an IL-6 and signal transducer and activator of transcription 3 (STAT3)-induced fashion[207-209]. Due to these properties, TAMs have been correlated with poor patient survival in multiple different cancer models[210], making them a potential target for anti-cancer therapy[211].

1.3.3 Tumour-associated macrophages in gastric cancer

In general, the biological function of TAMs in GC[212] appears similar to other cancer types. However, the clinical relevance of TAMs in GC are inconsistent between studies[211]. TAMs have been shown to be enriched in a stromal-associated EMT phenotype gene signature[213] and are associated with poor survival outcome[194, 214]. In contrast, they have also been correlated with increased tumour cell apoptosis and immune signalling which is, in turn, associated with good prognosis[215, 216].

These findings may reflect the multi-functionality of the TAMs but could also be the consequence of other factors unique to the gastrointestinal tract, such as the abundance of microbiomes[217]. As discussed earlier (§1.1.3.2), *H. pylori* is well recognised for its oncogenic role in GC[218]. *H. pylori*-activated macrophages *in vitro* were shown to exhibit elevated IL-1β, IL-12 and IL-23 compared to LPS-induced macrophages, suggesting a more pro-inflammatory phenotype[219]. Hence, TAMs in a *H. pylori*-infected GC may have been polarised into a more pro-inflammatory M1 than M2 status enabling them to prime the adaptive immune responses in the tumour[220]. However, *H. pylori* was shown to evade macrophage eradication via enhancing macrophage arginase-II (ARG2) expression[221], inducing apoptosis of infected macrophages via changing their mitochondrial-membrane permeability[222] and truncating their antigen-presentation ability[223, 224]. Moreover, the overall microbiota composition differs between paired non-malignant and GC tissues[225]. Therefore, how these microbial-induced regional changes affect overall immune response and the interaction with distant tumour regions within the stomach remains unclear.

1.3.4 Tumour-associated macrophages as therapeutic targets

Currently, evidence suggests that not only is focusing on the adaptive immune system important but targeting the myeloid components, such as macrophages, can have anti-tumour effects and may be an adjunct in increasing the efficacy of existing therapies[226]. TAMs are considered an important target for cancer therapy, due to their cancer/resistance promoting and immune suppressing properties[211]. Multiple methodologies are being developed to target TAMs based on different aspects of their function which can be summarised into three broad directions: (i) depletion, (ii) repolarisation and (iii) restoration of function.

1.3.4.1 Depletion

Clodronate-liposomes have been used to specifically deplete macrophages by targeting their phagocytic function, inducing macrophage apoptosis via disruption of the mitochondria inner membrane[227, 228]. In mouse models, systemic depletion of macrophages with clodronate-liposomes has been shown to improve therapeutic efficacy of anti-VEGF antibodies[229]. Similar systemic TAM depletion can be achieved with anti-CSF-1/CSF-1R molecules or

antibodies and a type I IFN-related suppression effect was observed in combination with cisplatin in a mouse mammary tumour model[230].

Local TAM depletion can be achieved by interfering with the CCL2/CCR2[231] and CXCL12/CXCR4[192] pathways, which are important chemoattractants for macrophages into the tumour microenvironment. CCL2/CCR2 blockade has been shown to significant decrease the CD11b+/Gr-1+ myeloid population and activate NK cells, but not T cells, in mouse primary liver tumours[232] and to reduce lung metastases in a mammary tumour model[233]. Trabectedin, a DNA binding drug that has been approved for soft tissue sarcoma treatments, was found to also selectively target TAMs by inducing cell apoptosis and reducing their CCL2 mRNA expression[234]. Small molecule inhibitors targeting CXCR4 have been shown to reduce cancer cell proliferation and invasion *in vitro* as well as to suppress tumour growth and metastasis *in vivo*[235, 236]. Multiple clinical trials targeting these macrophage attracting axes are being examined (Table 1.3.1). Some have demonstrated effective TAM reductions (NCT01444404).

While the depletion of overall macrophages or regional TAMs have shown to be promising anti-cancer approaches, these methods have so far not considered the polarisation status of these cells. A small proportion of M1-like macrophages within the M2-dominant microenvironment has been shown to be associated with improved GC survival[214, 237] and may possess anti-tumour and antigen-presenting abilities that are required for initiation of the Cancer-Immune cycle (Figure 1.2.2). More importantly, systemic depletion of macrophages can lead to a disturbance of body homeostasis[238]. To address these potential problems, ““repolarisation” and “restoration of function” TAM targeting approaches are being investigated.

Table 1.3.1 Clinical trials focusing on TAM depletion

Data from www.clinicaltrials.gov. Table[239, 240] updated from Mantovani *et al.,* 2017, and Poh and Ernst, 2018.

Target	Drug	Phase	n	Cancer type	Combined therapy	Complete (expected)	Result	Registry No.
CSF-1R inhibitor	Pexidartinib (PLX3397; Plexxikon)	1/2	24/25	Sarcoma, nerve-sheath tumours	C	2020	Ongoing	NCT02584647
		2	24	Melanoma	NA	2019	Ongoing	NCT02071940
		1	24	Prostate	R and hormone	2018	Ongoing	NCT02472275
		1/2	78	Solid tumours	Anti-PD1 ab	2018	NA	NCT02452424
		1	19	Pancreatic or colorectal	Anti-PDL1 ab	2019	Toxicity as expected.	NCT02777710
		3	120	PVNS or GCT-TS	NA	2019	Improved response rate and clinical benefits. Liver toxicity observed.	NCT02371369
		3	68	Breast	C	2020	Ongoing	NCT01596751
		1/2	81	Leukaemia, sarcoma, or neurofibroma	NA	2020	Ongoing. Drug well tolerated.	NCT02390752
		1/2	90	Acute myeloid leukaemia	NA	2018	NA	NCT01349049
		1/2	65	Glioblastoma	C and R	2019	Can be safely combined in newly diagnosed GBM.	NCT01790503
		1	74	Solid tumours	C	2018	NA	NCT01525602
		1/2	1920	Breast	C	2020	Ongoing	NCT01042379
	PLX7486 (Plexxikon)	1	59	Solid tumours / Pancreatic	NA	2018	NA	NCT01804530
	PLX3397 (Plexxikon)	1/2	132	Solid tumours	NA	2020	12/23 patients with partial response and 7 had stable disease.	NCT01004861

Ab: antibody. C: chemotherapy. R: radiotherapy. PVNS: pigmented villonodular synovitis. GCT-TS: giant cell tumours - tendon sheath.

Table 1.4.1 Clinical trials focusing on TAM depletion (Continued)

Target	Drug	Phase	n	Cancer type	Combined therapy	Complete (expected)	Result	Registry No.
Anti-CSF-1R antibody	LY3022855 (IMC-CS4; Eli Lilly)	1	178	Solid tumours	Anti-PDL1 /CTLA-4 ab	2018	NA	NCT02718911
		1	36	Breast or prostate	NA	2017	Drug well tolerated. Evidence of target engagement.	NCT02265536
		1	72	Solid tumours	NA	2018	NA	NCT01346358
	Emactuzumab (Roche)	1	310	Solid tumours	Anti-PDL1 ab	2019	Drug well tolerated.	NCT02323191
		1	217	Solid tumours	C	2018	Specific reduction of TAMs. No clinically anti-tumour activities.	NCT01494688
	AMG820 (Amgen)	1/2	116	Pancreatic, colorectal, or non-small-cell lung	Anti-PD1 ab	2019	Ongoing	NCT02713529
		1	25	Solid tumours	NA	2014	Tolerated with manageable toxicities. Limited anti-tumour activities.	NCT01444404
Anti-CCL2 antibody	CNTO888 (Centocor)	2	46	Prostate	NA	2011	NA	NCT00992186
		1	53	Solid tumours	C	2011	Drug well tolerated. No consistent changes in circulating tumour or endothelial cells.	NCT01204996
Anti-CCR2 antibody	MLN1202 (Millennium Pharmaceuticals)	2	44	Bone metastasis	NA	2012	Therapeutic effects in 14 patients.	NCT01015560
CCR2 antagonist	PF-04136309 (Pfizer)	1	44	Pancreatic	C	2016	Safe and tolerable.	NCT01413022
CXCR4 Inhibitor	Plerixafor (Mozobil; AMD3100)	1/2	30	Glioblastoma	C and R	2018	Drug well tolerated. No toxicities observed.	NCT01977677

Ab: antibody. C: chemotherapy. R: radiotherapy.

1.3.4.2 Repolarisation

The aim of this approach is to repolarise TAMs into an anti-tumour, or less pro-tumour and immune-suppressive phenotype[241]. The axis of Jumonji domain containing-3 (JMJD3), a histone 3 Lys27 (H3K27) demethylase, and IRF4, a regulator of anti-inflammatory macrophage response[242], has been shown to be an essential pathway for M2 macrophage development and its function during helminths infection, but not for the M1 responses[243]. However, this JMJD3/IRF4 axis has recently be reported to regulate the increased production of CCL17, a pro-inflammation cytokine, and the expression of MHC II in human monocyte and mouse macrophages post GM-CSF induction[244, 245]. These results suggest that targeting this pathway may be more complicated than a simple change in TAM polarisation status.

The hematopoietic cell kinase (HCK), a key regulator for the M2 macrophage development[246, 247] and extracellular matrix proteolysis[248], is another possible target. Inhibition of HCK has been shown to suppress M2 macrophage activation and to decrease STAT3-associated pathways which resulted in a reduced growth of colon xenograft tumours[249]. In addition, targeting the STAT3 and STAT6 signalling pathways has also been shown to reverse immune tolerance in human malignant glioma[250] and in mouse mammary tumour models[251], respectively.

PI3-kinase gamma (PI3Kγ) has recently been identified as a molecular switch controlling immune suppression[252]. PI3Kγ is highly-expressed in myeloid cells but not tumour cells[253, 254]. It functions through the Akt/mTOR pathway by inhibiting NF-κB while stimulating C/EBPβ[252]. Activation of PI3Kγ results in an enhanced myeloid cell trafficking, suppressed host immunity during inflammation and promoted tumour growth[255-257]. Selectively inhibiting macrophage PI3Kγ activity resulted in a restored T cell activation, reduced tumour growth and exhibited a synergistic effect with anti-PD1 antibody in a mouse model[258] and, more importantly, to be tolerable in a phase I clinical trial (NCT02637531; Table 1.3.2)[259].

CD40 is a costimulatory protein found on antigen presenting cells including macrophages[260]. Targeting CD40 with an antibody agonist activates TAMs and

induces tumour cell death in an IFN-γ-dependent manner[260] and the interaction of TAMs with CD4+ helper T cells induces macrophage-derived TNF-α and NO[261]. Sensitising TAMs with anti-CD40 treatments combined with CSF-1R inhibitors has been shown to rapidly repolarise the TAMs toward a pro-inflammatory phenotype which reinvigorated effective T cell functions even in checkpoint-insensitive tumours[262].

1.3.4.3 Restoration of macrophage function

Macrophages are known for their phagocytic ability[263] and are antigen-presenting cells[264, 265] that bridge the innate and adaptive immune systems. Therefore, approaches that aim to restore their phagocytic function are being explored.

The CD47/signal regulatory protein alpha (SIRP-α) axis is one of the most promising targets[266]. CD47 is an integrin-associated protein that plays an important role in cell self-recognition[267] and has been shown to be positively regulated by the oncogene *MYC*[268]. When it interacts with its ligand, SIRP-α, which is expressed highly on myeloid-lineage hematopoietic cells (e.g. macrophages and dendritic cells), a signal will be sent to downregulate their phagocytic ability[269, 270]. Numerous cancer types[271-274] have been shown to hijack this mechanism by upregulating their CD47 expression as a “don’t eat me” signal[275] to evade clearance by phagocytes[276].

Significant tumour reduction was observed in a mouse model post CD47/SIRP-α inhibition alone, and in combination with doxorubicin[277] and anti-PDL1 antibody[278]. In GC, CD47 expression correlates with tumour clones with higher proliferation rate and colony formation ability[279, 280], suggesting that CD47-targeting may be an attractive therapeutic approach. A phase I clinical trial of an anti-CD47 monoclonal antibody demonstrated antitumor effects in patients with advanced solid tumours[281] (NCT02216409; Table 1.3.3). The CD24/Siglec10 axis was recently identified exhibiting similar tumour/macrophage interactions as the CD47/SIRP-α axis. Blockade of this pathway robustly augmented the phagocytosis of all CD24-expressing human tumour cells *in vitro* and was synergistic with anti-CD47 therapy[282].

The therapeutic efficacy of restoration of TAM phagocytic function may be further improved by combining these approaches with other treatment agents, such as chemo-[283] and radiotherapies[284, 285], which are known to increase tumour cell death. These combinations increase the possibility of the adaptive immunity being primed by the repolarised-TAMs to achieve tumour elimination[275, 286]. However, antigen presentation seems to be more reliant on cells dying through necrosis rather than apoptosis[287, 288], suggesting diverse effects may be expected depending on the type of cell death induced by adjuvant therapies.

Other studies which utilise macrophages functions as drug carriers[289] are still in experimental state. These studies aim to overcome the limits in targeted drug delivery to solid tumours by combining macrophage phagocytic ability with their tumour-homing characteristics[290-292].

Table 1.3.2 Clinical trials focusing on TAM repolarisation

Data from www.clinicaltrials.gov. Table[239, 240] updated from Mantovani *et al.,* 2017, and Poh and Ernst, 2018.

Target	Drug	Phase	n	Cancer type	Combined therapy	Completed (expected)	Result	Registry No.
Agonistic anti-CD40 antibody	CP-870,893 (Pfizer; UPenn)	1	34	Solid tumours	C	2009	Safe and some biological and clinical responses were observed.	NCT00607048
		1	10	Pancreas	C	2013	NA	NCT01456585
	RO7009789 (Roche)	1	94	Solid tumours	Anti-ANG-2-VEGF Ab	2020	Ongoing	NCT02665416
		1	10	Pancreas	Chemo	2018	NA	NCT02588443
CD40 agonist antibody	Tremelimumab and CP-870 (CP-893; AstraZeneca)	1/2	32	Metastatic melanoma	Anti-CTLA-4 antibody	2016	2 patients had complete responses and 4 had partial responses.	NCT01103635
Vaccine	GM-CD40L vaccine	1/2	73	Lung	CCL21 cytokine	2019	No significant between vaccine immunogenicity and outcomes.	NCT01433172
STAT3 inhibitor	AZD9150 (AstraZeneca)	1	58	Metastatic hepatocellular carcinoma	NA	2015	Decreased tumourigenicity and increased chemo-sensitivity.	NCT01839604

Ab: antibody. C: chemotherapy.

Table 1.3.3 Clinical trials focusing on restoration of macrophage function

Data from www.clinicaltrials.gov. Table[239, 240] updated from Mantovani *et al.,* 2017, and Poh and Ernst, 2018.

Target	Drug	Phase	n	Cancer type	Combined therapy	Completed (expected)	Result	Registry No.
Anti-CD47 antibody	Hu5F9-G4 (Stanford U)	1	20	Myeloid leukaemia	NA	2019	Well tolerated and some biologic activity was observed.	NCT02678338
	CC-90002 (Celgene)	1	28	Myeloid leukaemia or myelodysplastic syndrome	NA	2018	NA	NCT02641002
		1	60	Advanced-stage solid or haematological malignancies	NA	2020	Ongoing	NCT02367196
SIRPα-Fc fusion protein	TTI-621 (Trillium)	1	260	Haematological malignancies / Solid tumours	Rituximab Nivolumab	2021	Ongoing	NCT02663518
Ab: antibody. C: chemotherapy.								

1.3.4.4 The role of TAMs in current checkpoint inhibition

Checkpoint inhibitors predominantly aim at the activation of adaptive immunity, but they also affect the macrophage population due to their intrinsic expression of checkpoint targets or corresponding ligands[293, 294].

The inhibition of PDL1 aims to block suppressive signalling between TAMs and tumour cells to T cells[132]. Enhanced macrophage proliferation was observed in mice and humans post anti-PDL1 antibody treatment, accompanied by elevated CD80 and MHC II expressions[295]. Similar effects were found with soluble CD80 and PD1 which drove macrophages toward a more pro-inflammatory phenotype[295]. Increased PD1 expression has been reported on *in vitro* polarised macrophages with LPS in an NF-κB-dependent manner[296] and with tumour-derived exosomes[297]. Macrophages highly expressing PD1 exhibit downregulated IL-12 and phosphorylated STAT1 expression in patients with chronic hepatitis C virus infection[298]. $PD1^+$ TAMs have been shown to possess limited phagocytic ability in human and mouse[107] and are associated with progression of GC[297]. Importantly, a combination of PD1/PDL1 blockade with an anti-CD47 antibody showed a synergistic therapeutic effect in an immune incompetent BALB/c $Rag2^{-/-}\gamma c^{-/-}$ mouse model, demonstrating the anti-tumour capacity of TAMs in the absence of the adaptive immune system[107]. Myeloid-specific ablation of PD1 was found to be more effective in decreasing tumour growth compared to T cell-specific PD1 ablation in a mouse melanoma model[299]. This anti-tumour immunity functioned through the induction of effector memory T cells and was facilitated by the inflammatory TAMs and dendritic cells with potential enhanced antigen-presenting properties[299].

More importantly, phenotypic remodelling of TAMs was observed in several studies with administration of checkpoint inhibition and was associated with the transition of the tumour microenvironment from immune cold to hot[300-304]. Significantly increased $iNOS^+$ and diminished $CCR2^+/CD206^+$ in myeloid cells and reduced regulatory T cells was observed in a mouse sarcoma model treated with anti-CTLA-4 plus anti-PD1 therapy[301]. TAMs have been identified as the primary source of CXCL9 and CXCL10 (immune cell chemoattractants) in the tumour microenvironment and are critical for anti-tumour immune

responses during checkpoint blockade[302, 303]. Dysfunctional CXCL9 production in TAMs through tumour-derived leukaemia inhibitory factor (LIF) was identified as a possible mechanism for cancer cells to impede lymphocytes infiltration[304].

In summary, these findings suggest that TAMs play important roles in modern checkpoint therapies. Repolarisation/activation of TAMs form an enhanced positive feedback within the Cancer-Immune cycle (§1.2.3), and are an attractive target for tumour eradication through harnessing host immunity.

1.4 Macrophage diversity and heterogeneity

Macrophages are a diverse population of cells[189] and their heterogeneity is well recognised[305]. Whilst the bipolar M1/M2 model nicely characterises the two macrophage phenotypes polarised *in vitro*, it was not completely reflective of the macrophage populations *in vivo*[171]. With the advance of single-cell RNA sequencing[306] and fate-mapping techniques, their multi-dimensional heterogeneity was revealed (i) in a spectrum model of phenotype/activation[307], (ii) with a finding of distinct cellular origins in organs[308], (iii) with spatial/metabolic immune reprogramming *in situ*[309], and (iv) the diversity between *in vitro-polarised*, mouse and human macrophages[310, 311].

1.4.1 Spectrum model of macrophage activation

Due to the complexity of phenotype/activation status observed in macrophage populations that extended beyond the simplified M1/M2 system, subpopulations within the M2 phenotype have been proposed including M2a, M2b, M2c and M2d[312] to specify different functional populations (Figure 1.4.1). M2a macrophages resemble the alternatively-activated M2 macrophages which are polarised with IL-4 and IL-13. These macrophages release high level of IL-10, TGF-β and are associated with type II inflammation, allergy and the killing of parasites[313]. M2c macrophages are polarised with IL-10, TGF-β and glucocorticoids, and have a similar cytokine release profile as the M2a macrophages but with an enhanced capacity in tissue remodelling, cellular matrix deposition[313, 314] and phagocytosis[315]. The M2b population is activated by immune complexes (ICs), IL-1 and LPS which results in a similar characteristic as the M1 macrophages in IL-1β, IL-6 and NO production as well as CD86 expression[316, 317]. However, these macrophages also exhibit an increase in IL-10 expression and protect mice from LPS toxicity[318], which put them within the broad M2 macrophage family. The M2d population is been described as a switch from a pro-inflammatory M1 to an angiogenic M2 phenotype, in an IL-6 and adenosine-dependent manner[319] (Figure 1.4.1). While the introduction of these *in vitro*-polarised macrophage subpopulations certainly assisted in the understanding of their heterogeneity, these subpopulations still fall short in precisely explaining the vast range of macrophage polarisation within tissues[183].

In light of this, Xue *et al.* reported a spectrum model of *in vitro* macrophage activation/polarisation[320] in 2014. Using non-supervised clustering methods to examine the transcriptomic patterns of human macrophages treated with 28 combinations of stimuli, their results revealed a multi-dimensional model consisted of 9 unique clusters of transcriptional signatures. In 2017, using cytometry by time-of-flight (CyTOF), TAMs with substantial complicated compositions were described in human clear cell renal cell carcinoma[321] and early lung adenocarcinoma[322]. These data suggest that the heterogeneity of TAMs not only existed within a terminal-differentiated macrophage population, but also could undergo dynamic *in situ* polarisation in different tumour microenvironments, as well as diverse cell origins (blood monocyte-derived or tissue-resident; further introduced in the following section). Using single-cell RNA sequencing techniques, rare macrophage populations have been identified in atherosclerosis[323], cancers[321, 322, 324, 325], and normal tissues[326, 327].

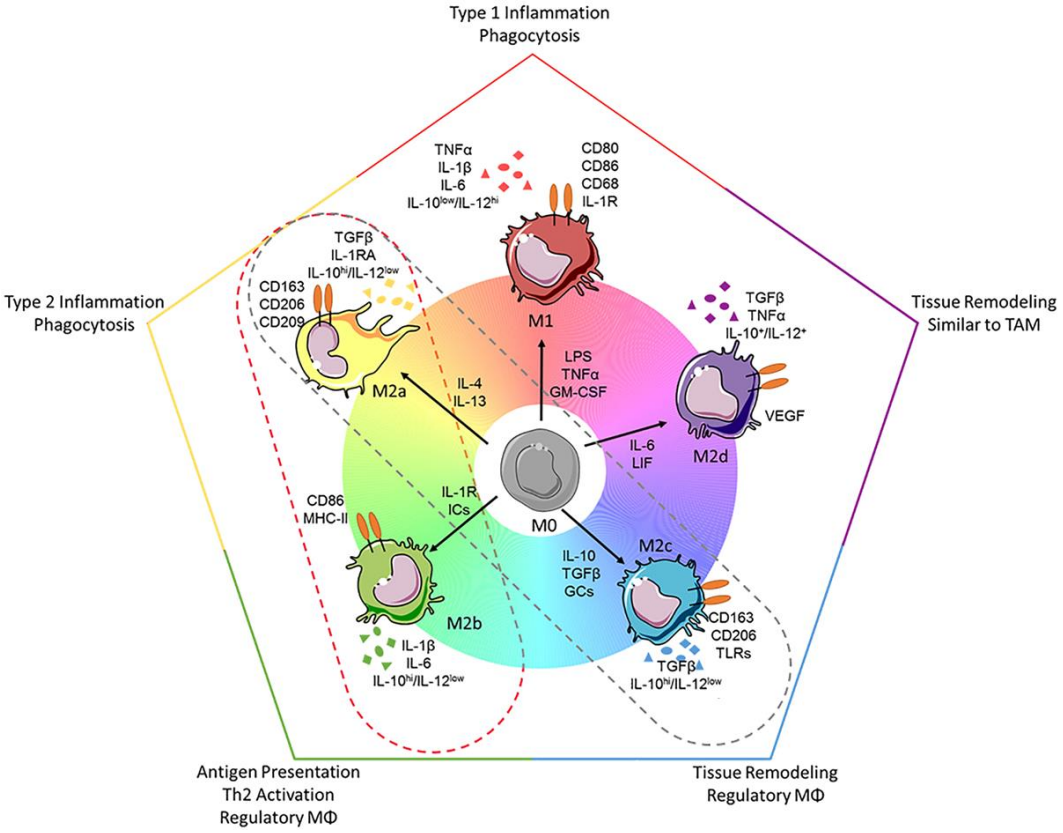


Figure 1.4.1 Polarisation spectrum of human macrophages

GCs: glucocorticoids. IC: immune complex. LIF: leukaemia inhibitory factor. Mϕ: macrophage. TAM: tumour-associated macrophage. VEGF: vascular endothelial growth factor. Modified[312] from Schliefsteiner *et al., Frontiers in Immunology,* 2017.

1.4.2 Tissue macrophages of dual origins

Macrophages are one of the gate-keepers of tissue homeostasis and are found in organs throughout the body[328] (Figure 1.4.2). Distinct tissue-resident macrophages, including microglia (brain), Kupffer cells (liver), alveolar macrophages (lung), red pulp macrophages (spleen), intestine macrophages, Langerhans cells (skin), and heart macrophages have been identified[328]. These macrophages are important in the maintenance of our neuronetworks[329], clearance of cellular waste disposals[330], protection against microbial debris and bacterial endotoxins[331], regeneration of red blood cells[332], and the facilitation of electrical conduction in the heart[333]. For a long while, these tissue-resident macrophages were thought to be replenished solely by blood monocytes[334, 335]. It was not until recently that using cell fate-mapping technology, the "dual origins" of tissue macrophages' embryonic precursors were identified[336, 337] (Figure 1.4.2 and Figure 1.4.3).

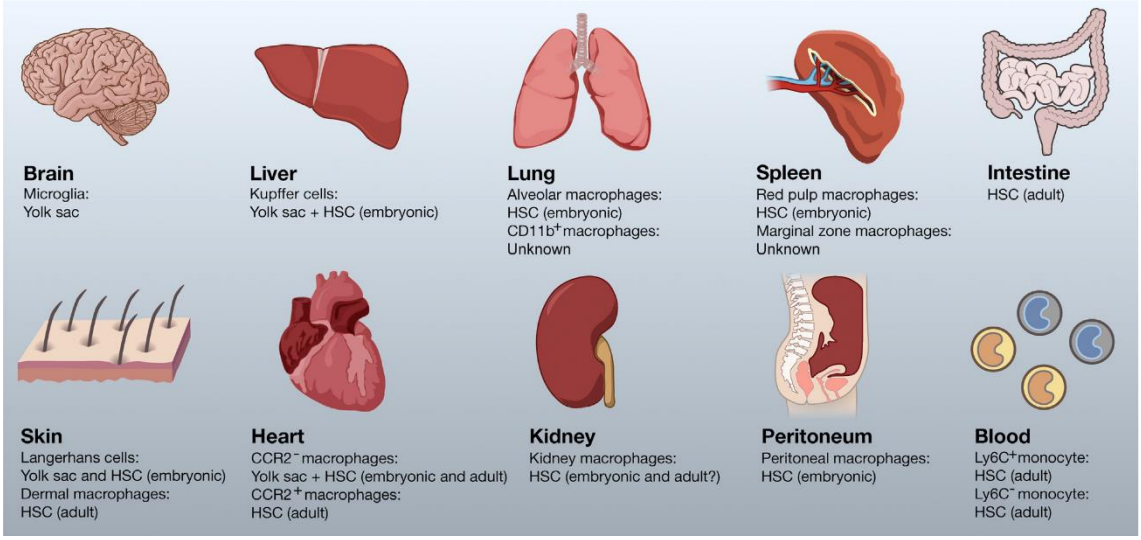


Figure 1.4.2 Tissue macrophages and their origins

HSC: hematopoietic stem cells. Modified[338] from Epelman *et al., Immunity*, 2014.

During mouse embryonic development, haematopoiesis takes place in the yolk sac where the first population of macrophage precursors appear (Figure 1.4.3). These macrophage precursors reside at the head region and then gradually migrate throughout the body via blood circulation. A second population of

precursors emerge days later within the foetal liver in a Myb-dependent manner[336], and translocate and remain in the bone-marrow throughout life. The microglia originates primarily from the yolk sac whereas the majority of other tissue macrophages are from the foetal liver[337]. Importantly, microglia and Kupffer cells have been shown to self-renew in adulthood whereas other tissue macrophages, such as intestinal[339], skin[340] and heart macrophages, are replenished constantly by blood monocytes[341]. There are no stomach-specific macrophage populations identified to-date: the muscularis propria macrophages have been shown to assist in the emptying of the stomach, yet their origin and turnover in the adult tissue have not been well addressed[342, 343].

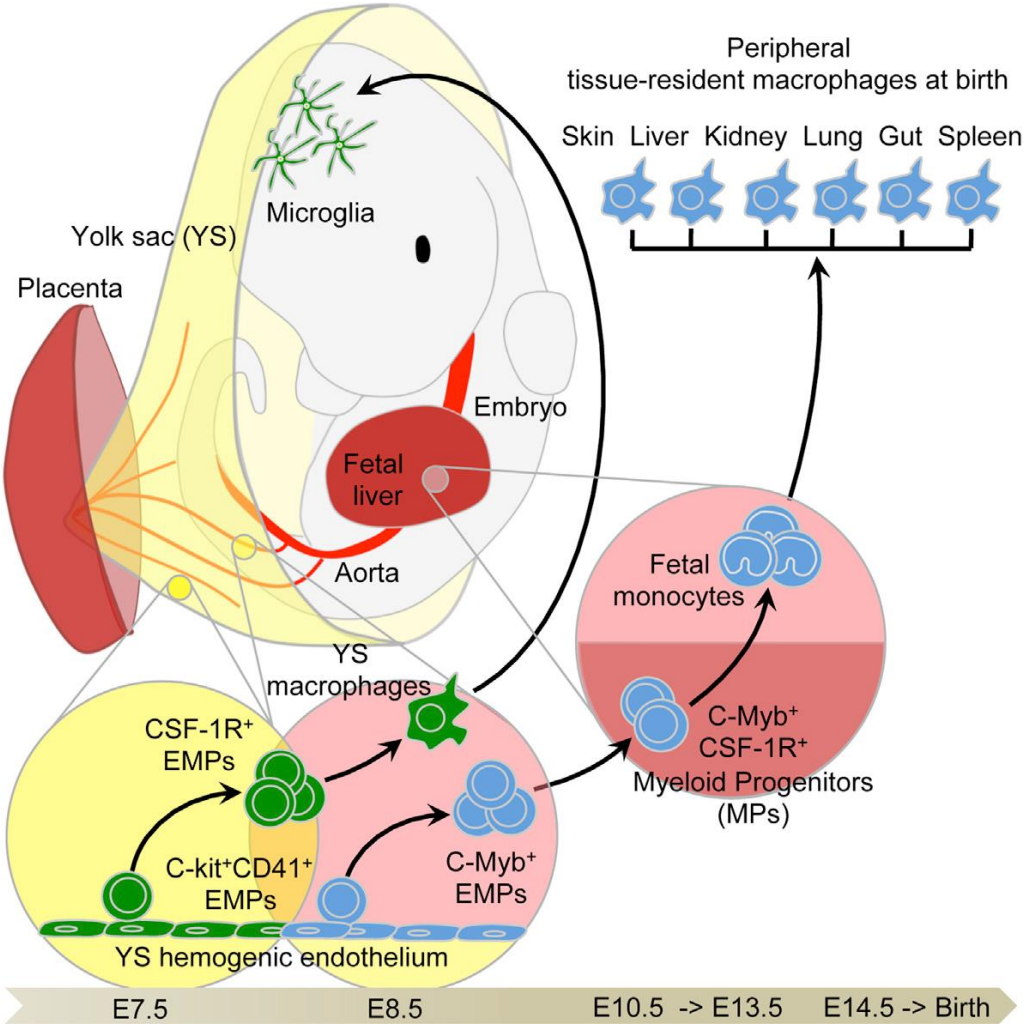


Figure 1.4.3 The dual origins of tissue macrophages

X axis: days in embryonic development. EMPs: erythro-myeloid progenitors. Graphic abstract[337] from Hoeffel *et al., Immunity,* 2015.

In cancers, the tumour microenvironment has been shown to nurture different TAM populations with distinct roles in cancer development[344, 345] (Figure 1.4.4). In a mouse pancreatic ductal adenocarcinoma model, TAMs of an embryonic origin were found to proliferate *in situ* and to exhibit a pro-fibrotic transcriptional profile indicating their roles in tissue remodelling and extracellular matrix formation[346]. In contrast, TAMs of hematopoietic stem cell (HSC) origin showed a higher expression in MHC molecules, IL-12, IFN-β and IFN-γ, enhanced antigen uptake and antigen presenting abilities as well as a lower PDL1 intensity, suggesting a more immune-active phenotype. However, these monocyte-derived TAMs also expressed a higher level of IL-4 and lower CD40, indicating some immune suppressive properties suggestive of their spectrum of activation status[346]. Similarly, this difference in functionality between myeloid cells of different origins was observed in mouse lung cancer. Monocytes and monocyte-derived TAMs were multi-functional whilst the tissue-resident TAMs were mainly tumour promoting[347], indicating distinct functionalities between TAMs of different origins.

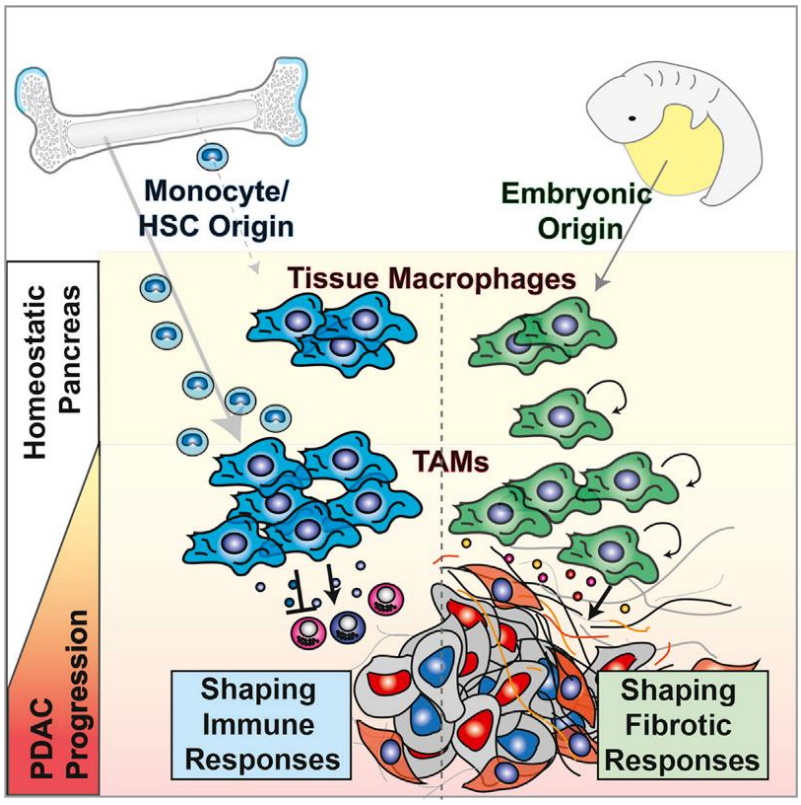


Figure 1.4.4 Opposed effects of macrophages on cancer progression

HSC: hematopoietic stem cell. Graphic abstract[346] from Zhu *et al., Immunity*, 2017.

When comparing TAMs in the human lung adenocarcinoma microenvironment to macrophages in normal lung tissue[322], TAMs expressed high levels of CD14, CD64, CD11c, IL-6 and a lower CD86, suggesting an enhanced inflammatory but immunosuppressive phenotype. However, how these two populations existed within the tumour was not examined in the study. Lastly, locational difference of macrophages of different origins was observed in addition to their functional diversities. Foetal-derived mammary gland macrophages were characterised with active scavenging ability and displayed preferential peri-ductal and perivascular localisation[348]. Microglia-related TAMs were found at the invasive front of mouse glioma while the blood-monocyte-derived TAMs resided at the intra-tumoural perivascular regions[324].

In summary, macrophages with different origins within the tumour microenvironment have been shown to exhibit distinct roles in the progression of cancers and contribute to another layer of complexity to their heterogeneity. Accumulating evidence has shown that understanding this diversity could assist in revealing their roles in cancer progression and in developing more precise therapeutic strategies[344].

1.4.3 Spatial and metabolic reprogramming of macrophages

The phenotype and activation state of macrophages are fine-tuned by metabolites present in the tumour microenvironment[309]. Multiple metabolic polarisation niches have been identified for macrophages[349] in addition to the iNOS/ARG-1 axis (Figure 1.3.1).

During the *in vitro* polarisation of M2 macrophages with IL-4, fatty acid-related mitochondrial oxidative phosphorylation (OXPHOS) is required for their energy consumption[350] through CD36 and STAT6-related pathways[350, 351]. Glutamine is largely consumed by M2 macrophages for the production of functional molecules[352] and the inhibition of glutamine-synthetase skews M2-polarised macrophages toward the M1 phenotype[353]. Cancer-derived succinate has also been shown to polarise M2 macrophage which facilitates tumour metastasis[354].

M1 macrophages switch their source of energy to glycolysis[355] for rapid response to signals and killing[349]. This process has been shown to be governed

by hypoxia-inducible factor 1 alpha[356] (HIF-1α) and is required for the overexpression of glucose transporter 1 (GLUT1), PKM2[357] and lactate dehydrogenase alpha (LDHA) which results in a lactate-associated environment and decreased pH[358] (Figure 1.4.5). NO produced from active M1 macrophage has been reported to impair their mitochondrial functions as to prevent their repolarisation to the M2 phenotype[359]. However, in the late stage of M1 macrophage activation, increased lactate was found to increase histone acetylation and promote the expression of M2-associated genes[360, 361].

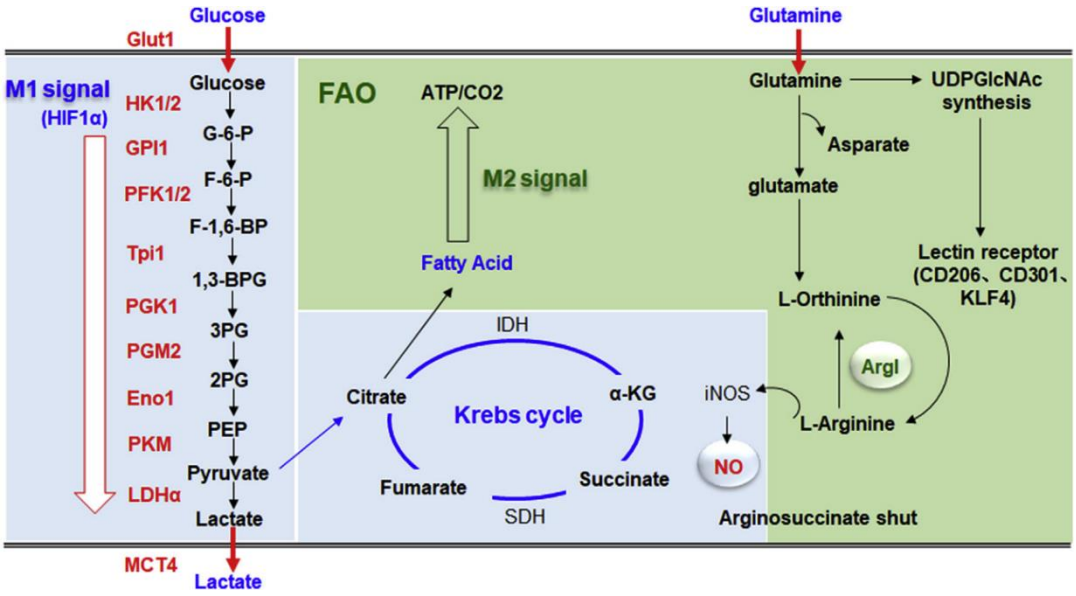


Figure 1.4.5 Metabolic reprogramming of M1/M2 macrophages

Different sources of energy supply employed by the M1 (blue) and M2 (green) macrophages. 1, 3-BPG: 1,3-bisphosphoglycerate. 2PG: 2-phosphoglyceric acid. 3PG: 3-phosphoglyceric acid. α-KG: α-ketoglutaric acid. ArgI: arginase 1. Eno1: enolase 1. F-6-P: fructose 6-phosphate. F-1, 6-BP: fructose-1, 6-bisphosphate. FAO: fatty acid oxidation. G-6-P: Glucose-6-phosphate. Glut1: glucose transporter 1. GPI1: Glucose-6-phosphate isomerase. HIF1α: hypoxia-inducible factor 1 alpha. HK1/2: hexokinase 1/2. IDH: isocitrate dehydrogenase. iNOS: inducible nitric oxide synthase. LDHα: lactate dehydrogenase alpha. MCT4: monocarboxylate transporter 4. NO: nitric oxide. PEP: phosphoenolpyruvic acid. PFK1/2: phosphofructokinase 1/2. PGK1: phosphoglycerate kinase 1. PGM2: phosphoglucomutase 2. PKM: pyruvate kinase. SDH: succinate dehydrogenase. TpI1: triosephosphate isomerase. UDPGlcNAc: N-glycosylation-essential uridine diphosphate N-acetylglucosamine. Image[349] from Wang, Liu, Yu *et al., Cancer Letters*, 2019.

This metabolic reprogramming of macrophage phenotypes is also found in cancers[349]. Tumour cells were known to favour glycolysis over OXPHOS even in aerobic conditions, as described by the Warburg effect[362]. TAMs have been shown to migrate to hypoxic regions with tumours in a CCL2/CCL5/CSF-1-dependent manner[363], where they support tumour proliferation and promote angiogenesis[364]. Interestingly, the transformation of a CD206^{high}Arg-1^{low} to a CD206^{low}Arg-1^{high} phenotype between normoxia and hypoxia was recently observed using an *in vitro* mouse macrophage cell line model. This process positively correlated with the lactate concentration in the surrounding media and was dependent on oxygen but not nutrients[365] (Figure 1.4.6). Collectively, this evidence suggests that the spatial distribution of these presumably more immune suppressive macrophages (Arg-1^{high}; as described in §1.3.1) was relevant to the diverse metabolic activities taking place within the tumour microenvironment (Figure 1.4.6).

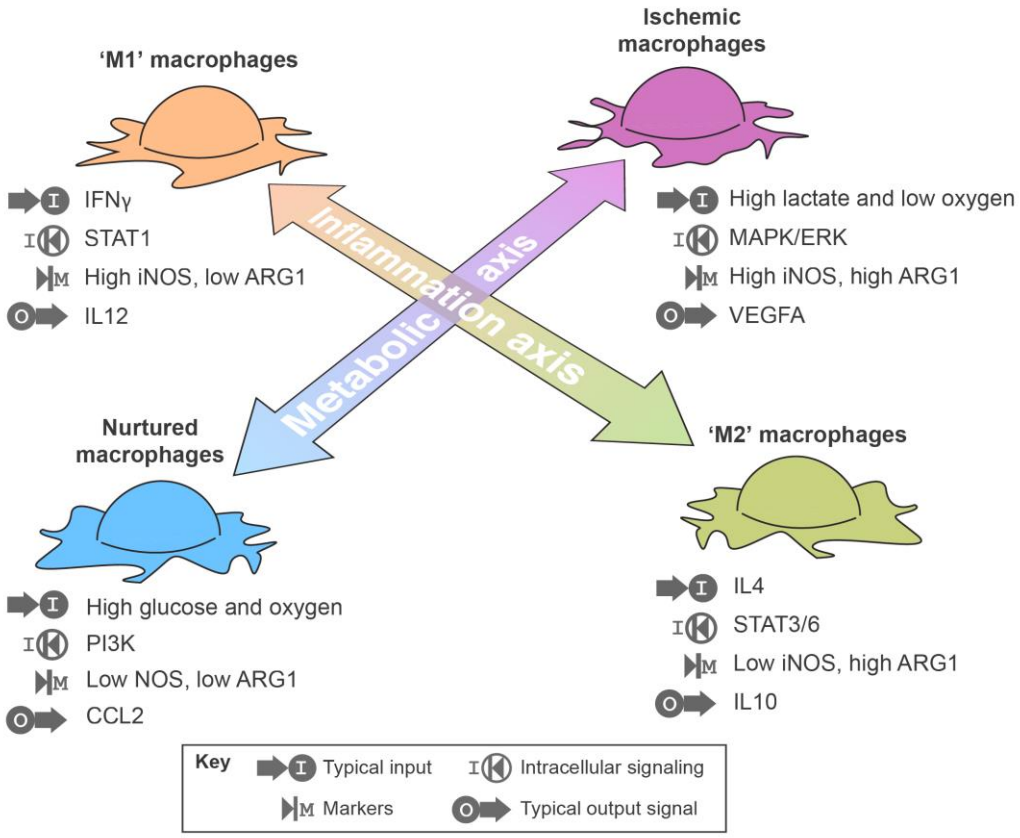


Figure 1.4.6 Metabolic reprogramming of macrophages in situ

Modified[309] from Hobson-Gutierrez and Carmona-Fontaine *et al., Disease Models & Mechanisms*, 2018.

1.4.4 Macrophages in non-infectious immunity and interaction with and other cells

Our current knowledge of macrophage polarisation/activation is mainly based on their interaction with bacteria and pathogens[366] and from *in vitro* culture systems[171]. Under a sterile inflammatory environment, such as cancers where the effect of foreign substances (e.g. LPS) on TAMs is limited, these responses may be different[171]. Indeed, while both LPS and IFN-γ were reported as mediators of M1 macrophage polarisation and similar responses on macrophages were observed, cellular signalling pathways triggered by these stimuli were not identical as separate or in combination[320, 367]. Macrophages primed with IFN-γ alone showed less production of pro-inflammatory cytokines (e.g. TNF-α, IL-6), whilst the IFN-γ and LPS-induced macrophages was found to selectively suppress TLR4-associated transcription (e.g. IL-10) resulting in a more severe and sustained inflammation[368].

During a sterile inflammation immune process, when stress or cellular damage-associated molecular patterns (DAMPs) are identified, activation of the innate and adaptive immune system takes place[369] (Figure 1.4.7). Long term IFN-γ production by Th1 cells can polarise macrophages into an M1 phenotype, compared to a more transient production of IFN-γ by the natural killer (NK) cells[307]. This M1 phenotype can be sustained by autocrine IFN-γ and co-stimulation of IL-12 and IL-18[370, 371] from other immune cells (e.g. Th1, macrophages, and dendritic cells). Pro-inflammatory M1 cytokines (e.g. IL-1β, IL-6, IL-23, TNF-α) could further contribute to the development of Th-17 cells[372] and the IL-17 producing CD8+ T cells[373] which attracts more immune cells into the region to further promote tissue inflammation[374]. Following removal of DAMP signals, clearance of cell debris by macrophages leads to a production of TGF-β[375], which enhances the resolution of inflammation and initiates wound healing. IL-4, produced by Th2 cells[376], basophils, mast cells and granulocytes[377], and IL-10 from regulatory T cells[378] and B cells[379], polarise macrophages into an M2-like phenotype for restoration of tissue homeostasis.

Sterile inflammation has also been shown to drive GC development in a STAT1-driven pro-tumourigenic manner. It was associated with the loss of NF-κB1 and

upregulation of PDL1 on the myeloid/epithelial cells and CTLA4/PD1 on the lymphocyte compartments[380, 381].

It remains unclear how this information applies specifically to macrophage polarisation *in situ* especially in the tumour where a dynamic mixture of different cytokines, chemokines and metabolites co-exist[382]. In addition, how the tumour microenvironments are being shaped by the different cell types and the interaction between GC and microbiome (§1.3.3) remains unclear. Hence, these challenges suggest that it would be beneficial to understand how these different immune cell populations are distributed and how they interact with each other and with the tumour cells in the tumour microenvironment.

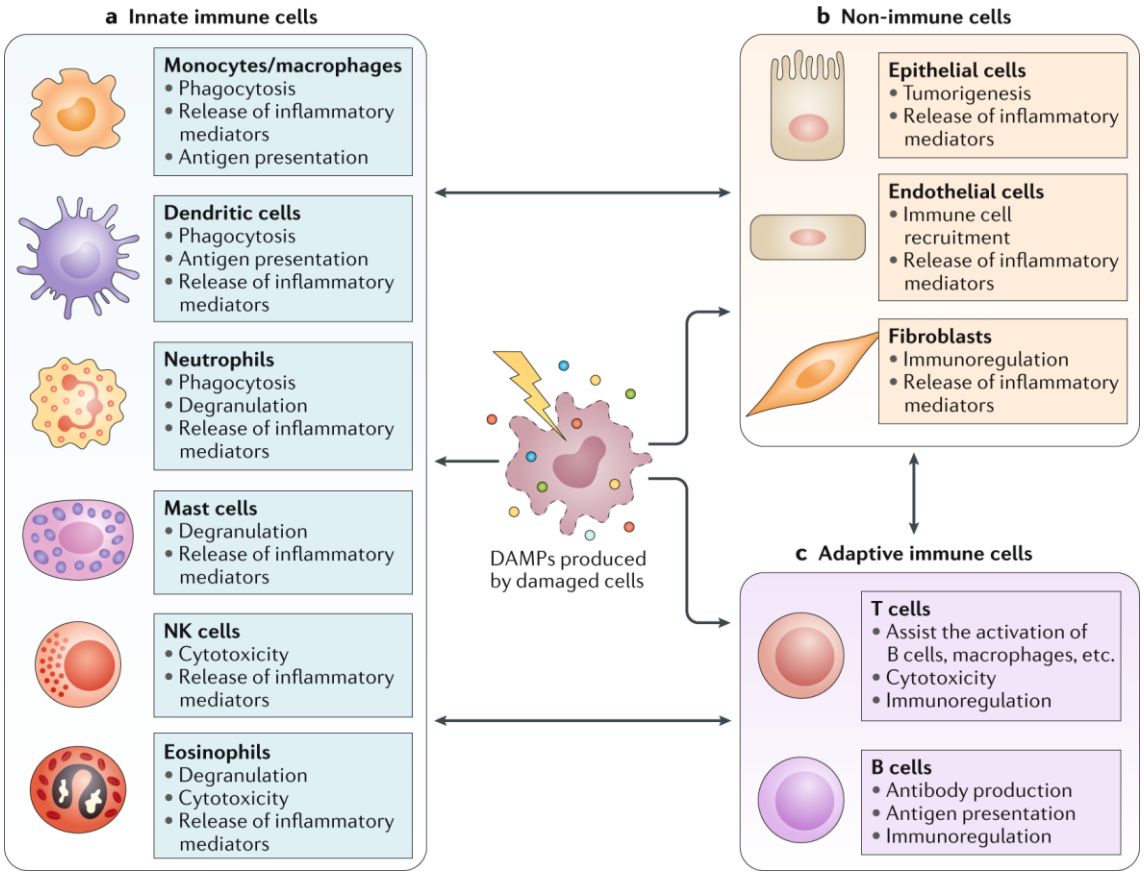


Figure 1.4.7 Sterile immune response

DAMPs: damage-associated molecular patterns. DCs: dendritic cells. NK: natural killer. Image[369] from Gong, Liu, Jiang *et al., Nature Review Immunology,* 2019.

1.4.5 Macrophage markers: Too similar and too different

The similarities between the macrophage populations polarised *in vitro* and between macrophages of different origins[383] is a huge obstacle for linking their counterparts *in vivo*[384]. To date, no exclusive markers are available to distinguish these populations, even those that are the best characterised. Arg-1 expression can be found on both M1 and M2 macrophages but at different levels[383, 385]. IL-10, a cytokine highly-expressed by M2 macrophages, is also produced by M1 macrophages at lower levels as a self-protective mechanism for reactive oxygen species[386-388]. Therefore, increasing evidence suggests that to better describe a specific population of macrophages, using a combination of different biomarkers is required.

The lack of similarity between *in vitro*-polarised and *in vivo*-characterised macrophages and between animal strains/species adds another layer of complexity and difficulty to understanding macrophage biology[310]. Firstly, the effect of a single agent on macrophage polarisation could be distinct in the presence of a secondary stimulus[320]. GM-CSF is commonly used to polarise M1 macrophages[171] as well as dendritic cells[389]. However, in combination with CCL18, macrophages were found to induce tumour cell EMT phenotype leading to tumour metastasis[390]. Importantly, the signalling feedback loops of the macrophages alone[386] and with the other cell types[391] could further complicate the dynamic of macrophage activation/polarisation within the tissues.

In animal models, the M1/M2 polarisation was found more pronounced in C57BL/6 than in BALB/c mouse strain[180], and multiple transcriptional differences were observed between different mouse strains regarding cell cycle, metabolic activity and immune response[392]. Moreover, human macrophage studies are complicated due to fundamental differences in comparison to mouse models[393]. While some conserved populations have been observed between the two species[394], signature markers of mouse macrophages, such as the characteristic iNOS/Arg-1 of the M1/M2 polarisation are not relevant in humans[311, 395]. In active murine macrophages, NO and iNOS expression was found to increase along with a crucial cofactor tetrahydrobiopterin (BH4) which stabilised the iNOS enzyme, however, this is not observed in human

macrophages[311]. Arginase activity was not induced in human IL-4/13 treated macrophages[396, 397]. In addition, F4/80, a classic macrophage marker used in mouse studies[398], is an eosinophil-specific receptor and is not expressed by human macrophages[399]. More recently, it was shown that human, unlike murine macrophages, do not to convert to glycolysis post LPS induction but rely on OXPHOS for energy supply[400]. E3 ubiquitin ligase, an enzyme that promotes the production of IL-1β in humans is not found in the mice[401] and TAMs have been shown to exhibit distinct RNA profiles between human and mouse glioblastoma models[402].

To address these problems, nomenclature and experimental guidelines[393, 403] have been proposed which suggest reporting macrophage populations based on the conditions of which they were polarised or identified with instead of referring them as M1/M2s. This would assist in the reproducibility of the populations which fits into the spectrum model of the macrophage activation.

1.5 Remaining challenges and Thesis aims

Accumulating evidence has shown that the complexity of macrophage population exceeds beyond the M1/M2 framework and that TAM heterogeneity is determined by their interaction with cytokines, chemokines and metabolites derived from the tumour cells, immune cells, other stromal cells and possibly between other TAM populations within the same milieu.

Challenges remain regarding how well these findings can translate from *in vitro* to *in vivo* mouse models, to humans, to gastric cancer and eventually to clinical practice. In addition, due to the tissue-destructive nature of investigational methods (e.g. CyTOF, single-cell RNA-seq) used in previous studies, it is not well understood how the different TAM populations are distributed and interacted among themselves and with other cell types *in situ*. Whilst some data showed that the distribution of TAMs in specific tumour anatomic regions could be clinically-associated in GC[216, 404], these studies were done using single or at most double-colour immunohistochemistry staining to identify macrophages which is now recognised as being inefficient to reflect macrophage heterogeneity. For these reasons, a careful reassessment of the role of macrophages and their clinical relevance in human gastric cancer is needed.

To address these challenges, this Thesis aims to investigate the pathophysiology of TAMs in GC including:

1. The spectrum model of TAMs
2. The distribution of TAMs taking into account their spatial context with the tumour cells and the other immune cells
3. The association of TAMs with the PDL1 expression, tumour microenvironment and clinical parameters
4. The similarity between human TAMs and *in vitro*-polarised macrophages

Chapter 2 : Materials and methods

2.1 MAUGIC cohort

The Molecular Analysis of Upper Gastrointestinal Cancer (MAUGIC) cohort was used for the studies from Chapter 3 to 7. This cohort consists of samples collected from 250 potentially resectable gastric and oesophageal cancer patients from 1999 to present (from 1999-2009[68] for this study). Written informed consent was obtained from all patients prior to sample collection. All procedures were ethically approved by the Individual Review Boards of the Peter MacCallum Cancer Centre and each of the tissue collection centres.

2.1.1 OPAL study cohort

A subset of 56 GC specimens from the MAUGIC cohort were identified as candidates for multiplex IHC and are referred to as the **OPAL study cohort**. The criteria for selection were (i) availability of large and good quality formalin-fixed paraffin-embedded (FFPE) tissue blocks of the primary cancer and (ii) comprehensive clinical information with at least 10 years follow-up data for survival analyses.

2.1.2 MAUGIC-Affy cohort

Ninety nine GC tissues (referred as the **MAUGIC-Affy cohort**) collected at the time of surgery were snap-frozen in liquid nitrogen and RNA was isolated with Trizol (Invitrogen) from the whole-tumour lysate using column chromatography (RNeasy, Qiagen). Microarrays were hybridised using U133+2 chips (Affymetrix) and scanned using the Genechip Scanner (Affymetrix) according to the manufacturer's protocols. Data was submitted to Gene Expression Omnibus (GEO; Series GSE51105[213]).

2.1.3 OPAL-Affy cohort

The OPAL-Affy cohort consisted of 34 patients with both multiplex IHC cell density data and whole-tumour-derived Affymetrix gene expression data.

2.1.4 Patient exclusion criteria for survival analysis

Overall survival (OS) was measured from the date of surgery to date of death of any cause. Relapse-free survival (RFS) was measured from date of surgery to date of first documented relapse. Within the **OPAL study cohort**, patients without cell density data within the tumour Core region were excluded from survival analysis. The Core was chosen as it comprises the majority of the tumour and because for some tumours, especially those with diffuse histology, tumour Edge and Margin were difficult to define. Three patients with known surgery-related deaths (within 100 days; sepsis, hyperkalaemia and pneumonia) and two with no recurrence data available were excluded from the OS and RFS analysis, respectively.

An online GC database (KMplot[405]), which contains six GC cohorts with patients from different ethnicities, was used for OS analysis as an independent dataset. Due to lack of relevant data, no patients were excluded as a result of surgical-associated death. The South Korean GC cohort available as part of the GC KMplot database (GSE62254), was analysed separately based on the authors recommendations. This is due to markedly different characteristics of this cohort (longer survival etc.) compared to the other cohorts.

2.1.5 Classifications of cancer subtype and inflammation status

Samples were classified histologically into intestinal, diffuse and mixed types[9] by an anatomical pathologist (Dr. Catherine Mitchell; C.M.). Samples were also classified molecularly based on the TCGA subtypes[31]. EBV burden was determined using *in situ* hybridisation (EBV Early RNA, Roche). IHC was used to identify MSI status with MLH1 (Leica, ES05, 1:50), PMS2 (Ventana, EPR3947), MSH2 (Ventana, G219-1129) and MSH6 (BD Biosciences, 44, 1:800) staining. MSI samples show the loss of MLH1 and PMS2 expression and retain MSH2 and MSH6 expression. Patients with diffuse subtype but neither EBV nor MSI were assumed as GS[68]. The remaining samples were defined as “Others” and not CIN due to lacking supporting evidence. Degree of inflammation of each GC tissue was scored by C.M. and assessed based on the infiltration of immune cells[406].

2.1.6 Cancer staging

The most recent AJCC manual is the 8th edition[69]. For this study, the AJCC 6th edition[67] is used for patient sample classification as this was the edition in use during the time of patient enrolment (from 1999-2009)[68].

2.2 Multiplex immunohistochemistry

2.2.1 Staining

Opal 7-colour kit (PerkinElmer, NEL811001KT) was used for multiplex IHC. 4µm FFPE sections were dewaxed and rehydrated on TRAJAN series 3 slides. First round antigen retrieval was performed using a pressure cooker (EDTA pH 8.0, 125°C, 3mins). Slides were cooled to room temperature (RT), washed with TBST/0.5% Tween (3 times, 3mins) and incubated with H_2O_2 (3%; 10mins). Slides were washed (3 times, 3mins) and blocked with blocking buffer (Dako, Glostrup, Denmark; 10mins). Primary antibody (prepared with 0.1% BSA, 1X TBS buffer) was applied and incubated at RT for 30mins. Slides were washed (3 times, 3mins) and an HRP-conjugated secondary antibody of the corresponding host species was incubated with the tissue (RT, 10mins). Slides were washed (3 times, 3mins) and TSA-dye was incubated with the tissue (RT, 10mins). Slides were washed (3 times, 5mins) and antigen was retrieved (EDTA, pH 8.0) using a microwave (100-150mW, 15mins). Slides were cooled to RT, washed (3 times, 3mins) and the staining procedure was repeated using different antibodies in the order listed in Table 2.2.1, Table 2.2.2, Table 2.2.3 and Table 2.2.4. Following antigen retrieval of the final antibody, slides were washed (3 times, 3mins) and nuclei were stained with DAPI (PerkinElmer; 5 mins). Slides were mounted with HardSet medium (Vectashield), coverslipped and sealed with nail polish. Anti-rabbit (PerkinElmer, NEF812001EA) or anti-mouse (PerkinElmer, NEF822001EA) secondary antibodies were used where applicable.

Four sequential sections of the same tissue blocks were stained with the (i) H&E, (ii) TAM, (iii) NOX2 and (iv) TIL panel, respectively.

Table 2.2.1 Multiplex tumour-associated macrophage (TAM) panel

Antibody details						
Antibody	**Company**	**Clone/Cat#**	**Host**	**Specificity**	**Marker**	**Location**
CD163	Cell Marque	MRQ-26	Mouse	Human	M2-like macrophage	membrane
CD68	Leica Biosystems	514H12	Mouse	Human	pan-macrophage	cytoplasm
CD206	Abcam	ab64693	Rabbit	Human, murine	M2-like macrophage	membrane
IRF8	Santa Cruz	E-9	Mouse	Human, murine	M1-like	nucleus
PDL1	Spring Bioscience	SP142	Rabbit	Human	immune checkpoint	membrane
AE1AE3	Leica Biosystems	NCL-L	Mouse	Human	pan-cytokeratin	membrane
DAPI	PerkinElmer	- -	- -	- -	cell nucleus	nucleus
pSTAT6	Abcam	ab28829	Rabbit	Human, murine	phospho-STAT6	cytoplasm
Staining conditions						
Antibody	**TSA-dye**	**Order**	**Control**	**Primary Ab***	**Secondary Ab***	**TSA-dye**
CD163	540	1	Liver	1:500	1:1000	1:50
CD68	570	2	Liver	1:100	1:500	1:50
CD206	620	3	Liver	1:6000	1:1000	1:50
IRF8	650	4	Tonsil	1:3000	1:1000	1:50
PDL1	520	5	Placenta	1:1000	1:1000	1:50
AE1AE3	690	6	Skin	1:200	1:1000	1:50
DAPI	- -	7	N/A	- -	- -	- -
pSTAT6[1]	520	5	Liver	1:100	1:1000	1:50

- Ab*: antibody. 1: pSTAT6 was used in replacement of PDL1 as a different panel

Table 2.2.2 Multiplex tumour-infiltrating T lymphocyte (TIL) panel

Antibody details						
Antibody	**Company**	**Clone/Cat#**	**Host**	**Specificity**	**Marker**	**Location**
CD3	Spring Bioscience	SP7	Rabbit	Human, murine	pan-T cell	membrane
CD8	ThermoFisher	4B11	Mouse	Human	cytotoxic T cell	membrane
CD4	Spring Bioscience	SP35	Rabbit	Human, murine	helper T cell	membrane
IRF8	Santa Cruz	E-9	Mouse	Human, murine	interferon-response	nucleus
FOXP3	BioSB	BSB 6762	Rabbit	Human	regulatory T cell	nucleus
AE1AE3	Leica Biosystems	NCL-L	Mouse	Human	pan-cytokeratin	membrane
DAPI	PerkinElmer	- -	- -	- -	cell nucleus	nucleus
Staining conditions						
Antibody	**TSA-dye**	**Order**	**Control**	**Primary Ab***	**Secondary Ab***	**TSA-dye**
CD3[1]	520	1	Tonsil	1:500	1:1000	1:50
CD8[1]	620	2	Tonsil	1:200	1:500	1:50
CD4[1]	650	3	Tonsil	1:100	1:1000	1:50
FOXP3[1]	570	4	Tonsil	1:100	1:1000	1:50
IRF8	540	5	Tonsil	1:3000	1:1000	1:50
AE1AE3	690	6	Skin	1:200	1:1000	1:50
DAPI	- -	7	N/A	- -	- -	- -

- Ab*: antibody. [1]: Conditions optimised based on Wang, 2019[407]

Table 2.2.3 Multiplex NOX2 panel

Antibody details						
Antibody	**Company**	**Clone/Cat#**	**Host**	**Specificity**	**Marker**	**Location**
CD163	Cell Marque	MRQ-26	Mouse	Human	M2-like macrophage	membrane
CD68	Leica Biosystems	514H12	Mouse	Human	pan-macrophage	cytoplasm
CD8	ThermoFisher	4B11	Mouse	Human	cytotoxic T cell	membrane
NOX2	Abcam	ab31092	Rabbit	Human, murine	gp91phox	membrane
PD1	BioSB	EP239	Rabbit	Human	immune checkpoint	membrane
AE1AE3	Leica Biosystems	NCL-L	Mouse	Human	pan-cytokeratin	membrane
DAPI	PerkinElmer	- -	- -	- -	cell nucleus	nucleus
Staining conditions						
Antibody	**TSA-dye**	**Order**	**Control**	**Primary Ab***	**Secondary Ab***	**TSA-dye**
CD163	540	1	Liver	1:500	1:1000	1:50
CD68	570	2	Liver	1:100	1:500	1:50
CD8	620	3	Tonsil	1:200	1:500	1:50
NOX2	650	4	Liver	1:600	1:1000	1:50
PD1	520	5	Tonsil	1:100	1:1000	1:50
AE1AE3	690	6	Skin	1:200	1:1000	1:50
DAPI	- -	7	N/A	- -	- -	- -
• Ab*: antibody						

Table 2.2.4 Mouse multiplex TAM panel

Antibody details						
Antibody	**Company**	**Clone/Cat#**	**Host**	**Specificity**	**Marker**	**Location**
F4/80	Cell Signaling	D2S9R	Rabbit	Murine	pan-macrophage	cytoplasm
CD206	Abcam	ab64693	Rabbit	Human, murine	M2-like macrophage	membrane
Mitochondria	Millipore			Human	Mitochondria	cytoplasm
DAPI	PerkinElmer	- -	- -	- -	cell nucleus	nucleus
Staining conditions						
Antibody	**TSA-dye**	**Order**	**Control**	**Primary Ab***	**Secondary Ab***	**TSA-dye**
F4/80	570	1	Liver	1:400	1:1000	1:50
CD206	620	2	Liver	1:10000	1:1000	1:50
Mitochondria	650	3		1:500	1:1000	1:50
DAPI	- -	4	N/A	- -	- -	- -
• Ab*: antibody						

2.2.2 Tissue imaging and image processing

Stained slides were imaged using a Vectra microscope (PerkinElmer, Massachusetts, USA). Whole slide scans were performed using the 10X objective lens and the regions of interests (ROIs) were identified with fixed-size stamps using the Phenochart software (PerkinElmer), based on the whole slide scan images. The smallest microscopy field available (1x1 [669x500 µm; 20X object lens] stamp) was used for the tumour Margin at the interface of the tumour and the adjacent normal tissue region. Regular field (2x2 [1338x1000

µm] stamp) was used for the tumour Core, Edge and for the adjacent normal tissue. All viable regions in each specimen were acquired with minimal overlap. Acquired images (Table 2.2.5) were analysed with the inForm software (PerkinElmer) for spectra-unmixing of fluorophores, tissue-component segmentation of tumour-cell (AE1AE3+) and stroma (AE1AE3-) regions and cell phenotyping for cells of interest.

Table 2.2.5 Number of images per region of interest per patient sample

Patient #	Core	Edge	Margin	Normal	Total	Patient #	Core	Edge	Margin	Normal	Total
497	43	8	46	5	102	***5263***	2	5	10	6	23
513	25	18	0	23	66	***5502***	33	3	0	3	39
514	36	0	0	0	36	***6000***	15	0	0	0	15
1971	0	4	3	17	24	***6765***	18	8	17	4	47
2173	20	0	0	5	25	***6844***	6	0	0	7	13
2333	0	11	0	25	36	***6848***	0	8	10	9	27
2433	5	5	10	4	24	***6881***	31	3	0	0	34
2529	13	5	0	0	18	***6932***	0	10	10	0	20
2655	9	0	0	0	9	***6937***	20	12	19	0	51
2690	3	0	0	4	7	***7136***	8	0	0	4	12
2692	8	5	15	16	44	***7335***	0	10	5	5	20
2757	6	0	0	0	6	***7419***	25	0	0	0	25
2804	7	0	0	0	7	***7422***	8	0	0	0	8
2852	18	11	9	10	48	***7424***	14	8	10	5	37
2906	13	4	0	3	20	***7572***	8	2	7	0	17
3010	0	5	7	8	20	***7632***	0	7	0	4	11
3062	17	8	0	0	25	***7698***	13	0	7	0	20
3331	12	0	0	0	12	***7868***	12	0	0	0	12
3376	25	3	8	3	39	***7934***	97	10	51	37	195
3468	11	0	4	0	15	***7945***	9	0	0	0	9
3710	19	0	0	0	19	***7988***	7	0	0	0	7
3722	68	0	0	0	68	***8138***	0	0	7	0	7
3958	18	18	17	8	61	***8269***	0	4	15	10	29
4080	21	4	7	0	32	***8693***	10	0	0	0	10
4088	24	0	7	5	36	***8897***	32	0	0	0	32
4325	15	0	0	0	15	***9445***	4	0	0	8	12
4715	20	0	0	0	20	***9817***	92	19	62	12	185
4891	9	6	14	10	39	***10574***	0	4	9	0	13
Sum	Core	Edge	Margin	Normal	Total	%	Core	Edge	Margin	Normal	Total
	929	228	386	260	1803		51.5	12.7	21.4	14.4	100

2.2.3 Cell phenotyping

A cell was only able to be phenotyped if it demonstrated positive nuclear DAPI staining. In 4µm sections with cells around 10-20µm, it is easy to slice through the edge of a cell and to score a negative result while the cell is in fact positive.

In addition, all cytoplasmic and membranous staining was evaluated within 5-10µm of DAPI. These approaches are used to minimise the scoring of markers adjacent to the cell nucleus can decrease the influence of macrophage dendrites.

Density of cells in each ROI was calculated by combining the cell counts from all images and normalised by the total area (cell/mm^2).

2.3 Cell culture

A luciferase tagged human gastric cancer cell line $MKN45^{408}$ was cultured in DMEM base media with 10% (w/v) foetal bovine serum, penicillin (100 U/ml) and streptomycin (100 µg/ml; Invitrogen, Carlsbad, CA) and was maintained at 37 °C in a humid incubator with 5% $CO_{2.}$.

2.4 In vivo experiment design

2.4.1 Mice

C57BL/6-Rag2<KO>γc<KO> mice (10-12 weeks) were bred and maintained under specific pathogen-free conditions in the Animal facility of the Peter MacCallum Cancer Centre. All experimental protocols were approved by the Animal Experimentation Ethics Committee (AEEC) of the Peter MacCallum Cancer Centre (E620).

2.4.2 Macrophage depletion

For depletion of all macrophages, clodronate-liposomes (Clodrosome®, Encapsula NanoSciences, Nashville, TN) were used. Depletion of CD206 (mannose receptor)-expressing macrophages was achieved using mannosylated clodronate-liposomes (m-Clodrosome®, Encapsula NanoSciences, Nashville, TN). Corresponding clodronate-lacking liposomes (Encapsome®, Encapsula NanoSciences) or mannosylated liposomes (m-Encapsome®, Encapsula NanoSciences) respectively were used as controls, 1X PBS (without Ca^{2+} and Mg^{2+}) was used as a negative control.

Mice were injected intraperitoneally (i.p.) with liposomes and PBS using 26G needles twice per week (3-4 day cycle). The weight, physical behaviour and condition of the mice were monitored daily. Antibiotics were i.p. injected during macrophage depletion period if necessary in signs of infection. Samples were collected at different time points to determine the depletion efficacy. Blood samples were collected on Day 3 and 10 post-drug injections (p.d.i.). Mice were anaesthetised with isoflurane, bled from the sub-mandibular vein approximately 100µl per 25g mouse. Peripheral blood mononuclear cells (PBMCs) were isolated and stained for flow cytometry analyses. Mice were bled and culled on Day 7, 14, 21 and 28 p.d.i. and PBMCs and organs were harvested for flow cytometry and IHC analyses, respectively.

2.4.3 Xenograft inoculation

MKN45 cells (0.5×10^6) were harvested and resuspended in Matrigel (50µl; ThermoFisher). Surgical procedures were performed as described previously[408]. Briefly, mice were anaesthetised using i.p. injection of ketamine/xylazine and placed in a dorsal position. Carprofen was administered prior to surgery for pain relief. Fur around the surgical area was clipped and sanitised with Betadine. A 5-10 mm incision was made through the skin and muscular layers. Forceps were used to expose the stomach. MKN45 cells were injected into the serosal layer of the stomach with a 28G insulin needle. The incision was sutured using the layered closure method.

2.4.4 Immunohistochemistry

Mouse stomachs were harvested, cleaned with 1X PBS (without Mg^{2+} and Ca^{2+}) and fixed with 4% PFA for 48 hours. Stomachs were divided in half and embedded in paraffin in both flat and perpendicular orientations. Tissue blocks were sectioned at 4 µm and were stained for histopathology. Single-stained IHC with an anti-human mitochondrial antibody (1:500, Millipore) for 1 hour at RT. Slides were washed and incubated with anti-rabbit antibody conjugated with HRP for 30 mins. Slides were washed (3 times, 3mins) and visualised with DAB chromogen kit (Dako) for 5 mins. Slides were washed (3 times, 3mins) and counterstained with Meyer's hematoxylin and multiplex IHC staining were performed as described in 2.2.1 with the antibodies in Table 2.2.4.

2.4.5 Invasion score

Tumour sections with single-stained IHC for human mitochondria was used to determine the invasiveness of tumours. Invasion score (number 0; Figure 8.3.21) was defined as having tumour located solely within the serosa (S) layer. Tumours which had invaded through the muscularis mucosa (MM) but not yet to the mucosa (M) was defined as having score (1) and the tumour that invaded through the MM into the M was defined as having score (2). All tumours with a score of 1 and 2 were considered invasive.

2.5 Flow cytometry

2.5.1 Mouse peripheral blood mononuclear cell

2.5.1.1 Sample preparation

Blood samples were collected (§2.4.3) in 0.5M EDTA. Stock red blood cell (RBC) lysis buffer (555899, BD) at room temperature (RT) was diluted to 1X with MilliQ water and combined with blood at a ratio of 10:1. Samples were vortexed and incubated at RT for 15 mins in the dark. Samples were centrifuged (300g, 5 mins), and the pellets were washed twice with 2ml PBS-/- (1X, without magnesium and calcium; Mg^{2+} and Ca^{2+}, respectively) then resuspended in FACS buffer (1mM EDTA, 0.1% Azide, 2% FCS mixed in 1X PBS-/-).

2.5.1.2 Antibody staining

Tubes were labelled for unstained, single-colour stained, fluorescence-minus-one (FMO) controls (optional), and for full stained cocktail (excluding viability dye). Counting beads (Trucount™ tube, 340334, BD) solution was prepared with FACS buffer. Antibody mix was prepared using Counting beads solution with the dilutions listed in Table 2.5.1. Cell blocking buffer was prepared with FACS buffer, 0.5% BSA and 1:50 CD16/CD32 Pure 2.4G2 antibody mix (553142, BD). Full stained antibody cocktail was prepared in Brilliant stain buffer (563794, BD) if multiple BV dyes were used.

Equal volume of samples was distributed into each well of a 96 well plate. The plate was centrifuged (1400g, 2 mins), and the supernatant was discarded. Blocking buffer (35 µl) was added to each well and incubated on ice (10 mins). FACS buffer (150 µl) as added to each well, centrifuged (1400g, 2 mins), and the supernatant was discarded. Antibody mix (35 µl) was added to the well where appropriate and was incubated on ice (25 mins). 1X PBS (1mM EDTA/protein-free; 150 µl) was added to each well, centrifuged (1400g, 2 mins), and the supernatant was discarded. The samples were washed again and 1X PBS (1mM EDTA/protein-free; 100 µl) to single colour controls. Viability dye solution was added to the sample wells and incubated (10 mins). FACS buffer (150 µl) was added to each well, centrifuged (1400g, 2 mins), and the supernatant was discarded. Washing steps were repeated and 100 µl Cytofix/Cytoperm buffer (554722, BD) / 4% Paraformaldehyde (PFA; 30525-89-4, Alfa Aesar) was added to each well and incubated (20 mins). FACS buffer (150 µl) was added to each well, centrifuged (1400g, 2 mins), and the supernatant was discarded. Washing steps were repeated and samples were resuspended in FACS buffer.

For intracellular staining, samples were washed twice with 1X Perm/Wash buffer (554723, BD) after being stained with viability dye. Antibodies were prepared in 1X Cytofix/Cytoperm buffer, added to each well and incubated (25 mins). Washing steps were repeated and 4% PFA (100 µl) was added to each well and incubated (20 mins). FACS buffer (150 µl) was added to each well, centrifuged (1400g, 2 mins), and the supernatant was discarded. Washing steps were repeated and samples were resuspended in FACS buffer.

Table 2.5.1 Mouse flow panel

Company	CAT No.	Clone	Mouse markers	Fluoro -chrome	Working dilution	
					PBMC	Tumour
BD Biosciences	564225	30-F11	CD45	BV786	1:500	1:500
BD Biosciences	563015	M1/70	CD11b	BV605	1:400	1:400
BD Biosciences	560596	AL-21	Ly-6C	APC-Cy7	1:200	1:400
BD Biosciences	560601	1A8	Ly-6G	PE-Cy7	1:400	1:400
BD Biosciences	565635	T45-2342	F4/80	BV480	- -	1:100
BioLegend	139311	X54-5/7.1	CD64	BV711	- -	1:100
ThermoFisher	12-1631-82	TNKUPJ	CD163	PE	- -	1:200
BioLegend	141704	C068C2	CD206	FITC	- -	1:100
BioLegend	137008	FA-11	CD68	APC	- -	1:700
BD Biosciences	564716	MIH5	PDL-1	BV421	- -	1:200
BD Biosciences	564997	Fixable Viability Stain 700			1:1500	1:4000
BD Biosciences	553142	Mouse CD16/CD32 Pure 2.4G2			1:50	
BD Biosciences	563794	Brilliant Stain Buffer			50µl per mix	
BD Biosciences	340334	Trucount Absolute Counting Tubes IVD			40µl / 1ml	

Table 2.5.2 Human flow panel

Company	CAT No.	Clone	Human markers	Fluorochrome	Working dilution (Tumour)
BD Biosciences	561863	2D1	CD45	APC-Cy7	1:200
BD Biosciences	560910	SK7	CD3	PE-Cy7	1:200
BD Biosciences	560916	B159	CD56	PE-Cy7	1:200
BD Biosciences	560911	HIB19	CD19	PE-Cy7	1:200
BD Biosciences	562254	G10F5	CD66b	PerCP-Cy5.5	1:200
BD Biosciences	742642	ICRF44	CD11b	BV786	1:200
BD Biosciences	745150	10.1	CD64	BV605	1:200
ThermoFisher	A15723	GHI/61	CD163	APC	1:200
BD Biosciences	551135	19.2	CD206	FITC	1:100
BD Biosciences	556078	Y1/82A	CD68	PE	1:200
BD Biosciences	563738	MIH1	PDL-1	BV421	1:100
BD Biosciences	564220	Human Fc Block Pure Fc1.3216			1:50
BD Biosciences	564997	Fixable Viability Stain 700			1:2000

2.5.2 Tumour samples

Tissue Digestion buffer was prepared with penicillin and streptomycin (0.02 ml/ml), collagenase IV (75U/ml), dispase (125 µg/ml), hyaluronidase (20 µg/ml) and DNAse I (0.1 µg/ml) in DMEM cell culture media (Gibco).

Human or mouse tumour samples were washed briefly with 1X PBS-/-. For mouse stomach tumours the visible tumour region was located and non-tumour stomach tissue was discarded.

Tumour was minced into smaller pieces using 2 scalpel blades (0206, Swann-Morton) in a 5cm cell culture dish (ThermoFisher) and was transferred into 5ml

of preheated Digestion buffer (10ml tube, ThermoFisher). The tube was incubated in bacterial shaker (1500rpm, 37°C, 20 mins). The single cell suspension was filtered through a 70 µm strainer into a 5cm cell culture dish and the remaining tissue that did not pass through the filter was gently minced with a syringe plunger (TERUMO) within the dish. The filtered medium was then transferred into a 15ml tube through a 40 µm strainer and centrifuged (300g, 5 mins). Cell pellets were washed twice with 1X PBS-/- and resuspended in FACS buffer (§2.5.1.1) for further staining (described in §2.5.1.2). If sample contained residual blood, RBC lysis steps were performed as described in 2.5.1.1.

2.5.3 Mouse spleen

Mouse spleen was removed and rinsed with 1X PBS-/-. The tissue was placed within a 70 µm strainer and put into a cell culture dish containing 1ml of 1X PBS-/- and was gently minced with a syringe plunger. The single-cell solution was then transferred into a 15ml tube through a 40 µm strainer and centrifuged (300g, 5 mins). Cell pellets were washed twice with 1X PBS-/- and incubated with 1 ml 1X RBC lysis buffer (10 mins, RT). Samples were topped up with 1X PBS -/-and centrifuged (300g, 5 mins). Cell pellets were washed twice with 1X PBS then resuspended in FACS buffer for further staining.

2.6 Analysis

2.6.1 Software and statistics

inForm[409] software was used to analyse the images acquired with the Vectra microscope. Image output from inForm showing the DAPI, AE1AE3, CD68 and CD163 or CD206 were validated with the Line profile function in ImagePro (Media Cybernetics) and with the 3D-density plot in ImageJ (Fiji Is Just ImageJ, FIJI). R software (version 3.3.1 for Windows) was used for the development of spatial distance analysis tool and for the interrogating the cell density information acquired with mIHC as well as the MAUGIC gene expression data. GraphPad prism version 7 and 8 (GraphPad Software, San Diego, USA) were used for statistical analysis. Reactiome[410, 411], an online bioinformatics tools for pathway analysis was used for interpretation of gene lists.

Mann-Whitney's U test (two-tailed), Wilcoxon matched-pairs test (two-tailed), Spearman and Pearson correlation, Chi-square analysis and Kaplan–Meier analysis (Log-rank, Mantel-Cox test) were used as appropriate with GraphPad prism version 7 and 8. P values lower than 0.05 were considered significant. Median value, non-parametric tests were used due to the non-Gaussian distribution of data.

2.6.2 Distance analysis

An Inter-cellular Spatial Analysis Tool[412] (ISAT) was developed using the R software in collaboration with Dr. Minyu Wang and Dr. Yu Sun. In brief, cells of a given phenotype were used as reference cell to calculate its distance to the nearest cell of different phenotypes using the x and y coordinates from the inForm raw data. The calculations were done for all combinations of cell types within the raw data sheet and the nearest distance of each cell was documented.

The effective density was calculated by using the number of cells within the cell type that fulfilled the distance criteria and normalized to the area of tissue (mm^2) and the effective percentage of a cell type was determined by normalising the cell counts of effective density to the total number of cells in the corresponding cell type. 10μm (nucleus to nucleus) was defined as an estimated direct contact distance between the cells.

2.6.3 R packages

The "limma" package[413] was used for normalising gene expressions of the **MAUGIC-Affy cohort**. "dplyr", "rowr", "gtools", "reshape" were used for data manipulation of the inForm raw data. "rgl", "plot3Drgl", "gplots" were used for data visualisation.

Chapter 3 : Establishing a model for the analysis of cellular phenotype and spatial interaction using multiplex immunohistochemistry

3.1 Introduction

3.1.1 Tumour-associated macrophages

Macrophages are one of the important components of the innate immune system[166]. Tumour-associated macrophages (TAMs) are abundant in GC[216] and are characterised by their plasticity and multiplicity of functions[189]. The abundance of TAMs is commonly correlated with poor cancer patient survival; however, their contributions to survival in GC[213, 216] are inconsistent between studies. This is possibly due to a range of TAM activation states and phenotypes and require further investigation. It is now recognised that TAMs are a mixture of different macrophages[307]. However, how these different macrophages populate *in situ* is not known mainly due to the limitation of technologies that have been used to facilitate these findings having a tissue-destructive procedures[320, 414, 415] (e.g. flow cytometry, single-cell RNA sequencing). To be able to focus specifically on the distribution of TAM populations *in situ*, the OPAL™ multiplex immunohistochemistry[409, 416] (mIHC) was selected as the method for this study.

3.1.2 Multiplex immunohistochemistry

The OPAL™ mIHC is an advanced staining technology developed by PerkinElmer which allows the simultaneous co-staining of up-to seven markers on a single formalin-fixed paraffin-embedded (FFPE) tissue section. While the number of markers that can be used in a mIHC panel remains limited compared to using Flow cytometry[417] or CyTOF[321, 322], the technology's strength is the ability to provide tissue-specific spatial data that allows transformation of a visual image into digital information. This digital information on individual cells allows for bioinformatic spatial analyses[418]. Given one of the major aims of the Thesis was to investigate heterogeneity of macrophages in the context of the

tumour microenvironment, mIHC provides a powerful tool to analyse TAMs in the different anatomical components of GC.

3.1.3 Regions of interest

TAMs are known to invade deep into the tumour Core and the hypoxic regions[137], but are also found to be associated with high PDL1 expression within the stroma[134] and with a stroma-related gene signature[213], suggesting that locational differences between different TAM populations may be present. To perform TAM spatial comparisons, a serially sectioned tissue from each sample block was stained with haematoxylin and eosin (H&E) and reviewed by a pathologist to identify the interface of tumour and normal tissue, in addition, different regions of interest (ROIs) were defined within the same specimen (Figure 3.1.1). Adjacent non-tumour normal tissue (N) was identified as the area within the specimen that was free of tumour. Margin (M) was defined as a strip of area, approximately 0.5 to 1 mm in width, based on the limited size of the smallest microscopy field, located at the interface of the tumour site and normal tissue. Edge (E) was a region, approximately 1 to 1.5 mm in width (based on the size of the medium microscopy field), starting immediately adjacent to the Margin into the tumour. Finally, the remainder of the inner tumour region was defined as Core (C). There may be potential bias of this approach due to the fact that the tumour/normal interface was determined based on observer knowledge and due to technical limitations of the OPAL multiplex IHC platform.

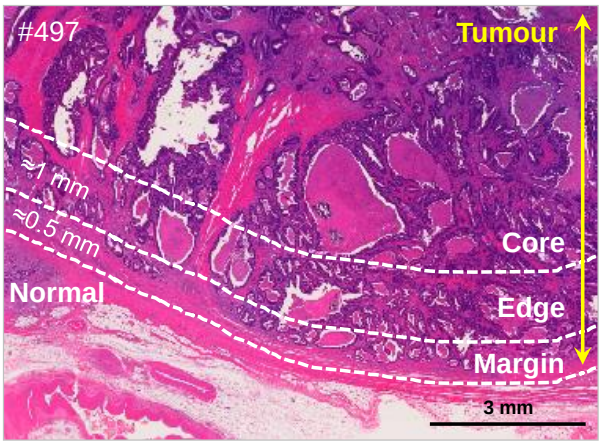


Figure 3.1.1 Defining regions of interest

Representative H&E staining of a GC patient sample (#497). Dashed line: approximate boundaries of ROI. Size of each ROI was based on the limited size of the microscopy fields.

3.1.4 Spatial analysis

Mixtures of TAM populations are known to co-localise in a shared tumour microenvironment[419-421]. However, their exact spatial relationship with each other and to the tumour cells are not known. Studies of spatial distribution of immune cells in the literature have been mainly focused on T cell populations and tumour cells using custom-built bioinformatic methods[422]. Therefore, taking advantage of the digital coordinate information from the mIHC platform, this Chapter aims to develop a bioinformatics tool to investigate TAM heterogeneity at a single-cell level.

The spatial analysis tool developed in this study was based on methods described by Carstens *et al,* 2017[422], Feng *et al.,* 2017[423], Lizotte *et al.,* 2016[424] and on the PerkinElmer website.

3.1.5 Selection of immunohistochemical markers

A total of seven surface and intracellular markers were utilised for mIHC and are referred as the multiplex TAM panel. DAPI was used for staining cell nuclei[425]. AE1AE3 (pan-cytokeratin) was chosen to identify tumour cells of an epithelial origin[426] and the immune-checkpoint marker PDL1 was included[129]. The remaining four markers, CD68, IRF8, CD206 and CD163, were selected to maximise the representation of macrophage phenotypes described in §1.4.1 within the limitations of the OPAL system.

CD68, or macrosialin, is one of the most well-established pan-macrophage markers[427-429]. It is a highly glycosylated protein that is predominantly expressed by mononuclear phagocytes[430, 431]. It is located on the surface of endosomes and lysosomes[432] and on the cell membrane[433]. CD68 has been shown to be functionally associated with oxidised low-density lipoprotein deposition[434], apoptotic cell clearance[435, 436] and antigen processing[437] but not directly to antigen presentation or its immune response[429, 438].

The interferon regulatory factor 8 (IRF8) was chosen as a marker for M1-like macrophages[439, 440] which was shown to be upregulated in these macrophages after induction by LPS[441] and IFN-γ[442]. IRF8 has been shown to drive macrophage differentiation[443] and maturation[444], enhance protective functions

against infections[440, 445] and antigen-presentation[446] and is associated with improved survival of patients with breast and renal cell carcinoma[442, 447].

The mannose receptor, CD206, is expressed broadly by the M2-like macrophages polarised with M-CSF, IL-4 and IL-13[183, 448, 449], TAMs[450] and certain dendritic cells[451, 452]. Tissue-resident macrophages[453] (e.g. peritoneal, interstitial and alveolar macrophages) also express CD206 at different levels[454]. Functionally, CD206 is associated with phagocytosis[455], antigen cross-presentation[451, 452], and the clearance of excess glycoproteins from the circulation[456].

Elevation of CD163 is more restricted to subsets of macrophages, especially the M2c population polarised with IL-10 but not with IL-4 and 13[313, 457-459]. CD163 is also a marker for liver-resident macrophage[460] (Kupffer cells), peri-vascular macrophages[461] and for TAMs[237, 462]. Functionally, CD163 is a high-affinity scavenger receptor targeting the haptoglobin-hemoglobin complex[463] and high mobility group box 1 (HMGB1) protein[464], and acts as a sensor for bacteria[465]. Both CD206 and CD163 on macrophages can be cleaved from the cell membrane upon activation; therefore, soluble forms of these receptors have been proposed as biomarkers in pulmonary tuberculosis[449] and liver cirrhosis[460], respectively.

3.2 Aims

Aim 1: To optimise a multiplex immunohistochemistry panel for macrophage markers

Aim 2: To develop a bioinformatic analytic tool which allows for the determination of spatial relationships between macrophages and tumour cells in the context of GC

Aim 3: To define and validate bioinformatic criteria used for spatial analysis comparisons which reflect the visual co-localisation of the cells in an image

Major findings on the characterisation of TAM populations from the Chapter have been published[466]. The manuscript is included as Appendix 1.

3.3 Results

3.3.1 Cohort selection

56 FFPE GC specimens from 56 different patients were selected from the MAUGIC cohort (see Section 2.1) representing known GC histological and molecular subtypes. These cases were also selected on the basis of: (i) availability of comprehensive clinical information and (ii) adequate tissue to allow good quality multiplex IHC staining. They will be referred to as the "**OPAL study cohort**". All patients had undergone surgical resection and had at least 10 years follow-up[68]. Figure 3.3.1 is a Consort diagram that outlines the selection of 56 patients that satisfied all the criteria to be included in the **OPAL study cohort**. (Figure 3.3.1 and Table 3.3.1). Potential bias may exist for the size of the study cohort; however, due to technical limitations, only a subset of patients of the MAUGIC cohort can be included for this approach.

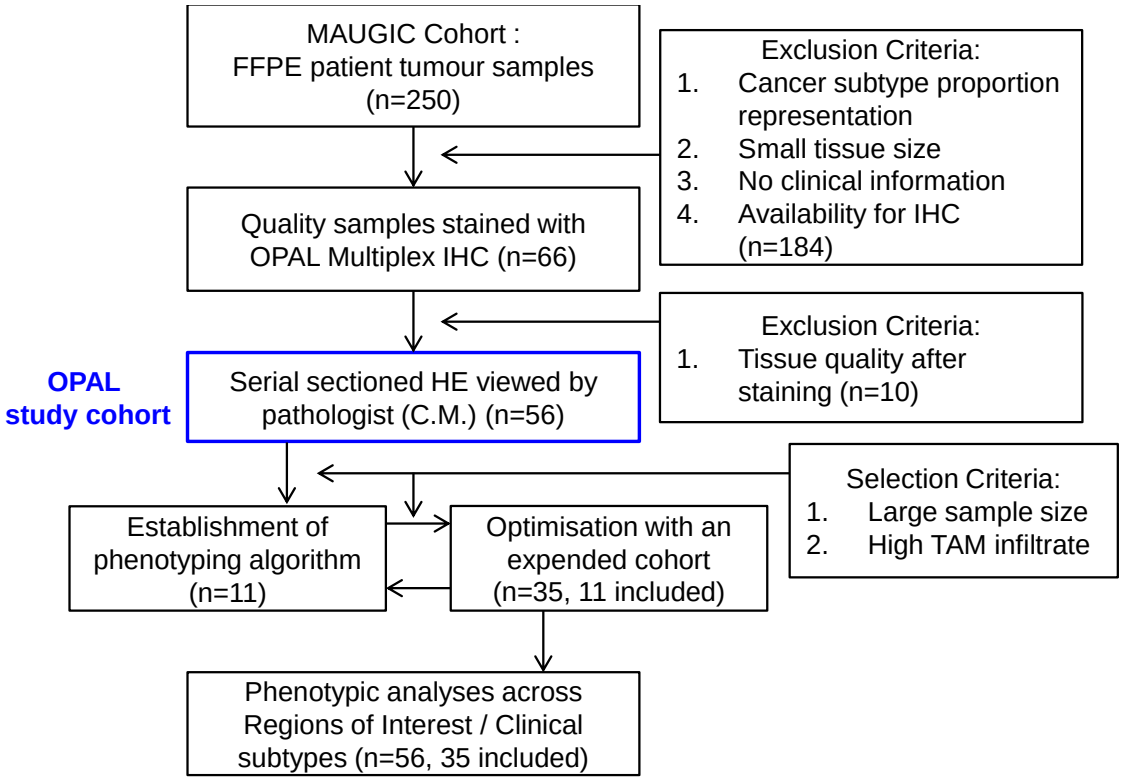


Figure 3.3.1 Consort diagram of OPAL study cohort

Table 3.3.1 Clinical and pathological characteristics of the OPAL study cohort

Groups		n	% in cohort	Groups		n	% in cohort
Age	40-49	5	8.93	T stage	T1	3	5.36
	50-59	16	28.57		T2	13	23.21
	60-69	12	21.43		T3	39	69.64
	70-79	16	28.57		T4	1	1.79
	80-89	6	10.71	N stage	N0	23	41.07
	90-99	1	1.79		N1	18	32.14
Gender	Female	20	35.71		N2	10	17.86
	Male	36	64.29		N3	5	8.93
Histological subtype (Laurén)	Intestinal	37	66.07	M stage	M0	53	94.64
	Diffuse	18	32.14		M1	3	5.36
	Mixed	1	1.79	AJCC 6th	AJCC 1+2	29	51.79
Molecular subtype (TCGA)	EBV	4	7.14		AJCC 3+4	27	48.21
	MSI	9	16.07	Recurrence	Yes	30	53.57
	GS	17	30.36		No	24	42.86
	Other	26	46.43		ND	2	3.57
ND: Not documented. Table from[466].							

3.3.2 Multiplex immunohistochemistry panel optimisation

Each of the selected macrophage markers in the mIHC panel was first optimised individually using appropriate positive controls (Figure 3.3.2A) to establish optimal antibody concentration (Table 2.2.1). For the purpose of multiplexing, markers were then assigned tyramide signal amplification (TSA)-dyes of different wavelengths (Figure 3.3.2B) to avoid spectral overlap between targets located at same regions of the cells (Table 2.2.1 and Figure 3.3.2C). The quality of staining was further assessed using a separate image-analysis program (ImageJ; Figure 3.3.2D and E) and compared between different GC patient tissues to confirm that the final antibody panel selection and ordering were appropriate for the majority of tissues in the **OPAL study cohort** (Figure 3.3.3). The optimised conditions for this panel are listed in Table 2.2.1 and a library containing a spectrum signature of each TSA-dye was built using the single-stained positive control tissues (Figure 3.3.2A; related to Table 2.2.1).

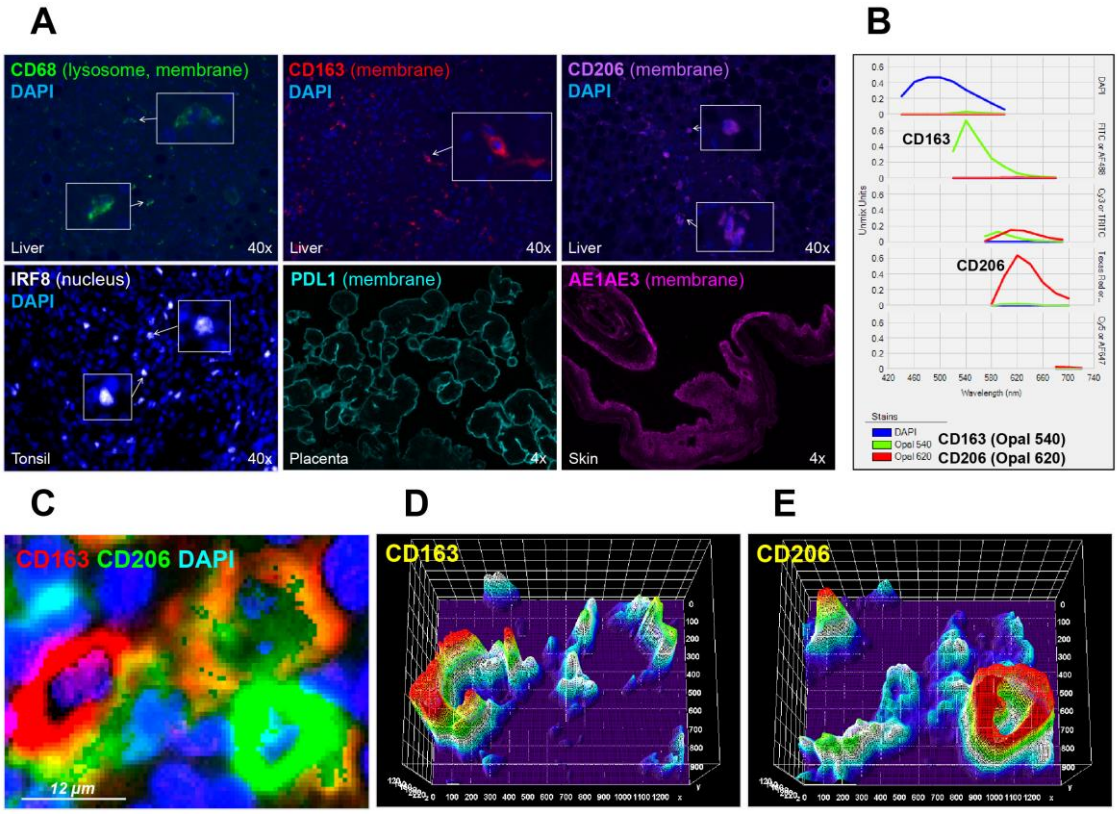


Figure 3.3.2 Optimisation of multiplex TAM panel

(A) Single-stained IHC of multiplex TAM panel markers on corresponding control tissues. Cellular location of each marker is as labelled, related to Table 2.2.1. The same images were used for the establishment of a spectrum library of each TSA-dye. (B) Examples of spectrum library showing macrophage marker allocated on TSA-dyes of different spectral wavelengths with minimum overlaps. (C) Co-localised CD163+ (CD206-; left), CD163+CD206+ (middle) and CD206+ (CD163-; right) macrophages. 3D-marker intensity plots of (D) single-stained CD163 and (E) CD206 from (C). Data analysed with inForm and ImageJ.

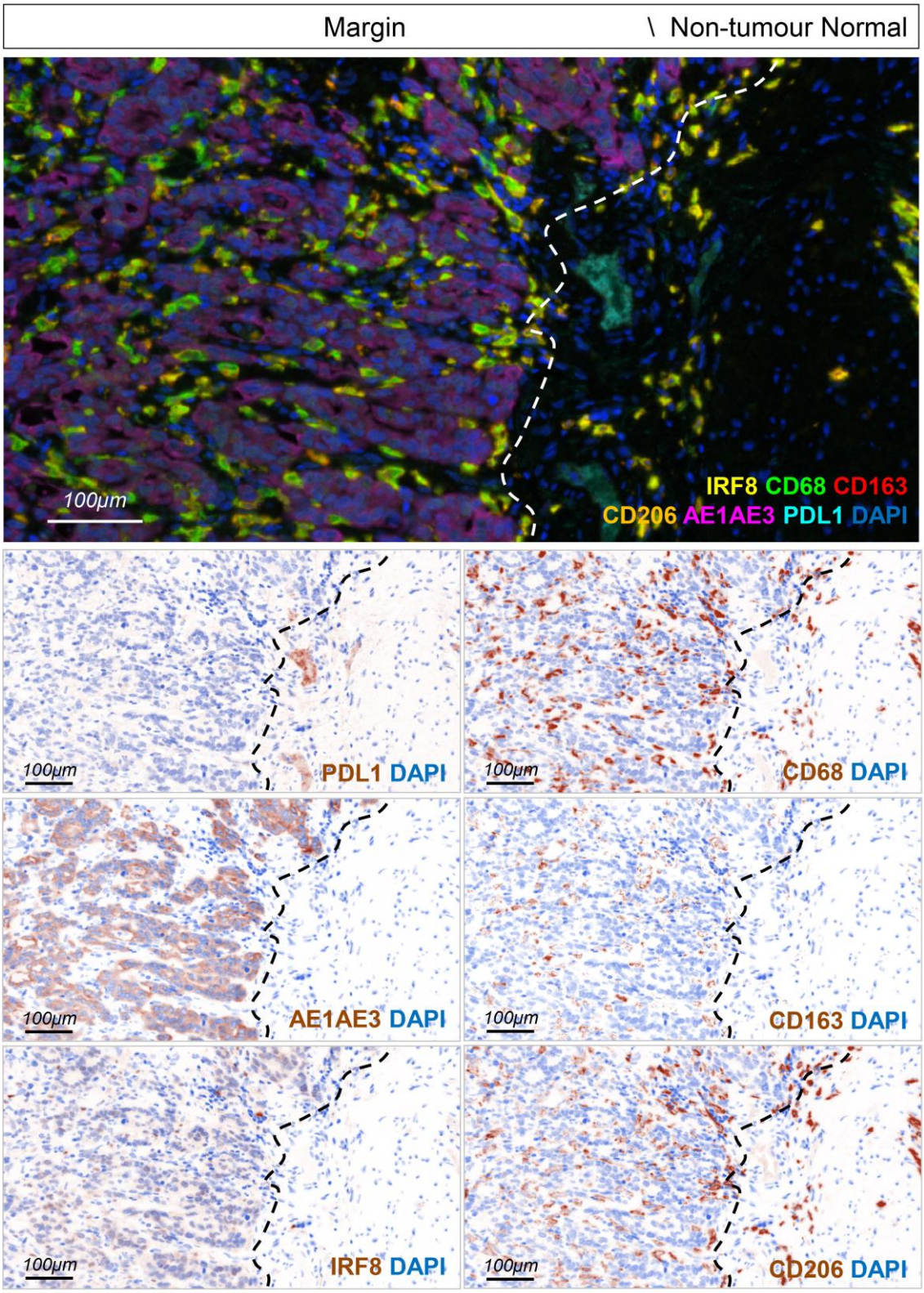


Figure 3.3.3 Optimised multiplex TAM panel

Representative images of composite and single-stained multiplex TAM panel. Dashed line: interface of tumour Margin and adjacent non-tumour normal tissue.

3.3.3 Cell phenotyping

A tissue section from each of the fifty-six selected GC cases (Table 3.3.1) was stained with the optimised multiplex TAM panel and imaged using the Vectra microscope. A total of 1803 high power images comprising 929 from the Core (52%), 228 from the Edge (13%), 386 from the Margin (21%), and 260 from the adjacent Normal tissue (14%) were acquired across the ROIs (Table 2.2.5). Images from eleven high quality, representative tissues within the OPAL study cohort were selected and spectrally-unmixed using inForm software (Figure 3.3.1 and Figure 3.3.3). These images were then viewed thoroughly for establishing a supervised algorithm with inForm for subsequent tissue-area segmentation (Figure 3.3.4) and cell phenotyping based on the theoretical gating strategy derived from the literature for TAMs[183, 417, 420] (Figure 3.3.5 and Figure 3.3.6). Tissue areas, including tumour-nest[137] (AE1AE3+) and stroma (AE1AE3-), were segmented in each image (Figure 3.3.4).

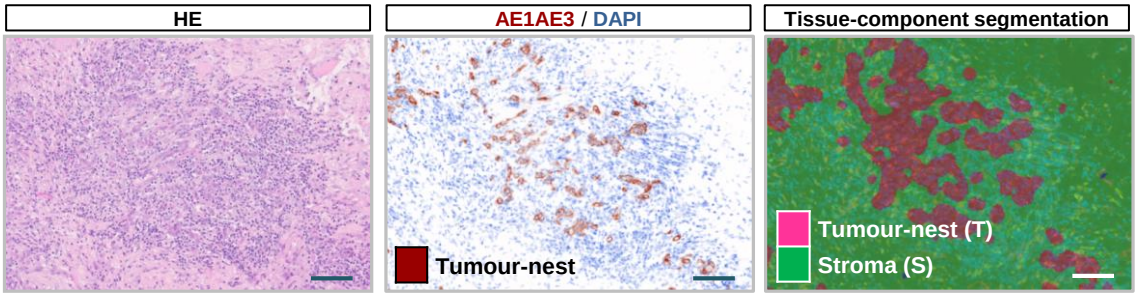


Figure 3.3.4 Definition of tumour-nest and stromal areas

Representative H&E, single-stained IHC, and tissue-component segmentation of the same region analysed using inForm software. Figure from[466].

Twenty-four additional cases of the OPAL study cohort were then included for further optimisation of the algorithm. Finally, all fifty-six cases of the **OPAL study cohort** were analysed with the optimised algorithm on a case by case basis (Figure 3.3.1). Macrophages were first identified based on positive staining for the pan-macrophage marker CD68 and negative AE1AE3 staining (Figure 3.3.5A and Figure 3.3.6). With the unique co-expression of macrophage markers, seven major TAM populations were identified and characterised in GC using the gating strategy (Figure 3.3.5A).

Macrophages were then further divided into subpopulations based on the positivity and intensity of other markers (Figure 3.3.5B and Figure 3.3.6). Two populations classified as ‘M1-like’ TAM populations were identified based on negative staining of CD206 and CD163 and five ‘M2-like’ TAM populations were also defined (Figure 3.3.5A and Appendix 2B). The CD68+ macrophages were only positive for CD68, whereas the CD68+IRF8+ TAMs were characterised with positive nuclear IRF8 staining (Figure 3.3.5C, Figure 3.3.6 and Appendix 2A). CD68++CD163+ TAMs could be distinguished from CD68+CD163+ TAMs based on significantly different levels of CD68 expression (represented with an additional plus sign), and both were in the absence of CD206 (Figure 3.3.5 and Figure 3.3.7). Populations negative for CD163 staining were separated using differential CD206 expression into CD68+CD206++ and CD68+CD206+ (Figure 3.3.5, Appendix 2C and 2D). The final CD68+CD163+CD206+ population expressed all three markers (Figure 3.3.5 and Appendix 2B).

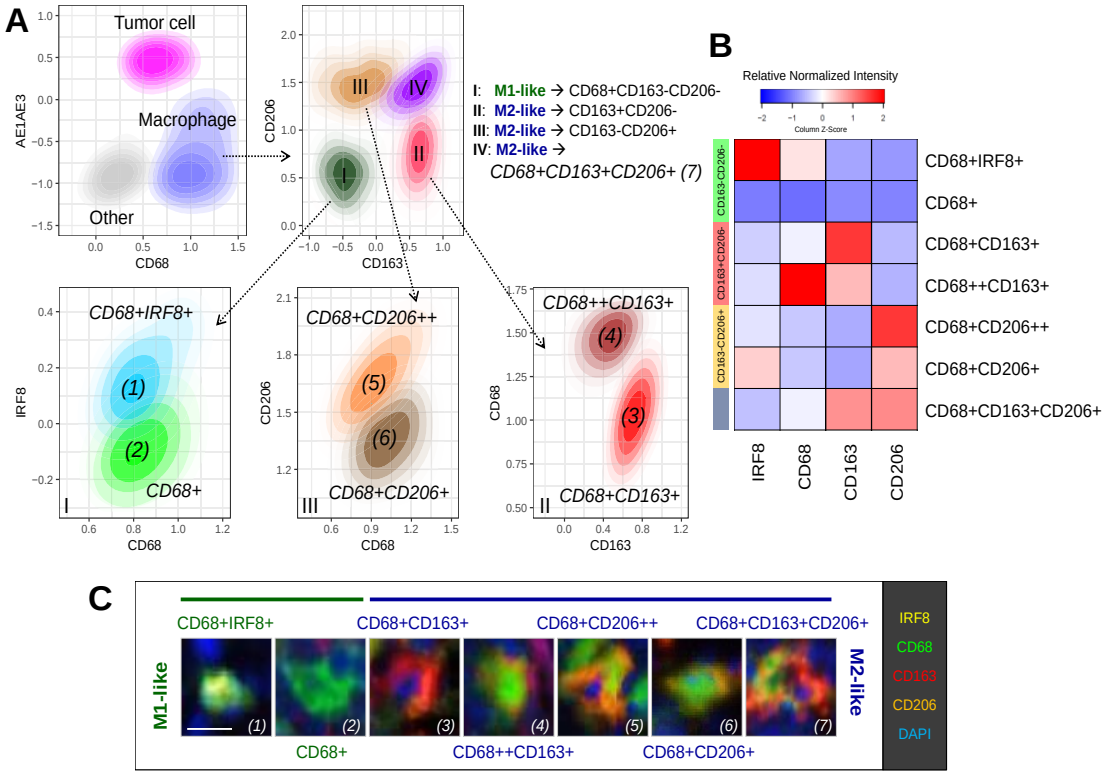


Figure 3.3.5 Seven predominant TAM populations in gastric cancer

(A) Multiplex IHC TAM marker gating strategy of different cell populations. (B) Combined marker signature of each TAM population. (C) Representative images of predominant TAM populations. Numbers on the image correspond to the numbered cell populations in (A). Figure from[466].

The individual TAMs for all patients were plotted based on their CD68, CD163 and CD206 intensities (Figure 3.3.8A) providing evidence of a spectrum of macrophages in three-dimensional space. The average intensity of each marker was determined on a per patient basis (Figure 3.3.8B) confirming that all seven TAM populations were represented within each individual patient specimen.

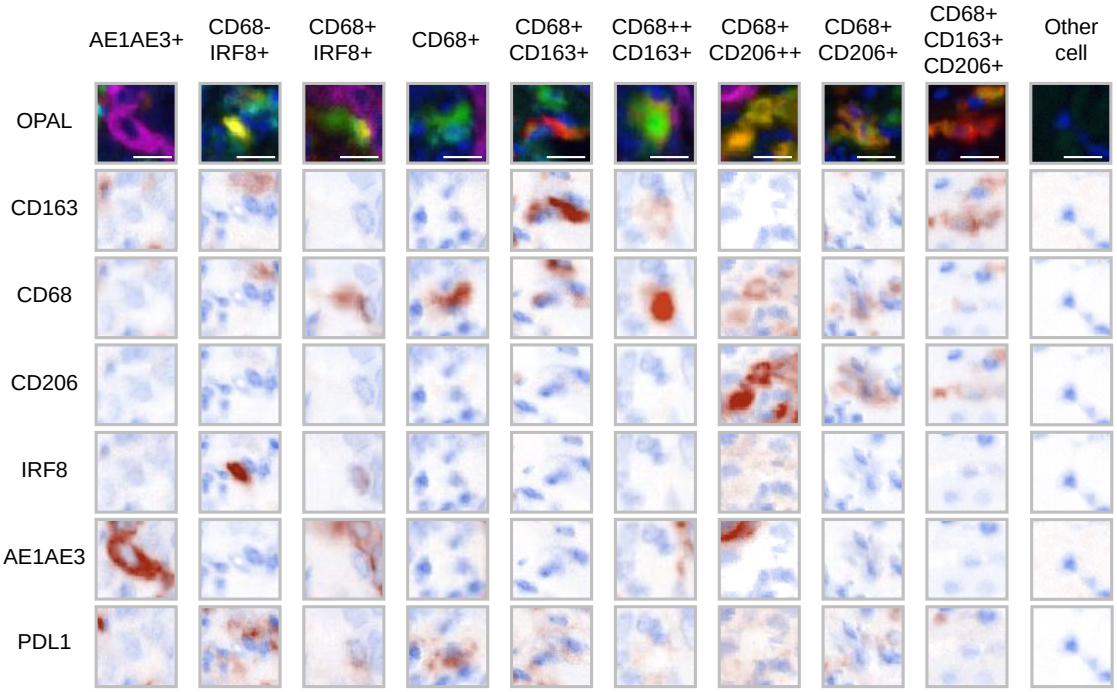


Figure 3.3.6 Representative images of cell populations defined with the multiplex TAM panel

Yellow: IRF8, Green: CD68, Red: CD163, Orange: CD206, Magenta: AE1AE3, Cyan: PDL1, Blue: DAPI. Single-stained IHC colour: Blue: DAPI, Brown: Positive staining of markers as indicated (+). Relative intensity between cell types is represented (++). Scale bar: 10 µm. Image from[466].

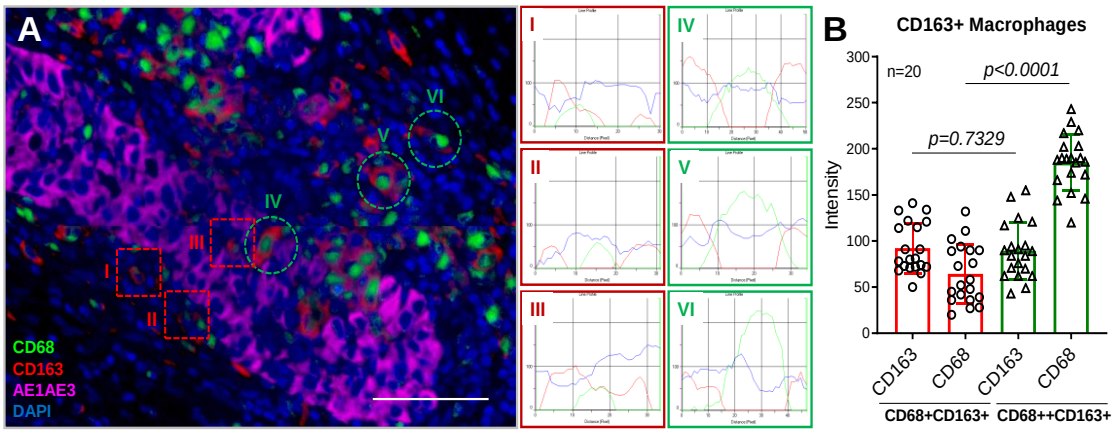


Figure 3.3.7 Distinguishing CD163+ (CD206-) M2-like TAM populations

(A) Representative image of the CD68+CD163+ and CD68++CD163+ TAMs and marker intensity of CD68 and CD163 on TAMs analysed with the ImagePro software. Intensity of markers on numbered cells were plotted in the matched numbered plots. Red square: CD68+CD163+ TAMs, Green circle: CD68++CD163+ TAMs. X axis: Distance in pixels, Y axis: Intensity of marker. Colours in the plots: CD163 (red), CD68 (green) and DAPI (blue). Scale bar: 100 µm. (B) Quantification of the maximum intensity of CD68 and CD163 expressed on the TAMs (n=20 for each population) in (A). Bar and error bars represent mean ± SD, Mann-Whitney U test. Figure from[466]. Similar validation with ImagePro on the CD206+ (CD163-) TAM populations is provided in Appendix 2C and D.

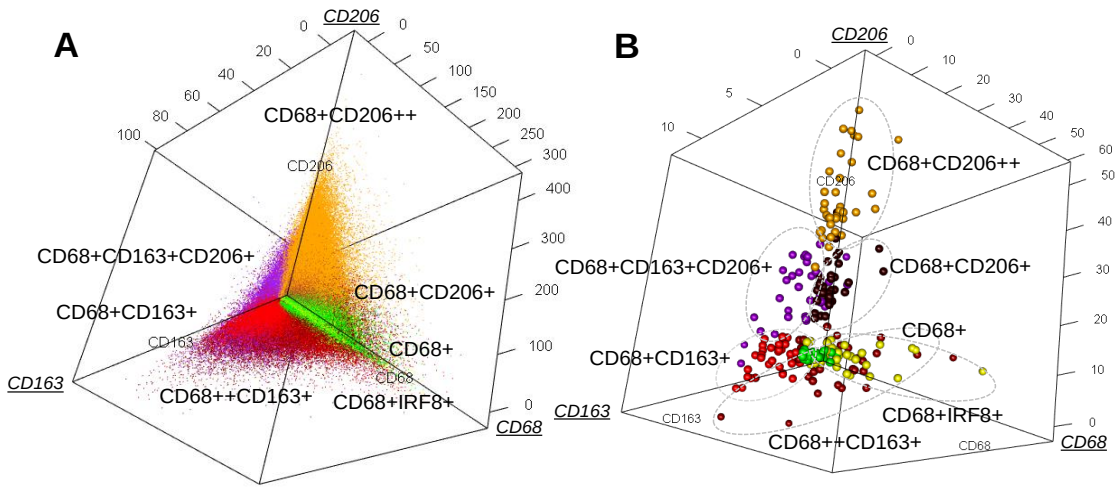


Figure 3.3.8 Three-dimensional distribution of macrophage markers

(A) Single cell intensity of individual cells (n=8.5×10^6 from 56 patients). (B) Average intensity of individual patient samples (n=35 with high quality Core region data). Figure from[466].

3.3.4 Validation of cell phenotyping

To validate the performance of the supervised inForm phenotyping algorithm across different patient samples and ROIs, 100 cells were randomly subsampled from the different TAM populations per patient within each ROI in the tumour regions (Core, Edge, and Margin) as a validation cohort. The subsampling was repeated 2000 times to create 2000 validation cohorts. Three different aspects were validated including (i) the "robustness" of the algorithm, (ii) the "number" of TAM populations identified with mIHC, and (iii) the consistency and reproducibility of TAM population using different methods.

Firstly, the statistical robustness of the algorithm (Figure 3.3.9A) was examined by comparing the median TAM marker expression signatures of each TAM population in each patient per ROI in each validation cohort with the overall expression signature of the study cohort (Figure 3.3.5B) using Pearson correlation ($p<0.05$). The results showed that for each patient subsampled data, the robustness of TAM phenotyping was over 99% in the Core and Edge and at least 96% accurate at the Margin across repeated testing (Figure 3.3.9A).

Secondly, the number of TAM populations identified with the multiplex TAM panel was assessed with an unsupervised clustering method using a subset of the subsampled validation cohorts (n=500 of the 2000). The "within group sum of squares" values of different ROIs were computed using the K-means unsupervised clustering method[31, 467] (Figure 3.3.9B). According to the "elbow" method[467] for clustering, the results showed that for all ROIs, the optimal number of clusters was between 5 and 7 (Figure 3.3.9B). This was consistent with the results from the supervised algorithm which identified seven predominant TAM populations.

Lastly, the consistency and reproducibility of the TAM groupings were compared between the unsupervised (K-mean) clustering and the supervised (inForm) methods. The median marker expression signature of each cluster determined with the unsupervised method was compared (Pearson correlation) with the expression signature of TAM populations identified with inForm (Figure 3.3.5B). TAM population was defined as "rediscovered" if the two signatures

significantly passed the correlation test ($p<0.01$). The rediscovery rate was calculated for each TAM population per ROI (Figure 3.3.9C).

The results indicated that within the optimal clustering range (5-7), all TAM populations could be rediscovered, and could better describe the differences between marker signatures of the data compared to the use of 2-4 clusters (Figure 3.3.9C). However, due to the limited number of markers able to be used for multiplex IHC compared to flow cytometry and CyTOF, the unsupervised clustering method cannot clearly differentiate between the CD68++CD163+/CD68+CD163+ pair and the CD68+CD206++/CD68+CD206+ pair (Figure 3.3.10). This explains why seven TAM populations can be identified even when only 5-6 unsupervised clusters were used (Figure 3.3.9C). Nevertheless, using the gating strategy described with the supervised methods and with visual images (Figure 3.3.5), the data clearly showed that there were morphological, distributional and marker intensity differences between these TAM populations (Figure 3.3.5, Figure 3.3.6, Figure 3.3.7 and Appendix 2). When population of TAMs were restricted to be a specific location (Figure 3.3.7), it is reasonable to assume that these TAMs may have biological relevance.

Collectively, the results from these analyses suggest that (i) the phenotyping robustness of the inForm algorithm was above 96% across different ROIs, (ii) the number of TAM populations characterised with the supervised method was within the optimal number of clusters defined by the unsupervised clustering method, and (iii) the distribution of TAMs should be taken into account when identifying TAM populations. This has often been ignored in other studies using unsupervised clustering methods based purely on expression of markers.

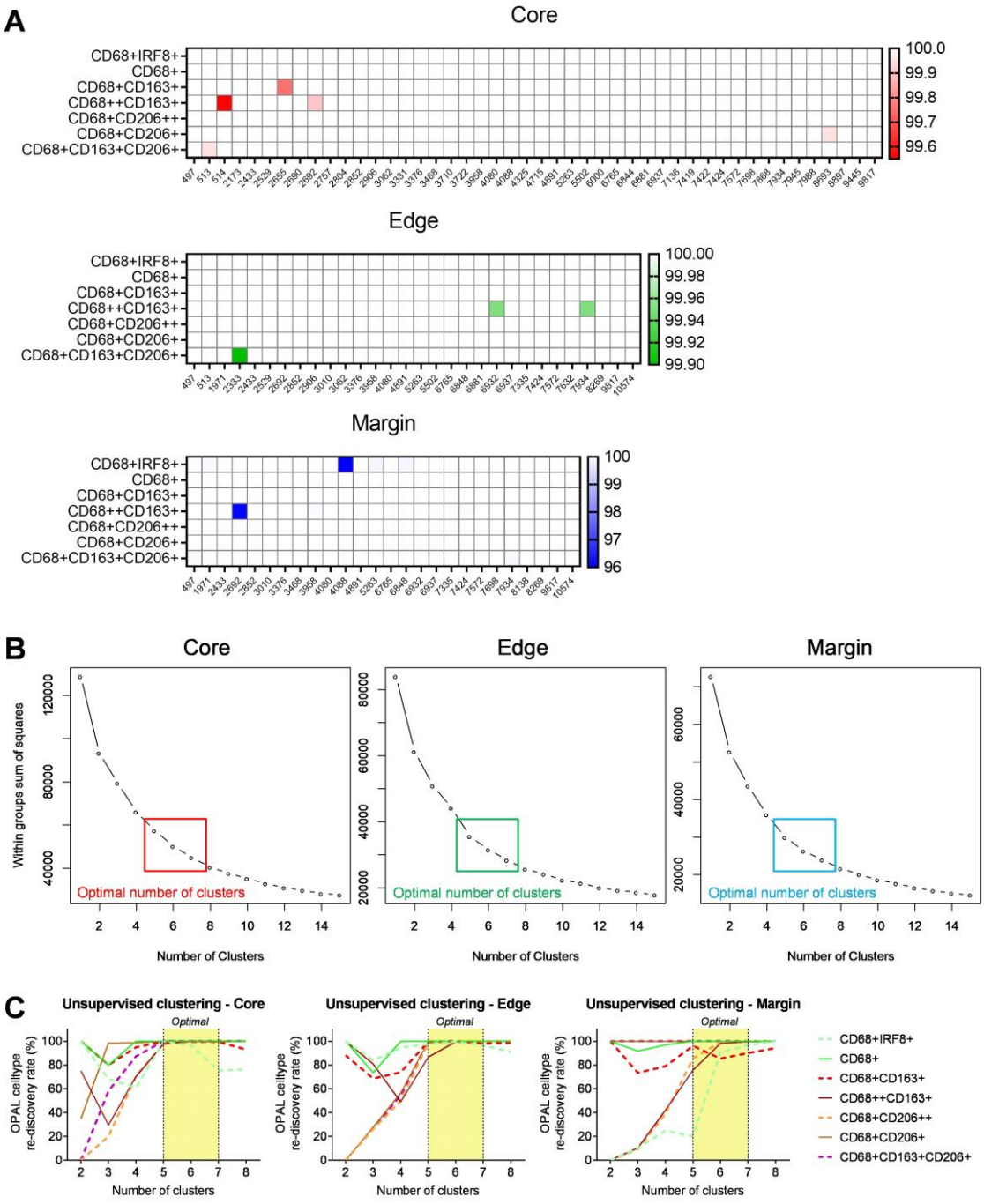


Figure 3.3.9 Validation of cell phenotyping robustness

(A) Heatmaps representing the subsampling robustness of each TAM population per patient (bottom) across ROIs (Pearson correlation, $p<0.05$) compared to overall marker signatures in Figure 3.3.5B. Scale: Accuracy (%) out of 2000 repeats. (B) Theoretical optimal number of clusters defined with the "elbow" method of clustering. (C) TAM population rediscovery-rate of randomly selected samples compared to inForm supervised phenotyping. Discovery-rate determined with Pearson correlation ($p<0.01$) comparing selected cells to the overall marker signatures in Figure 3.3.5B. Figure from[466].

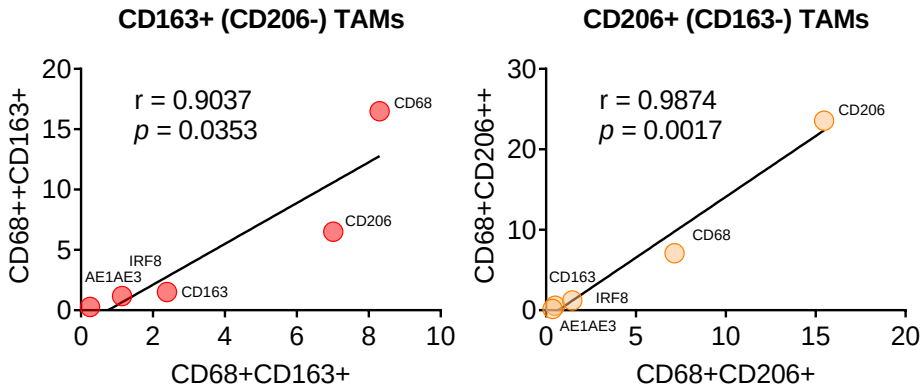


Figure 3.3.10 Pearson correlations between TAM populations

Correlation of combined marker signatures of CD163+ (CD206-) and CD206+ (CD163-) TAM populations in Figure 3.3.5B. X and Y axis: marker normalised intensity.

3.3.5 Distance analysis criteria and model setup

In addition to comparing TAM composition between ROIs, an R software-based bioinformatic package (collaborations with Dr. Minyu Wang and Dr. Yu Sun) was developed to spatially resolve TAM heterogeneity at a cell-to-cell resolution.

In brief, this package, termed “Inter-cellular Spatial Analysis Tool” (ISAT)[412], extracts the x and y coordinates of each cell on an image, and calculates the distance of an individual cell of a cell population (reference cell, RC) to every individual cell in any other given population (nearest cell, NC) within the image (Figure 3.3.11A).

The minimum nucleus-to-nucleus distance of the each RC to NC was documented and the median value of the minimum distance of each RC population (Figure 3.3.11B) was determined for all RC-to-NC combinations (Table 3.3.2). Median, but not average, distance was used for comparisons between RC populations due to the non-Gaussian distribution of the data (Figure 3.3.11C) and because the average could be affected by extreme values in this context.

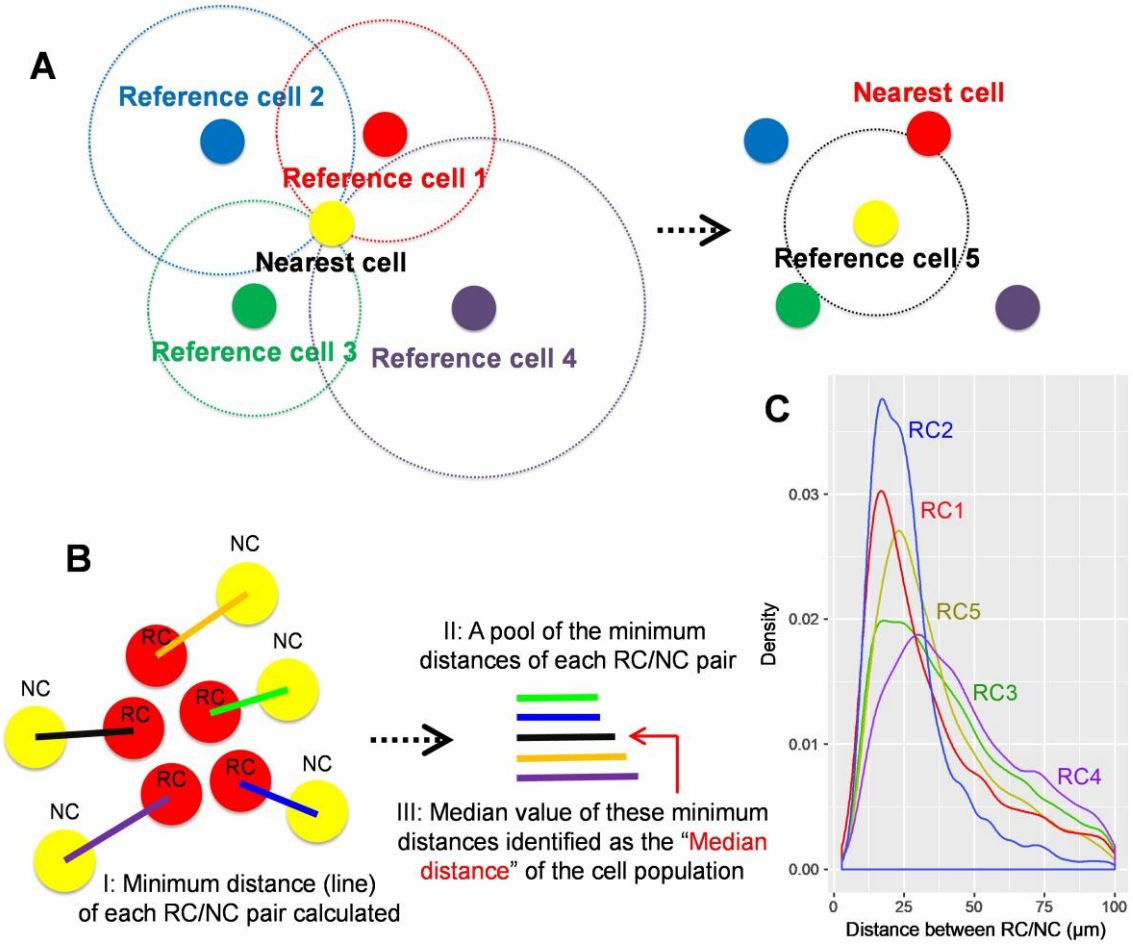


Figure 3.3.11 Diagram of the spatial distribution analysis

(A) Identification of the nearest neighbouring cell (NC) of each reference cell (RC). RC5 (yellow) is the NC for RC1 to 4, and RC1 (red) is the NC of RC5. (B) The minimum distance (each line) was calculated between each RC/NC pair and the median value of these minimum distances was identified as the "Median distance" of the cell population. (C) Non-Gaussian distribution of the distance data between RC/NC pairs. Y axis represents the probability density function calculated with the Kernel density estimation. Plotted with "ggplot2" in R plot.

Table 3.3.2 Median distance between cell populations of the multiplex TAM panel

Core - Median distance (μm) / Nearest cell	Reference cell							
	CD68+ IRF8+	CD68+	CD68+ CD163+	CD68++ CD163+	CD68+ CD206++	CD68+ CD206+	CD68+ CD163+ CD206+	AE1AE3+
CD68+IRF8+	--	73.04	80.93	65.82	96.91	75.92	97.85	71.01
CD68+	15.95	--	16.68	15.63	17.92	14.23	16.86	26.79
CD68+CD163+	49.23	42.8	--	32.15	51.03	51.52	35.57	62.65
CD68++CD163+	37.52	40.59	29.52	--	47.73	46.36	38.76	50.24
CD68+CD206++	41.92	32.91	37.25	38.3	--	27.95	20.56	42.27
CD68+CD206+	56.66	51.31	55.23	56.29	55.78	--	48.67	67.18
CD68+CD163+CD206+	47.63	35.62	25.12	34.95	24.71	30.29	--	52.18
AE1AE3+	12.31	21.74	17.87	16.9	20.34	15.02	23.8	--

- Red / White / Blue: Smallest / Medium / Largest value of each row.

To define which cell type(s) should be referred to as reference and nearest cell, for the interest of this study and to fit the bioinformatics tool design, both tumour and TAM populations were used as RCs and NCs and the results were compared (Figure 3.3.12). The multiplex IHC images showed that certain TAM populations were preferentially located within specific tumour regions. If tumour cells were used as RCs, TAM populations located in different ROIs would still be identified as the NCs irrespective of their location (Figure 3.3.12A). This issue can be circumvented if the TAMs are used as the RCs, and takes into account the preferred location of the TAMs in the tumour microenvironment (Figure 3.3.12B).

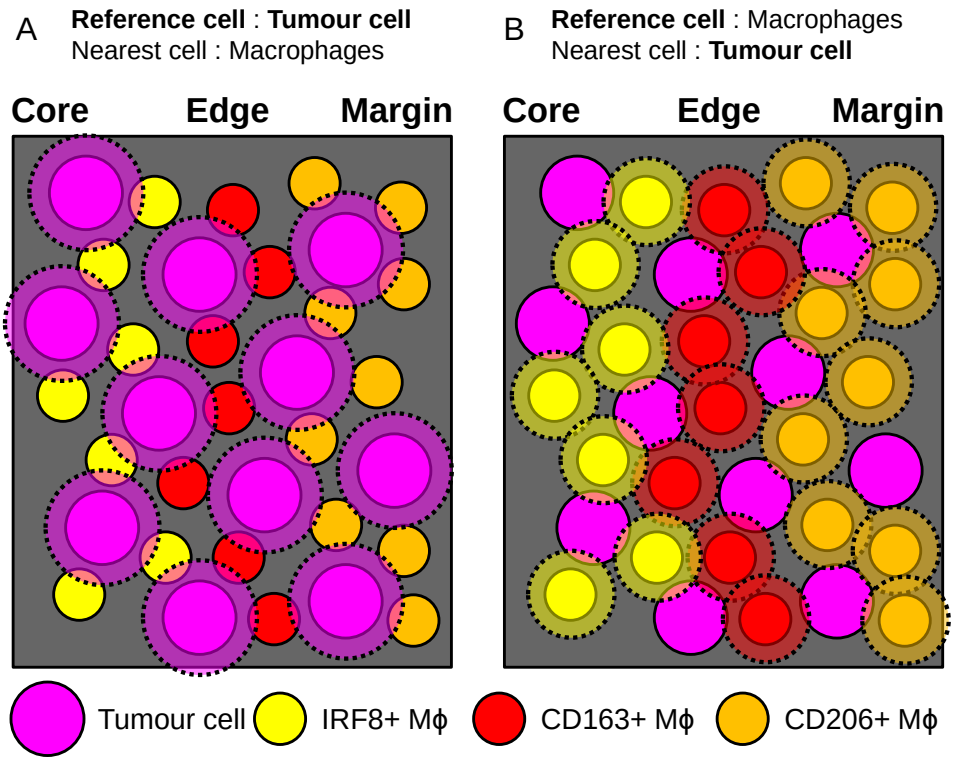


Figure 3.3.12 Reference and nearest cell population selection

Dashed line and semi-transparent coloured area: distance with the nearest cell of each reference cell. Related to Figure 3.3.11A.

The correlations between cell density and the median distance of each cell population were investigated (Spearman correlation; Figure 3.3.13). TAMs were used as RCs as described in Figure 3.3.12, and their distance to the tumour cells (NCs) was calculated (Table 3.3.2). The results showed that there were no correlations between the density of RCs and their distance to NCs, suggesting that TAMs were not randomly distributed in the tumour microenvironment (Figure 3.3.13A and Figure 3.3.14). On the contrary, the tumour cell density negatively correlated with the minimum distance of every TAM population suggesting that there was no locational preference from the tumour cells (Figure 3.3.13B and Figure 3.3.14). These results further support the decision of using TAMs as RCs rather than using the tumour cells for subsequent studies.

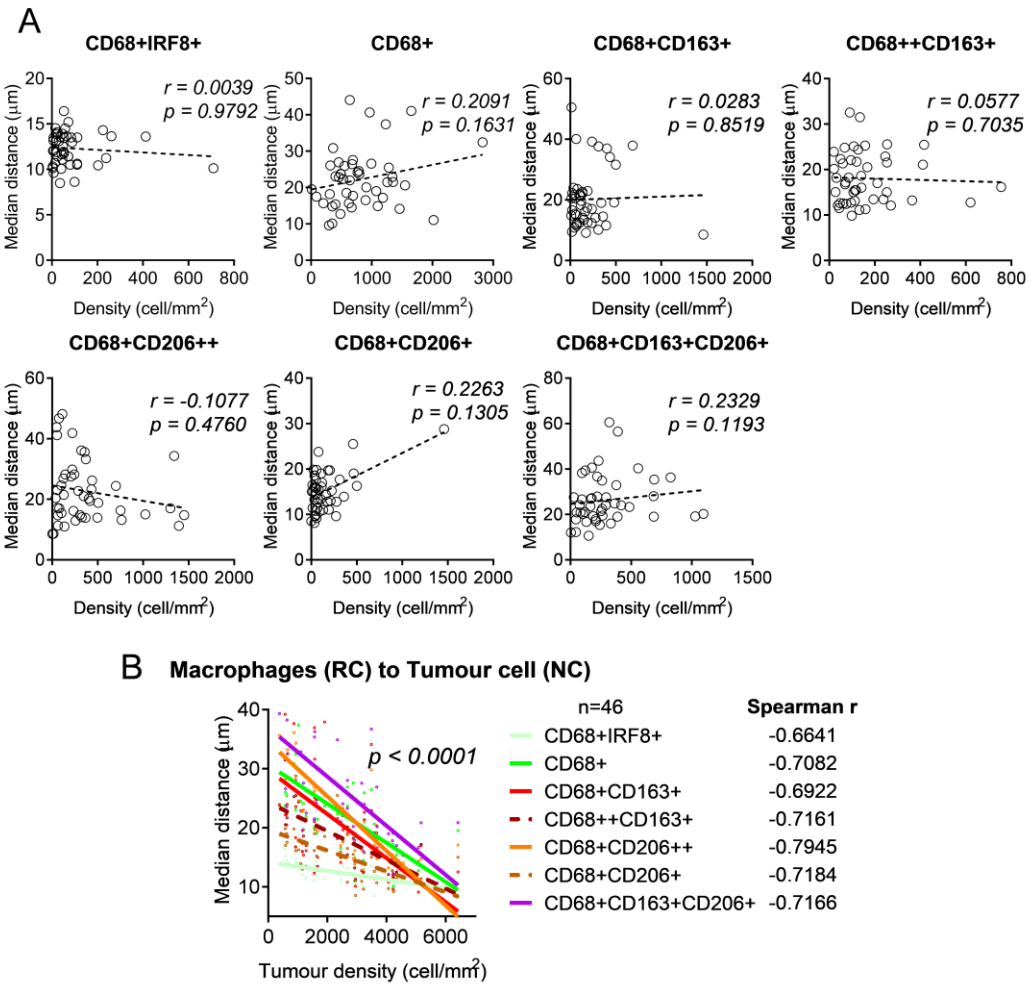


Figure 3.3.13 Correlation of cell density and minimum distance

Spearman correlation between the median distance of each TAM population (RC) to tumour cell (NC) and density of (A) corresponding TAM population and (B) tumour cell.

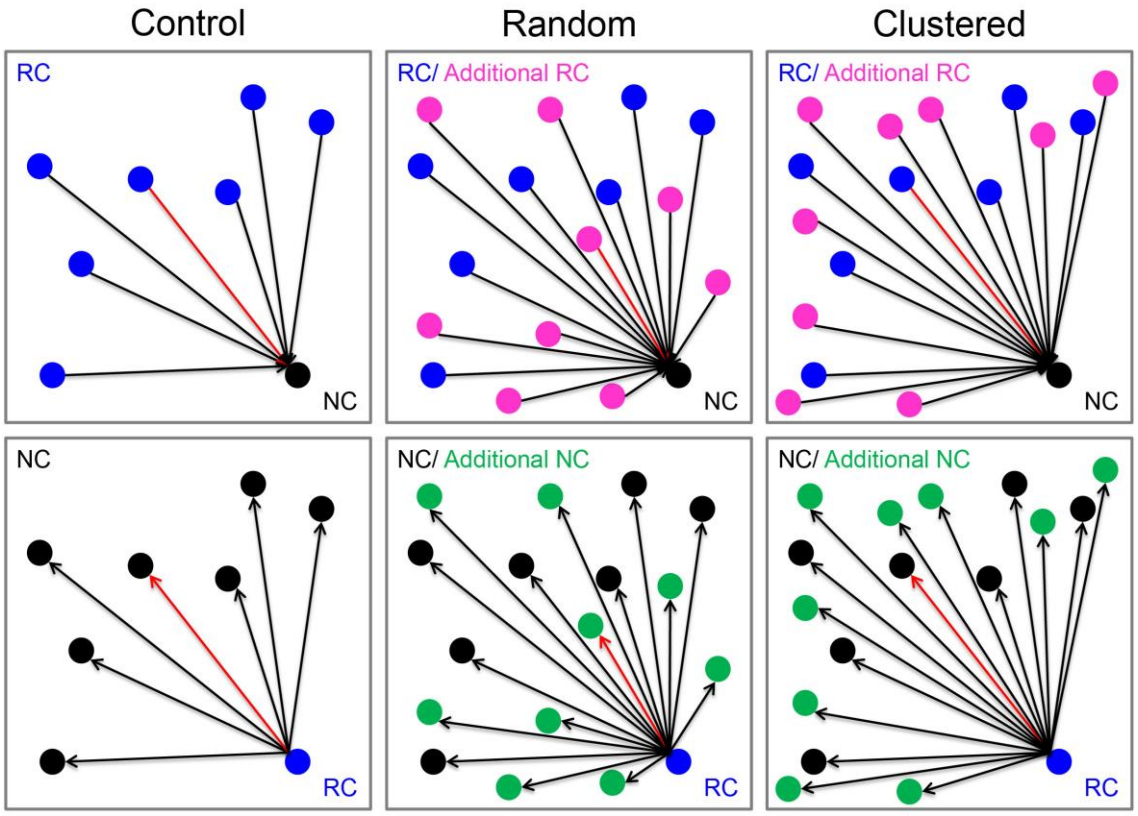


Figure 3.3.14 Schematic relationship of increased cell density with median distance between RC/NC

Median distance reduces if the increase in RCs (pink; or NCs in green) were of random distribution and remains similar if the RCs (or NCs) were clustered.

Finally, to define a bioinformatic distance threshold for direct contact between RCs and NCs that could reflect the actual visual co-localisation of cells in an image, the distances of cells in direct contact were analysed with the ImagePro software (Figure 3.3.15). Cell pairs in direct contact were identified and the distance between the nuclei were labelled (1 pixel equals 0.5µm; n=20 pairs). The results show that the median direct contact distances in different ROIs were similar: approximately 8.5 µm with an upper 95% confidence interval at around 9.5 µm. Based on this result, a 10 µm threshold between cells was defined as direct contact for the analysis.

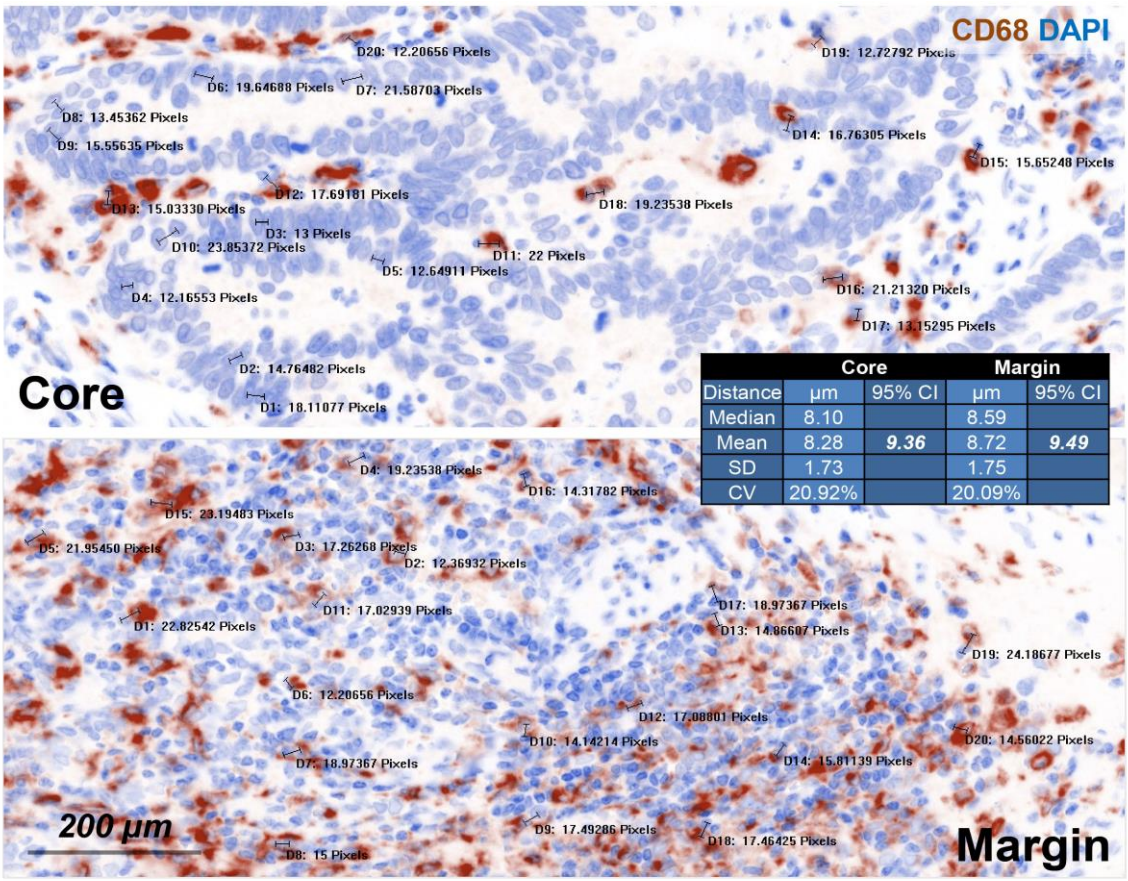


Figure 3.3.15 Defining direct contact distance criterion between cells

Twenty cell pairs (as numbered) per ROI were randomly selected and were used to define the numeric distance of visual direct contact. Cells were identified visually with the ImagePro software and their distances in between were identified labelled (in pixel, 1 pixel = 0.5 µm). Statistical results are presented in the Table.

3.4 Discussion and Conclusions

In this Chapter, an **OPAL study cohort** (n=56) was selected from the MAUGIC cohort and characterised using the multiplex TAM panel to reveal a high-dimensional, non-linear spectrum model of TAMs in GC. Seven predominant TAM populations were first identified and characterised based on distinct expression of the markers using a supervised approach. This result was then tested with bioinformatic unbiased clustering methods and it was found that the robustness of the supervised method was above 96% accurate in all tumour regions (Core, Edge, and Margin) and that all TAMs were present in all patient samples.

In this Chapter, the creation of a distance analysis tool (ISAT) was described. This was developed and used to validate the relationship between cell density and distance in FFPE tissue at single-cell resolution. The rationale for the use of TAMs as reference cells was outlined to investigate their relationship with tumour cells (defined as nearest cells). Distance of TAMs to tumour cells did not correlate with their overall densities suggesting that the distribution of TAMs was not random but clustered, which might be biologically relevant. A threshold of 10 µm was determined as the criterion to represent visual direct contact of cells observed on the image and will be used for further analyses.

3.4.1 Summary

In summary, this Chapter outlines the earliest part of the Thesis and describes the creation of platforms to enable objective analysis for use in subsequent Chapters that will investigate the spatial heterogeneity of TAMs *in situ*.

Chapter 4 : Spatial mapping of tumour-associated macrophages

4.1 Introduction

It is now recognised that TAMs are comprised of a diverse population of macrophages[189]. However, it remains unclear if certain TAMs populated in specific regions of the tumour and how their spatial location and cellular interactions within the tumour microenvironment may be relevant to clinical characteristics and outcomes of GC patients. In addition, while TAMs have been shown to express high PDL1[295, 468] and were correlated with the stromal PDL1-expressing patterns in GC[134], it has not been investigated if PDL1 was associated with a specific TAM population(s). This may potentially be used as an alternative biomarker or more specific therapeutic target for future treatments, but has not been included in current clinical stratification[130] of patients for immune checkpoint therapy[126] .

To explore these questions, in this Chapter aims to investigate the spatial distribution of the TAM populations (Figure 3.3.5) identified in the previous Chapter. The ISAT spatial method was utilised to measure the distribution of these TAMs to tumour cells in different regions of interest (Core, Edge and Margin; defined in Figure 3.1.1). In addition, PDL1 expression on each TAM population was determined per patient and at single cell level and was compared with proposed methods for defining PDL1-positivity in the literature. Finally, clinical parameters were tested with the TAM densities and also interrogated using both their PDL1 intensity and PDL1+ cell number.

4.2 Aims

Aim 1: To compare the spatial distribution of TAM populations across different regions of interest, in relation to tumour cells and between TAM populations

Aim 2: To investigate the PDL1 expression on different TAM populations

Aim 3: To investigate clinical associations with TAM cell density, cell distribution and PDL1 expression

Major findings on the spatial distribution and PDL1 expression of TAM populations from the Chapter have been published[466]*. The manuscript is included as Appendix 1.*

4.3 Results

4.3.1 Distribution of TAMs across different tumour regions

To examine the distribution of TAMs in the GC microenvironment, the spatial density of the seven TAM populations identified in Chapter 3 (Figure 3.3.5) was analysed within different regions of interest (ROIs). A significant increase in the overall TAM density was found within the tumour (Core, Edge and Margin) compared to the adjacent non-tumour normal regions (Figure 4.3.1A). The TAMs exhibited a more M2-like phenotype at the Margin compared to a significant increased proportion of M1-like TAMs in the Core (Figure 4.3.1B).

The distribution of each TAM population was explored (Figure 4.3.1C and D) and the CD68+CD163+CD206+, CD68+CD206++ and CD68+ macrophages were found to be abundant in all ROIs. However, given their dominant presence in the adjacent normal tissue (grey; Figure 4.3.1C), they are likely to be associated with the normal-tissue macrophages than tumour-associated macrophages. CD68+CD163+CD206+ macrophages accumulated at the Margin and decreased toward the inner Core. In contrast, the number of CD68+IRF8+ macrophages increased significantly from the Margin into the Core which contributed to the shift of the M1-like to M2-like ratio across these regions (Figure 4.3.1B and Appendix 1 Figure S3B). The higher densities

observed for the CD68+CD163+, CD68++CD163+ and CD68+CD206+ macrophages within the tumour compared to the normal tissue suggested that these populations may have been polarised by the local tumour microenvironment (Figure 4.3.1C and D).

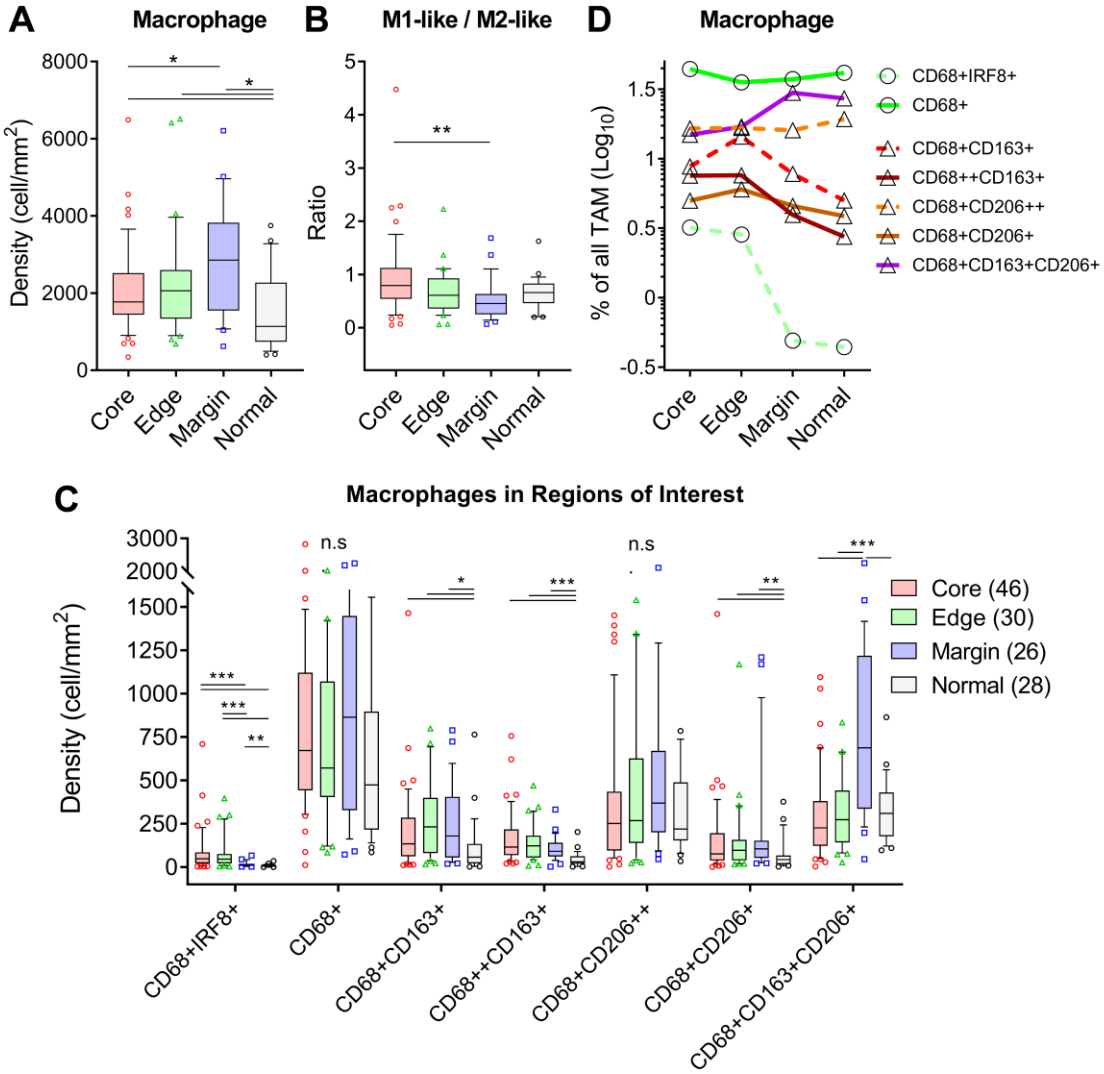


Figure 4.3.1 Distribution of overall macrophage across regions of interest

(A) Overall TAM density (B) M1-like to M2-like TAM ratio. Core: n=46, Edge: n=30, Margin: n=26, Normal: n=28. (C) Each TAM population density. (D) Percentage of TAM populations in all TAMs. Box and whiskers represent mean ± 10-90 percentile. Each point represents one patient. Line represent mean of each TAM population. *p<0.05, **p<0.01 comparing between ROIs. Mann-Whitney U test. Figure from[466].

The spatial relationship of TAMs with respect to the tumour-nest and stromal areas (defined in Figure 3.3.4) was further examined (Figure 4.3.2). The CD68+CD163+CD206+ macrophages were located primarily in the stroma of matched patient samples across different regions of interest. In contrast, CD68+IRF8+ macrophages, were not only more abundant in the Core than at the Margin (Figure 4.3.1D), but were preferentially located within the tumour-nest than in the stroma (Figure 4.3.2). The CD68+CD206+ population was found to be specific to the tumour-nest area (Figure 4.3.2A) but was not related to different ROIs (Figure 4.3.2B).

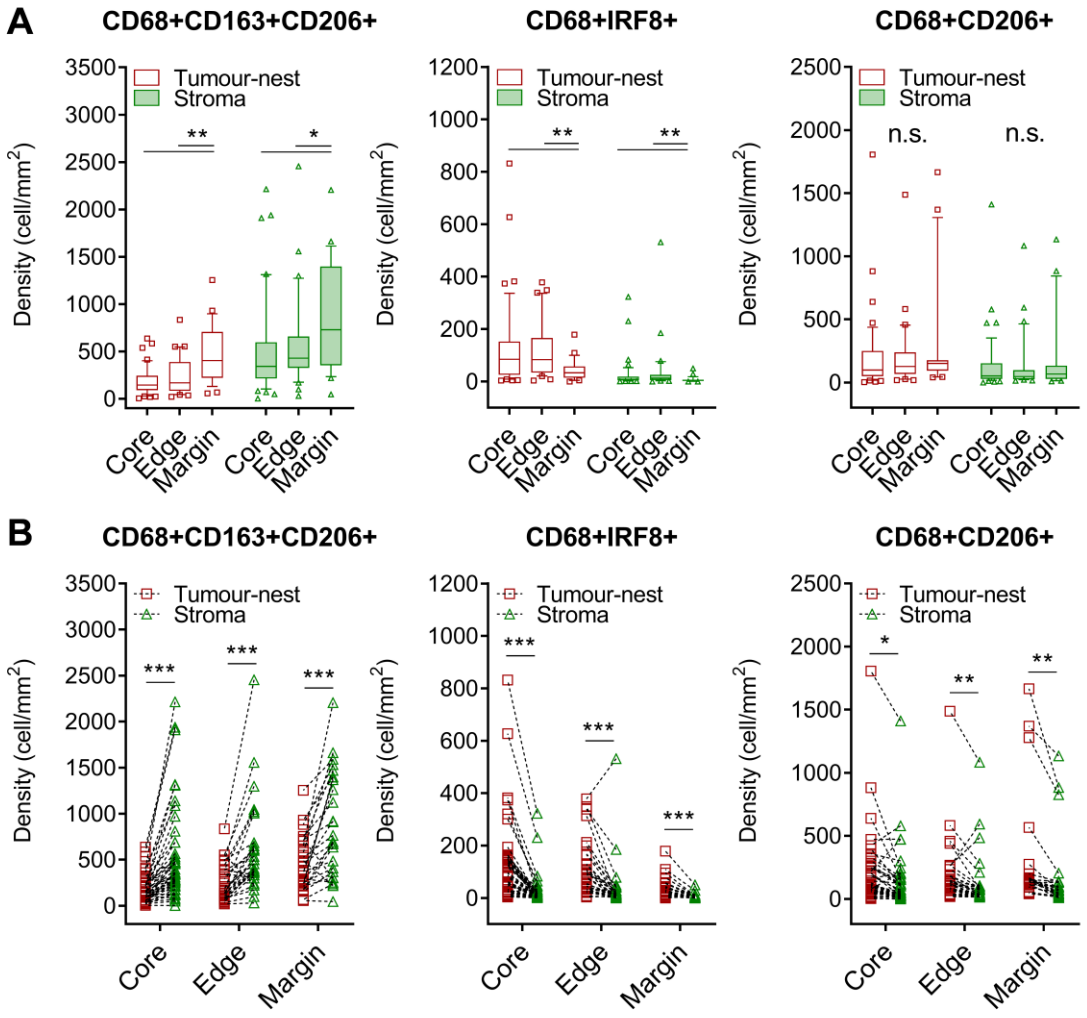


Figure 4.3.2 Distribution of TAMs between tumour areas across ROIs

Density of selected TAM populations between the Tumour-nest and Stroma areas (A) among the ROIs and (B) in matched (dash line) patient samples. Mean ± 10-90 percentile. Each point represents one patient. *p<0.05, **p<0.01, ***p<0.001 and not significant (n.s.) comparing between ROIs. Mann-Whitney U test. Figure from[466].

An analysis of TAMs in GCs of different histological subtypes indicated that a lower cell density was observed in the diffuse subtype compared to the intestinal subtypes (Figure 4.3.3A). Using the more recently described TCGA molecular subtypes (Figure 4.3.3B), cell density was found to be lower in the GS subtype in comparison to the MSI, EBV and Others subtypes (related to §2.1.5). Similar trends were observed in both tumour Core and Edge but not at the Margin, reflecting the locational preference of TAM populations across different ROIs (Figure 4.3.3). No other differences in TAM populations between the tumour-nest and stromal areas and between clinical parameters were found (Appendix 1Figure S3C and F).

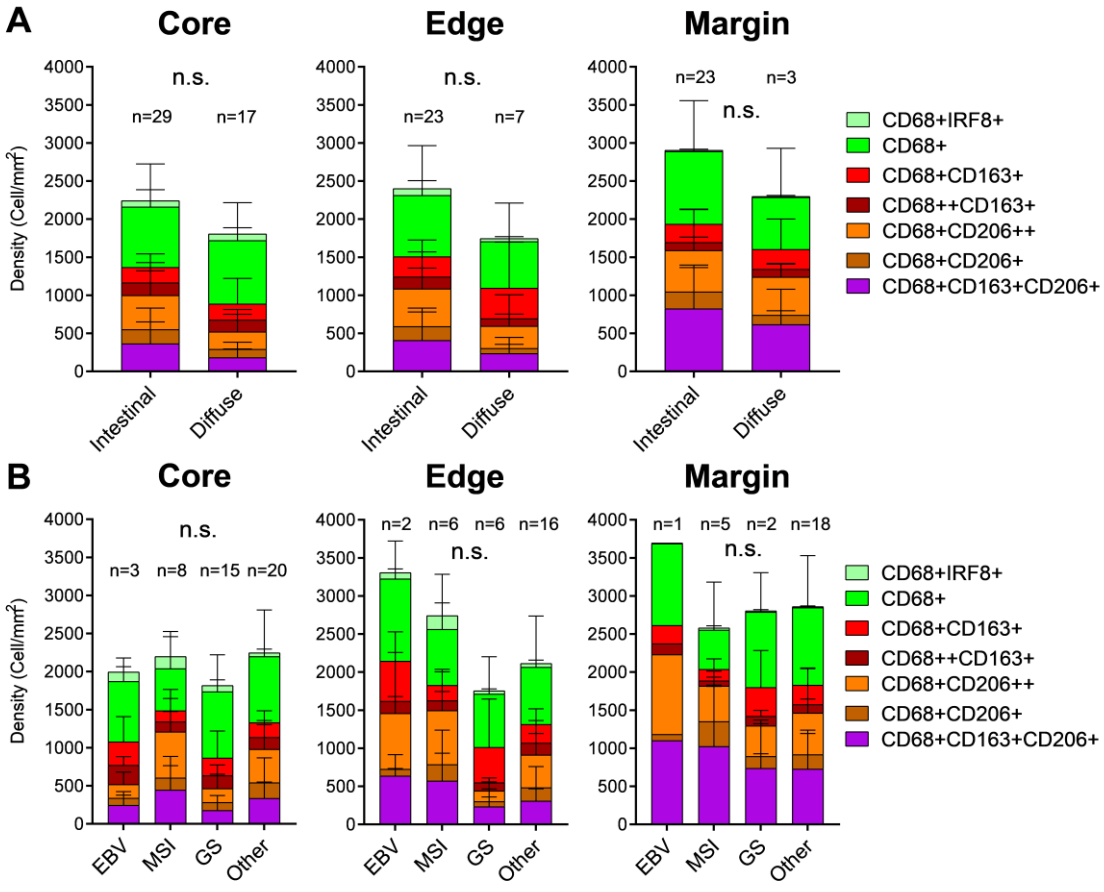


Figure 4.3.3 Density of TAM populations of different cancer subtypes

Bar and error bars represent mean ± SD. Not significant (n.s.) comparing between cancer (A) histological and (B) molecular subtypes. Mann-Whitney U test. Figure from[466].

4.3.2 Distribution of TAMs in proximity to tumour cells

The observation that certain macrophages were enriched within specific tumour areas (Figure 4.3.2), indicated that the proximity of TAMs to tumour cells might influence their phenotype. To further study these localisation patterns[404, 420, 422], the spatial bioinformatics tool, ISAT[412], described in Chapter 3 was utilised (Figure 4.3.4).

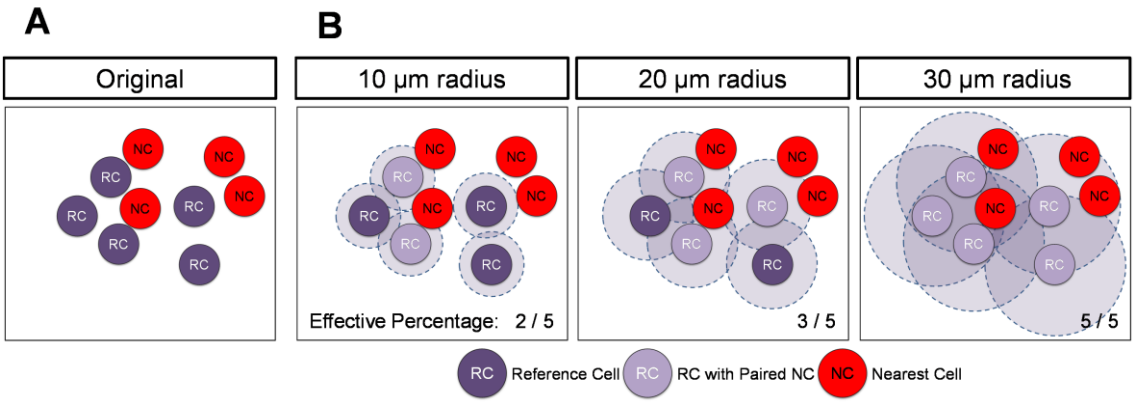


Figure 4.3.4 Schematic illustration of the spatial distance analysis

Each reference cell (RC) was paired with a neighbouring nearest cell (NC) in 10 µm increments from its nucleus. Effective percentage represents the proportion of RC that had a paired NC in a given distance. Related to Figure 3.3.11. Figure from[466].

Distances between cells within the Core were analysed and the CD68+IRF8+ macrophages were identified as the closest population to the tumour cells with a median distance of 12.3 µm (Figure 4.3.5A). In contrast, the CD68+CD163+CD206+ macrophages were furthest from the tumour cells (23.8 µm) and the other TAM populations located within this distance range. The distribution patterns of TAMs to tumour cells found at the Edge and Margin was then compared with the Core (Figure 4.3.5). The data showed that the median distance of TAMs to tumour cells at the Edge was very similar to the Core (Figure 4.3.5A and B). At the Margin, although the distance of TAMs to tumour cells were much further (Figure 4.3.5C and Table 3.3.2), the distribution patterns remain similar to those in the Core and Edge (Figure 4.3.5D). The CD68+IRF8+ macrophages remained the closest TAM population to the tumour cells (15.1 µm), followed by the CD68+CD206+ and the CD68++CD163+ TAMs. The CD68+CD163+CD206+ macrophages had the furthest median distance

from the tumour cells but were not different to the CD68+ and CD68+CD206++ TAMs as a population (Figure 4.3.5D). These data suggest that, although the actual distances between TAMs and tumour cells may be different across ROIs possibly due to the degree of immune infiltration, the distribution patterns of TAMs to tumour cells were similar between the Core, Edge and the Margin.

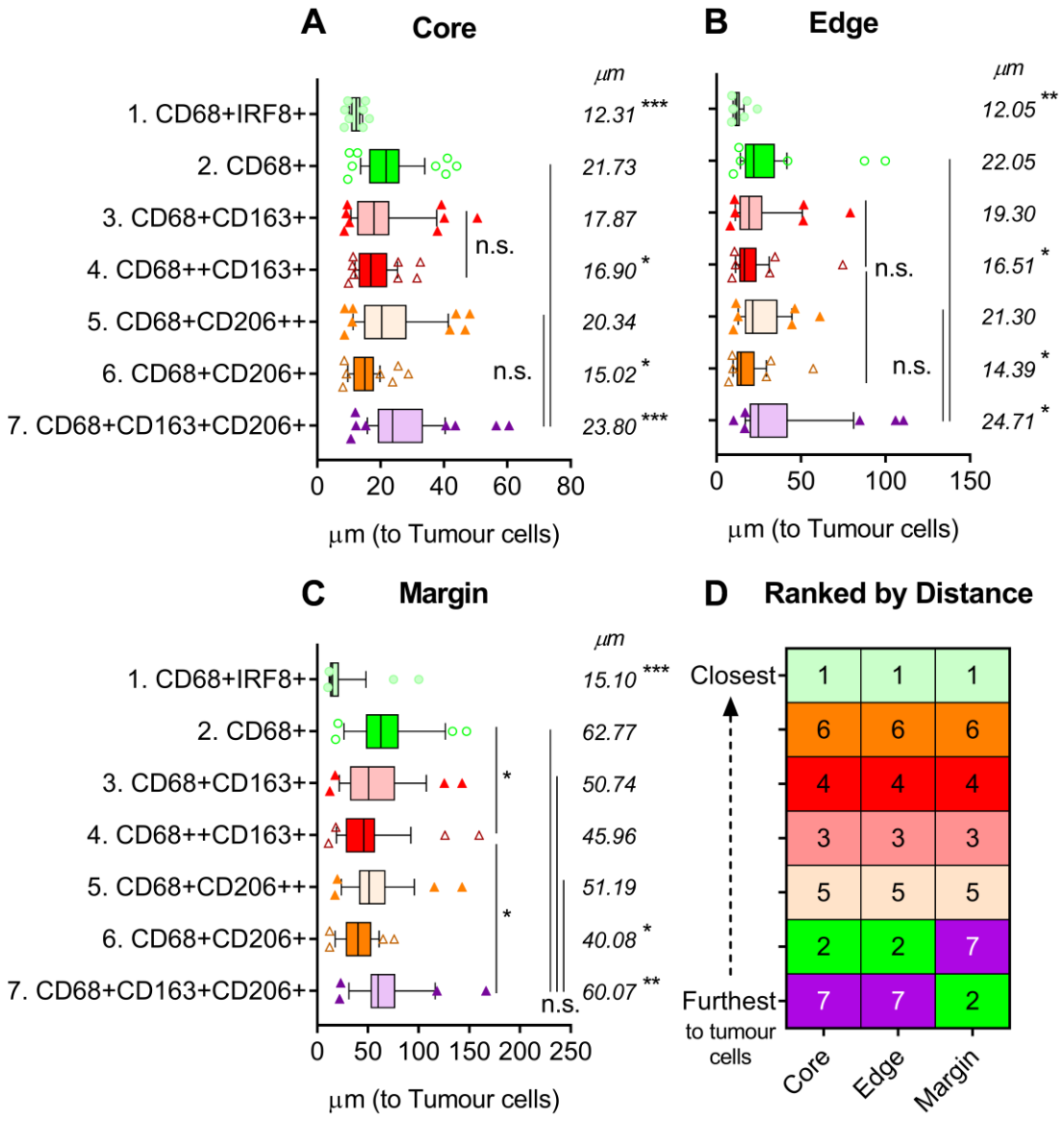
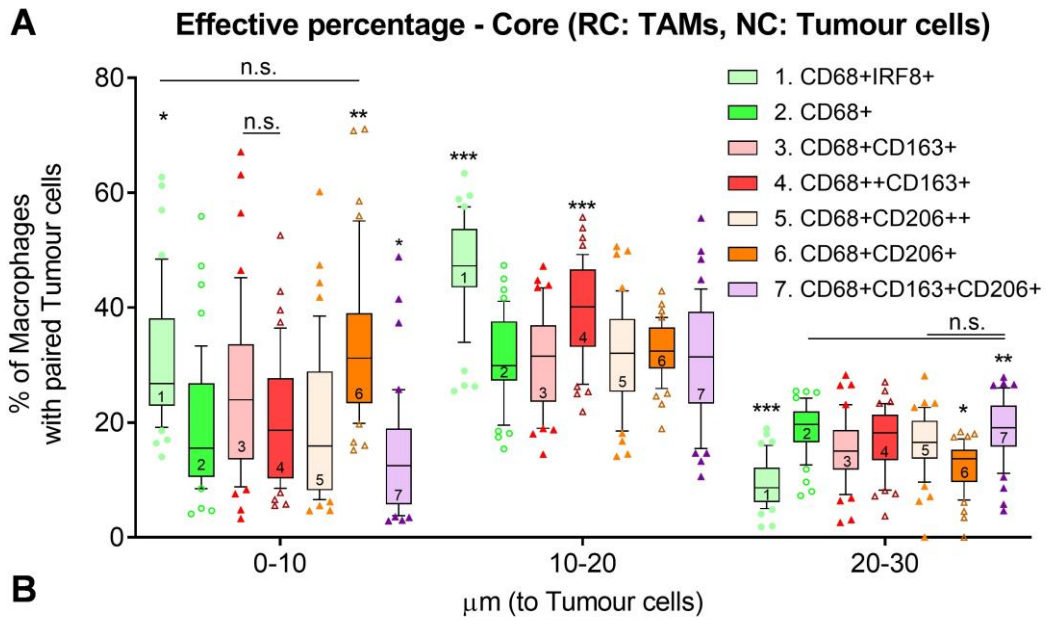


Figure 4.3.5 Median distance of TAMs to tumour cell in regions of interest

Median distance of TAM populations (RCs) to tumour cells (NCs) in the (A) Core (n=46), (B) Edge (n=30) and (C) Margin (n=26). (D) TAM populations, numbered as in (A), ranked by their distance to tumour cells in each ROI. Mean ± 10-90 percentile. Each point represents one patient. *p<0.05, **p<0.01, ***p<0.001 and not significant (n.s.) comparing between TAM populations. Mann-Whitney U test. Figure from[466].

To incorporate both cell proximity and quantity, an “effective percentage” parameter was introduced (Figure 4.3.6A). Effective percentage represents the proportion of macrophages that had a tumour cell within a defined distance (Figure 4.3.4B). In the Core, significantly higher percentages of the CD68+CD206+ (31%) and the CD68+IRF8+ (27%) macrophages had tumour cells within a 10 µm radius (Figure 4.3.6A and Appendix 1, Figure S4B). The CD68+CD163+CD206+ macrophages were the least associated with tumour cells (12%) within this range. When the distance was extended to within 10-20 µm, the CD68+IRF8+ macrophages (47%) remained the major population associated with tumour cells. The CD68++CD163+ macrophages (40%) were the next most abundant (Figure 4.3.6 and Appendix 1 Figure S4B) and the CD68+CD163+CD206+ macrophages remained the most abundant population beyond 20 µm from the tumour cell (Figure 4.3.6B).



Effective percentage (%): 0-20 µm							
TAMs	1	2	3	4	5	6	7
Median	77.60	45.04	56.90	58.63	48.01	65.36	43.02
Average	78.19	50.24	56.46	59.48	51.14	65.74	44.90
SD	10.22	17.61	20.22	18.08	20.17	13.90	19.42

Figure 4.3.6 Effective percentage of TAM populations in the Core

Effective percentage (A) within 10 µm increments and (B) within 0-20 µm. #: TAMs numbered as in (A) Mean ± 10-90 percentile. Each point represents one patient. *p<0.05, **p<0.01, ***p<0.001 and not significant (n.s.) comparing between TAM populations. Mann-Whitney U test. Figure from[466].

These results indicate that, despite being a large population within the tumour, the majority of CD68+CD163+CD206+ macrophages were located at a distance approximately 2-3 average cell-lengths (defined in Figure 3.3.15) from the tumour cells. The majority of the CD68+IRF8+ macrophages (78%) had tumour cells within 20 µm radius of their nucleus (Figure 4.3.6B). All TAM-tumour pairings peaked within 10-20 µm, a distance which would start to put cells into direct contact with each other. This suggests that this distance may be the zone for TAM polarisation or phenotypic change *in situ*, and could potentially be used as a threshold for partitioning the tissue for subsequent genomic/proteomic analyses.

In summary, the data showed that major TAM populations differed phenotypically between the tumour and adjacent normal tissue (Figure 4.3.1). Similar phenotypic difference and distribution patterns were observed in macrophages that were more proximal to the tumour cells (Figure 4.3.5 and Figure 4.3.6) across the Core, Edge and Margin.

4.3.3 Association of TAM populations and patient clinical outcomes

The relevance of TAMs to relapse-free survival (RFS) and overall survival (OS) was assessed. Patients in the **OPAL study cohort** were grouped based on their TAM densities in the tumour Core. The Core was chosen as it comprises the majority of the tumour mass and also because some tumours, especially the diffuse GC, do not have a definitive Edge and Margin. In a univariate analysis of outcome, CD68++CD163+ TAMs were associated with improved RFS, but not OS (Figure 4.3.7A and Appendix 1 Figure S5D). While this was an interesting finding, this observation did not reach statistical significance after multivariate analysis incorporating known clinical prognostic factors (Table 4.3.1).

The effective density (0-10 µm), which reflected the absolute number of macrophages that had a tumour cell within a 10 µm radius (defined as direct cell-to-cell contact in Figure 3.3.15), was used as a more refined measurement of potential contact-mediated function. The results showed that patients with a higher effective density of CD68++CD163+ macrophages had significantly

improved RFS and OS (Figure 4.3.7B) when compared to patients with lower TAM density. No other TAM population was found to be associated with patient survival (Appendix 1 Figure 4 and 5).

There were no survival differences found if only proximity or cell proportion (median distance, effective percentage; Appendix 1 Figure S4C and 4E) but not cell number (overall density, effective density) was used for patient stratification. These data indicate that the influence of TAM on patient survival was relevant to both the number of macrophages and their proximity to tumour cells, suggesting that the spatial location of TAMs, in addition to their overall density, should be considered as a factor on survival.

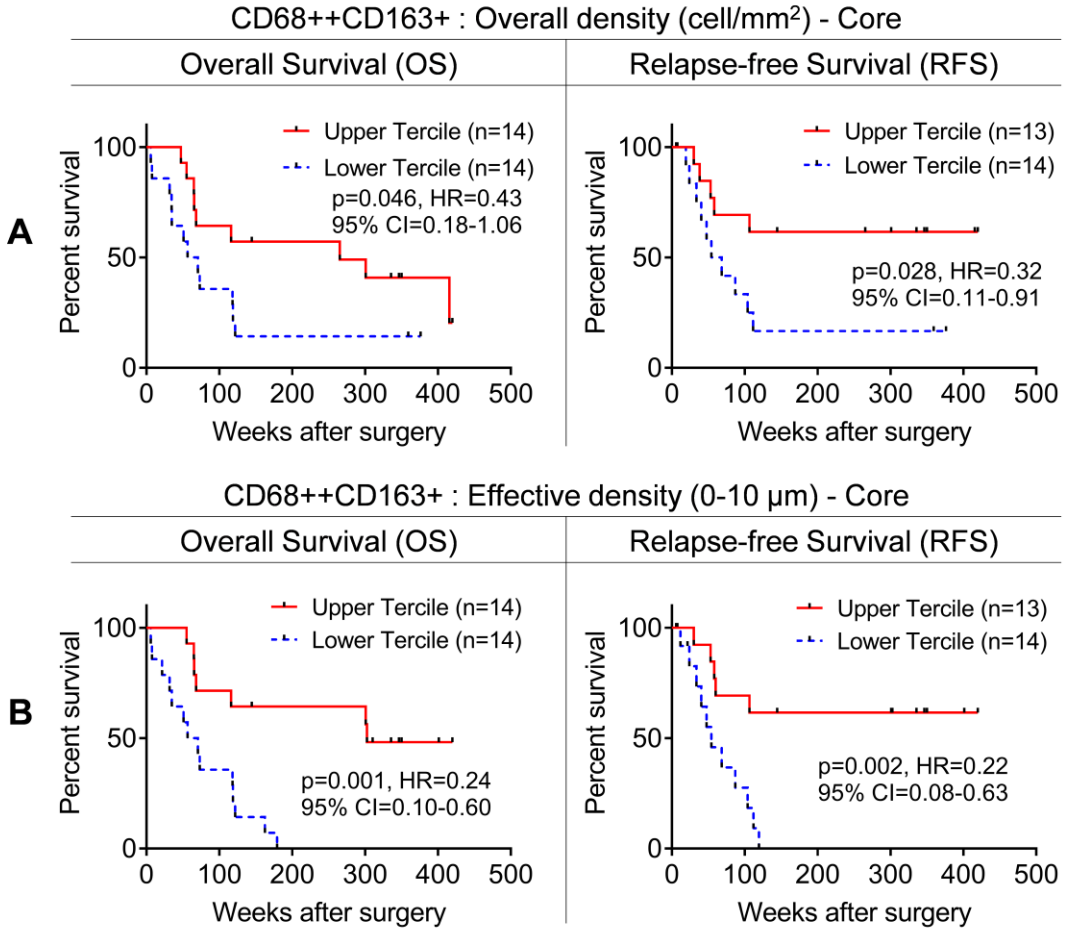


Figure 4.3.7 OS and RFS based on CD68++CD163+ TAM density

(A) Overall density. (B) Effective density (0-10 µm) in the tumour Core. Effective density (0-10 µm): the number of TAM that had a tumour cell within a 10 µm radius. Upper tercile (density > 2/3 of the patients in the cohort; red line). Lower tercile (density ≤ 1/3 of patients in the cohort; blue dash line). Log-rank (Mantel-Cox) test. Figure from[466].

Table 4.3.1 Multivariate analysis of clinical parameters and CD68++CD163+ TAM density

Parameters	Coefficients	Standard error	t Stat	P-value
Age	-0.1145	0.0487	-2.3488	0.0246
T Stage	0.3435	0.1202	2.8582	0.0071
N Stage	0.3603	0.1460	2.4682	0.0186
M Stage	0.2669	0.2248	1.1874	0.2431
AJCC 6th	-0.2682	0.1471	-1.8236	0.0768
TCGA	-0.5830	0.1275	-4.5720	0.0001
CD68++CD163+ density	-0.0921	0.0684	-1.3456	0.1871

- Linear regression. Table from[466].

4.3.4 Co-localisation of TAM populations

The heterogeneity of TAM populations within the same tumour microenvironment is well recognised[137, 183], but their interaction has not been well described in GC. To understand the possible interaction between these macrophage populations, their density correlations within the tumour Core were investigated. The CD68+IRF8+ macrophages were significantly enriched in an environment with increased CD68++CD163+ and CD68+CD206+ TAMs, but negatively associated with the CD68+CD206++ and CD68+CD163+CD206+ TAMs. The CD68++CD163+ population further co-localised with the CD68+ and CD68+CD163+ TAM, which was, in turn, significantly correlated with the CD68+CD163+CD206+ population (Figure 4.3.9). Principal component analyses (PCA) was applied to interrogate these correlation patterns and the results indicate that, although the CD68+IRF8+, CD68++CD163+ and CD68+CD206+ macrophages co-existed within the same tumour (Figure 4.3.8), the two M2-like TAMs were more closely clustered than with the IRF8+ M1-like TAM (Figure 4.3.9A). Similarly, the CD68+CD206++ and the CD68+CD163+CD206+ macrophages clustered with each other rather than with the CD68+ TAMs (Figure 4.3.9A), even though all three populations were abundant across all regions of interest (Figure 4.3.1C). Collectively, these data suggest that the macrophage populations from each end of the broad M1/M2 spectrum tend to relate more closely with each other, which may be related to the specific tumour microenvironment context of these TAMs (Figure 4.3.9). Interestingly, the CD163+ (CD206-) and the CD206+ (CD163-) TAMs were negatively correlated (Figure 4.3.8) and were located far apart (Figure 4.3.9B).

These results suggest that the environmental factors may be distinct and contribute to the polarisation of these TAM populations *in situ*.

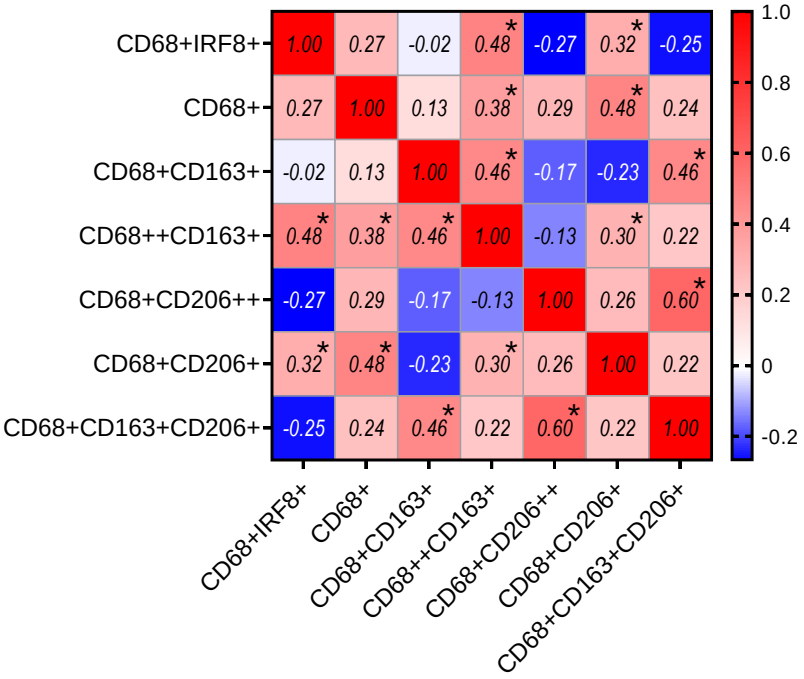


Figure 4.3.8 Density correlations of TAMs in the tumour Core

Red/White/Blue: positive/no/negative correlation. *: p<0.05, Spearman. Figure from[466]. Correlation coefficients are as labelled in each cell.

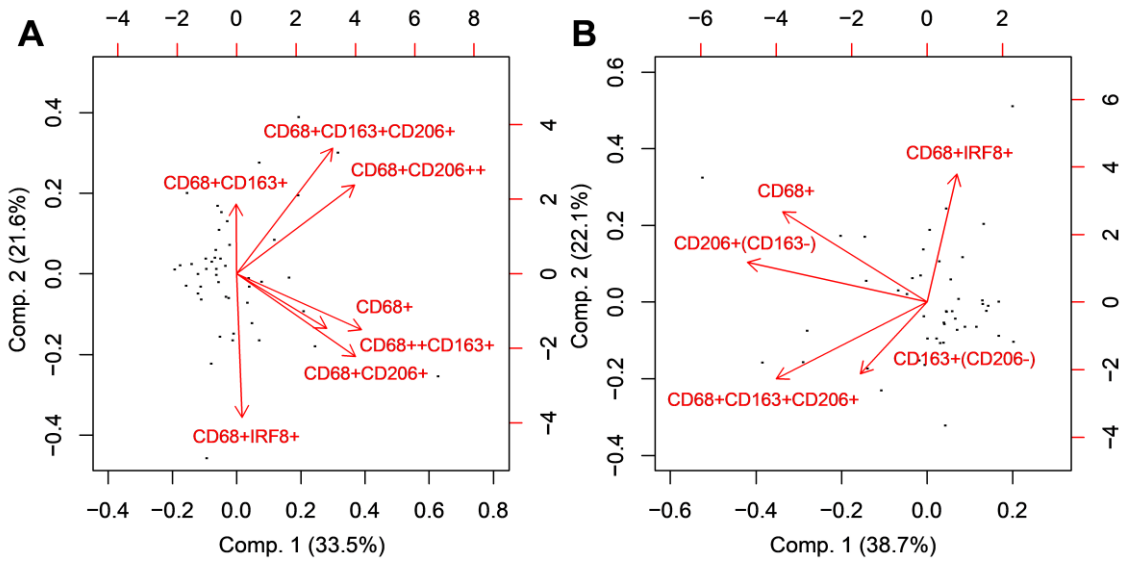


Figure 4.3.9 Principal component analyses of TAM density in the Core

(A) All seven TAM populations. (B) Collapsed M2-like TAM populations based on CD163/CD206 positivity. Figure from[466].

4.3.5 PDL1 expression on multiplex IHC-characterised TAMs

Anti-PDL1 antibodies have been assessed as a potential therapeutic for GC[125] and PDL1 expression was shown to be highly associated with the presence of TAMs in GC[134].

The data showed PDL1 was expressed by all TAMs (Figure 4.3.10A); however, the CD68+CD206+ macrophages exhibited a significantly higher mean PDL1 expression per patient compared to the other populations (Figure 4.3.10B). It is recognised that the heterogeneous PDL1-expression pattern in the tumour microenvironment is dependent on cell location, cell density and intensity for each cell (Figure 4.3.10A). Therefore, PDL1 expression on the individual cells was analysed across all ROIs. It was observed that all cell types, including macrophages and tumour cells, had a proportion of high PDL1-expressing cells (Figure 4.3.10C).

Using the mean PDL1 expression across individual cells in the cohort as a threshold of positivity, which corresponded to visible PDL1 staining of cells within the images (Figure 4.3.11A), 32% of all cells irrespective of cell types were identified as PDL1-positive (Figure 4.3.11B).

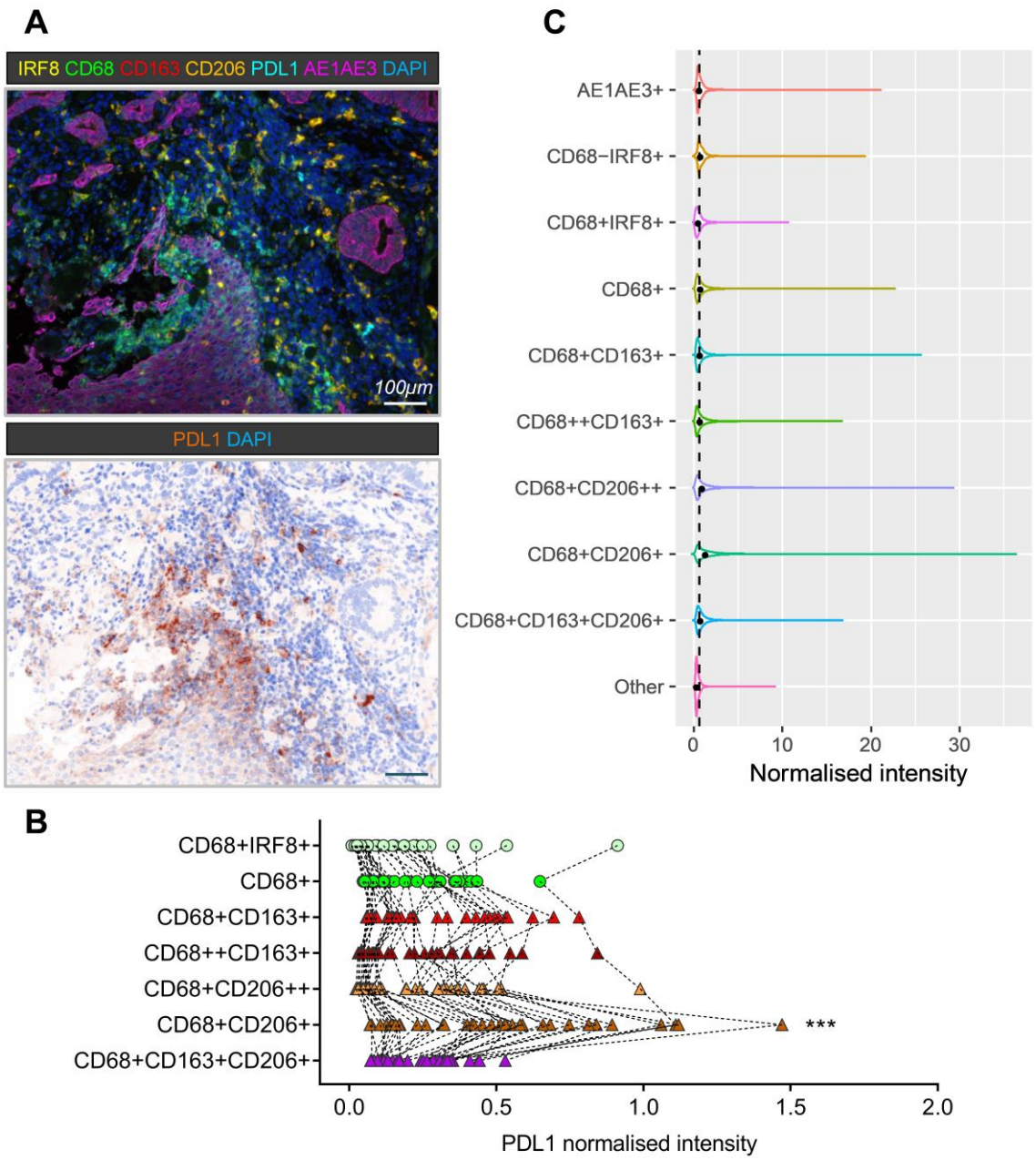


Figure 4.3.10 PDL1-expression in GC tissue and on TAM populations

(A) Representative composite and single-stained IHC images. (B) PDL1-expression on each TAM population averaged per patient Core. Bar and error bars represent mean ± SD. Each line and point represents one patient (n=35). ***p<0.001 comparing between TAM populations. Mann-Whitney U test. (C) Single-cell PDL1 expression on cell populations. Figure from[466].

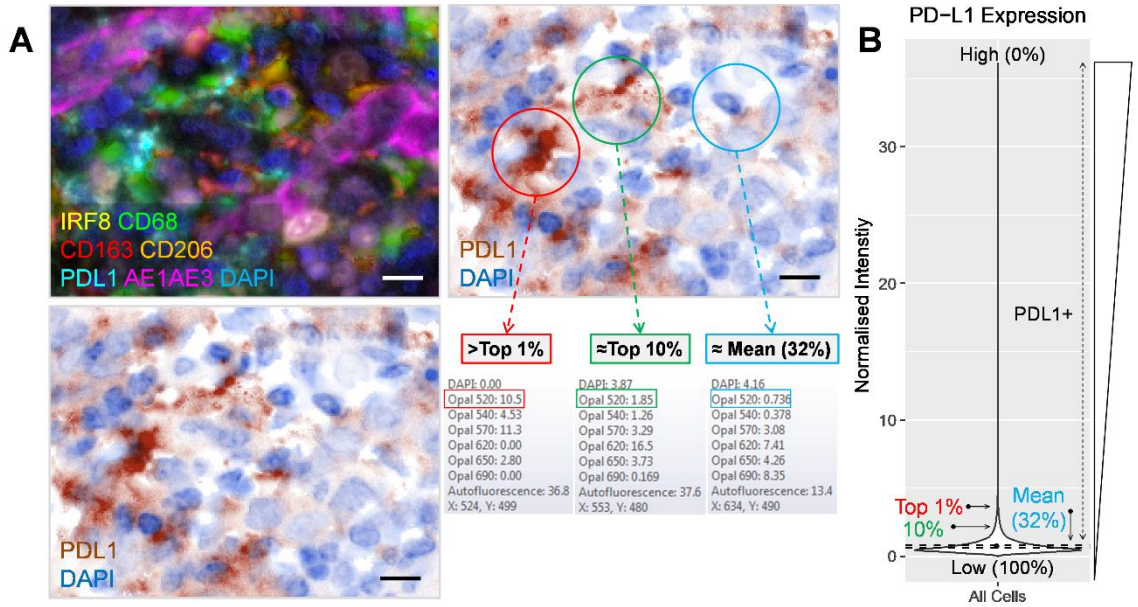


Figure 4.3.11 Definitions of different PDL1 intensity criteria

(A) Representative visual examples of different intensity criteria of the cells marked as red (highest Top 1% pf PDL1 expression), green (Top 10 %) and blue (above mean, 32%). Different criteria defined using single-cell PDL1 expression across all cell types in Figure 4.3.10C. Scale bar: 10 µm. (B) Equal number (10^4) of cells per patient (n=56, all ROIs included) were randomly selected to normalise between sample sizes. Cells were pooled as a sampling cohort and ranked via their PDL1-positivity from High (0%) to Low (100%). Distribution of PDL1-expression on individual cells in a sampling cohort regardless of cell types. 32% of total cells were defined as PDL1+ with the mean expression of the cohort. Top 1% and 10% of the cells with high PDL1 expression are indicated. Figure from[466].

Whilst the total number of PDL1+ macrophages (regardless of population) was similar to the total number of PDL1+ tumour cells, the number of TAMs with PDL1 expression in the top 10% of expression was higher than tumour cells (Figure 4.3.11B, Figure 4.3.12A and B). A more detailed interrogation of the data identified three abundant PDL1+ TAM populations, namely CD68+, CD68+CD206++ and CD68+CD163+CD206+ (Figure 4.3.12A).To control for the differences in total cellular infiltrate (Figure 4.3.1C), the percentage of PDL1+ cells in each population was compared (Figure 4.3.12C). All three CD206+ TAM populations contained at least 36% of cells that were PDL1+ (Figure 4.3.12C). However, although the percentages of PDL1+ cells within the CD206+ macrophages were similar, the intensity of PDL1 was different (Figure

4.3.12D). CD206+ (CD163-) macrophages exhibited the highest PDL1 expression, whereas the CD68+CD163+CD206+ macrophages were homogeneously distributed among different intensities. These results showed that the CD68-only (CD68+; high in number) and the CD206+ TAMs (high in number and percentage of cell type) were the main PDL1-expressing populations in our cohort. The high mean PDL1 expression on CD68+CD206+ observed per patient was due to having a larger proportion of PDL1+ cells (Figure 4.3.12C).

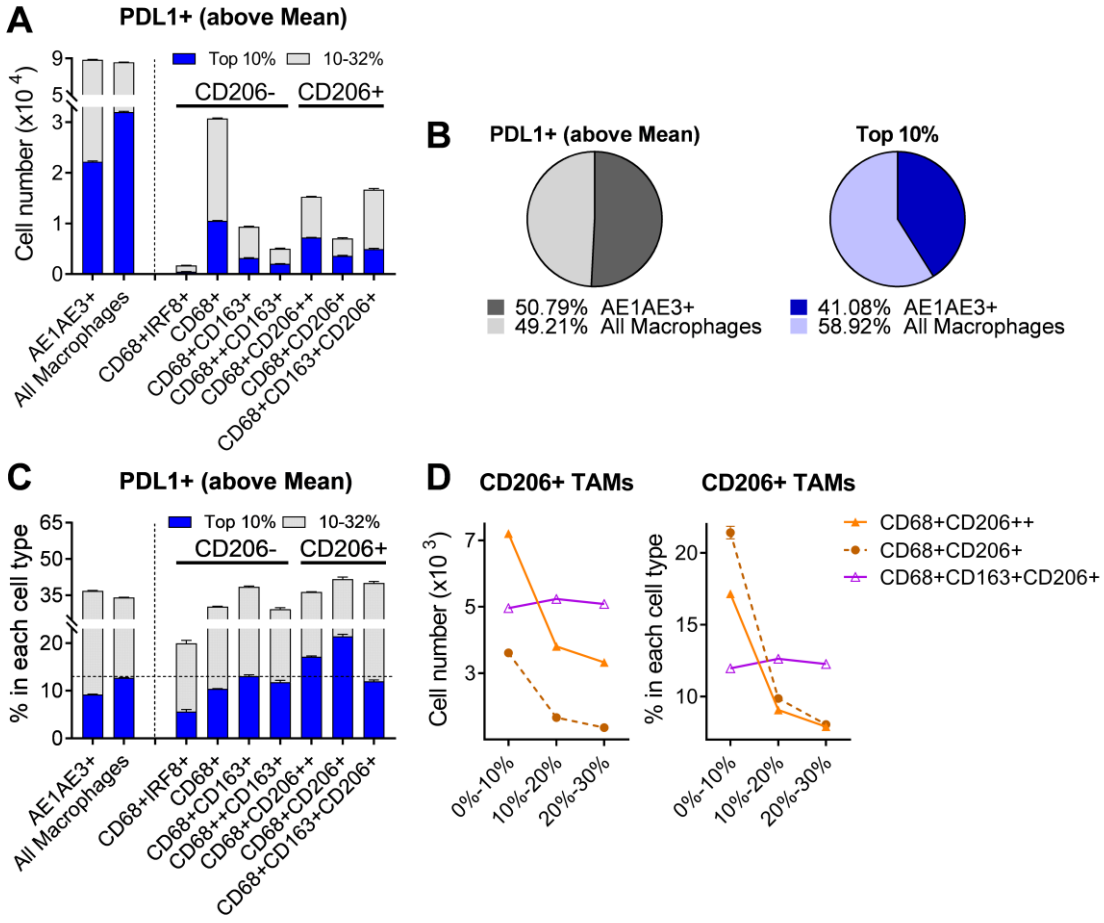


Figure 4.3.12 TAM PDL1 status defined at single-cell level

(A) Cell number and (B-C) percentage different PDL1 intensity-expressing cells in each cell type. (D) Cell number and percentage in each CD206+ TAM population. Bar and error bars represent mean ± SD of five subsampling cohorts described in Figure 4.3.11B. Figure from[466].

To investigate the correlation of PDL1+ TAMs with different GC subtypes, TAM populations with the highest PDL1 intensities from each patient were identified. Top 1% PDL1 expression of the cohort reflects a strong visible PDL1 staining in our cohort (Figure 4.3.11) and is a similar selection criterion[130] used clinically to determine patient PDL1-status. PDL1-high patients (n=44) were referred as having any TAMs represented in the top 1% of the total cell population (Figure 4.3.11B) whereas the PDL1-low patients (n=12) had no TAMs expressing PDL1 in the top 1%.

Among the PDL1-high patients, the CD68+ macrophages were predominant in tumours of the GS and diffuse subtypes, whereas the CD68+CD206++ macrophages were enriched in the MSI/Others and intestinal subtypes (Figure 4.3.13A and B). Additionally, TAMs in the GS and diffuse cancer subtypes had significantly lower median PDL1 expression (Figure 4.3.13C and D). Whilst significant association between PDL1+ TAM in GC subtypes was observed, no substantial survival differences using TAM-PDL1 intensities were found (Figure 4.3.14). Indeed, PDL1 expression of each patient tissue was more predictive of its GC subtype than the TAM composition within (Table 4.3.2).

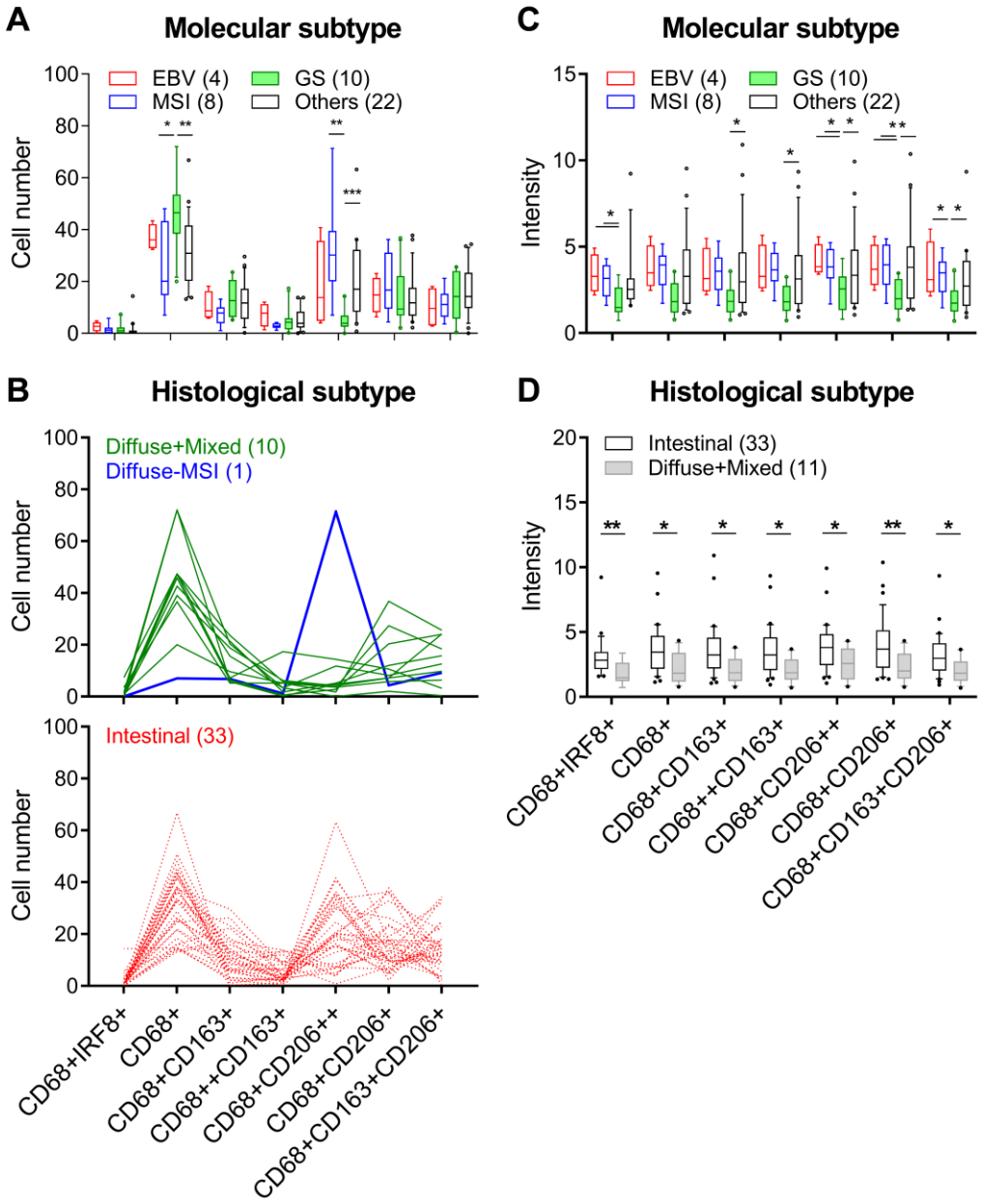


Figure 4.3.13 Relevance of PDL1-high TAMs between GC subtypes

Predominant PDL1-high TAM populations between GC (A) molecular and (B) histological subtypes. Median PDL1 expression on TAM between GC (C) molecular and (D) histological subtypes. Box and whiskers represent mean ± 10-90 percentile. Each point/line represents one patient. *p<0.05, **p<0.01, ***p<0.001 comparing between TAM populations. Mann-Whitney U test. Figure from[466].

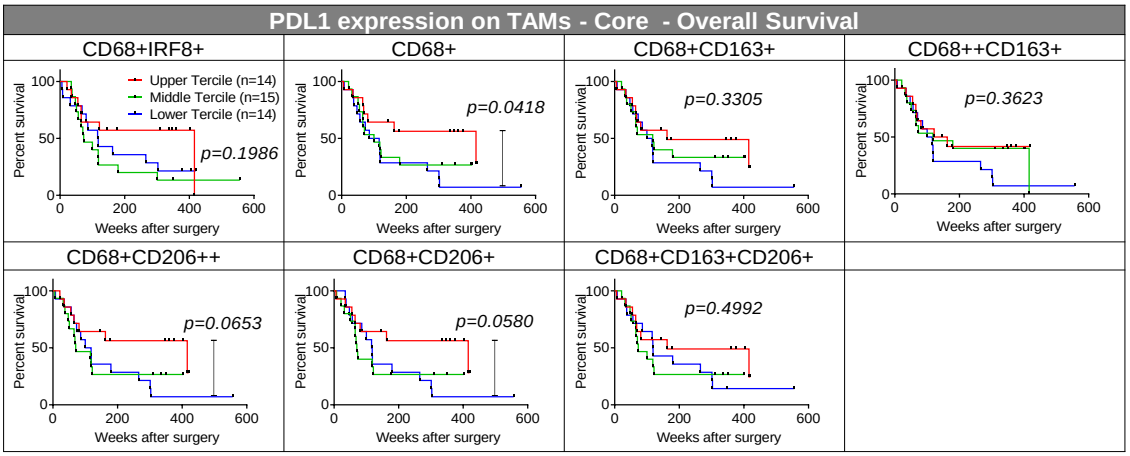


Figure 4.3.14 TAM PDL1-intensity-stratified patient overall survival

Upper tercile (density > 2/3 of the patients in the cohort; red line), Middle tercile (1/3 < density < 2/3 of patients in the cohort; green line). Lower tercile (density ≤ 1/3 of patients in the cohort; blue line). Log-rank (Mantel-Cox) test. Figure from[466].

Table 4.3.2 Clinical parameters of TAM PDL1-intensity-stratified patients

Median PDL1 intensity		Cancer subtypes (number of patients)				TNM stages				AJCC 6th stages	
TAMs	Tercile	Intestinal	Diffuse +Mixed	EBV+MSI	GS +Others	T3+T4	T1+T2	N2+N3	N0+N1	3+4	1+2
CD68+ IRF8+	Upper	12	2	6	8	11	3	2	12	7	7
	Medium	7	8	1	14	9	6	5	10	6	9
	Lower	8	6	2	12	11	3	5	9	8	6
	X^2	0.0817		0.0432		0.4329		0.3801		0.6496	
CD68+	Upper	12	2	6	8	10	4	4	10	7	7
	Medium	11	4	2	13	11	4	3	12	7	8
	Lower	4	10	1	13	10	4	5	9	7	7
	X^2	0.0043		0.0451		0.9912		0.6397		0.9785	
CD68+ CD163+	Upper	12	2	6	8	10	4	3	11	6	8
	Medium	10	5	2	13	12	3	5	10	9	6
	Lower	5	9	1	13	9	5	4	10	6	8
	X^2	0.0219		0.0451		0.6397		0.7731		0.5630	
CD68++ CD163+	Upper	12	2	6	8	10	4	3	11	6	8
	Medium	10	5	2	13	12	3	5	10	10	5
	Lower	5	9	1	13	9	5	4	10	5	9
	X^2	0.0219		0.0451		0.6397		0.7731		0.2151	
CD68+ CD206++	Upper	13	1	6	8	10	4	3	11	6	8
	Medium	9	6	2	13	11	4	6	9	10	5
	Lower	5	9	1	13	10	4	3	11	5	9
	X^2	0.0072		0.0451		0.9912		0.4329		0.2151	
CD68+ CD206+	Upper	13	1	6	8	12	2	4	10	8	6
	Medium	9	6	2	13	10	5	3	12	8	7
	Lower	5	9	1	13	9	5	5	9	5	9
	X^2	0.0072		0.0451		0.3801		0.6397		0.4788	
CD68+ CD163+ CD206+	Upper	12	2	6	8	11	3	3	11	7	7
	Medium	9	6	2	13	11	4	5	10	9	6
	Lower	6	8	1	13	9	5	4	10	5	9
	X^2	0.0614		0.0451		0.6950		0.7731		0.4230	

- X^2: Chi-square test. Table from[466].

4.3.6 PDL1 expression on fresh sample-isolated TAMs

To validate the findings regarding high PDL1 expressions on CD68-only and CD206+ TAMs, fresh tumour biopsies (n=3 patients, 2-3 biopsies per patient) were obtained from GC patients undergoing surgery and were analysed using flow cytometry (Table 2.5.2 and Figure 4.3.15).

The pan macrophage marker CD68 previously used in multiplex IHC was not ideal for use in FACS as staining intracellular markers requires fixation and permeabilisation of the cells to mediate interaction of the epitope and antibody. This would limit future functional experiments requiring viable cells (e.g. co-culturing with tumour cells and T cells, single-cell RNA-seq). To circumvent this issue macrophages were defined as $CD45^{+}CD11b^{+}CD64^{+}$ as a recognised group of markers specific for macrophages[417] (Figure 4.3.15A). CD163 and CD206 were further used to subdivide the identified macrophage populations into different populations similar to those defined with the multiplex IHC approach. PDL1 was included in the flow staining panel and the median PDL1 intensities on these TAM populations were compared (Figure 4.3.15B).

PDL1 intensity was found to vary between patient samples (Figure 4.3.16A). Higher PDL1 expression was observed on the CD206+ (CD163-) TAM population (Figure 4.3.16B). This result showed that the $CD163^{-}CD206^{-}$ (R6 population; presumably the CD68-only TAMs identified with mIHC) and the $CD163^{-}CD206^{+}$ TAMs exhibited the most intense PDL1 expression (Figure 4.3.12). Reassuringly, these data suggest that the findings were reproducible with different detection methods and confirmed the consistently higher PDL1-intensities on the CD206+ TAMs compared to the CD163+ (CD206-) macrophage population.

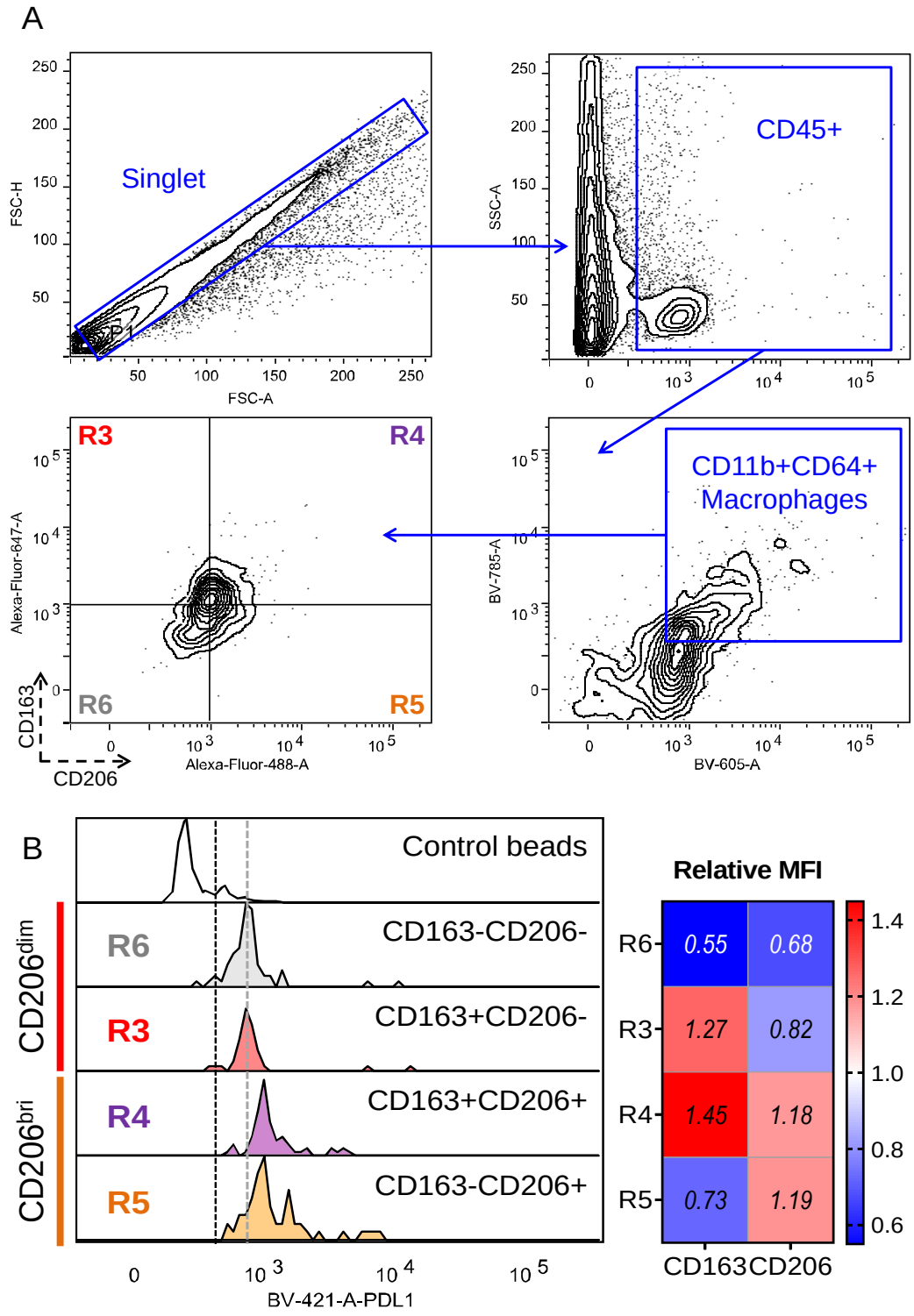


Figure 4.3.15 Analysing macrophages using flow cytometry

(A) Gating strategy used for Flow analysis. Gated based on non-stained negative control beads. (B) CD163/CD206 intensity classified TAM populations and combined marker signatures of each group. MFI: median fluorescence intensity.

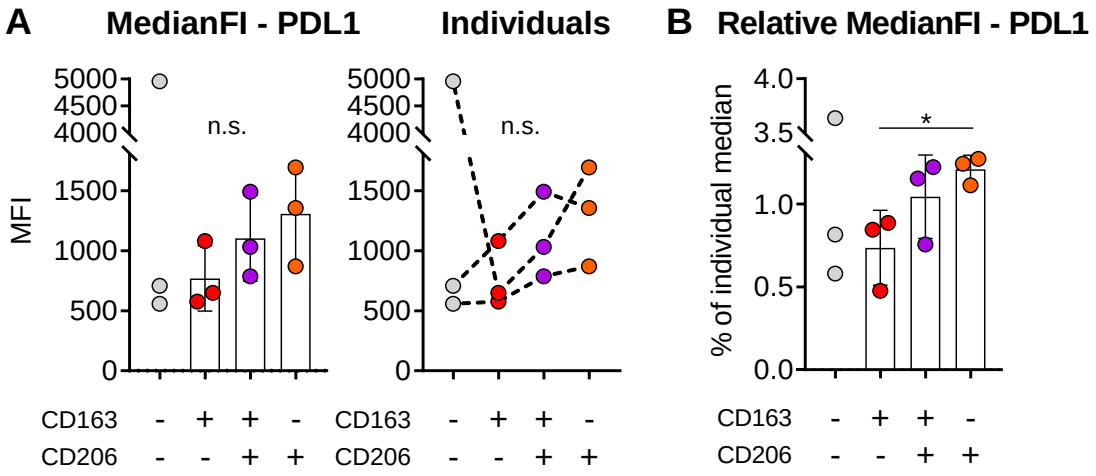


Figure 4.3.16 PDL1 median intensity on CD163/CD206 TAMs

(A) Original PDL1 intensity of each patient. Dashed line: data of the same patient. (B) PDL1 intensity of each patient sample normalised with the median intensities of all CD11b+CD64+ macrophages per patient (n=3). Bar and error bars represent mean ± SD. Each point represents one patient. *p<0.05 and not significant (n.s.) comparing between TAM populations defined in Figure 4.3.15. Mann-Whitney U test. Positive (+) and negative (-) represent positivity of the marker labelled. MFI: median fluorescence intensity.

4.3.7 Marker expression on TAMs between the tumour-nest and stroma

CD68-only and the CD206+ TAMs were identified as the populations with the highest PDL1 expression. Using the tumour Core as the region of interest, the distribution of TAMs regarding their PDL1 status was further assessed by comparing the expression changes of PDL1 on TAMs at the interface between the tumour-nest (T) and stroma (S) areas (TS; Figure 4.3.17 and Figure 4.3.18).

The mean PDL1 expression defined the threshold for PDL1-positivity as described in Figure 4.3.12 and Figure 4.3.13A. Using these criteria, the level of PDL1 expression by tumour cells (AE1AE3+) was at the threshold and the other non-macrophage cells (Other) were negative (Figure 4.3.18). Most TAMs expressed PDL1 below this threshold in the stroma but showed a progressive increase of PDL1 with increasing proximity to the tumour cell. The PDL1 expression on CD163+ and CD68+CD206+ macrophages were found to be

continuously upregulated as they became more embedded in the tumour-nest. The CD68+CD206+ macrophages were the only PDL1+ population detected in the stroma (Figure 4.3.18 and Figure 4.3.19A). A similar pattern of PDL1 expression in other ROIs was observed and the lower PDL1 expression in the diffuse and GS cancer subtypes was confirmed (Figure 4.3.19B and C).

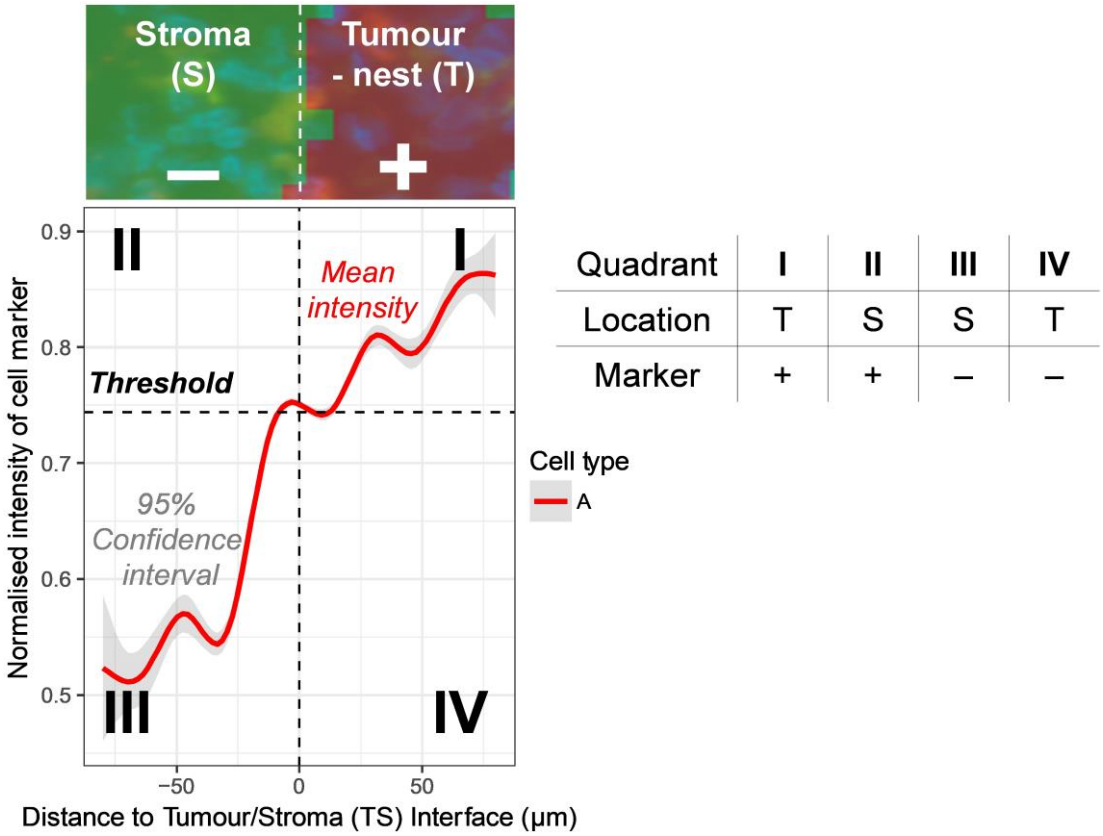


Figure 4.3.17 Schematic model of marker intensities between the tumour-nest and stroma

Intensity change of markers between the tumour-nest (T) and stroma (S) areas was determined by randomly assigning equal number of cells (n=500, minimum number available between samples) from both areas per patient (within the Core). The intensity of the marker of interest was plotted with its mean value (red) and the 95% confidence intervals (grey). The interface between TS areas was defined as point zero, positive and negative values on the x-axis indicate the tumour-cell and the stroma region, respectively. Thresholds were applied to define the positivity of markers. Quadrants: I: cell type A located in the tumour-nest and is positive (+) of the marker tested. II: stroma, positive. III: stroma, negative (–). IV: tumour, negative. Figure from[466].

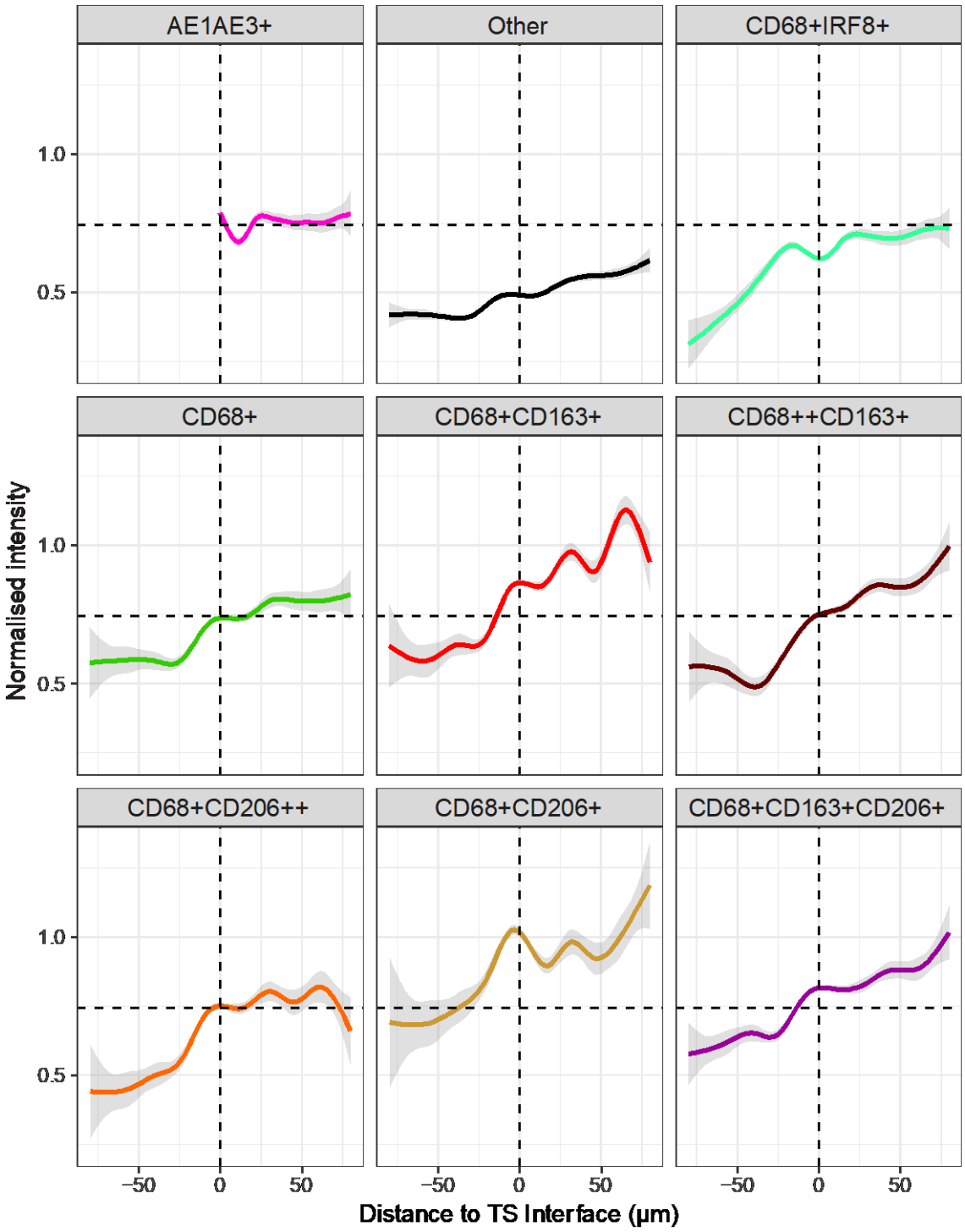


Figure 4.3.18 Change in PDL1 expression with distance from the TS interface

Threshold: mean PDL1 expression defined in Figure 4.3.11. Figure from[466].

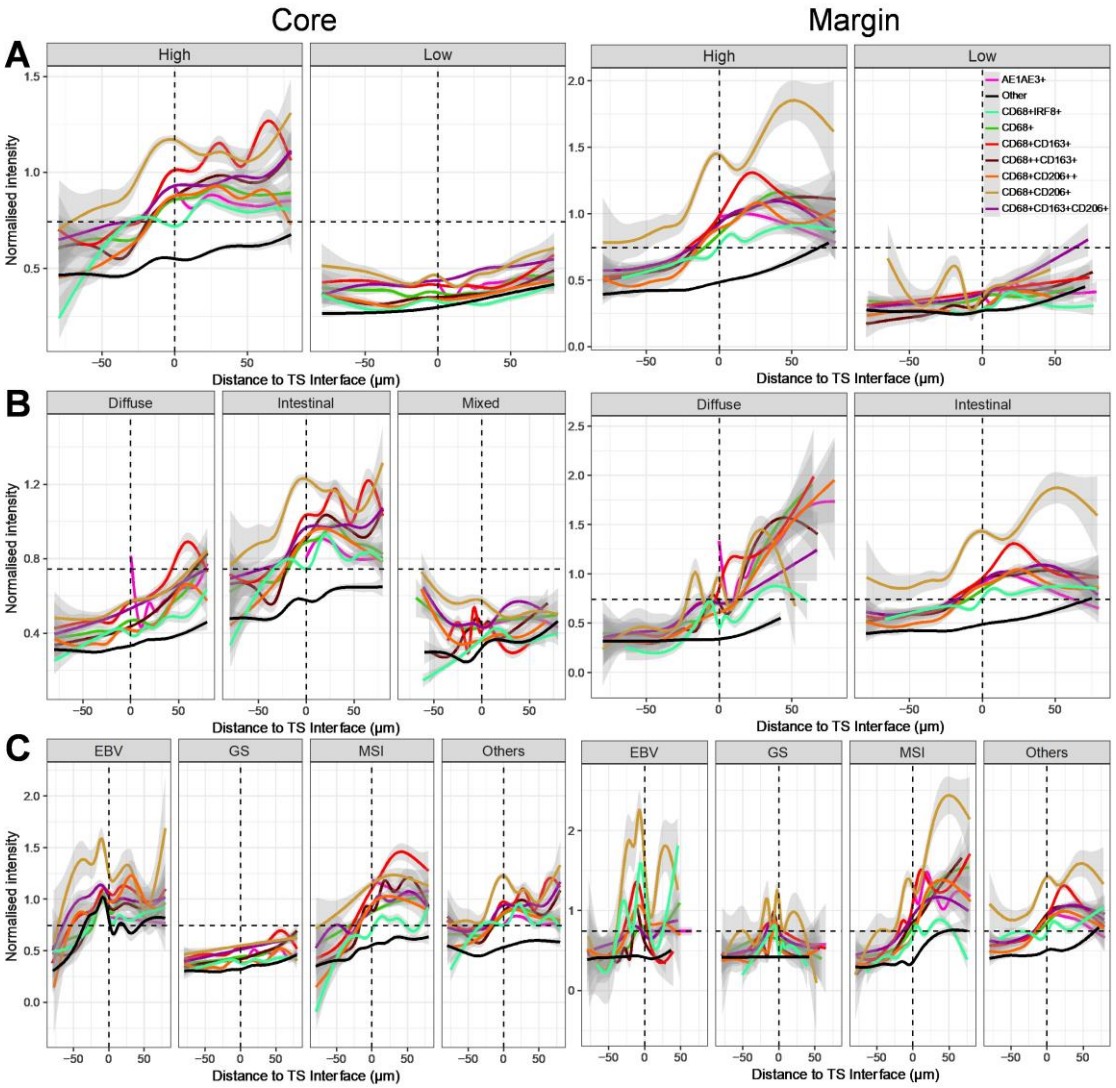


Figure 4.3.19 PDL1 expression on TAMs at the TS interface

(A) PDL1^{High} and PDL1^{Low} samples grouped with the TAMs >Top1% of the OPAL study cohort and with (B) histological and (C) molecular GC subtypes. Figure from[466].

Markers expressed by macrophages are often functionally related to their activation status[183]. Therefore, the expression of CD68, CD163 and CD206 on each TAM population between the TS areas was compared using the mean expression of each macrophage marker of tumour (AE1AE3+) and non-macrophage (Other) cells as baseline thresholds (Figure 4.3.20).

The CD163+ and CD68+IRF8+ macrophages exhibited a minimal 2-fold increase in their CD68 expression between the TS areas and this was induced approximately 25 µm before engaging the TS interface (Figure 4.3.20A). The

CD206+ (CD163-) and CD68-only TAMs exhibited relatively little change. The results suggest that the CD163+ and CD68+IRF8+ macrophages may differ in their phagocytic abilities[315, 429] compared to the CD206+ (CD163-) macrophages due to the differential expression of CD68 and that the induction of this marker does not require direct contact between the TAMs and the tumour cells.

With increasing proximity to tumour cells, an increase in CD163 expression (measured by intensity) was observed in all CD163+ TAMs (Figure 4.3.20B). Interestingly, unlike CD68 and CD163, the expression of CD206 on each TAM population was not different across the TS areas and only the CD68+CD206++ macrophages showed a slight increase in expression within the tumour-nest Figure 4.3.20C). However, considering that the CD68+CD206+ TAMs were predominately located within the tumour-nest (Figure 4.3.2), these results suggest that the overall CD206 expression on the CD206+ (CD163-) macrophages (CD68+CD206++ and CD68+CD206+) decreased as they were more proximate to the tumour cells (or tumour-nest area).

Surprisingly, the IRF8 expression on the CD68+IRF8+ macrophages decreased within the tumour-nest compared to those in the stroma Figure 4.3.20D). This may be related to distribution difference of the cellular source of IFN-γ (e.g. T cells), the more immune suppressive microenvironment near the tumour cells, or may indicate a transition from a $CD68^{low}IRF8^{high}$ into a $CD68^{high}IRF8^{low}$ phenotype that is biologically relevant to their function required in different regions of the tumour (Figure 4.3.20A and D). Importantly, a higher PDL1 expression was found on these intra-tumoural CD68+IRF8+ populations (Figure 4.3.19). This result suggests that, despite the fact that the number and proportion of PDL1+ CD68+IRF8+ TAMs were the lowest among all TAMs (Figure 4.3.12B), their close proximity to tumour cells may confer immunosuppressive properties to other immune cells[469, 470]. IRF8 expression on all other TAM populations increased slightly when they were located in the tumour-nest, which may imply a certain degree of further maturation[444] of these macrophages.

In summary, these data confirmed the plasticity of TAMs between tumour areas and showed that the proximity of TAMs to tumour cells was an important and definitive factor to their phenotypic differences. These results also revealed that although the classification of seven predominant macrophage populations were robust in a whole tumour setting, fine tuning of different markers on individual TAMs at a µm scale within each TAM population may be one of the reasons for the spectrum of phenotypes observed *in situ*.

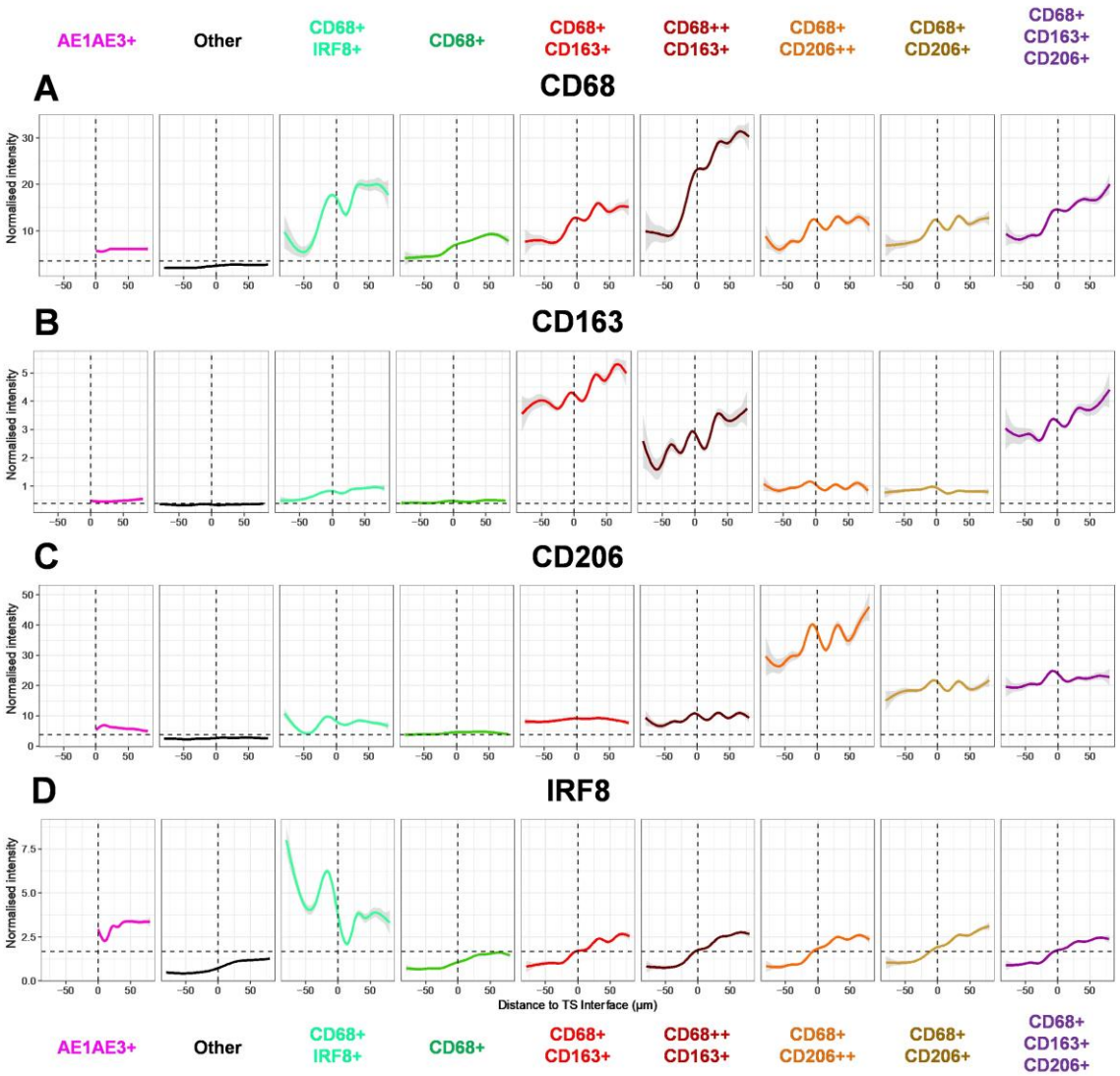


Figure 4.3.20 Change in macrophage marker expression with distance from the TS interface

Cell types are as labelled and coloured. Thresholds: mean expression of (A) CD68, (B) CD163 and (C) CD206 (D) IRF8 on the tumour and non-macrophage (Other) cells. Figure from[466].

4.3.8 PDL1-positive cell density-stratified patient overall survival

Patients were stratified based on the mean PDL1 intensity on TAMs defined in Figure 4.3.11 and no significant advantages in overall survival (OS) were observed between the different groups (Figure 4.3.14). This result is consistent with existing literature claiming that PDL1 was an imprecise marker of patient survival[471, 472] and of response to checkpoint blockades[125, 126]. In addition, patient groupings using PDL1 intensity on TAMs were more predictive of GC subtypes (Table 4.3.2) and overall high PDL1 expression was particularly relevant to the EBV/MSI and Intestinal subtypes[31, 473, 474].

However, it is acknowledged that the intensity of a marker on FFPE tissues may vary between studies due to different tissue-fixation methods, antigen-retrieval processes, and concentration of antibody, as well as the staining methods used (multiplex or traditional IHC). Therefore, to be able to compare our findings with the literature, in addition to using PDL1 expression on TAMs (§4.3.5), the overall number of PDL1+ cells were used to investigate if it could be predictive of patient overall survival in our cohort. The survival data was interrogated based on the density of each cell type (Figure 4.3.21 to Figure 4.3.23), defined by different PDL1-positivity criteria (above mean, Top 10% and 1%; defined in Figure 4.3.11).

Interestingly, the CD68+IRF8+ M1-like macrophages, which did not appear to have survival relevance when the PDL1 intensity on TAMs was used as a patient-stratifying factor (Figure 4.3.14), showed favourable survival predictions incorporating PDL1+ cell density regardless of which criteria were used (Figure 4.3.21 to Figure 4.3.23). Given that the IRF8 and PDL1 can both be upregulated in response to IFN-γ exposure[475], high numbers of PDL1+CD68+IRF8+ macrophages could possibly reflect an IFN-γ enriched tumour microenvironment. This may correlate with the survival advantage observed in patients with high non-macrophage (Other, negative of all markers; e.g. T cells) and the non-macrophage IRF8+ (CD68-IRF8+; solely positive of IRF8) cell populations (Figure 4.3.21 to Figure 4.3.23). The CD163+ TAMs also showed some favourable predictive value using different PDL1-positivity criteria,

especially the CD68++CD163+ population, which is already a predictor of improved relapse-free survival (RFS) regardless of its PDL1 status (Figure 4.3.7).

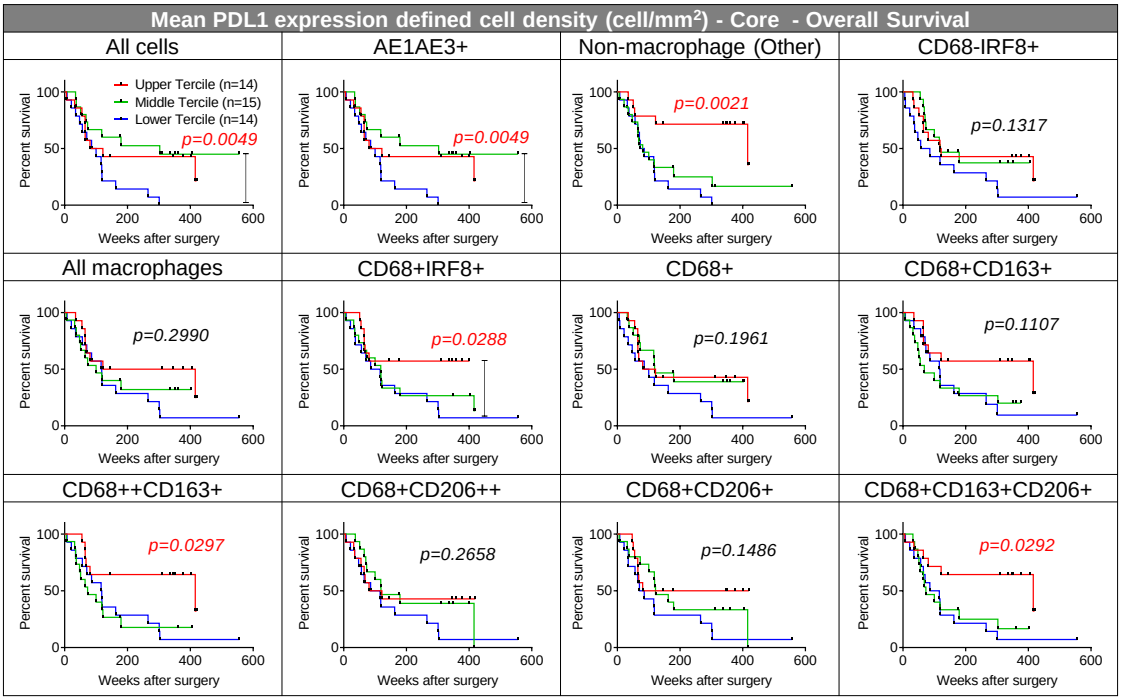


Figure 4.3.21 Overall survival based on TAM density (PDL1; Mean)

Cell positivity was determined with the threshold of mean PDL1 expression of the **OPAL study cohort** (defined in Figure 4.3.11). Patients were then stratified into three groups using the number of PDL1 positive cells and overall survival was plotted. Upper tercile (density > 2/3 of the patients in the cohort; red line), Middle tercile (1/3 < density < 2/3 of patients in the cohort; green line). Lower tercile (density ≤ 1/3 of patients in the cohort; blue line). Log-rank (Mantel-Cox) test.

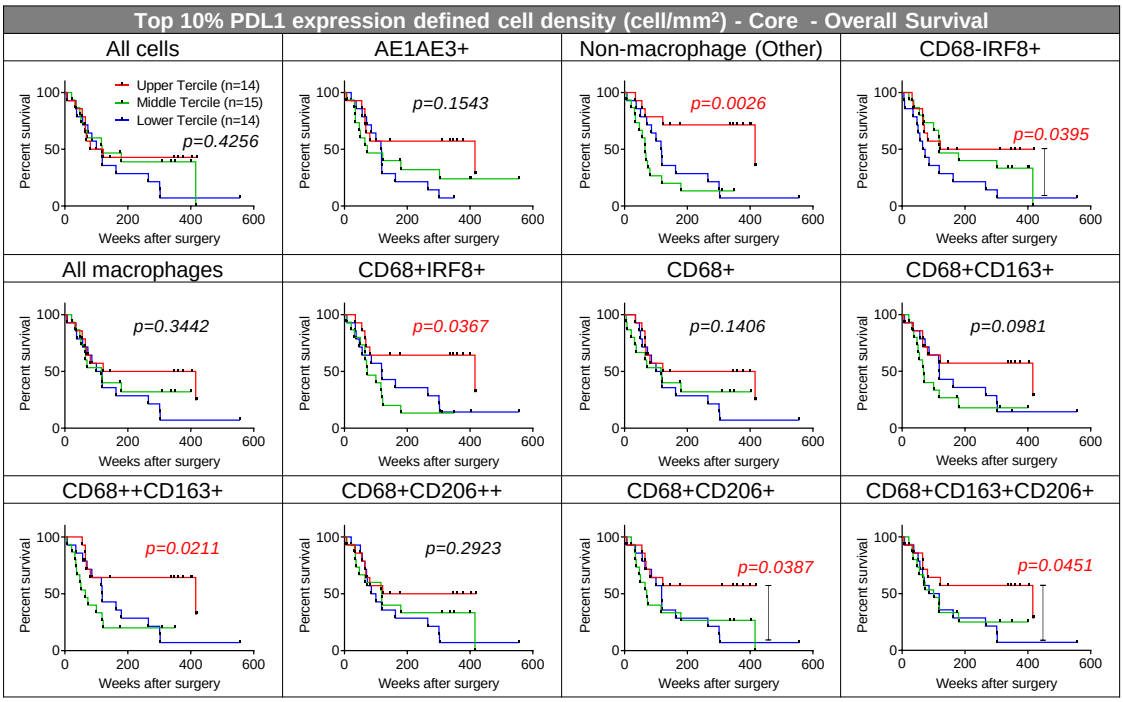


Figure 4.3.22 Overall survival based on TAM density (PDL1; Top 10%)

Cell positivity determined with the highest Top 10% of PDL1 expression for patient stratification as described in Figure 4.3.21.

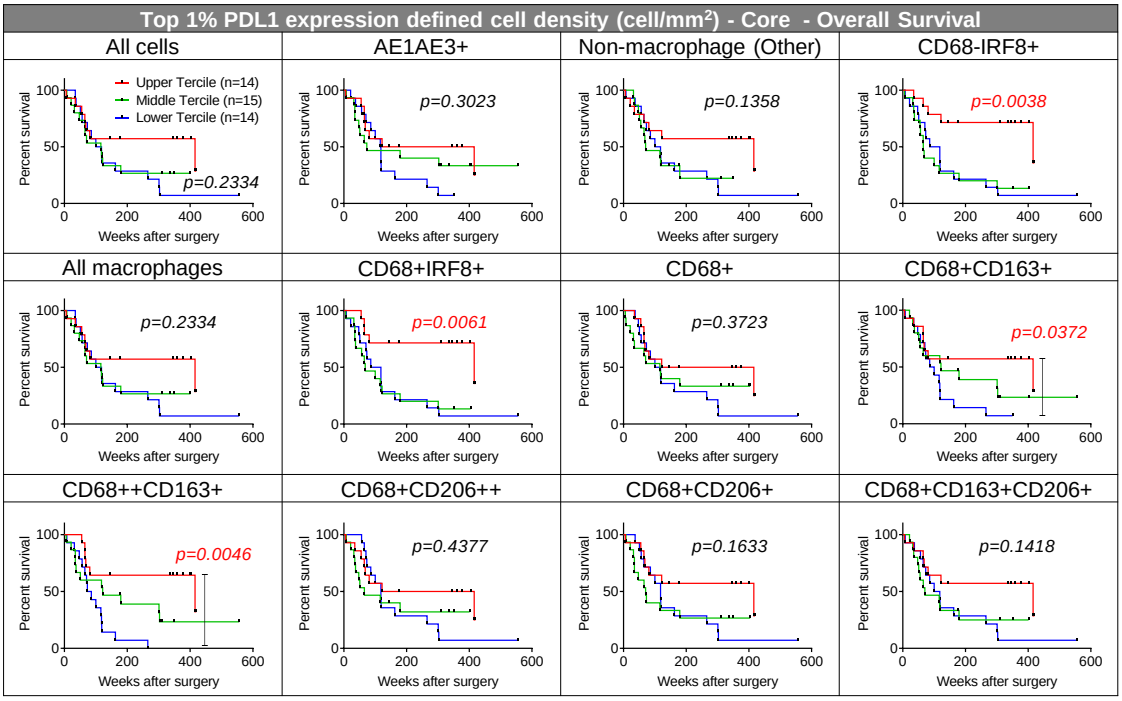


Figure 4.3.23 Overall survival based on TAM density (PDL1; Top 1%)

Cell positivity determined with the highest Top 1% of PDL1 expression for patient stratification as described in Figure 4.3.21.

When comparing the survival data to other clinical parameters between the patients with different PDL1+ cell densities in a univariate analysis, the separation of patients was highly associated with GC histological subtypes and in some cases with the molecular subtype (Table 4.3.3). It is well recognised that cancer subtype is a predictor of survival[31, 213]; and the results indicate clearly that the PDL1 expression in GC tissue was predominantly associated the cancer subtypes than the total density, PDL1 intensity, the density of PDL1+ TAMs and the presence of which TAM populations are in the tumour.

Table 4.3.3 Clinical parameters of patients grouped with PDL1+ cells

PDL1-expression stratified, Cell density-associated Overall Survival											
Clinical parameters		Histological (Laurén)		Molecular (TCGA)		T stage		N stage		AJCC 6th	
Cell types	Threshold	Intestinal	Diffuse +Mixed	EBV +MSI	GS +Others	3+4	1+2	2+3	0+1	3+4	1+2
All cells	Top 1%	0.022		0.045		0.640		0.304		0.215	
	Top 10%	0.022		0.177		0.773		0.304		0.848	
	Positive (<32%)	0.022		0.054		0.773		0.315		0.979	
AE1AE3+	Top 1%	0.022		0.020		0.991		0.240		0.215	
	Top 10%	0.037		0.020		0.773		0.773		0.848	
	Positive (<32%)	0.037		0.054		0.304		0.315		0.650	
CD68-IRF8+	Top 1%	0.007		0.177		0.433		0.380		0.979	
	Top 10%	0.022		0.646		0.433		0.092		0.650	
	Positive (<32%)	0.001		0.714		0.304		0.076		0.735	
Other	Top 1%	0.004		0.177		0.433		0.991		0.848	
	Top 10%	0.002		0.005		0.640		0.060		0.063	
	Positive (<32%)	0.001		0.020		0.380		0.105		0.179	
Tumour-associated macrophages populations											
All macrophages	Top 1%	0.022		0.045		0.640		0.304		0.215	
	Top 10%	0.022		0.177		0.773		0.304		0.563	
	Positive (<32%)	0.022		0.223		0.773		0.105		0.848	
CD68+ IRF8+	Top 1%	0.007		0.005		0.773		0.380		0.848	
	Top 10%	0.007		0.005		0.695		0.380		0.423	
	Positive (<32%)	0.022		0.045		0.315		0.240		0.848	
CD68+	Top 1%	0.002		0.177		0.991		0.060		0.063	
	Top 10%	0.007		0.177		0.640		0.060		0.063	
	Positive (<32%)	0.037		0.714		0.433		0.240		0.979	
CD68+ CD163+	Top 1%	0.061		0.054		0.695		0.695		0.650	
	Top 10%	0.015		0.177		0.380		0.773		0.735	
	Positive (<32%)	0.061		0.646		0.380		0.773		0.367	
CD68++ CD163+	Top 1%	0.007		0.020		0.773		0.380		0.735	
	Top 10%	0.015		0.045		0.991		0.304		0.215	
	Positive (<32%)	0.022		0.177		0.640		0.380		0.563	
CD68+ CD206++	Top 1%	0.004		0.177		0.773		0.304		0.063	
	Top 10%	0.004		0.045		0.773		0.304		0.215	
	Positive (<32%)	0.022		0.177		0.433		0.076		0.650	
CD68+ CD206+	Top 1%	0.022		0.005		0.640		0.380		0.011	
	Top 10%	0.137		0.005		0.640		0.380		0.215	
	Positive (<32%)	0.022		0.177		0.072		0.380		0.423	
CD68+ CD163+ CD206+	Top 1%	0.004		0.177		0.433		0.773		0.848	
	Top 10%	0.002		0.177		0.122		0.773		0.479	
	Positive (<32%)	0.022		0.301		0.773		0.315		0.650	

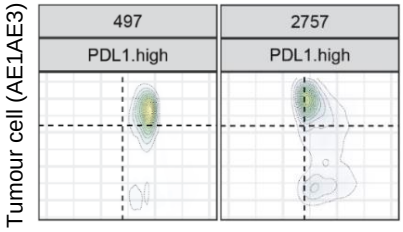
- P-value comparing between different patient groups (e.g. intestinal with diffuse) in each clinical parameter (e.g. of Histological GC subtype), determined with Chi-square analysis.

Lastly, given the high number of PDL1+ TAMs and PDL1+ tumour cells observed at single cell level (Figure 4.3.12), patients were stratified using different PDL1-intensity criteria on their PDL1+ cell populations (Figure 4.3.24A and B; defined in Figure 4.3.11).

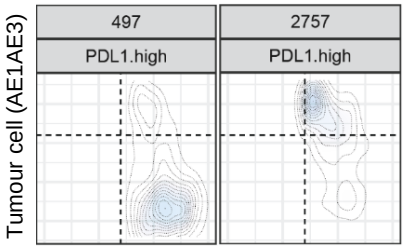
It was found that in patients with similar clinical parameters (Figure 4.3.24C), distinct primary source of high PDL1-expressing cells (AE1AE3+ tumour cells or CD68+ TAMs; Figure 4.3.24D) were observed. Patients with PDL1-expression from both tumour cells and TAMs were associated with improved overall but not relapse-free survival compared to the patients with PDL1-positivity from only tumour cells or TAMs (Figure 4.3.25).

Interestingly, this patient grouping based on the primary source of PDL1 was independent of other clinical parameters (Table 4.3.4), including GC subtypes, a parameter which were identified to be related to the overall expression of PDL1 in the microenvironment using PDL1+ cell intensity and density (Table 4.3.2 and Table 4.3.3). These data indicate that although GC subtype-associated PDL1-positivity could reflect the overall immunity and the corresponding immune suppression, it was not determinant of which cell population to be PDL1 positive.

A >Mean (32%)



B >Top 10%



C

Clinical parameters		#497	#2757
GC classification	Histological	Intestinal	Intestinal
	Molecular	Other	EBV
Stage	T	3	3
	N	0	0
	M	0	0
	AJCC^{6th}	2	2
Recurrence (days)		NA	Yes (210)
Overall survival (days)		2910	386

D

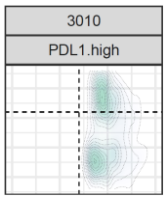
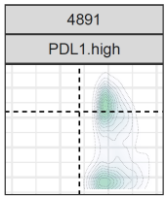
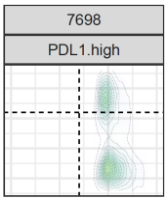
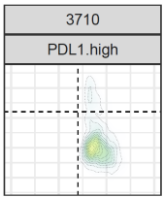
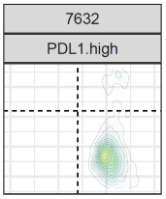
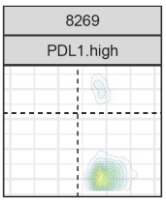
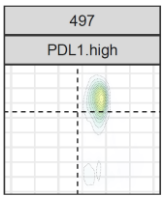
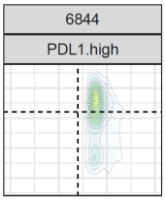
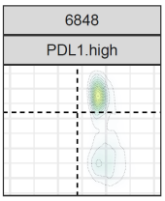
PDL1+ cell /	Different source of PDL1-positivity groups			
	I	II	III	IV
Tumour cell (Y axis)	-	+	-	+
Macrophage (X axis)	-	+	+	-
Representative samples (n=3) ***PDL1 threshold***: Mean intensity of the OPAL study cohort	PDL1 negative	  	  	  

Figure 4.3.24 Cellular source of PDL1 in gastric cancer patients

(A) Clinical parameters of patients in (B) and (C). (B) PDL1+ tumour cells and TAMs defined using the mean PDL1 expression of the OPAL study cohort. Threshold defined in Figure 4.3.12. (C) >Top 10% of PDL1+ cells. (D) Representative cellular profiles of patients with different sources of high PDL1-expressing cells. I: PDL1-negative patients. II-IV: PDL1-positive patients with PDL1 expressed by (II) both tumour cells (AE1AE3+; y axis) and TAMs (CD68+; x axis), (III) primarily TAMs and (IV) primarily tumour cells.

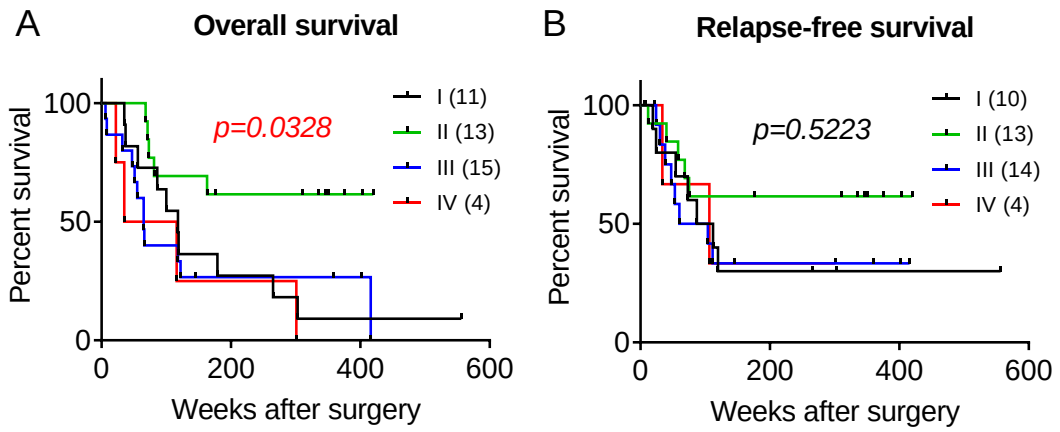


Figure 4.3.25 Survival based on PDL1 cellular source

Cell positivity was determined with the threshold of mean PDL1 expression of the **OPAL study cohort** (defined in Figure 4.3.11 Patients were stratified into four groups (number of patients in black brackets) based on the categories defined in Figure 4.3.24D and their (A) overall and (B) relapse-free survival was compared. Group I: PDL1-negative (black). II: PDL1 expressed by both tumour cells and TAMs (green). III: PDL1 expressed only by tumour cells (blue). IV: PDL1 expressed only by TAMs (red). Log-rank (Mantel-Cox) test.

Table 4.3.4 Clinical parameters of patients grouped with PDL1 cellular source

Group	PDL1+ cell	Cancer Subtypes (number of patients)				TNM Stages				AJCC Stages	
		Intestinal	Diffuse +Mixed	EBV +MSI	GS +Others	T3+T4	T1+T2	N2+N3	N0+N1	3+4	1+2
I	negative	4	7	1	10	7	4	3	8	3	8
II	T and M	9	4	3	10	8	5	3	10	6	7
III	T	12	3	5	10	13	2	4	11	9	6
IV	M	2	2	0	4	3	1	2	2	3	1
Chi-square		0.1271		0.3311		0.4383		0.7687		0.2693	

T: AE1AE3+ tumour cell. M: CD68+ macrophage.
Group I: PDL1-negative. II: PDL1 expressed by both tumour cells and TAMs. III: PDL1 expressed only by tumour cells. IV: PDL1 expressed only by TAMs.

4.3.9 Combined positive score of PDL1

A *Combined Positive Score* (CPS) method was recently proposed to define the PDL1-postivity of tissues for treatment stratification[130]. This method, in addition to using just cell densities and PDL1-positivity as described in the sections above, defines the relative "balance" of immunity/immune suppression to overall tumour burden (Table 4.3.5). To investigate if CPS could add survival predictive value in our model, different scores for each patient were calculated and their overall survival data were interrogated.

Table 4.3.5 Combined Positive Score (CPS) for PDL1-positivity

Selection criteria	PDL1-positivity	PDL1+ cell of interest	Comparing cells
1%[1]	>Mean intensity (32%)	All cell types	Total cells
CPS[2]	>Mean intensity (32%)	All cell types	Total tumour cells
MIDS[3]	>Mean intensity (32%)	TAMs and other cells	Total tumour cells
TPS[4]	>Mean intensity (32%)	Tumour cells	Total tumour cells
CPS (Mean TAM)	>Mean intensity (32%)	TAMs	Total tumour cells
CPS (10% TAM)	>Top 10%	TAMs	Total tumour cells
CPS (1%TAM)	>Top 1%	TAMs	Total tumour cells
1: Current threshold for clinical definition of PDL1-positivity. 2: Combined positive score. 3: Mononuclear immune cell density score. 4:Tumour proportion score[130].			

First, different scores were compared between GC subtypes (Figure 4.3.26) which were identified as the major influence of their PDL1 expression in previous analyses. The results showed that the diffuse/mixed subtype had lower scores across all comparisons (Figure 4.3.26A) but it was not as definitive for the molecular GC subtypes (Figure 4.3.26B). Using a >1% threshold to identify PDL1+ tissues (standard threshold used in clinics), the results were consistent with our previous findings that the diffuse/mixed and GS GC subtypes had less PDL1+ cases in our cohort (Table 4.3.6). Interestingly, no survival relevance was found using different scores which aimed to define the "balance" in the microenvironment (Figure 4.3.27). One explanation may be that, although diffuse/mixed and GS cancer subtypes had relative lower CPSs, some patients characterised with elevated CPSs (Figure 4.3.26A) were not due to their higher number of PDL1+ cells but to their lower number of tumour cells (Figure 4.3.28). This suggests that using the "ratio" between cells as a patient stratification criterion was not ideal across all GC cases.

In summary, using both PDL1 intensity on cells and PDL1+ cell number, overall high PDL1 expression in the tissue was highly correlated with gastric cancer subtypes and was associated with improved overall survival in our cohort. However, these correlations may differ between cell types and also depend on which PDL1-positivity criteria were used. For survival prediction, PDL1+ cell density was a more informative measurement compared to using the intensity of PDL1 on cells or the ratios (or balance) between cell populations. This may be due to the variation between FFPE tissues and the lower tumour cell characteristic of the diffuse and GS subtypes, which normally have a shorter survival.

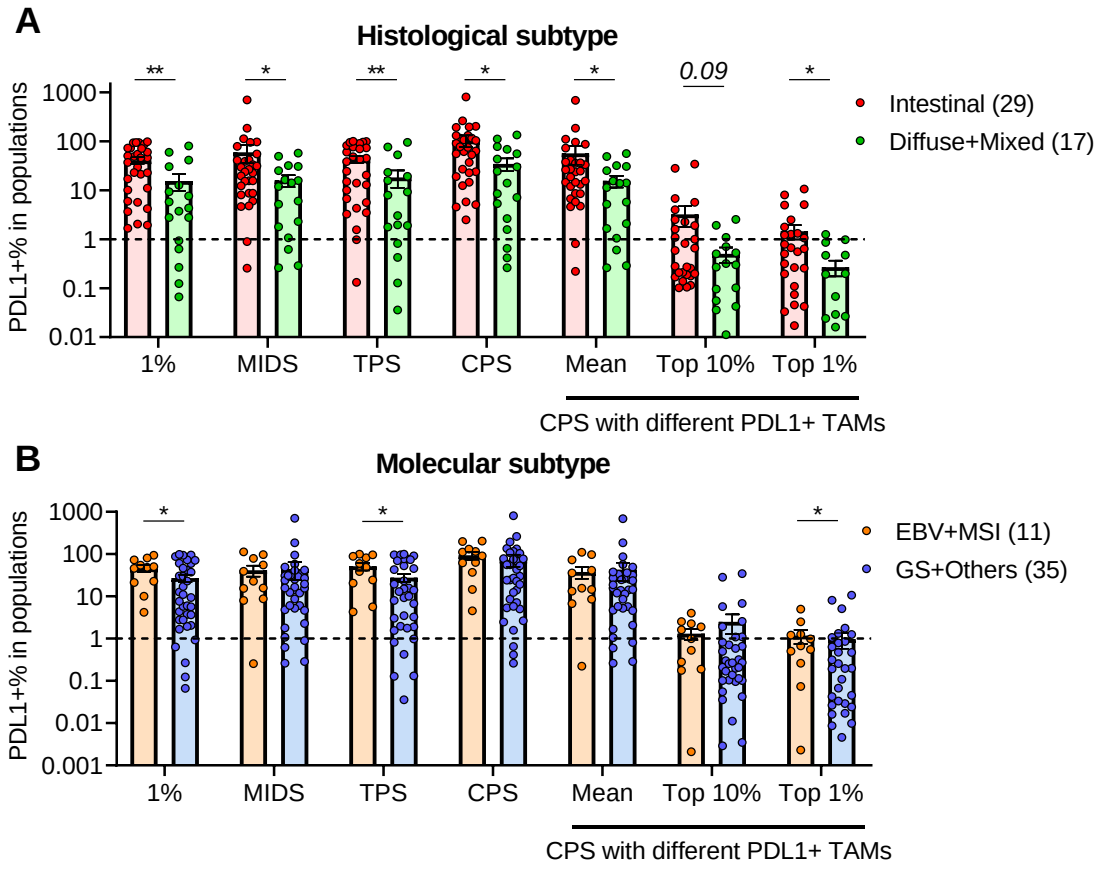


Figure 4.3.26 Combined positive scores between GC subtypes

(A) Histological and (B) molecular GC subtypes. Bar and error bars represent mean ± SD. Each point represents one patient. *p<0.05 comparing between GC subtypes. Mann-Whitney U test.

Table 4.3.6 Percentage of PDL1-positive cases in cohort defined with different combined positive scores

GC subtype	n	PDL1+ % in population						
		1%[1]	CPS[2]	MIDS[3]	TPS[4]	CPS (32% TAM)	CPS (10% TAM)	CPS (1%TAM)
Intestinal	29	100.00	100.00	93.10	93.10	93.10	34.48	31.03
Diffuse	17	70.59	82.35	82.35	76.47	82.35	17.65	5.88
EBV	3	100.00	100.00	100.00	100.00	100.00	33.33	33.33
MSI	8	100.00	100.00	87.50	100.00	87.50	50.00	37.50
GS	15	66.67	80.00	80.00	66.67	80.00	20.00	6.67
Other	20	100.00	100.00	95.00	90.00	95.00	25.00	30.00

1: Current threshold for clinical definition of PDL1-positivity. 2: Combined positive score.
3: Mononuclear immune cell density score. 4: Tumour proportion score.

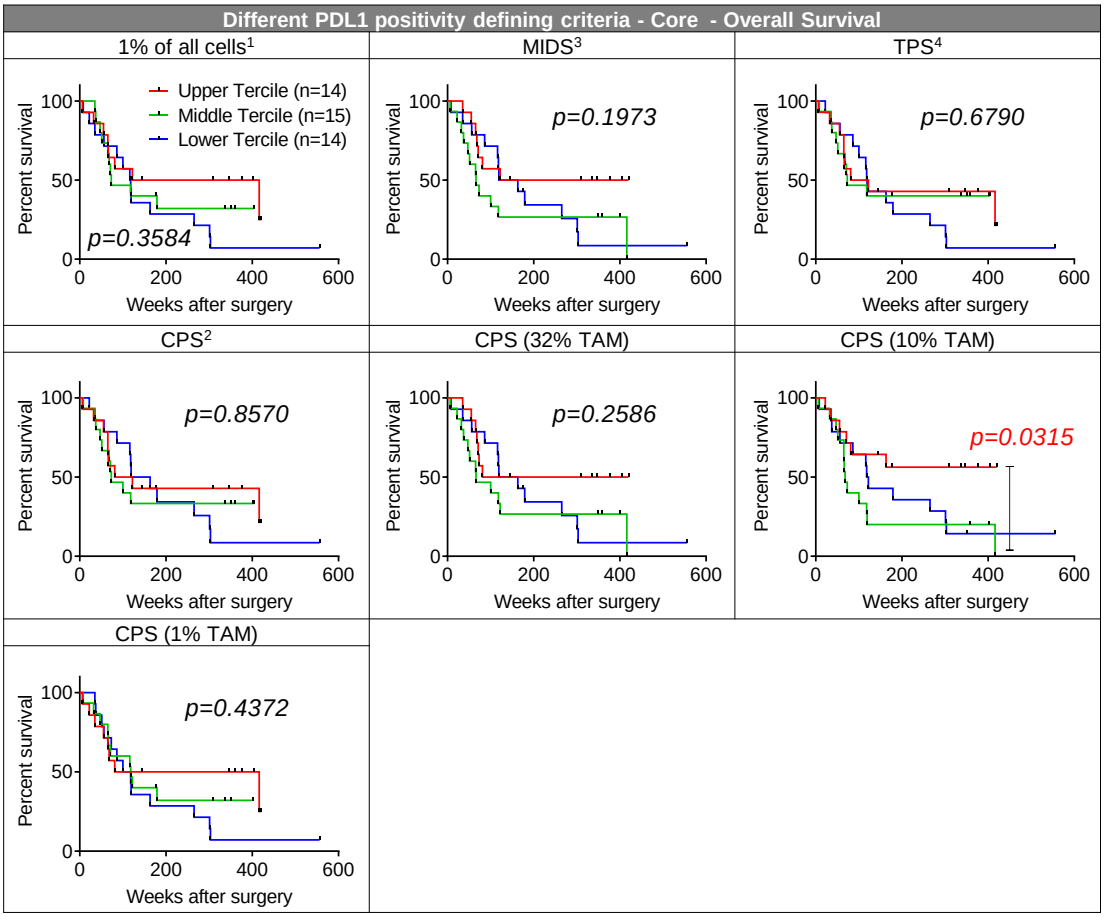


Figure 4.3.27 Overall survival based on different combined positive scores

Patients were stratified into three groups using different CPS criteria labelled on each column and overall survival was plotted. Upper tercile (density > 2/3 of the patients in the cohort; red line), Middle tercile (1/3 < density < 2/3 of patients in the cohort; green line). Lower tercile (density ≤ 1/3 of patients in the cohort; blue line). Log-rank (Mantel-Cox) test. 1: Current threshold for clinical definition of PDL1-positivity. 2: Combined positive score. 3: Mononuclear immune cell density score. 4: Tumour proportion score.

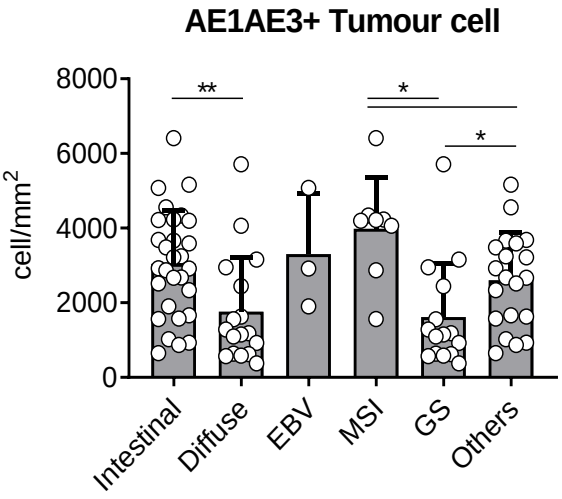


Figure 4.3.28 Tumour cell density between different GC subtypes

Bar and error bars represent mean ± SD. Each point represents one patient. *p<0.05, **p<0.01 comparing between GC subtypes. Mann-Whitney U test. N: Intestinal (29), Diffuse (17), EBV (3), MSI (8), GS (15), Others (20).

4.4 Discussion and Conclusions

In this Chapter, the anatomical distribution of the seven TAM populations described in the previous Chapter was investigated in detail and a spatial spectrum model of TAMs in GC was established. TAM heterogeneity was displayed not only at mm scale between the tumour and non-tumour regions, but also at μm scale in proximity to tumour cells. The relative increase or decrease of macrophage markers on individual TAMs between different regions could be contributed to the presence of the spectrum of macrophage phenotypes (Figure 4.4.1), possibly related to the metabolic activities in the corresponding tumour-related regions[309, 365] and the cytokine diffusion distance, which shows the effective range of these cytokines, within the tissue[476-478].

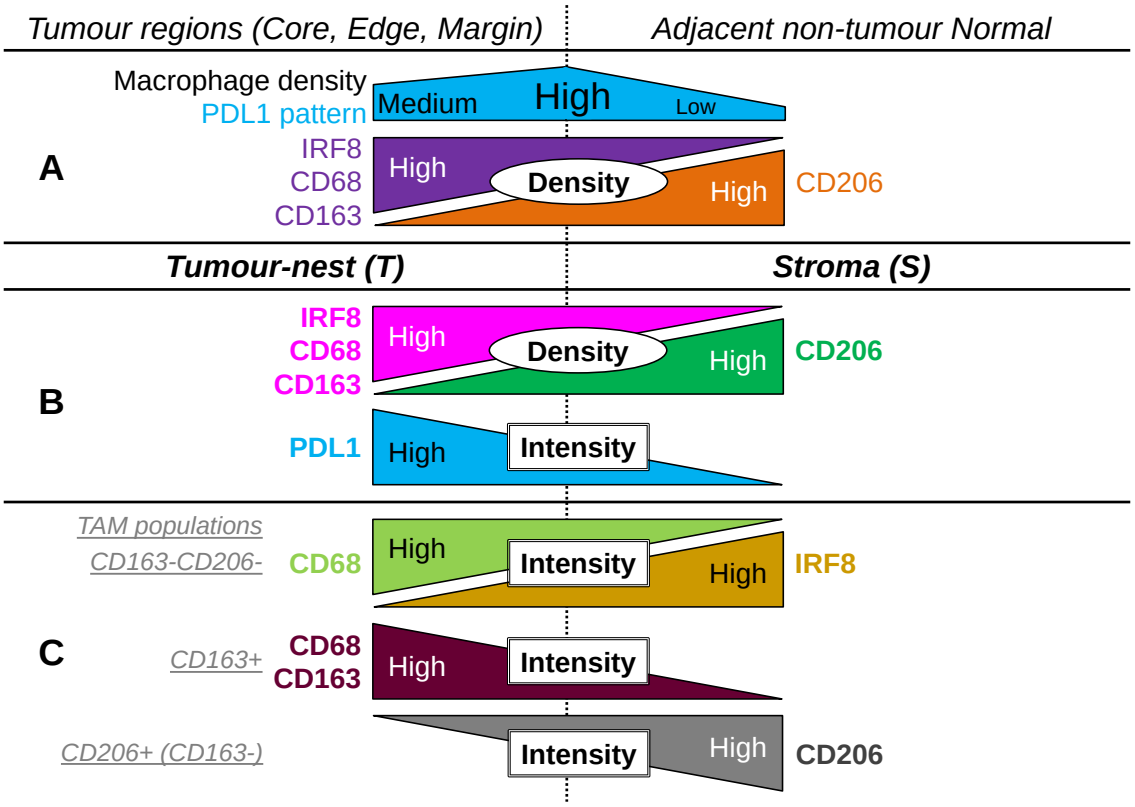


Figure 4.4.1 TAM density and intensity distribution between tumour locations

The distribution of TAM density between tumour/non-tumour regions and between tumour-nest/stroma areas were similar, which was related to an overall decrease of CD206 and an increase of CD68, IRF8 and CD163 expression on TAMs when more proximate to tumour cells (Figure 4.4.1A and B). However, these changes were not uniformly present in all TAM populations but were restricted to certain subpopulations (Figure 4.4.1C). An inverse trend of CD68 and IRF8 intensity was found on the CD68+IRF8+ TAMs, which were predominantly located within the tumour Core, particularly within the tumour-nest. The CD163+ TAM populations (CD68+CD163+, CD68++CD163+ and CD68+CD163+CD206+) behaved similarly in that both CD68 and CD163 expression increased on these TAMs when nearing the tumour cells. Interestingly, a negative correlation between the CD163+ (CD206-) and the CD206+ (CD163-) TAMs was found, suggesting that the environmental factors which polarised these M2-like marker-expressing macrophages may be distinct.

The PDL1 expression pattern displayed in the tissue correlated with the distribution of TAMs (Figure 4.4.1A) and the CD206+ TAMs were identified as

the population with the most intense PDL1 expression. However, survival analyses showed that the PDL1 status of patients was predominantly influenced by their cancer subtype, some with the density of different TAM phenotype and certainly not with the “ratio” between cells. The previously published CPS[130] method was not informative in predicting patient OS in our cohort. However, this result indicates that, unlike the commonly used “cytotoxic/regulatory T cell” ratio for interrogating patient survival[479, 480], which represents the balance between anti-tumour/anti-immune activities, CPS with PDL1 was more complicated. While PDL1 expression on a range of cell types represents the existence of immune suppression, it can be induced by IFN-γ which reflects an active immune response within an immune-escaped tumour microenvironment. Therefore, due to this complexity in interpreting the actual influences of PDL1 in the tissue, identifying the cell origin of PDL1 expression would be important. In addition, given that the CPS was designed to stratify and evaluate patient responses to immune checkpoint blockade, it will be interesting to test if CD206 and/or CD68 plus PDL1 could confer better stratification and prediction of response compared to using CPS alone if a cohort of anti-PD1/PDL1 treated patient becomes available. These therapies are not yet government subsidised for gastric cancer patients in Australia.

The finding of the multiplex IHC was validated with flow cytometry with fresh human GC biopsies. This result suggests that 1-3 randomly acquired biopsies from GC patients contained sufficient material for the determination of PDL1 status on TAMs. More importantly, the reproducibility of the results between different methods indicates that a rapid PDL1-status check may be performed clinically given it takes only three hours to measure PDL1 by flow cytometry compared to days to measure with multiplex IHC.

Potential bias may exist with this relatively small and subjectively selected OPAL study cohort, especially when compared with clinical parameters. However, including other unused cases from the MAUGIC cohort would not improve the power of the study due to the lower quality of tissue, lack of suitability for performing mIHC (ethanol fixed tissues are not applicable) and the

lack of comprehensive clinical information. Other cohorts or methods will be needed to validate the findings from this study.

4.4.1 Limitations

The sensitivity and specificity of the antibodies are limiting factors in mIHC-based studies. Whilst CD68 is a recognised mononuclear phagocyte marker, low CD68 expression can also be found on cell types such as fibroblasts and endothelial cells[429, 481] and the performance of the antibody may differ between antibody clones[482]. As a result, the CD68-only population referred to in this study is likely to contain a proportion of non-macrophage cells of different cell origins; therefore, limited conclusions were made on this population of cells. In addition, PDL1-positivity may differ between different antibody clones[129]. It was shown that different PDL1 antibodies exhibited huge differences in sensitivity towards both tumour cells and immune cells under similar staining conditions[129]. This provided the rationale for not only defining PDL1 expression with an arbitrary threshold but to analyse the intensity of staining of individual cells as shown in this study.

4.4.2 Summary

In summary, the results in this Chapter clearly demonstrate TAM spatial heterogeneity at both macro- and micro level. The distribution of TAM *in situ* was not random but was highly associated with their relative distance to the tumour cells. The CD68++CD163+ TAMs were associated with a favourable prognosis of the patients, and both cell number and proximity of TAMs to tumour cells were important. The CD68-only and CD206+ TAM populations were associated with high PDL1 expression in our cohort. However, the overall PDL1 status of each sample was more associated with the cancer subtypes than the presence of macrophage subpopulations.

Collectively, the data in this Chapter highlight potential influences of tumour microenvironment on TAM heterogeneity in gastric cancer, both phenotypically and presumably functionally. Therefore, the data indicate that to decipher the complicated TAM composition *in situ*, a more detailed interrogation of the tumour microenvironment was required.

Chapter 5 : Transcriptomic landscape of tumour-associated macrophage

5.1 Introduction

In the previous Chapter, the distribution of TAMs was identified as relevant to an overall decrease of CD206 and an increase of CD68, IRF8 and CD163 expression on TAMs when more proximate to tumour cells. In addition, while the CD68-only and CD206+ TAMs were identified as the TAM populations with the highest correlations with strong PDL1 expression, the PDL1 status of patients was predominantly influenced by their cancer subtype. These results highlight the importance of understanding the different tumour microenvironment which may contribute to TAM heterogeneity in GC.

Environmental factors derived from the tumour cells, immune cells, and other stromal cells in the tumour microenvironment are known to contribute to the dynamic process of macrophage polarisation *in vivo*[365, 483]. In this Chapter, to investigate this in the human GC setting, environmental gene signatures for each TAM population identified with multiplex IHC were derived using the matched cell density and Affymetrix gene profiling data from the same patient. These gene signatures were further interrogated with pathway analysis methods to decipher the complicated TAM composition *in situ*, to understand what cell types or signals might be driving the polarisation of TAMs in complex milieu, and to define possible factors that may be related to the differences between different TAM populations identified using multiplex IHC.

5.1.1 Resources

(A) **OPAL study cohort** (n=56): defined in Chapter 3

(B) **MAUGIC-Affy cohort** (n=99): whole tumour-derived Affymetrix gene profile obtained at the time of tissue collection

(C) **OPAL-Affy cohort** (n=34): overlap between the (A) and (B)

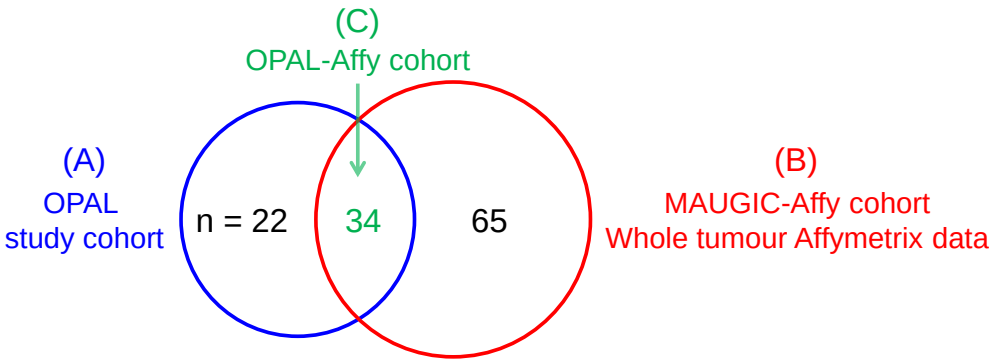


Figure 5.1.1 Defining different resource cohorts

Described in Materials and methods (§2.1).

5.2 Aims

Aim 1: To generate an environmental gene-signature of each TAM population characterised in this study

Aim 2: To compare the gene-signature between multiplex IHC-characterised TAM populations with *in vitro*-polarised macrophages

Aim 3: To investigate the influence of the TME on TAM polarisation *in situ*

Aim 4: To investigate possible reasons underlying the positive association of the CD68++CD163+ TAMs with improved patient survival

Major findings on the environmental signatures of TAM populations from the Chapter have been published[466]. The manuscript is included as Appendix 1.

5.3 Results

5.3.1 Definitions of gene/density correlation groups

To investigate the influence of tumour microenvironment on TAMs *in situ*, thirty-four patients (**OPAL-Affy cohort**; Figure 5.1.1) having both multiplex IHC cell density data (**OPAL study cohort**) and whole-tumour-derived Affymetrix gene profiles (**MAUGIC-Affy cohort**) were identified.

Using the **OPAL-Affy cohort** (n=34), individual genes in the Affymetrix database were tested with the cell density of each TAM population (Figure 5.3.1A), and the genes that had significant correlation with cell density were identified (Spearman correlation, $p<0.05$). These identified genes were referred as the "environmental gene signature" for each TAM population (Figure 5.3.1A), due to the fact that the Affymetrix gene profiles were generated with whole-tumour lysates which included both tumour and stromal compartments making the specific cellular origins of these genes difficult to deconvolute (§2.1.2).

A gene signature of a TAM population consisted of multiple smaller gene groups (Figure 5.3.1B; defined with unsupervised clustering method), including genes that were either positively or negatively correlated with the increase in cell density (Figure 5.3.1A and B). Some gene groups were cell population unique (X and Z in Figure 5.3.1A, Figure 5.3.1B and C), whilst others were shared genes referred as the "crosstalk" genes (Y in Figure 5.3.1A, Figure 5.3.1B and C). Within the crosstalk genes, a proportion had an inverse correlation between the different cell populations (Figure 5.3.1B and D), whereas the others had concurrent positive or negative correlations with cell density. Gene groups with positive and negative correlations with cell density were also present in the population unique signature (Figure 5.3.1A and B).

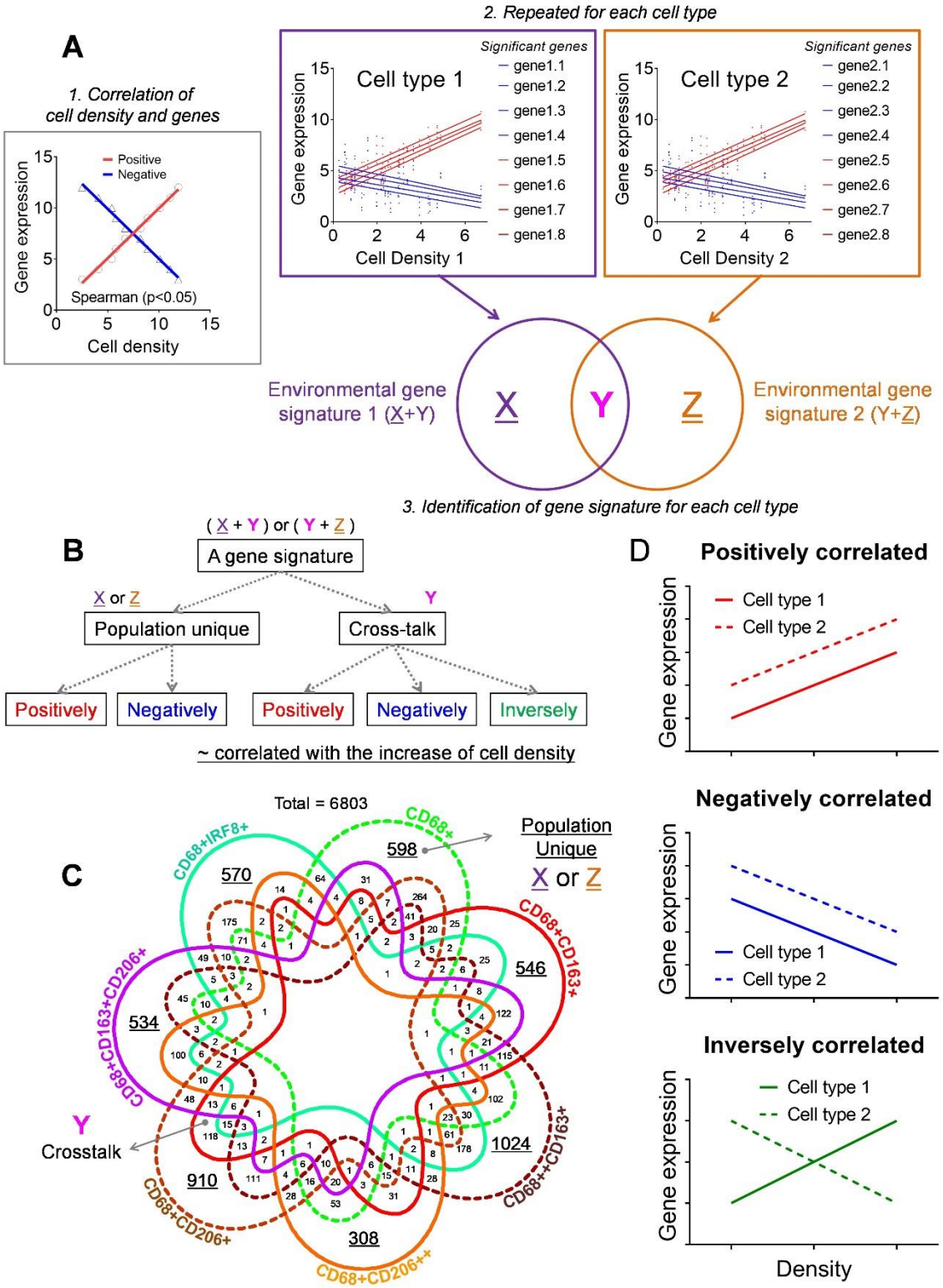


Figure 5.3.1 Definitions of gene/density correlation groups

(A) Spearman correlations (p<0.05) of cell density with gene expression were used to identify gene signatures for each TAM population. (B) Constitution of gene groups (X and Z: population unique; Y: crosstalk) in a gene signature of a cell population. (C) Representation of population

unique and cross-talk gene groups of the gene signatures. (D) Representations of positively, negatively and inversely correlated genes with density within the cross-talk gene group.

5.3.2 Gene signatures between mIHC-characterised TAMs

To acquire biological information from these TAM signatures, genes in different gene groups were interrogated with Reactome[411], an online pathway database, to determine the most relevant pathways associated with the gene groups. Significant pathways (false discovery rate, FDR<0.05; corrected with Benjamini-Hochberg[410]) were labelled for each TAM comparison (from Figure 5.3.2 to Figure 5.3.9).

5.3.2.1 M1-like TAM populations

The gene groups between M1-like macrophage populations, defined by the lack of CD163 and CD206 expression, were compared (Figure 5.3.2). The results showed that in a tumour with an increased number of both M1-like TAM populations (#B, Figure 5.3.2), an upregulation of TP53-regulated cell death and Insulin-like growth factor 2 (IGF2) gene signatures were observed. The CD68-only population was associated with the release of cytochrome C (#E) whilst the CD68+IRF8+ macrophages showed a unique signature of NF-κB activation (#C). These results suggest that the M1-like macrophage populations may have been controlling the actively growing tumours (high IGF2 signalling[484, 485]) by inducing tumour apoptosis[486, 487].

CD68+	CD68+ IRF8+	#	Associated pathways	FDR <0.05
P		A	1. Regulation of gene expression in beta cells 2. Regulation of TP53 activity through phosphorylation	
P	P	B	1. Insulin-like growth factor-2 mRNA binding proteins* 2. TP53 regulated transcription of cell death genes*	Y
	P	C	1. Generic Transcription Pathway 2. TRAF6 mediated NF-kB activation	
N	P	D	1. Mitochondrial iron-sulfur cluster biogenesis 2. Regulation of TP53 activity through methylation	
P	N	E	1. TP53 regulated cytochrome C release* 2. TP53 regulated transcription of cell death genes	Y
	N	F	1. Transcriptional activation of p53 responsive genes 2. Protein-protein interactions at synapses	
N	N	G	1. Neurotransmitter receptors and postsynaptic signal transmission 2. Integration of energy metabolism	
N		H	1. WNT mediated activation of DVL 2. Mitochondrial translation termination	

Figure 5.3.2 M1-like macrophages

Red: genes with positive (P) correlations with cell density. Blue: negative (N) correlations. White: no correlations, unique signatures of either cell populations. Associated pathways identified with the Reactome database. *: FDR<0.05 (Benjamini-Hochberg[410]).

5.3.2.2 CD163+ (CD206-) TAM populations

The CD163-positive but CD206-negative macrophage populations were investigated (Figure 5.3.3). These two TAM populations, CD68+CD163+ and CD68++CD163+, mainly differed in CD68 expression, which was shown to be upregulated when a macrophage was proximate to the tumour-nest (Figure 4.3.20A). In the gene group analysis, the CD68+CD163+ macrophages correlated with IL-4 and 13 (#C), suggesting a closer relationship with the true alternatively-activated M2 (or M2a[307, 488]; §1.4.1) macrophages polarised *in vitro* with IL-4 and IL-13. The CD68++CD163+ macrophages exhibited signatures related to strong immune signalling (IL-4, IL-13 and IL-10) and also the remodelling of extracellular matrix (ECM; #A, Figure 5.3.3). Having the IL-10 signature suggest that the CD68++CD163+ population may be related more to M2c[307, 457] macrophage and the presence of the IL-10 cytokine in the microenvironment may be one of the definitive factors between the locational differences of the two populations.

Both the CD163+ (CD206-) TAM populations negatively correlate with cell cycle-associated signatures, suggesting that cells in the tumour may have been less proliferative where these TAMs were abundant. Both of the populations were associated with TGFβ and STAT5 signalling (#B), and had an inverse relationship with IGF2 (anti-apoptotic[489] and enhanced cell proliferation[484]) and transcriptional regulation, indicating different rates of cell growth within the tumours where these TAM populations were abundant.

CD68+ CD163+	CD68++ CD163+	#	Associated pathways	FDR <0.05
	P	A	1. Signalling by Interleukins* (IL-10 / 4 & 13) 2. Extracellular matrix organization* 3. Cytokine signalling in Immune system* 4. Assembly of collagen fibrils and other multimeric structures* 5. Nuclear Receptor transcription pathway*	Y
P	P	B	1. Activation of STAT5 2. IL-2 / 7 / 9 / 15 / 21 signalling 3. TGFBR2 MSI frameshift mutants in cancer	
P		C	1. Nonsense-Mediated Decay (NMD)* 2. Interleukin-4 and Interleukin-13 signalling*	Y
P	N	D	1. Nuclear Receptor transcription pathway* 2. Generic Transcription Pathway*	Y
N	P	E	1. Insulin-like Growth Factor-2 mRNA Binding Proteins* 2. Metabolism of RNA*	Y
N		F	1. Cell Cycle, Mitotic* 2. Signalling by FGFR2	Y
N	N	G	1. TP53 regulated DNA repair genes* 2. Polo-like kinase mediated events 3. Cell Cycle, Mitotic	Y
	N	H	1. G0 and Early G1 2. G1/S-Specific Transcription	

Figure 5.3.3 CD163+ (CD206-) macrophages

Red: genes with positive (P) correlations with cell density. Blue: negative (N) correlations. White: no correlations, unique signatures of either cell populations. Associated pathways identified with the Reactome database. *: FDR<0.05 (Benjamini-Hochberg).

5.3.2.3 CD206+ (CD163-) TAM populations

The expression of CD206 on TAMs was found to decrease when macrophages were proximate to the tumour-nest (Figure 4.3.20C). As a consequence, the CD68+CD206+ TAMs were found to localise near the tumour cells whilst the CD68+CD206++ TAMs were more associated with the stroma and non-tumour tissues (Figure 4.3.1C and Figure 4.3.2). The gene profile of the CD68+CD206+ macrophages was associated with a unique signature of IL-6 and enhanced immune signalling (#A, Figure 5.3.4), whereas the CD68+CD206++ macrophages were more associated with an anti-apoptotic (IGF2; #B), IL-7-related (#G) and anti-inflammatory environment (decrease in IL-36[490]; #E).

CD68+ CD206+	CD68+ CD206++	#	Associated pathways	FDR <0.05
P		A	1. Interleukin-6 signalling* 2. Signalling by Interleukins 3. MAPK1/3 (ERK2/1) activation	Y
	P	B	1. Insulin-like growth factor-2 mRNA binding proteins* 2. Regulation of TP53 activity through methylation	Y
P	P	C	1. RUNX1 interactions 2. Sodium/Proton exchangers	
P	N	D	1. Defective SLCO1B1/3 2. Threonine catabolism	
	N	E	1. Regulation of TP53 expression 2. NOTCH2 intracellular domain regulates transcription 3. RUNX3 regulates NOTCH signalling 4. Interleukin-36 pathway	
N	N	F	1. Uptake and function of anthrax toxins 2. Deactivation of the beta-catenin trans-activating complex	
N	P	G	1. Interleukin-7 signalling* 2. MyD88/IRAK4 deficiency (TLR2/4) 3. Chromatin organization	Y
N		H	1. RUNX3 regulates CDKN1A transcription 2. Transcriptional activation of p53 responsive genes 3. Transcriptional activation of cell cycle inhibitor p21	

Figure 5.3.4 CD206+ (CD163-) macrophages

Red: genes with positive (P) correlations with cell density. Blue: negative (N) correlations. White: no correlations, unique signatures of either cell populations. Associated pathways identified with the Reactome database. *: FDR<0.05 (Benjamini-Hochberg).

5.3.2.4 The CD68+CD163+CD206+ populations

The CD68+CD163+CD206+ macrophages were numerous in both tumour and non-tumour regions and were found to accumulate at the tumour Margin (Figure 4.3.1C). High CD163 and CD206 expression have been reported on unpolarised (naïve) macrophages[414], which might explain their abundance in the normal tissue and their most distant spatial relationship with the tumour cells (Figure 4.3.5). Additionally, the reduction of CD206 expression and increased CD163 expression on TAMs observed between the non-tumour normal tissue into the tumour-site (Figure 5.3.5) indicates that a proportion of the CD68+CD163+CD206+ TAMs may represent a transient phenotype between the CD163+ (CD206-) near the tumour and the CD206+ (CD163-) TAMs at the Margin. To understand the possible change between these TAM populations, the gene signature of the CD68+CD163+CD206+ macrophages was compared to the CD163+ (CD206-) and the CD206+ (CD163-) TAM populations in Figure 5.3.6 and Figure 5.3.7, respectively.

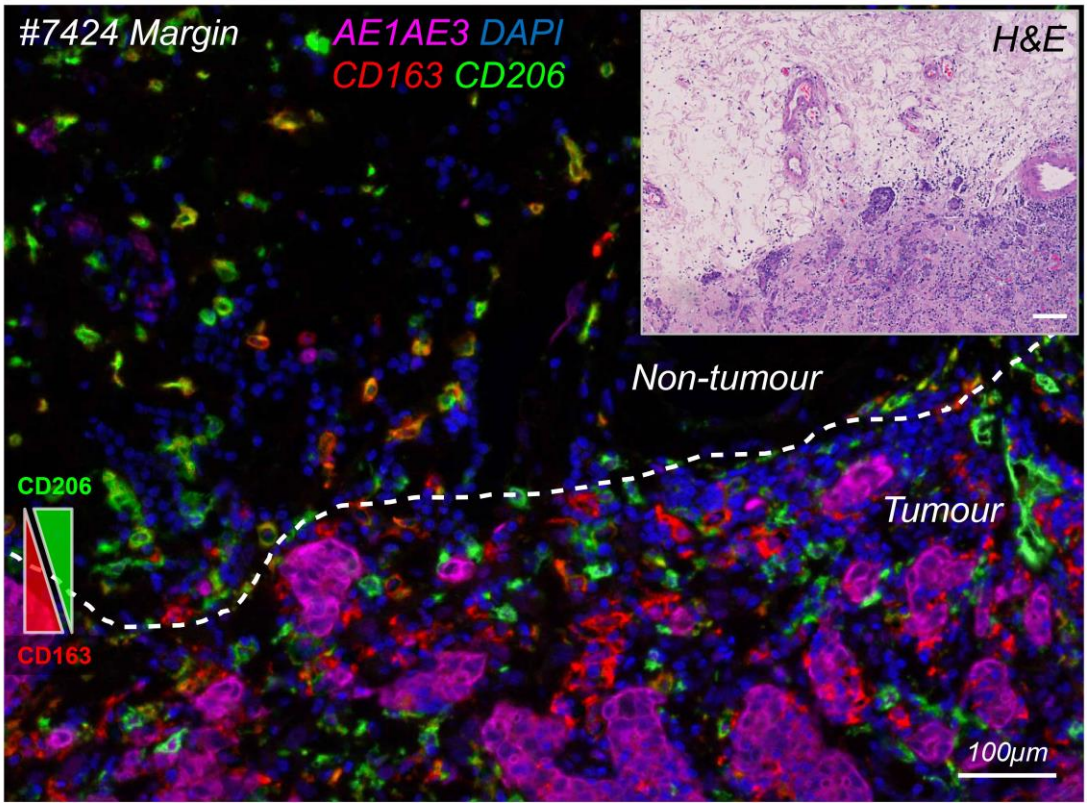


Figure 5.3.5 Differential CD163/CD206 expression at the Margin

Representative multiplex IHC and H&E images. Dashed line: interface of tumour Margin and adjacent non-tumour normal tissue.

When compared with the CD163+ (CD206-) TAMs, the results showed that the CD68+CD163+CD206+ population was more M2a-like which correlated with IL-4 and 13 (#F, Figure 5.3.6) and not with IL-10 (#A). It was not associated with STAT5 signalling (#C), was negatively associated with cell cycle genes (#I, J and M), and, interestingly, with the activation of T-cell receptor (TCR), PD1 signalling and the development of regulatory T cells (#E). These results suggest that the CD68+CD163+CD206+ macrophages at the Margin might be functionally associated with the infiltration of T lymphocytes.

There was not much similarity found in the CD68+CD163+CD206+ macrophages compared to the CD206+ (CD163-) populations (Figure 5.3.7). The CD68+CD163+CD206+ macrophages exhibited the unique signature associated with T cells and M2a-like phenotype (#F, Figure 5.3.7), as described above (Figure 5.3.6), and merely shared a IL-7 signature (#E, Figure 5.3.7) with the CD68+CD206++ macrophages that was also abundant in the non-tumour tissue (Figure 4.3.1C). These data suggest that the CD68+CD163+CD206+ macrophages may relate to the CD163+ (CD206-) population more than the CD206+ (CD163-) population.

CD68+ CD163+ CD206+	CD68+ CD163+	CD68++ CD163+	#	Associated pathways	FDR <0.05
		P	A	1. Signalling by Interleukins* (IL-10, 4 & 13) 2. Extracellular matrix organization* 3. Immune system*	Y
P		P	B	1. Generation of second messenger molecules 2. Interleukin-7 signalling 3. TCR signalling	
	P	P	C	1. STAT5 signalling (IL-2/7/9/15) 2. Synthesis of pyrophosphates in the cytosol	
	P		D	1. Nonsense-Mediated Decay (NMD)* 2. SHC-mediated cascade:FGFR1*	Y
P			E	1. Translocation of ZAP-70 to Immunological synapse* 2. Phosphorylation of CD3 and TCR zeta chains* 3. PD1 signalling* 4. Attenuation phase* 5. Generation of second messenger molecules* 6. HSF1-dependent transactivation* 7. RUNX1 and FOXP3 controlled Treg development* 8. Interferon gamma signalling	Y
P	P		F	1. TP53 regulated cell cycle* 2. Interleukin-4 and Interleukin-13 signalling*	Y
		N	G	1. Alpha-defensins 2. Negative control of E2F targeted transcription 3. Cell cycle	
	N	N	H	1. TP53 regulated transcription of DNA repair genes* 2. Transcriptional regulation by TP53* 3. Cell Cycle, Mitotic* 4. Cell Cycle	Y
N		N	I	1. RUNX2/1 regulated genes*	Y
N	N		J	1. Cell Cycle, Mitotic* 2. Signalling by FGFR2*	Y
	N	P	K	1. Metabolism of RNA* (CD44)	Y
	N		L	1. Cell cycle	
N			M	1. RNA Polymerase II transcription termination 2. Mitochondrial translation elongation 3. Regulation of TP53 expression	

Figure 5.3.6 All CD163+ macrophages

Red: genes with positive (P) correlations with cell density. Blue: negative (N) correlations. White: no correlations, unique signatures of either cell populations. Associated pathways identified with the Reactome database. *: FDR<0.05 (Benjamini-Hochberg).

CD68+ CD163+ CD206+	CD68+ CD206++	CD68+ CD206+	#	Associated pathways	FDR <0.05
		P	A	1. Interleukin-6 signalling* 2. Signalling by Interleukins 3. MAPK1/3 (ERK2/1) activation 4. IL-3, IL-5 and GM-CSF signalling	Y
	P	P	B	1. RUNX1 interacting co-factors 2. Linoleic acid (LA) metabolism	
	P		C	1. Insulin-like growth factor-2 mRNA binding proteins* 2. Regulation of TP53 expression	Y
P	P		D	1. Opioid signalling 2. Chemokine receptors bind chemokines	
P		P	E	1. FOXO-mediated transcription of cell cycle genes 2. Interleukin-7 signalling*	Y
P			F	1. Translocation of ZAP-70 to Immunological synapse* 2. Generation of second messenger molecules* 3. Phosphorylation of CD3 and TCR zeta chains* 4. PD1 signalling* 5. Attenuation phase* 6. Costimulation by the CD28 family 7. Interleukin-4 and Interleukin-13 signalling 8. RUNX1 and FOXP3 controlled Treg development 9. Interferon-gamma signalling	Y
	P	N	G	1. Interleukin-7 signalling* 2. MyD88/IRAK4 deficiency (TLR2/4)	Y
		N	H	1. RUNX3 regulated CDKN1A transcription 2. Transcriptional activation of p53 responsive genes	
	N	N	I	1. Uptake and function of anthrax toxins 2. Signalling to ERK5	
N		N	J	1. RUNX1 regulated transcription 2. TP53 regulated transcription of cell death genes	
N	N		K	1. Regulation of TP53 expression 2. RUNX3 regulated immune response / cell migration	
	N	P	L	1. Defective SLCO1B3 causes hyperbilirubinemia 2. Threonine catabolism	
	N		M	1. NOTCH2 intracellular domain regulates transcription 2. RUNX3 regulates NOTCH signalling 3. Interleukin-36 pathway	
N		P	N	1. Signalling by FGFR in disease* 2. PI3K Cascade*	Y
N			O	1. Transport of mature transcript to cytoplasm 2. G0 and Early G1	

Figure 5.3.7 All CD206+ macrophages

Red: genes with positive (P) correlations with cell density. Blue: negative (N) correlations. White: no correlations, unique signatures of either cell populations. Associated pathways identified with the Reactome database. *: FDR<0.05 (Benjamini-Hochberg).

5.3.2.5 CD68+CD163+ and CD68+CD206+ TAMs

A negative density correlation between the CD68+CD163+ and the CD68+CD206+ TAMs was observed within the M2-like spectrum (Figure 4.3.8). This result suggests that the CD68+CD163+ and the CD68+CD206+ TAMs were not concurrently abundant at a whole-tumour level, despite the obvious trend in the CD163 and CD206 changes observed (Figure 5.3.5), showing that these two TAM populations can still be found within the same microenvironment of a tumour.

When comparing the gene signatures of the two TAM populations, the IL-4/13 and IL-6 signatures were confirmed for the CD68+CD163+ and the CD68+CD206+ populations, respectively (#A and #D, Figure 5.3.8). The two populations share a positive association with IL-12 (#B), and a negative association with cell death signalling (#G). The CD68+CD163+ macrophages were correlated with the enhancement of cell cycle arrest (#C) and the downregulation of cell proliferation (#F), whilst the CD68+CD206+ macrophages had positive association with cell proliferation (#C) and possible interactions with other cell types (#D and #E; CTLA4, and FGFR2 with T lymphocytes and fibroblasts, respectively).

These results suggest that the difference in abundance of between the two TAM populations at the whole-tumour level may be related to the proliferation status of cells, and also the dominant immune compositions of individual tumours. Within the same tumour, these TAMs might interact with different cellular targets, or were polarised with the by-products of cell cycle modulation and/or immune activity.

CD68+ CD206+	CD68+ CD163+	#	Associated pathways	FDR <0.05
	P	A	1. Nonsense Mediated Decay (NMD) 2. IL-4 and IL-13 signalling	
P	P	B	1. JAK-STAT signalling after IL-12 stimulation* 2. IL-12 signalling*	Y
N	P	C	1. Transcriptional regulated cell cycle arrest*	Y
P		D	1. IL-6 signalling* 2. Signalling by Interleukins 3. MAPK1/3 (ERK2/1) activation 4. CTLA4 inhibitory signalling 5. IL-3, IL-5 and GM-CSF signalling	Y
P	N	E	1. Signalling by FGFR2* 2. PI3K/AKT signalling in cancer *	Y
	N	F	1. Cell cycle, Mitotic* 2. Insulin-like Growth Factor-2 mRNA Binding Proteins*	Y
N	N	G	1. RUNX1 regulated transcription* 2. TP53 regulated transcription in cytochrome C release	Y
N		H	1. TFAP2 (AP-2) family regulated transcription 2. WNT mediated activation 3. Function of SMAD2/4 in cancer	

Figure 5.3.8 Inversely correlated TAMs: CD68+CD163+/CD68+CD206+

Red: genes with positive (P) correlations with cell density. Blue: negative (N) correlations. White: no correlations, unique signatures of either cell populations. Associated pathways identified with the Reactome database. *: FDR<0.05 (Benjamini-Hochberg).

5.3.2.6 CD68+IRF8+ and CD68+CD163+CD206+ TAMs

The M1-like CD68+IRF8+ macrophages and the M2-like CD68+CD163+CD206+ macrophages were negatively correlated based on density (Figure 4.3.8), distributed among different tumour regions (Figure 4.3.1C) and were located the closest (12.3μm) and furthest (23.8μm) relative to tumour cells, respectively (Figure 4.3.5). The comparison of gene signatures between these populations confirmed an association of IL-1, NF-κB signalling (#A, Figure 5.3.9) with the CD68+IRF8+ macrophage and the IL-4/13 pathways (#D) with the CD68+CD163+CD206+ macrophages, as described above (Figure 5.3.2 and Figure 5.3.6). Both of the TAM populations showed positive correlations with active immunity (#B) but inversely correlated with cell death-related genes (#C) and extra-cellular matrix-associated pathways (#E, Figure 5.3.9). These results, in combination with their spatial location, infer an immune-relevant transition from a less inflamed environment in the distant normal tissue

into a more inflamed environment within the tumour regions. This pattern may be recapitulated at the microscopic scale between stroma and the tumour-nest that is within the 10-20μm from the tumour cells where the percentage of all TAM/tumour cell pairs peaked (Figure 4.3.6).

In summary, these data indicate that the heterogeneity of macrophages was influenced by their spatial distribution to the tumour cells in a very close range. The diffusion distance[476-478] of tumour-cell-derived cytokines and chemokines may be a controlling factor, additionally, other cells located within the microenvironment (e.g. T cells and fibroblasts; as associated with certain TAM population signatures), that cannot be defined with the current panel, may also play an important role in the polarisation of TAMs *in situ*.

CD68+ CD163+ CD206+	CD68+ IRF8+	#	Associated pathways	FDR <0.05
	P	A	1. Insulin-like Growth Factor-2 mRNA binding proteins 2. TRAF6 mediated NF-kB activation 3. Assembly of the ORC complex at the origin of replication 4. Other interleukin signalling 5. IL-1 processing	
P	P	B	1. Generation of second messenger molecules* 2. TCR signalling* 3. HLA-DQB1	Y
N	P	C	1. TP53 regulated cell death genes*	Y
P		D	1. IL-7 signalling 2. IL-4 and IL-13 signalling 3. Development of regulatory T lymphocytes	
P	N	E	1. Heat shock factor 1 (HSF1) activation* 2. Degradation of the extracellular matrix	Y
	N	F	1. Transcriptional activation of cell cycle inhibitor p21 2. FOXO-mediated transcription of cell death genes	
N		G	1. Signalling by FGFR2 2. RMTs methylate histone arginine 3. Transport of mature transcript to cytoplasm 4. Cell cycle	

Figure 5.3.9 Inversely correlated TAMs: CD68+IRF8+/ CD68+CD163+CD206+

Red: genes with positive (P) correlations with cell density. Blue: negative (N) correlations. White: no correlations, unique signatures of either cell populations. Associated pathways identified with the Reactome database. *: FDR<0.05 (Benjamini-Hochberg).

5.3.2.7 CD68++CD163+ TAM enriched tumour microenvironment

In §4.3.3, a survival advantage was found in patients with a higher CD68++CD163+ TAM density (n=14, >66% of the **OPAL study cohort**) compared to the patients with lower density (n=14, <33%; Figure 4.3.7). To explore possible mechanisms underlying this observation, the **MAUGIC-Affy cohort** (n=99) was clustered with the environmental gene signature derived from the CD68++CD163+ TAMs density (Figure 5.3.10). This result showed that two main clusters of patients were identified using the unsupervised clustering method and the major pathway differences between the groupings were in immune response and cell proliferation (Figure 5.3.10).

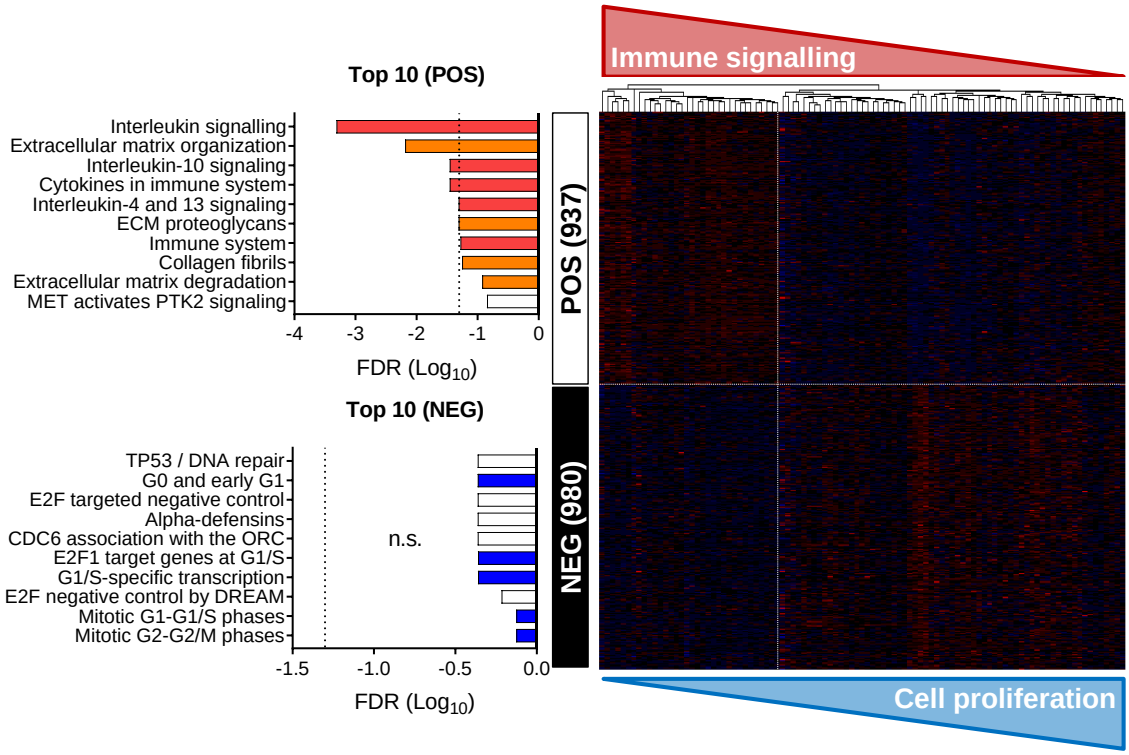


Figure 5.3.10 Unsupervised clustering of MAUGIC-Affy cohort with CD68++CD163+ TAM gene signature

Heatmap key: Red/Black/Blue: positive/no/negative spearman correlation. Most relevant pathways identified with the Reactome database. Pathway key: Red/Orange/Blue/White: Immune/Extracellular-matrix/Cell-cycle/Other related. Dashed line: FDR=0.05. n.s.: not significant.

A refined gene signature was developed using the genes that were within the associated pathways (Figure 5.3.10) that were most significantly correlated ($p<0.001$; Spearman correlation) with the CD68++CD163+ TAM density (Figure 5.3.11). Patients were stratified into High and Low groups based on the median expression of this refined gene signature using an unsupervised clustering method (Figure 5.3.11). This signature was validated using the extended **MAUGIC-Affy cohort** to expand patient number for testing their survival relevance and was tested using an online GC survival database[405] (n=348). Patients with an above median level of expression of this signature in both cohorts had improved overall survival (Figure 5.3.12).

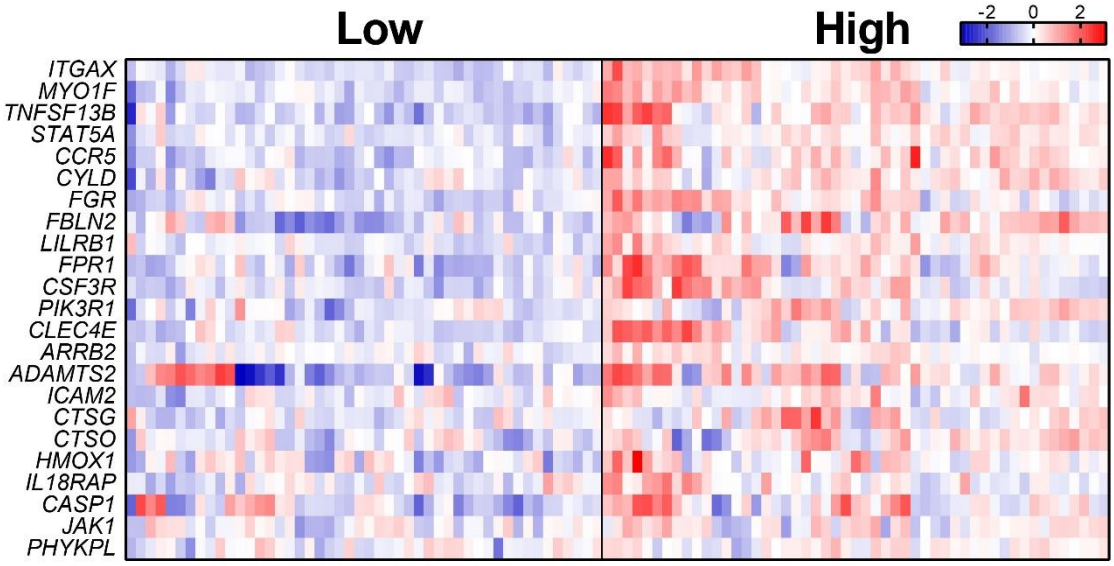


Figure 5.3.11 Patients in the MAUGIC-Affy cohort grouped using a refined CD68++CD163+ TAM signature

This refined gene signature was identified from the genes within the CD68++CD163+ TAM density-derived environmental signature (§5.3.2.2), using the criteria of (i) the gene expressions that were most significantly correlated its cell density ($p<0.001$, Spearman correlation), and (ii) were within the significantly-associated pathways (FDR<0.05) in Figure 5.3.11. Key: relative gene expression. Figure from[466].

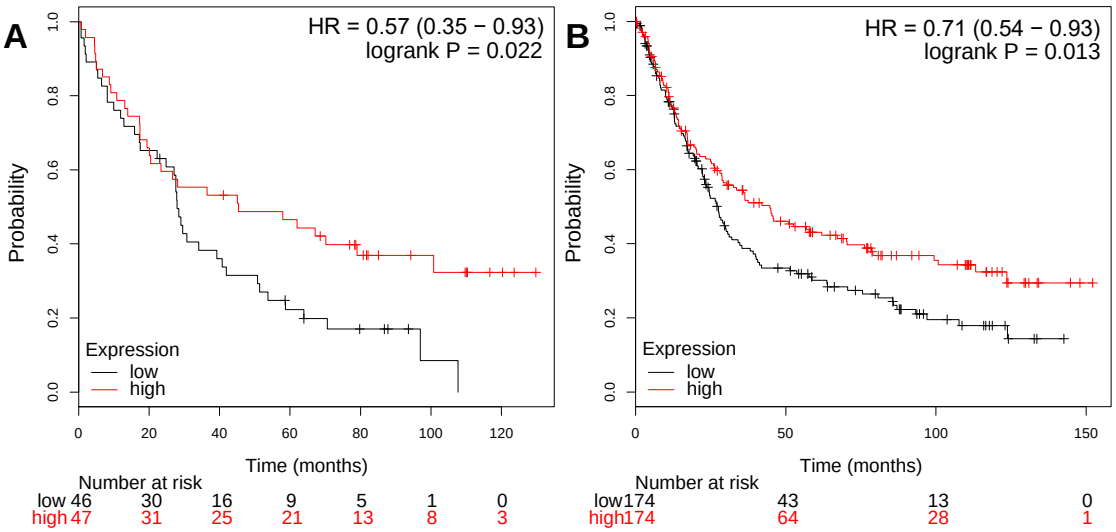


Figure 5.3.12 Validation of patient overall survival classified by the refined CD68++CD163+ TAM signature

(A) MAUGIC-Affy cohort (n=93 from the KMplot[405]; GSE51105). (B) Combined GC cohort (KMplot n=248; GSE14210, GSE15459, GSE22377, GSE29272 and GSE51105). Log-rank (Mantel-Cox) test. Figure from[466].

The immunological features of patients grouped with the refined CD68++CD163+ TAM gene signature (Figure 5.3.11) were then compared. Upregulation of both M1-like and M2-like macrophage and also T and NK cell related genes were observed (Figure 5.3.13A and B). This grouping of the **MAUGIC-Affy cohort** was also correlated with the increased inflammation scores[406] in patient samples as determined by a pathologist (C.M.; Figure 5.3.13C), suggesting that high CD68++CD163+ TAM density reflects an enhanced overall host immune response that could be one reason for the improved patient survival observed on univariate analysis (Figure 4.3.7).

Oxygen levels have been previously reported as an important factor contributing to TAM polarisation *in situ*[365]. To investigate if tumour hypoxia could be involved in the polarisation of the CD68++CD163+ TAMs, a hypoxia-related gene signature[491], as well as angiogenesis-associated genes (e.g. *VEGF*), were compared between the patient groups (Figure 5.3.13D). Interestingly, increased expression of *HIF1A* and decreased *VEGFA* were observed in patients with higher expression of the refined CD68++CD163+ TAM gene signature (defined

in Figure 5.3.11), suggesting a more hypoxic and less angiogenic microenvironment where these TAMs were abundant. However, the fold changes of the genes between patient groups were not substantial (0.28 and 0.42 for the *HIF1A* and *VEGFA*, respectively) indicating that these may be regional effects within the microenvironment rather than a global change in the tumours. Interestingly, while the *VEGFA* was downregulated in these tumours, the elevation of *VEGFB* and *VEGFC* may suggest a provoked vessel survival[492] and the lymphangiogenesis[493, 494] associated with these genes, respectively.

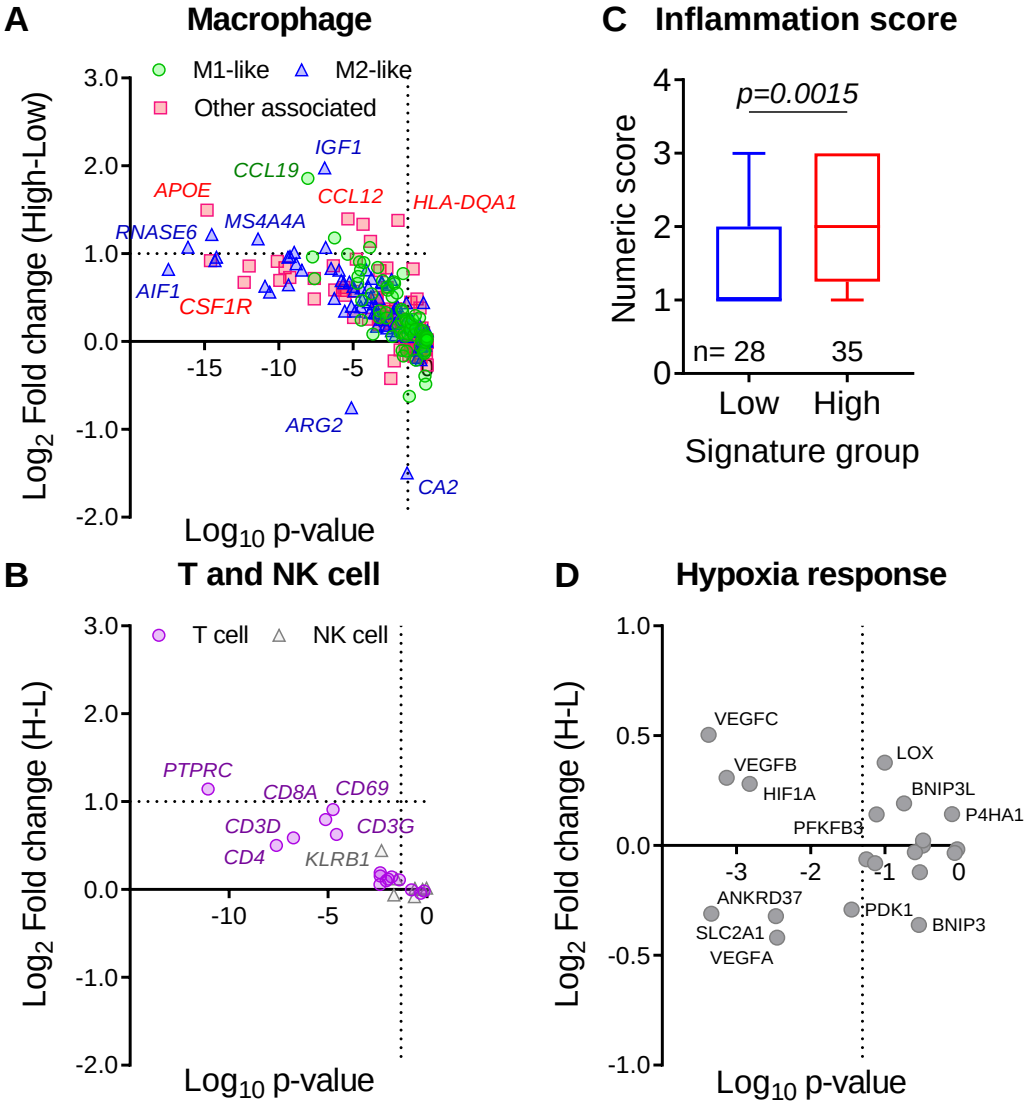


Figure 5.3.13 Gene comparisons between the High-Low patient groups

(A) Macrophage associated genes. (B) Selected T and NK cell related genes. (C) Inflammation score determined by a pathologist (C.M.). (D) Hypoxia-associated genes. Vertical dashed line: p value=0.05. Mann-Whitney U test. Figure from[466].

5.3.2.8 An overview of TAM spectrum heterogeneity with associated TME

Gene signatures of all seven TAM populations were combined and clustered using an unsupervised method to gain an overall interpretation of the macrophage system in GC (Figure 5.3.14). TAM populations were associated with immune and transcriptional regulation-associated pathways but to a different extent (Figure 5.3.14). Some were correlated with more specific cytokines (e.g. IL-1, 6 and 10), whereas others were associated with broader and more generic cellular functions (e.g. transcription, DNA repair).

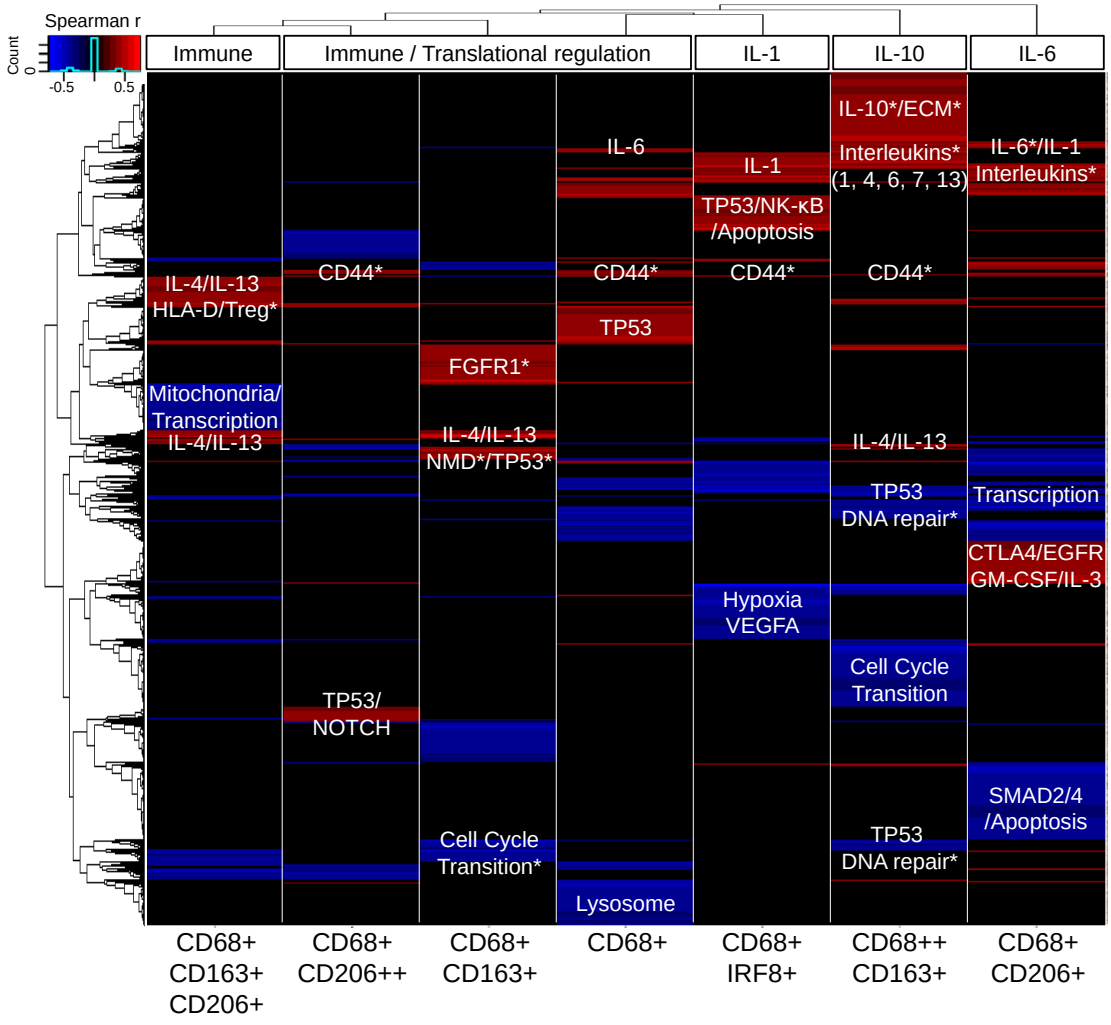


Figure 5.3.14 Unsupervised clustering of TAM-associated environmental signatures and associated pathways

List of genes that were significantly correlated with each TAM population density of matched patient samples (n=34; **OPAL-Affy cohort**) identified (Spearman). Red/Black/Blue: positive/no/negative correlation. *: FDR<0.05 (Benjamini-Hochberg). Figure from[466].

5.3.3 Characterisation of TME with *in vitro*-polarised macrophage gene signature

The gene signature analyses described in Section 5.3.2 suggest that a more detailed TAM characterisation method may assist in deciphering whole-tumour-derived gene expression data to reveal the existence of different TAM populations. Further investigation were performed to examine if using known gene signatures that characterise *in vitro*-polarised macrophages could have similar effects. A list of 217 differentially-expressed genes (Appendix 3) between the *in vitro*-polarised M1/M2 macrophages was identified by cross referencing published studies focusing on describing genomic changes macrophage phenotypes[171, 183, 313, 448, 495-497] and was tested with the **MAUGIC-Affy cohort** (n=99).

The **MAUGIC-Affy cohort** was first interrogated with the gene list with multiple unsupervised hierarchical clustering methods (e.g. complete, single, average, ward.D2). A subgroup of patients (n=9, red arrow; Figure 5.3.15) was found to always cluster together and had relatively high expression of specific genes. Further analysis was performed by comparing the differentially-expressed genes between this subgroup of patients (n=9) to the rest of the cohort (n=90); a large number of M1-like macrophage associated genes (e.g. *IDO1*, *IFNG*, *CXCL9*, *CXCL10*) were observed to be differentially expressed between the groups (Figure 5.3.16A).

A more refined *in vitro* macrophage signature was generated by selecting the significantly differentially-expressed genes ($p<0.05$) that had an absolute binary logarithmic fold change (FC) value greater than one (Figure 5.3.16B). Interestingly, three out of five macrophage-associated markers that were used in the multiplex IHC panel were also identified using this approach (CD163, CD206 and PDL1; Figure 5.3.16B). However, within this refined macrophage signature, all but one gene was upregulated within the nine patients; therefore, it was not possible to distinguish between the genes from either side of the macrophage polarisation spectrum. This result was similar to the result comparing patients with high CD68++CD163+ TAMs showing that genes associated with both M1 and M2 macrophage were elevated (Figure 5.3.13A).

To further investigate this matter, genes within the refined signature were correlated with each other using a Pearson correlation (Figure 5.3.17). As expected, the majority of the genes were highly and positively correlated (coloured in red). However, surprisingly, genes from either side of the *in vitro* polarisation spectrum tended to cluster together (arrows; Figure 5.3.17). This result suggests that there existed subtle differences between TAM populations in the whole-tumour-derived samples, however, these cannot be easily separated by gene expression profiles alone.

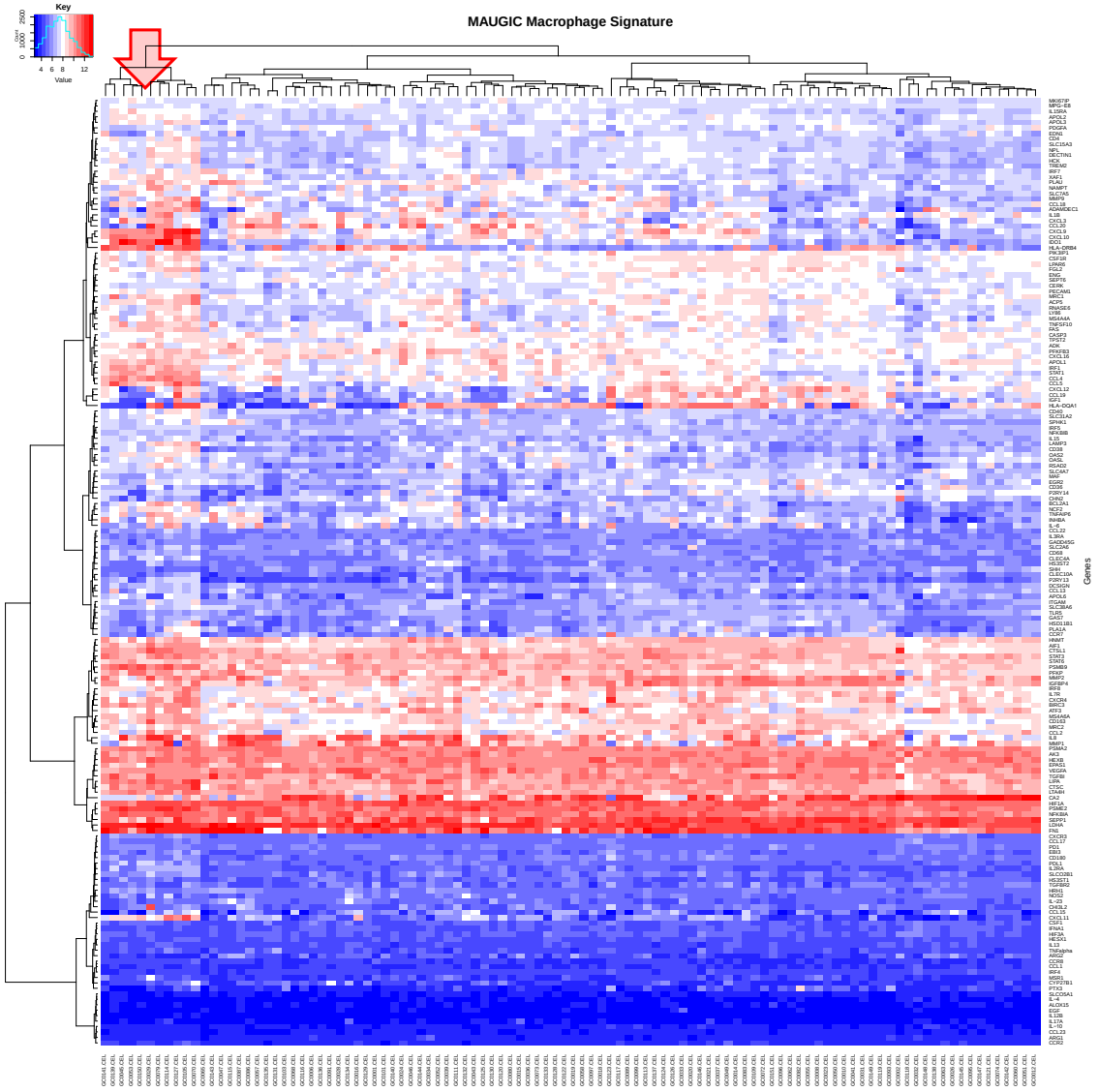


Figure 5.3.15 Interrogation of MAUGIC-Affy cohort with in vitro macrophage gene signature

Red arrow: a group of patient (n=9) identified having higher expression of a gene signature with different clustering method. Red/White/Blue: positive/no/negative correlation. Unsupervised clustering (ward.D2) using R software.

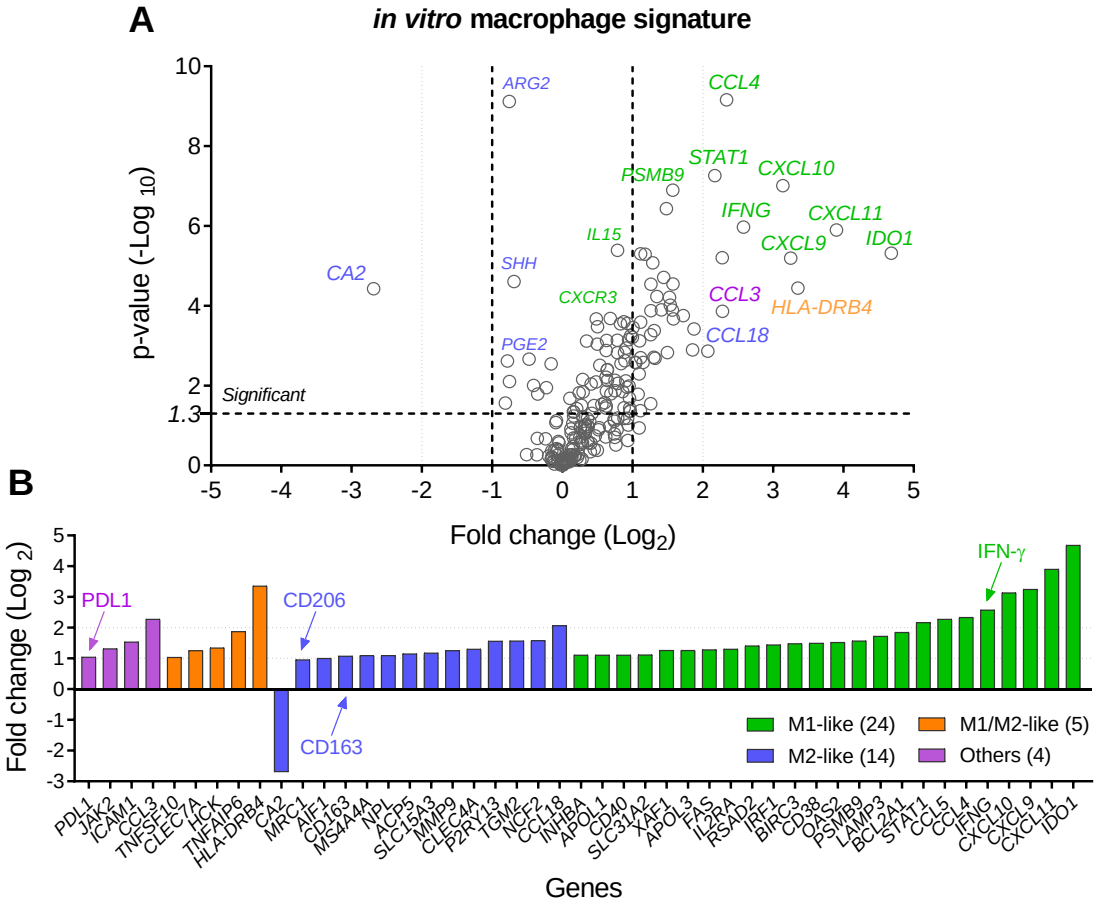


Figure 5.3.16 A refined in vitro macrophage gene signature

(A) Differentially-expressed genes ($p<0.05$) and (B) the genes with absolute fold change >1 between the Red-arrow-marked patients (n=9) in Figure 5.3.15 with the rest (n=90) of the MAUGIC-Affy cohort. Mann-Whitney U test.

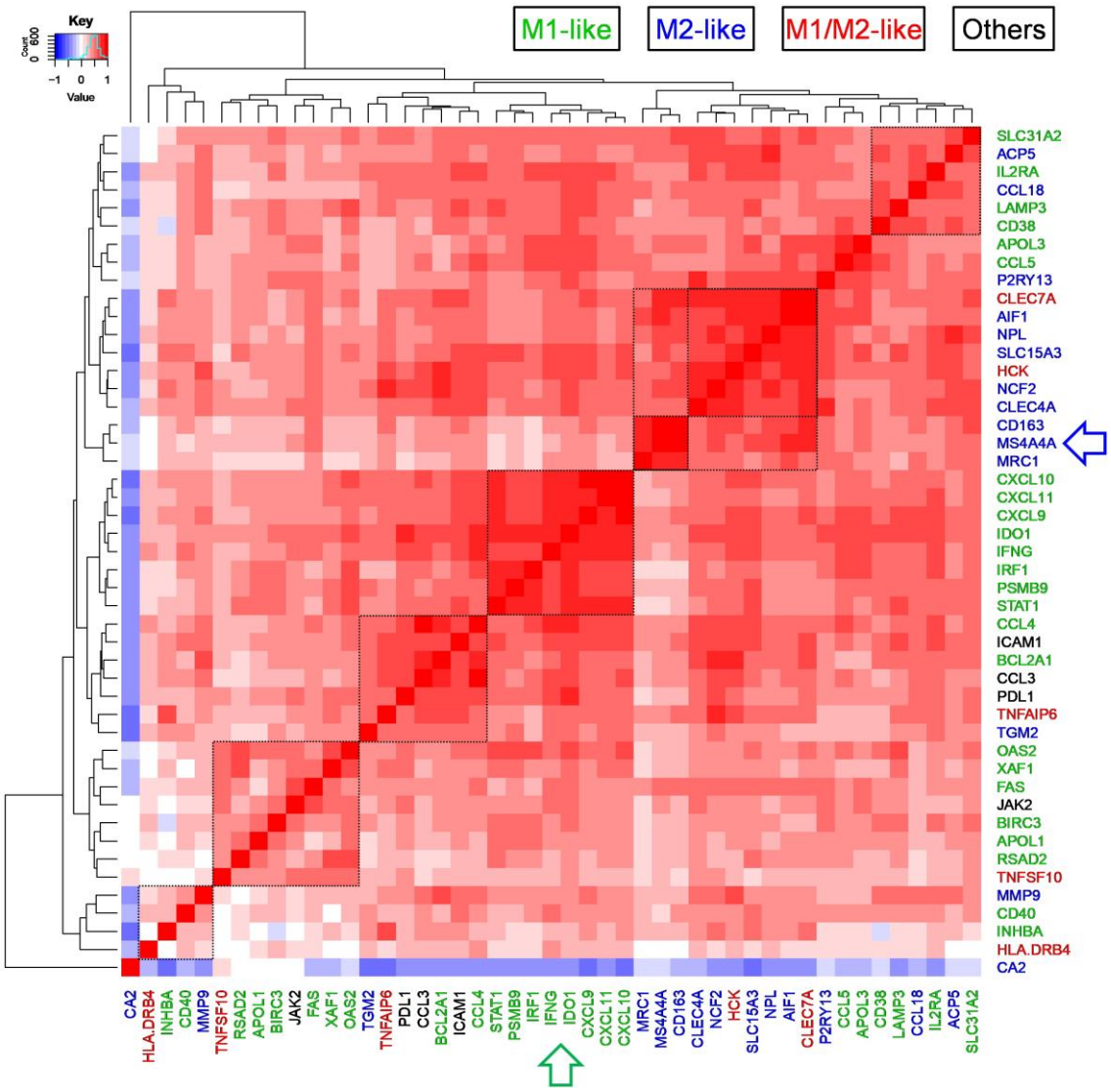


Figure 5.3.17 Gene-gene correlations of the refined macrophage signature

Pearson correlation of genes in Figure 5.3.16B in the MAUGIC-Affy cohort. Red/White/Blue: positive/no/negative correlation.

To explore possible associations between clinical parameters and macrophage gene signatures, an unsupervised clustering method was used to group patients in the **MAUGIC-Affy cohort** into three groups using the refined *in vitro* macrophage signature (Figure 5.3.18). Higher percentages of patients with EBV/MSI and Intestinal GC subtypes were identified in the High/Medium-expressing groups compared to the Low-expressing group (Figure 5.3.19), which aligned with the literature showing these patients were associated with higher immune signalling[31]. Indeed, patients in the High gene-expression group were confirmed to have higher immune signature genes associated with T cells, macrophages, and NK cells-associated genes (Figure 5.3.20). These patients also had relatively improved overall and relapse-free survivals, but were not statistically significant which may be due to low numbers in our cohort (Figure 5.3.21A). An elevated inflammation score and a lower BMI was found associated with the High gene-expression patients compared with the Low gene-expression ones (Figure 5.3.21B and C). No other clinical parameters were found to be associated with the patient groupings (Figure 5.3.22).

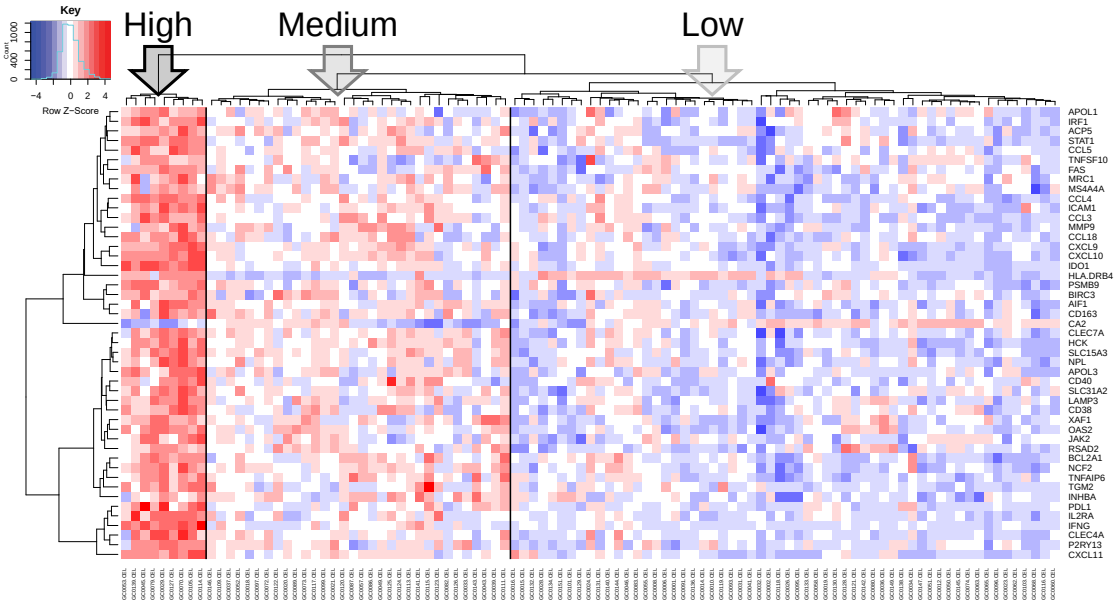
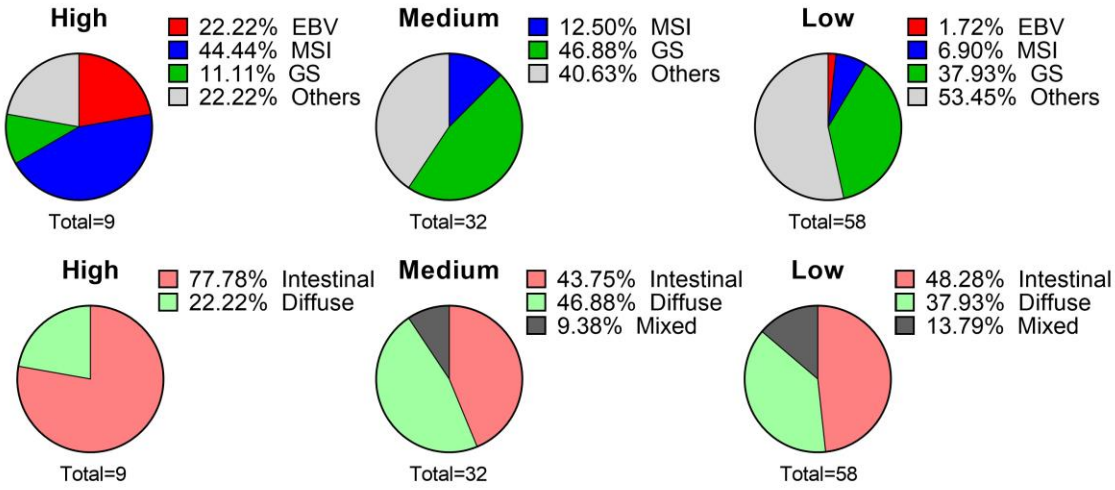


Figure 5.3.18 Stratification of the MAUGIC-Affy cohort with the refined in vitro macrophage signature

Red/White/Blue: positive/no/negative correlation. Clustered with unsupervised method (ward.D2) using R software.



Classifications	Subtypes	High	Medium	Low	Total
Molecular (TCGA)		9	32	58	99
Histological (Lauren)		9	32	58	99
Number of patient					
Molecular	EBV	2	0	1	3
	MSI	4	4	4	12
	GS	1	15	22	38
	Others	2	13	31	46
Histological	Intestinal	7	14	28	49
	Diffuse	2	15	22	39
	Mixed	0	3	8	11

2-way ANOVA	
TCGA (*p-value*)	
Row Factor	*0.172*
Column Factor	*0.161*
Lauren (*p-value*)	
Row Factor	*0.042*
Column Factor	*0.020*

Figure 5.3.19 Cancer subtype between patient groups

Patient cancer subtype compared between patient groups defined in Figure 5.3.18.

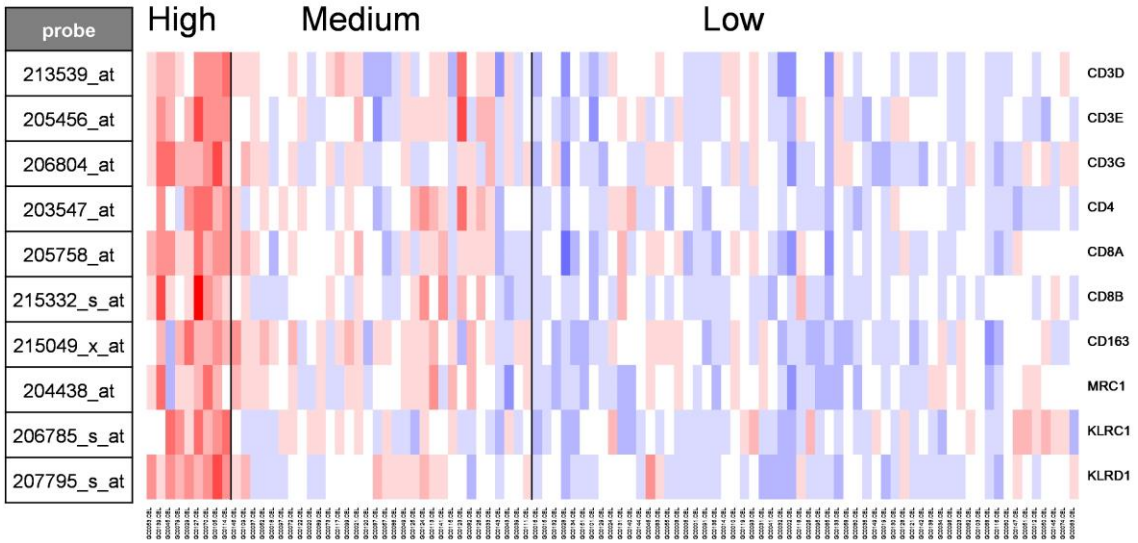


Figure 5.3.20 Immune related genes between patient groups

Red/White/Blue: positive/no/negative correlation. Supervised clustering of data based on patient groups defined in Figure 5.3.18.

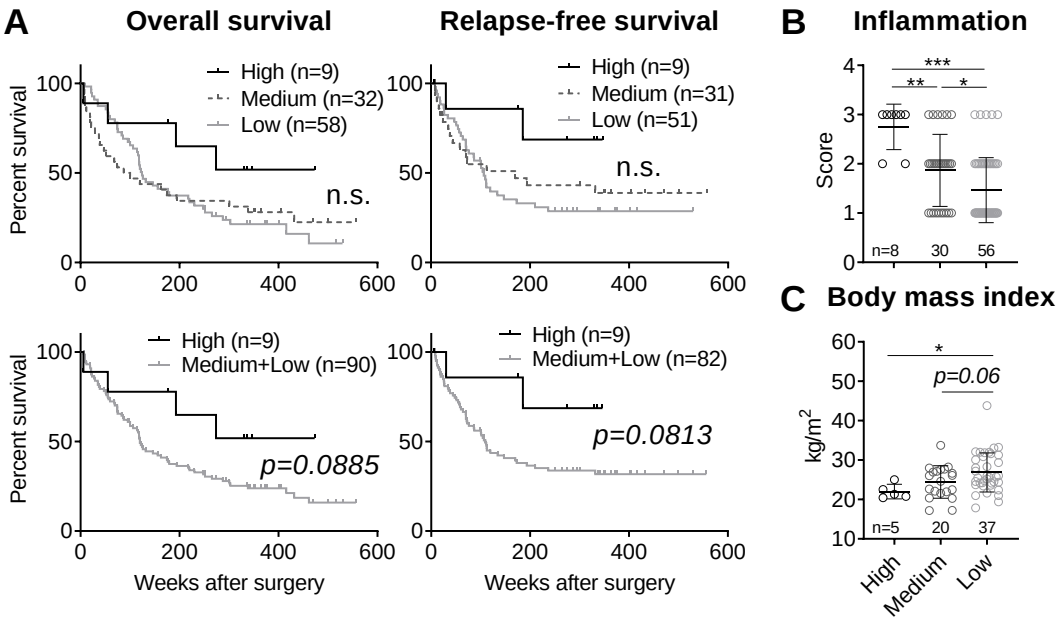


Figure 5.3.21 Survival and significant clinical relevance between patient groups

(A) Survival relevance, (B) inflammation score and (C) BMI compared between patient groups defined in Figure 5.3.18.

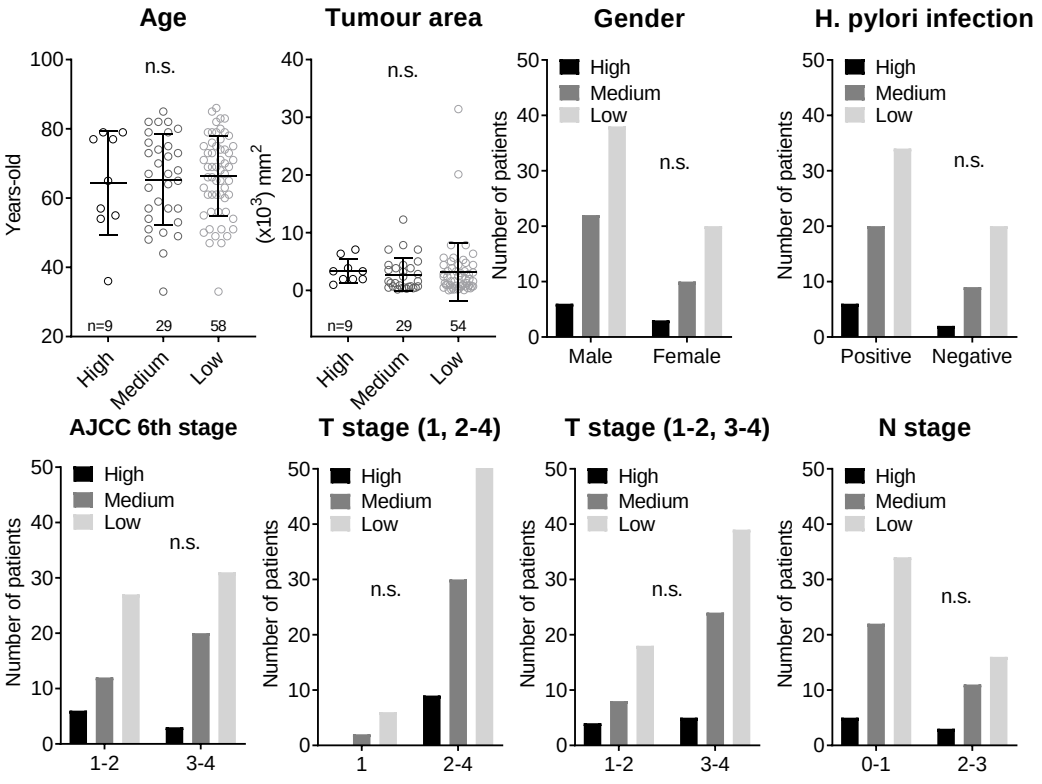


Figure 5.3.22 Non-significant clinical relevance between patient groups

Clinical parameters compared between patient groups defined in Figure 5.3.18.

5.3.4 Expression of phospho-STAT6 on TAM populations

The CD206 expression in TAMs was identified to be closely related to significantly up-regulated expression of PDL1. The majority of CD206+ macrophages preferentially located in the adjacent non-tumour normal region, at the tumour Margin and within the tumour stroma. More importantly, the gene signatures of the CD206+ macrophages associated with a more classic M2-like, anti-inflammatory and immune suppressive activity. To investigate if additional markers associated with IL-4/13 signalling could assist to more specifically define these TAM populations, the phosphorylation status of STAT6[498, 499] (pSTAT6) was selected. It is known that IL-4 and IL-13 can induce the phosphorylation of STAT6 which activates downstream gene expression related to macrophage M2 polarisation[500] and promote tumour growth[501]. Five patient samples from the **OPAL study cohort** with the most abundant CD206+ macrophages in the tumour Core were identified and were stained with a multiplex IHC panel consisting pSTAT6, CD68, CD163, CD206, AE1AE3 and DAPI (Table 2.2.1; Figure 5.3.23 to Figure 5.3.25).

In adjacent normal tissue within the tumour specimens, pSTAT6 staining was found to be either expressed by the CD206+ macrophages or cells neighbouring the TAMs (Figure 5.3.23). The pSTAT6+CD206+ TAMs can be found within different tumour regions, and occasionally with much higher pSTAT6 expression compared to the macrophages within the adjacent normal tissue (Appendix 4). However, the majority of the CD206+ TAMs were pSTAT6 low or negative and numerous pSTAT6+ non-macrophage cells were found in different tumour regions (Appendix 4).

However, no differential expression of pSTAT6 on TAMs was observed between the CD163+ (CD206-) and CD206+ (CD163-) populations, but the pSTAT6+ non-macrophage cells had a trend in accumulating close to the tumour cells (Figure 5.3.24). High pSTAT6 expression was also found in the tertiary lymphoid structures (Figure 5.3.25). Given their appearance and location preferences, these high pSTAT6 non-macrophage cells could possibly be T[502] or B cells[503].

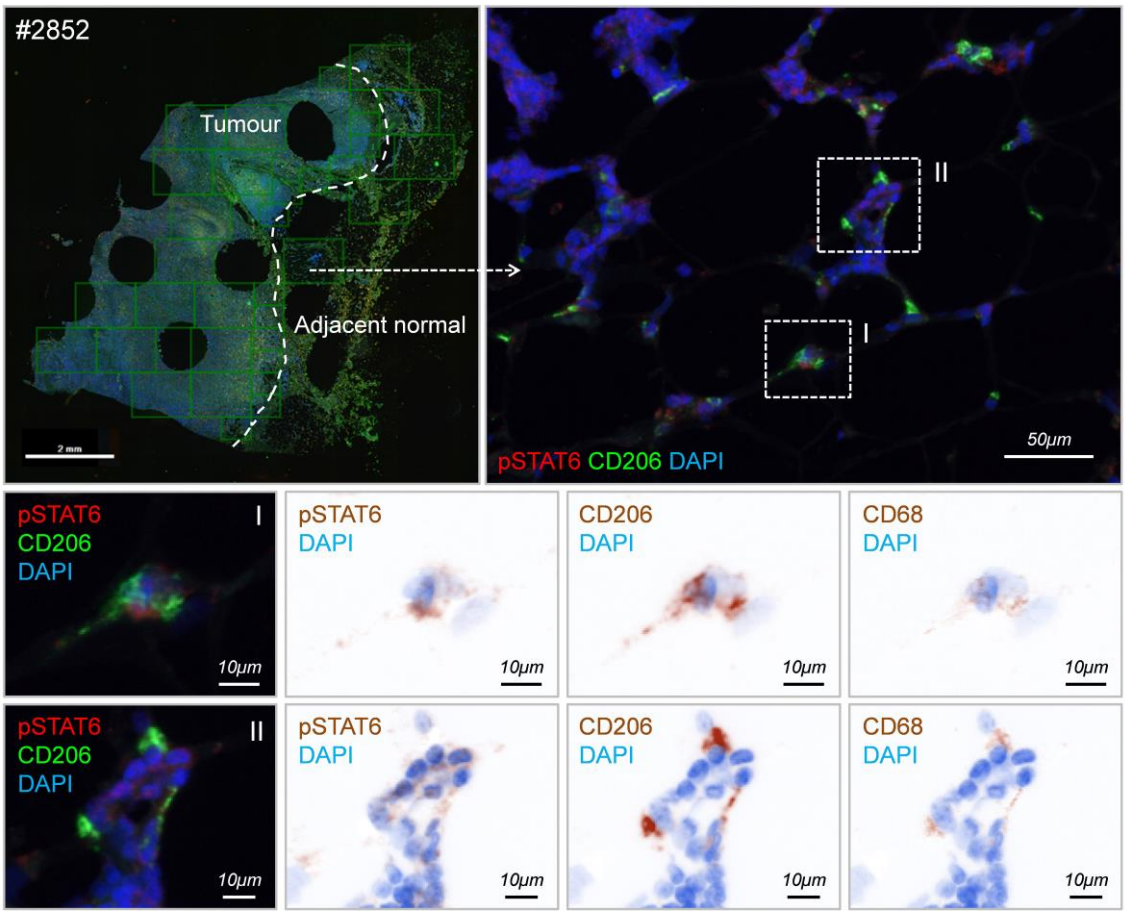


Figure 5.3.23 Phospho-STAT6 staining in GC specimen

Representative composite and single-stained IHC images of phosphor-STAT6 (pSTAT6) staining on macrophages within the adjacent non-tumour normal tissue of a GC specimen.

Although pSTAT6 was not differentially expressed by the TAM populations, interestingly, the CD163+ TAMs seemed to localise preferably within the pSTAT6-positive regions in the tumour regions irrespective of the presence of tumour cells (Figure 5.3.24), but rarely in or near the tertiary lymphoid structure (Figure 5.3.25). These results suggest that, in addition to the influence of tumour cells on TAMs, the cytokines or chemokines from these pSTAT6+ cells, possibly lymphocytes, might also be important factors in their heterogeneity *in situ*.

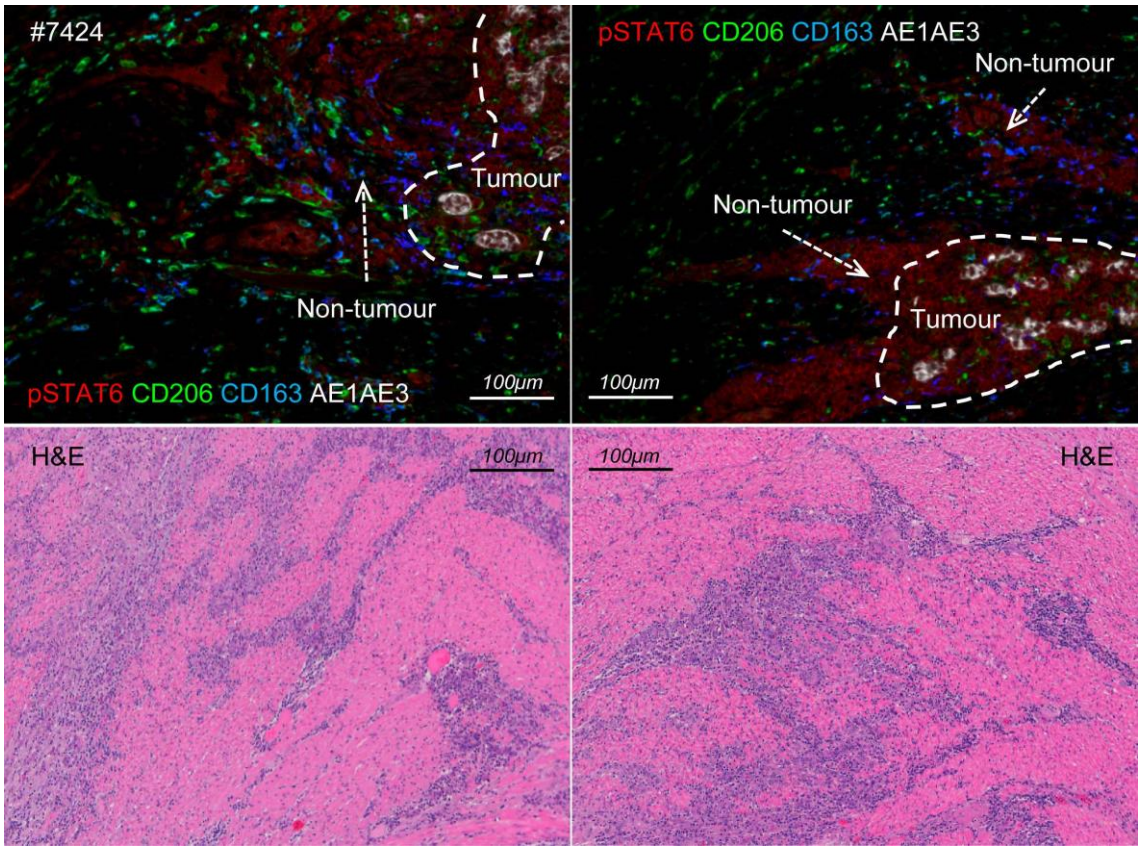


Figure 5.3.24 pSTAT6 staining on TAM populations within the tumour Core

Representative multiplex IHC and H&E images. Dashed line: interface of tumour and stroma.

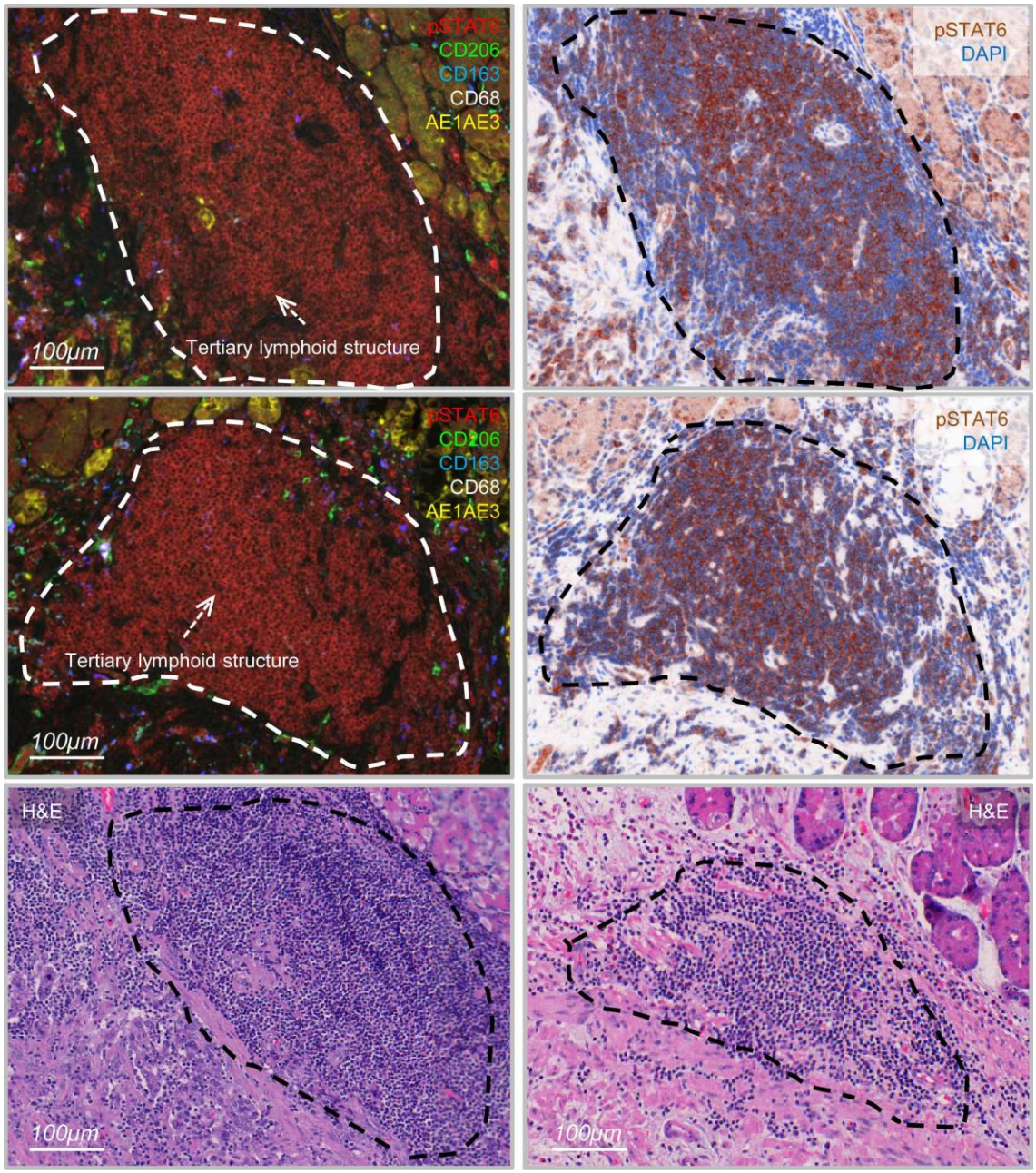


Figure 5.3.25 pSTAT6 staining at the tertiary lymphoid structure in GC tissue

Representative multiplex IHC and H&E images. Region within dashed line: tertiary lymphoid structure.

5.4 Discussion and Conclusions

5.4.1 Gene signatures between mIHC-characterised TAMs

In this Chapter, environmental gene signatures for each of the seven TAM populations identified with multiplex IHC in Chapter 3 were generated and compared. Pathways were associated with the gene groups in an environmental gene signature which acted partly as a validating approach for the IHC cell phenotyping with the properties of the markers chosen for the multiplex TAM panel (§3.1.5), but also as a mean to assign further putative functions to each TAM population. The results showed that the TAM populations characterised in this study may recapitulate some of the different macrophage subtypes proposed by others using *in vitro* polarisation methods (Figure 5.4.1).

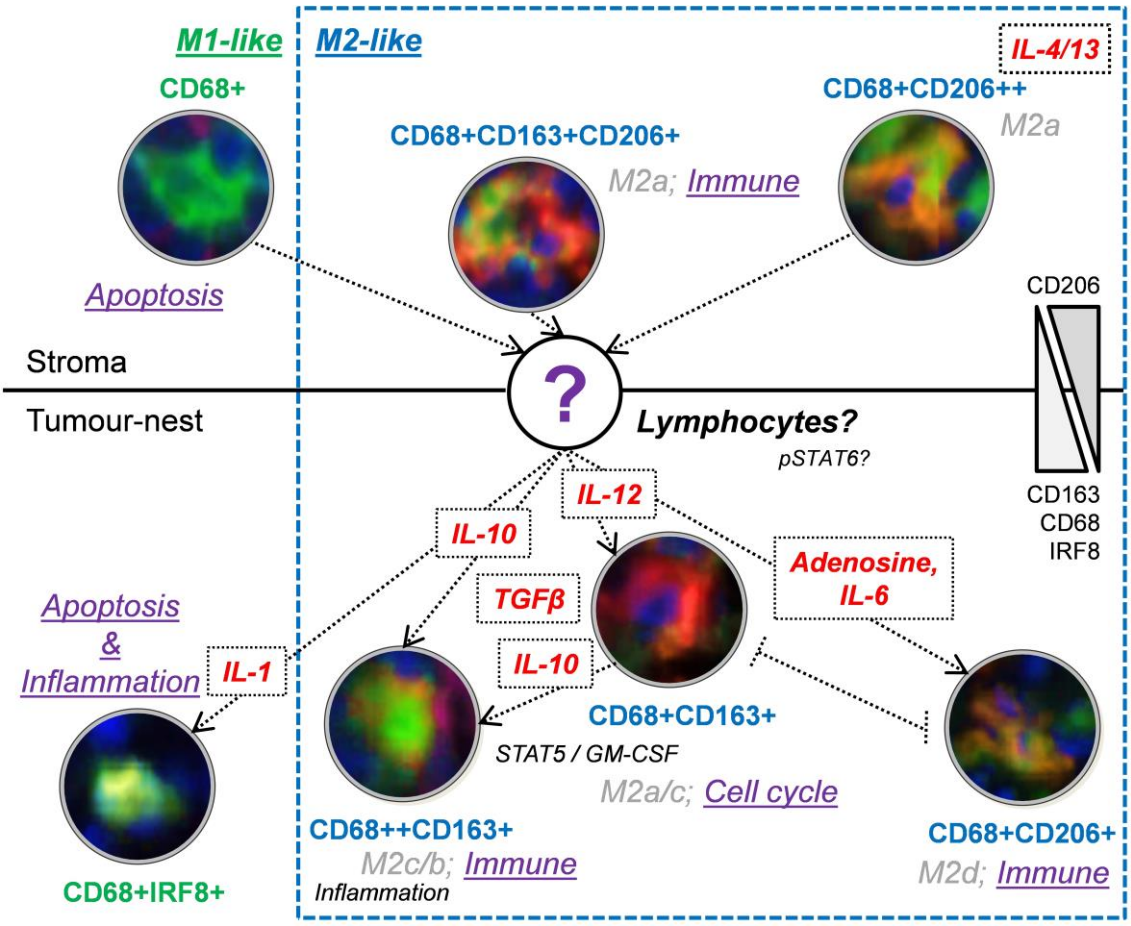


Figure 5.4.1 Schematic model of spatial macrophage polarisation in situ

Label keys: Grey: putative close approximation of *in vitro* macrophage subtype. Purple: Most relevant pathway related to each TAM population. Red: chemokine signature associated with each TAM population.

Both M1-like macrophages (CD68+ and CD68+IRF8+) were most significantly associated with apoptotic and cell death signalling. However, the two TAM populations had different association with the release of cytochrome C and NF-κB activation which suggest that these two TAM populations may reflect different stages of an apoptotic cascade. The CD68-only population might be abundant in an earlier or more active phase[504] whilst the CD68+IRF8+ macrophages were present in a later and readily inflamed environment when apoptosis was being maintained[505, 506].

The CD68+CD163+ TAMs exhibited a more *in vitro*-polarised M2a-like macrophage gene signature that associated with only IL-4 and 13. Whereas the CD68++CD163+ TAMs, that exhibited a higher expression of CD68, had an additional IL-10 signature which infer an association with the M2c phenotype (macrophage subtypes as described in §1.4.1). The CD68++CD163+ TAMs were associated with improved patient survival in the previous analyses (Figure 4.3.7). In conjunction with their gene expression profiles, this suggests that the CD68++CD163+ macrophages were enriched in a more anti-apoptotic, IL-10 enriched, cell mobility promoted (ECM degradation) environment compared to the CD68+CD163+ macrophages. However, interestingly, both CD163+ (CD206-) TAM populations exhibited a STAT5 signature, which is broadly considered as an M1-like macrophage marker[507] and has been shown to upregulate post LPS[508], IL-6[507] and GM-CSF[509] induction. Additionally, although CD163 has been described as a monocyte/macrophage specific marker[510, 511], CD163 has been found to be upregulated in a proportion of dendritic cells (DCs) polarised *in vitro* from blood monocytes[512, 513] during inflammation[514-516]. Therefore, based on the results from this Chapter, the functional associations of the CD68++CD163+ TAMs cannot yet determine if these macrophages were (i) more immune suppressive and anti-inflammatory, or (ii) more pro-inflammatory and may confer some DC-like functionality that assisted with the cell killing; alternatively, (iii) they may be bystanders in the microenvironment to mop up debris post cell death which requires further investigation.

The CD68+CD206+ macrophages that were identified as having the most abundant PDL1+ proportion in our cohort (Figure 4.3.12) were associated with

IL-6 signalling. This result suggests that these TAMs may be related to the anti-inflammatory M2d macrophage population polarised *in vitro* with IL-6 and adenosine[183]. Macrophages have been shown to be skewed toward an M2d status in an IL-6 autocrine[496, 517], and adenosine A_{2A}-dependent fashion that were independent of IL-4[518]. High adenosine in the tumour microenvironment is known to suppress T cell function by inhibiting their TCR signal transduction[519, 520]. Blockage of overall macrophage-derived IL-6 could promote T lymphocyte proliferation as well as their IFN-γ response in preclinical models[521, 522]. Additionally, IL-6 and leukaemia-inhibitory factor (LIF) were found to facilitate monocyte differentiation into TAMs[496]; however, *in vitro* IL-6-induced macrophages did not show an upregulation in PDL1[414]. Collectively, these data suggest that the $CD206^{low}$ TAMs (CD68+CD206+) may be more immune suppressive than the $CD206^{high}$ TAMs (CD68+CD206++) due to their high PDL1 expression, their M2d-like phenotype, in addition to their close proximity to the tumour cells (Figure 4.3.2). However, the high PDL1 expression on the CD206+ population observed in this study may have been due to simultaneous or secondary induction of multiple factors.

Overall, the M2-like (CD163+ and CD206+) TAM populations were broadly characterised with an IL-4/13 related pathway whilst the M1-like (CD163- and CD206-) showed a relationship with cell apoptosis and pro-inflammatory cytokines (e.g. IL-1; Figure 5.3.14). The CD68+CD163+CD206+ macrophages were more closely related to the CD163+ (CD206-) than the CD206+ (CD163-) populations and may be acting as a wall of T cell suppression at the Margin of the tumour. IL-6, IL10 and IL-12 may be important drivers of further TAM polarisation of the M2-like populations *in situ* which was dependent not only on the different tumour regions, but also on the cytokine influence and spatial distributions from other immune compartments (e.g. pSTAT6+ T and B cells) in the microenvironment.

One limitation from this study of whole tumour-derived gene expression analysis is noise from other cell types, especially from tumour cells. Therefore, a gene could have multiple functions in different pathways that would be dependent on the cell of origin. Nevertheless, the environmental gene signatures identified

with mIHC density results, together with the pattern of density distribution between regions of interest (Figure 4.3.1C and Figure 4.3.2) and the co-localisation pattern (Figure 4.3.8 and Figure 4.3.9), may reflect the dynamic process of macrophage polarization *in situ*.

5.4.2 Characterisation of TME with *in vitro*-polarised macrophage gene signature and pSTAT6 staining

In this Chapter, differentially-expressed *in vitro*-polarised M1/M2 macrophage genes were identified from the literature and were used to interrogate the **MAUGIC-Affy cohort**. The results showed that using the *in vitro*-polarised M1/M2 macrophage genes, a small proportion of patients can be identified and their enhanced immune signatures and inflammatory statuses were similar to those identified with multiplex IHC incorporating more detailed macrophage phenotyping. However, in general, using gene signatures alone was not sufficient enough to identify the different macrophage populations or to draw strong conclusions about how the immune cells were associated with patient parameters.

Interestingly, patients identified having high *in vitro*-polarised macrophage genes exhibited an elevated inflammation score (Figure 5.3.21), similar to the patients grouped with the refined CD68++CD163+ TAM signature (Figure 5.3.11). This may be partially explained by the downregulated CA2 expression of the High gene-expression group (Figure 5.3.16). CA2 encodes the enzyme Carbonic anhydrase 2 which was found to be highly-expressed by mouse macrophages compared to other cell types (e.g. tumours, endothelial cells, fibroblasts)[523]. CA2 has been shown to enhance Th2 (IL-4/13) responses[524] and mast cell-mediated inflammation[525]. These data suggest that the tumour microenvironments within the High gene-expression patients were associated with a Th1-driven inflammation. This imbalance between Th1/Th2 inflammation[526] may be related to the significant difference in BMI between the patient groups (Figure 5.3.21) since obesity is viewed as a chronic but low-grade inflammation state[527]. Obesity has been reported to reduce the cytotoxic property of NK cells due to intra-cellular lipid accumulation[528] and to promote macrophages that resemble TAMs[529]. Therefore, there may also be a systemic

metabolic reprogramming of the immune activities in the patients in different BMI groups, however, more samples would be required for further investigation.

pSTAT6 was selected as the downstream target of the IL-4/13 signalling pathways to examine if it could more specifically identify certain TAM populations. However, pSTAT6 was not a discriminative marker for the macrophages and other cell types *in situ*. Some high pSTAT6 expression was found on TAMs supporting the fact that these pathways are important for macrophages[499]. However, a combination of other markers are needed to further investigate its significance for the TAM populations identified in this study.

5.4.3 Summary

In summary, in this Chapter, environmental gene-signatures were successfully generated for each of the TAM population defined in Chapter 3 using mIHC. The data indicate that these TAM populations identified *in situ* may resemble some of the macrophage populations polarised *in vitro*. Importantly, interrogation of the whole tumour-derived gene profile in conjunction with the more detailed TAM characterisation data and multiplex IHC could help to decipher the complicated composition of the TAM/tumour relationship *in situ,* but not with the *in vitro*-polarised macrophage gene signature alone. Moreover, it also revealed the importance of including a broader view of other immune cells for their possible contributions to TAM heterogeneity in the GC microenvironment.

Chapter 6 : Interactions between tumour-associated macrophages and tumour-infiltrating T lymphocytes

6.1 Introduction

In the previous Chapter, environmental gene signatures were generated for each TAM population identified with multiplex IHC to investigate their possible interactions with the tumour microenvironment. These results identified certain cytokines (e.g. IL-1, 6 and 10) that may be critical for TAM polarisation *in situ* and suggest possible contributions of other immune cells to shaping TAM heterogeneity in the GC microenvironment.

TAMs and tumour-infiltrating T lymphocytes (TILs) are two of the most abundant and well characterised immune populations in the tumour microenvironment (TME)[294]. The interactions between these cell types have long been recognised and studied[530, 531] in different disease models[532, 533] and the Th1/Th2 classification was the exemplar that allowed the creation of the M1/M2 bipolar model[169]. The TAMs and TILs have been reported to exhibit different functionalities in the TME that are related to pro- and anti-tumoural roles, respectively[294]. In addition, the difference in their spatial location within the tumours has been described as being “inversely correlated”[189] with TILs more commonly restricted to the stromal areas whilst the TAMs infiltrated deeper into the tumour-nest (Figure 6.1.1). Importantly, given the observation in Chapter 5 that the pSTAT6+ non-macrophage cells could possibly influence TAM spatial distribution/polarisation *in situ*, this Chapter aims to investigate the association of TIL and TAM populations.

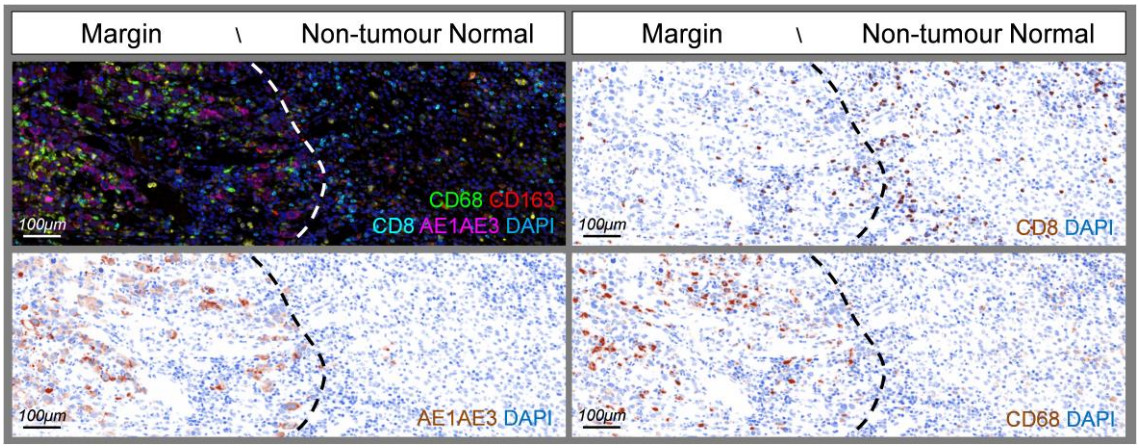


Figure 6.1.1 Inverse locations of TAMs and TILs within gastric cancer

CD68+ macrophages are found to locate within the AE1AE3+ tumour Margin whilst the CD8+ T cells were excluded from the tumour. Dashed line: interface of tumour Margin and adjacent non-tumour normal tissue.

6.2 Aims

Aim 1: To characterise the TIL landscape in the tumour Core region

Aim 2: To investigate the spatial relationships of TAMs and TILs to tumour cells

Aim 3: To investigate the influence of TILs on TAM polarisation and possible immune cell interactions through gene expression

Aim 4: To investigate possible reasons underlying the positive association of CD68++CD163+ TAMs with improved patient survival

6.3 Results

6.3.1 Multiplex TIL panel staining and cell phenotyping

To investigate the TIL profile, a multiplex TIL panel[407] was designed and optimised: CD3 was used as a pan-T lymphocyte marker, CD4 and CD8 were selected as markers for the helper and cytotoxic T cells, respectively, and the forkhead box P3 (FOXP3) was a signature marker for the regulatory T cells[418] (Figure 6.3.1, Figure 6.3.2 and Table 2.2.2). IRF8 was included in the panel due to the observations from previous Chapters that (i) the CD68-IRF8+ cells, as well as pSTAT6+ non-macrophage cells, had a location preference in the intra-tumoural tertiary lymphoid structures (Figure 6.3.3 and Figure 5.3.25), (ii) a high percentage of CD68-IRF8+ cells expressed PDL1 (Figure 6.3.4), and (iii) the presence of these cells was associated with improved patient survival (Figure 4.3.22 and Figure 4.3.23), suggesting they may be a population of interferon-associated T lymphocytes[534].

A subset (n=43) of samples from the **OPAL study cohort** (n=56) stained using the multiplex TAM panel in Chapter 3 were chosen based on the presence of tumour Core region and the availability of survival data. For this analysis, the adjacent, sequential sections of the tissue block were stained with the multiplex TIL panel (Figure 6.3.1).

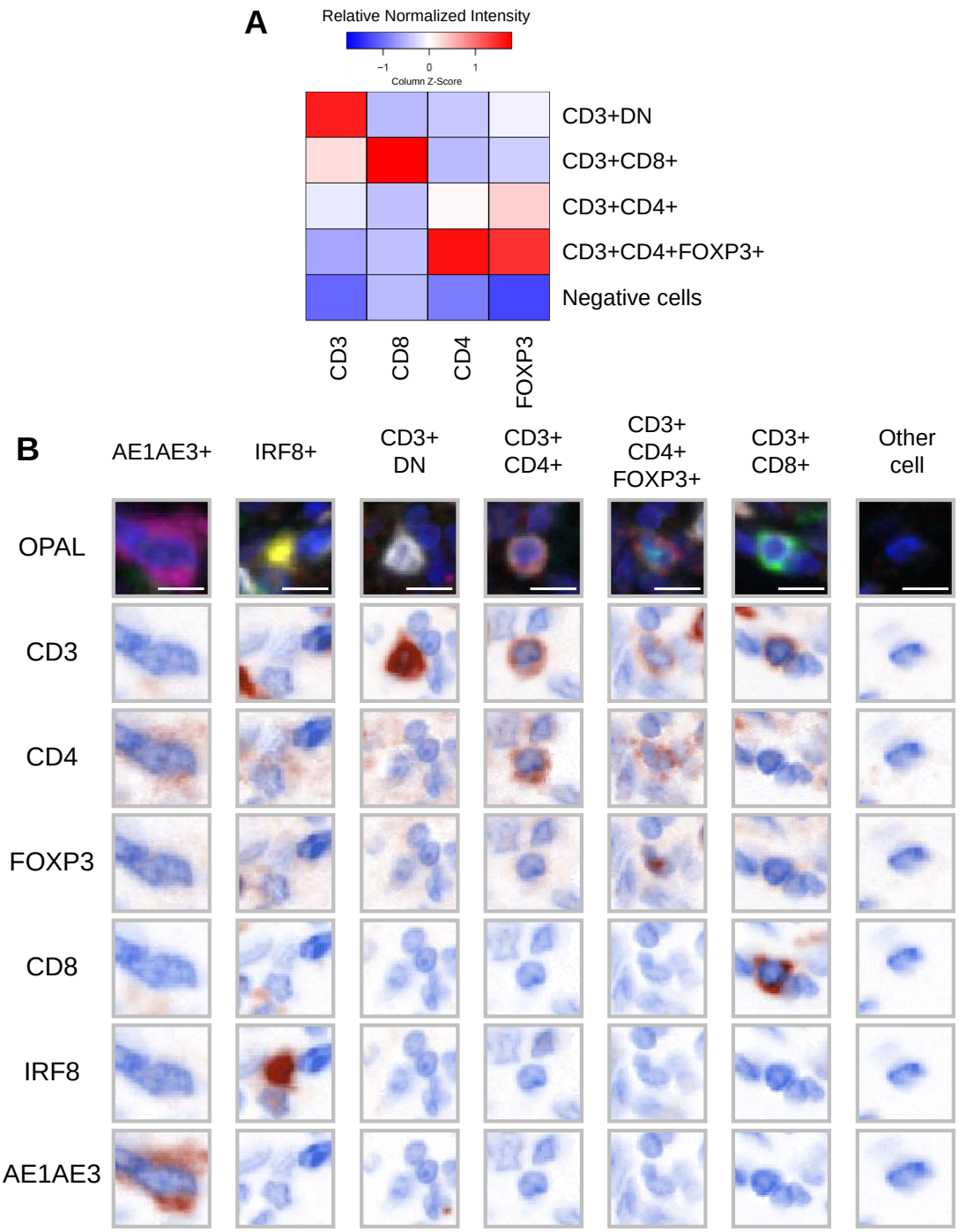


Figure 6.3.1 Cell populations identified with the multiplex TIL panel

(A) Combined marker signature of each TIL population. Negative cells are the “Other cell” in (B). (B) Representative images of cell populations in gastric cancer defined with the multiplex TIL panel. DN: Double negative of CD4 and CD8. Yellow: IRF8, White: CD3, Red: CD4, Green: CD8, Magenta: AE1AE3, Cyan: FOXP3, Blue: DAPI. Single-stained IHC colour: Blue: DAPI, Brown: Positive staining of markers as indicated (+). Scale bar: 10 µm.

Images were segmented and cells were phenotyped into different TIL populations with the inForm software as described in Chapter 3 (§3.3.3). Images from different regions of interest (ROIs; Figure 6.3.2) showed similar staining location patterns to the pSTAT6+ cells described in Chapter 5 (Figure 5.3.25), supporting the hypothesis that some of the non-macrophage pSTAT6+ populations might be T lymphocytes. Unfortunately, the T cell populations were all negative of IRF8 (Figure 6.3.1B), leaving the identity of this interesting cell population undetermined.

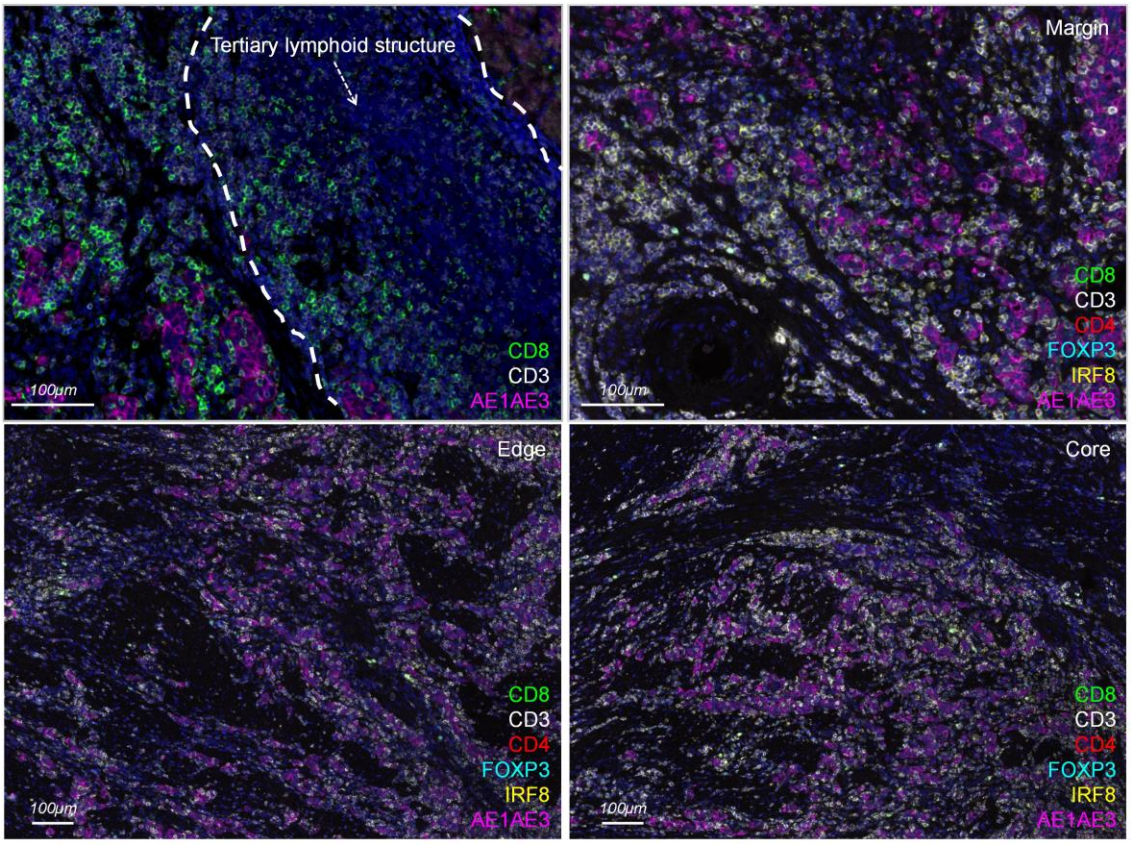


Figure 6.3.2 Representative images of the multiplex TIL panel

Similar regions of interest obtained from the same patient (#7424) as in Figure 5.3.24 and Figure 5.3.25 investigating pSTAT6 expression on TAMs.

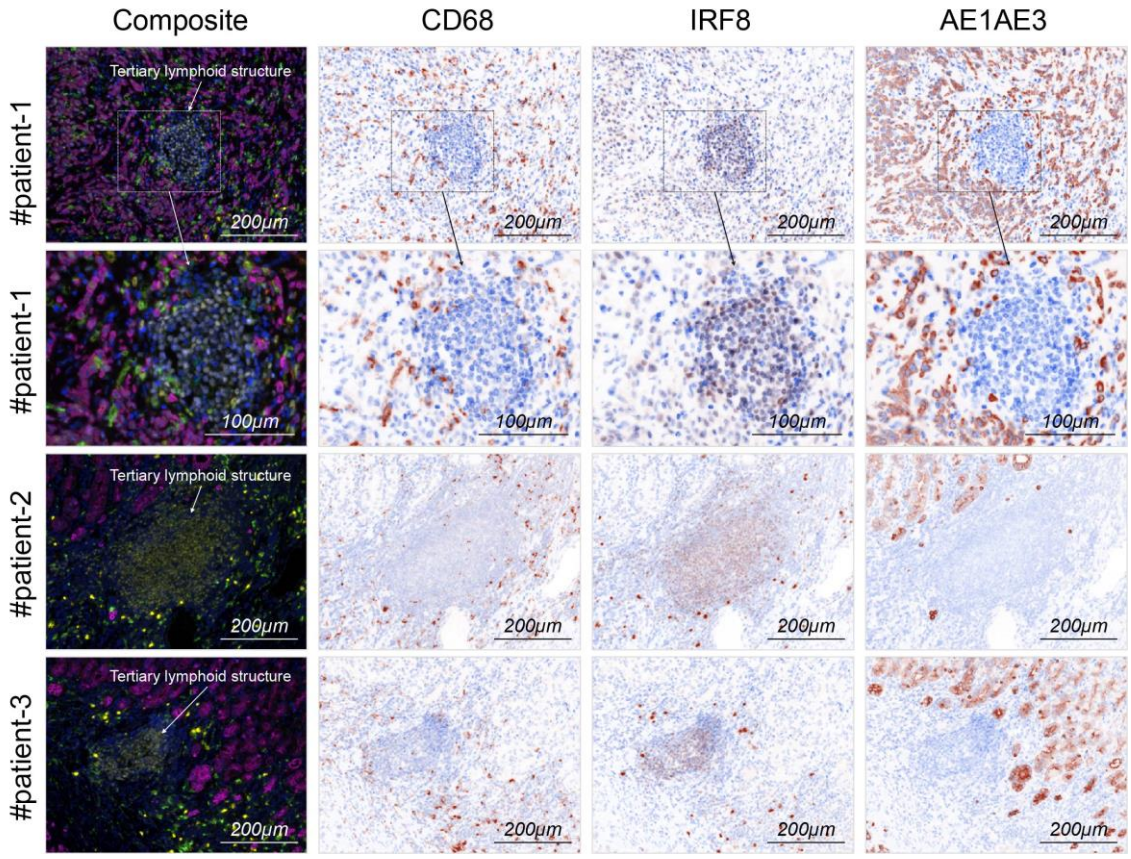


Figure 6.3.3 CD68-IRF8+ cells located in tertiary lymphoid structures

Data of the multiplex TAM panel showing the locational preference of CD68-IRF8+ cells in different patient samples. Yellow: IRF8, Green: CD68, Magenta: AE1AE3, Blue: DAPI. Single-stained IHC colour: Blue: DAPI, Brown: Positive staining of markers as indicated.

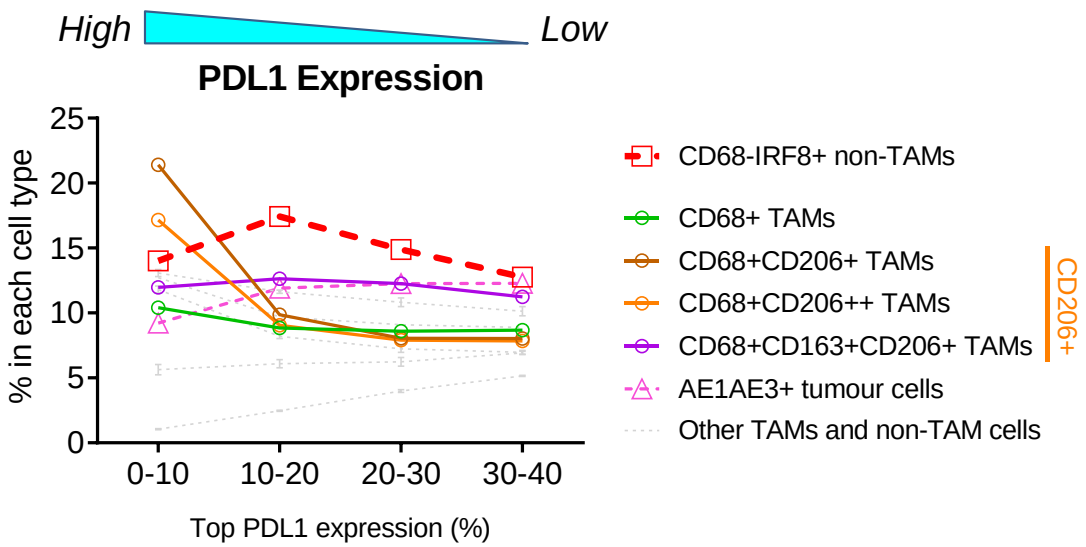


Figure 6.3.4 High PDL1 expression on CD68-IRF8+ cells

PDL1 expression on cell populations defined in Figure 4.3.11 and Figure 4.3.12. Figure from[466].

6.3.2 Density correlations between the TAMs and TILs

Tumour Core was selected as the region within a tumour specimen to compare the difference between the TAMs and TILs. The Core was chosen as it comprises the majority of the tumour and because for some tumours, especially those with diffuse histology, tumour Edge and Margin were difficult to define. This could also minimise the influence due to “tissue loss” between sequential sections.

The total TAM (CD68+) to total TIL (CD3+) ratio in the tumour Core was 3:1 (Figure 6.3.5A), and the two immune systems positively correlated in the tumour Core (Figure 6.3.5B). To examine the potential interaction of TAMs and TILs, the density correlation between the individual TAM and TIL populations was compared (Figure 6.3.6). It was notable that all the TIL populations were positively correlated with each other as well as to all the TAM populations (Figure 6.3.6A) whilst some of the TAMs were negatively correlated with the other TAMs as previously described (Figure 4.3.8). Higher correlations were observed between individual TAM populations than between individual TIL populations and the CD3+CD8+ T cells were the TIL population that was most highly associated with the TAMs (Figure 6.3.6B). These results suggest that, as a whole, both innate and adaptive immune systems were concurrently present in the tumour, either working together or reflecting the balance of an immune-escaped microenvironment with the coexistence of both pro- and anti-tumour immunity. TILs may have been recruited into the TME as a group whereas the recruitment of TAMs may differ depending on the environmental signals of each individual tumour.

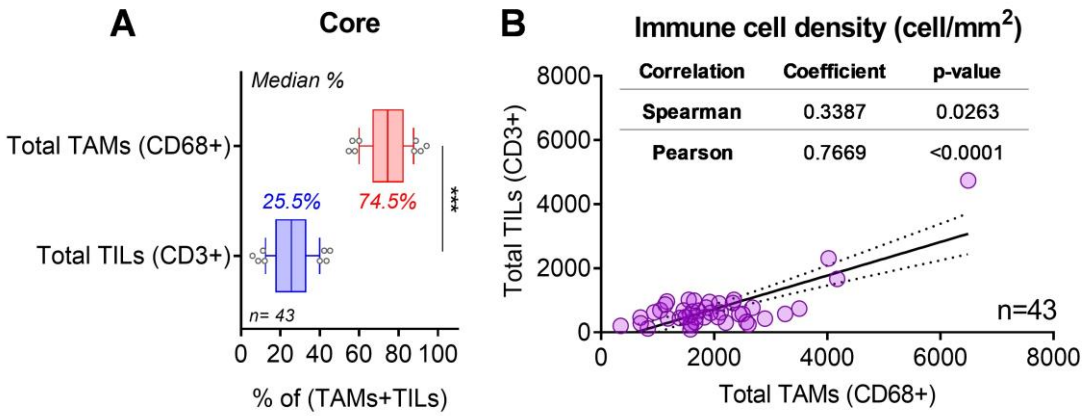


Figure 6.3.5 Association between TAMs and TILs in the Core

(A) Percentage of TAMs and TILs in total TAMs plus TILs. Box and whiskers represent mean ± 10-90 percentile. Each point represents one patient. ***p<0.001 comparing between TAMs and TILs. Mann-Whitney U test. (B) Density correlations between TAMs and TILs. Solid and dashed line represent linear fitted line with 95% confidence intervals.

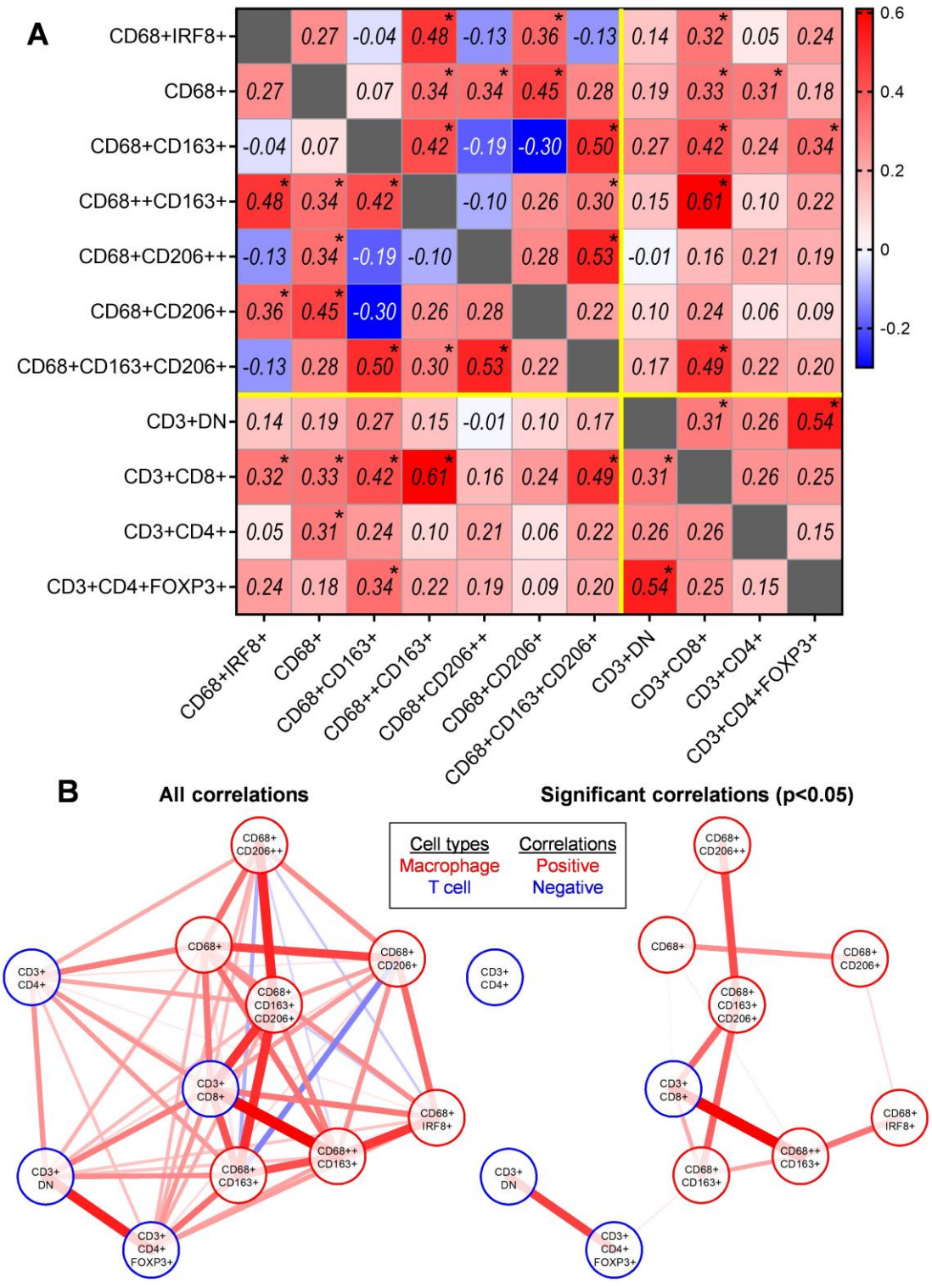


Figure 6.3.6 Density correlation of TAMs and TILs in the tumour Core

(A) Heatmap of Spearman correlation (n=43) and (B) Density qgraph map ("qgraph" package in R) between each of the TAM and TIL population. Increased line width in the qgraph map corresponds to increased significance of density correlations. Red/Blue: positively/negatively correlated. CD3+DN: double-negative of CD4 and CD8. Correlation coefficients are as labelled in each cell.

6.3.3 Spatial TIL distribution relative to tumour cells

To understand the spatial distribution of TILs in the TME, the ISAT package (§3.3.5) was applied to the TIL dataset. The distance of TILs to tumour cells was extracted from the matrix (Figure 6.3.7). The CD3+CD4+FOXP3+ regulatory T cells were the closest to the tumour cells with a median distance of 12.65 µm and the CD3-only (CD3+DN, double-negative) T cells were located furthest away (27.31 µm) from the tumour cells. The CD3+CD4+ helper and CD3+CD8+ cytotoxic T cells both had a median distance of approximately 2-3 cell-to-cell (as defined in Figure 3.3.15) distance from the tumour cells.

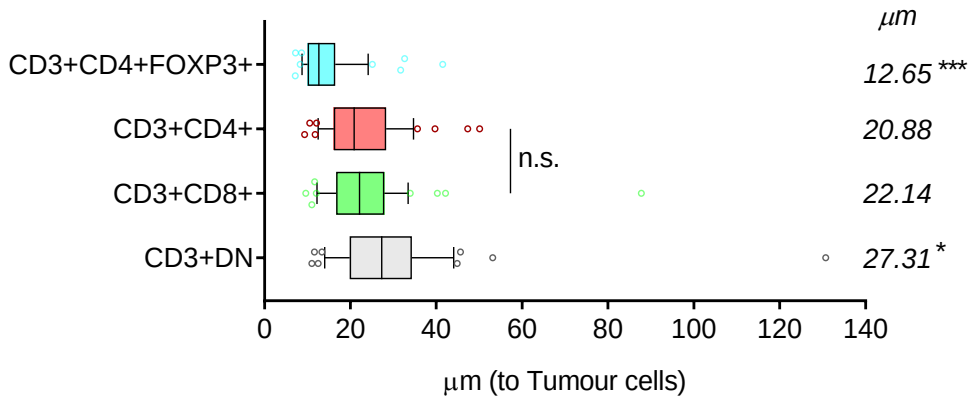


Figure 6.3.7 Median distance of T cell populations to tumour cells

TILs were used as reference cells and tumour cells as nearest cells in the Core region (n=43). Box and whiskers represent mean ± 10-90 percentile. Each point represents one patient. Numbers represent median distance of each TIL population to tumour cells. *p<0.05, ***p<0.001 and not significant (n.s.) comparing between TIL populations. Mann-Whitney U test.

6.3.4 Spatial relationship between TAMs and TILs

The data which determined the distance of TAMs (Figure 4.3.5) and TILs (Figure 6.3.7) from the tumour cells were combined to investigate the spatial relationship between the innate and adaptive immune systems. A median value (approximately 20 µm) of the overall distance of each immune cell population to tumour cells was used as the threshold to define bioinformatically the tumour-nest and stromal regions of the microenvironment (Figure 6.3.8A).

The spatial distribution pattern of immune cells in our cohort was similar to the published data[189] which suggests that the TILs were more commonly found in the stroma whereas some TAM populations could infiltrate into the tumour-nest. The infiltration depth of each immune population was independent of their overall cell densities (Figure 6.3.8B). A significant percentage of CD68+IRF8+ TAMs (78%), CD3+CD4+FOXP3+ TILs (72%), CD68+CD206+ TAMs (65%) and CD68++CD163+ TAMs (59%) resided within the tumour-nest whilst the CD68+CD163+CD206+ TAMs (43%) and the CD3+DN TILs (36%) were located in the stroma (Figure 6.3.9). The relative location of immune cells may be used to infer functionally relevant interactions between populations of cells that were proximate to each other.

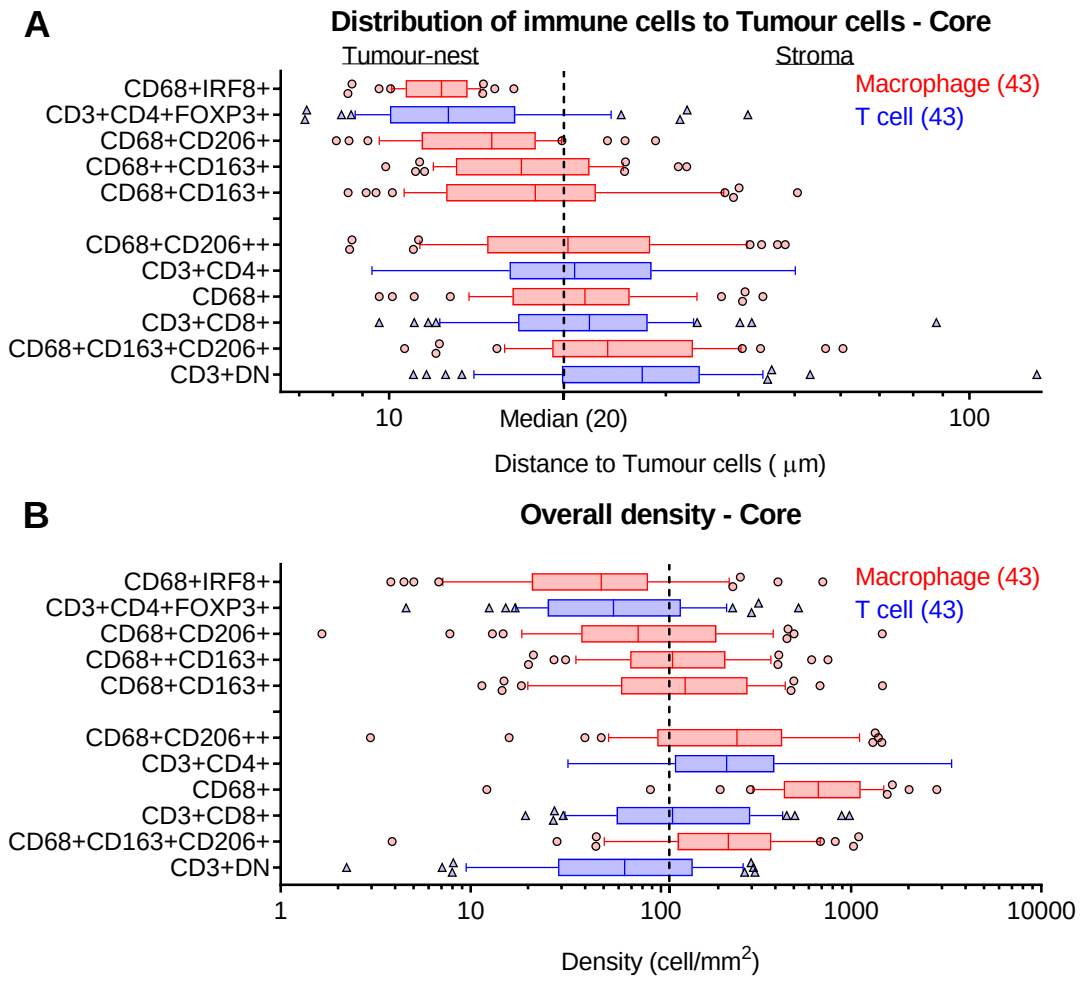


Figure 6.3.8 Median distance defined tumour microenvironment

(A) Median distance of cell populations to tumour cells. (B) Corresponding cell density of each cell population. Dashed line shows median distance or density of each cell population.

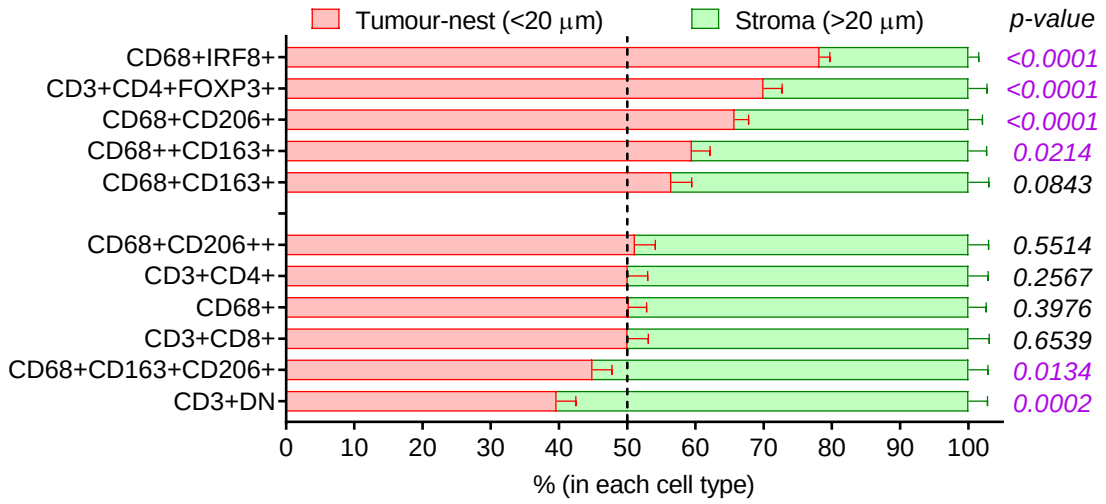


Figure 6.3.9 Distribution of immune cell populations with distance defined TME

Tumour-nest and stroma defined with the median immune cell to tumour cell distance identified in Figure 6.3.8. n=43. P-value comparing cell density between the tumour-nest and stromal areas of each cell population. Mann-Whitney U test.

The density correlations of TAMs and TILs in the tumour-nest and the stroma were then compared (Figure 6.3.10). All immune cells showed a much higher and more significant correlation in the stroma than in the tumour-nest (Figure 6.3.10A). This result suggests that all TAMs and TILs were present in the TME of an individual tumour; however, only certain cell populations were within the tumour-nest. Interestingly, the CD68++CD163+ macrophage and the CD3+CD8+ T cell pair had the highest correlation in both tumour-nest and stroma (Figure 6.3.10B), despite their differences in median distance to the tumour cells and overall densities (Figure 6.3.8). These results suggest that these two cell populations may be functionally related to each other or were attracted to/being polarised within a similar microenvironment.

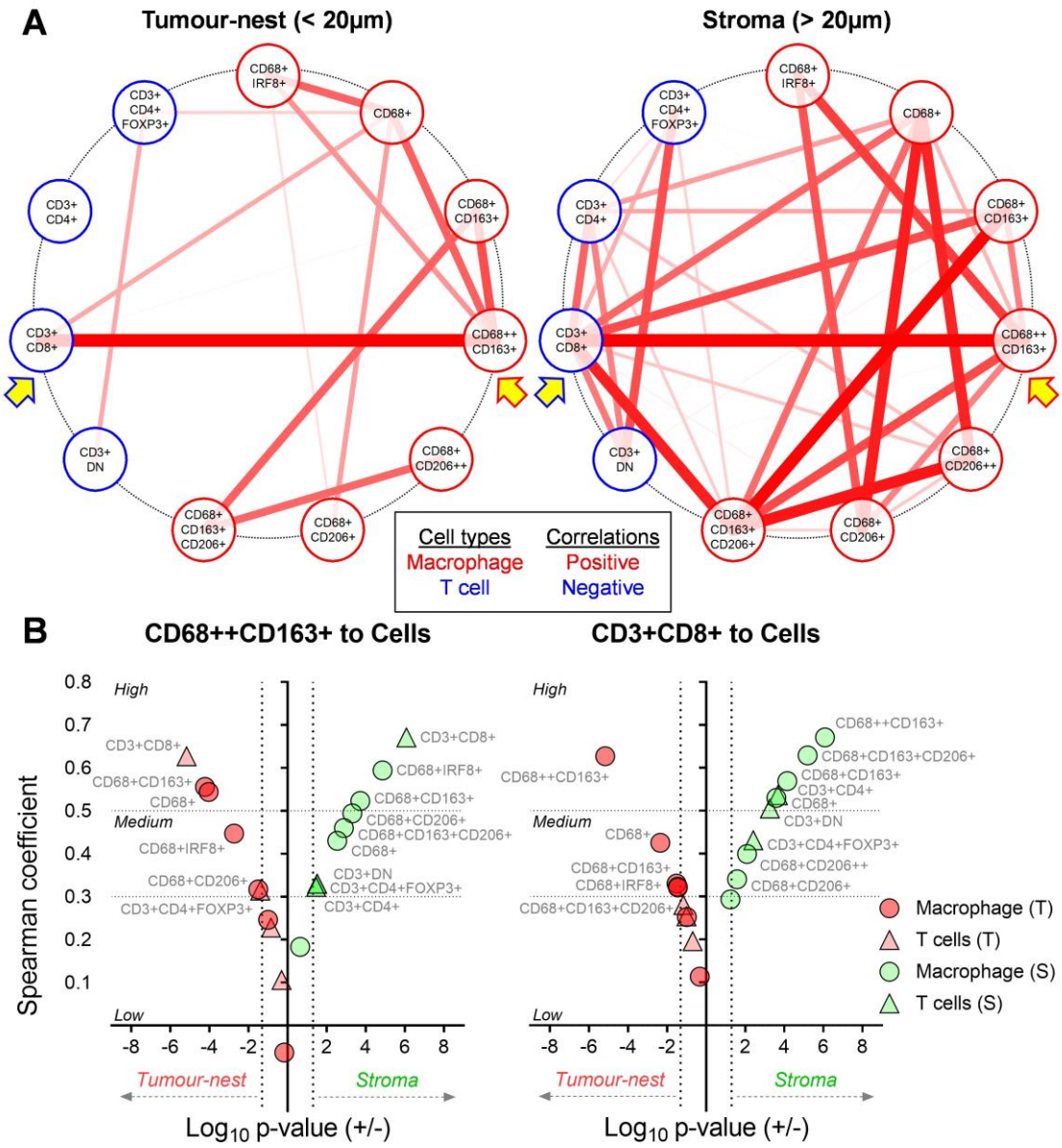


Figure 6.3.10 Correlation of TAMs and TILs in tumour areas

(A) Density qgraph map of Spearman correlation ($p<0.05$) between all cell types within the tumour-nest (T) and stroma (S). Arrows identify the TAM/TIL pair with the highest density correlations in tumour-nest and stroma. Red/Blue line: positive/negative correlation. Increased line width in the qgraph map correspond to increased significance of density correlations. (B) Spearman correlations for the CD68++CD163+ TAMs and the CD3+CD8+ TILs. Cell populations with significant ($p<0.05$) density correlations are labelled.

The spatial distribution data (Figure 6.3.8) of each patient was grouped based on different clinical parameters, and the EBV/MSI GC molecular subtype appeared to be the most significant factor for enhanced immune infiltration

depth (Figure 6.3.11) and not other parameters (Table 6.3.1). The overall median distance of immune cells to tumour cells of patients with EBV/MSI GC subtype was 14.3 µm compared to 20.5 µm of patients with GS/Others GC subtype (Figure 6.3.11). This increase (43%; 20.5/14.3) in the infiltration depth into the tumour-nest was independent of their overall cell densities (Figure 6.3.12 and Table 6.3.2).

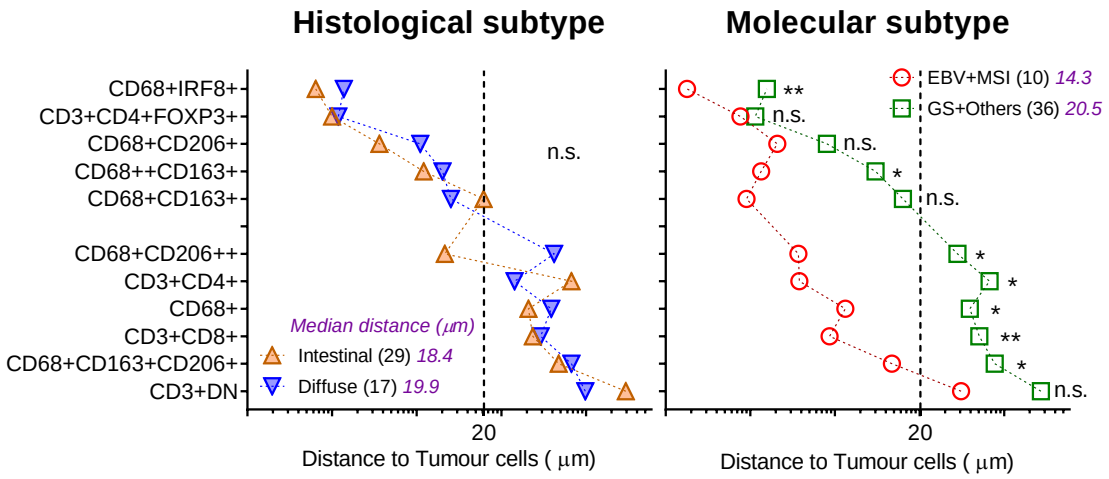


Figure 6.3.11 Immune cell distance to tumour cells by GC subtypes

Symbols represent median distance. Black brackets: cases. Lines: GC subtype. Vertical dashed line: overall median distance of immune cells to tumour cell defined in Figure 6.3.8. *p<0.05, **p<0.01 and not significant (n.s.) comparing between GC subtype. Mann-Whitney U test.

Table 6.3.1 Clinical parameters associated immune distance to tumour

Clinical parameter / Immune population	Age 70 Above / Below	Gender Male/ Female	T stage 1+2/ 3+4	N stage 0+1/ 2+3	AJCC 6th 1+2/ 3+4	Inflammation 1 / 2+3	Recurrence Yes / No	*H. pylori* + / (- & NA)
Number in each group	20 / 26	31 / 15	12 / 34	33 / 13	24 / 22	18 / 28	22 / 24	18 / 28
CD68+IRF8+	*0.587*	*0.440*	*0.325*	*0.686*	*0.531*	*0.037*	*0.129*	*0.128*
CD3+CD4+FOXP3+	*0.303*	*0.052*	*0.230*	*0.964*	*0.995*	*0.956*	*0.871*	*0.224*
CD68+CD206+	*0.891*	*0.698*	*0.908*	*0.668*	*0.944*	*0.225*	*0.524*	*0.035*
CD68++CD163+	*0.969*	*0.986*	*0.644*	*0.576*	*0.423*	*0.351*	*0.198*	*0.022*
CD68+CD163+	*0.882*	*0.977*	*0.356*	*0.550*	*0.227*	*0.399*	*0.210*	*0.056*
CD68+CD206++	*0.625*	*0.338*	*0.811*	*0.576*	*0.510*	*0.104*	*0.416*	*0.062*
CD3+CD4+	*0.645*	*0.753*	*0.580*	*0.223*	*0.024*	*0.898*	*0.750*	*0.108*
CD68+	*0.701*	*0.610*	*0.210*	*0.923*	*0.703*	*0.730*	*0.506*	*0.070*
CD3+CD8+	*0.559*	*0.994*	*0.795*	*0.219*	*0.131*	*0.710*	*0.297*	*0.120*
CD68+CD163+CD206+	*0.869*	*0.835*	*0.990*	*0.647*	*0.439*	*0.664*	*0.640*	*0.098*
CD3+DN	*0.614*	*0.617*	*0.037*	*>0.999*	*0.876*	*0.166*	*0.895*	*0.162*
Median Distance (µm)	18.2 / 18.4	18.2 / 18.6	16.8 / 18.9	17.9 / 19.5	17.0 / 19.2	19.0 / 17.8	19.6 / 17.1	21.6 / 16.2

- P-values (*italic values*) between groups determined with Mann-Whitney U test

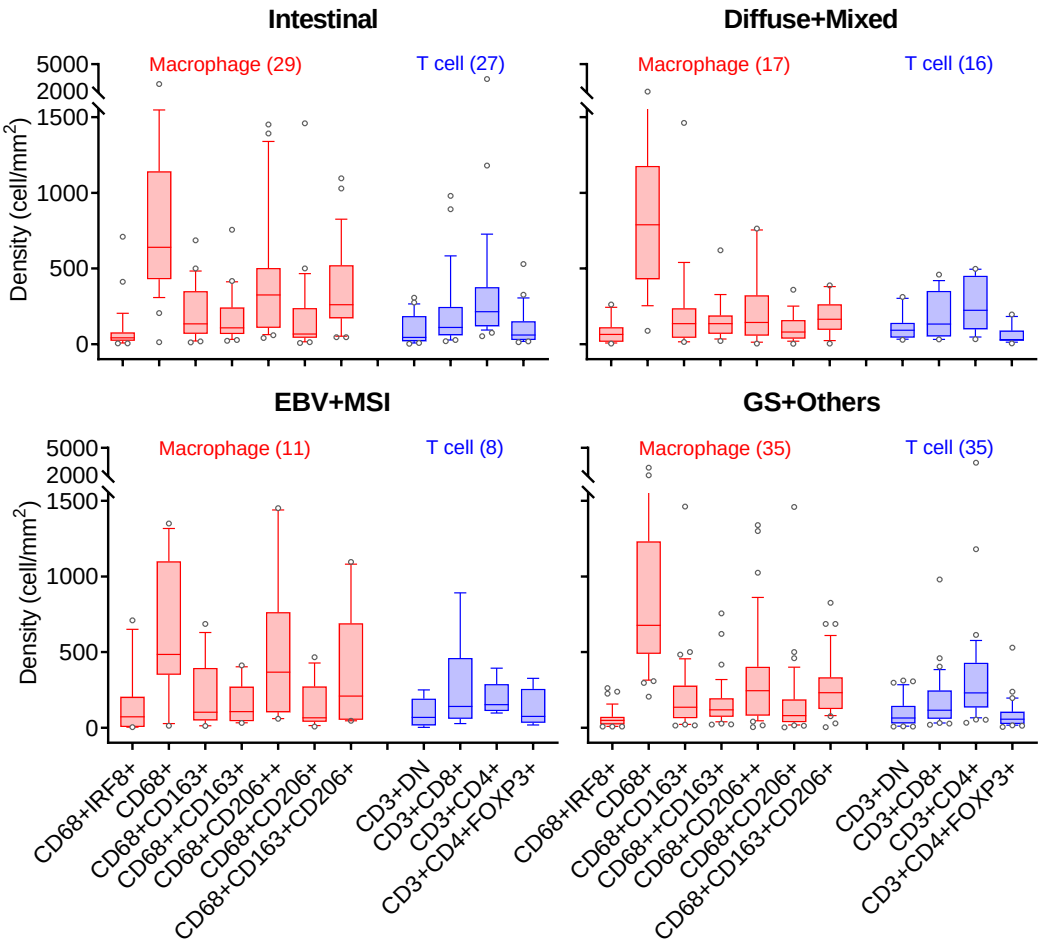


Figure 6.3.12 Immune cell densities between different GC subtypes

Cell Densities within tumour Core. Box and whiskers represent mean ± 10-90 percentile. Each point represents one patient. Differences between each immune cell population are presented in Table 6.3.2.

Table 6.3.2 Immune cell densities between different GC subtypes

Density (cell/mm^2)			
Cell types		Laurén (p-value)	TCGA (p-value)
Macrophage	CD68+IRF8+	0.299	0.761
	CD68+	0.669	0.210
	CD68+CD163+	0.404	0.559
	CD68++CD163+	0.770	0.939
	CD68+CD206++	0.042	0.346
	CD68+CD206+	0.719	0.899
	CD68+CD163+CD206+	0.028	0.722
T cell	CD3+DN	0.130	0.819
	CD3+CD8+	0.700	0.613
	CD3+CD4+	0.794	0.178
	CD3+CD4+FOXP3+	0.064	0.317
• Differences between each immune cell populations presented in Figure 6.3.12 • Determined with Mann-Whitney U test			

In summary, by comparing the spatial distribution of TAMs and TILs to the tumour cells, an inverse distribution pattern was observed in our cohort which is consistent with existing literature[189]. Interestingly, it has been shown that the regulatory T cells were one of the main sources of IL-10 and the helper T cells could generate IL-4/13 and also IL-10 in the TME[535]. The regulatory T cells and the helper T cells were found to locate within the tumour-nest and stroma, respectively (Figure 6.3.8). The difference in preferential localisation between these T cells may be associated with the polarisation of macrophages between different tumour areas and be related to the CD206/CD163 distribution patterns observed within different pSTAT6+ regions (Figure 5.3.24). In addition, the high correlation between the CD68++CD163+ macrophages and the CD3+CD8+ T cells might explain their association with improved patient survival (Figure 4.3.7). These hypothesised connections were further investigated below.

6.3.5 TIL environmental gene signature and survival

To further understand the tumour microenvironment with reference to TIL populations and how TILs may be influencing TAM polarisation, environmental gene-signatures were generated for each TIL population (Figure 6.3.13) using the methods described in Chapter 5 (Figure 5.3.1). The CD3+CD8+ T cells exhibited a unique signature of enhanced immune signalling (IL-2) and activation of TCRs (#A, Figure 6.3.13). The CD3+CD4+FOXP3+ T cell density was correlated with the *FOXP3* and *CTLA4 genes*, which were signature markers for the regulatory T cell (#D). Interestingly, these two populations shared upregulated IFN-γ and cell apoptosis signalling (#E), suggesting that more cell death might be present where these cells were abundant. However, the CD3+CD4+FOXP3+ TILs also shared an increased IFN-γ regulation signature with the CD3+DN T cells (#F), and an inverse signature associated with cell senescence with the CD3+CD8+ T cells (#G), indicating the multi-functional property of this cell population or the existence of different subpopulations with distinct functions[536]. The CD3+CD4+ T cells were found to associated with reduced IL-10 (#N) but may be related to an enhanced IL-12 signature (#J), suggesting that a higher Th1 compared to a Th2 response might be occurring in the tumours. Interestingly, this result was not in keeping with the hypothesis that the Th2 cytokines might be affecting the TAM polarisation within the tissue areas before they encounter the tumour cells (pSTAT6+ patterns; Figure 5.3.24). A possible explanation for this might be that the gene expression data was derived from homogenised whole-tumour tissue rather than specific regions.

When comparing the survival data stratified by the density of different TIL populations, interestingly, the CD3+CD4+FOXP3+ T cells were found to be associated with improved OS and RFS in our cohort; however, this was not the case for the other TIL populations (Figure 6.3.14).

CD3+ DN	CD3+ CD4+	CD3+ CD4+ FOXP3+	CD3+ CD8+	#	Associated pathways	FDR <0.05
			P	A	1. Cytokine signalling in immune system* 2. Signalling by interleukins*(IL-2)* 3. Toll-like receptor cascades*	Y
P				B	1. Degradation of the extracellular matrix 2. Receptor-type tyrosine-protein phosphatases	
P			P	C	1. Ca2+ pathway 2. G beta:gamma signalling through PI3Kgamma	
		P		D	1. Development of Tregs* (*FOXP3, CTLA4*)	Y
		P	P	E	1. Apoptosis 2. IFN-γ signalling (*PML;HLA-DQB1;JAK1*)	
P		P		F	1. Signalling by Non-receptor tyrosine kinases* 2. Regulation of IFNγ signalling (*SOCS1/3*)	Y
		P	N	G	1. Oncogene / oxidative stress induced senescence* 2. Binding of TCF/LEF:CTNNB1 to target gene promoters* 3. Regulation of ERBB4 signalling (WNT/PTK6)*	Y
N			N	H	1. Activation of gene expression by SREBP* 2. Metabolism of steroids / cholesterol*	Y
			N	I	1. DNA methylation 2. RNA polymerase I promoter opening	
	P			J	1. Neutrophil degranulation 2. TP53 regulated cell cycle genes 3. NF-κB / IL-12 signalling	
N				K	1. Protein ubiquitination 2. Function of SMAD2/4 in cancer	
		N	N	L	1. Calcitonin-like ligand receptors 8 2. NOTCH signalling	
		N		M	1. ER to Golgi transport 2. TFAP2 (AP-2) family regulated transcription	
	N			N	1. Signalling by interleukins* 2. IL-4/10/13 signalling	Y
N		N		O	1. FGFR3 signalling	

Figure 6.3.13 T cell density-derived environmental signatures

Density of each TIL population of the **OPAL-Affy cohort** (n-34) was correlated with their matched whole-tumour-derived gene expression data. The environmental signature of each TIL population was identified. Red: genes with positive (P) correlations with density. Blue: negative (N) correlations. White: no correlations, unique signatures of either cell populations. Associated pathways identified with the Reactome database. *: FDR<0.05 (Benjamini-Hochberg).

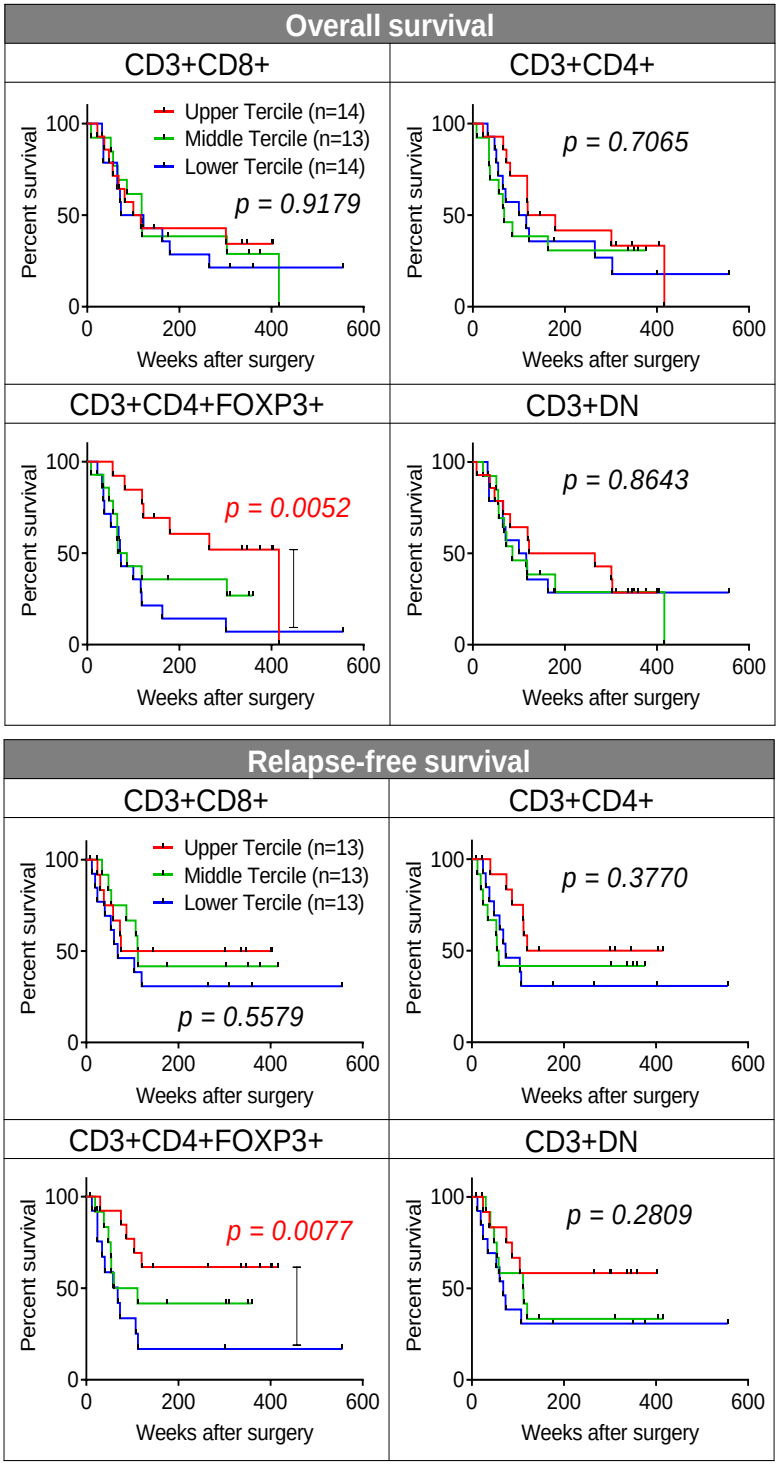


Figure 6.3.14 Overall and relapse-free survival based on TIL density

For each TIL population, patients were stratified into three groups using the overall density calculated in the tumour Core. Overall and relapse-free survival were plotted. Upper tercile (density > 2/3 of the patients in the cohort; red line), Middle tercile (1/3 < density < 2/3 of patients in the cohort; green line). Lower tercile (density ≤ 1/3 of patients in the cohort; blue line). Log-rank (Mantel-Cox) test.

6.3.6 Combined TAM/TIL-associated gene signature and patient survival

To assess whether the high correlation with CD3+CD8+ TILs could explain the survival advantage observed in patients with increased number of CD68++CD163+ TAMs, patients were stratified into different groups with their combined cell density and immune cell ratio (Figure 6.3.15A); however, no survival differences were observed (Figure 6.3.15B).

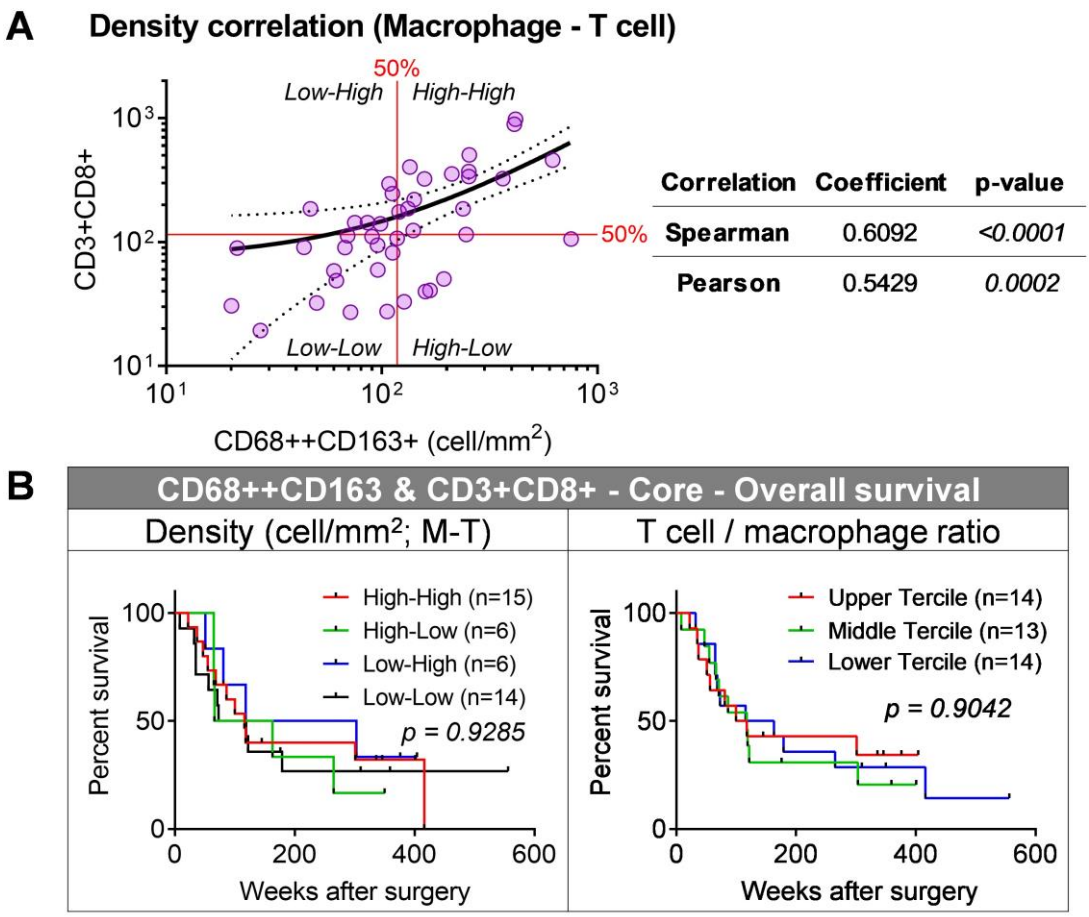


Figure 6.3.15 Stratification of patients with TAM and TIL combined density and ratio

(A) Patients (n=43) were stratified into four groups with median densities of CD68++CD163+ TAMs and CD3+CD8+ TILs as cut-offs. (B) Patients overall survival was interrogated between the four groups, or (C) The T-cell to macrophage ratio of each patient was determined. Patients were then stratified into three equivalent groups (Upper, middle and lower tercile) for survival analysis

Gene signatures of the two populations were compared to investigate a possible interaction between the two cell types (Figure 6.3.16). The co-existence of CD68++CD163+ TAMs and CD3+CD8+ TILs in the same TME was characterised by an enhanced signature of immune signalling (#A, Figure 6.3.16) and a negative association with cell cycle-related genes (#D-F). These results indicate that strong overall immunity can be found in the tumours where the two cell populations were abundant; however, this did not have any influence on patient survival (Figure 6.3.15B). The CD68++CD163+ TAMs were characterised with a unique IL-4/IL-13 and extra-cellular matrix associated signalling (#B), whilst the CD3+CD8+ T cells correlated with the activation of TCRs, interaction with chemokines and, interestingly, with PD1 signalling (#C). These findings suggest that the functional status (e.g. activated or exhausted) of the CD3+CD8+ cytotoxic T cells might be important to take account of in addition to the overall density.

CD3+ CD8+	CD68++ CD163+	#	Associated pathways	FDR <0.05
P	P	A	1. Immune system* 2. Signalling by Interleukins* (IL-2 / 10 / 21) 3. Cytokine signalling in immune system*	Y
	P	B	1. Degradation of extracellular matrix* (MMP9/14) 2. IL-4 and IL-13 signalling*	Y
P		C	1. Translocation of ZAP-70 to Immunological synapse* 2. PD1 signalling (PDCD1LG2/CD247) 3. Phosphorylation of CD3 and TCR zeta chains 4. Chemokine receptors bind chemokines	Y
	N	D	1. Cellular response to hypoxia 2. Cell cycle	
N	N	E	1. Cell cycle 2. Transcription of E2F targets	
N		F	1. DNA methylation 2. RNA polymerase I promoter opening 3. Activation of matrix metalloproteinases (MMP2/8/13/15)	

Figure 6.3.16 Environmental gene signatures of CD68++CD163+ TAM and CD3+CD8+ TILs

Red: genes with positive (P) correlations with cell density. Blue: negative (N) correlations. White (- -): no correlations, unique signatures of either cell populations. Associated pathways identified with the Reactome database. *: FDR<0.05 (Benjamini-Hochberg).

To understand the global change in the TME which contains different immune cell components, principal component analysis (PCA) was performed on the gene signature data (Figure 6.3.17 and Appendix 5).

The M1-like TAMs (CD68+IRF8+ and CD68+) clustered more closely with each other compared to other M2-like TAM populations (Figure 6.3.17A). The CD68+CD163+CD206+ TAMs were more closely associated with CD68+CD163+ TAMs than with the CD206+ (CD163-) populations as shown in Figure 5.3.6 and Figure 5.3.7. Interestingly, the CD68+IRF8+ and CD68++CD163+ TAMs, as well as the CD3+CD8+ and CD3+CD4+FOXP3+ TILs, that had either high density correlations in the tumour Core (Figure 6.3.6 and Figure 4.3.9) or relevance to survival (Figure 4.3.7 and Figure 6.3.14), were not all clustered together (Figure 6.3.17A). The CD3+CD8+ TILs shared an IFN-γ signature with the CD3+CD4+FOXP3+ TILs (Figure 6.3.13) and an enhanced immune signalling with the CD68++CD163+ TAMs (Figure 6.3.16) which may explain their clustering in a PCA plot. The CD68+IRF8+ TAMs were associated with increased inflammation, IL-1 signalling and apoptosis, and were, therefore, separated from the others (Figure 6.3.17B and Appendix 5).

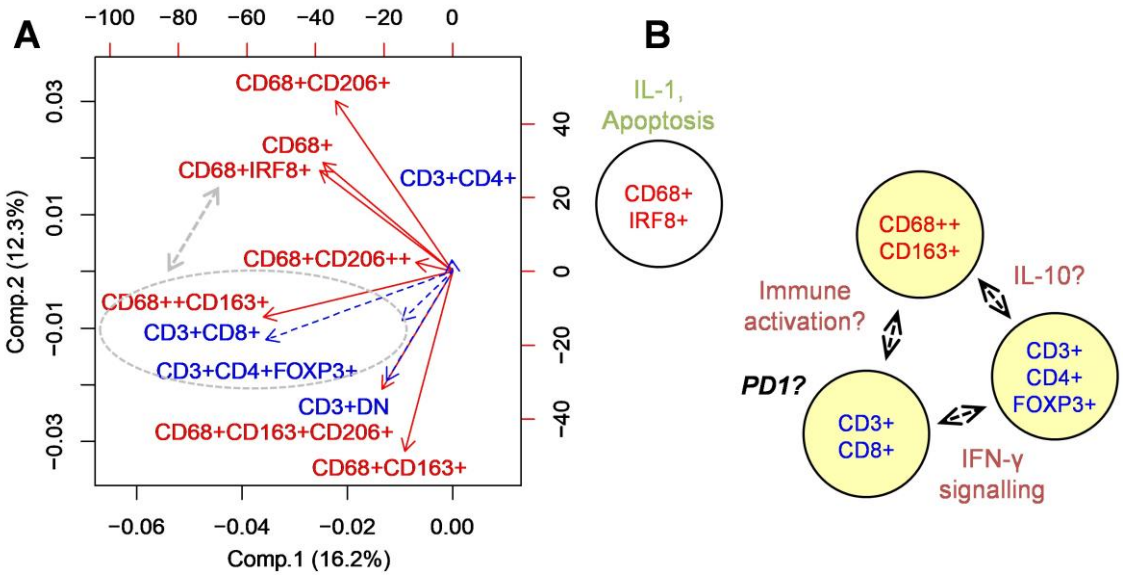


Figure 6.3.17 PCA of TAMs and TILs with population gene signatures

(A) Dashed circle and arrow in grey: immune cell populations identified with the most relevance with OS in the survival screen. (B) Schematic relationship between the cell populations.

These data suggest that, although different immune cells may show significant density correlations (CD68++CD163+ and CD68+IRF8+ TAMs; Figure 4.3.8) or have similar survival association with outcome (CD68++CD163+ TAMs and CD3+CD4+FOXP3+ TILs; Figure 4.3.7 and Figure 6.3.14), the reasons or mechanisms behind these observations may not be identical and investigating the signalling pathways in the TME might be informative.

To further obtain an overview of the innate and adaptive immune landscape of gastric cancer, seven major pathways, with known macrophage functions based on the literature[137, 183, 190, 240, 307], were identified (Appendix 6A). The enrichment of genes in each pathway was examined for each immune gene signature (Figure 6.3.18 and Appendix 6B-D).

Overall, the TAMs were more associated with EMT and Stromal-related pathways, whereas the TILs were correlated with active immune responses (Immune and Antigen presentation). Surprisingly, the M1-like CD68+IRF8+ signature had a minimal correlation with immune responses, suggesting that these macrophages may be functionally suppressed despite being enriched for cell death/cell cycle-related genes. On the other hand, the M2c-like CD68++CD163+ TAMs had the highest enrichment in active immunity and antigen-presenting capability among all the TAMs which were accompanied by an elevated extra-cellular matrix degradation signature. These results suggest that, despite the expression of the M2-like marker, CD163, the overall effect of this TAM population may be anti-tumoural. The high correlation of this population with the CD3+CD8+ TILs suggests that the TAMs might have been activating the cytotoxic T cells by presenting them with tumour antigens, clearing the way for them by degrading the cellular matrix leading to the enhancement of cell death and a reduced cell cycle-related signatures of the CD3+CD8+ TILs.

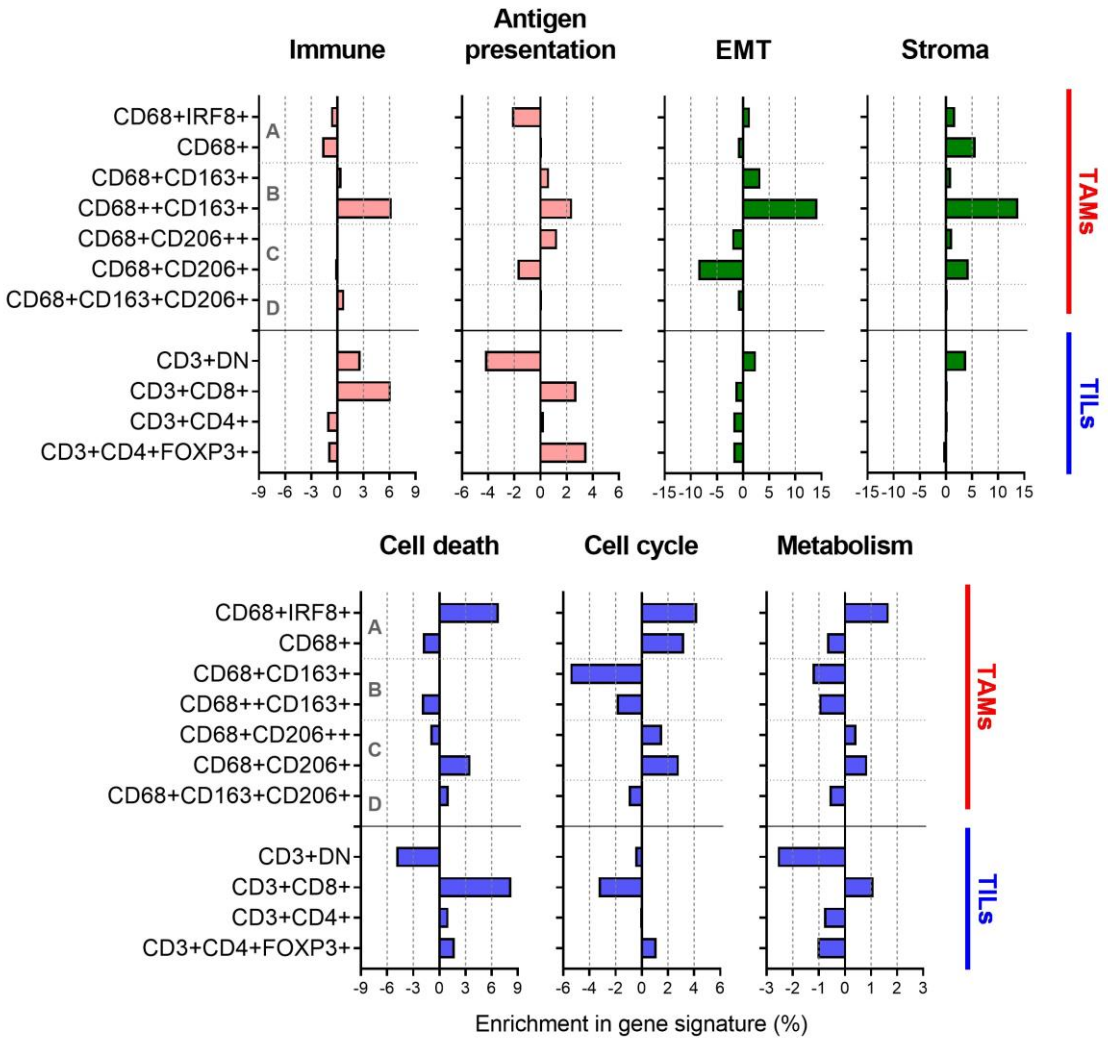


Figure 6.3.18 Association of immune populations to pathway categories

Enrichment of gene in each pathway determined for each immune environmental gene signature. EMT: Epithelial–mesenchymal transition. A: M1-like TAMs. B: CD163+ (CD206-) TAMs. C: CD206+ (CD163-) TAMs. D: CD163+CD206+ TAMs.

6.4 Discussion and Conclusions

6.4.1 Spatial and transcriptomic relationship between the TAMs and TILs

This Chapter constitutes a natural progression from the findings reported in Chapters 4 and 5 that showed TIL-associated genes and spatially distributed lymphocyte-like cells were found to correlate with *in situ* characterised TAMs. An additional multiplex IHC panel was designed to characterise the TIL landscape within the **OPAL staining cohort** (§3.3.1). TIL population densities and their distances to tumour cells were investigated and compared with the TAM results. Overall, TAMs and TILs were found to be positively correlated within the same tumour. This result suggests that both innate and adaptive immune systems were present simultaneously in the tumour, which categorises the patients into immune "hot" or "cold"[537, 538]. However, the majority of the TILs were excluded from the tumour-nest except for the CD3+CD4+FOXP3+ regulatory T cells, along with the CD68+IRF8+, CD68++CD163+ and CD68+CD206+ TAMs. This pattern of co-localisation suggests that the microenvironment surrounding the tumour cells may be more inflamed and immune active (CD68+IRF8+ and CD68++CD163+ TAMs), but were also accompanied by a higher degree of immune suppression (CD3+CD4+FOXP3+ TILs and CD68+CD206+ TAMs).

The GC molecular subtype was identified as a major influencing factor associated with enhanced immune infiltration in our cohort. The EBV/MSI patients had an overall 43% enhancement in the infiltration depth of the immune cells compared to the GS/Others subtypes, which might explain their improved survival outcome. Interestingly, this enhanced migration toward tumour cells was not related to the total number of infiltrating cells in a sample. Previous studies have reported that EBV/MSI subtypes were enriched in immune signalling[31] which infer the immune cell density in these tumours were higher; however, these studies analysed whole-tumour-derived samples without consideration of a relative spatial location *in situ*.

In addition to defining tumours into immune “hot” and “cold” based on their overall density, the distribution pattern of immune cells in the microenvironment of solid tumours can be divided into “homogeneous” or “excluded” based on their relative distribution to tumour cells[537, 538] (Figure 6.4.1). In a tumour with a “homogeneous” tumour-immune distribution pattern, the nearest distance of immune cells to tumour cells will be shorter compared to the ones with an “excluded” pattern (Figure 6.4.1). This difference can be identified using the spatial analysis tool developed in this study and was described as having an enhanced immune infiltration depth into the tumour-nest (Figure 6.3.9).

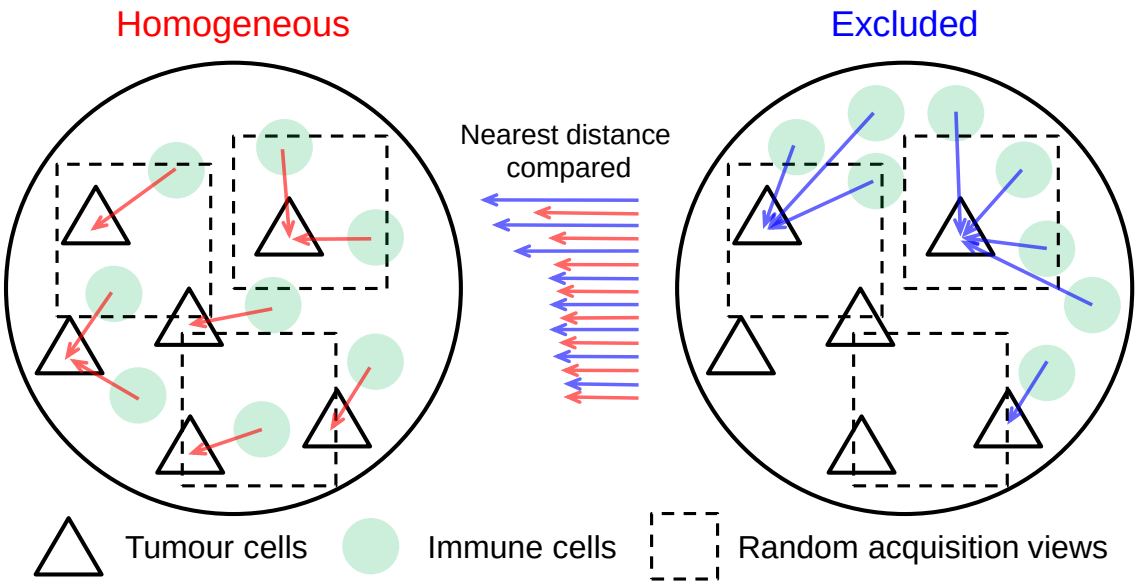


Figure 6.4.1 Tumour-immune cell distribution pattern

Homogeneous tumour-immune distribution pattern will increase the likelihood of immune cells been included in a piece of randomly acquired sample and be interpreted as having higher overall immune cell number compared to the patients with an excluded distribution pattern.

Compared to the whole-tumour-derived methods[31], especially between patients with similar total amounts of immune infiltrates but with different distribution patterns, a “homogeneous” tumour will increase the likelihood of immune cells being included in a randomly acquired sample (Figure 6.4.1). This may be interpreted as having a higher overall immune cell number compared to the patients with an “excluded” distribution pattern. In this study, the increased proximity of immune cells to tumour cells was found to be able to identify

patients with improved OS independently of cancer subtype (Figure 4.3.7 and Appendix 1 FigureS5). These results suggest that the distribution of cells may explain why cancer subtype or immune signatures were not precise biomarkers for patient survival prediction and their response to therapy in GC[126].

Collectively, the data from this study suggest that taking a biopsy may not be fully representative of the heterogeneous immune content of the whole tumour. Tumour-nest sampling could be optimal in determining a patient's immune status because it reflects a depth of immune penetration. Samples from adjacent stromal components, if applicable, may (i) improve the accuracy in identifying the patients with immune "excluded" patterns compared to overall immune cold patients, and (ii) provide a more precise evaluation of the TME as different immune cells have locational preferences.

The multiplex TIL panel staining confirmed that the pSTAT6+ non-macrophage cells resembled the TILs in both morphology and distribution patterns within the TME. Using the spatial and transcriptomic signature of the TAMs and TILs generated in this study, the TAMs were found to be associated with EMT, stromal and cell cycle-related pathways whilst the TILs were associated with active immune signalling. The relationship between different TAM and TIL populations could be described spatially, relative to tumour cells at µm scale, and transcriptomically on a global tumour level. However, it was difficult to investigate in detail to why the CD163+ TAM populations were more abundant within the pSTAT6+ cell enriched regions (Figure 5.3.24) since the exact spatial distribution data between the TAMs and TILs to tumour cells were collected on different tissue sections. The co-staining of immune markers on the same tissue section is required for a more detailed analysis.

6.4.2 Influence of TAMs and TILs on patient survival relevance

The relevance of cell density and gene expression on survival was also investigated in this Chapter. Surprisingly, the CD3+CD4+FOXP3+ regulatory T cell was identified to be the most strongly associated with improved survival compared to all the other immune populations. The shared IFN-γ signalling of this population with the CD3+CD8+ TILs might be an explanation; however, the regulatory T cells also exhibited an IFN-γ regulation and cell senescence

signature[539]. These results may indicate dual functionality[540] or mixed populations[536] within the CD3+CD4+FOXP3+ TILs. Indeed, IL-12 has been shown to stimulate CD4+FOXP3^{low} T cells to produce more IFN-γ[541] *in vitro* compared to the CD4+FOXP3^{high} T cells[536]. This evidence suggests that, similar to TAMs, the complexity of the regulatory T cell populations[542] may not be easily deconvoluted with a single stain for FOXP3 and additional markers are needed to identify their subpopulations[542-544] (This is being pursued by other researchers in my lab independently).

The CD68++CD163+ TAMs were found to be associated with improved patient survival in our cohort (Figure 4.3.7). The CD68++CD163+ TAMs and the CD3+CD8+ TILs were the most highly correlated pair in both tumour-nest and stroma, suggesting that their co-existence may be independent of the presence of tumour cells. Importantly, the abundance of these TAMs and TILs in the tumour correlated with multiple enhanced immune-associated pathways; however, this was not predictive of patient survival. A more detailed analysis of their population-associated-gene-signatures revealed that PD1 signalling could be important in defining the activation status of the CD3+CD8+ TILs. The CD68++CD163+ TAMs, contrary to the currently accepted M2-like properties, were associated with upregulated immune cytokines and antigen-presentation that might be assisting the CD3+CD8+ TILs in keeping tumour cells in check. However, additional functional markers are required in the same multiplex IHC panel to test this hypothesis.

6.4.3 Summary

In summary, the work in this Chapter showed that TILs can be successfully identified and characterised. Their spatial and transcriptomic relationship with TAMs were investigated. A high density-correlation of the CD3+CD8+ TILs with the CD68++CD163+ TAMs was identified within both tumour-nest and stroma suggesting a possible interaction between these immune populations.

Chapter 7 : Evaluation of interactions between the CD68++CD163+ TAMs and CD8+ TILs

7.1 Introduction

From the results in Chapter 6, the CD68++CD163+ TAMs were found to be highly correlated with CD3+CD8+ TILs in both the tumour-nest and stroma (Figure 6.3.10). It was thought at first that this correlation may explain the favourable survival associated with this TAM population; however, no survival benefit was observed with CD3+CD8+ TIL density alone or in combination with the CD68++CD163+ TAMs. Results suggested that staining of both immune populations on the same section, along with functional markers, was important in determining their interaction and impact on the tumour microenvironment (TME) and for investigating their clinical relevance. From the gene-signature analyses between these TAMs and TILs, PD1 signalling was identified as a potential target for the CD3+CD8+ TILs (Figure 6.3.16); however, appropriate functional markers for the CD68++CD163+ TAMs have not yet been identified.

PD1 is an inhibitory receptor which is upregulated on active T cells post antigen stimulation and is a major component of immune checkpoint therapies in cancer[97]. PD1 expression has been shown to increase on CD8+ TILs with enhanced granzyme B production reflecting their state of activation[545, 546]. However, in an environment of persistent antigen exposure, such as cancer, high PD1 expression was found on CD8+ T cells and was associated with loss of T cell effector functions termed “exhaustion”[111]. Based on these properties, PD1 was selected as the functional marker for the CD3+CD8+ TIL population for further study.

This Chapter aims to identify a marker for the CD68++CD163+ TAMs which will allow for further investigation into possible mechanisms underlying their association with improved survival, their ambiguous M1/M2-like properties, and possible interaction with the CD3+CD8+ TILs, utilising PD1 as a functional marker for the TILs.

7.2 Aims

Aim 1: To investigate possible reasons underlying the positive association of CD68++CD163+ TAMs with improved patient survival

Aim 2: To identify a functional marker for CD68++CD163+ TAMs

Aim 3: To investigate the spatial relationship between the CD68++CD163+ TAMs, CD8+ TILs and functional markers

Aim 4: To investigate the clinical relevance of different immune cell populations

7.3 Results

7.3.1 Identification of NOX2 as a potential functional marker for TAMs

Based on the observation that the CD68++CD163+ macrophages (presumably M2-like) were associated with favourable survival and the CD68+IRF8+ (presumably M1-like) macrophages were not (Figure 4.3.7 and Appendix 1 Figure 4D), the genes inversely correlated between these TAM populations and their associated pathways were identified with Reactome[410] (Figure 7.3.1; methods described in Chapter 5). These genes confirmed the previous findings (Figure 6.3.18), showing that CD68+IRF8+ TAMs are more associated with increased apoptosis-related genes whilst the CD68++CD163+ TAMs correlated with upregulated antigen presenting properties.

Cytochrome b beta (*CYBB*; Figure 7.3.1B), also known as the nicotinamide adenine dinucleotide phosphate H (NADPH) oxidase 2 (*NOX2*) gene, was the gene most highly associated with the pathways identified for the CD68++CD163+ TAMs, and had the highest correlation with improved GC survival (Figure 7.3.2 and Appendix 7). This *NOX2* gene encodes a membrane-located protein gp91^{phox}, a subunit of the NADPH oxidase (Figure 7.3.3) which is responsible for generating reactive oxygen species (ROS) in macrophages[547] and has been shown to enhance antigen presentation of dendritic cells[548-550].

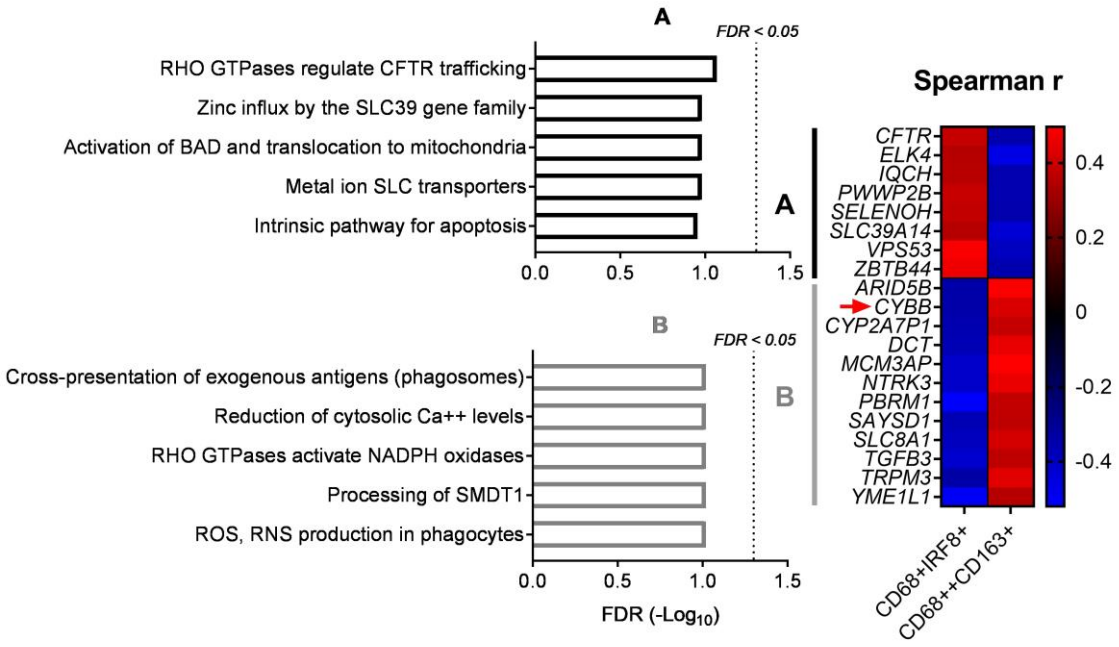
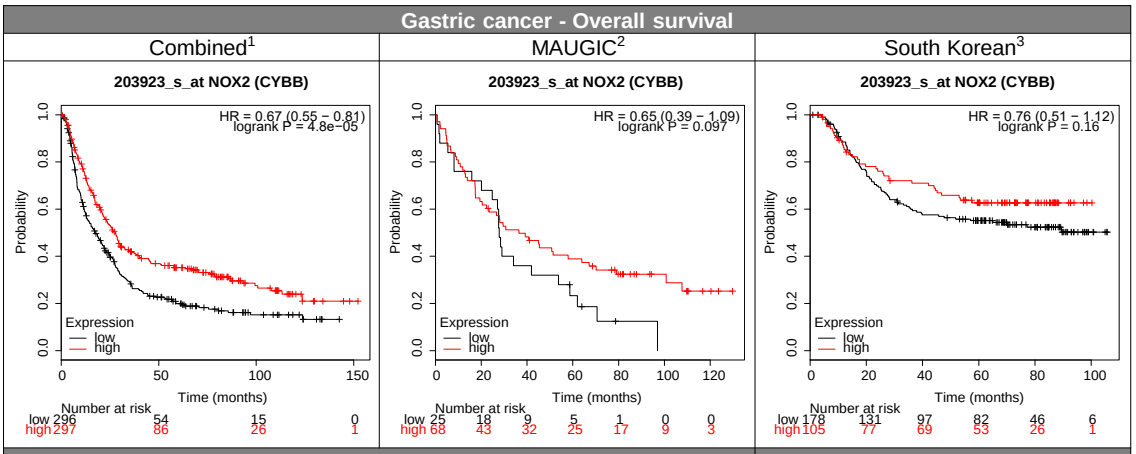


Figure 7.3.1 Inverse gene signatures between the CD68++CD163+ and CD68+IRF8+ TAM

(A) Genes and pathways positively correlated with CD68+IRF8+ TAMs and negatively with CD68++CD163+ TAMs were identified with Reactome. (B) Reverse correlations of (A). Red/Blue: gene expressions positively/negatively correlated with increased TAM densities as labelled.



Median survival (month)				Upper quartile (month)	
high	27.9	high	36.4	high	26.27
low	17.4	low	27.8	low	20.13

Figure 7.3.2 Survival relevance NOX2 (CYBB) on GC overall survival

1: n=593; GSE14210+GSE15459+GSE22377+GSE29272+GSE51105. 2: GSE51105 (n=93). 3: GSE62254 (n=283); analysed separately. This cohort has much improved overall patient survival due to early-stage screening programs for GC. Upper quartile survival compared due to no median survival reached. Log-rank (Mantel-Cox) test. Survival plots generated with KMplot[405].

To confirm the correlation with NOX2 was not random, genes of other subunits of the NADPH oxidase (Figure 7.3.3) were correlated with the cell densities of different immune populations (Table 7.3.1). This result showed that 67% (4 out of 6) of these subunits were associated with the CD68++CD163+ TAM and CD3+CD8+ TIL pair and not with the other immune populations, suggesting that this pathway may be important for their combined functions.

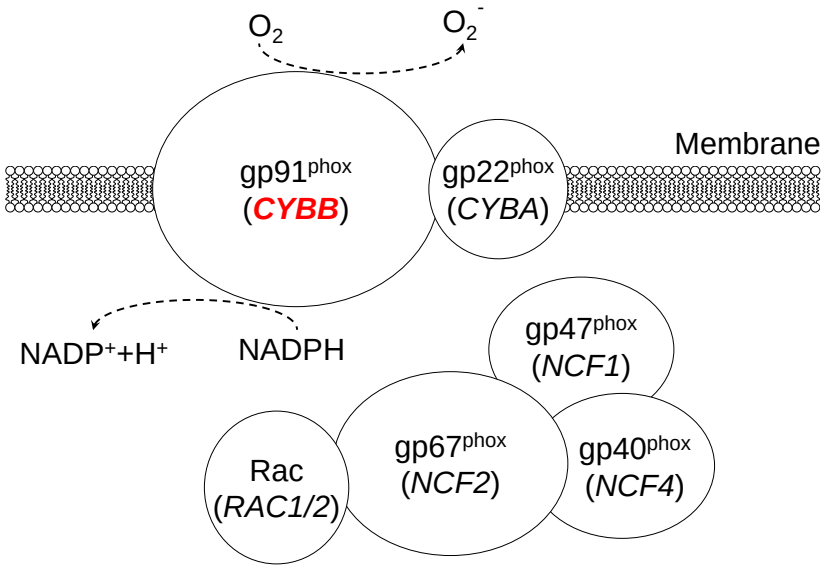


Figure 7.3.3 Subunits of the NADPH oxidase complex

Table 7.3.1 Correlations of the subunits of the NADPH oxidase complex

NADPH oxidase (Spearman density/gene correlation)							
Subunit		p22phox	gp91phox	p47phox	p67phox	p40phox	Rac
gene		*CYBA*	*CYBB*	*NCF1*	*NCF2*	*NCF4*	*RAC1/2*
Macrophage	CD68+IRF8+	0	-0.349	0	0	0	0
	CD68+	0	0	0	0	0	0
	CD68+CD163+	0	0	0	0	0	0
	CD68++CD163+	0.35	0.423	0	0.375	0	0
	CD68+CD206++	0	0	0	0	0	0
	CD68+CD206+	0	0	0	0	0	0
	CD68+CD163+CD206+	0	0	0	0	0	0
T cell	CD3+DN	0	0	0	0	0	0
	CD3+CD8+	0	0.449	0	0	0.409	0
	CD3+CD4+	0	0	0	0	0	0
	CD3+CD4+FOXP3+	0	0	0	0	0	0

These data suggest that the improved patient survival observed with the CD68++CD163+ macrophages may be due a NOX2-associated enhancement of antigen-presentation to the CD3+CD8+ T cells, whose functional status could be defined by their PD1 expression. To test this hypothesis, a multiplex NOX2 panel was designed which incorporated CD68 and CD163 to identify TAMs, CD8 to identify TILs, AE1AE3 for tumour cells and with NOX2 and PD1 as functional markers for the TAMs and TILs, respectively (Figure 7.3.4 and Table 2.2.3).

The multiplex NOX2 panel was optimised with positive controls of each antibody and the NOX2 staining was found to be expressed on normal human liver macrophages (co-stained with CD68 and CD163; Figure 7.3.4A) but not on other liver cells. Some NOX2+ non-macrophages were present in normal human tonsil (Figure 7.3.4A) and in the GC tissue (referred as NOX2+ in Figure 7.3.4B and Figure 7.3.5). These cells could possibly represent dendritic cells[550], neutrophils[551] or myeloid-derived suppressor cells[552] (MDSCs; only in the tumour). The **OPAL study cohort** was stained with this panel, and images were acquired and phenotyped as different cell populations using methods described in Chapter 3. Visually and statistically, the CD68++CD163+ TAMs were found to express enhanced NOX2 at the protein level (Figure 7.3.4B and Figure 7.3.5), supporting the gene-expression data and the hypothesis that the CD68++CD163+ TAMs are associated with NOX2 signals in the tumour microenvironment.

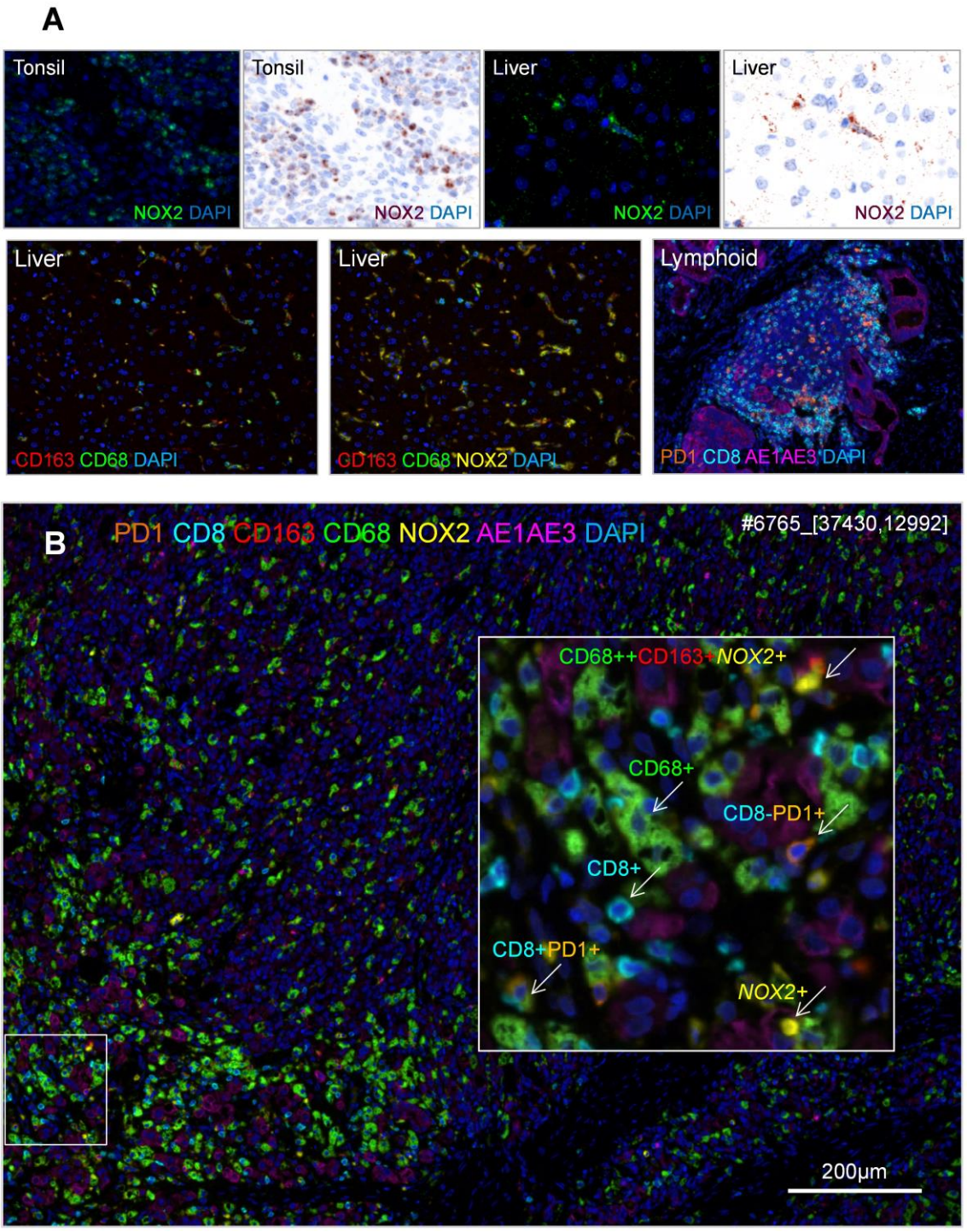


Figure 7.3.4 Representative images of the multiplex NOX2 panel

(A) Composite and single-stained IHC images optimised NOX2 and PD1 antibody on positive control tissues. (B) Composite image and cell populations identified with the optimised multiplex NOX2 panel.

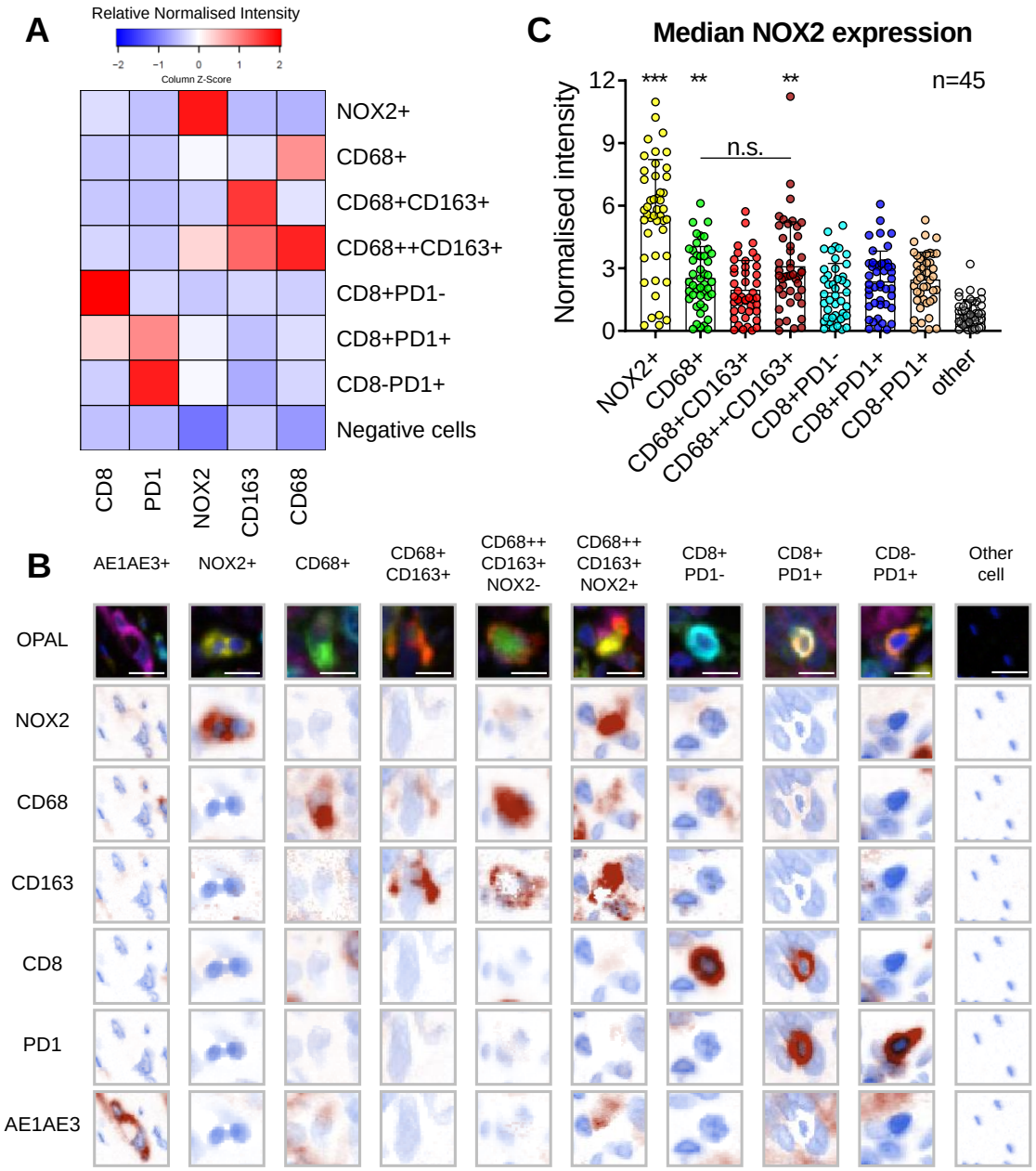


Figure 7.3.5 Marker signatures and representative images of cell types identified with the multiplex NOX2 panel

(A) Combined marker signatures of the cell populations identified with the multiplex NOX2 panel. NOX2+ cells are defined as non-macrophage cells expressing NOX2, may represent dendritic cells[550], neutrophils[551] or myeloid-derived suppressor cells[552]. Negative cells are the other cells in (B) and (C) that are without any expressions in all markers used in the panel. (B) Representative single-cell composite and single-stained IHC images of each cell population. Scale bar: 10 µm. (C) NOX2 intensity compared between different cell populations. Bar and error bars represent mean ± SD. Each point represents one patient. **p<0.01, ***p<0.001 and not significant (n.s.) comparing between cell populations. Mann-Whitney U test.

7.3.2 Validation between multiplex TAM, TIL and NOX2 panels

In previous Chapters, the TAM (Chapter 3) and TIL (Chapter 6) populations were characterised on separate tissue sections from the same patients. To ensure conformity of results generated from different tissue sections from the same patient tissue block (Appendix 8), different variables (e.g. density, distance, survival groupings) determined for the CD68++CD163+ TAMs and the CD8+ TILs characterised with the multiplex NOX2 panel were compared with the results of the multiplex TAM and TILs panels,.

The results showed that the densities of the CD68++CD163+ TAMs and CD8+ TILs, identified using the multiplex NOX2 panel, were consistent with the previous TAM/TIL panels (Appendix 8A and E). There were no differences between their median distances to tumour cells identified between panels (Appendix 8B and F). Their survival association results were identical. The TAMs were associated with an improved patient survival while the TILs were not (Appendix 8C and G). The groupings of the individual patients in the survival groups were compared and only 6 out of 46 patients had discordant results (13%; Appendix 8D and H), reflecting the heterogeneity of immune densities between different slides from the same block[553]. In conclusion, the validation data of different variables between mIHC panels suggest that the methods developed and the results generated in this study were reproducible and comparable.

7.3.3 Distribution of multiplex NOX2 panel-characterised cells

To investigate the relationships between the CD68++CD163+ TAMs and CD8+ TILs, the density and distance between cell populations were calculated and compared (Figure 7.3.6). Overall, there were more TAMs (all CD68+) than CD8+ TILs in the tumour Core (Figure 7.3.6A and B); the CD68++CD163+ TAMs accounted for a median 15.3% of all TAMs and 13.3% of the CD8+ TILs were PD1+ (Figure 7.3.6C and D), showing that these cells of interest were not the predominant immune populations by number within the tumour microenvironment.

When comparing the median distance of cell populations to tumour cells (defined in Figure 3.3.12), the CD68++CD163+ TAMs were the closest (16.62µm, within the tumour-nest; Figure 7.3.6E). The CD8+ TILs, irrespective of their PD1 status, were preferentially located beyond 20µm of a tumour cell. This finding was similar for the non-CD8 PD1+ cells (CD8-PD1+), possibly representing other non-cytotoxic T cells[554] (Figure 7.3.6E).

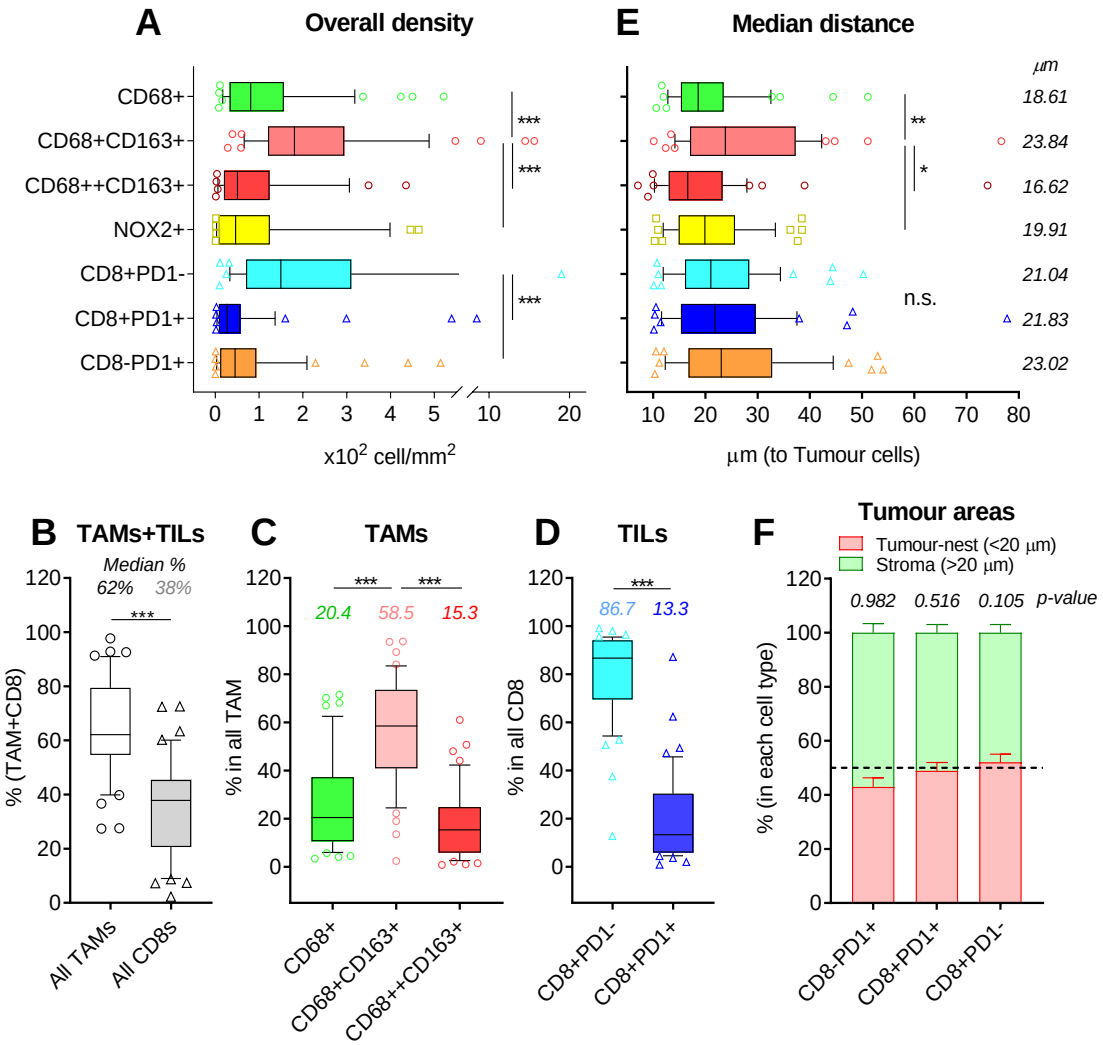
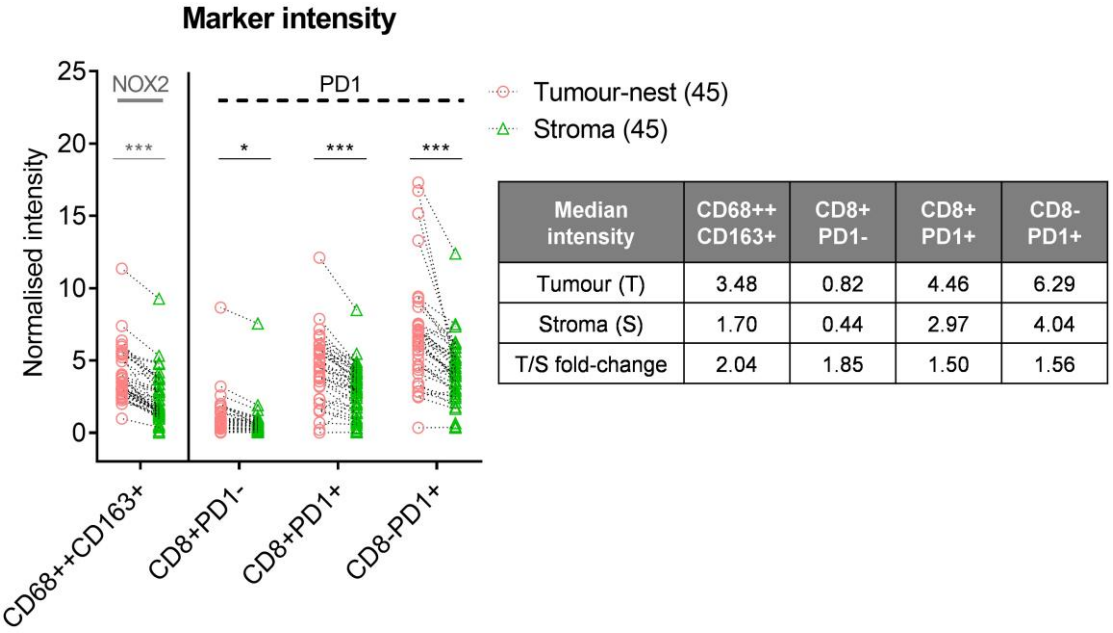


Figure 7.3.6 Characteristics of TAMs and TILs in the tumour Core

(A) Density and (B) percentage of TAMs and TILs in both TAMs and TILs and in (C-D) individual populations. (E) Median distance of cell populations to tumour cells. Box and whiskers represent mean ± 10-90 percentile. Each point represents one patient. ***p<0.001 comparing between cell populations. (F) Distribution of TILs between tumour areas. Error bar: SEM. P-value comparing between tumour areas. Dashed line: 50%. Mann-Whitney U test.

Further characterisation did not identify any differences in the spatial distribution of the CD8+PD1-, CD8+PD1+, and the CD8-PD1+ cells between the tumour-nest and the stroma (Figure 7.3.6F). However, higher PD1, as well as NOX2 intensity, on the corresponding TILs and TAMs, respectively, were observed within the tumour-nest (Figure 7.3.7). These data suggest that the PD1 positivity on TILs was not related to their proximity to tumour cells but might be related to other factors within the tumour-nest.



Median intensity	CD68++ CD163+	CD8+ PD1-	CD8+ PD1+	CD8- PD1+
Tumour (T)	3.48	0.82	4.46	6.29
Stroma (S)	1.70	0.44	2.97	4.04
T/S fold-change	2.04	1.85	1.50	1.56

Figure 7.3.7 NOX2 and PD1 expression on TAMs/ TILs between tumour-nest and stroma

NOX2 or PD1 expression was determined for defined cell types within the tumour-nest (T) and stromal (S) compartment of the **OPAL study cohort** (n=45). Dashed lines represent paired patient samples. Table shows the median intensity and ratio of the functional markers within and between tumour areas. *p<0.05 and ***p<0.001. Mann-Whitney U test.

To investigate if the co-existence of TAMs and TILs was associated with elevated PD1 expression on CD8+ TILs, their density correlations in the tumour Core were compared within the multiplex NOX2 panel (Figure 7.3.8). The cell density of CD68++CD163+ TAMs was found to correlate with the NOX2+ non-macrophages, all the other TAM populations, and the total number of the CD8+ TILs (Figure 7.3.8). Interestingly, the CD68++CD163+ TAMs were found to be highly correlated with the CD8+ TILs positive for PD1 (CD8+PD1+) but not with the PD1-negative population (CD8+PD1-; yellow squares in Figure 7.3.8). In contrast, the CD68+CD163+ TAMs correlated only with the CD8+PD1- TILs and not with the CD8+PD1+ TILs (yellow squares; Figure 7.3.8A). These findings were confirmed by correlating the TIL densities of the multiplex NOX2 panel with the TAM and TIL specific panels (yellow squares in Figure 7.3.8B).

When comparing the density correlations of the PD1+ cells with the other TAM populations in the multiplex TAM panel, the CD8-PD1+ cells significantly correlated with the CD68-only, CD68+CD206++ and the CD68+CD163+CD206+ TAMs (Figure 7.3.8B), which were the populations with the highest PDL1+ densities and expression in the tumour microenvironment identified in this study (Figure 4.3.12). This suggested possible interactions between these populations and that the patients with high number of these immune populations might be potential candidates for checkpoint therapies targeting PDL1/PD1.

However, the CD68+CD206+ TAMs, which were largely PDL1+, did not correlate with any of the other PD1+ populations (Figure 7.3.8B). This suggests that despite the presence of PDL1, this TAM population may be immune suppressive through a PD1/PDL1 independent mechanism (e.g. IL-6; related to Figure 5.3.4). The CD8+ TILs and PD1+ cells identified with the multiplex NOX2 panel were all positively correlated with the majority of TILs in the T cell specific panel (Figure 7.3.8B), supporting previous findings that the different T cell populations might function or were recruited into the microenvironment as a group (Figure 6.3.10).

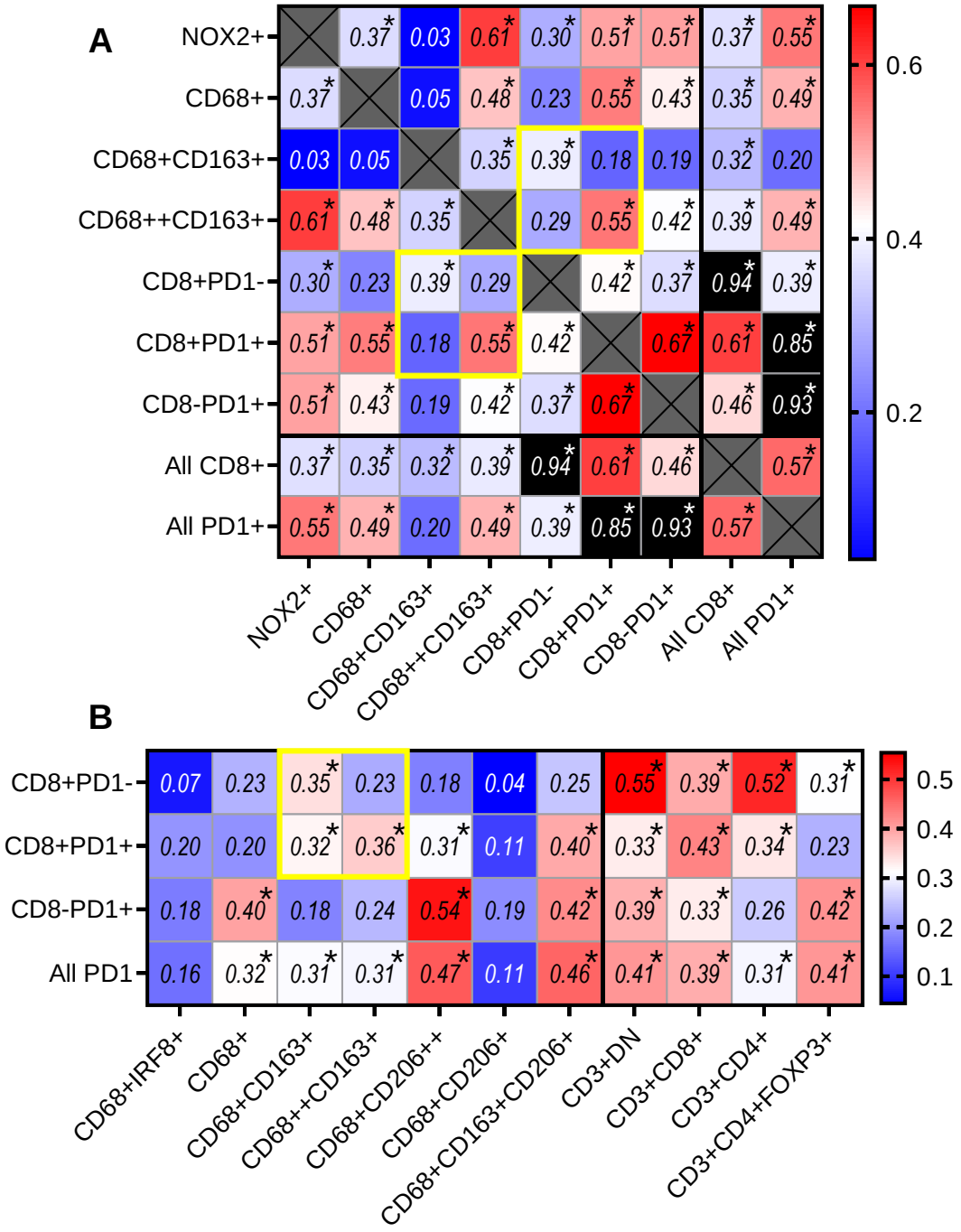


Figure 7.3.8 Cell density correlations of the multiplex NOX2 panel

(A) Density correlation of cell populations within the multiplex NOX2 panel. n=45. Correlation coefficients are as labelled in each cell. (B) Density correlation of cells identified with the multiplex NOX2 panel with the cells identified with the TAM and TIL panels. n=43. Red/White/Blue: Above/at/below median value. All CD8+: CD8+PD1- plus CD8+PD1+. All PD1+: CD8+PD1+ plus CD8-PD1+. Black: high correlation due to cell grouping methods. Grey: correlation with its own density. Yellow square: correlation between the CD8+PD1± TILs and the CD68+(+)CD163+ TAMs. *: $p<0.05$. Spearman correlation.

7.3.4 Refining CD68++CD163+ TAMs with NOX2 intensities

The CD68++CD163+ TAMs were found to possess an elevated NOX2 expression (Figure 7.3.5A) and their positive correlation with the CD8+PD1+ TILs (Figure 7.3.8) may support the hypothesis that the NOX2 pathways are important for their combined functions. However, not only did the intensity of NOX2 on CD68++CD163+ TAMs vary between patient samples (Figure 7.3.5C) but also not all TAMs expressed similar amount of NOX2 (Figure 7.3.5B). These data suggest that the expression of NOX2 on this TAM population was heterogeneous and an additional separation of TAMs based on their NOX2 intensities was required to refine TAM phenotypes.

In order to use NOX2 expression to more precisely phenotype TAMs, the minimum NOX2 intensity of the NOX2+ non-macrophage cells of each patient, corresponding to their visual positive staining, was used as individual baseline levels for defining the NOX2 positivity of TAMs in each sample (Figure 7.3.9A). In addition, the median intensity of the NOX2+ non-macrophage cells in the staining cohort was used as a reference to compare between different patient samples and to further divide the NOX2-positive TAM population into High and Low-expressing subgroups (Figure 7.3.9A).

The results showed that TAMs with different NOX2 positivity could be found within each patient sample but the majority of the CD68++CD163+ TAMs were grouped as NOX2-positive (Figure 7.3.9B), with a ratio of POS to NEG around 3:1 (Figure 7.3.9B). However, the majority (86%) of the POS CD68++CD163+ TAMs were $NOX2^{Low}$ and only 14% were $NOX2^{High}$ (Figure 7.3.9C). The expression of NOX2 on the CD68++CD163+ TAMs was independent of GC subtypes (Figure 7.3.9D), a factor that was found to significantly influence immune infiltration depth and PDL1 expression in patient samples in this study (§6.3.4, §4.3.8 and §4.3.9).

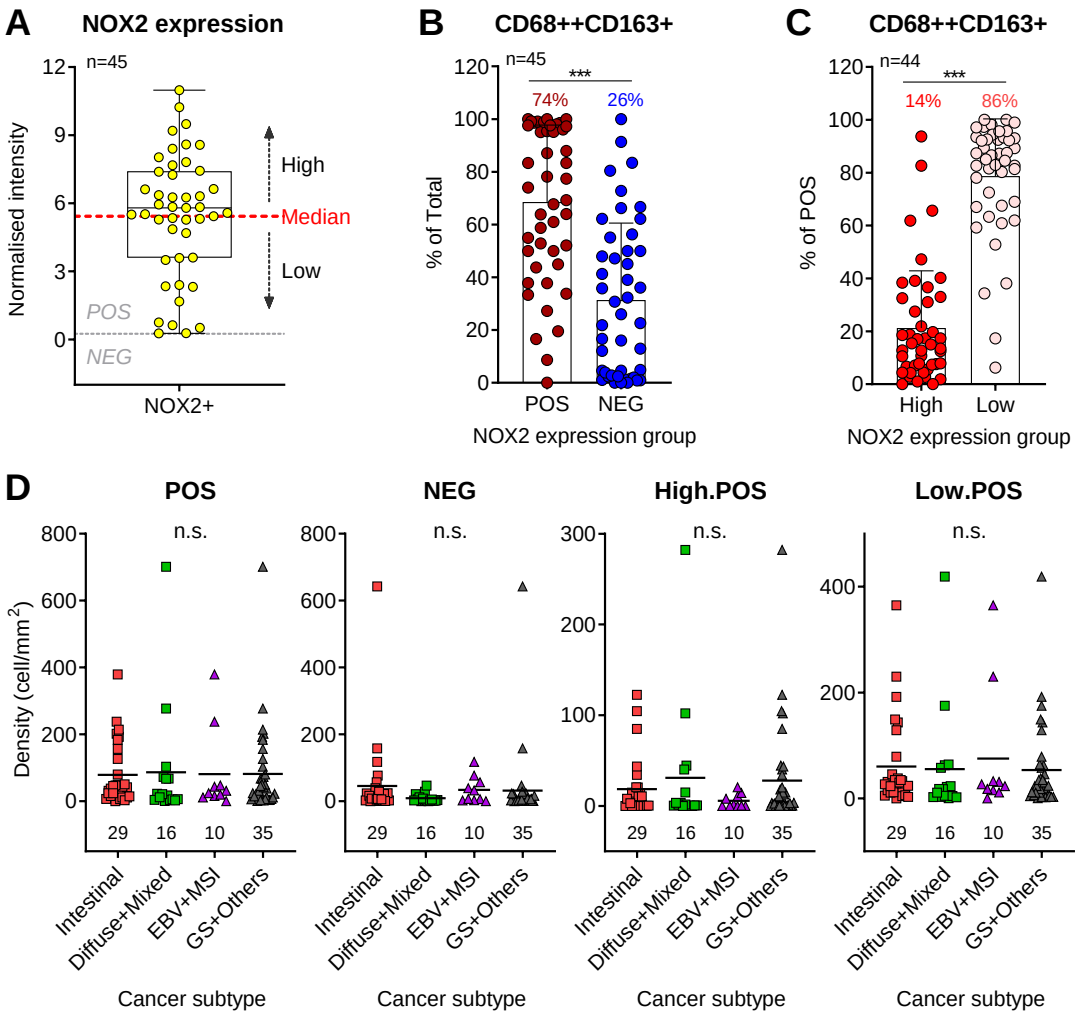


Figure 7.3.9 NOX2-expression refined CD68++CD163+ TAM

(A) NOX2-expression criteria used for refining CD68++CD163+ TAMs into NOX2-negative, high NOX2-positive and low NOX2-positive subpopulations. (B) Percentage of NOX2-positive and negative TAMs in all CD68++CD163+ TAMs in each patient sample (n=45). Median percentage of each group as labelled. (C) Percentage of High and Low NOX2-expressing TAMs in all NOX2-positive TAMs (n=44; one patient had no NOX2-positive TAMs). (D) Density of NOX2-definded TAMs between different GC subtypes. Bar and error bars represent mean ± SD. Each point represents one patient. Number of patients in each group are labelled. ***p<0.001 comparing between TAM populations and GC subtypes. Mann-Whitney U test.

7.3.5 NOX2 intensity-refined TAM density correlation

The density correlations with the NOX2-refined CD68++CD163+ TAMs was then compared with the other cell populations within the multiplex NOX2 panel (Figure 7.3.10). The NOX2+ non-macrophage cells significantly correlated with the NOX2+ TAMs (POS), albeit with different intensities, suggesting that the induction of NOX2 was systemically increased in the tumour; however, it was not associated with cancer subtypes (Figure 7.3.9C).

The NOX2-negative CD68++CD163+ TAMs had no correlation with any of the other cell types other than the total number of CD68++CD163+ TAMs (Figure 7.3.10A). Interestingly, the NOX2-positive TAMs significantly correlated with the CD8-PD1+ cells and all CD8+ TILs (irrespective of their PD1 status; Figure 7.3.10A). Within the CD8+ TIL population, CD68++CD163+ TAMs have higher density correlation with the PD1+ than the PD1- TILs; more importantly, these correlations between the TAMs and CD8+ TILs (irrespective of their PD1 status) were found to elevate as the NOX2-expression on TAMs increased (Figure 7.3.10B). These results showed that the PD1 expression on CD8+ TILs positively correlated with the NOX2 intensity on the CD68++CD163+ TAM and the two populations co-exist within the same tumour. Collectively, these data suggest that the systemic elevated NOX2 in the tumour could be immune related.

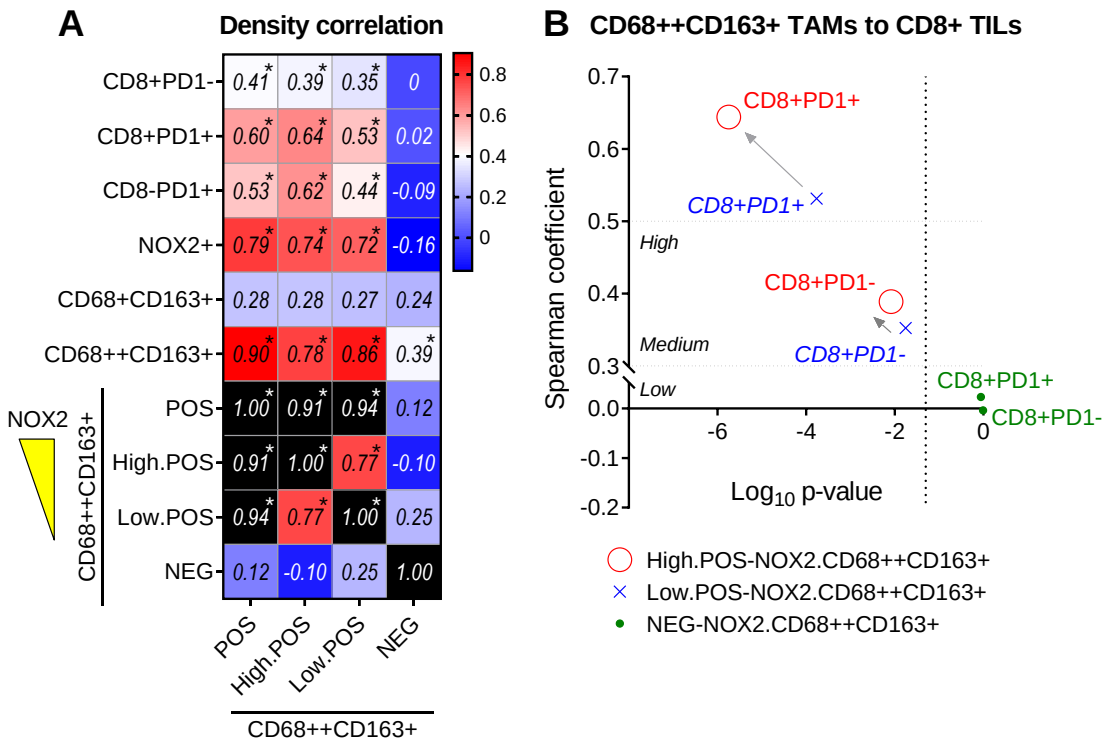


Figure 7.3.10 Density correlations of NOX2-refined CD68++CD163+ TAMs

(A) Density correlation of NOX2-intensity-refined CD68++CD163+ TAM populations with other cell types identified with the multiplex NOX2 panel. Red/White/Blue: Above/at/below median value. POS: High.POS plus Low.POS. Black: high correlation due to cell grouping methods. (B) Correlation between the CD68++CD163+ TAMs of different NOX2 intensities with CD8+ TILs of different PD1 positivity. Arrow: increased correlation as NOX2 expression on TAMs increased. *: $p<0.05$. Spearman correlation. Correlation coefficients are as labelled in each cell.

7.3.6 Functional marker expression on TAMs and TILs in proximity

Findings from the previous sections identified (i) a tumour-independent density correlation between the CD68++CD163+ TAMs and the CD3+CD8+ TILs in the tumour-nest and stroma (Figure 6.3.10) and (ii) the co-existence of NOX2-expressing CD68++CD163+ TAMs and PD1-expressing CD8+ TILs within the same tumour (Figure 7.3.10). However, the median distance between the CD68++CD163+ TAMs (RC) to CD8+PD1+ TILs (NC) was 82.3µm (66.2µm for the reverse comparison; Figure 7.3.11A), which was much further than their respective distances to tumour cells (16.62 and 21.83µm for the TAMs and TILs, respectively; Figure 7.3.11A and Figure 7.3.6D). Therefore, the high density correlation between the NOX2-expressing CD68++CD163+ TAMs and PD1-expressing CD8+ TILs may have been a random event that occurred in the same tumour.

To investigate if these functional markers (NOX2 and PD1) changed when the TAMs and TILs come in close contact, both cell types were used as reference cells (RCs) to calculate their distances to their corresponding nearest cells (NCs; Figure 7.3.11B). A distance of 50 µm was defined as the maximum diffusion distance of cytokines based on the literature[476-478]. Using this distance as threshold, the expression of functional markers on the TAMs and TILs within 50-60 µm was used as the baseline level of marker positivity for the corresponding cells. The marker intensity in each 10 µm increment of proximity (starting from 0) was compared (i) to the marker intensity within the 50-60 µm interval and also (ii) to within the 0-10 µm interval (defined as direct contact; Figure 7.3.11B and Figure 7.3.12). These comparisons represent (i) the degree of alteration of a functional marker when the cells were neared and (ii) when the intensity of a functional marker may have plateaued, respectively.

A

Median distance (μm) / Nearest cell	Reference cell	
	CD68++ CD163+	CD8+ PD1+
CD68++CD163+	--	66.24
CD8+PD1+	82.34	--
AE1AE3+	16.62	21.83

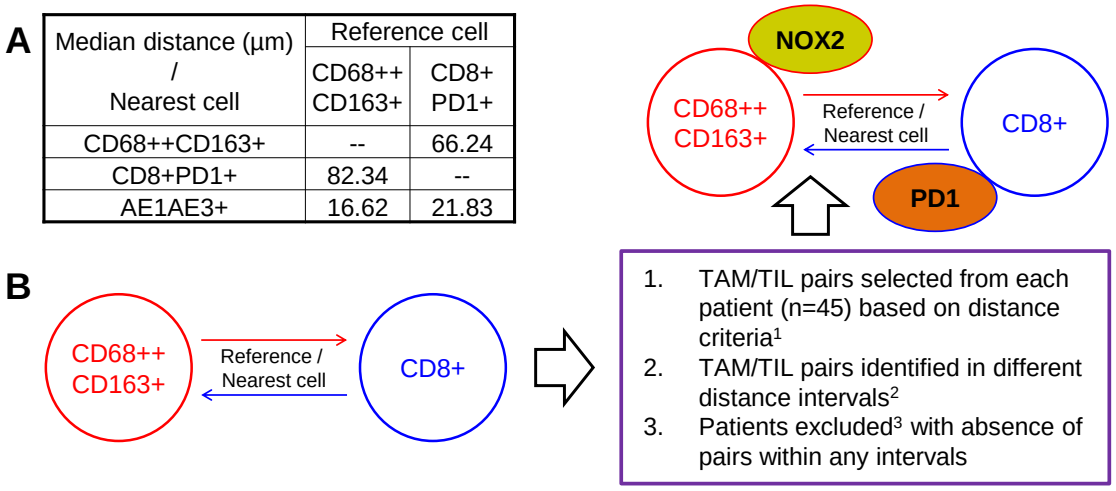


Figure 7.3.11 Proximity of NOX2-expressing TAMs and PD1-expressing TILs

(A) Median distance between cell populations. (B) Schematic graph of analysing spatial NOX2 and PD1 expression on TAMs and TILs. The TAMs and TILs were both used as reference cells and the TAM/TIL pairs were identified for each patient (n=45). 1: 50μm was used as the maximum cytokine diffusion distance[476, 477]. 2: TAM/TIL pairs were grouped within each 10 μm increments of proximity from 0-10 to 50-60 μm. 3: Patients with absence of pairing data in any of the distance intervals were excluded from the paired analysis. 9 patients were excluded when TILs (remaining n=36) were used as reference cells. 3 patients were excluded when the TAMs were used as RCs (remaining n=42). Functional marker intensities in each distance interval was compared with the intensities on corresponding cells within 50-60 μm and with the intensities when in direct contact (0-10 μm).

Significant increases of functional markers were observed on the corresponding cells when in proximity with each other (Figure 7.3.12and Appendix 9). When comparing the change in median PD1 expression on CD8+ TILs when TILs were used as RCs (Figure 7.3.12A), PD1 increased approximately 20% when the two cell types were in direct contact (0-10 μm) compared to when they were 50-60 μm apart (Figure 7.3.12A). In addition, when in direct contact, PD1 expression on TILs was higher than in all other distance intervals compared, whose intensity levels showed no difference with 50-60 μm (Figure 7.3.12A). When using CD8+ TILs as NCs (Figure 7.3.12B), PD1 on CD8+ TILs was also found to increase once they neared the TAMs within 50 μm. More importantly, an up to 70% elevated PD1 intensity was found on these TILs when in direct contact with the TAMs compared to when 50-60 μm apart and was significantly

higher than on the TILs in any other intervals compared (Figure 7.3.12B). These results suggest that the strongly enhanced PD1 on CD8+ TILs may have been more direct-contact dependent than through cytokine interactions with the TAMs.

As for NOX2 expression on TAMs, a 30% enhanced NOX2 was found on TAMs when analysed as RCs and comparing the direct contact pairs to the ones within 50-60 µm (Figure 7.3.12C). This gradual increase in NOX2 intensity was observed once the TAMs and TILs were within 50 µm of proximity and reached maximum expression within 20 µm with each other (10-20µm; Figure 7.3.12C). Interestingly, only subtle changes in NOX2 expression were found on TAMs when used as NCs in different distance intervals (Figure 7.3.12D). These results indicate that the changes in NOX2 expression on TAMs were related to their proximity with TILs which could be associated with paracrine or autocrine release of cytokines, and NOX2 expression plateaued before the cells came into direct contact (0-10µm). These findings could also infer that one TIL may not be sufficient to induce the NOX2 expression on a TAM (Figure 7.3.12D), but one TAM was sufficient to enhance the PD1 expression on a TIL (Figure 7.3.12B).

In summary, current data in this Chapter showed that (i) both the NOX2-expressing CD68++CD163+ TAMs and PD1-expressing CD8+ TILs co-existed in the same tumour (Figure 7.3.10) and that (ii) the expression of these functional markers increased on corresponding cell types as the TAMs and TILs were located in close proximity with each other (Figure 7.3.12).

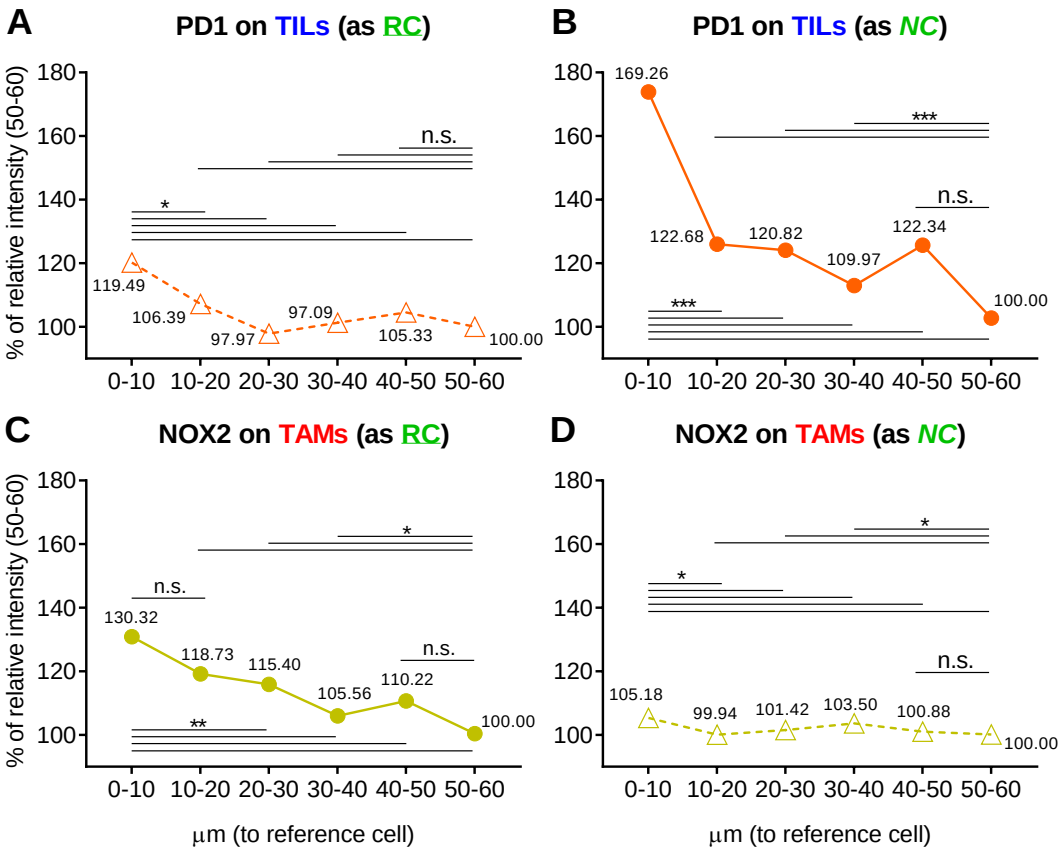


Figure 7.3.12 Functional marker expression on TAMs and TILs in proximity

Median PD1 expression (numbered with each point) on CD8+ TILs (blue) when TILs were used (A) as reference cells (RCs; green underlined) or (B) as nearest cells (NCs; green italic). Median NOX2 expression on CD68++CD163+ TAMs (red) when TAMs were used (C) as RCs or (D) as NCs. Lines represent median intensity of NOX2/PD1 expressions on corresponding TAMs/TILs. Intensities of the markers on the cells within each distance interval were normalised to the intensities within 50-60 µm. Orange: PD1 expression. Yellow: NOX2 expression. Functional marker intensities in each distance intervals were compared with the intensities on corresponding cells within 50-60 µm and with the intensities when in direct contact (0-10 µm). n=36 in (A) and (B). n=42 in (C) and (D). Patient exclusion methods are described in Figure 7.3.11. Wilcoxon matched-pairs test. *p<0.05, ***p<0.001 and not significant (n.s.) comparing marker intensity between distance intervals.

7.3.7 Survival relevance of individual TAM and TIL densities

The results from analysing functional marker differences between cells may support the hypothesis that the CD68++CD163+ TAMs and CD8+ TILs may be interacting through NOX2/PD1 associated mechanisms. However, while CD68++CD163+ TAMs were associated with improved survival (Figure 4.3.7), CD3+CD8+ TILs and their combined density with CD68++CD163+ TAMs were not (Figure 6.3.14 and Figure 6.3.15). Therefore, patient overall survival was evaluated by using of NOX2 and PD1 markers to improve prognostication.

The overall density and the effective density (0-10µm; related to Figure 4.3.7), representing the density of cells in direct contact with a tumour cell, were extracted from the data. Overall survival was compared between three patient groups that were stratified based on the two different density parameters of cell populations identified with the multiplex NOX2 panel (Figure 7.3.13 and Figure 7.3.14; as described in §4.3.3).

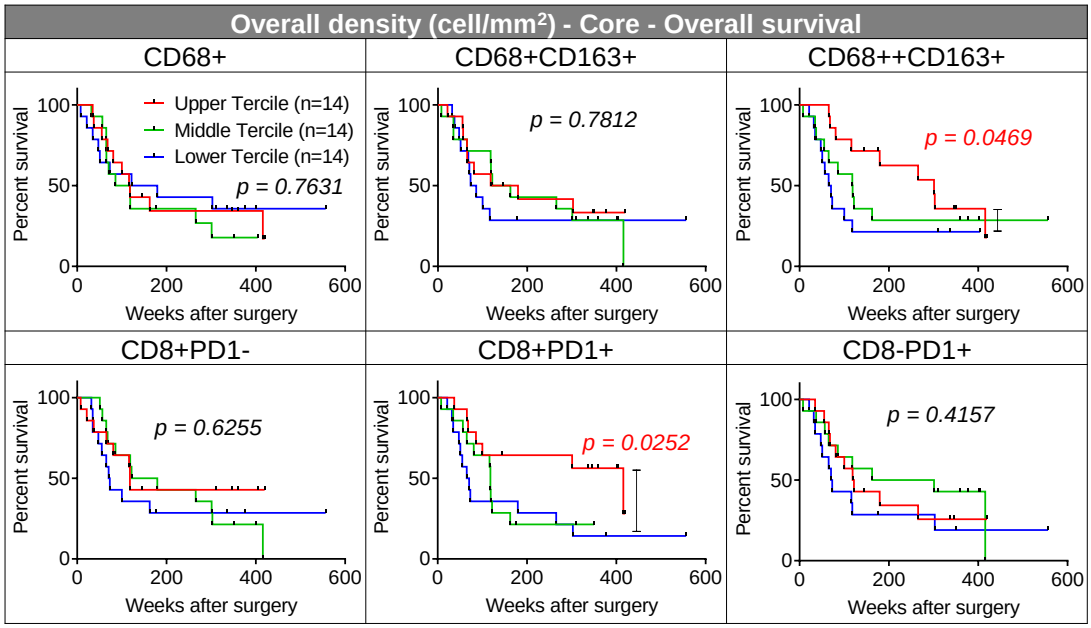


Figure 7.3.13 Overall survival based on overall cell density

Patients were stratified into three groups using the overall densities of different cell populations and their overall survival was compared. Upper tercile (density > 2/3 of the patients in the cohort; red line), Middle tercile (1/3 < density < 2/3 of patients in the cohort; green line) Lower tercile (density ≤ 1/3 of patients in the cohort; blue line). Log-rank (Mantel-Cox) test.

Using overall density, the results confirmed the CD68++CD163+ TAM as a predictor of improved survival and not the other TAM populations (Figure 7.3.13 and Appendix 1 Figure S4). With the utilisation of PD1, the increase in CD8+PD1+ TILs overall density identified patients with excellent survival whilst the CD8+PD1- and CD8-PD1+ populations did not (Figure 7.3.13).

Using effective density (0-10µm; Figure 7.3.14), the results confirmed and validated that this parameter, which reflect both the quantity and infiltration depth of intra-tumoural immune cells, was a more reliable selection factor to predict patients with good outcome than using overall density (Figure 4.3.7).

Collectively, these results indicate that revealing the spatial distribution as well as the functional status of the TILs was clinically relevant and that these putative antigen-experienced CD8+ T cells may be important for patient survival.

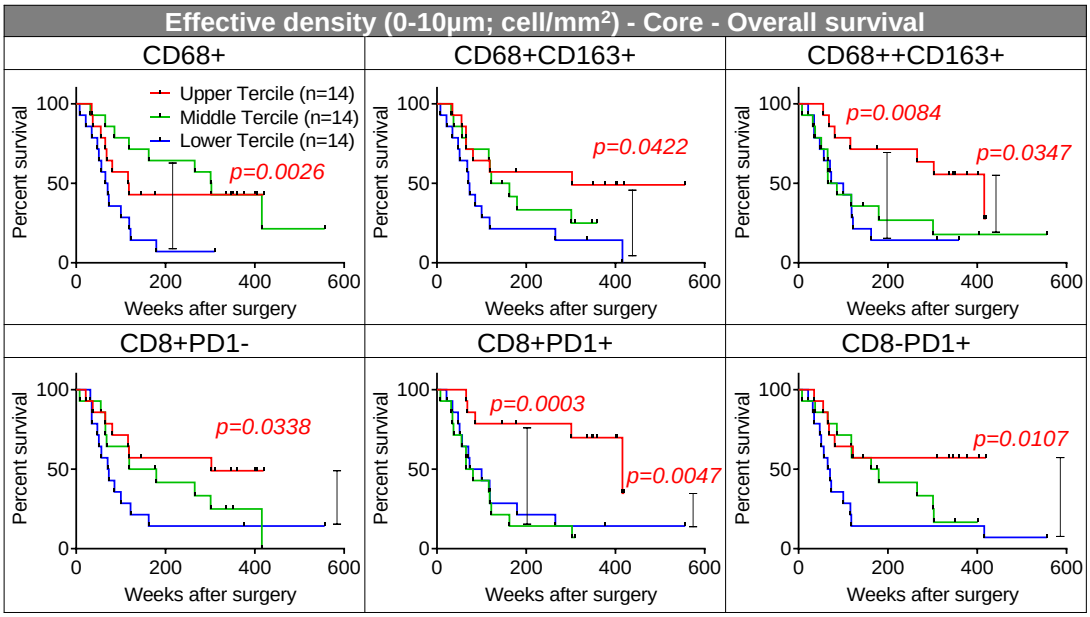


Figure 7.3.14 Overall survival based on effective density (0-10 µm)

Patients were stratified into three groups using the Effective density (0-10 µm) of different cell populations and their overall survival was compared. Effective density (0-10 µm) represents the number of cells that were within 10 µm of tumour cells, defined in Figure 4.3.7. Upper tercile (density > 2/3 of the patients in the cohort; red line), Middle tercile (1/3 < density < 2/3 of patients in the cohort; green line). Lower tercile (density ≤ 1/3 of patients in the cohort; blue line). Log-rank (Mantel-Cox) test.

To evaluate whether NOX2 expression could be used to further improve the survival prediction of the CD68++CD163+ TAMs, patients were stratified with the overall density of NOX2-intensity refined CD68++CD163+ TAMs (Figure 7.3.15; populations defined in Figure 7.3.9). Interestingly, the results showed that including NOX2 did not provide additional survival benefits. It was found that the patients who were within the upper-tercile of the study cohort based on TAM densities, had not only higher TAM number and improved survival, these TAMs also expressed enhanced NOX2 intensity compared to the patients with less cell density and poor survival outcome (Figure 7.3.15).

The findings from this and previous sections showed that: (a) CD68++CD163+ TAMs were associated with improved survival (Figure 7.3.13; related to Figure 4.3.7), (b) the majority (74%) of the TAMs were NOX2-postive (Figure 7.3.9B), and (c) different NOX2-expressing TAMs and the overall CD68++CD163+ TAM density all had positive density correlations (Figure 7.3.10A).

Collectively, these data indicate that the abundance of CD68++CD163+ TAMs and the elevated NOX2 expression on these TAMs were concurrent events within the same tumour microenvironment. These results also suggest that, unlike the favourable survival prediction value of PD1 on CD8+ TILs (Figure 7.3.14), NOX2 was not an additive positive selection factor for the CD68++CD163+ TAMs compared to using their overall density to identify patients with improved overall and relapse-free survival (Figure 7.3.15).

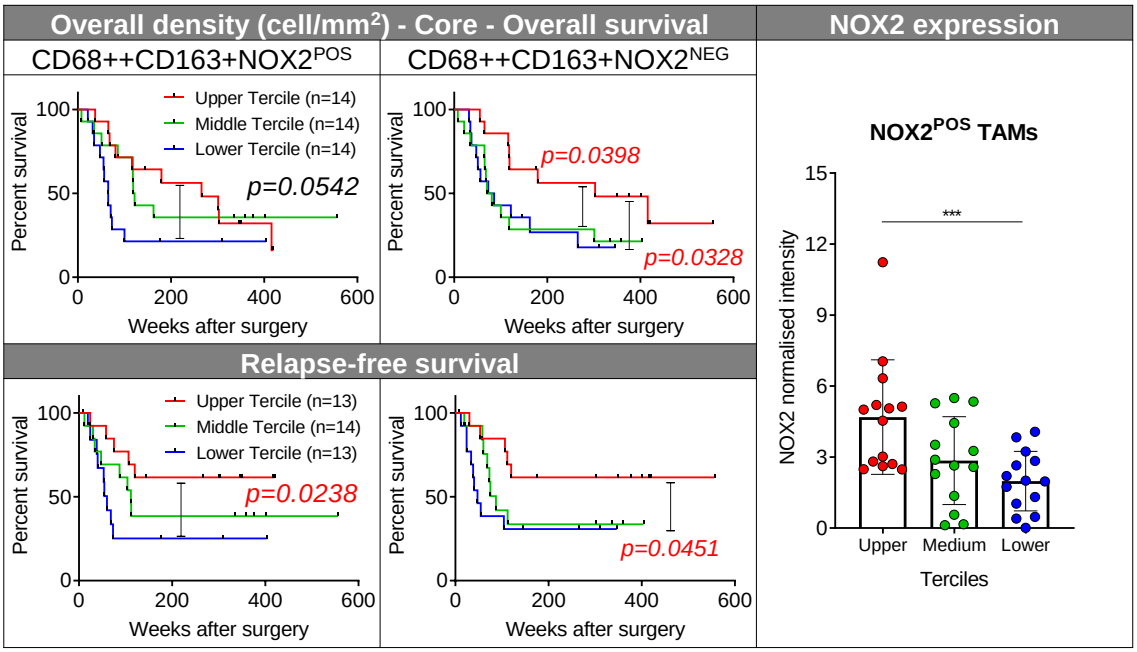


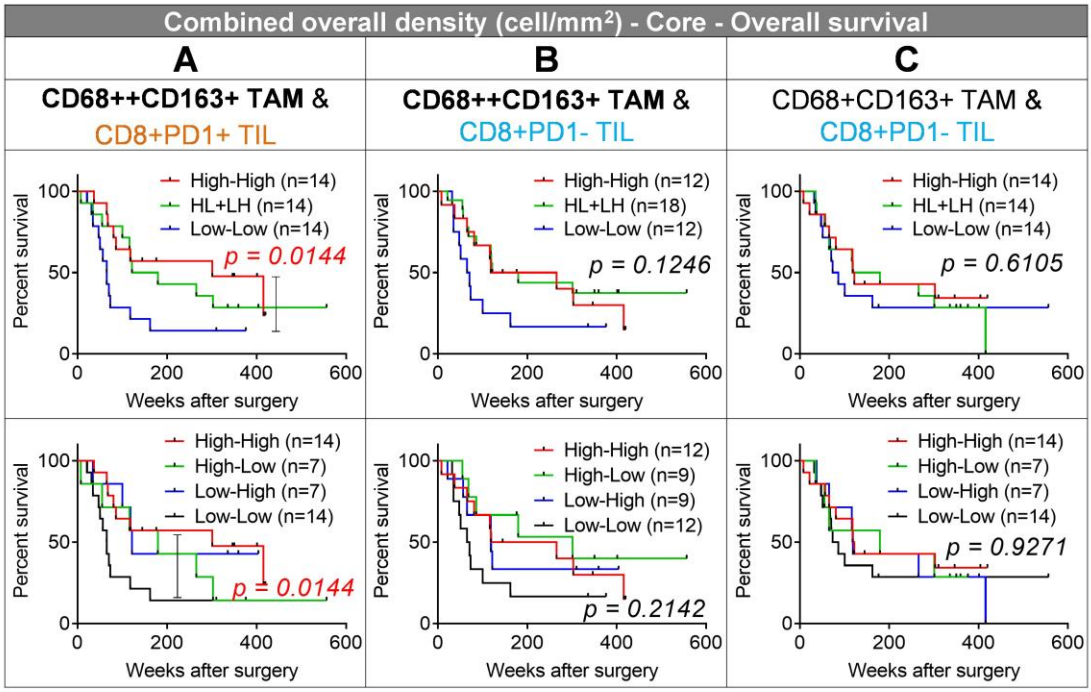
Figure 7.3.15 Survival based on NOX2-refined CD68++CD163+ TAM density

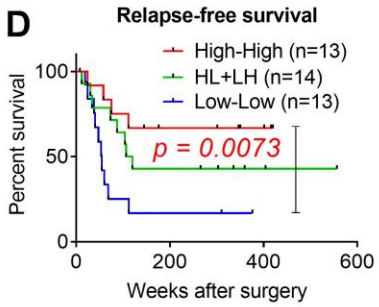
Patients were stratified into three groups using the overall density of CD68++CD163+ TAMs with different NOX2 positivity and their overall and relapse-free survival were plotted. Upper tercile (density > 2/3 of the patients in the cohort; red line), Middle tercile (1/3 < density < 2/3 of patients in the cohort; green line). Lower tercile (density ≤ 1/3 of patients in the cohort; blue line). Log-rank (Mantel-Cox) test. (B) NOX2 expression on TAMs in patient groups stratified with TAM density. Bar and error bars represent mean ± SD. Each point represents one patient. ***p<0.001 comparing between patient groups. Log-rank (Mantel-Cox) and Mann-Whitney U test.

7.3.8 Survival relevance of TAM and TIL combined densities

The combined analysis of TAM and TIL cell density was then used as a stratification criterion of patient overall survival (Figure 7.3.16 and Appendix 10; methods as described in Figure 6.3.15A). The results showed that the patients with high CD68++CD163+ TAM and concurrently high CD8+PD1+ TIL density had an improved overall survival (Figure 7.3.16A). This was not seen in combination with the CD8+PD1- population (Figure 7.3.16B), nor with the combined densities of the CD68+CD163+ TAMs and CD8+PD1- TILs pair (Figure 7.3.16C) which also significantly co-localised within the same tumour (Figure 7.3.8). The patients abundant intra-tumoural CD68++CD163+ TAMs and CD8+PD1+ TILs showed more durable survival without tumour and lower

percentage of cancer recurrence which could be one of the reasons for their improved overall survival (Figure 7.3.16D). These results indicate possible interactions of the CD68++CD163+ TAM and the CD8+PD1+ TIL pair, and the co-existence of both cell types at high cell number was required within the same tumour to show its effectiveness (High-High group in Figure 7.3.16A and D).





Recurrence (%)	TAM - TIL		
	High-High	HL+LH	Low-Low
Yes	30.77	57.14	76.92
No	69.23	42.86	23.08
Total (n)	13	14	13
p-value	**High-High**	**HL+LH**	**Low-Low**
High-High	- -	0.1682	0.0183
HL+LH	0.1682	- -	0.2760
Low-Low	0.0183	0.2760	- -

Figure 7.3.16 Survival based on TAM / TIL combined density

Patients were stratified into different groups with median densities as cut-offs of corresponding cell populations and their (A-C) overall survival, (D) relapse-free survival and incidence of recurrence were compared. High-High (patients with above median densities of both TAMs and TILs). High-Low (HL; patients with above median density of TAMs but below of TILs). Low-High (LH; patients with below median density of TAMs but above of TILs). Low-Low (patients with below median densities of both TAMs and TILs). Method as described in Figure 6.3.15A. (A-D) Log-rank (Mantel-Cox) and (D) Chi-square test.

Further stratification of NOX2-postive expression on TAMs (Figure 7.3.17) did not provide much additional survival benefit for patient stratification compared to using their overall densities (Figure 7.3.16). However, interestingly, a subgroup of patients with very poor outcome (Low-Low in Figure 7.3.17) was identified with the combined densities of NOX2-negative TAMs with the CD8+ TILs regardless of their PD1 status. These data support previous findings (Figure 7.3.15) that the NOX2 marker did not confer much additive value for the CD68++CD163+ TAMs on patients with improved survival as a positive selection factor due to the concurrent high density with enhanced NOX2 expression. However, NOX2 may be used as a negative selection marker to identify patients with low immune infiltration, non-activated cell status (NOX2 and PD1 negative), and therefore, very poor outcome (Figure 7.3.17).

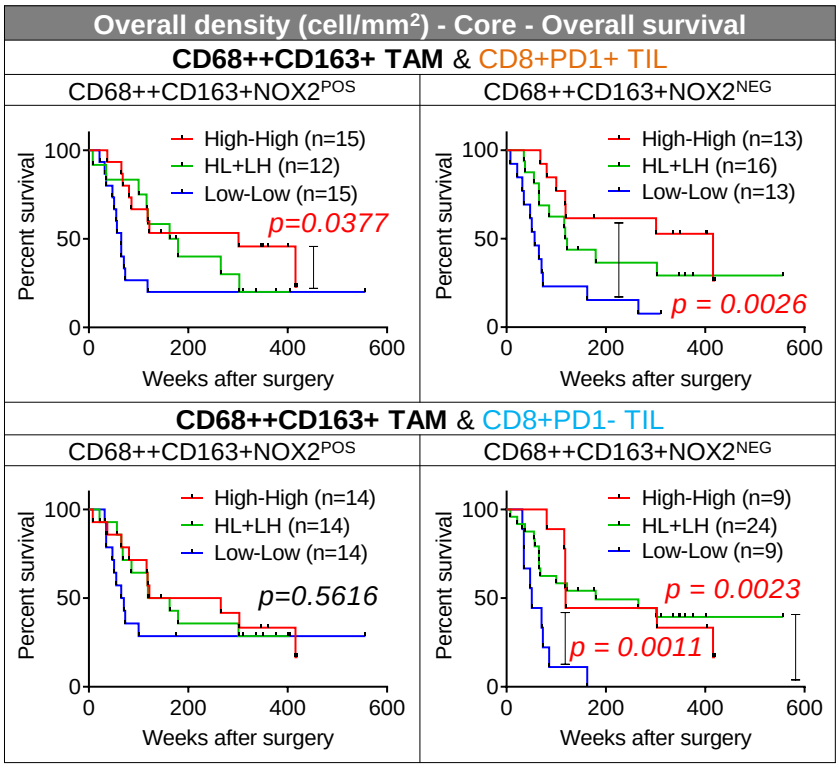


Figure 7.3.17 Overall survival based on NOX2-refined TAM / TIL combined density

Patients were stratified into four groups with the median densities of corresponding cells as cut-offs. Overall survival was interrogated between the combined patient groups. High-High (patients with above median densities of both TAMs and TILs). High-Low (HL; patients with above median density of TAMs but below of TILs). Low-High (LH; patients with below median density of TAMs but above of TILs). Low-Low (patients with below median densities of both TAMs and TILs). Log-rank (Mantel-Cox) test.

High density correlation was found between the CD68++CD163+ TAMs and CD3+CD8+ TILs in both tumour-nest and stroma (Figure 6.3.10) and an upregulation of NOX2 and PD1 on TAMs and TILs, respectively, was observed when these cells come in close contact (Figure 7.3.12). These data suggest that these TAM/TIL pairs in different distances from each other may be functionally discrete. To investigate if the co-localisation of the TAMs and TILs was survival relevant, patients were grouped based on the number of TAM/TIL pairs in the Core and their overall survival between groups was compared. Interestingly, unlike the relative distance of TAMs and TILs to tumour cells which showed strong indicative values on survival (Figure 4.3.7, Figure 7.3.13 and Figure 7.3.14), the proximity between the TAMs and TILs was not a reliable selection factor to predict patients with good outcome (Figure 7.3.18 and Figure 7.3.19).

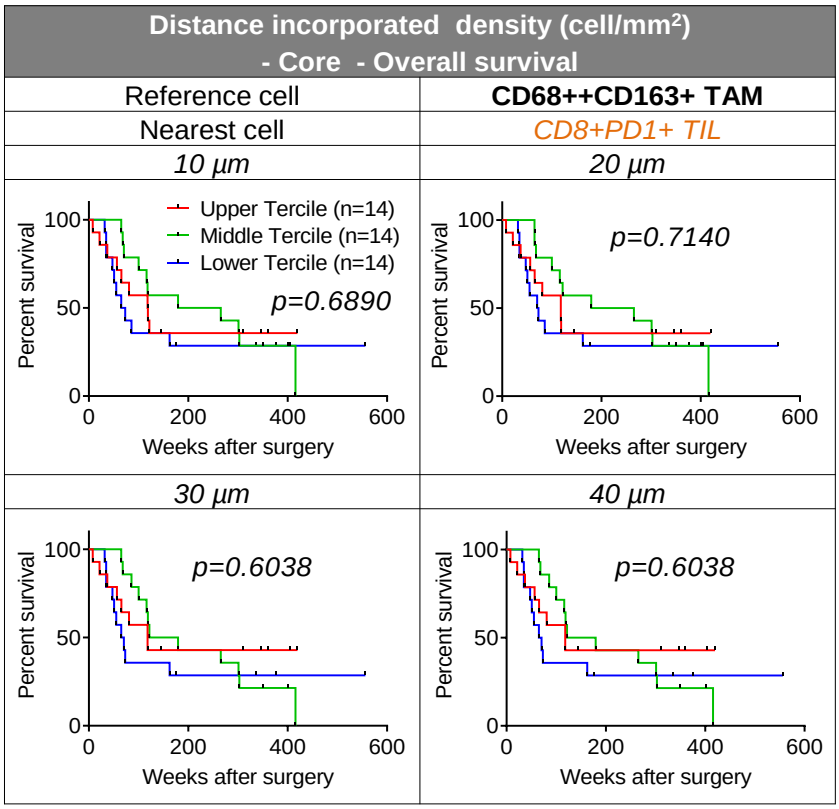


Figure 7.3.18 Overall survival based on TAM/TIL (RC/NC) pairing proximity

CD68++CD163+ TAMs were used as reference cell (RC) and the CD8+PD1+ TILs were used as nearest cell (NC).Patients were stratified based on the number of TAM/TIL pairs in different distance ranges into three groups and overall survival was plotted. Upper tercile (density > 2/3 of the patients in the cohort; red line), Middle tercile (1/3 < density < 2/3 of patients in the cohort;

green line). Lower tercile (density ≤ 1/3 of patients in the cohort; blue line). Log-rank (Mantel-Cox) test.

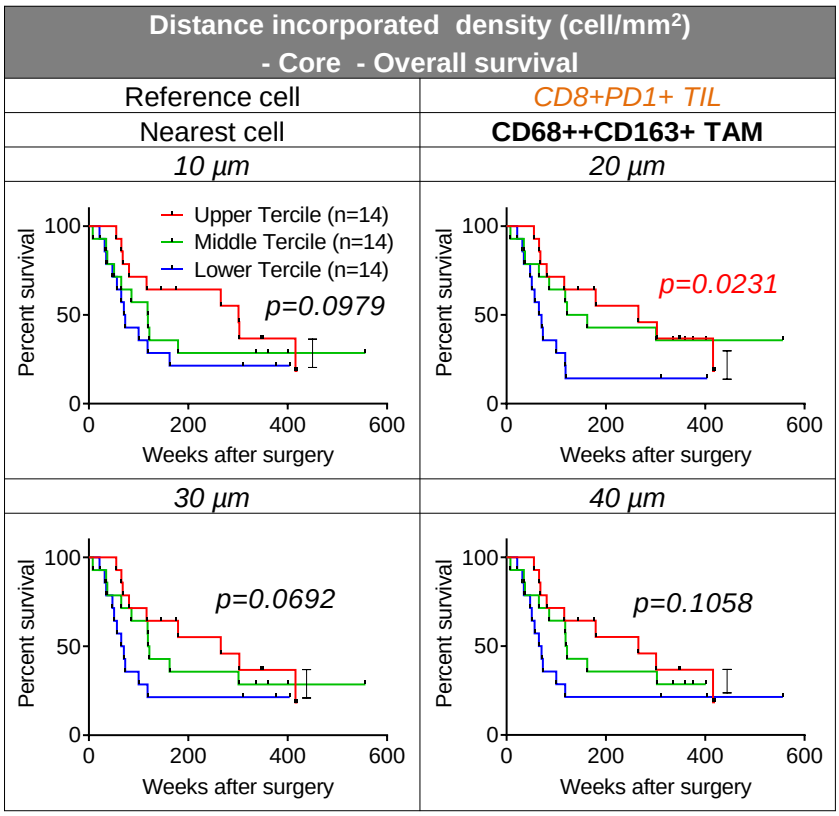


Figure 7.3.19 Overall survival based on TAM/TIL (NC/RC) pairing proximity

CD8+PD1+ TILs were used as reference cell (RC) and the CD68++CD163+ TAMs were used as nearest cell (NC). Patients were stratified based on the number of TAM/TIL pairs within a given range (um) were determined and overall survival was plotted. Upper tercile (density > 2/3 of the patients in the cohort; red line), Middle tercile (1/3 < density < 2/3 of patients in the cohort; green line). Lower tercile (density ≤ 1/3 of patients in the cohort; blue line). Log-rank (Mantel-Cox) test.

These results indicate that, whilst the co-localisation of TAMs and TILs may suggest possible interactions between the immune systems, their relative distance or infiltration depth to tumour cells may better describe the enhanced immunological processes in the tumour, as indicated with “effective density” (§4.3.3, Figure 4.3.7 and Figure 7.3.14). The proximity of immune cells alone did not fully account for their spatial distributions in a tumour-orientated setting (Figure 7.3.20A). Therefore, these data indicate that the relative distance of these TAM/TIL pairs to the tumour cells will need to be determined to assess their possible impact on the tumour population (Figure 7.3.20B).

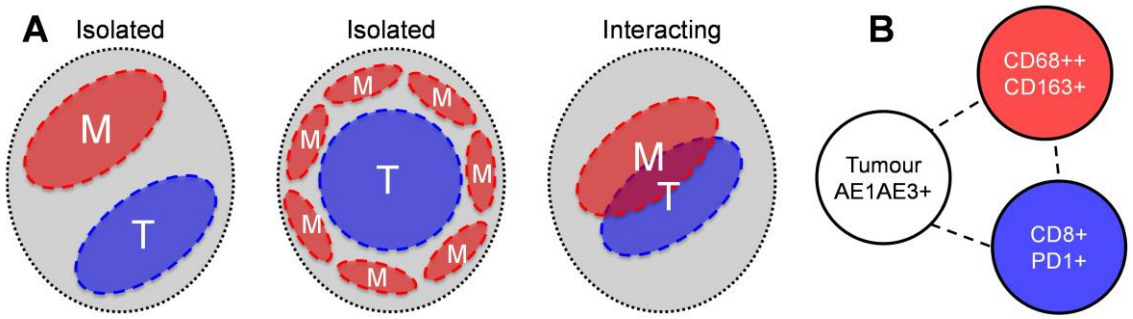


Figure 7.3.20 Possible cell distribution patterns in the shared microenvironment

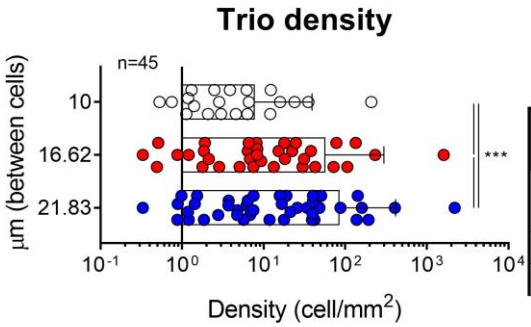
M and T: macrophage and T cell. (A) Different distribution patterns between cells types; Cells may be interacting (right) or isolated from each other and with their distribution patterns being irrelevant (left) or relevant (middle) to tumour regions (e.g. Core, Edge, Margin; defined in Figure 3.1.1) (B) Identification of the Immune/Tumour trios in proximity with each other.

7.3.9 Survival relevance of the Immune/Tumour Trio density

Thus far, positive associations were observed in patient overall survival with individual and combined immune cell overall density (Figure 7.3.13, Figure 7.3.15 and Figure 7.3.16) and with effective density (0-10µm) which reflect the quantity and proximity of immune cells to tumour cells (Figure 7.3.14). No associations were found with the number of TAM/TIL pairs within the microenvironment (Figure 7.3.18 and Figure 7.3.19), suggesting that the location of these immune cell pairs to tumour cells, referred as the Immune/Tumour trio (Figure 7.3.20B), could be crucial. This parameter combines both the cell density and spatial location information in order to determine their overall effect on patient survival.

The Immune/Tumour trio which is comprised of an AE1AE3+ tumour cell, a CD68++CD163+ TAM and a CD8+PD1+ TIL (Figure 7.3.20B) was identified in each patient (Figure 7.3.21). Three different distance thresholds between individual cells were used to define the trios: (i) 10µm was defined as direct contact (based on Figure 3.3.15), (ii) the median distance of CD68++CD163+ TAMs (16.62µm; identified in Figure 7.3.6C) to tumour cells (referred as Median TAM) and, (iii) the median distance of CD8+PD1+ TILs (21.83µm; identified in Figure 7.3.6C) to tumour cells (referred as Median TIL).

The results revealed a large patient-to-patient variation in the number of the Immune/Tumour trio (Figure 7.3.21). Due to the low likelihood of the co-localisation of all three cell types, the average trio density with different distance thresholds was below 100 trios per mm^2, suggesting that, even when different cell types showed significant high correlations in the same tumour (Figure 6.3.10), not all of them might be co-localised within a short distance that may be biologically relevant (Figure 7.3.21). However, a small number of patients exhibited up to 1000 trios within their tumour specimen, showing a very strong immune infiltration into the tumour-nest and suggesting possible interactions between the different cell types (Figure 7.3.21).



Trio density	Direct contact	Median (TAM)	Median (TIL)
µm between cells	10	16.62	21.83
Median	0.00	6.53	7.50
Mean	7.80	56.91	85.44

Figure 7.3.21 Immune/Tumour trio densities with different distance thresholds between cells

Median (TAM): median distance of the CD68++CD163+ TAMs (red) to tumour cells (white). Median (TIL): median distance of the CD8+PD1+ TILs (blue) to tumour cells. Triangles above the Table correspond to the Immune/Tumour trios as defined in Figure 7.3.20B of different distance criteria. Both distance were identified in Figure 7.3.6D. ***p<0.001 comparing between distance criteria. Wilcoxon matched-pairs test.

The number of trios was divided by the overall density of each of the tumour cell, TAM and TIL, respectively, to control for the differences in cell number between populations (Figure 7.3.22A). The trio percentage of each cell type, defined as the proportion of cells that was interacting with the other cell populations, was compared (Figure 7.3.22B-D). The tumour cells, which dominated the tumour Core in number (Figure 7.3.22A), had approximately 0.01% tumour cells (on average) engaged directly with the CD68++CD163+ TAMs and CD8+PD1+ TILs (Figure 7.3.22B). About 3% and 5% of the CD68++CD163+ TAMs and CD8+PD1+ TILs directly engaged within the trios, respectively (Figure 7.3.22B). The percentage in each of the cell types included in the trio increased as the distance threshold increased such that both the percentage of TAMs and TILs increased approximately 10-fold when the distance increased from 10µm to 21.83µm (2.99% to 31.90% and 5.21% to 51.18%, respectively; Figure 7.3.22B-D). Lastly, while enhanced immune infiltration depth was previously observed in patients with EBV/MSI cancer subtypes (Figure 6.3.11), no differences were found in trio densities or percentages between different GC subtypes (Appendix 11), suggesting some patients with GC/Others GC subtypes also had similar Immune/Tumour trios in their tumours compared with the EBV/MSI patients.

Collectively, these data suggest that only a small proportion of cells within the tumour microenvironment were within direct contact distance with each other and that there were less TAMs (31.90%) engaged within the trios compared to the TILs (51.18%; Figure 7.3.22D) when the same distance criterion was applied.

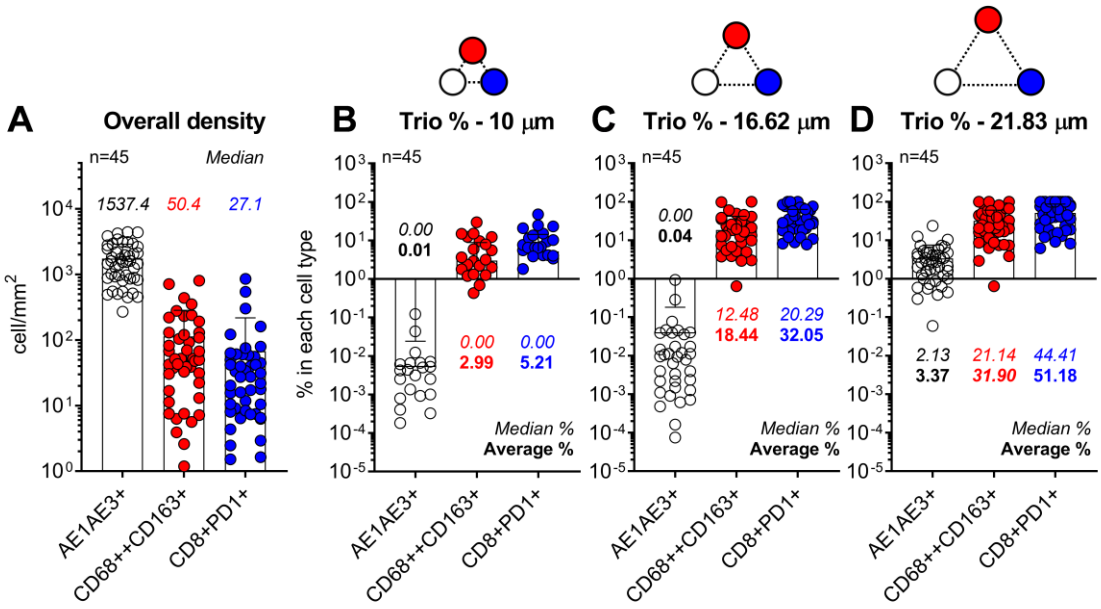


Figure 7.3.22 Immune/Tumour trio percentage in each cell type

(A) Overall density of the cell populations labelled. (B-D) Trio percentage in each cell populations of different trio distance criteria. Triangles above the panel B to D correspond to the Immune/Tumour trios as defined in Figure 7.3.20B of different distance criteria.

To investigate if the difference in percentage of cells engaged in the Trio was due to the difference in overall density between the TAMs and TILs (Figure 7.3.22A) or may also be related to their proximity to tumour cells (Figure 7.3.6), overall cell densities of TAMs and TILs were correlated with their trio percentage in each cell type (Figure 7.3.23).

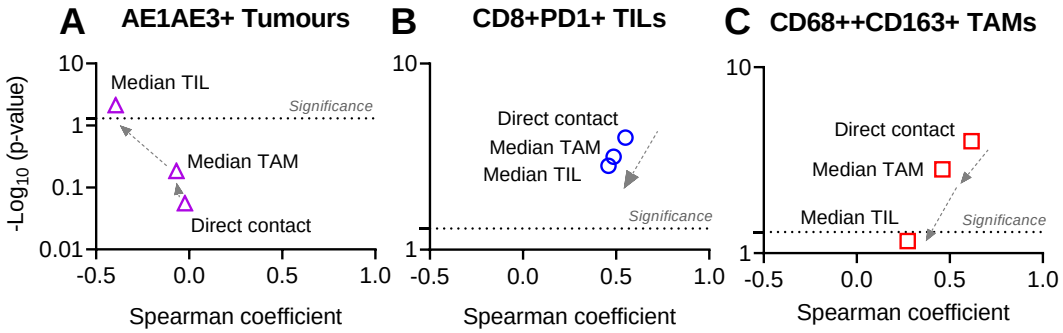


Figure 7.3.23 Correlations of trio density with percentage in each cell type

Trio density and percentage of (A) tumour cells, (B) CD8+PD1+ TILs and (C) CD68++CD163+ TAMs in each cell type that were engaged in a trio with other cells were compared using the Spearman correlation. Arrows show increase in distance threshold from direct contact (10µm) to Median TAM (16.62 µm) and then to Median TIL (21.83 µm). Above dashed line: $p<0.05$.

The results showed that in tumour cells (Figure 7.3.23A), negative correlations were found between trio percentage and cell density and the significance of correlation increased as the distance threshold increased from using direct contact (10µm) to using Median TIL (21.83µm). This observation was because there were more tumour cells than TAMs and TILs (Figure 7.3.22A) in the tumour Core and that as the distance from the tumour cell increases, more Immune/Tumour trios can be identified (Figure 7.3.23A), suggesting a random distribution pattern of the tumour cell (Figure 3.3.14).

The positive correlation between the percentage of trio and cell density was observed for the CD8+PD1+ TILs despite the slight decrease in significance as the distance threshold increase (Figure 7.3.23B). This result indicates that the CD8+PD1+ population was more randomly distributed (defined in Figure 3.3.14),

which supports previous results showing that they had no locational preference within the microenvironment (Figure 7.3.6F).

Interestingly, the trio percentage and cell density of CD68++CD163+ TAMs were found to be positively correlated within a short distance but not when the distance increased beyond the median distance of TAMs to tumour cells (Median TAM; Figure 7.3.23C). This result reflected the previous observations that the distribution of CD68++CD163+ TAMs reside predominantly in the tumour-nest (Figure 6.3.8), therefore increasing the distance surrounding these TAMs beyond a certain threshold would not increase the possibility of identifying Immune/Tumour trios.

Collectively, these data suggest that the number and percentage of the Immune/Tumour trio were related to both cell densities and the distribution of each cell type. These data also confirmed previous findings regarding the heterogeneous distribution of the CD68++CD163+ TAMs in the tumour (Figure 4.3.1, Figure 4.3.2 and Figure 6.3.9), and suggest that to homogenise these TAMs in the microenvironment or to create an environment favourable for the repolarisation of these TAMs might be possible future therapeutic approaches, if indeed these cells were truly antigen-presenting and immune-promoting (Figure 6.3.18).

Finally, to assess the predicted survival benefit of the Immune/Tumour trio which takes into account both cell density and spatial location of multiple cell components, patients were stratified by the trio densities of different distance thresholds (Figure 7.3.24). The results showed that the increase of all trio densities with different distance criteria correlated with improved survival. Importantly, although the number of trios was very few when counting the ones that were in direct contact (Figure 7.3.21), this method characterises the patients into Yes (with) or No (without) any trios presented in the sample. An on-and-off criterion like this may be more applicable clinically, compared to using continuous variables (density or percentage) which often vary between patient cohorts. This result suggests that if a patient had any tumour cell, CD68++CD163+ TAM, CD8+PD1+ TIL trios in direct contact within their tumour Core, the patient will possibly have a longer lifespan, which could be due to the high immune cell number, enhanced infiltration depth, and more active immune system.

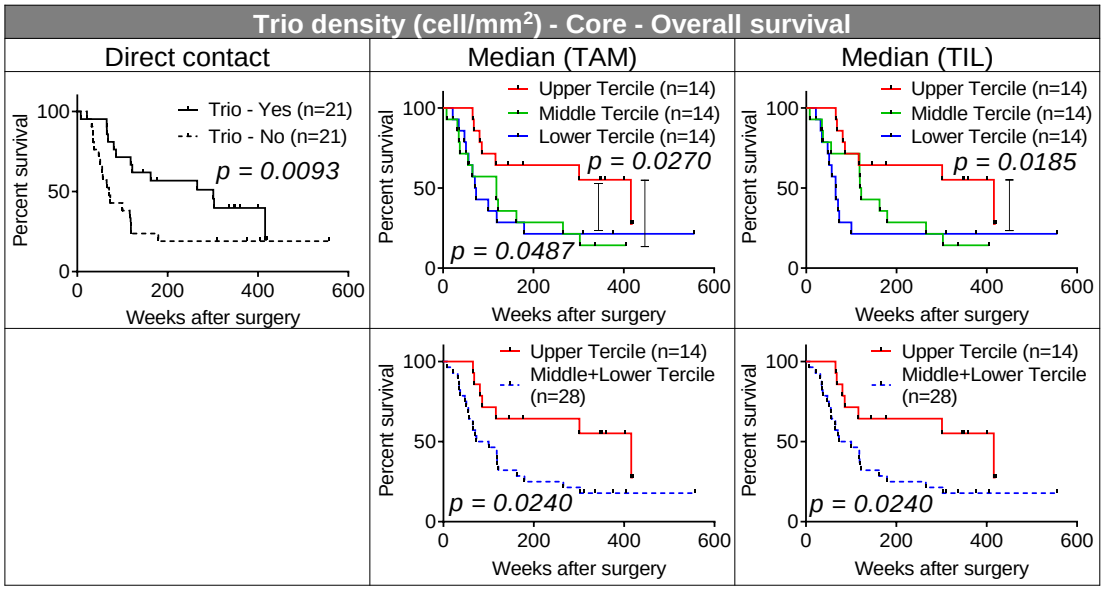


Figure 7.3.24 Overall survival based on Immune/Tumour trio density

Patients were stratified into different groups using the number of trios with different distance criteria and overall survival was plotted. Yes (with) or No (without) any trio present in the sample. Upper tercile (density > 2/3 of the patients in the cohort; red line), Middle tercile (1/3 < density < 2/3 of patients in the cohort; green line). Lower tercile (density ≤ 1/3 of patients in the cohort; blue line). Log-rank (Mantel-Cox) test.

7.4 Discussion and Conclusions

7.4.1 NOX2 as a possible functional marker for CD68++CD163+ TAMs

In this Chapter, approaches were taken to investigate possible mechanism(s) behind the survival advantage observed in the patients with elevated CD68++CD163+ TAM density. Gene signatures of CD68++CD163+ and CD68+IRF8+ TAMs were compared given their positive density correlation within the same tumour, but difference in survival prognosis. This comparison revealed a NADPH oxidase-relate gene (NOX2) that was enriched in the tumours with abundant CD68++CD163+ TAMs and also CD3+CD8+ TILs. In macrophages, presence of NOX2 has been shown to suppress autocrine IL-10 post LPS induction to sustain a pro-inflammatory phenotype[555] (Figure 7.4.1). In the absence of NOX2, macrophages can self-polarise with IL-10 into an anti-inflammatory phenotype[555]. Importantly, NOX2 has been reported to be involved in antigen presentation of dendritic cells[548-550] by preventing the acidification and proteolysis of proteins in phagosomes. Collectively, evidence suggest that NOX2 may play an critical role in regulating macrophage polarisation; however its role in antigen presentation by different macrophage subtypes has not been well described.

In view of the literature, and given previous observations that the CD68++CD163+ TAMs were associated with active immune and possible antigen-presenting signalling at a whole-tumour level (Figure 6.3.18), further investigation were conducted to determine if NOX2 was expressed by the CD68++CD163+ TAMs in our cohort which may help explain their association with enhanced tumour inflammation (Figure 5.3.13C) and putative antigen-presenting ability (Figure 6.3.18). A multiplex NOX2 panel, including TAM/TIL markers with NOX2/PD1 was designed, optimised, validated and characterised in detail, including cellular density, distribution and survival.

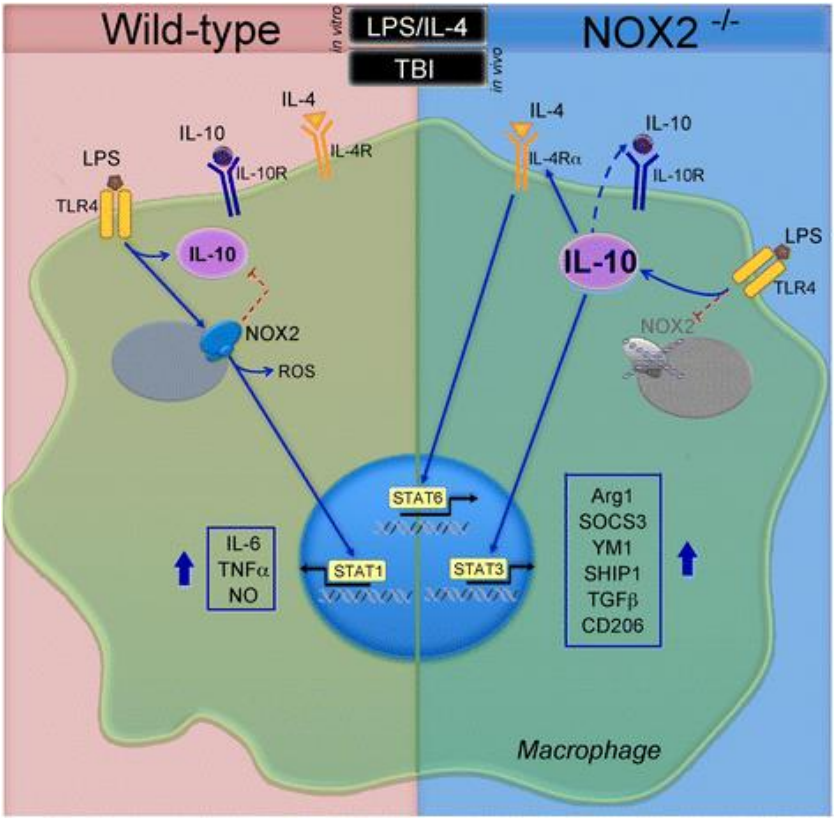


Figure 7.4.1 Schematic role of NOX2 in macrophage polarisation

Image[555] from Barrett *et .al., Journal of Neuroinflammation,* 2017.

7.4.2 NOX2+ TAMs co-localise with PD1+ TILs

High NOX2-expression on the CD68++CD163+ TAMs was confirmed visually with images and quantified at the cell population and single-cell level. NOX2-High CD68++CD163+ TAMs and CD8+PD1+ TILs were found to significantly co-exist within the same tumour microenvironment. By comparing the intensity of these functional markers in different distance intervals, the data infer that (i) the upregulation of PD1 on TILs may be direct contact dependent whilst (ii) the enhancement of NOX2 on TAMs could be more paracrine-related. This may reflect (i) the direct contact dependent activation of TILs by the TAMs and (ii) the upregulation of NOX2 by possible IFN-γ[556, 557] release from the activated TILs within the same environment, respectively.

When in direct contact, the median intensity of both NOX2 and PD1 functional markers significantly increased by approximately 20%-30% on the corresponding reference cells (RCs), up to 70% of PD1 on the nearest TILs, but only by 5% on the nearest TAMs, compared to when the TAMs and TILs were 50-60µm apart.

These results may be due to the fact that when a TAM/TIL pair was identified, other TAM or TIL may exist in the surrounding area which may also be influencing the NOX2 or PD1 expression on cells (Figure 7.4.2A and B). As a limitation of the multiplex IHC method and bioinformatic spatial analysis, the exact cell-to-cell influence is difficult to analyse. However, data from this study suggest that a TAM (as RC) may be sufficient to induce the PD1 expression on multiple surrounding TILs (as nearest cells, NCs; Figure 7.4.2C), given their elevated overall expression within a tissue (Figure 7.3.12B). Whilst a TIL (as RC) may not be as potent as the TAMs in influencing the NOX2 expression on nearby TAMs (as NCs; Figure 7.4.2D): even though the NOX2 on the reference TAM was induced (Figure 7.3.12B), the overall NOX2 signal may have been diluted by the surrounding NOX2-negative TAMs (Figure 7.3.12D).

Moreover, previous data in this study showed that (i) CD68++CD163+ TAMs were found more commonly within the tumour-nest than in the stroma (Figure 6.3.9) but was not observed for the CD8+ TILs (Figure 6.3.9 and Figure 7.3.8E); (ii) PD1 expression on CD8+ TILs was found to be increased in the tumour-nest (Figure 7.3.7) but the distribution pattern of TILs was not related to their proximity to tumour cells (Figure 7.3.6F). These data suggest that the marker expression of the TAM/TIL pairs discovered in the stroma may be different to those in the tumour-nest (Figure 7.4.2). Collectively, these findings indicate that the number of surrounding cells and the location in which these interactions take place could be important factors.

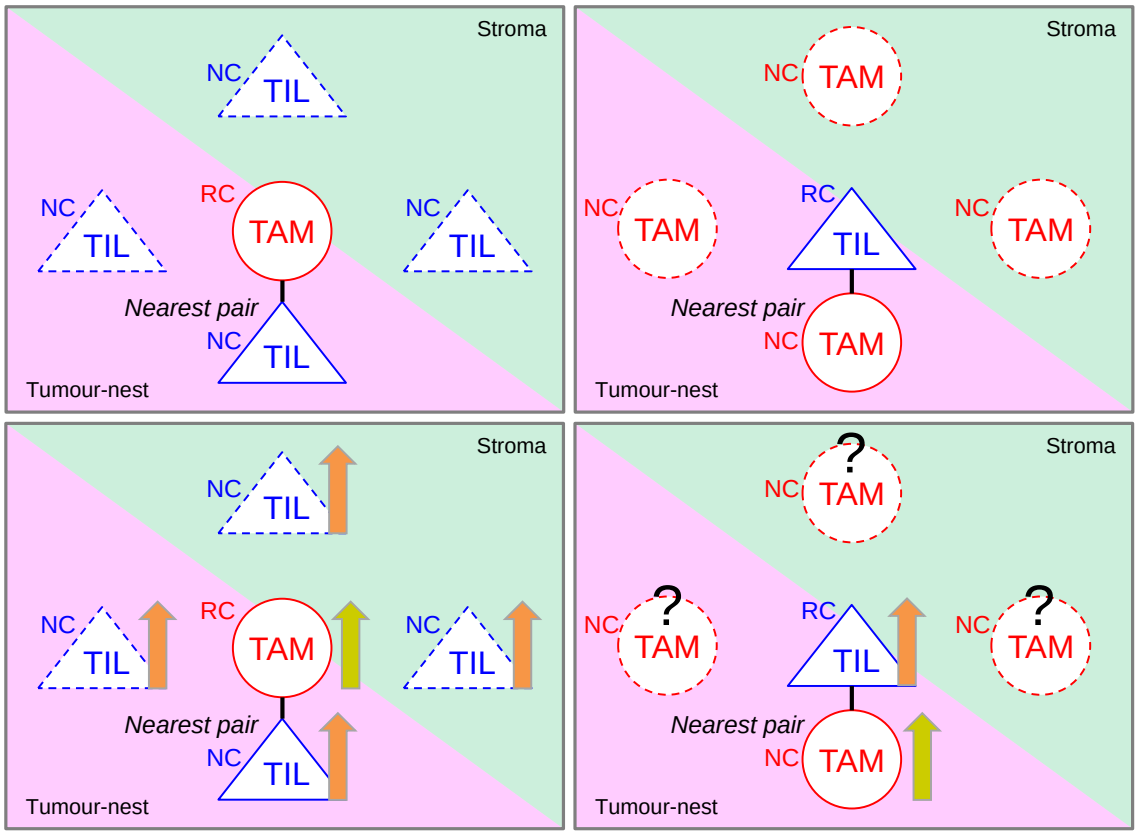


Figure 7.4.2 Schematic model of NOX2/PD1 expression on TAMs and TILs in proximity to each other

When a nearest TAM/TIL pair was identified, other TAM or TIL may exist in the surrounding area which may also be influencing the NOX2 or PD1 expressions on cells. In Figure 7.3.12, PD1 was found to be elevated on CD8+ TILs (as both RC and NC) when in close proximity with CD68++CD163+ TAMs. Similarly, increased NOX2 was observed on TAMs when used as RCs but not NCs. These data suggest that a TAM may be sufficient to induce the PD1 expressions on multiple surrounding TILs, whilst a TIL may not be as potent as the TAMs in influencing the NOX2 expressions on nearby TAMs. RC/NC: reference/nearest cell. Black line: nearest RC/NC pair. Dashed circle/triangle: other possible surrounding cells. Orange/Yellow arrows: PD1/NOX2 expression. Pink/Green: tumour-nest and stromal areas.

7.4.3 NOX2 and PD1 status on TAMs and TILs improves their survival prediction

Survival analysis showed that including PD1 as a measure of the functional status of the CD8+ TILs significantly improved their survival predictive value with the PD1+ TIL population being positively associated with improved overall survival (Figure 7.3.13). NOX2 expression on TAMs did not show additive value

as a positive selection criterion to the patient groupings given that the CD68++CD163+ TAMs had concurrently higher NOX2 expression (Figure 7.3.15). However, in combination with the TIL density, NOX2-refined TAMs may be useful as a negative selection marker to identify the patient with low immune infiltration and less activation, which in turn may relate to a very poor survival outcome (Figure 7.3.17).

7.4.4 Proximity of immune cells to tumour cells outweighs the proximity between immune cells for survival analysis

No survival advantage to patients was observed when their CD68++CD163+ TAMs and CD8+PA1+ TILs were in close proximity with each other. However, there was a survival benefit when these two immune cell types were in close proximity with the tumour cells, both individually and as Trios. These results suggest that while the possible interactions of immune cell populations could be important in altering their immune phenotypes and may be related to their functional status (discussed in §7.4.2), the ability to have a direct effect on the tumour cell, as inferred by proximity in this study, had a more profound association with patient survival.

Importantly, the results from Trio density and percentage showed that, on average, only 3-5% of the TAMs and TILs in each cell population were in direct contact with each other and with the tumour cells. This result revealed that, while the CD68++CD163+ TAMs and the CD8+ TILs strongly correlated within the tumour-nest and stroma and were the pair with the highest correlation compared to all other immune cells (Figure 6.3.10), only very small proportions were within contact distance with the tumour cells. These results indicate that to investigate the interaction of cells, the actual spatial co-localisation of the cells of interest should be identified in addition to just using correlation tests which may be misleading and does not take account the region of the tumour where the cells reside.

In the previous Chapter, immune cell infiltration was found to be higher in patients with EBV/MSI GC subtypes compared to those with GS/Others subtypes, and was independent of the densities of individual cell populations

(Figure 6.3.11). However, univariate analysis of immune cell density, distribution and cell marker expression with clinical parameters often showed no significant correlations with GC subtype and with other clinical parameters (e.g. age, cancer stages)[468]. This was also true when comparing the NOX2 and PD1 status on the TAMs and TILs, respectively. These results indicate that, while in general the EBV/MSI patients exhibited a stronger immune response[31] and were associated with high overall PDL1 expression in our cohort (§4.3.8 and §0), some patients in the GC/Others category also possessed an enhanced immunity (Figure 4.3.13, Figure 6.3.12 and Figure 7.3.9B), and these patients may have a chance to benefit from checkpoint blockade. These observations may explain why GC subtypes and PD1/PDL1 staining were imprecise markers for GC survival[133, 558] and response to therapy[126]. However, one of the limitations is that these experiments were done as univariate analyses that are difficult to test in a multivariate model.

7.4.5 Limitations

The data presented in this Chapter clearly showed the possible interactions between the TAMs/TILs that may be working through the NOX2/PD1-related mechanism. However, without appropriate knockout models and functional assays it is difficult to make conclusions on the cause and effect between these markers and between the immune cell types using only multiplex IHC. The current data could not fully test the hypothesis that the survival advantage observed for the patients with elevated CD68++CD163+ TAMs was due a NOX2-associated enhancement of antigen-presentation of TAMs to CD3+CD8+ T cells, whose functional status could be defined with their PD1 expressions. Further studies are needed to investigate different aspects of this hypothesis.

7.4.5.1 Identifying the functionality of NOX2-expressing TAMs

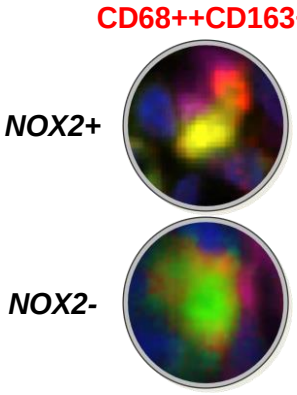
While no functional assays have been performed to assess the role of NOX2 in this TAM population, some clues may be found from the nature of the markers expressed by the TAMs and the gene signatures of cases where these TAMs were enriched.

Firstly, NOX2 has been shown to be highly expressed by macrophages, but also by dendritic cells (DCs) to a lesser extent[559]. As a result, macrophages were found to produce more reactive oxygen species (ROS) than other cell types[550]. In addition, macrophages have been shown to have a higher expression of vacuolar proton adenosine triphosphatase ($V\text{-}H^+$-ATPase), a universal proton pump[560], compared to DCs, which results in a more acidic phagosome/endosome/ lysosome environment in macrophages (pH 5.7) than in DCs (pH 7.7)[559]. Due to the difference in pH, macrophages were identified as having more rapid and proficient antigen degradation[561] through active lysosomal proteases[562] at this pH. The DCs, on the other hand, have been shown to specialise in limiting protease abundance[563] and activity[550], and regulating the transport and modification of MHC molecules[564]; therefore, were more advanced in immune initiation with antigen presentation. Macrophages with a *NCF1* mutation (a critical subunit of the NADPH oxidase complex, Figure 7.3.3) have been shown to engage in the priming of T cells in the absence of ROS, but were T cell suppressive in the presence of ROS *in vitro*[565]. ROS has been reported to modulate the macrophage immunosuppressive phenotype through the upregulation of PDL1[566] and to promote tumour initiation and growth; however, these effects may differ between tumour models[567]. More importantly, due to the complexity and plasticity of TAMs within the microenvironment, tumour-isolated TAMs have been shown to express high levels of antigen-presentation molecules[346] and be efficient for priming cytotoxic T cell for specific tumour killing *in vitro*[468].

Secondly, the influence of CD68++CD163+ TAM population may be related to their expression of CD163. During inflammation and activation by LPS[568], oxidative stress[569], and TLR signalling[570], the soluble truncated peptide of CD163 (sCD163)[571] was found to be cleaved from the macrophage membrane by the metalloprotease, ADAM metallopeptidase domain 17 (ADAM17)[572, 573]. sCD163 has been shown to suppress lymphocyte proliferation[574-576] post antigen exposure and was proposed as a blood biomarker in multiple inflammatory and infectious diseases[577-581]. However, the way in which this information fits with the specific CD68++CD163+ macrophage population identified in the cancer tissue requires further investigation.

Thirdly, IL-10, a cytokine associated with the CD68++CD163+ TAM environmental gene signature in this study, has traditionally been considered as being immune suppressive[582]. However, paradoxically, increasing evidence in the literature is demonstrating its supportive effect on CD8+ T cell dependent anti-tumour activities[583, 584]. Administration of IL-10 has been reported to prevent CD8+ T cells apoptosis through a dendritic cell-mediated process[583] and to promote intra-tumoural T cell activation and enhance its proliferation[585, 586]. It has also been shown that IL-10-induced macrophages have an elevated phagocytic activity[315] and some antigen presenting M2 macrophages also express MHC molecules[183]. IL-10-polarised macrophages exhibited a medium ROS production compared to IFN-γ and IL-4-polarised ones[459] (highest and lowest, respectively).

Collectively, to understand the true functions of the CD68++CD163+ TAMs, it is crucial to determine if those TAMs with high NOX2 expression were more pro-inflammatory[555, 587], showed higher expression of MHC molecules[588, 589], and associated with enhanced or delayed production of ROS and antigen degradation ability (related to upregulated CD68 expression[437]; Figure 7.4.3).



Phenotype	Putative functions (?)
High NOX2	Pro-inflammatory
	Antigen presentation
	Antigen degradation
	ROS production
High CD68	Enhance phagocytosis
	Delayed degradation

Figure 7.4.3 Putative functions of the CD68++CD163+ TAM

Additional markers are required to be included in the same multiplex IHC panel and *in vitro* experiments will need to be conducted to further access the pro- or anti-immune properties[389, 429, 549] of the CD68++CD163+ TAMs. Red: CD163. Green: CD68. Yellow: NOX2. Blue: DAPI.

7.4.5.2 Identifying the functionality of the PD1-positive TILs

While PD1 has been shown to be upregulated on activated T cells post antigen stimulation[590], high PD1 expression also identifies exhausted, dysfunctional

TILs in cancer[546]. These exhausted TILs could be further characterised with T-cell immunoglobulin and mucin-domain containing-3 (TIM-3) and lymphocyte-activation gene 3 (LAG-3)[591], and with the reduction of IFN-γ production[546]. Therefore, exhaustion and functional cytokine markers are needed to elucidate the functions of the different PD1-expressing CD8+ TILs identified in this study (Figure 7.4.4). T cell factor 1 (TCF1/*tcf7*) and CD39/CD103 could be used to help interpret activation status. These markers identify the stem-like CD8+ TIL populations with proliferative property post immune checkpoint administration[589, 592, 593] and as tumour-antigen-experienced/exhausted populations[594-597], respectively. Observations from this study suggest that the PD1 expression on CD8+ TILs was independent of their distance to tumour cells (Figure 7.3.6F), and inclusion of these markers could possibly reveal the locational differences of these different PD1-expressing TILs.

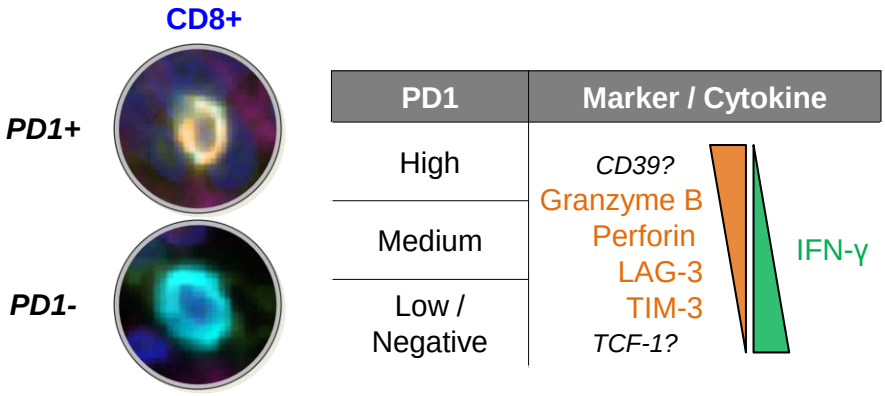


Figure 7.4.4 Marker and cytokine profile of CD8+ TILs with different PD1 positivity

PD1 (orange) positivity on CD8+ (cyan) TILs has been shown to correlate with their activation, but also exhaustion in cancer. Further functional markers will need to be incorporated within the same multiplex IHC panel to investigate if these TILs were immune active or exhausted. Data[545, 546, 594] from Kansy *et al., Cancer Researc*h, 2017, Thommen *et al., Nature Medicine,* 2018, and Chen and Ji *et al., Immunity,* 2019.

7.4.5.3 Impact on the tumour microenvironment

The CD68++CD163+ TAMs correlated with increased tumour hypoxia and decreased angiogenesis[598] from gene-expression analyses in this study (Figure 5.3.13D); therefore staining of HIF1α and CD31 (endothelial cell marker[201]) may

be incorporated to the multiplex IHC panel to validate these findings and confirm their identities when more colours were available with the technology.

Moreover, additional response markers (e.g., cell death markers) on the tumour cells that were grouped as a trio with the immune cells will be useful to determine the actual function of the immune cells. As mentioned earlier, it is difficult to make conclusions about the cause and effect of these cells in the TME. Alternative explanations for the current results include:

1) A NOX2-expressing TAM is immune-promoting and is sufficient to induce the PD1 expression and activation of surrounding TILs (Figure 7.4.2)
2) The cytokines derived from the activated PD1-expressing TILs are responsible for inducing NOX2 expression on the TAMs (opposite to 1)
3) TAMs are an immune suppressive subtype that are recruited to suppress the actives TILs and to induce T cell exhaustion
4) These cells were not functionally related; rather the TAMs were located in the same regions as the TILs coincidentally to mop up debris associated with active killing

7.5 Summary

In summary, the work described in this Chapter showed that NOX2 was first identified through gene expression analysis and an mIHC panel was designed to contain markers to characterise immune cells as well as functional markers, NOX2 and PD1. NOX2 was shown to be highly expressed by the CD68++CD163+ TAMs to confirm the findings from a gene-expression level at a protein level. The expression of the NOX2 and PD1 increased as the TAMs and TILs come in direct contact, suggesting a possible mechanistic relationship between these cells. Inclusion of functional markers on cells, and density combined spatial distribution of the immune cells to tumour cells all increased the prognostic value compared to using just overall cell density alone.

Additional *in vitro* experiments or more cell type-specific mIHC panels are needed to resolve the true function of these TAMs and TILs and their impact on patient survival.

Chapter 8 : Investigating the Influence of macrophages on tumour invasion in a mouse model

8.1 Introduction

The data from Chapter 4 and 5 showed that (i) the CD206+ group of TAMs was associated with high PDL1 expression (Figure 4.3.12), (ii) the CD68+CD206+ TAMs were located in close proximity to tumour cells (Figure 4.3.5) and were associated with immune suppressive gene signatures (Figure 5.3.4) and (iii) the CD68+CD206++ and CD68+CD163+CD206+ TAMs were abundant in normal stomach tissue, especially at the tumour Margin (Figure 4.3.1). These results suggest the CD206+ TAMs may have possible roles in immune suppression, tumour invasion, cell trafficking between the tumour sites and surrounding stroma, and that targeting the CD206+ macrophage population may be therapeutically beneficial.

In light of these findings, this Chapter aims to utilise an existing mouse xenotransplantation model of gastric cancer established by my laboratory[213] to examine the influence of the CD206+ macrophage subgroups on tumour invasion. The C57BL/6-Rag2<KO>γc<KO> mouse strain was chosen for being severely immunocompromised[599] (lacking T, B and NK cells), and thus suitable for studying macrophage biology. Clodronate was used as the agent for macrophage depletion[229] (as discussed in §1.3.4.1); clodronate-liposomes (Clodrosome®, Encapsula NanoSciences) and mannosylated clodronate-liposomes (m-Clodrosome®, Encapsula NanoSciences) were utilised to deplete either (i) overall macrophages[229, 600] or (ii) CD206+ macrophages[601, 602], respectively (Figure 8.1.1 and Methods).

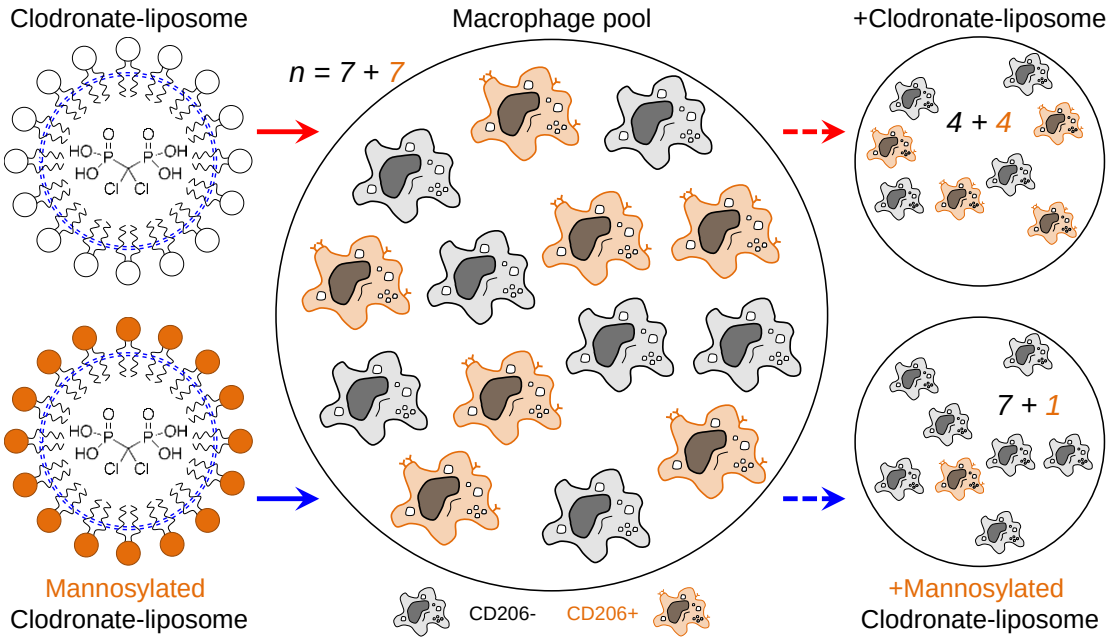


Figure 8.1.1 Schematic graph of macrophage depletion design

Clodronate-liposome (overall) / Mannosylated clodronate liposome (selective) CD206+ macrophage depletion, respectively. Mannose receptor: CD206. Numbers represent selective depletion of macrophage populations.

8.2 Aims

Aim 1: To establish and optimise a working macrophage depletion model with healthy, tumour-free mice

Aim 2: To investigate the role of macrophages in tumour invasion using an orthotopic xenograft gastric cancer model

8.3 Results

8.3.1 Optimisation of *in vivo* macrophage depletion system

The depletion efficacy and optimal protocol for each of the different clodronate-liposome constructs were first evaluated in a safety study with tumour-free, healthy C57BL/6-Rag2<KO>γc<KO> mice. Doses were determined based on published studies which have utilised these compounds[229, 600].

Mice (12 per group) were injected intraperitoneally with indicated concentrations of clodronate-liposomes (Figure 8.3.1A and Appendix 12) twice per week[603] (3-4 day cycle) for four weeks. Each mouse was bled from the sub-mandibular vein, and three mice per group were culled per week (Figure 8.3.1B). The depletion efficacies of both overall and CD206+ macrophages in different organs were determined using multiplex IHC and flow cytometry.

A

Experimental groups	Concentration (per dose)	Mice per group/week	Duration (week)	Total mice per group
1. PBS	0.1, 0.2, 0.25 and 0.5 mg / mouse	3	4	3*4 = 12
2. Control liposome				
3. Control mannosylated-liposome				
4. Clodronate-liposome				
5. Mannosylated clodronate-liposome				
Total number				12*5 = 60

B

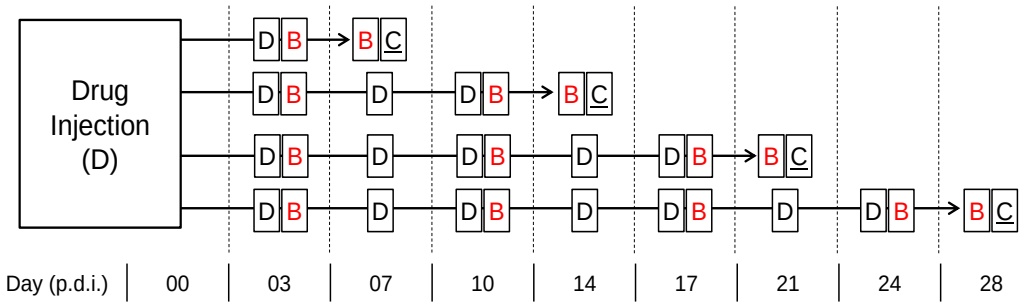


Figure 8.3.1 Design of toxicity/safety study

(A) Number of mice in each experimental group. (B) Clodronate toxicity safety timeline of an experimental group described in (A). Each line represents mice (n=3) that have undergone the same experimental procedures but were collected at different time points. Samples were collected per week for determining depletion efficacies of both overall and CD206+ macrophages in different organs. p.d.i.: post-drug injection. D: Macrophage depletion drug injection. B: Blood sample collected via sub-mandibular vein. C: Mice culled and organs harvested. Each arrow represents the timeline of independent groups with the same experimental design.

Based on previous studies in the literature, overall animal health, survival, body weight, and liver damage were used as indicators of drug toxicity in the animals[604]. Drug-related death was observed when mice were dosed with 0.25 and 0.5 mg/dose clodronate-liposome of both constructs, whilst no depletion was achieved with 0.1 mg/dose (Appendix 12A, B and C). No drug related death occurred and no weight loss of the mice was observed using the

concentration of 0.2 mg/dose biweekly (Figure 8.3.2 and Appendix 12 A). An approximately 43% depletion of blood macrophage-like populations[393, 605] (Figure 8.3.3A; defined as $CD45^{+}CD11b^{+}Ly6G^{-}LyC^{low/neg}$, presumably derived from the $CD45^{+}CD11b^{+}Ly6G^{-}LyC^{high}$ monocytes) by both clodronate-liposome constructs was maintained throughout the 4-week period (Figure 8.3.3B). No liver damage was observed (Figure 8.3.4A) compared to using the 0.5mg/dose biweekly dose (Appendix 12D). An up-to 80% depletion of liver macrophages[606, 607] (defined as F4/80+ and F4/80+CD206+; Figure 8.3.4B) was observed across the 4 weeks (Figure 8.3.4C and Figure 8.3.5). These results indicate that 0.2mg/dose of clodronate-liposome biweekly was the optimal experimental condition.

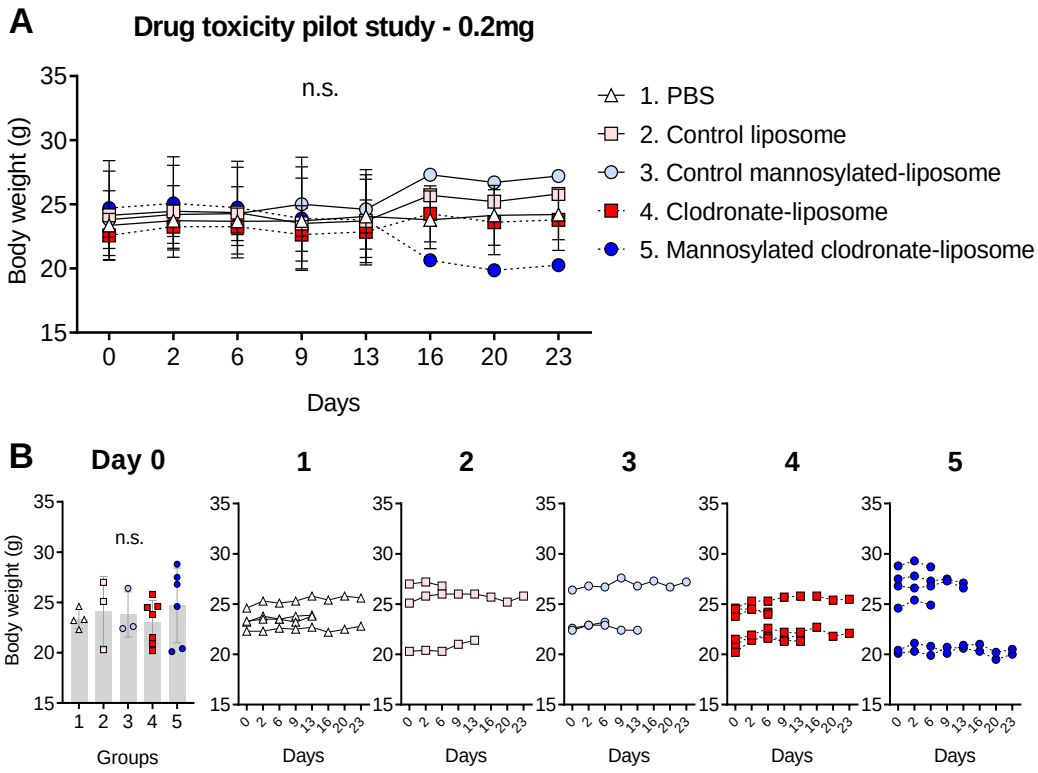
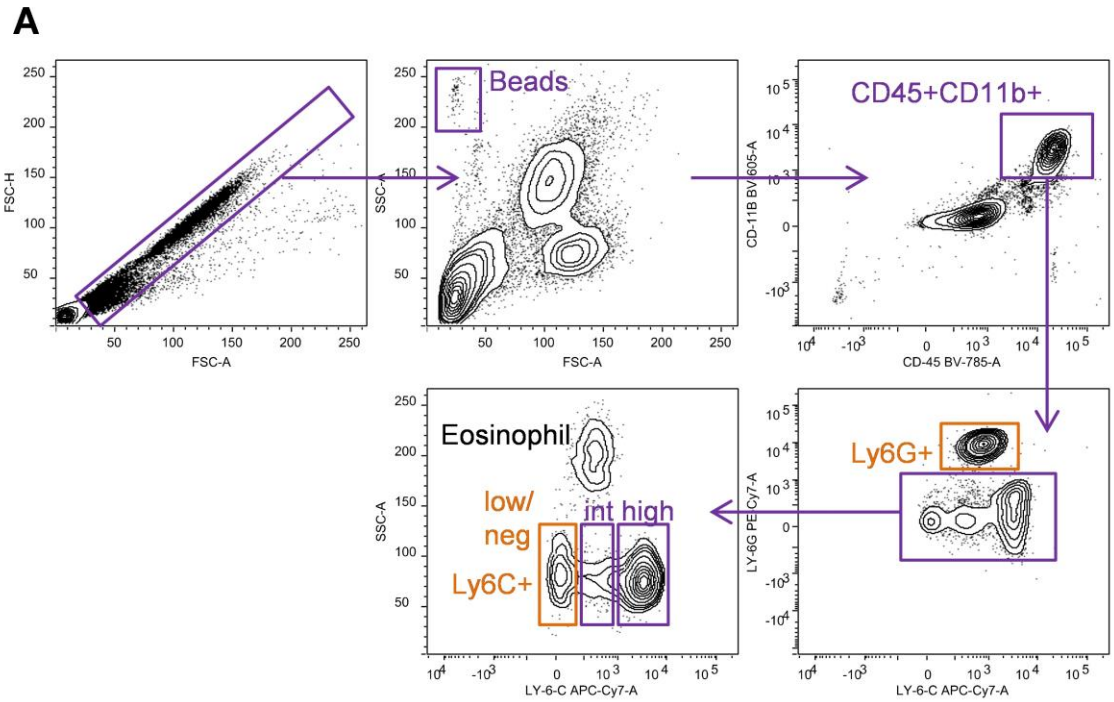
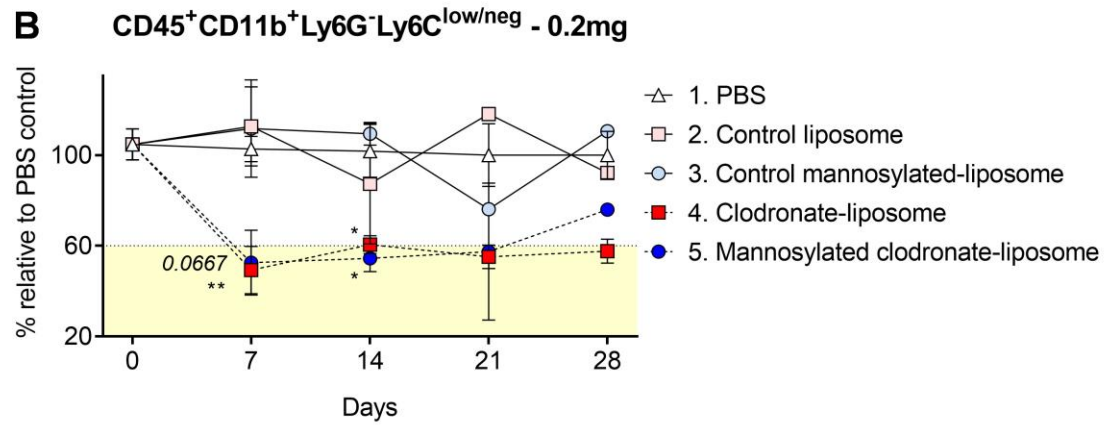


Figure 8.3.2 Mouse body weight change in safety study

Each coloured symbol represents each data collection time point of each group. (A) Each line (solid and dashed) represents each group. (B) Each line represents individual mice. Variations in weight between individual mice were observed with male mice being heavier than females. Bar and error bars represent mean ± SD. Not significant (n.s.) comparing (A) drug injected groups to PBS control and (B) between experimental groups. Mann-Whitney U test.





CD45+CD11b+Ly6G-Ly6C$^{low/neg}$ (Median % relative to PBS control)					
Concentration/dose	0.2mg				
Days	7	14	21	28	**Depletion efficacy[d]**
1. PBS	100.00	100.00	100.00	100.00	0%
2. Control liposome	106.09	87.37	118.12	92.07	0.92%
3. Control mannosylated-liposome	103.96	109.38	76.10	110.53	-6.7%
4. Clodronate-liposome	55.12	57.03	55.10	57.58	43.9%
5. Mannosylated clodronate-liposome	33.56	54.13	57.41	75.88	44.2%

Figure 8.3.3 Flow gating strategy of mouse PBMC and depletion efficacy – safety study

(A) Gating strategy used in flow analysis of macrophage-like population in PBMC. (B) Relative percentage of macrophage-like population of each experimental group normalised to PBS control. [d]: depletion efficacy determine by comparing the median % of remaining macrophage-like cells across 4 weeks to PBS control. N as defined in Figure 8.3.1. Each line represents each experimental group. Each point represents each data collecting time point. *p<0.05, and **p<0.01 comparing clodronate-liposome injected groups to PBS control. Mann-Whitney U test.

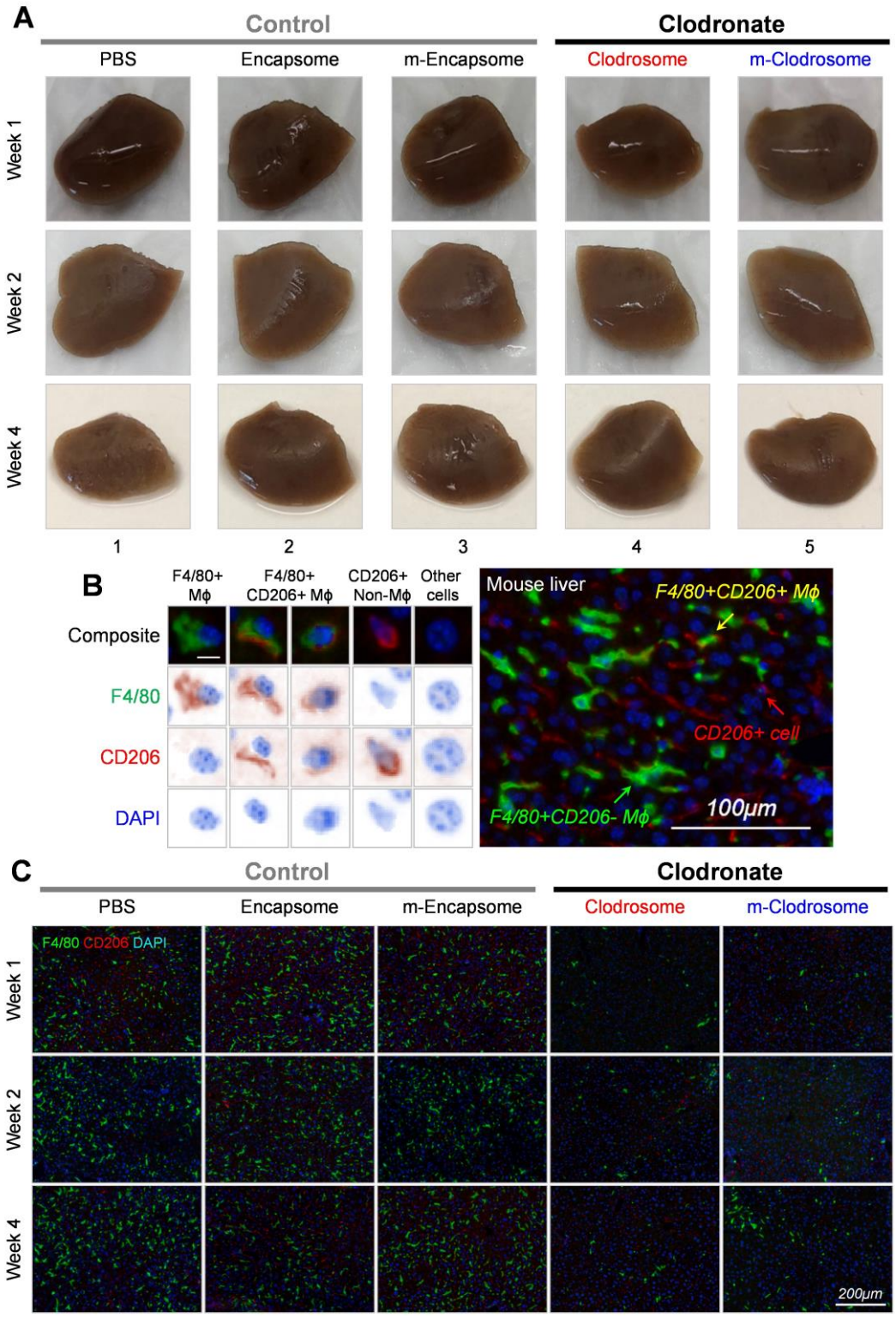


Figure 8.3.4 Mouse liver morphology and representative images of liver macrophage – safety study

(A) Appearance of representative mouse liver tissues. (B) Representative cell populations within the liver in the PBS control group of Week 1. Mϕ: macrophage. (C) Representative images of depletion efficacy in the liver of different experimental groups. Encapsome/m-Encapsome (mannosylated): control liposomes: liposomes without clodronate.

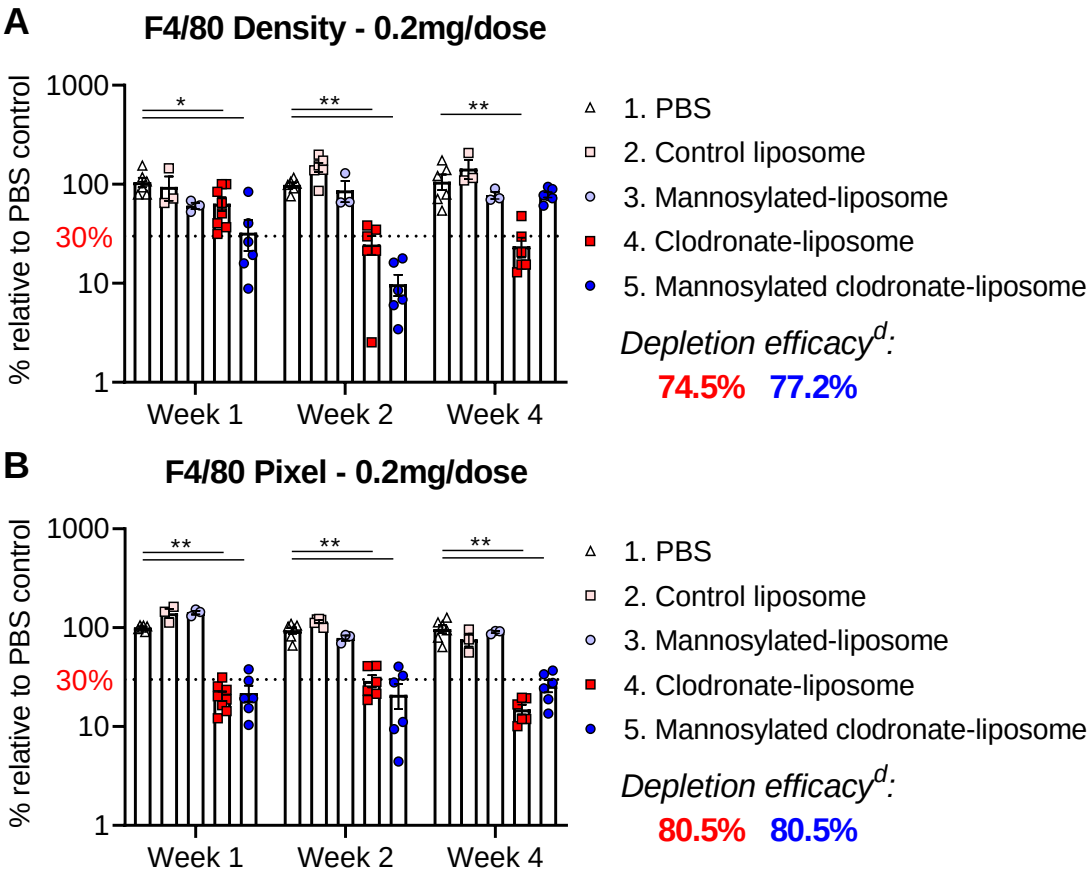


Figure 8.3.5 Quantification of mouse liver macrophage depletion efficacy – safety study

Depletion efficacy determined with (A) density-based analysis by inForm and (B) Pixel-based analysis by ImagePro. [d]: depletion efficacy comparing the median % of remaining F4/80+ macrophages across 4 weeks to PBS control. Data normalised to PBS control. Bar and error bars represent mean ± SD. N as defined in Figure 8.3.1. Each point represents each image. Three randomly acquired images per mouse. *p<0.05, **p<0.01, comparing between experimental groups of the same week. Mann-Whitney U test.

8.3.2 Xenograft tumour implantation

To investigate the role of macrophages during tumour progression and invasion, a mouse intra-gastric xenograft model was utilised[408]. Individual mice were bled a week prior to xenograft implantation to confirm that there were no differences in PBMC populations and body weights between litters, cages and genders (Figure 8.3.6).

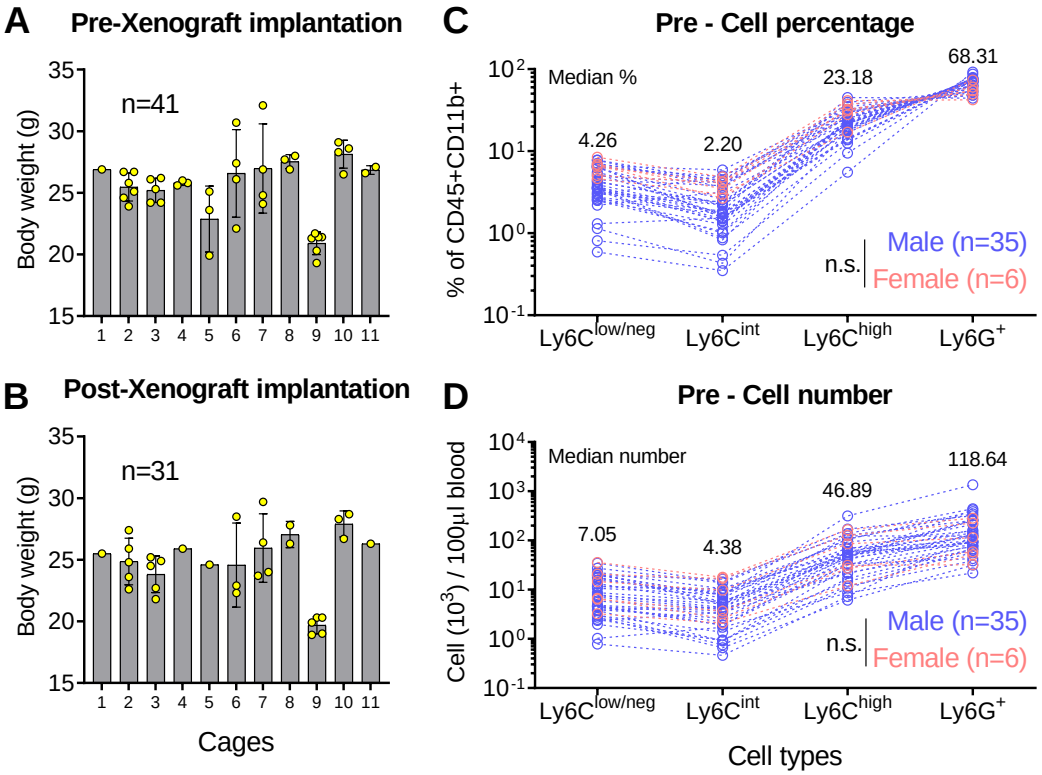
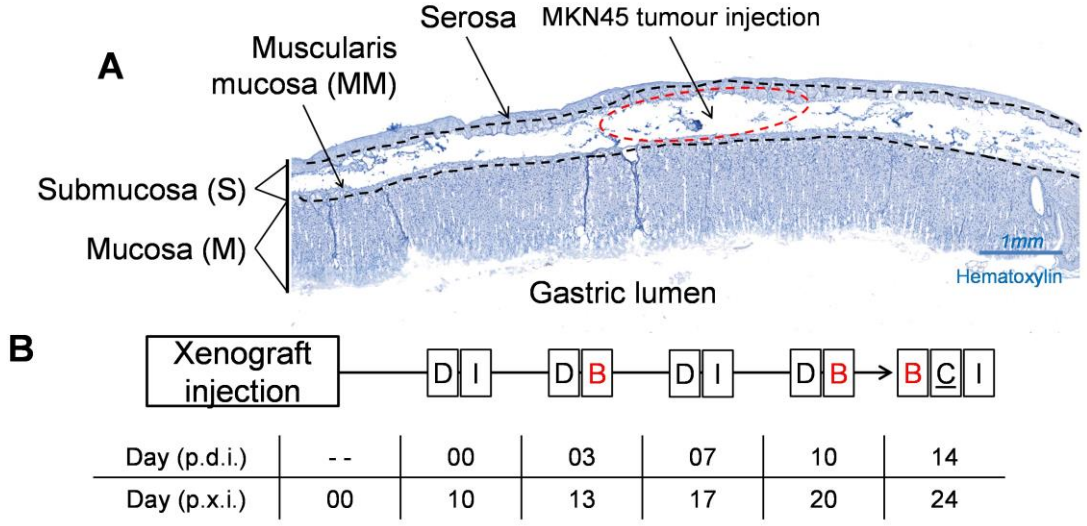


Figure 8.3.6 Baseline control of mice in experiment pre-clodronate treatment

Mice from different litters were housed in separate cages and their body weights were compared (A) pre- and (B) post-xenograft implantation. Female mice (Cage 9) were in general smaller in size compared to male mice (other cages). (C) Percentage and (D) Number of cell populations of interest between individual mice (n=41) determined with flow cytometry pre-xenograft implantation. Bar and error bars represent mean ± SD. Each line/point represents one mouse. Not significant (n.s.) comparing between male and female mice. Mann-Whitney U test.

Xenograft implantation was carried out by injecting luciferase-tagged human gastric cancer cells (MKN45)[408] into the serosal layer of the mouse stomach (Figure 8.3.7A and Method). This is an inverse-invasion tumour model compared to human gastric cancers which normally initiate from the inner mucosa layer then invade outward to the serosa (§1.1.4.1; Figure 8.3.8). The MKN45 cell line was chosen for its moderate invasive and metastatic properties compared to other GC cell lines[408]. Mice were imaged one week post tumour cell inoculation to detect cancer cells with the bioluminescent IVIS system. Clodronate-liposomes (0.2 mg/dose, biweekly; Figure 8.3.3 and Figure 8.3.4) were injected on day ten post tumour cell implantation at the dosage and frequency determined in the safety study (Figure 8.3.7B).



Xenograft intra-gastric implantation				
MKN45 ($0.5x10^6$ per mouse)				n = 41
Macrophage depletion				
Group	Concentration	Mice per group	Duration (week)	Total number of mice
1. PBS	0.2 mg / dose / biweekly	9	2	31
4. Clodronate-liposome		11		
5. Mannosylated clodronate-liposome		11		

Figure 8.3.7 Experimental design of macrophage depletion in tumour-bearing mice

(A) Representative image of mouse stomach layers showing tumour cell injection site. (B) Experimental timeline. p.d.i.: post-drug injection. p.x.i.: post-xenograft implantation. Numbers: days with experiment procedure. D: Macrophage depletion drug injection. B: Blood sample collected via sub-mandibular vein. I: Luciferin injected for non-invasive tumour imaging. C: Mice culled and organs harvested.

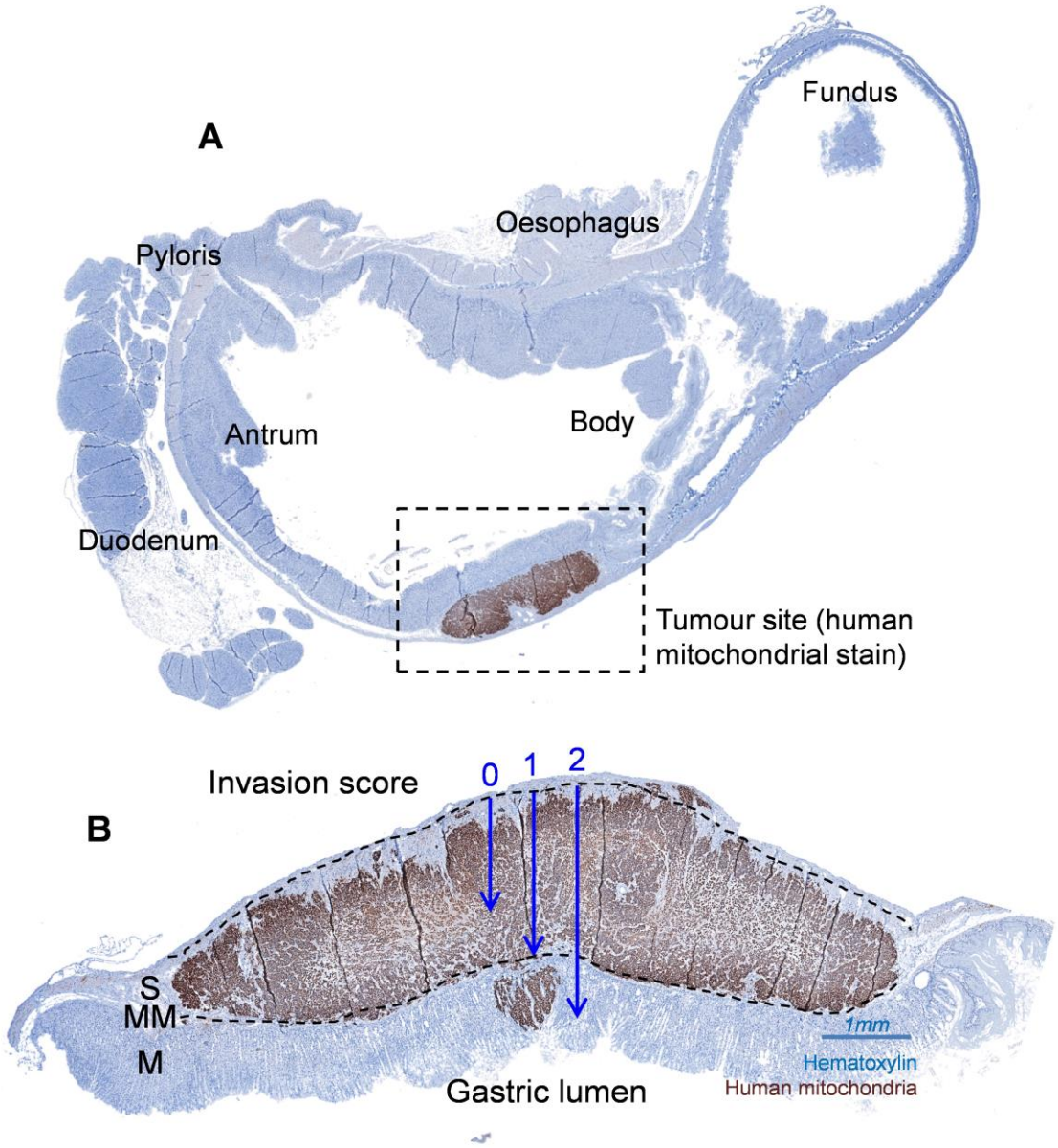


Figure 8.3.8 Definitions of gastric cancer invasion

Representative (A) whole mouse stomach and tumour injection site (dashed rectangle). Brown: human mitochondria stains xenograft tumour cells. Blue: hematoxylin counter stain. (B) Definitions of invasion score: 0 = tumour located within the serosa (S) layer. 1 = tumour invaded through the muscularis mucosa (MM) but not yet to the mucosa (M). 2 = tumour invaded through the MM into the M. Anything above a zero is invasive. Dashed line: primary tumour site.

8.3.3 Effect of macrophage depletion on tumour progression

8.3.3.1 Body weight

Ten mice have had developed tumours by day 10 post tumour-implantation whilst others remained tumour-free (n=21; Table 8.3.1). All tumour-implanted mice were treated with different clodronate-liposome constructs and consistent results with the previous safety study were observed in that neither construct affected mouse body weight (Figure 8.3.9A). No differences in body weight were observed between tumour and non-tumour-bearing mice and between male and female mice (Figure 8.3.9B).

Table 8.3.1 Number of mice between experimental groups

Groups / n	Group 1	Group 4	Group 5	*Total*
Total mice per group	9	11	11	*31*
Tumour-bearing mice at the start of depletion	4	3	3	*10*
Tumours developed during depletion	2	1	3	*6*
Total tumour-bearing mice	6	4	6	*16*
Mice culled during depletion*	0	1	1	*2*
Tumour-bearing mice at the end of depletion	*6*	*3*	*5*	*14*
Non-tumour-bearing mice at the end of depletion	*3*	*7*	*5*	*15*

- Group 1: PBS control.
- Group 4: Clodronate-liposome.
- Group 5: Mannosylated clodronate-liposome.
- *: both tumour-bearing mice. Lose of weight due to inflammation.

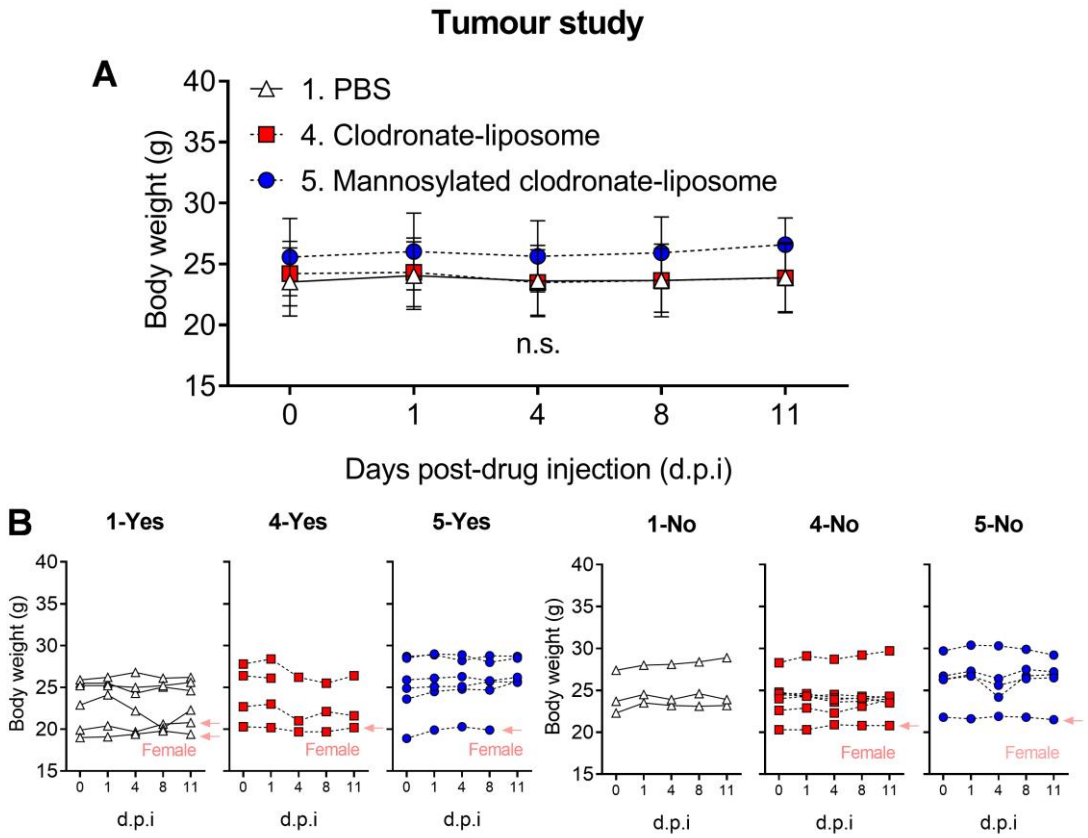


Figure 8.3.9 Mouse body weight change in tumour study

(A) Mouse weight throughout the experimental period. Day 0 indicates the first day of liposome injection. Each coloured symbol represents each data collecting time and each line represents each group. (B) Body weight of tumour-bearing (Yes) and non-tumour-bearing (No) mice. Pink arrow: female mice. N as defined in Table 8.3.1. Each line represents individual mice. Bar and error bars represent mean ± SD. Not significant (n.s.) comparing between experimental groups. Mann-Whitney U test.

8.3.3.2 Macrophage depletion in PBMC and splenic macrophages

Depletion of blood macrophage-like cells ($CD45^{+}CD11b^{+}Ly6G^{-}LyC^{low/neg}$; defined in Figure 8.3.3) in both groups injected with clodronate-liposome constructs was maintained at 65% throughout the 2 week experimental period compared to PBS controls (Figure 8.3.10A). However, when comparing the number of macrophage-like cells per ml of blood (Figure 8.3.10B), the results showed that it was elevated in each of the mice compared to their individual baselines (Day 0; before clodronate-liposome injection) regardless of the experimental group (Figure 8.3.6B). No differences were found between tumour-bearing and non-tumour-bearing mice of the same experimental group (Figure 8.3.11). These data suggest that the presence of systemic inflammation in mice that resulted in an elevated macrophage-like cells in the PBMC may be related to the surgical procedures rather than the presence of the tumours. Importantly, the results indicate that the depletion effect in peripheral blood observed in the clodronate-liposome injected groups was due to a relatively mild increase in macrophage-like cells compared to PBS controls, than a reduction of cell number compared to their individual baseline levels.

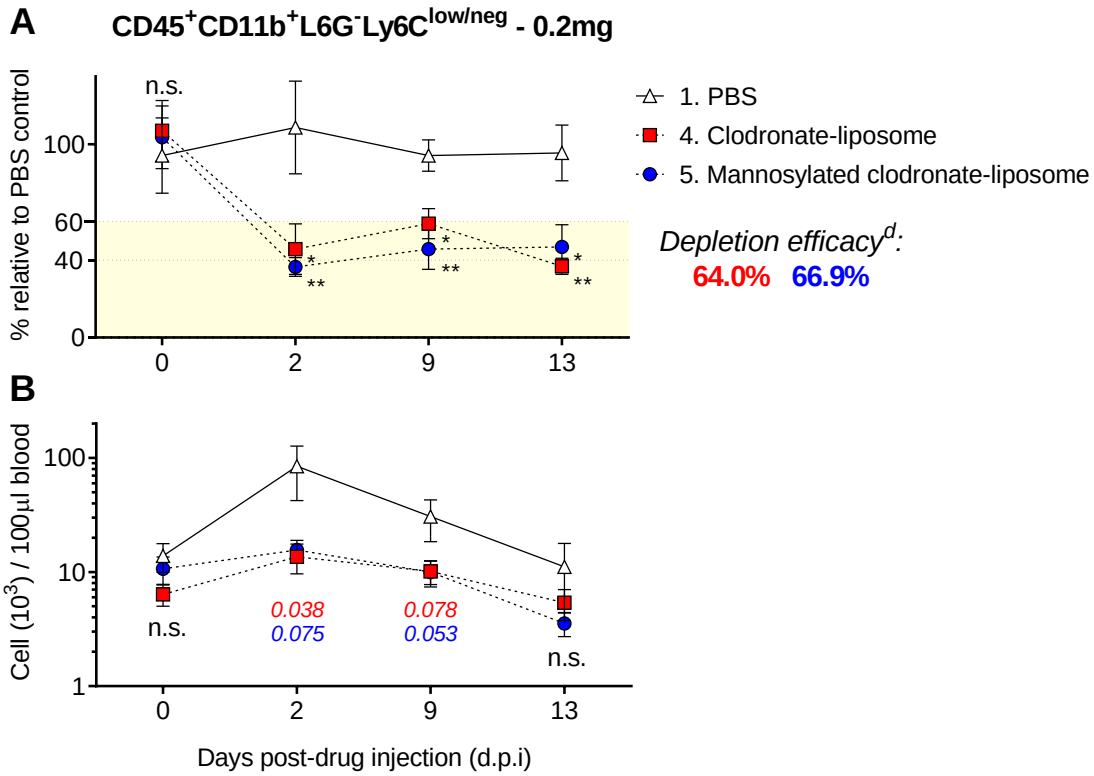
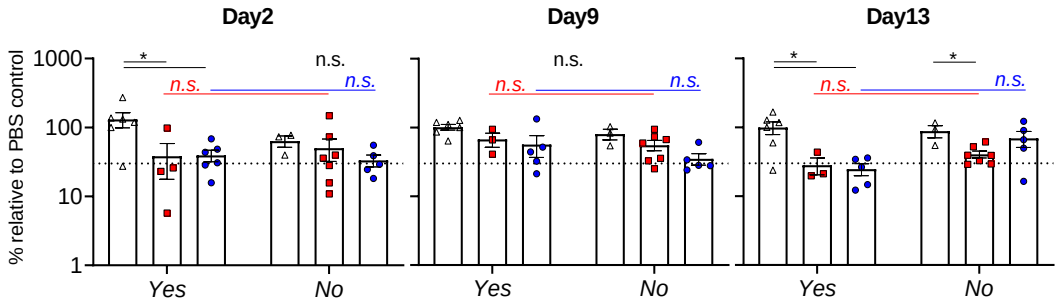


Figure 8.3.10 Mouse PBMC depletion efficacy – tumour study

Percentage of macrophage-like population of each experimental group (A) Normalised to PBS control and (B) absolute cell number determined with counting beads. Each line represents each group. [d]: depletion efficacy comparing the median % of remaining macrophage-like population across 2 weeks to PBS control. N as defined in Table 8.3.1. Each point represents each data collecting time point. Numbers labelled in (B) represent p-value of clodronate-liposome (red) and mannosylated clodronate-liposome (blue) groups compared to PBS control, *p<0.05, **p<0.01 and not significant (n.s.) comparing clodronate-liposome groups to PBS control. Mann-Whitney U test.



CD45+CD11b+Ly6G-Ly6C$^{low/neg}$ (Median % relative to PBS control)									
Tumour-bearing									
Duration	Day2			Day9			Day13		
Groups	1	4	5	1	4	5	1	4	5
Yes	125.70	24.43	37.19	105.51	65.92	44.08	108.80	21.19	26.45
No	73.22	35.99	29.25	83.17	59.50	28.12	93.86	39.22	66.12
p-value	*0.167*	*0.527*	*0.662*	*0.262*	*0.517*	*0.548*	*0.548*	*0.267*	*0.056*
Depletion efficacy*									
Groups	1	4	5	1	4	5	1	4	5
Yes	- -	75.565	62.81	- -	34.08	55.92	- -	78.81	73.55
No	- -	64.01	70.75	- -	40.5	71.88	- -	60.78	33.88

Figure 8.3.11 Mouse PBMC depletion efficacies of tumour and non-tumour-bearing mice

Depletion efficacy of macrophage-like population of each experimental group normalised to PBS control. 1: PBS control (white). 4: clodronate-liposome (red). 5: mannosylated clodronate-liposome (blue). Yes: tumour-bearing. No: non-tumour-bearing mice. [d]: depletion efficacy comparing with median % of remaining macrophage-like population across 2 weeks to PBS control. N as defined in Table 8.3.1. Bar and error bars represent mean ± SD. Each point represents one mouse. *p<0.05 and not significant (n.s.) comparing between experimental groups. Mann-Whitney U test.

The depletion of mouse splenic macrophages was measured by flow cytometry and by including F4/80 as a more specific macrophage marker for the mouse (defined as CD45^{+}CD11b^{+}Ly6G^{-}Ly6C$^{low/neg}$F4/80^{+}; Figure 8.3.12A). F4/80 was found to be upregulated on mature macrophages in the tissue and therefore was not ideal for the blood samples[393, 608]. The results showed that clodronate-liposomes could specifically deplete the F4/80-positive populations (Figure 8.3.12B) with an efficacy of around 95% (Figure 8.3.12C and Figure 8.3.13). There was no difference observed between the two liposome constructs (Figure 8.3.12C) and between tumour and non-tumour-bearing mice (Figure 8.3.13).

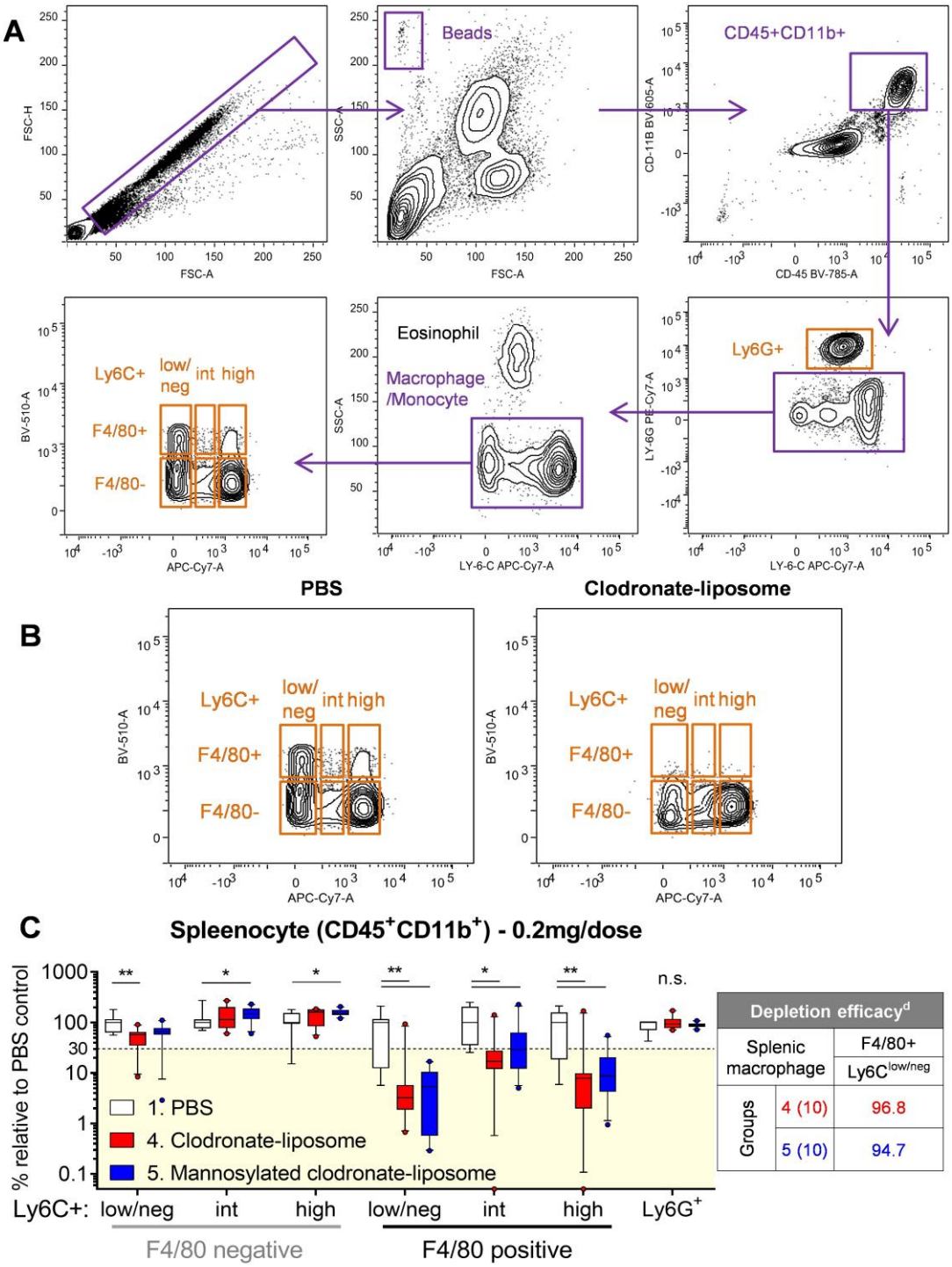
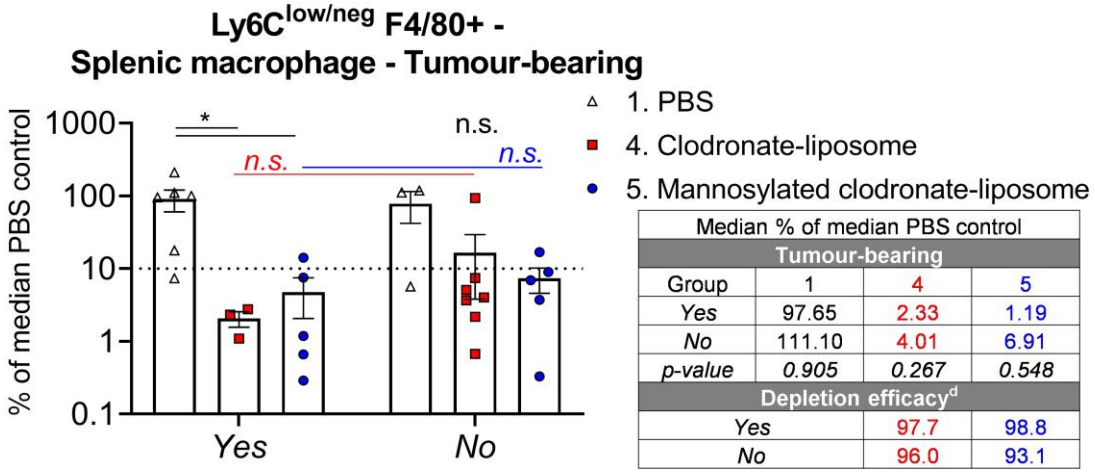


Figure 8.3.12 Gating strategy and depletion efficacy of mouse splenic macrophages

(A) Gating strategy used for flow analysis. (B) Representative macrophage depletion results between PBS control and clodronate-liposome. (C) Depletion of the cell populations of each experimental group normalised to PBS control 2 weeks post-drug injection. [d]: median % of splenic macrophages compared to control. N as defined in Table 8.3.1. Box and whiskers represent mean ± 10-90 percentile. Each point represents one mouse. *p<0.05, **p<0.01,

***p<0.001 and not significant (n.s.) comparing between experimental groups. Mann-Whitney U test.



Median % of median PBS control			
Tumour-bearing			
Group	1	4	5
Yes	97.65	2.33	1.19
No	111.10	4.01	6.91
p-value	*0.905*	*0.267*	*0.548*
Depletion efficacy[d]			
Yes		97.7	98.8
No		96.0	93.1

Figure 8.3.13 Depletion efficacy of splenic macrophages in tumour and non-tumour-bearing mice

Depletion efficacy of the cell of interest of each experimental group normalised to PBS control. Yes: tumour-bearing. No: non-tumour-bearing mice. [d]: median % of splenic macrophages compared to PBS control. N as defined in Table 8.3.1. Bar and error bars represent mean ± SD. Each point represents one mouse. *p<0.05 and not significant (n.s.) comparing between experimental groups. Mann-Whitney U test.

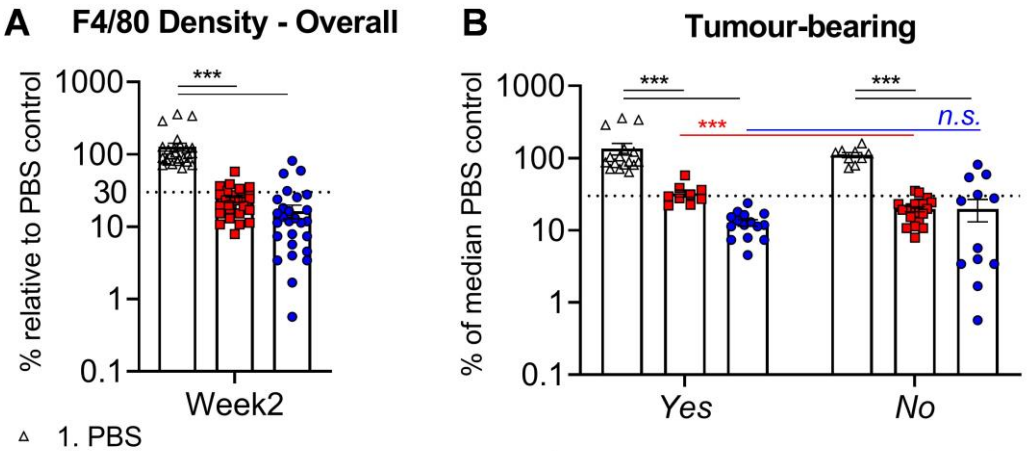
8.3.3.3 Macrophage depletion in liver and lung macrophages

Macrophage depletion in the liver and lung were assessed with multiplex IHC staining of F4/80 and CD206. Approximately 80% depletion of liver macrophages was observed in both tumour and non-tumour-bearing groups and across different clodronate-liposome constructs, consistent with the safety study results (Figure 8.3.14A). A difference in macrophage number was found in the non-tumour-bearing mice compared to tumour-bearing mice within the clodronate-liposome injected group but not in the control or the mannosylated clodronate-liposome injected mice (Figure 8.3.14B).

Interestingly, F4/80+ liver macrophages were found to exhibit very low co-expression of CD206 (3%; Figure 8.3.15A) compared to lung macrophages[609, 610] (22%; Figure 8.3.15B and C). These results suggest that the expression of CD206 on F4/80+ macrophages was tissue specific. Indeed, the mannosylated

clodronate-liposomes could more specifically deplete F4/80+CD206+ macrophages in the lung compared to the non-targeted clodronate-liposomes (Figure 8.3.16A). Macrophage depletion levels were higher with both clodronate-liposome constructs in the non-tumour-bearing than tumour-bearing mice, suggesting a possible systemic immune influence from a gastric tumour to the distant lung (Figure 8.3.16B).

In summary, these results showed that different organs had different levels of macrophage depletion (blood: 65%; spleen: 95%; liver: 80%; lung: 45%), which might reflect distinct microenvironments and also differential rates that the macrophage pools were replenished in each organ.



Median % relative to PBS control			
Overall			
Group	1	4	5
F4/80	100.0	22.9	11.6
Depletion efficacy[d]		77.1	88.4

Median % relative to PBS control			
Tumour-bearing			
Yes	88.98	29.40	11.87
No	115.25	19.15	3.98
p-value	*0.550*	*0.001*	*0.383*
Depletion efficacy[d]			
Yes		70.6	88.1
No		80.9	96.0

Figure 8.3.14 Depletion efficacy of liver macrophages in tumour and non-tumour-bearing mice

Depletion of F4/80+ liver macrophages normalised to PBS control in (A) all (regardless of tumour status) and (B) between tumour-bearing (Yes) and non-tumour-bearing (No) mice. [d]: median % of liver macrophages compared to PBS control. N as defined in Table 8.3.1. Bar and error bars represent mean ± SD. Each point represents each image. Three randomly acquired images per mouse. ***p<0.001 and not significant (n.s.) comparing between experimental groups. Mann-Whitney U test.

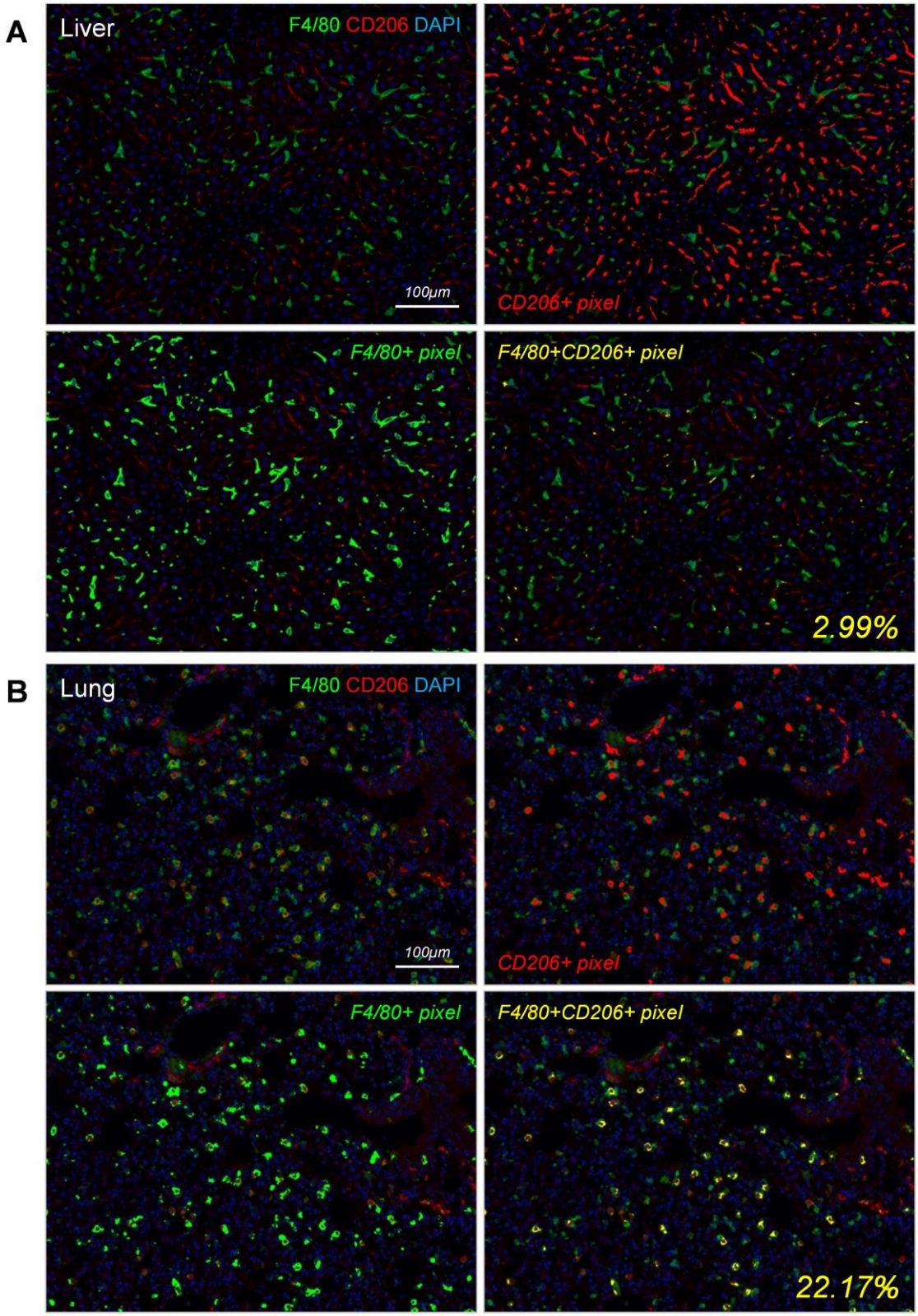
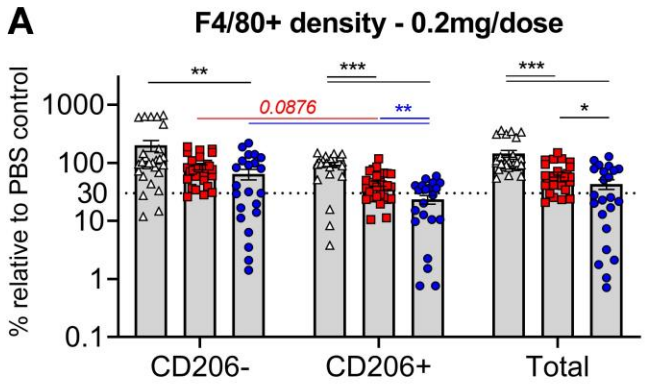
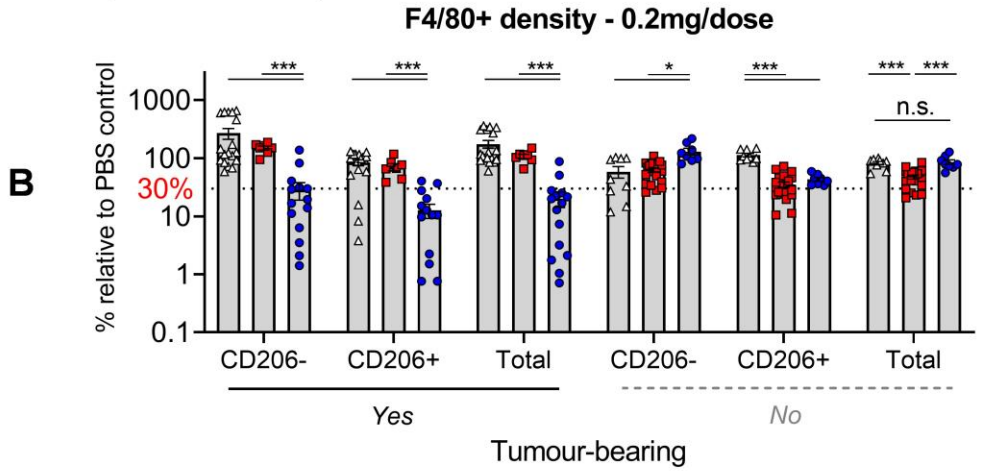


Figure 8.3.15 Representative images of liver and lung macrophages

(A) Liver macrophages. Scale bar: 100 μm. (B) Lung macrophages. Scale bar: 100 μm. Green: F4/80. Red: CD206. Yellow: co-staining of F4/80 and CD206. Blue: DAPI. Percentage showing the proportion of F4/80+ macrophage co-expressing CD206.



Median % relative to PBS control			
Overall			
F4/80+ macrophages	Groups		
	1	4	5
CD206-	100.00	77.62	31.46
CD206+	100.00	38.36	20.29
Total	100.00	57.02	25.29
Depletion efficacy[d]			
CD206-		22.4	68.5
CD206+		61.6	79.7
Total		43.0	74.7



Median % relative to PBS control								
Tumour-bearing					**Depletion efficacy[d]**			
F4/80+ macrophage		1	4	5	F4/80+macrophage		4	5
Yes	CD206-	124.82	150.35	16.78	Yes	CD206-	-30.8	83.22
	CD206+	98.88	66.89	10.52		CD206+	33.11	89.48
	Total	113.16	111.58	16.84		Total	-11.58	83.16
No	CD206-	43.43	65.73	115.39	No	CD206-	34.27	-15.39
	CD206+	103.76	31.55	42.91		CD206+	68.45	57.09
	Total	88.46	54.02	78.63		Total	45.98	21.37
p-Value	CD206-	*0.0024*	*<0.0001*	*0.0001*	mice (n)	1	4	5
	CD206+	*0.1895*	*0.001*	*0.0001*	Yes	6	3	5
	Total	*0.0019*	*<0.0001*	*<0.0001*	No	3	7	5

Figure 8.3.16 Depletion efficacy of lung macrophages in tumour and non-tumour-bearing mice

Depletion efficacy of F4/80+ lung macrophages of each experimental group normalised to PBS control in (A) all and (B) between tumour-bearing (Yes) and non-tumour-bearing (No) mice. [d]: median % of liver macrophages compared to PBS control. N as defined in Table 8.3.1. Bar and error bars represent mean ± SD. Each point represents each image. Three randomly acquired images per mouse. *p<0.05, **p<0.01, ***p<0.001 and not significant (n.s.) comparing between experimental groups. Mann-Whitney U test.

8.3.3.4 Macrophage depletion at the tumour site

Macrophage depletion in the stomach was evaluated with multiplex IHC and, surprisingly, no depletion was observed despite the systemic reduction of macrophages in multiple organs (Figure 8.3.12). In addition, F4/80+ macrophages with different CD206 expression levels were observed in different regions of the tumour and stomach. Macrophages within the stomach mucosa had negligible CD206 expression (2%; I in Figure 8.3.18C and D). CD206 on macrophages increased in the submucosa and serosa layers (II: 14%), in oesophagus (III: 39%) and more than half of the macrophages in the duodenum were CD206-positive (IV: 64%; Figure 8.3.18B). The CD206 expression pattern on mouse mucosal macrophages was distinct from human gastric mucosal macrophages in which the majority were CD206-positive (Figure 8.3.19), reflecting a difference between human and mouse. Interestingly, a similar CD206 expression/distribution pattern was observed across the mouse tumour regions compared to human GC. Mouse CD206+ macrophages were also found to be preferentially located at the peri-tumoural rather than intra-tumoural regions (Figure 8.3.20; related to Figure 4.3.20).

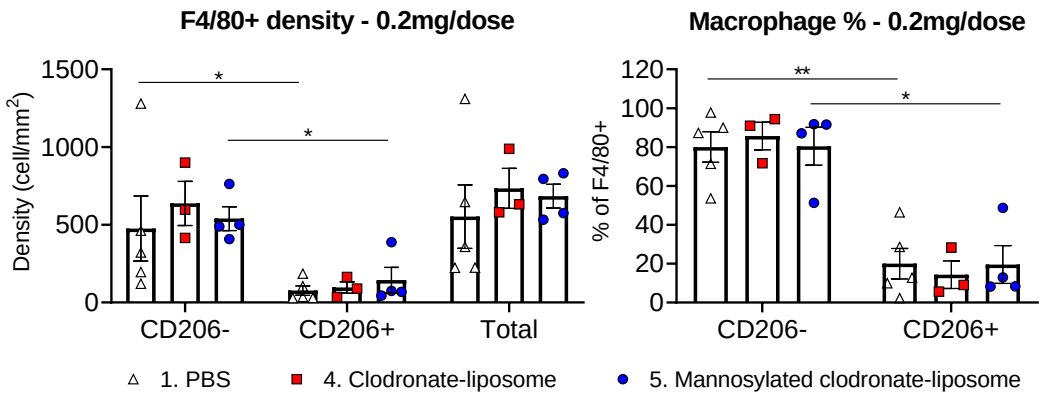


Figure 8.3.17 Depletion efficacy of gastric tumour-associated macrophages

Depletion efficacy of the cell of interest of each experimental group normalised to PBS control. All mice were tumour-bearing. N as defined in Table 8.3.1. Bar and error bars represent mean ± SD. Each point represents one mouse. *p<0.05, **p<0.01, ***p<0.001 and not significant (n.s.) comparing between experimental groups. Mann-Whitney U test.

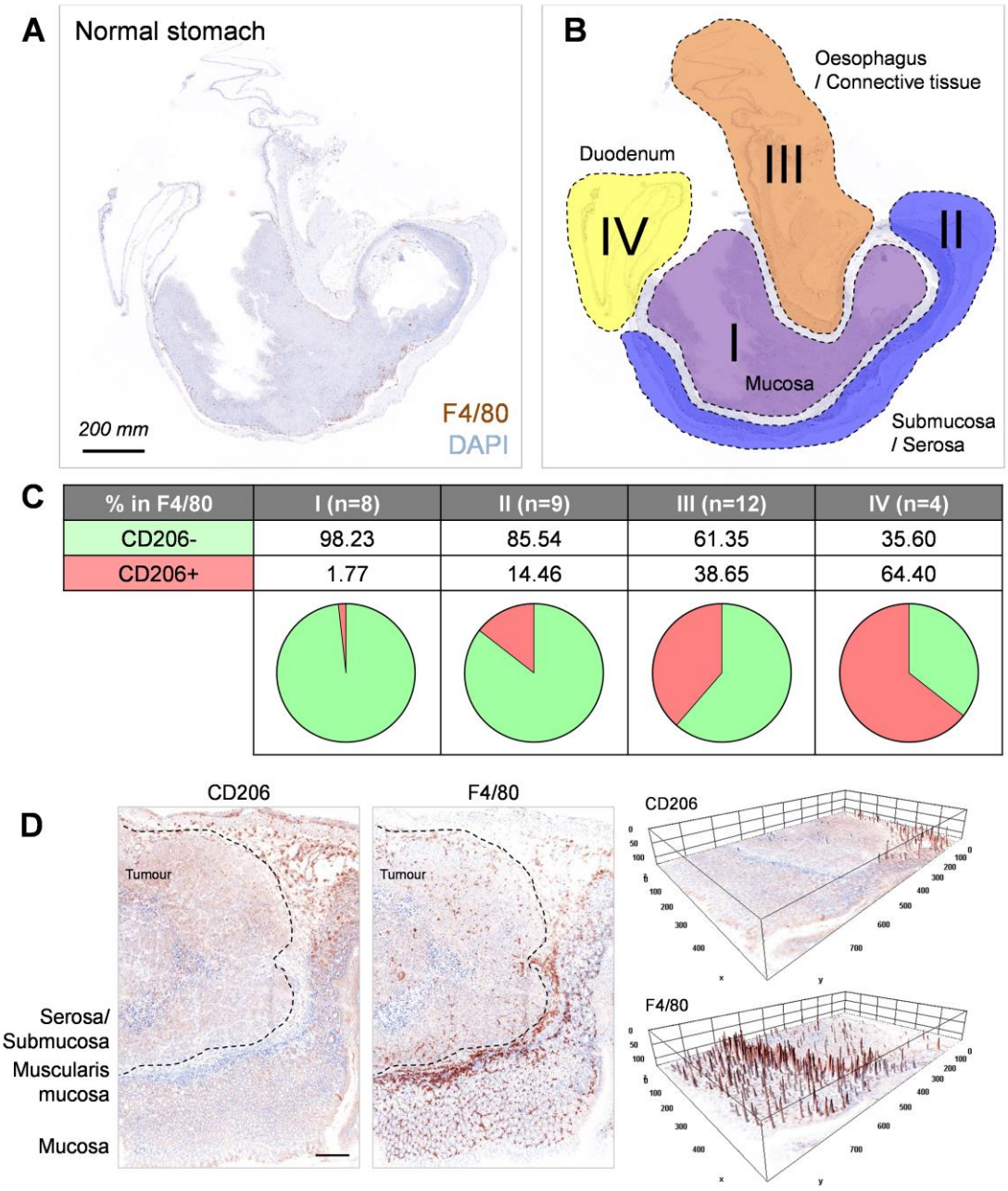


Figure 8.3.18 Quantitation of CD206 expression on different gastric macrophage populations

Representative images of the (A) whole mouse stomach and the (B) identification of different regions of a PBS control mouse. (C) Pie charts represent the median percentage of F4/80+ macrophages that were also CD206+ in the corresponding stomach regions described in (B) of control mice. (D) Representative 2D and 3D single-stained IHC images of CD206 and F4/80 showing the distribution of mouse macrophages with different marker signatures. Dashed line: tumour site. Brown: CD206 or F4/80 staining. Blue: DAPI. Scale bar: 100 µm.

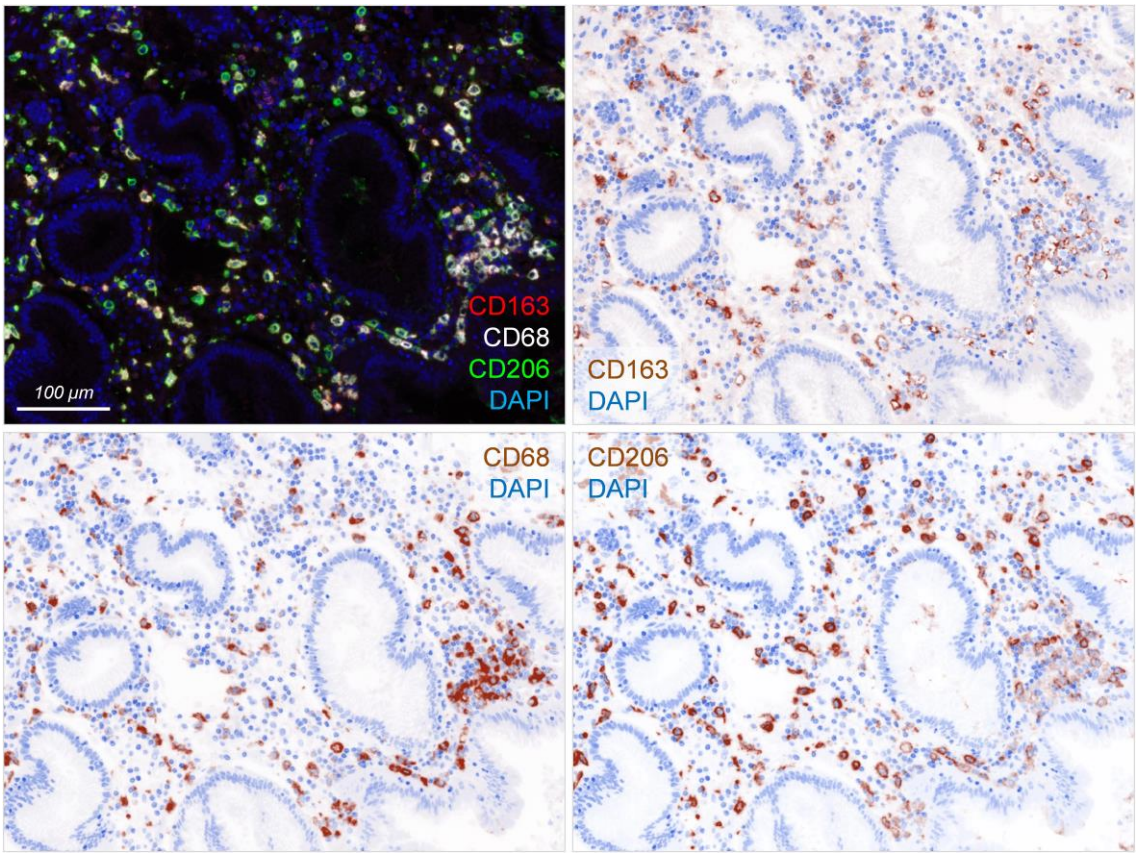


Figure 8.3.19 Representative images of human mucosal macrophages

Composite and single-stained IHC images of human mucosal macrophage expressing both CD206 and CD163.

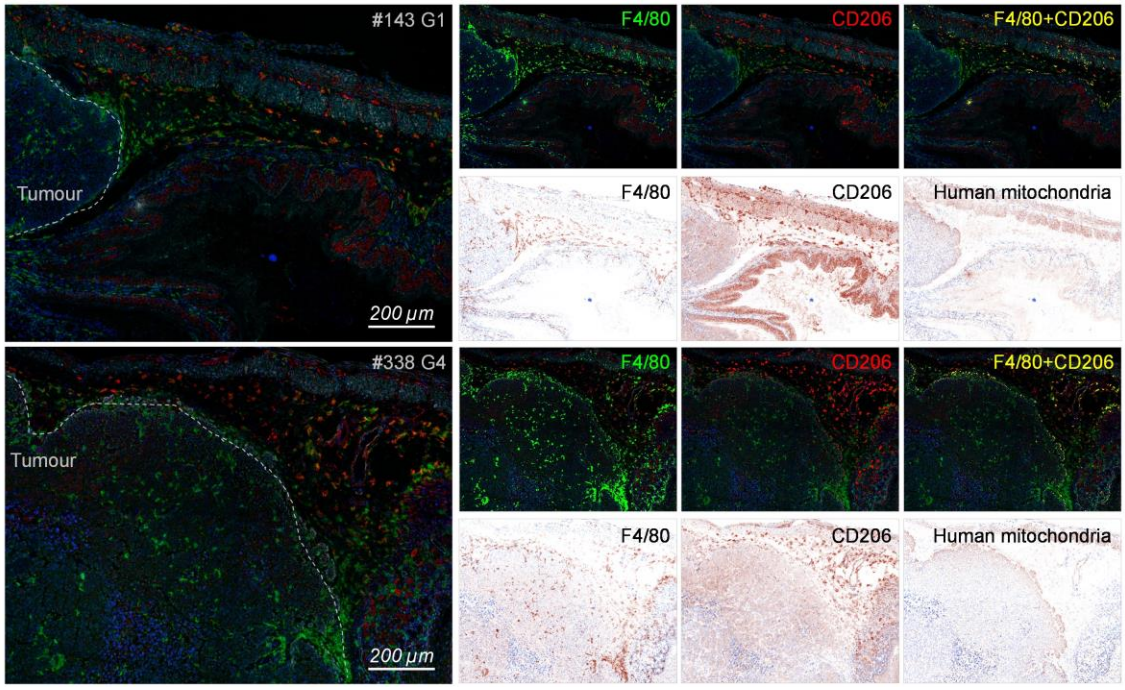


Figure 8.3.20 Representative images of mouse gastric tumour macrophage populations

Representative composite and single-stained IHC images of differential CD206 and F4/80 expressions on macrophages populations between tumour site and adjacent non-tumour normal tissue within the stomach. Human mitochondria stains xenografted tumour cells. Mouse macrophages exhibited a higher CD206 expression at the peri-tumour regions and not within the tumour.

Collectively, these findings reflect a fundamental difference between human and mouse macrophages that reside in the stomach and this should be taken into consideration in future study designs. The data also suggest that the ways in which the tumour microenvironment influences the CD206 expression on macrophage between tumour regions (e.g. metabolic activities[365]) might be similar between species.

Lastly, tumour development and invasion (defined in Figure 8.3.8) between the different experimental groups were compared. There were no significant differences in macrophage number in the stomach between groups, and no differences were found in the degree of invasion or primary tumour formation (Figure 8.3.21).

A

Gender	Group	n	Invasion score
F	1. PBS control	9	2
M			2
M			1
M			NA
M			2
F			1
F	4. Clodronate -liposome	3	2
M			2
M			2
M	5. Mannosylate clodronate -liposome	5	2
M			2
M			2
M			2
M			NA

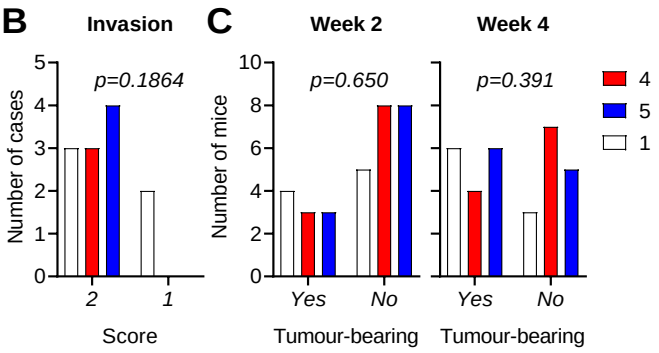


Figure 8.3.21 Invasion scores and tumour- formation

(A) Table shows the number of mice in each experimental group with tumour identified with the bioluminescence imaging and were culled for (B) invasion scoring. F and M: female and male mice, respectively. n: Number of mice per group. NA: no tumour found therefore no scoring. Invasion score: determined based on worst case scenario, stomach with any tumour cell that meet the invasion scoring criteria (defined in Figure 8.3.8). (C) Tumour-formation determined with bioluminescence imaging. Weeks represent the weeks post-xenograft implantation. Yes: tumour-bearing. No: non-tumour-bearing mice. Bars represent the total number of mice in each condition. Chi-square analysis comparing between conditions.

8.4 Discussion and Conclusions

In this Chapter, to investigate the role of CD206+ TAMs on tumour progression and invasion, an *in vivo* model of tumour invasion and clodronate-based depletion of macrophages was used. A safety study was initially performed to determine the efficacy and safety of the clodronate liposomes; a dose regime of 0.2mg per mouse at a frequency twice per week was determined as the optimal conditions for maximal macrophage depletion without toxicity. Under these conditions a reduction of blood macrophage-like cells (40-65%) and liver macrophages (80%) was achieved with no associated drug-related weight loss or organ damage.

The orthotopic mouse model for GC was utilised for the determination of tumour invasion with and without the presence of different macrophage populations. In this instance host macrophage depletion in the spleen (96%) and lung (45%) were also evaluated. However, surprisingly, no macrophage depletion was

found in the tumour regions, and no differences in tumour growth, and degree of invasion was observed (Table 8.4.1). The mannosylated clodronate-liposome was utilised as a method to target specifically the CD206+ macrophages[601, 602]. It showed a higher depletion efficacy and were more specifically to the CD206+ macrophages in the lung; however, not in other organs examined. These unexpected results may be due to: (i) the time frame of sample collection, (ii) the replenishing speed of different CD206-expressing macrophage populations in different organs, (iii) the efficacy of mannose targeting or (iv) the differences between mouse and human macrophages.

Table 8.4.1 Summary of macrophage depletion at different organs

#	Organ	Depletion* %	Mannose specific targeting		Higher depletion efficacy	Observed group
1	Blood	40-65	*NA*		*NA*	- -
2	Spleen	96	*NA*		*NA*	- -
3	Liver	82	*NA*		Non-tumour-bearing mice	Clodronate-liposome
4	Lung	45	*YES*		Non-tumour-bearing mice	Both liposome constructs
5	Tumour	0	NA		- -	- -
*: Median depletion level across both clodronate-liposome constructs.						

Firstly, tumour samples were harvested 4 days post final clodronate-liposome injection. It was observed that by this stage the macrophage-like cells in the blood in some mice had started to recover but not in the other organs. This may be due to the fact that liver and spleen macrophages were the tissue-resident populations that normally do not replenish from the blood monocytes as quickly as in the lung and intestine[338, 611]. Mucosal macrophages have been shown to be continuously replenished by circulating monocytes in the intestine and colon[339, 612] and this may be similar throughout the gastrointestinal tract[343].

Therefore, in a chronically inflamed stomach tumour with rapid replenishment of blood monocyte-derived macrophage, four days post-drug injection may have been too long to observe any changes in macrophage number at the tumour site. Tumour tissues harvested at earlier time points (e.g. one day post-drug

injection) would be needed to examine the dynamics of macrophage depletion in the stomach. If depletion at an early time points was observed, then a more frequent dosing regimen will need to be re-evaluated to study the role of macrophages during tumour progression and invasion. In addition, the tumour take rate in this study was roughly 40% which could be improved with more concentrated cell solutions for future experiments. Moreover, peritoneal macrophages and intestinal and colonic tissues could be collected for comparison as organs that may have more similarities with the stomach. These organs were not collected in the current study because they were tumour-negative based on bioluminescent tumour detection via the IVIS system. However, they could be used as a reference of macrophage populations with different CD206 expressions in future studies.

Secondly, the measure of macrophage populations expressing different levels of CD206 within the same organ and between different organs may help to explain the different depletion results observed in this study. The mannosylation of clodronate-liposome was thought to increase the specificity towards the CD206+ macrophages. However, given that the principle of targeting macrophages with liposomes was based on their phagocytic ability, it is not clear how much additive effect conjugating mannose on liposomes could provide compared to non-conjugated ones due to the fact that the CD206+ macrophages have been shown to also exhibit higher phagocytic ability[613]. The efficacy mannosylation on liposomes could be assessed using an *in vitro*-polarised macrophage system by comparing macrophage depletions between mannose conjugated and non-conjugated liposome constructs of different concentrations with the macrophage of the same CD206 expression.

Differential CD206 expression was observed between macrophage populations between mouse organs in this study. Liver macrophages expressed very low levels of CD206 (3%); therefore, may explain why there were no differences were observed between the two liposome constructs. Spleen macrophages exhibited strong expression of CD206[427, 614]; however, they were almost completely depleted with clodronate-liposome alone and not much of an additive effect could have been observed with the mannosylated construct.

Indeed, in the lung, the depletion efficacy was more pronounced in the mannosylated clodronate-liposome group, suggesting an additive depletion effect for the CD206 macrophage. The lung is comprised of tissue-resident alveolar macrophages ($CD206^{high}$) as well as interstitial macrophages[615, 616] ($CD206^{low}$). The alveolar macrophages originate from the yolk sac and foetal liver whereas the interstitial macrophages originate and are constantly replenished by bone marrow precursors[617, 618]. The dynamic changes between these cell populations in tumour and non-tumour-bearing mice may explain their differential response to depletion but more investigation is required to further explore their relationship with systemic immunity from a distant tumour.

To achieve a more specific CD206+ macrophage depletion, a different route of targeting these macrophages that is not dependent on their phagocytic ability could be considered (e.g. small peptides[619], antibodies[345], nanoparticles[620]) to avoid ablating the effect of specific targeting.

Collectively, the depletion results from different organs indicate that the tolerance of macrophage populations to clodronate-liposome differed between regions of the body and will need to be evaluated separately.

Lastly, differences between mouse and human macrophages were observed. The macrophage population in the mouse stomach mucosa lacked CD206 expression, which was in contrast to observations in the human stomach mucosa. Further experiments are required to determine whether this phenomenon was (i) a true difference between the two species, or (ii) due to an issue of animals hosted in a relatively clean laboratory environment or (iii) to this specific mouse strain given that CD206 has been shown to upregulate on human macrophages after *H. pylori* infection[219] and that CD206 expression on mouse gastric mucosal macrophages has been previously reported[343].

The differences in CD206-expression on mucosal macrophages between mouse and human suggest that the xenograft mouse model may not fully recapitulate the biology of tumour-macrophage interaction at the mucosa and muscularis mucosa regions seen in humans if the CD206 receptor on TAMs was really functioning. However, the trend of a decreasing pattern of CD206

expression from the non-tumour toward the tumour region observed in the human GC samples was also observed in the mouse stomach tumours. These data indicate that the mechanisms (e.g. oxygen level[365]) underlying macrophage polarisation may be conserved between species and will be informative if an exclusive marker(s) between these TAM populations could be identified using the mouse model.

If future validation results show that mouse gastric macrophages were indeed resistant to clodronate-liposome depletion, suggesting that this *in vivo* model might be inappropriate for investigating local tumour invasion, it could possibly be utilised as a mouse GC model of liver metastasis. Consistent and high macrophage depletion in the liver were observed in this study and all mice (9 out of 9) have been reported to exhibit liver metastases by week 6 post-xenograft implantation using this model[408].

8.4.1 Summary

In summary, a working model system allowing for the depletion of macrophages using clodronate-liposomes was established. However, this will need further optimisation to obtain depletion at the stomach tumour site. Distinct CD206 expression on macrophages and variable response to drug-induced macrophage depletion were found across different mouse organs, between mouse gastric anatomic regions and between human and mouse samples, reflecting the heterogeneity and its exciting challenges of studying macrophage biology that should be considered in future experiments.

Chapter 9 : Discussion, Future directions and Conclusions

Characterisation of tumour-associated macrophages (TAMs) has been challenging due to (i) their plastic phenotype in response to exogenous stimuli[621], (ii) the lack of specific markers to distinguish between macrophages of different activation states and origins[414], (iii) technical difficulties for spatial analysis[309], and (iv) the inherent differences between species[395]. Despite extensive characterisation of *in vitro*-polarised macrophages[622] and TAMs in mouse and human cancer models, the distribution, putative function of these cells in GC remains unclear. Likewise, important questions remain unresolved of the *in situ* interaction of macrophage populations with each other and other cell types within the GC milieu, and the influence this imparts on clinical outcomes.

To address these challenges, multiplex IHC (mIHC) was utilised as a central part of this Thesis due to its ability to enable co-staining of up-to seven markers simultaneously and its capability of digitalising cellular information for bioinformatic analyses (**Chapter 3**). Spatial analysis tools were developed (**Chapter 3**) to interpret cell-to-cell interactions and changes in marker expression *in situ* at single-cell resolution (**Chapter 4**). Cellular density information collected from mIHC was correlated with Affymetrix gene expression profiles of the matched patient samples to generate cell-specific environmental gene signatures (**Chapter 5**). These signatures were used to investigate the putative functions and interaction of TAMs within the tumour microenvironment and with tumour-infiltrating T lymphocytes (TILs; **Chapter 5** and **6**, respectively), to compare with *in vitro* characterised TAM populations in the literature (**Chapter 5**) and to validate with published patient cohorts (**Chapter 5**). Additional mIHC panels were established for further cellular interaction studies between the TAMs and TILs (**Chapter 6** and **7**). Finally, influences of specific TAM populations, identified with mIHC, on tumour invasion were evaluated with an *in vivo* mouse model (**Chapter 8**).

9.1 Discussion

Heterogeneity remains a major problem for macrophage studies which limits our understanding of their therapeutic implications[623] and biological function *in situ*[171]. This Chapter discusses how the findings from this Thesis could assist in addressing current challenges and facilitate our understanding of TAMs as described in §1.4, with respect to their:

1. Spectrum model of activation[307, 320]
2. Multiplicity of origin[346]
3. Spatial and metabolic reprogramming by the tumour microenvironment[309]
4. *In situ* interaction with other cells[468]
5. Fundamental differences between human and animal macrophage biology[311, 395]

9.1.1 Spectrum model of macrophage activation

Using multiplex IHC, different TAM populations that goes beyond the bipolar classification were observed within the GC microenvironment in this study. Whilst the spectrum model[307, 320] of macrophage activation has greater detail in describing macrophage biology compared to the simplified M1/M2 model, how this data can be applied to interpret the biological relevance of macrophages has not been well described in the literature.

The novel data presented in this Thesis on the GC spectrum macrophage model with cellular spatial resolution provides important insight into this matter.

9.1.1.1 Macrophage nomenclature and classification

The M1 and M2 macrophages have been referred to as spectrum extreme phenotypes in some studies[624-626]. However, in this study, data show that all TAMs characterised *in situ* with either CD163 or CD206 staining (presumably M2-like) were associated with a certain level of IL-4/13 signalling. This was found to be associated especially with the macrophage populations within the non-tumour adjacent normal region, but varied in other unique signatures to intra-tumour TAMs (Figure 9.1.1). This may be, in part, due to the basal requirement of M-CSF (CSF-1), a critical factor for macrophage survival and proliferation in tissues[184, 627] and *in vitro*[320], which is known to drive

macrophages toward a M2-like phenotype. Because of this, the majority of the tissue-resident macrophages in the steady state were described as more M2-like than M1-like[183, 628]. These data suggest that, at least in the GC tumour setting, the M2 phenotype (by definition associated with IL-4 and IL-13) was not an “extreme” subdivision of TAM populations but was among the different TAM populations and may even possibly be a more general or upstream phenotype of the other TAM subpopulations that were exposed to additional stimuli.

In summary, the information from this Thesis could be important for the nomenclature of macrophages[403] and act as a baseline to assist future hierarchical clustering studies deciphering the spectrum of macrophages in GC and other malignancies.

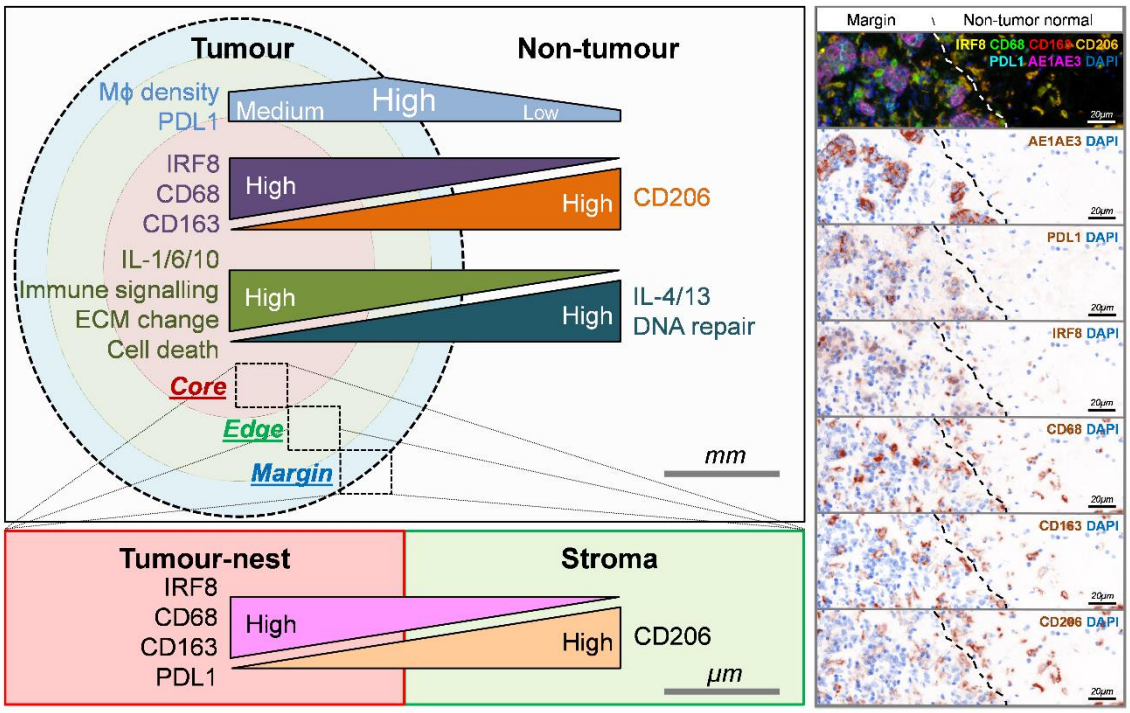


Figure 9.1.1 Schematic spatial and transcriptomic model of TAMs in GC

A proposed model proposes that TAM density and marker expression vary between GC tumour regions. Distinct marker expression profiles on TAMs were associated with their population disparity between the tumour site and non-tumour tissue and between the tumour-nest and stroma. TAM populations were associated with signature pathways which may help inform on their function and polarization status. A similar trend of marker changes on TAMs was observed between the tumour-nest and stroma across different tumour regions (Core, Edge or Margin). Mϕ: macrophage. ECM: extra-cellular matrix. Figure from[466].

9.1.1.2 Functional differences between TAMs within tumour regions

In the literature, CD206 and CD163 are commonly categorised as M2 markers[307] and are used widely and interchangeably to identify M2-like macrophages[212, 629]. However, the results from the present study demonstrate the clear differences between the CD206+ (CD163-) and CD163+ (CD206-) TAMs. These macrophages differed in their predominant spatial location, PDL1 status, and proportion size which suggest distinct biological functions in GC (Figure 9.1.1).

CD206 expression has been shown to be related to the protective function of ROS in macrophages[630] and to be involved in cross-presentation of dendritic cells[451]. However, previous studies that targeted CD206 with antigens resulted in cytotoxic T cell tolerance instead of activation *in vivo*[631, 632] via induction of CTLA-4 through direct interaction with CD45[633]. Combined with information from the present study, this infers that CD206+ TAMs may be T cell-suppressive, given their high PDL1 expression and locational preference at the tumour Margin and stroma, overlapping with the location of TILs in our GC cohort.

CD163 is a functional haptoglobin-hemoglobin and HMGB1 scavenger receptor[464] and has been shown to be upregulated on macrophages polarised with IL-10[457]. CD163+ macrophages were shown (i) to localise at perivascular regions within tissues[461], (ii) to exhibit the highest phagocytic ability compared to other *in vitro*-polarised phenotypes[315] and (iii) to clear apoptotic debris through efferocytosis via enhanced MerTK[634] (a phagocytic receptor which is under investigation as a TAM-targeting candidate[635]). Additionally, it has been reported that the IL-10-induced macrophage signature was found to coexist with the IFN-γ-induced macrophage signature during early stages of burn-related wound tissue, but was then gradually decreased and reverted into an IL-4/13-dominant environment[457]. Therefore, the observation in this study that high accumulation of CD163+ (CD206-) TAMs found within the tumour Core and tumour-nest (§4.3.1 and §6.3.4), may represent the TAMs that have been polarised by the leaky nature of the tumour vasculature[636] and functioning to clear tumour cellular debris from active inflammation-related death.

However, interestingly, IL-10 has also been shown to reduce inflammation-induced macrophage phagocytosis of healthy host cells[637]. TAMs have also been shown to effectively prime T cells[468] (as discussed in §7.4.5.1). Therefore, it is crucial to confirm if the subset of CD68++CD163+ TAMs which highly expressed NOX2 were more pro-inflammatory and pro-immune[555] or extremely immune suppressive[638] and tissue regenerative[457]. This would have fundamental implications for future therapeutic applications.

In summary, the data from this study support recent publications advocating the reassessment of using the bipolar M1/M2 classification[171] and indicate that CD206 and CD163 are not interchangeable markers. Co-staining of both CD206 and CD163 on the same tissue is required for future studies focusing on TAM heterogeneity *in situ* to discriminate between these TAM populations.

9.1.1.3 Identifying cell populations for specific therapeutic and diagnostic targeting

Using the spatial information derived in this study, the generally-accepted concept that “cell abundance positively correlates with functional importance” may be challenged.

In bioinformatic analyses of high dimensional data (e.g., flow cytometry and CyTOF[639], and single-cell RNA sequencing[640]), a decent size of a cell cluster and a high cell type frequency are often used as parameters to evaluate the quality of unsupervised clustering. However, in this study, the median distance of immune cells to tumour cells and cell populations that were embedded in the tumour-nest (presumably with more chance of interacting with the tumour cells) were found to be independent of their overall density. Just 13% of the CD8+ TILs were PD1-positive (CD8+PD1+), and only 3% of the CD68++CD163+ TAMs and 5% CD8+PD1+ TILs were in direct contact within the Immune/Tumour trios. These parameters, however, were more characteristic of patient survival than overall immune densities, suggesting that the effector immune cells were not of the ones with the highest number within the tumour microenvironment. These data align with other studies demonstrating that the proximity of immune cells to tumour cells[422] and other immune cells[423]

correlates with better prognosis of patients with pancreatic and oral squamous cell cancer, respectively. Importantly, in this Thesis, it was confirmed that both the quantity and location of immune cells to tumour cells were important for predicting patient survival in GC, with the proximity of immune cells to tumour cells being more important than proximity between different immune cells. A recent publication has shown that despite the elevated CD8+ TILs number observed within human lung and colorectal tumours, a large proportion were CD39-negative non-tumour-specific bystanders[595]. This suggests that the overall abundance of immune cells does not fully denote functional importance.

Multiple approaches for targeting TAMs have been explored with targeting of CD206-positive[619, 641] or CD163-positive[638] populations showing therapeutic promise in mouse models. The findings from this study suggest that if the same compounds/antibodies examined in these studies[619, 638, 641] were used to treat a GC patient, the combination of both may have synergistic effects if the CD163+ TAMs are truly immune suppressive. In addition, given the high expression of CD206 and CD163 on resident macrophages in the lung[453] and liver[460], respectively, this dual targeting of CD206+ plus CD163+ TAMs may have different the overall side effects related to macrophage depletion compared to using a single reagent alone.

Additionally, given their high PDL1 expression, therapies targeting the CD206+ TAMs may be combined with anti-PD1/PDL1 inhibitors[642] or be utilised as biomarker for patient stratification. Alternatively, targeting the angiogenesis-promoting CD163+ TAMs[643] could potentially be combined with other anti-VEGF agents to overcome macrophage-mediated drug resistance[644]. Moreover, a combination of macrophage targeting and radiotherapy[285] that results in removing macrophages within hypoxic regions after stereotactic radiation[201, 365] could possibly reduce the pro-tumour effect of TAMs[364] and limit the invasiveness of tumour cells[192, 645].

Importantly, the spatial distribution differences between the CD206+ and CD163+ TAMs could possibly be used for enhancing the precision of non-invasive tumour imaging[646]. Radioisotope-labelled antibodies (or fragments) targeting CD206[647, 648] or CD163[649] on macrophages are being developed for

PET imaging. The results from this study suggest that using a CD163 targeted PET tracer may provide a more precise identification of the tumour Core, whilst using a CD206 tracer alone or in combination with CD163 may assist in identifying the interface between the tumour site and normal gastric tissue.

In summary, the data in this study demonstrate how obtaining spatial information, in addition to overall cell density, could inform the identification of the true effective immune populations in the tumour as candidates for future studies and for more precise targeted diagnosis and therapy.

9.1.1.4 PDL1 expression on macrophages and immune therapy

The PD1/PDL1 axis is currently the most intensively examined immune checkpoint therapy for GC and many other solid tumours[650]. PDL1 immunohistochemical staining of tumours has been used as a biomarker for patient selection[126]; however, is now recognised that PDL1 is not a good predictor of patient survival[651] and response to treatments[126].

One study suggested that the expression of PDL1 on both GC tumour and stromal cells was associated with poor overall survival[133], whilst another study showed that PDL1 on both tumour and infiltrating immune cells was a predictor of improved overall survival[558]. Additionally, PDL1-positivity was only 50% predictive of response in metastatic GC patients undergoing PD1 inhibition[126]. Interestingly, it has recently been shown that heterogeneous origins of PDL1-expressing cells had a distinct influence on the immune system during early lung cancer development[468]. PDL1-expressing tumour cells were found to exhibit T-cell suppressive properties whilst PDL1-expressing TAMs (defined as $CD11b^{+}CD14^{+}HLA\text{-}DR^{+}$) were not inhibitory of cytotoxic T cell cytokine production or proliferation[468, 652]. Instead, TAM-derived PDL1 functioned as a self-protective mechanism for the macrophages during antigen presentation to effector cytotoxic T cells[468]. Although it is necessary to verify if these findings from other tumour models also exist in GC and if any functional differences exist between the CD163+ and the CD206+ TAMs as identified in this study, these data demonstrate that the source of PDL1 within the tumour microenvironment may not all be immune suppressive, and is grounds for further investigation with

the aim of more precise patient stratification in the use of checkpoint inhibitors (Figure 4.3.24).

In summary, the PDL1-analysing methods developed and the CD68/CD206 biomarker identified in this study could potentially be utilised and tested in a checkpoint-treated GC cohort with the potential to derive a more precise method for patient stratification.

9.1.2 Multiplicity in TAM origin

Tissue-resident and monocyte-derived macrophages were previously found to have opposing effects on tumour carcinogenesis using bone-marrow transplantation mouse models[346] (§1.4.2). However, functions of human macrophages cannot be determined using this methodology and there are no exclusive markers to distinguish these macrophage populations from each other[384].

While the markers used in the present study were not able to differentiate macrophages of different origins on their own, using a combination of marker signatures and spatial information, it was possible to identify the macrophage populations that were more abundant in the adjacent non-tumour tissue (e.g. the CD68-only, CD68+CD206++ and the CD68+CD163CD206+ macrophages) compared to the TAMs within tumour regions (Core, Edge and Margin). Surprisingly, the CD68+CD163+CD206+ macrophages, which express both M2-like markers, were found to be consistently located furthest from the tumour cells. This suggests that they were not the main population affecting tumour cells directly and may be bystanders co-existing in the microenvironment. These CD68+CD163+CD206+ macrophages showed accumulation at the tumour Margin and exhibited relatively high PDL1 similar to the CD206+ (CD163-) TAMs, but the environmental gene signature of these macrophages was more related to the CD163+ (CD206-) TAMs.

In a recent study, a subset of CD163+CD206+ omentum tissue-resident macrophages with high T-cell membrane protein 4 (TIM-4) expression has been shown to promote metastatic spread of ovarian cancer[653]. M-CSF-differentiated but unpolarised naïve macrophages have been shown to co-express CD163

and CD206[414]. Based on this evidence, it is possible that the CD68+CD163+CD206+ macrophages identified in this Thesis consist of several different populations, including (i) true tissue-macrophages, and (ii) a transient phenotype between the CD163+ (CD206-) and CD206+ (CD163-) populations (especially the macrophages that accumulate at the Margin), and (iii) recruited but unpolarised naïve macrophages (which may explain their distant relationship with the tumour cells). These data may reflect the differences in distribution between macrophages of different origins reported in the literature showing that the tissue-resident macrophages were located at the invasive front of a tumour whilst monocyte-derived TAMs resided at the intra-tumoural regions in a mouse glioma model[324] (§1.4.2).

In summary, the data in this Thesis show that, using a combination of multiple markers in conjunction with spatial information, it was possible to identify macrophage populations that were either more associated with normal tissue or with tumour. These macrophages could then be sorted from fresh GC tissue collected from different regions of a tumour for subsequent single-cell RNA transcriptional analyses to identify more specific markers and gene signatures to better characterise these different TAM populations.

9.1.3 Spatial and metabolic reprogramming of macrophages

A key finding of this Thesis is the heterogeneous but organised distribution of TAM populations across different regions of interest and tumour area. These data demonstrate that the distribution of TAMs was not random but was highly influenced by their proximity to tumour cells. There was an overall decrease of CD206 cells when moving nearer tumour cells. In contrast, there was an increase in IRF8, CD68 and CD163 expression on TAMs closest to the tumour core (tumour-nest; Figure 9.1.1). These gradual changes in markers between regions and areas of the microenvironment contributed to the spectrum of TAM populations observed in this study and could be related to (i) the dynamic metabolic activities in different regions[365] (§9.1.3.1 and §1.4.3) and (ii) the diffusion threshold of cytokines within the tissue[476-478] (§9.1.3.2).

9.1.3.1 Reflecting on the dynamic polarisation of TAMs *in situ*

The interaction between TAM populations remains relatively undescribed compared to other, better characterised, cell types such as T cells[422]. The diversity of both pro- and anti-inflammatory cytokines in a shared location can contribute to their heterogeneity[654] and the co-existence of different populations may not just reflect the interaction between terminally differentiated subtypes but also reflect the dynamic plasticity inherent to macrophages and the change from one phenotype to another[365]. For example, IL-1β and IL-6 are produced by pro-inflammatory macrophages[655] and the low level of autocrine IL-10 from these macrophages can serve as a self-protective mechanism[386-388] which can potentially polarise adjacent macrophages into M2-like phenotypes. In this study, the CD68+IRF8+, CD68+CD206+ and CD68++CD163+ TAMs were found to co-exist in the same tumour and correlated with increased in IL-1-, IL-6- and IL-10-associated pathways, respectively. Moreover, *IL-1β* is an early response gene and *IL-6* is a late response gene in inflammation[656, 657], suggesting that the co-existence of different TAM populations may also reflect their dynamic polarisation process in tissues[658] that was been captured in a snapshot of time.

In addition to the influence of environmental cytokines and chemokines on macrophage polarisation, reduced oxygen levels have been shown to be associated with a reduction in CD206 on an *in vitro* cultured mouse macrophage cell line[365]. This hypoxic response could be a reasons for decreased CD206 on TAMs closer to the GC tumour Core in human (Figure 9.1.1), as well as on mouse stomach TAMs (Figure 8.3.20) in this study.

In summary, the findings in the present study indicate there is utility in a more detailed TAM sub-classification based on co-localisation information that may help deconvolute whole tumour-derived gene expression data to understand the tumour microenvironment.

9.1.3.2 Identifying polarisation distance thresholds *in situ*

The diffusion distance of cytokines *in situ* is difficult to determine and likely differs between cytokines[478, 659]. Previous studies have examined the signalling of TNF-α in macrophages and IL-2 in T cells, using *in vitro* reporter systems

combined with computational modelling[476-478]. Interestingly, a distance of 40-50 µm was reported in these studies[476-478] to be the estimated maximum diffusion distance *in situ*. The median distance of TAM populations to tumour cells identified in this Thesis was within 10-30 µm and the number of TAM-tumour pairings all peaked within 10-20 µm of the tumour cells in the tumour Core, within this estimated cytokine diffusion range.

The 0-10 µm distance was defined in this Thesis as the criterion which resembled direct cell-cell interaction between neighbouring cells (§3.3.5). Therefore, this 10-20 µm zone with the maximum paring of TAMs and tumour cells could be viewed as the window where paracrine/autocrine effects of the TAMs convert into direct-contact interactions with the tumour cells. Importantly, using the spatial analysis methods developed in this study, the enhancement of NOX2 on the CD68++CD163+ TAMs was observed starting when 40µm apart and reached maximum when in 20µm in proximity with the CD8+ TILs (§7.3.6). In contrast, the PD1 expression on the CD8+ TILs was only upregulated when the TAMs and TILs were in direct contact. These findings suggest that, in combination with tissue-microdissection and cell-isolation techniques, the different distance thresholds (0-10 [direct contact], 10-40 [paracrine] and >50 µm) could potentially be used for partitioning the tissue for subsequent genomic/proteomic analyses[660] for future studies investigating TAM polarisation or phenotypic change *in situ*.

In summary, the data of this Thesis can (i) be used to generate hypotheses on how different immune cell populations communicate within the tissue and (ii) be utilised as additional variables to be put into computational models[476-478] to investigate cytokine/chemokine diffusion distance thresholds *in situ*.

9.1.3.3 Implication as a tumour microenvironment biomarker

In this Thesis, the distribution of TAM populations within the GC tumour was identified to be dependent on their proximity to tumour cells. However, no substantial associations were observed between TAM populations and clinical parameters, with the exception of survival-relevance of CD68++CD163+ TAMs. Clinical parameters including cancer subtypes and tumour staging, clearly define the progression of GC, but fail to inform on the heterogeneous and

dynamic change of the tumour microenvironment which is influential for TAM polarisation *in situ*[309]. This plasticity of TAMs may explain the inconsistency between studies attempting to identify TAM biomarkers of patient outcomes[211, 468]. However, due to this faithfulness of TAMs in reflecting environmental stimuli[309, 645], it makes them the ideal biomarker for studying different metabolic activities within the tumour microenvironment. It is technically difficult to stain each of the cytokines and chemokines in a tissue and, in addition, would be impossible to determine the "balance" of these pro- and anti-tumour signalling in the microenvironment with current technology. However, the detection of TAM populations may be more practical. A change from an anti- to a pro-inflammatory tumour microenvironment post immune checkpoint therapies has been reported in mouse models and was characterised by the shift from a CD206-dominant to an iNOS-dominant macrophage phenotype[301]. In this study, the abundance of CD68++CD163+ TAMs was related to an elevated inflammation score of patients and reflected the overall enhanced immune signalling in these tumours. Lastly, with the advance in computational machine learning, "immune context", which incorporates the density and distribution of multiple cell types, is now being examined as a biomarker by others[661]. This may increase the value of TAMs as indicators of a response to cancer therapies.

In summary, using the detailed TAM subgrouping methods described in this study, TAMs potentially could be utilised as critical references for studying the complicated and heterogeneous tumour microenvironment which is now considered as one of the drivers of GC progression[213] and indicators of choice of therapy and response[147].

9.1.4 Interaction of macrophages with other cells

9.1.4.1 TAM interaction with TILs

TAMs and TILs are two well documented immune infiltrates in GC[404, 650] and their spatial and transcriptomic interactions were investigated in this Thesis. TAM and TIL densities were found to be positively correlated within tumours suggesting the possible interaction between the innate and adaptive immune systems. Interestingly, the CD163 expression on TAMs was found to increase on TAMs nearer tumour cells, and was enhanced specifically within the clusters

of pSTAT6+ non-macrophage/tumour cells whose locational pattern resembled T cells. This suggest that the TILs, in addition to tumour cells, could be contributing to the polarisation of specific TAM populations *in situ*.

Helper T cells[662], regulatory T cells[663], tumour cells[664] and the monocytes/macrophages themselves[546] have all been reported as being the source of IL-10 which was identified as the cytokine related to the CD163+ (CD206-) TAMs in this Thesis. Interestingly, IL-10/IL-35-positive regulatory T cells have been shown to promote CD8+ T cell exhaustion[665] and activated regulatory T cells were found to secrete IL-13 and promote macrophage efferocytosis during inflammation resolution through a self-enhancing IL-10/STAT3-associated pathway[666].

In this study, the environmental gene signatures were compared between each TAM and TIL population. Their correlation was (i) described at the whole tumour scale (§5.3.2, §6.3.5 and §6.3.6), and (ii) a schematic model was generated by combining these results with their spatial distribution relative to tumour cells (Figure 9.1.2). However, the key factors as to why the CD163+ TAMs were enriched within the pSTAT6+ non-TAM cell regions, and the distribution of TAMs and TILs around tumour cells within regional microenvironments remain undetermined. These results indicate that inclusion of the staining of candidate cytokines within the gene signatures (e.g., IL-1, IL-6 and IL-10), as well as other cellular and microenvironment markers (e.g., cell death markers; as discussed in §7.4.5), are required to further elucidate the drivers of these dynamic interactions between cells.

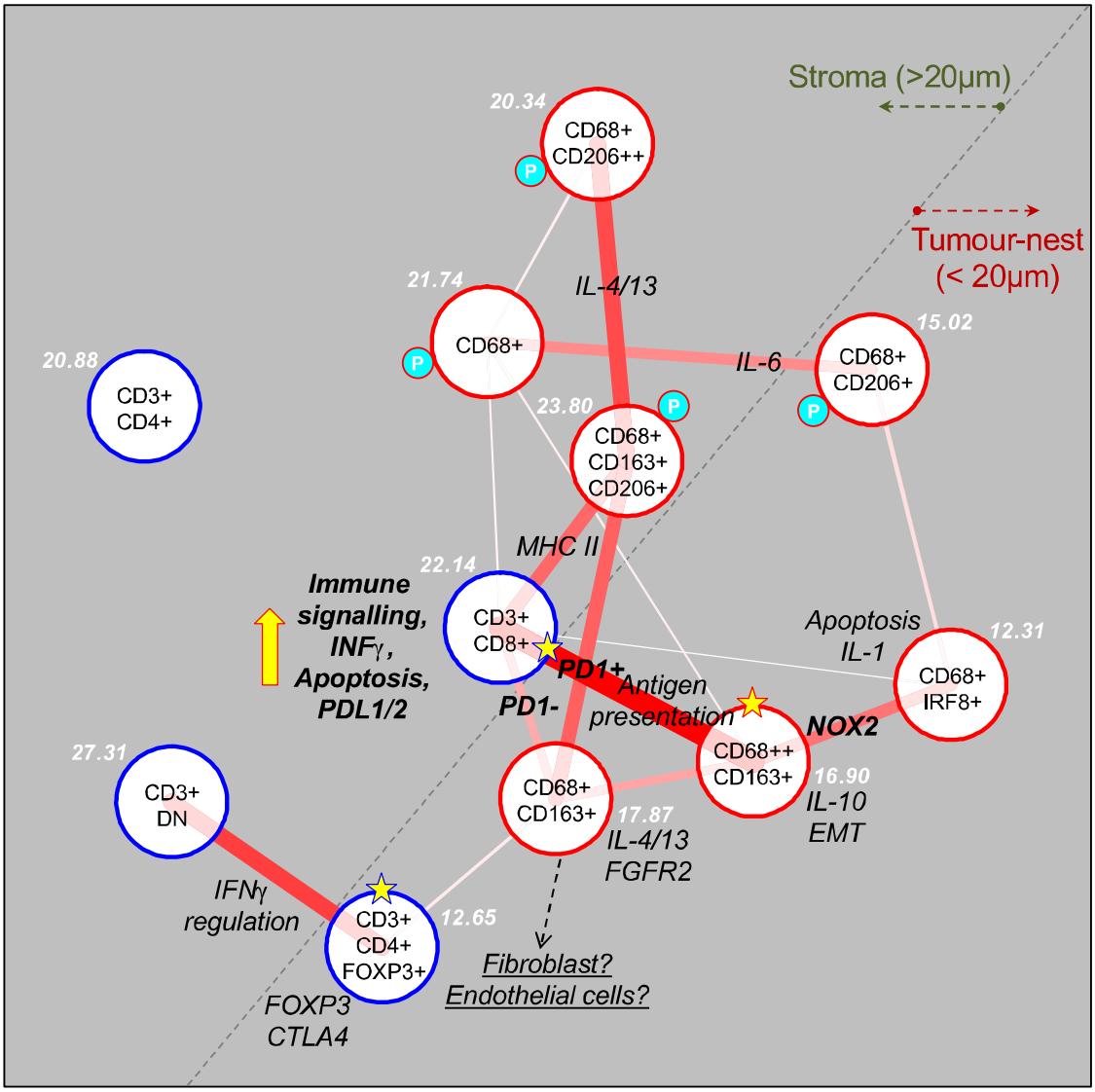


Figure 9.1.2 Schematic spatial and transcriptomic model of the TAMs and TILs within tumour Core

TAM and TIL populations are distributed unevenly between the tumour-nest and stroma and located at different distances to tumour cells. Each immune population is associated with a unique environmental gene signature and share different signalling pathways between immune cells. The CD68++CD163+ TAMs, CD8+PD1+ TILs and the CD3+CD4+FOXP3+ TILs are associated with improved patient survival in our cohort. Dashed line: distance (20 μm from tumour cell) defined tumour-nest and stroma. Red/Blue circle: TAM/TIL populations labelled. Lines connecting circles: significant Spearman correlation between cell populations. Thickness of lines represents significance of correlation. Number labelled on the circles: median distance of each population to tumour cells. Black labels: associated pathways/genes/markers unique to each cell population or shared between populations. Star sign: significant positive association with patient survival. Cyan P circle: PDL1-expressed populations.

The observation that TILs were related to the distribution of certain TAM populations may be one of the reasons for the limited therapeutic effects observed in clinical trial data targeting TAMs alone[667] and for why immune checkpoint blockade and chimeric antigen receptor (CAR) T cell therapy were less effective in solid tumours[668]. Due to the important roles of tissue-resident macrophages in non-tumour organs (as described in §1.4.2), the efficacy of current non-discriminant TAM-targeting approaches (§1.3.4) are limited so that overdosing of these drugs could lead to life-threatening side effects in humans[669] and in mice, as shown in the safety study in this Thesis (§8.3.1). The small proportion of TAMs that survived the targeting approaches could have been repolarised by both TILs and tumour cells into the functional TAMs needed for tumour survival given that macrophages have been shown to impede CD8 T cells in reaching the tumours[670]. This evidence suggests that to enhance the efficacy of anti-tumour effects of these therapeutic approaches, targeting both TILs and TAMs is required. Indeed, CAR T cells engineered to express IL-12 were shown to enhance anti-tumour effects via a macrophage-mediated response in mouse that was antigen independent[671]. Dual targeting of the innate and adaptive immune systems in mice with anti-CD47 (§1.3.4.3) and anti-PD1/PDL1 showed synergistic effects with checkpoint inhibitors against solid tumours and circulating tumour cells[278] by limiting tumour cell immune evasion[672].

These advances in the literature outline the demand for elucidating the possible interactions between the CD68++CD163+ TAMs and CD8+ TILs that could be associated with the NOX2/PD1 axis observed in this Thesis. This includes the actual functions regarding the TAM's immune promoting/suppressive property and the TIL's immune activated/exhausted status (as discussed in §7.4.5). Depending on the real effects of these TAMs, NOX2 inhibitors[673] or enhancers[674] could be tested in combination with checkpoint inhibitors as future therapeutic approaches. Bi/tri-specific antibodies[675, 676] that targets CD163 and CD8 could be developed to function as cellular linkers to facilitate the engagements of TAM/TIL pairs if they were cooperative. Blocking antibodies, such as targeting the MerTK (highly-expressed by the IL-10-polarised

macrophages[634] and TAMs[635]) and the PD1 on TILs, may be applied to avoid communications between these cells of interest.

In summary, published studies as described above suggest that dual targeting of innate and adaptive immunity may enhance the efficacy of immune checkpoint therapies. The NOX2/PD1 axis between the CD68++CD163+ TAMs and the CD8+ TILs identified in this study may be a novel target for future therapeutic approaches and the mechanism behind these cells is important to reveal.

9.1.4.2 TAM interaction with other cell types

In addition to TILs, cancer-associated fibroblasts (CAFs) are one of the stromal populations that have been shown to influence macrophage polarisation and function[677]. The co-existence of macrophages and fibroblasts has been shown to facilitate the formation of primary gastric organoids[678]. Feedback loops between these cell types via CSF-1 and platelet-derived growth factor (PDGF) were identified for maintaining tissue stability[391]. CAFs were found to promote M2 macrophage polarisation and coordinated with them to suppress NK cells functions in colorectal cancer[679]. Importantly, CAFs were shown to promote PDL1 expression on neutrophils via the IL6/STAT3 pathway and foster immune suppression[680]. This evidence suggest that the CAFs may be especially associated with the CD206+ TAMs, which were more stroma-oriented, accumulated at the tumour margin and may also be inducing their high PDL1 expression.

Dendritic cells[681], mast cells[682], myeloid-derived suppressor cells[683] (MDSCs) and NK cells[684] have all been reported to be associated with the TAM functions or with GC progression in the literature. While no specific data on these interactions were investigated in this study due to limitations in the number of antibodies with the OPAL multiplex IHC system, it would be an interesting area to pursue as a future direction. A better understanding of the cooperation of the whole immune/stroma system could elucidate the role of TAMs and their polarisation *in situ*.

9.1.5 Macrophage markers: Too similar and too different

One of the most challenging aspects of characterising macrophages is the lack of exclusive markers between populations[384]. In this study, although none of the markers were exclusive and overlapped between TAM populations and tumour regions, using their combined marker signatures with spatial information could enhance the interpretation and identification of different TAM populations *in situ* through their relative distances to tumour cells and between immune cells. Moreover, the inclusion of functional markers (e.g. PDL1, NOX2, and PD1), in addition to lineage markers, could provide further information on the status of activation of immune cells and improve our understanding of their putative functions within the tumour environment and ultimately their impact on clinical outcomes.

Interestingly, a significant difference in the CD206 expression on macrophages in the gastric mucosa of mouse and humans was observed in **Chapter 8**. This result highlights the need to carefully assess the use of animal models in translating macrophage-related findings into humans. However, the pattern of decreasing CD206 from the stroma toward the tumour region was conserved between species and also between tumours in mice at different locations, suggesting a certain level of similarity in CD206 regulation that may be due to the level of hypoxia[365]. Given the difficulty in accessing human tissues, using mouse models for the identification of regulators of CD206 and for functional studies will remain an informative tool.

9.1.6 The roles of macrophages in gastric cancer

The overall aim of this Thesis was to elucidate the roles of macrophage populations in gastric carcinogenesis and their putative functions at spatial and transcriptomic levels. Multi-function and plasticity are the hallmarks of macrophages[240] and were reflected in the gene signatures derived from this study (Figure 9.1.3).

A number of gene signatures were used or generated in this study including:

(i) Published by Busuttil *et al.*[213] which utilised the MAUGIC-Affy cohort to identify the stromal-gene correlation with macrophages in GC

(ii) Refined literature-derived, *in vitro*-polarised macrophage signatures (Figure 5.3.16) which characterised a specific subset of patient with high immunity

(iii) Overall CD68++CD163+ TAM-derived environmental gene signatures (genes correlated with cell density; Figure 5.3.10)

(iv) The refined CD68++CD163+ TAM signature (genes identified with pathway analyses; Figure 5.3.11)

(v) Highly-upregulated genes between patients grouped with the refined CD68++CD163+ TAM gene list (High-to-Low in Figure 5.3.11).

These TAM gene signatures were associated with cellular functions ranging from (i) stromal[213] and epithelial–mesenchymal transition to (ii) immune response[415] and inflamed tumour microenvironment[137] (Figure 9.1.3). These data may be one of the reasons why the influence of macrophages in gastric cancer literature is so diverse. Macrophages are involved in a variety of biological process and most studies only focus on a subset of those biological activities, making it difficult to de-convolute their specific function when looking at an entire tumour microenvironment.

In summary, careful evaluation of the relationship of different macrophage populations with the tumour microenvironment, among macrophages and with other cell types are required. Accepting their spectrum of phenotype or activation state[320] with spatial information[420, 466], combining RNA profiles at the single cell level[306], and integrating the information from other immune cell types with machine learning[661] and system immunology[685], could improve our understanding of this mercurial cell type.

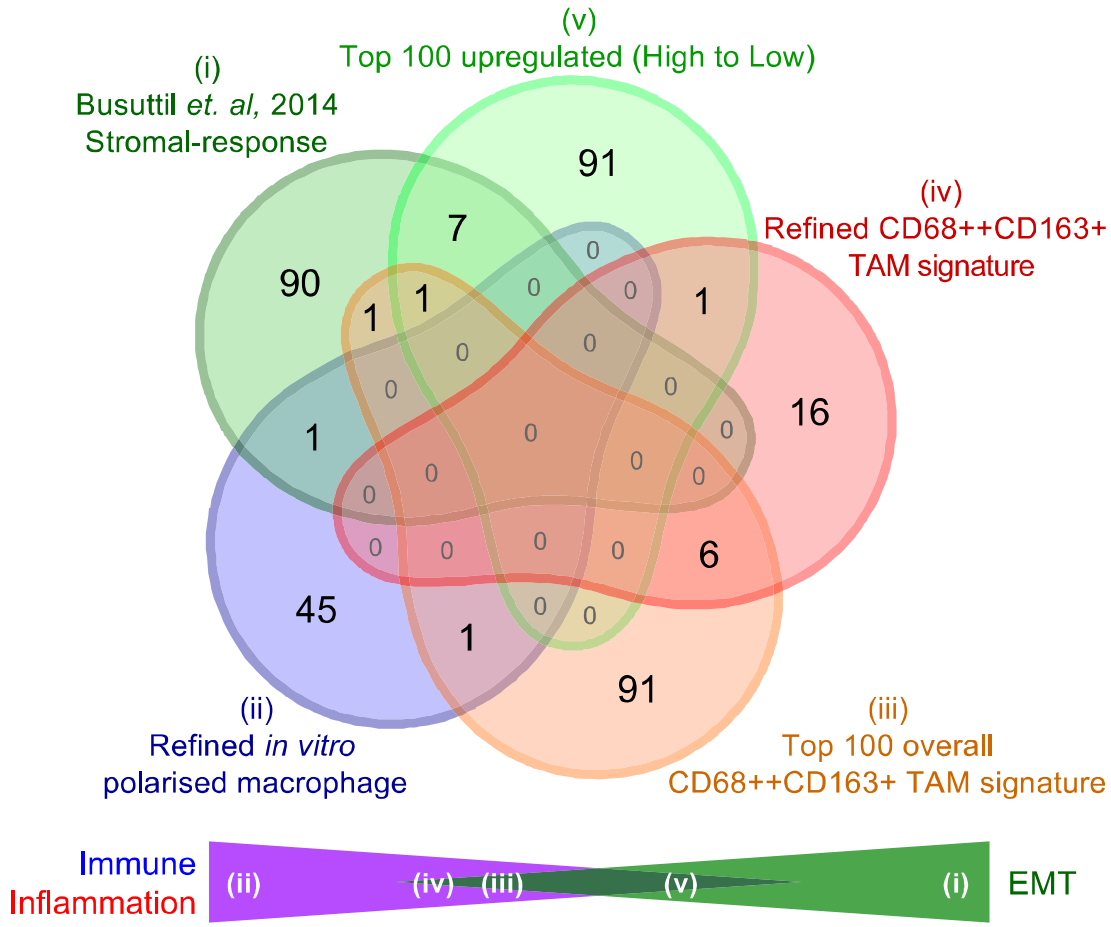


Figure 9.1.3 Multi-function and plasticity of macrophages in gastric cancer

EMT: epithelial-mesenchymal transition. (1) Stromal genes[213] identified by Busuttil *et al.* to be associated with macrophage in GC. (2) Refined *in vitro*-polarised macrophage genes related to Figure 5.3.16. (3) Top 100 overall and (4) refined CD68++CD163+ TAM-derived environmental gene lists related to Figure 5.3.10 and Figure 5.3.11, respectively. Identified with Spearman correlations between density and gene expression for (3), and further incorporating associated pathways for (4). (5) Top 100 upregulated (fold change) genes between patients grouped with the refined CD68++CD163+ TAM gene list (High to Low in Figure 5.3.11).

9.2 Limitations

9.2.1 Subjective phenotyping and criterion setting

While mIHC was superior in characterising the spatial heterogeneity of TAMs, the number of TAM populations identified in this study was restricted due to the limitation of the technology (e.g. number of colours available) and marker availability (e.g. cytokines) compared to using other techniques (e.g. flow cytometry, CyTOF, single-cell sequencing)[320, 322]. Therefore, similar to any other types of IHC studies, subjectiveness in mIHC remains a problem that is inherent in the technology.

In this study, the results from subjective cell phenotyping were validated with unsupervised clustering methods, with the combination of marker signatures, with gene signatures from published literature and with online cancer survival cohorts demonstrating the reproducibility of the findings. Absolute expression thresholds to define marker positivity were difficult to determine between and within patient samples, the use of relative expression (high/low) for the marker was more appropriate. However, whether these differences in intensity represented cell types with different functionality require further investigation which will require isolation of TAM populations of interest for genomic/proteomic analyses in future studies.

Last but not least, it cannot be overemphasised that the results from this Thesis do not advocate that “seven” is the optimal grouping for TAMs but rather it was referred as seven “predominant” populations. The groupings were based on the four TAM markers used with mIHC within the setting of GC. This number can be further refined if additional markers are incorporated and may change if the same panel were applied to another cancer model.

9.2.2 Correlation is not causation

Environmental gene signatures were generated with cell densities in this study to provide putative identities of these cell populations within the tumour microenvironment and were used as surrogates of the cellular density information for the samples that were not available for mIHC techniques. However, these were done in the context of whole-tumour lysates where cells of

gene expression origin were unknown. The gene expression data would have been affected by the dominant cell types with higher proportion among all cells within the tumour. Therefore, further work is required to investigate the origin of these genes for more specific therapeutic implications.

Importantly, while survival associations were made with some TAM and TIL populations in this study, these analyses were done by comparing patient survival to tumour samples *ex vivo*. Further investigations are needed to evaluate if an enhanced immune infiltrate observed within the tumour microenvironment could reflect to their systemic immune activity and the efficiency of their immune system in killing malignant cells. Non-tumour samples (e.g. blood) collected from the same patients may be utilised as additional biomarkers to determine their immune activities.

9.3 Remaining challenges and future directions

This Thesis demonstrates how spatial information assists the utilisation of the macrophage spectrum model[307, 320] to elaborate on the putative function of TAMs *in situ*. Remaining challenges include overcoming the limitations discussed in the previous section (§9.2) and the identification of the spatial properties of additional markers that were not included in this study.

Firstly, to improve the specificity of macrophage classifications, the inclusion of additional lineage markers (e.g. CD45, CD11b), is required. However, this approach will need to compromise markers used for macrophage population classification if using the current mIHC method. A possible alternative approach could be the use of the newly-developed Imaging Mass Cytometry technique, which allows co-staining of 40 markers simultaneously on a single tissue section[686-688]. This technique, similar to CyTOF, utilises the spectral signatures of metal isotopes to overcome the spectral-overlap of traditional light-based fluorescent dyes for more sensitive and precise detection of biological targets. This could improve the specificity of TAM classification and also aid in refining TAM populations. More importantly, functional markers for the CD68++CD163+ TAMs and CD8+PD1+ TILs, as discussed in §7.4.5, and lineage markers for other cell types can be incorporated to gain a more comprehensive view of the interaction of cells *in situ*. In addition to visualising markers of interest, spatial transcriptomic methods[660, 689, 690] which allow gene profiling at selected regions of a tissue section could be applied. These techniques, involve either (i) tissue segmentation of specific regions followed by RNA extraction or (ii) acquire RNA profiles of a tissue region directly using microscope slide-attached primers, providing additional spatial information in parallel to allow gene expression compared to single-cell RNA sequencing. However, these technologies are limited in resolution with the diameter of approximately 100 µm compared to the majority of cell distances to tumour cells identified in this study that were described as being within 20 µm, suggesting the spatial transcriptomic methods may not yet be ideal for identifying cells of origin.

Secondly, the combination of single-cell RNA-seq with mIHC or Imaging Mass Cytometry of the same sample could help improve the subjective nature of the

imaging methods by combining spatial data and quantitative gene expression data. These complementary results could provide the functional status of each TAM population and inform the appropriate thresholds for marker positivity within a continuous spectrum model[307, 320]. Genes of interest from the sequencing data could then be validated with the imaging method at a protein level similar to the multiplex NOX2 panel described in this Thesis and to confirm the signal origins within the microenvironment.

Finally, it is unavoidable that functional assessments of targets and information from these types of studies need to be conducted in appropriate model systems. Functional assessments of these targets will need to be validated *in vitro* (e.g. co-culturing of TAMs and TILs with tumour cells using 3-D migration/invasion assays) and *in vivo* for specific therapeutic targeting purposes and could be tested on different cancer models given the possible different nature of immune context observed in this study (§7.4.5 and §9.1.4.1).

9.4 Concluding remarks

Macrophages are diverse populations of cells[189] with great therapeutic potential in cancer[240]. In this Thesis, I aimed to explore the presence, biology and clinical influence of the spectrum[320] tumour-associated macrophage model in the context of gastric cancer. As a result, I

1. Established multiplex IHC and bioinformatic platforms for understanding cell-to-cell interactions *in situ*
2. Outlined the spectrum model[320] of tumour-associated macrophages and their tumour-orientated spatial heterogeneity at both macro and micro levels
3. Generated environmental gene signatures which may reflect the interactive process between immune cells and with the tumour microenvironment
4. Presented the similarities between tumour-associated macrophages and *in vitro*-polarised macrophage populations and further summarised possible cytokines that may be relevant to their polarisation *in situ*
5. Identified the CD206+ TAM population as most relevant to high PDL1 expression
6. Proposed the NOX2/PD1 axis as a possible mechanism underlying improved patient survival associated with the CD68++CD163+ TAMs and CD8+ TILs
7. Established an *in vivo* macrophage depletion protocol in a mouse model of gastric cancer invasion and metastasis

More importantly, I provided the insight of how a spectrum macrophage model with spatial content can be utilised to interpret their biological interactions within gastric cancer. I demonstrated the importance of using high-resolution characterisation (i) to understand the role of macrophages in tissues, (ii) to identify the effective immune populations as potential therapeutic targets and prognostic indicators and (iii) to understand the dynamic interactive immune landscape in gastric cancer.

Appendices

Appendix 1 Macrophage spatial heterogeneity in gastric cancer defined by multiplex immunohistochemistry, Nature Communications, 2019 (Main and Supplementary data)

nature COMMUNICATIONS

ARTICLE

https://doi.org/10.1038/s41467-019-11788-4 OPEN

Macrophage spatial heterogeneity in gastric cancer defined by multiplex immunohistochemistry

Yu-Kuan Huang[1,2,3], Minyu Wang[1,2,3], Yu Sun[2,3], Natasha Di Costanzo[1], Catherine Mitchell[4], Adrian Achuthan[3], John A. Hamilton[3,5], Rita A. Busuttil[1,2,3] & Alex Boussioutas[1,2,3]

Tumor-associated macrophages (TAMs), one of the most abundant immune components in gastric cancer (GC), are difficult to characterize due to their heterogeneity. Multiple approaches have been used to elucidate the issue, however, due to the tissue-destructive nature of most of these methods, the spatial distribution of TAMs in situ remains unclear. Here we probe the relationship between tumor context and TAM heterogeneity by multiplex immunohistochemistry of 56 human GC cases. Using distinct expression marker profiles on TAMs, we report seven predominant populations distributed between tumor and non-tumor tissue. TAM population-associated gene signatures reflect their heterogeneity and polarization in situ. Increased density of CD163+ (CD206−) TAMs with concurrent high CD68 expression is associated with upregulated immune-signaling and improved patient survival by univariate, but not multivariate analysis. CD68-only and CD206+ TAMs are correlated with high PDL1 expression.

[1] Upper Gastrointestinal Translational Research Laboratory, Peter MacCallum Cancer Centre, Melbourne, Victoria 3000, Australia. [2] Sir Peter MacCallum Department of Oncology, The University of Melbourne, Victoria 3010, Australia. [3] Department of Medicine, Royal Melbourne Hospital, The University of Melbourne, Victoria 3010, Australia. [4] Department of Pathology, Peter MacCallum Cancer Centre, Melbourne, Victoria 3000, Australia. [5] The Australian Institute for Musculoskeletal Science (AIMSS), The University of Melbourne and Western Health, St. Albans, Victoria 3021, Australia. Correspondence and requests for materials should be addressed to A.B. (email: alex.boussioutas@petermac.org)

Gastric cancer (GC) is one of the leading causes of cancer-related deaths worldwide[1]. This may, in part, be attributed to different GC subtypes, heterogeneous tumor microenvironments (TME) and/or limited treatment options[2]. GC is commonly described using histological criteria into intestinal, diffuse and mixed subtypes[3]. More recently, an integrated genomics-based approach reported by TCGA[4] revealed four GC molecular subtypes: Epstein-Barr virus-positive (EBV), microsatellite instability (MSI), chromosomal instability (CIN), and genomically stable (GS), with each subtype demonstrating different TMEs and clinical outcomes[2]. The EBV and MSI GC subtypes are associated with higher degrees of immune signaling and therefore are candidates for immune-checkpoint therapies (ICT), including those targeting programmed death ligand 1 (PDL1)[5]. PDL1 expression has been used to stratify GC patients for ICT, however, is an imprecise biomarker of response[6] suggesting a requirement for more stringent selection criteria.

Upregulated PDL1, detected in approximately 40% of GC cases, has been positively associated with tumor-associated macrophage (TAM) infiltration[7]. TAMs are one of the most abundant immune components in cancers[8] and are characterized by their plasticity and multiplicity of function, contribution to tumor metastasis, immune suppression, and resistance to therapy[9]. However, the role of TAMs in GC is conflicting. TAMs were shown to be related to a stromal-associated gene signature and poor patient outcome[10], but have also been correlated with a high degree of tumor cell apoptosis and good prognosis[11]. This disparity may be associated with their heterogeneity within individual tumors[12,13].

TAMs are a diverse population of cells[14]. The bipolar M1/M2 paradigm which describes the polarization of macrophages in cell culture with lipopolysaccharide (LPS) and interferon-γ (IFN-γ) (M1) or interleukin-4 (IL-4) and IL-13 (M2) has been widely used to classify TAMs[15]. However, accumulating evidence suggests that this is an oversimplification and their complexity would be better described as a dynamic spectrum of phenotypes[16]. Macrophages were shown to exhibit distinct transcriptomes in response to different in vitro stimuli[17] and high-dimensional TAM heterogeneity has been described in different tumor models[18,19]. Advances in single-cell sequencing has significantly improved our understanding of the myeloid compartments[20]. However, due to the limitations of these methods which destroy the tumor architecture, the spatial relationship between different TAM populations in situ remains a significant problem[21].

In the current study, we sought to comprehensively investigate the TAM spatial heterogeneity in GC, and additionally, to determine their relevance to PDL1 and patient survival. A multiplex immunohistochemistry (m-IHC) panel consisting of surface and intracellular markers was designed: CD68, an endosomal/lysosomal glycoprotein that is highly expressed by the mononuclear phagocytes, was used as a pan-macrophage marker[22–24]; scavenger (CD163) and mannose (CD206) receptors are highly expressed by the M2-like macrophages[8,25–27], while interferon regulatory factor 8 (IRF8) is upregulated in M1-like macrophages[28] and was associated with their functions[29–31]; the immune-checkpoint marker PDL1 was incorporated; and AE1AE3 (pan-cytokeratin) was used for identifying tumor cells[32].

Using this panel, we describe seven predominant TAM populations characterized by specific combinations of markers on individual cells. Location, PDL1 expression, and environmental transcriptome signature associated with each population are determined. Our results reveal the spatial distribution of TAM heterogeneity in situ in GC and highlight how TAM characterization with m-IHC may provide further information on macrophage polarization in different tumor anatomic regions. This may assist in the identification of possible therapeutic targets.

Results

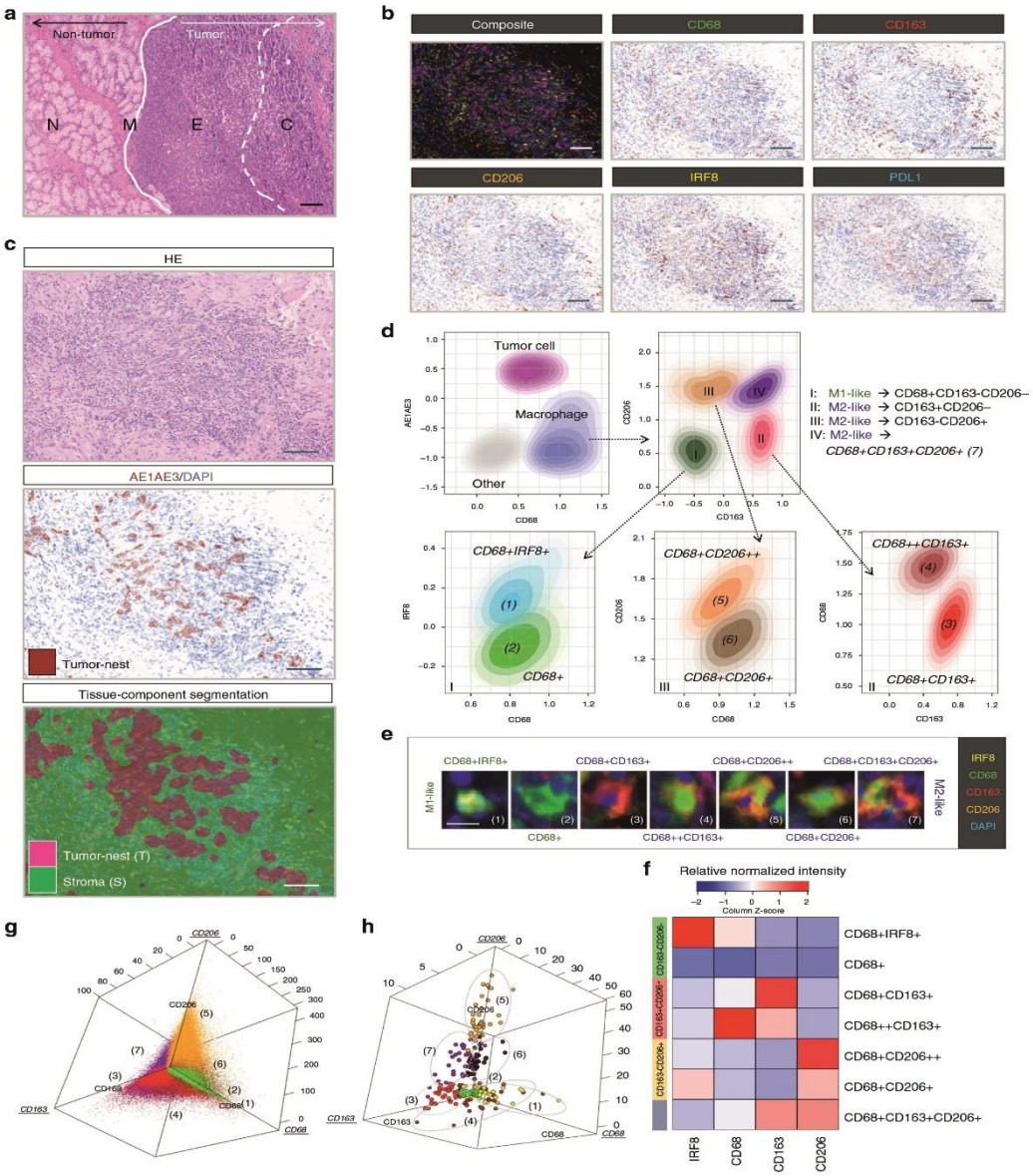
Experimental definitions and conditions. To investigate the macrophage landscape within GC, 56 full-face formalin-fixed, paraffin-embedded (FFPE) patient samples were selected (Supplementary Table 1; see Methods section). An H&E-stained tissue section was reviewed by an anatomical pathologist (C.M.) to identify tumor core (C, major body of the tumor mass), edge (E), margin (M), and non-tumor normal (N), which we refer to as regions of interest (ROI). These represent tumor position relative to surrounding tissue (Fig. 1a; see Methods). The serially sectioned tissue was stained with the m-IHC panel (Fig. 1b, c). A total of 1800 high power fields (C: 52%, E: 13%, M: 21%, N: 14%) were imaged across all patient ROI. A supervised image analysis system (inForm[33]) was used to segment each image into tumor-nest[34] (AE1AE3+) and stromal (AE1AE3−) areas (Fig. 1c). In addition, cell phenotyping data were obtained based on the pattern of marker expression (Fig. 1d–f).

Characterization of macrophage populations. Macrophage marker expression was analyzed at a single-cell level and seven major populations were characterized and validated (Fig. 1d–f, Supplementary Figs. 1, 2). Criteria for identifying macrophages were CD68 positive and AE1AE3 negative staining. Macrophages were further subdivided based on the positivity and relative intensity of other markers[8,27,35].

Two M1-like TAM populations were identified based on the absence of CD163 and CD206. The CD68+IRF8+ TAMs had high nuclear IRF8 staining, whereas the CD68+ macrophages were only positive for CD68 (negative for other markers). Five M2-like TAM populations were identified by the presence of CD163 and/or CD206. The CD68+CD163+ and CD68++CD163+ TAMs were distinct from each other with the latter population having significantly higher CD68 expression (Supplementary Fig. 1c–e). TAM populations expressing negligible CD163 were characterized using differential expression of CD206, referred to as CD68+CD206++ and CD68+CD206+ (Supplementary Fig. 1f, g). The final population, CD68+CD163+CD206+, expressed both M2-like markers.

The individual TAMs for all patients were plotted based on the intensity of CD68, CD163, and CD206 (Fig. 1g) providing evidence of a spectrum of macrophage populations. The average intensity of each marker was then determined on a per patient basis (Fig. 1h) confirming that these populations are represented within each individual patient sample and ROI (Supplementary Fig. 2).

Distinct distribution of TAM populations across ROI. To examine the TAM distribution within the microenvironment, we analyzed the spatial density of the populations, characterized above, within different ROI. A significant increase of the overall macrophage density was observed within the tumor regions (core, edge, and margin) compared with the adjacent normal tissue (Fig. 2a). The TAMs exhibited a more M2-like phenotype at the margin whilst a significant increase in proportion of M1-like TAMs was seen in the core (Fig. 2b). The distribution of each TAM population was then explored (Fig. 2c). The CD68+, CD68+CD206++ and CD68+CD163+CD206+ macrophages were abundant in all ROI but given their dominant presence in the adjacent normal tissue (white circle; Fig. 2c and Supplementary Fig. 3a), they could be associated with the normal-tissue macrophages more than tumor-associated macrophages. CD68+CD163+CD206+ macrophages accumulated at the margin and decreased toward the core. In contrast, the CD68+IRF8+ macrophages increased significantly from the margin into the core which contributed to the shift of the M1-like to M2-like ratio (Fig. 2b and Supplementary Fig. 3b).



Higher densities of CD68+CD163+, CD68++CD163+, and CD68+CD206+ macrophages were found within the tumor regions when compared with normal tissues suggesting that these populations were polarized according to their location in the tumor microenvironment (Fig. 2c).

The localization of TAMs with respect to the tumor-nest and stromal areas (defined in Fig. 1c) was further examined. The CD68+CD163+CD206+ macrophages were located primarily in the stroma across matched patient samples (Fig. 2d, e). In contrast, CD68+IRF8+ macrophages, were more abundant in the

Appendix 1 Continued

Fig. 1 Identification and characterization of macrophage populations. **a** Regions of interest (ROIs): adjacent normal tissue (N), margin (M), edge (E), and core (C). Scale bar: 100 μm. **b** Representative composite and single-stained IHC images of the multiplex IHC panel. Scale bar: 100 μm. **c** H&E, single-stained AE1AE3, and tissue-component segmentation of the same region. Scale bar: 100 μm. **d** Multiplex IHC panel design: gating strategy for each TAM population (numbered). **e** Seven major TAM populations. Positivity (+) of corresponding markers and relative intensity between populations is indicated. Scale bar: 10 μm. **f** Marker signatures used for TAM population characterization in patient samples ($n = 35$). Relative normalized intensity: relative original intensity of each marker divided by exposure time. **g**, **h** 3D plots showing the intensities of TAM populations from (**g**) single cells ($n = ~8.5 \times 10^6$ from 56 patients) and (**h**) averaged per patient ($n = 35$). Unit of axis: Normalized intensity. Key: Orange: CD68+CD206++, Brown: CD68+CD206+, Green: CD68+, Yellow: CD68+IRF8+, Dark red: CD68++CD163+, Red: CD68+CD163+, and Purple: CD68+CD163+CD206+. TAM populations are as numbered in (**d**) and (**e**)

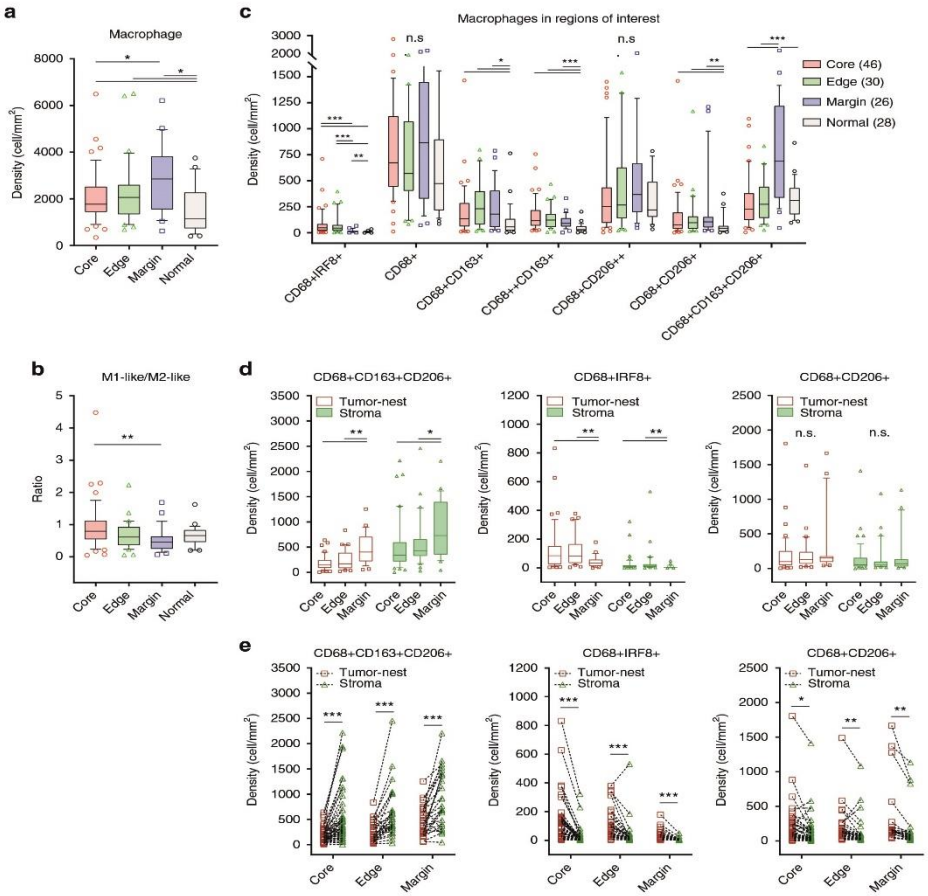


Fig. 2 Distinct distribution of TAM population densities across regions of interest. **a**–**c** Spatial distribution of TAM populations: **a** Overall TAM density, **b** M1-like to M2-like ratio, and **c** Density of each TAM population. Core (red circle): $n = 46$, edge (green triangle): $n = 30$, margin (blue square): $n = 26$, normal (white circle): $n = 28$. **d**, **e** Density of selected TAM populations between the Tumor-nest (dark red square) and Stroma (dark green triangle) areas (**d**) among the ROIs and (**e**) in matched (dash line) patient samples. Box and whiskers represent mean ± 10–90 percentile. Each point represents one patient. $^*p < 0.05$, $^{**}p < 0.01$, $^{***}p < 0.001$ and not significant (n.s.). Mann–Whitney *U* test

core compared with the margin (Fig. 2c, d), and were located within the tumor-nest than in the stroma (Fig. 2e). The CD68+CD206+ population was also found to be more specific to the tumor-nest area (Fig. 2e) but did not differ among the ROIs (Fig. 2d). No other quantification of TAM densities were significant between the tumor-nest and stromal areas and were independent of GC subtypes and clinical parameters (Supplementary Fig. 3c–f).

TAM composition is associated with tumor cells. The observation that certain macrophage populations were enriched in the tumor region (Fig. 2e), suggested the proximity of TAMs to tumor cells might influence their phenotype. To further study these localization patterns[36], a bioinformatics tool (ISAT; see Methods[37]) which determines the nucleus to nucleus distances between any two cell types was developed (Fig. 3a).

Distances between cells within the tumor core were analyzed and identified the CD68+IRF8+ macrophages as the population located in closest proximity to the tumor cells with a median nucleus-to-nucleus distance of 12.3 μm (Fig. 3b). In contrast, the CD68+CD163+CD206+ macrophages were furthest from the tumor cells (median distance 23.8 μm). The distribution patterns of TAM populations relative to tumor cells at the edge and margin were similar to those in the core (Supplementary Fig. 4a).

To incorporate both cell proximity and quantity, an "effective percentage" parameter was introduced (Fig. 3a). This represents the proportion of macrophages that had a tumor cell within defined distance criteria. A significantly higher percentage of the CD68+CD206+ and the CD68+IRF8+ macrophages had tumor cells within a 10 μm radius (median effective percentages of 31 and 27%, respectively; Fig. 3c and Supplementary Fig. 4b). The CD68+CD163+CD206+ macrophages (12%) were the least associated with tumor cells within this range.

When the distance was extended to within 10–20 μm, the CD68+IRF8+ macrophages (47%) remained the major population associated with tumor cells. The CD68++CD163+ macrophages (40%) were the next most abundant (Fig. 3c and Supplementary Fig. 4b) and the CD68+CD163+CD206+ macrophages remained the abundant population beyond 20 μm from the tumor cell (Fig. 3c, d).

These results indicate that despite being a large population within the tumor, the majority of CD68+CD163+CD206+ macrophages were located at a distance approximately 2–3 average cell-lengths from the tumor cells. The majority of the CD68+IRF8+ macrophages (78%) had tumor cells within 20 μm radius of their nucleus (Fig. 3d). All TAM-tumor pairings peaked within 10–20 μm, a distance which would put cells into direct contact with each other. This suggests that this distance may be the zone for TAM polarization or phenotypic change in situ, and could potentially be used as a threshold for partitioning the tissue for subsequent genomic/proteomic analyses.

Collectively, our data show that the predominant TAM population differs phenotypically between the tumor and adjacent normal tissue (Fig. 2). The same phenotypic differences were observed in macrophages proximal to the tumor cells (Fig. 3b–d).

Influence of TAMs on patient survival. To assess the relevance of TAMs to relapse-free survival (RFS) and overall survival (OS), patients were stratified based on the density of TAMs within the tumor core (Supplementary Fig. 5a–c). The core was chosen as it comprises the majority of the tumor mass and also because some tumors, particularly those of diffuse histology, do not have a definitive margin.

In a univariate analysis of outcome, TAMs expressing CD68++CD163+ within the core were associated with improved RFS, but not OS (Fig. 3e and Supplementary Fig. 5d). This observation did not reach statistical significance after multivariate analysis incorporating known clinical prognostic factors (Supplementary Fig. 5e).

The effective density (0–10 μm), which reflected the absolute number of macrophages that had a tumor cell within a 10 μm radius (defined as direct contact), was used as an additional measurement. The results showed that patients with a higher effective density of CD68++CD163+ macrophages had significantly longer RFS and OS (Fig. 3f and Supplementary Fig. 4d) when compared with patients with lower TAM density. No other TAM population was found to be associated with patient survival (Supplementary Figs. 4c–f, 5).

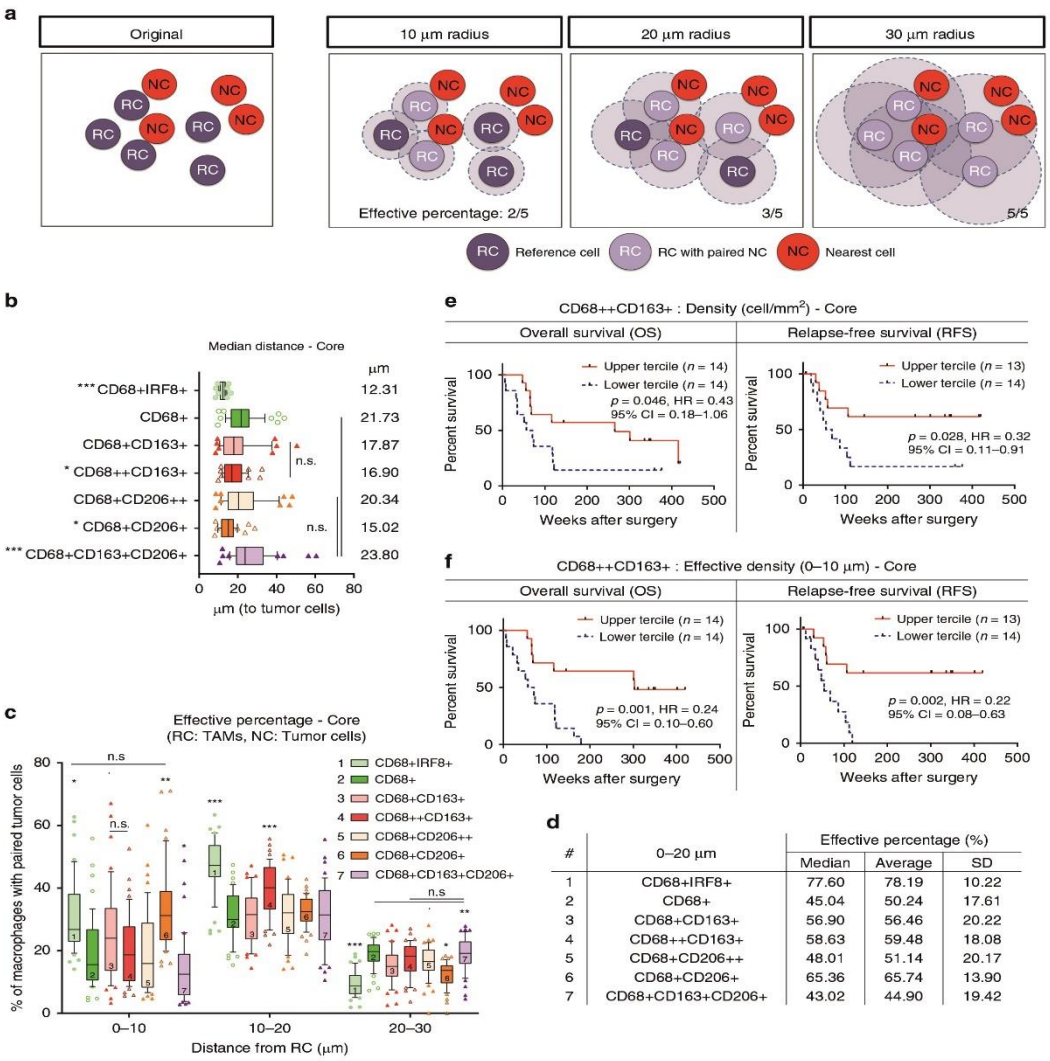
There were no survival differences found if only proximity or cell proportion (median distance, effective percentage; Supplementary Fig. 4c, e) but not cell number (overall density, effective density) was used as patient classifying factors. These results indicate that the influence of CD68++CD163+ macrophages on patient survival could be relevant to both the number of macrophages and their proximity to tumor cells. In summary, our data indicate that to determine the influence of TAMs on tumor cells and patient survival, location in addition to population density, should be taken into consideration.

Different TAMs co-localize in a same tumor microenvironment. The co-existence of different TAM populations in the tumor microenvironment has been recognized previously[8,34], but their interaction is not well studied in GC. To understand the possible interaction between these macrophages, first the co-localization of TAMs within the tumor core was investigated. The CD68+IRF8+ macrophages were significantly enriched in an environment with increased CD68++CD163+ and CD68+CD206+ TAMs, but negatively associated with the CD68+CD206++ and CD68+CD163+CD206+ TAMs. The CD68++CD163+ population was further co-localized with the CD68+ and CD68+CD163+ TAM, which was, in turn, significantly related to the CD68+CD163+ CD206+ populations (Fig. 4a and Supplementary Fig. 6a).

Environmental signatures reflect TAM polarization in situ. Environmental factors which contribute to the dynamic process of macrophage polarization in vivo[38] might be the cause of TAM co-localization patterns. To further study the influence of these factors, the TAM densities in the core were correlated with whole tumor-derived transcriptomic microarray data (Affymetrix U133+ 2)[10] derived from the same patient ($n = 34$) to generate TAM population-specific environmental gene signatures (Fig. 4b).

The genes that were significantly correlated ($p < 0.05$; Spearman correlation) with each TAM density were identified as the signature for each TAM population. The most relevant pathways associated with each signature were further determined using Reactome[39] (Fig. 4b). These signatures comprised of the genes that were population unique and also some shared elements between populations (Supplementary Fig. 6b). Significant pathways (FDR < 0.05; Benjamini-Hochberg[40]) are listed in Supplementary Fig. 6c.

Microenvironments with abundant CD68+IRF8+ TAMs were characterized by an increase in IL-1 signaling and inflammatory/apoptotic cell death pathways (Fig. 4b). The CD68++CD163+ population was characterized specifically by increased IL-10, extra-cellular matrix (ECM) organization, other interleukin signaling pathways and the down-regulation of DNA repair pathways. The CD68+CD206+ population was defined by enrichment in multiple interleukin signaling pathways, especially IL-6. The CD68+CD163+CD206+ population showed



d

#	0–20 μm	Effective percentage (%)		
		Median	Average	SD
1	CD68+IRF8+	77.60	78.19	10.22
2	CD68+	45.04	50.24	17.61
3	CD68+CD163+	56.90	56.46	20.22
4	CD68++CD163+	58.63	59.48	18.08
5	CD68+CD206++	48.01	51.14	20.17
6	CD68+CD206+	65.36	65.74	13.90
7	CD68+CD163+CD206+	43.02	44.90	19.42

Fig. 3 TAM composition is associated with their proximity to tumor cells. **a** Schematic illustration of the distance analysis involving reference cell (RC) and nearest cell (NC). Each RC was paired with a neighboring NC in 10 μm increments from its nucleus. Effective percentage represents the proportion of RC that had a paired NC in a given distance. **b** Median distance of TAM populations (RC) to tumor cell (NC). Box and whiskers represent mean ± 10–90 percentile. Each dot represents one patient. Core: $n = 46$. *$p < 0.05$, **$p < 0.01$, ***$p < 0.001$ and not significant (n.s.). Mann–Whitney U test comparing between TAM populations. Circle: M1-like macrophages. Triangle: M2-like macrophages. **c**, **d** Effective percentage of TAM populations in the core (**c**) within 10 μm increments and (**d**) within 0–20 μm. **e**, **f** Overall survival (OS) and relapse-free survival (RFS) classified by the (**e**) overall CD68++CD163+ TAM density and the (**f**) effective density (0–10 μm) in the tumor core. Effective density (0–10 μm): the number of TAM that had a tumor cell within a 10 μm radius. Upper tercile (density > 2/3 of the patients in the cohort; red line), Lower tercile (density ≤ 1/3 of patients in the cohort; blue dash line). Log-rank (Mantel-Cox) test

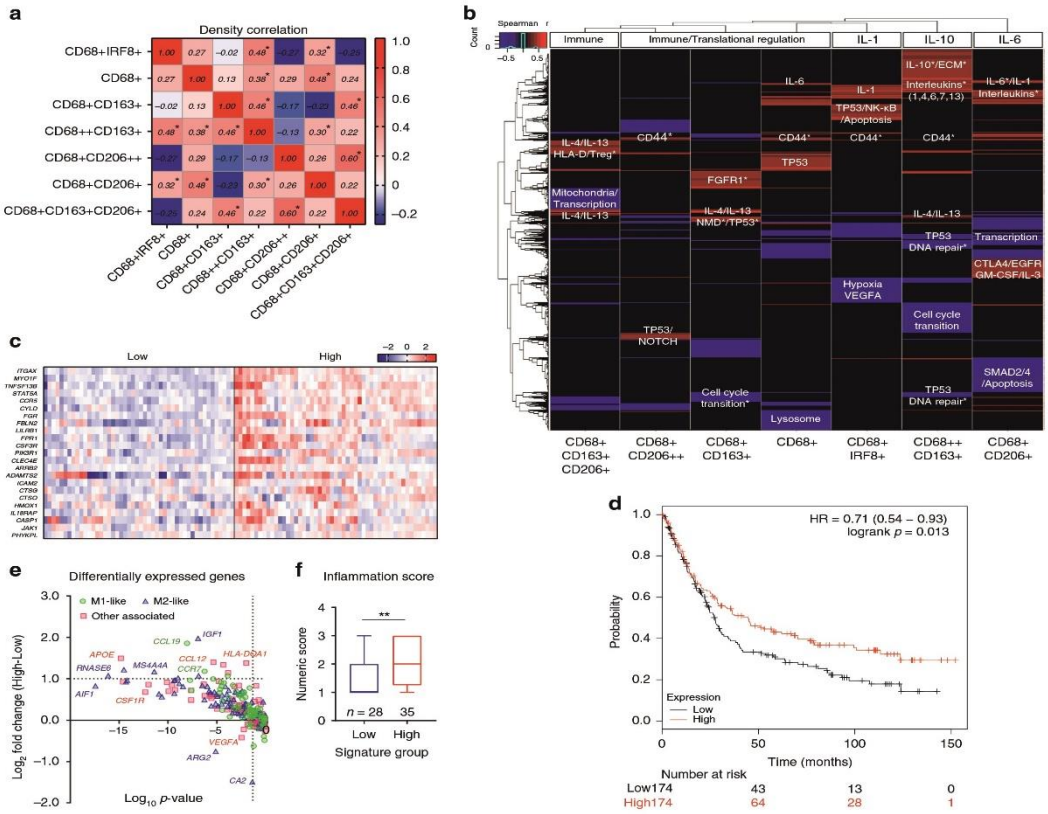


Fig. 4 High CD68++CD163+ TAM density reflects a more inflamed microenvironment and enhanced immune-cell infiltration. **a** Spearman correlation of TAM population densities in the tumor core. Red/white/blue: positive/no/negative correlation. *$p < 0.05$. **b** Unsupervised clustering of TAM-associated environmental signatures and associated pathways. List of genes that were significantly correlated with each TAM population density of a matched patient sample ($n = 34$) were identified with the Spearman correlation. Red/black/blue: positive/no/negative correlation. *FDR < 0.05 (Benjamini-Hochberg[40]). **c** Patients in the MAUGIC cohort ($n = 99$) grouped using a refined CD68++CD163+ TAM signature (gene expression most significantly correlated with cell density, $p < 0.001$; Spearman correlation). Key: relative gene expression. **d** Validation of patient overall survival classified by the refined CD68++CD163+ TAM signature using KMplot[41]. Above (red) and below (black) the median expression of the gene signature. Log-rank (Mantel-Cox) test. **e** Differentially expressed macrophage-associated genes, and **f** inflammation scores between the high-low patient groups in the MAUGIC cohort. Box and whiskers represent mean ± 10–90 percentile. **$p < 0.01$. Mann–Whitney *U* test

upregulation in IL-4/IL-13 signaling pathways and genes relevant to the development of regulatory T cells. These results, together with the pattern of density distribution between ROIs (Fig. 2c) and the co-localization pattern (Fig. 4a), may reflect the dynamic process of macrophage polarization in situ.

High density of TAMs reflects an inflamed microenvironment. To explore possible reasons underlying the survival advantage in patients with an enriched CD68++CD163+ population, a refined gene signature using the genes that were most significantly correlated ($p < 0.001$; Spearman correlation) with its density within the core was developed (Fig. 4c). This signature was validated using our extended patient cohort ($n = 99$; Fig. 4c, Supplementary Fig. 6d, e). A publically available online GC survival database ($n = 348$)[41] was then tested, patients with above median level of expression of this signature had an improved overall survival (Fig. 4d).

To investigate the immunological features of patients grouped with the refined CD68++CD163+ TAM gene signature (Fig. 4c), differentially expressed macrophage and other immune-cell related genes were compared. Upregulation of both M1-like and M2-like macrophage and also T and NK cell related genes were observed (Fig. 4e and Supplementary Fig. 6f). This also correlated with increased inflammation scores[42] as determined by a pathologist (C.M.; Fig. 4f) and with high CD3+CD8+ T cell number in the core (Supplementary Fig. 6g). These data suggest

that high CD68++CD163+ TAM density reflects an enhanced host immune response and could be one reason for the improved patient survival seen on univariate analysis.

High PDL1 expression in CD68-only and CD206+ macrophages. Inhibition of PDL1 by ICT has been assessed as a potential therapeutic for GC[5]. The data presented in this study show that PDL1 is expressed by all TAMs (Fig. 5a), however, the CD68+CD206+ macrophages had significantly higher mean PDL1 expression per patient compared with the other TAM populations (Fig. 5b). Given the pattern of PDL1 in the tumor microenvironment was related to cell location, cell number and intensity on each cell (Fig. 5a); PDL1 expression on the individual cells across all ROIs was further analyzed. It was observed that all cell types, including macrophages and tumor cells, had a proportion of cells with high PDL1 expression (Supplementary Fig. 7a). Using the mean PDL1 expression across individual cells in the cohort (visible PDL1 staining; Supplementary Fig. 7b) as a threshold of positivity, thirty two percent of all cells (irrespective of cell types) were defined as PDL1+ (Fig. 5c and Supplementary Fig. 7b, c; see Methods).

The number of PDL1+ macrophages (regardless of population) was similar to the number of PDL1+ tumor cells. More TAMs were within the top 10% of the PDL1+ cells in our cohort (Fig. 5d). A more detailed interrogation of the data identified three abundant PDL1+ TAM populations, namely CD68+, CD68+CD206++ and CD68+CD163+CD206+ (Fig. 5d and Supplementary Fig. 7c). To control for differences in the cellular infiltrate (Fig. 2c) that may influence the absolute number, the percentage of PDL1+ cells in each cell type was compared. All three CD206+ TAM populations had at least 36% of cells that were PDL1+ (Fig. 5d and Supplementary Fig. 7c). However, although the percentages of PDL1+ cells within the CD206+ macrophages were similar, their intensity expression patterns were different (Fig. 5e). CD206+ (CD163−) macrophages exhibited most intense expression, whereas the CD68+CD163+CD206+ macrophages were equally distributed among different intensities.

These results showed that the CD68-only (high in number) and the CD206+ TAMs (high in number and percentage of cell type) were the main PDL1-expressing populations in our cohort. The high mean PDL1 expression on CD68+CD206+ observed per patient was due to having a larger proportion of PDL1+ cells (Fig. 5d).

PDL1 expression on TAMs is associated with cancer subtype. To associate PDL1+ TAMs with different GC subtypes, we identified the TAM population with the highest PDL1 intensities from each patient. PDL1-high patients ($n = 44$) were categorized by having any TAMs represented in the top 1% of the total cell population (Fig. 5c and Supplementary Fig. 7b). Among the PDL1-high patients, the CD68+ macrophages were predominant in the GS and diffuse subtypes, whereas the CD68+CD206++ macrophages were enriched in the MSI and intestinal subtype (Fig. 5f). In addition, TAMs in the GS and diffuse cancer subtypes had significantly lower median PDL1 expression (Fig. 5g). Whilst we found a significant association between PDL1+ TAM in GC subtypes, we did not find substantial survival differences using TAM-PDL1 expression (Supplementary Fig. 7d). Indeed, the PDL1 expression was more predictive of cancer subtype than TAM composition (Supplementary Fig. 7e).

High PDL1+ TAMs are located in the tumor-nest. From the results above, TAM populations with the highest PDL1 expression were identified. Using the tumor core as the region of interest, the location of these PDL1+ TAMs was further investigated by comparing the expression changes of PDL1 on TAMs at the interface between the tumor-nest (T) and stroma (S) areas (TS; Fig. 6a, b).

The mean PDL1 expression defined the threshold for PDL1 positivity as described in Fig. 5c. Using this threshold, the level of PDL1 expression by tumor cells (AE1AE3+) was at the threshold and the other non-macrophage cells (Other) were negative (Fig. 6b). Most TAMs expressed PDL1 below this threshold in the stroma but showed a progressive increase of PDL1 with increasing proximity to the tumor cell. The CD163+ and CD68+CD206+ macrophages were found to continuously upregulate PDL1 as they became more embedded in the tumor-nest. The CD68+CD206+ macrophage was the only PDL1+ population detected in the stroma (Fig. 6b and Supplementary Fig. 8a). We found a similar pattern of PDL1 expression in other ROIs and confirmed lower PDL1 expression in the GS and diffuse cancer subtypes (Supplementary Fig. 8).

Macrophage marker expression differed between tumor areas. Markers expressed by macrophages often reflect their function[8]. The change in macrophage markers at the TS interface was investigated using the mean expression of CD68, CD163 and CD206 of tumor (AE1AE3+) and non-macrophage (other) cells as baseline thresholds (Fig. 6c–e).

The CD163+ and CD68+IRF8+ macrophages exhibited a minimal twofold increase in their CD68 expression between the TS areas and this was induced ~25 μm before engaging the TS interface (Fig. 6c). The CD206+ (CD163−) and CD68-only TAMs had relatively little changes. The results suggested that the CD163+ and CD68+IRF8+ macrophages may differ in their phagocytic abilities[22] compared with the CD206+ (CD163−) macrophages and the induction of CD68 did not require direct contact between the TAMs and the tumor cells.

With increasing proximity to tumor cells, an increase in CD163 expression was observed in all CD163+ macrophages (Fig. 6d). Interestingly, unlike CD68 and CD163, the expression of CD206 on each TAM population was not differential across the TS areas and only the CD68+CD206++ macrophages showed slightly increased expression within the tumor-nest (Fig. 6e). However, the CD68+CD206+ TAMs were predominately located within the tumor-nest (Fig. 2e) suggesting that the overall CD206 expression on the CD206+ (CD163−) macrophages (CD68+CD206++ plus CD68+CD206+) decreases as they near the tumor cells.

Discussion

Characterization of TAMs in GC has been complicated due to their adaptive changes to environmental stimuli[38], the lack of exclusive markers between populations[43] and the differences between human and animal models[44]. Hence, despite intensive investigation on macrophage heterogeneity[9,20], the distribution of different populations in situ remains unclear in humans. Accumulating evidence suggests that using a combination of markers would be a more reliable approach to distinguish between populations or activation states[21]. Techniques to study TAM populations include IHC[27,45,46], CyTOF[18], flow cytometry[35,47], and single-cell sequencing[20,48]. While the multiplex IHC utilized in this study was limited to using a few cell markers, its strength was its ability to spatially resolve TAM heterogeneity.

Here we describe the use of multiplex IHC on human GC tissues to characterize TAM populations in a spatial context and ultimately their association with clinical outcomes based on the proximity of TAMs to tumor cells. We have identified TAM

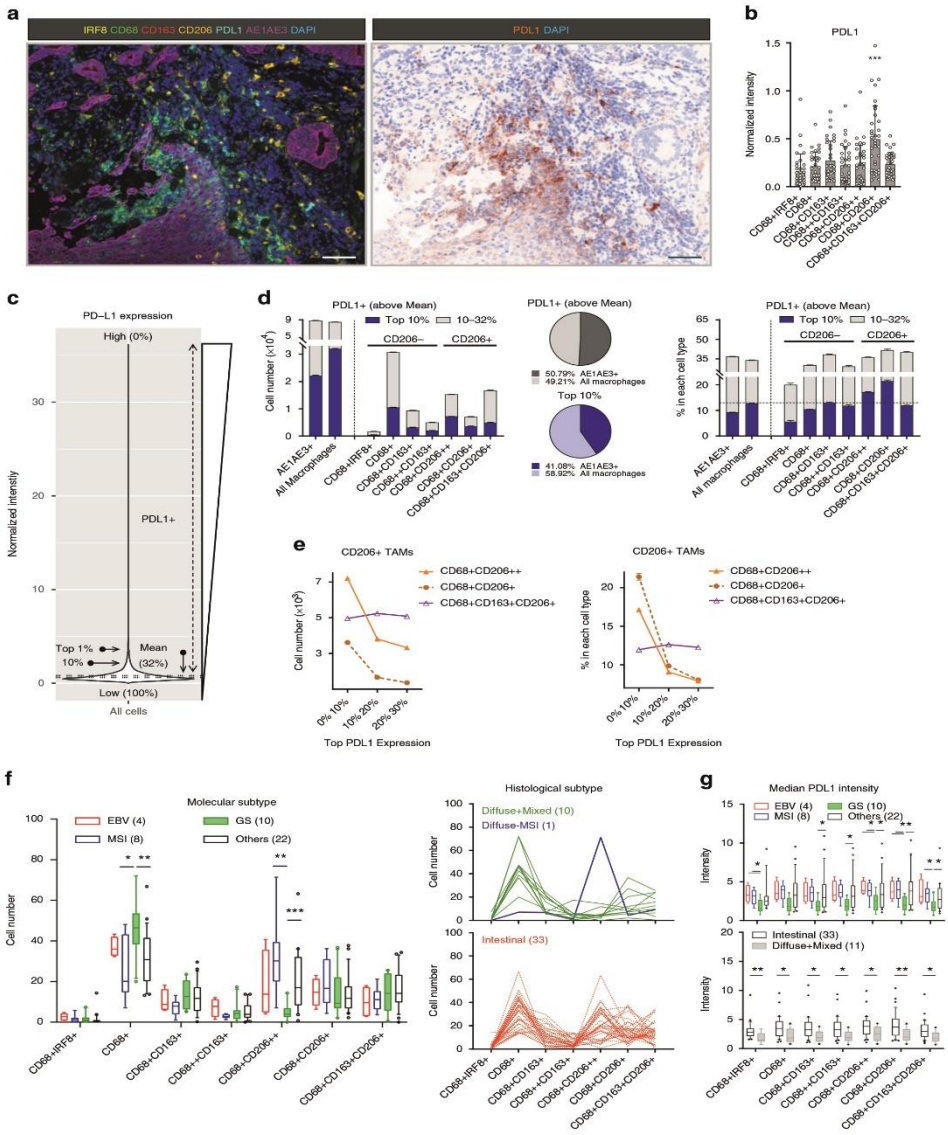
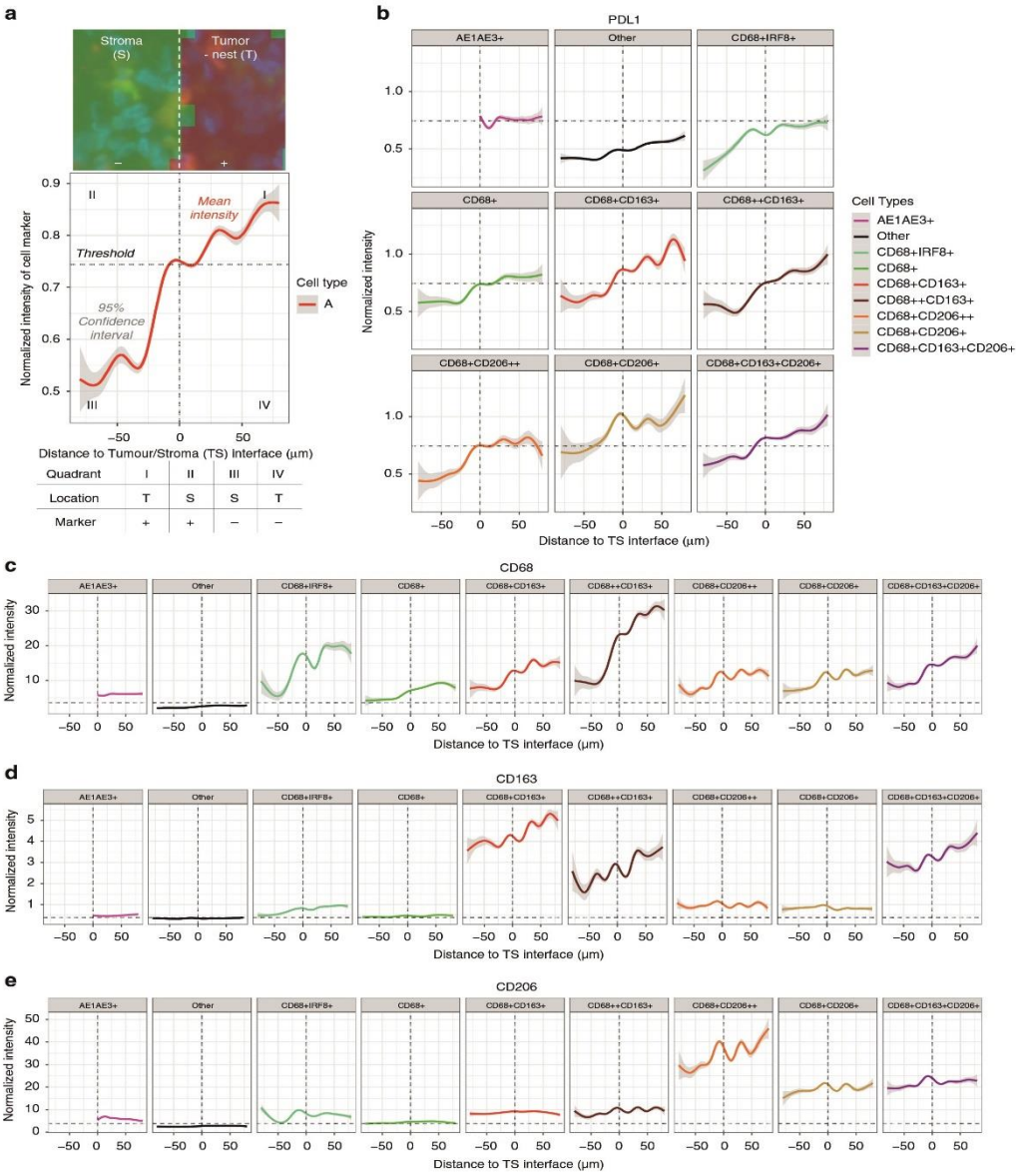


Fig. 5 PDL1 expression in GC is both TAM and GC subtype associated. **a** Representative images of PDL1 expression in the tumor core. Scale bar: 100 µm. **b** Mean PDL1 intensity per patient ($n = 35$) for each TAM population. Error bars represent mean ± SD. **c** Distribution of PDL1 expression on individual cells in a sampling cohort regardless of cell types. Equal number (10^4) of cells per patient ($n = 56$, all ROIs included) were randomly selected to normalize between sample sizes. Cells were pooled as a sampling cohort. 32% of the cohort was defined as PDL1+ with the mean expression of the cohort. **d** Cell number and percentage of different PDL1 intensity expressing cells in each cell type. Error bars represent mean ± SD of five independent randomly selected subsampling cohorts. **e** PDL1 expression patterns of CD206+ TAMs: Cell number and percentage in each population. Error bars represent mean ± SD. $n = 5$. **f** Cell number and **g** median PDL1 expression on TAM populations in patients grouped by different GC subtypes. Box and whiskers represent mean ± 10–90 percentile. Each point/line represents one patient. $^*p < 0.05$, $^{**}p < 0.01$, $^{***}p < 0.001$, and not significant (n.s.) Mann–Whitney *U* test



population-specific environmental gene signatures and pathways that provide some information on the influence of the microenvironment on these TAM populations and their putative functions (Fig. 7).

We report seven predominant TAM populations distributed in a nonlinear spectrum based on the staining of four markers. The majority of the CD68+IRF8+ TAMs (78%) were within 20 µm of tumor cells. This proximity may reflect the functional gradient of

Fig. 6 Macrophage marker expression differed between the tumor-nest and stroma. **a** Tumor-nest (red, T) and stroma (green, S) areas in each image were segmented using inForm software (see also Fig. 1b). Intensity change of markers between the TS regions was determined by randomly assigning equal number of cells ($n = 500$, minimum number available between samples) from both areas per patient (core). The marker of interest was plotted with the mean (red) and the confidence intervals (gray). The interface between TS regions was defined as point zero, positive and negative values on the *x*-axis indicate the tumor cell and the stroma region, respectively. Thresholds were applied to define the positivity of markers. Quadrants: I: cell type A located in the tumor-nest and is positive (+) of the marker tested. II: stroma, positive. III: stroma, negative (–). IV: tumor, negative. **b** Change in PDL1 expression with distance from the TS interface for each macrophage population. Threshold: mean PDL1 expression defined in Fig. 5c. **c**–**e** Change of (**c**) CD68, (**d**) CD163, and (**e**) CD206 expression with distance from the TS interface. Thresholds: mean expressions of CD68, CD163, and CD206 on the tumor and non-macrophage cells (Other)

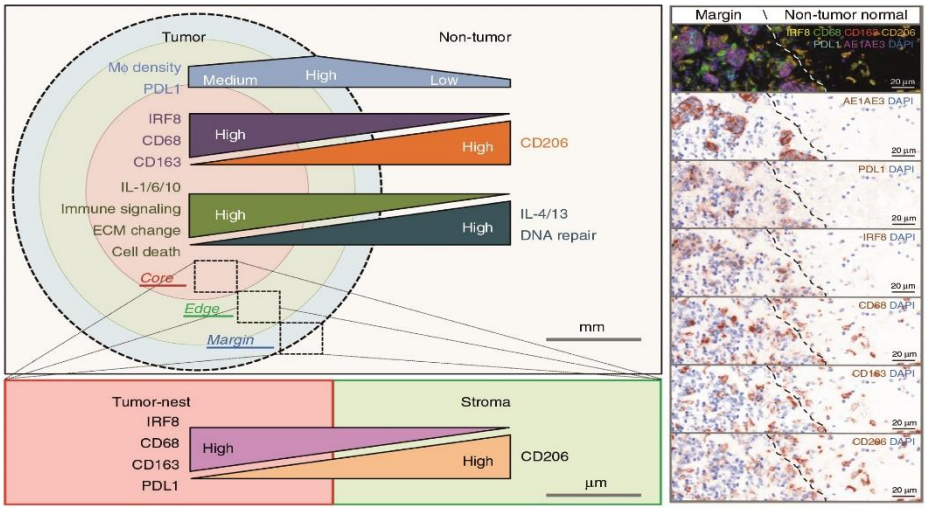


Fig. 7 Schematic model of spatial macrophage heterogeneity in anatomic regions in gastric cancer. A proposed model suggesting that TAM density and marker expression varies between GC sample regions. Distinct marker expression profiles on TAMs were associated with their population disparity between the tumor site and non-tumor tissue and between the tumor-nest and stroma. TAM populations were associated with signature pathways which may help inform of their function and polarization status. Similar trend of marker changes on TAMs were observed between the tumor-nest and stromal compartments within different tumor regions (core, edge, or margin). Mϕ: macrophage. ECM: extra-cellular matrix

cytokines such as interferons[28] which are thought to trigger M1-like macrophage polarization but also suggests that these TAMs may function through direct contact with a tumor cell. Micro-environments enriched with this TAM population were characterized by the increase of IL-1 related genes and cell death signaling. However, these M1-like TAMs did not significantly impact on patient survival which may be due to their relatively low number compared with the other M2-like TAM populations.

Surprisingly, the CD68+CD163+CD206+ macrophages, expressing both M2-like markers, were abundant in the tumor regions but were consistently located furthest from the tumor cells. This suggests that they may not be the main population affecting the tumor cells directly. Our data show an inverse relationship between CD163 and CD206 expression on TAMs as they near the tumor cells. The CD68+CD163+CD206+ population may include some cells that are of a transient phenotype between the CD163+ (CD206−) and CD206+ (CD163−) populations and also some unpolarized macrophages that co-express CD163 and CD206[43].

The effects of TAMs on GC patient outcome in the existing literature are conflicting. These studies[25,26] invariably use either single staining of CD68 or dual staining in combination with either CD163 or CD206 to identify TAMs using the useful but oversimplified bipolar model[49]. Our data support recent publications advocating the reassessment of using bipolar classification[15,17] and our findings suggest that the presence of CD68+CD163+CD206+ TAMs could possibly dilute out the contributions of smaller populations which may have prognostic value, such as the CD68++CD163+ TAMs.

In a univariate analysis we found that clinical outcome was associated with TAM number and their proximity to tumor cells, highlighting the importance of investigating the distribution of cells. This proximity to tumor cells suggests that cell–cell contact and/or paracrine effects are key to their function.

Interestingly, the high number of CD68++CD163+ TAMs in close proximity to the tumor cell resulted in improved prognosis of patients in our cohort. Although we are unable to describe a cell-specific mechanism to explain this observation, clues may be found from the environmental signatures associated with this TAM population and the nature of the markers expressed. Functionally, CD68 has been shown to be the receptor for apoptotic cells and may be involved in antigen processing[22]. CD163 is a high affinity haptoglobin-hemogobin and HMGB1 scavenger receptor[50] and has been found to be

upregulated on macrophages polarized by IL-10, but not IL-4[51], which is consistent with our findings of higher IL-10-associated signaling pathways in cases where CD68++CD163+ macrophages were abundant. CD163+ macrophages have been shown to localize at perivascular areas[52], clear apoptotic debris, and engage in endocytosis[53]. This evidence suggests that the CD68++CD163+ TAMs may function in the clearance of dead cells, tissue remodeling and anti-inflammatory processes. High numbers of this population near the tumor cell may reflect an enhanced immunological response in these particular tumors.

While high CD68++CD163+ TAM density proximal to the tumor correlated with improved survival in univariate analysis, this was not confirmed in a multivariate model incorporating known prognostic clinical parameters (e.g., age, tumor stage). Larger cohorts are required to confirm our observation.

The interactions between TAM populations have been relatively difficult to determine compared with other more established cell types (e.g., T cells[36]). The diversity of both pro- and anti-inflammatory cytokines in a shared location can contribute to their heterogeneity[54] and the co-existence of different populations might not just reflect the interaction between terminally differentiated subtypes but also reflect the plasticity inherent in macrophages and the change from one phenotype to another[8,55]. For example, IL-1β and IL-6 are produced by pro-inflammatory macrophages[56]. Low level of autocrine IL-10 from these macrophages can serve as a self-protective mechanism[57,58], which can potentially polarize adjacent macrophages into M2-like phenotypes. In our data, we found the CD68+IRF8+, CD68+CD206+, and CD68++CD163+ macrophages to be co-localized in the same tumor and were correlated with the increase of IL-1-, IL-6-, and IL-10-associated pathways, respectively. These results suggest that the co-existence of different TAM populations could resemble their dynamic polarization process in tissue[59], and when more detailed TAM subgroupings were applied, this co-localization data could potentially be used for the deconvolution of whole tumor-derived gene expression data. In addition, it would be difficult to determine the balance of cytokine and chemokines in the TME even by staining every possible target, but the detection of TAMs may be more pragmatic.

Collectively, our results show that CD163 and CD206 clearly stain different TAM populations and that not all M2-like marker-expressing macrophages might be affecting tumor cells directly[34]. The compositions of TAM populations change not only in millimeter scale between the tumor site and the adjacent normal tissue but also within microns of the tumor cells. These phenotypic differences are due to the relative changes in the expression of CD68, CD163, and CD206 at different distances from the tumor cells and could be associated with different environmental stimuli, possibly related to the metabolic activities in different regions[55] and the propagation threshold of cytokines within the tissue[60,61]. Conclusively, our data demonstrate that TAMs in situ are not just randomly distributed but are influenced by their proximity to tumor cells and the tumor microenvironment.

Consistent with previous reports[4], PDL1 was more highly expressed in the EBV and MSI GC subtypes in our cohort. PDL1 expression was not restricted to a specific cell type but our results showed that PDL1+ TAMs accounted for around 50% of all PDL1+ cells and exhibited some of the highest PDL1 expression. The CD68-only and CD206+ macrophages were identified to be the major PDL1+ populations. These findings raise the possibility of combining checkpoint inhibitors with macrophage targeting strategies in future immunotherapy studies for GC. Given our finding of specific high PDL1 expression on the CD206+ TAMs, the combination of PDL1 and CD206 could potentially be utilized as an alternative biomarker to PDL1 alone, to identify and stratify patients as candidates for ICTs[6,62]. Moreover, we found PDL1 expression by all TAMs, including the M1-like populations, increased when they were located within the tumor-nest. This result suggests that, despite the fact that the number and proportion of PDL1+CD68+IRF8+ TAMs were the least among all TAMs, their close proximity to tumor cells may confer immunosuppressive properties to other immune cells. This data highlight the complexity of the role of TAMs in GC in vivo where a spectrum of TAM populations coexist, and may represent plasticity that does not easily reconcile with the in vitro M1/M2 model.

There are certain limitations to an m-IHC study and the sensitivity and specificity of the antibodies used is a limiting factor. Whilst CD68 is a recognized mononuclear phagocyte marker, low CD68 expression can be found on other cell types[22]. As a result, the CD68-only population is likely to contain a proportion of non-macrophage cells. In addition, PDL1 positivity may differ between different antibody clones[62]. This provided the rationale for not only defining PDL1 expression with an arbitrary threshold but to analyze the intensity of staining of individual cells. Third, due to the limitations associated with the number of markers that can be used per sample, the number of TAM populations identified in our study was restricted compared with studies using other techniques[18,19]. This number can be further refined if additional markers are incorporated, therefore, we do not state that we defined the optimal grouping for TAMs but investigated the spatial distribution of the populations we can distinguish. Last, whilst we were able to characterize the heterogeneity of TAM populations by associated environmental gene signatures, this was in the context of whole tumor tissue, where cells of gene expression origin are unknown. Further work is required to investigate the origin of these genes for more specific therapeutic implications. This will require single-cell isolation from fresh samples and detailed TAM phenotyping.

In conclusion, our results outline the spatial resolution of macrophage heterogeneity in gastric cancer. We describe the different environmental gene signatures which may reflect the interactive process between macrophage populations in situ and identify the CD206+ macrophages to be most relevant to high PDL1 expression. Our data demonstrate that the heterogeneity of macrophages within the tumor is present at both macro- and micro-levels due to the gradient change of different markers. We emphasize the importance of using high resolution characterization to investigate the roles of macrophage populations in a tissue setting, to identify potential therapeutic candidates and to understand the immune landscape of gastric cancer.

Methods

Study cohort and selection criteria. The Molecular Analysis of Upper Gastro-Intestinal Cancer (MAUGIC) cohort consists of 250 cases of gastric and esophageal cancer patients from 1999 to present (This study was restricted from 1999 to 2009[63]). Written informed consent was obtained from all patients prior to sample collection. All procedures were ethically approved by the Individual Review Boards (IRB) of the Peter MacCallum Cancer Centre and at each of the collection centers.

Specimens from 56 GC specimens from different patients representing all GC cancer subtypes and with comprehensive clinical information were selected. All patients had undergone surgical resection and had at least 10 years follow-up. Eleven cases comprised the phenotyping algorithm training cohort (inForm, PerkinElmer, Massachusetts, USA) and 35 (training cohort included) were used for optimization. All 56 patients were analyzed independently. Three patients with immediate surgery-associated deaths and two with no recurrence data were excluded for overall-survival and relapse-free survival analysis, respectively.

Classifications of cancer subtype and inflammation status. GC tissues were classified by an anatomical pathologist (C.M.) into intestinal, diffuse, and mixed types[3]. In situ hybridization was used to determine EBV burden (EBV Early RNA, Roche). MSI cases were identified using IHC for MLH1 (Leica, ES05, 1:50), PMS2 (Ventana, EPR3947), MSH2 (Ventana, G219-1129), and MSH6 (BD Biosciences,

44, 1:800). Tumors showing loss of MLH1 and PMS2 expression, with retention for MSH2 and MSH6 were regarded as microsatellite unstable. Patients classified as diffuse but non-EBV and non-MSI were assumed as GS. The remaining patients were termed "others" and not CIN due to lacking supporting evidence. Degree of inflammation of each GC tissue was scored by a pathologist (C.M.) based on the infiltration of immune cells.

Multiplex IHC staining protocol. Opal 7-colour kit (PerkinElmer, NEL811001KT) was used for multiplex IHC. Four micrometers of FFPE sections were dewaxed and rehydrated. In the first round antigen was retrieved with a pressure cooker (EDTA pH 8.0) at 125 °C for 3 min. Slides were cooled to room temperature (RT), washed with TBST/0.5% Tween (3 times, 5 min) and incubated with H_2O_2 (3%) for 10 min. Slides were washed and blocked with blocking buffer (Dako, Glostrup, Denmark) for 10 min. Primary antibody, CD163 (Cell Marque, MRQ-26, 1:500, dye540), was incubated at RT for 30 min. Slides were washed and an HRP-conjugated secondary antibody was incubated at RT for 10 min. TSA dye (1:50) was applied for 10 min after washes. This was repeated five more times using the following antibodies, CD68 (Leica Biosystems, 514H12, 1:100, dye570), CD206 (Abcam, Ab64693, 1:6000, dye620), IRF8 (Santa Cruz, E-9, 1:3000, dye650), PDL1 (Spring Bioscience, SP142, 1:2000, dye520), and multi-cytokeratin (Leica Biosystems, NCL-L-AE1/AE3, 1:200, dye690). For second and subsequent rounds antigen retrieval was performed in EDTA (pH 8.0) buffer using a microwave (100–150 mW, 15 min). Nuclei were stained with DAPI (PerkinElmer) and mounted with medium (HardSet, Vectashield). Secondary antibodies anti-rabbit (PerkinElmer, NEF812001EA) or anti-mouse (PerkinElmer, NEF822001EA) were used at a 1:1000 dilution.

Regions of interest (ROIs). The interface of tumor and normal tissue was identified by a pathologist (C.M.). Definitions of the ROIs are as follows: Normal adjacent to tumor (N): the area within the specimen but not within the tumor. Margin (M): the area at the interface of the tumor and normal tissue. Edge (E): the area from interface into the tumor (approximately 1–1.5 mm; depth defined by the limited size of the microscopy field). Core (C): the rest of the tumor.

Multiplex IHC imaging and inForm analysis. Slides were imaged using a Vectra microscope. Whole slide scans were performed using the ×10 objective lens. ROIs were selected with fixed-size stamps in Phenochart (PerkinElmer), based on the previously acquired whole slide scan images. 1 × 1 (669 × 500 µm; ×20 object lens) stamp was used for the Margin and 2 × 2 (1338 × 1000 µm) for the Core, Edge, and Normal. As many viable regions as possible in each specimen were selected with minimal overlap. Acquired images ($n = 1800$) were analyzed with inForm for tissue-component segmentation of tumor-cell (AE1AE3+) and stroma (AE1AE3–) regions and cell phenotyping. Density of cells in each ROI was calculated by combining the cell counts from all images and normalizing by the total area (cell/mm^2).

Robustness of TAM population phenotyping. TAM population phenotyping robustness was tested by randomly subsampling ($n = 2000$) equal number of cells ($n = 100$) from each of the populations per patient within each ROI (Core, Edge, and Margin). The combined-marker signature of the subsampled cells was compared with the signature of the bulk population (Pearson correlation). The number of TAM populations was tested using the K-means clustering method[4] (Fig. S2).

ImagePro image analysis. Image output from inForm showing the DAPI, AE1AE3, CD68 and CD163 or CD206 were validated with the Line profile function in ImagePro (Media Cybernetics).

R analysis. An Inter-cellular Spatial Analysis Tool (ISAT[37]) was developed using the R software (version 3.3.1 for Windows) for the distance analysis. Distance between two cell nuclei was calculated using the x and y coordinates from the inForm raw data. Each cell of the same phenotype was used as a reference cell to calculate its distance to the nearest cell of different phenotypes. The effective percentage of a cell type was calculated by counting the number of cells within the cell type that had the nearest distance which that fulfilled the distance criteria and normalized to the total number of cells in that cell type. The effective density was calculated by using the number of cells within the cell type that that fulfilled the distance criteria and normalized to the area of tissue (mm^2). 10 µm (nucleus to nucleus) was defined as an estimated direct contact distance between the cells.

For PDL1 single-cell expression analysis, to determine a uniform threshold for PDL1 positivity across patients and to normalize for different cell number between patient samples for further analyses, five test cohorts were sampled with equal number of cells (10^4) per patient. Cells were randomly assigned using the "sample_n" function of the "dplyr" package.

Microarray. RNA from fresh-frozen GC tissue ($n = 99$) collected at the time of surgery was isolated with Trizol (Invitrogen) and column chromatography (RNeasy, Qiagen). Microarrays were hybridized using U133+ 2 chips (Affymetrix) and scanned with the Genechip Scanner (Affymetrix). Data were previously submitted to Gene Expression Omnibus (GEO; Series GSE51105[10]).

Environmental gene signatures. Patients with available core region for multiplex IHC and whole tumor microarray data available were selected ($n = 34$). Environmental gene signatures of each TAM subtype was generated by correlating the cell density results with the gene expression data ($p < 0.05$; Spearman correlation, assuming nonlinear data distribution). Most relevant pathways associated with each signature were identified with the Reactome database. A refined CD68++CD163+ TAM signature was generated using the genes within the significantly associated pathways (FDR < 0.05; Benjamini-Hochberg) and most highly correlated with cell density ($p < 0.001$; Spearman correlation).

KMplot survival analysis. Patient survival was interrogated with the refined CD68++CD163+ TAM gene signature using the online database KMplot[41] survival of the MAUGIC dataset (GSE51105) and a combined cohort (GSE14210, GSE15459, GSE22377, GSE29272, and GSE51105) were interrogated.

Statistics. GraphPad Prism 7.0 software (GraphPad Software, San Diego, USA). Mann–Whitney U test (two-tailed), Spearman and Pearson correlation, Chi-square analysis and Kaplan–Meier analysis (Log-rank, Mantel-Cox test) were used as appropriate. P values lower than 0.05 were considered as significant.

Reporting summary. Further information on research design is available in the Nature Research Reporting Summary linked to this article.

Data availability

Source data for figures [Fig. 1a–h; Fig. 2; Fig. 3b–f; Fig. 4a, c, e, f; Fig. 5a, c–f, Fig. 6] are provided with the paper. Microarray data are available online (GSE51105). Other data that support the findings of this study are available from the corresponding author [A.B.] upon reasonable request.

Code availability

The Inter-cellular Spatial Analysis Tool (ISAT) package for R used in the study is available online[37].

Received: 15 January 2019 Accepted: 31 July 2019
Published online: 02 September 2019

References

1. Bray, F. et al. Global cancer statistics 2018: GLOBOCAN estimates of incidence and mortality worldwide for 36 cancers in 185 countries. *CA Cancer J. Clin.* **68**, 394–424 (2018).
2. Cristescu, R. et al. Molecular analysis of gastric cancer identifies subtypes associated with distinct clinical outcomes. *Nat. Med.* **21**, 449–456 (2015).
3. Lauren, P. The two histological main types of gastric carcinoma: diffuse and so-called intestinal-type carcinoma. An attempt at a histo-clinical classification. *Acta Pathol. Microbiol Scand.* **64**, 31–49 (1965).
4. Cancer Genome Atlas Research, N. Comprehensive molecular characterization of gastric adenocarcinoma. *Nature* **513**, 202–209 (2014).
5. Muro, K. et al. Pembrolizumab for patients with PD-L1-positive advanced gastric cancer (KEYNOTE-012): a multicentre, open-label, phase 1b trial. *Lancet Oncol.* **17**, 717–726 (2016).
6. Kim, S. T. et al. Comprehensive molecular characterization of clinical responses to PD-1 inhibition in metastatic gastric cancer. *Nat. Med.* **24**, 1449–1458 (2018).
7. Harada, K. et al. Tumor-associated macrophage infiltration is highly associated with PD-L1 expression in gastric adenocarcinoma. *Gastric Cancer* **21**, 31–40 (2018).
8. Roszer, T. Understanding the mysterious M2 macrophage through activation markers and effector mechanisms. *Mediat. Inflamm.* **2015**, 816460 (2015).
9. Mantovani, A., Marchesi, F., Malesci, A., Laghi, L. & Allavena, P. Tumour-associated macrophages as treatment targets in oncology. *Nat. Rev. Clin. Oncol.* **14**, 399–416 (2017).
10. Busuttil, R. A. et al. A signature predicting poor prognosis in gastric and ovarian cancer represents a coordinated macrophage and stromal response. *Clin. Cancer Res.* **20**, 2761–2772 (2014).
11. Ohno, S. et al. The degree of macrophage infiltration into the cancer cell nest is a significant predictor of survival in gastric cancer patients. *Anticancer Res.* **23**, 5015–5022 (2003).
12. Ruffell, B. & Coussens, L. M. Macrophages and therapeutic resistance in cancer. *Cancer Cell* **27**, 462–472 (2015).

Appendix 1 Continued

13. Liu, J. Y. et al. Distribution pattern of tumor associated macrophages predicts the prognosis of gastric cancer. *Oncotarget* **8**, 92757–92769 (2017).
14. Murray, P. J. Nonresolving macrophage-mediated inflammation in malignancy. *FEBS J.* **285**, 641–653 (2018).
15. Murray, P. J. et al. Macrophage activation and polarization: nomenclature and experimental guidelines. *Immunity* **41**, 14–20 (2014).
16. Ginhoux, F., Schultze, J. L., Murray, P. J., Ochando, J. & Biswas, S. K. New insights into the multidimensional concept of macrophage ontogeny, activation and function. *Nat. Immunol.* **17**, 34–40 (2016).
17. Xue, J. et al. Transcriptome-based network analysis reveals a spectrum model of human macrophage activation. *Immunity* **40**, 274–288 (2014).
18. Lavin, Y. et al. Innate immune landscape in early lung adenocarcinoma by paired single-cell analyses. *Cell* **169**, 750–765 (2017).
19. Chevrier, S. et al. An immune atlas of clear cell renal cell carcinoma. *Cell* **169**, 736–749 (2017).
20. Bassler, K., Schulte-Schrepping, J., Warnat-Herresthal, S., Aschenbrenner, A. C. & Schultze, J. L. The myeloid cell compartment—cell by cell. *Annu. Rev. Immunol.* **37**, 269–293 (2019).
21. Hobson-Gutierrez, S. A. & Carmona-Fontaine, C. The metabolic axis of macrophage and immune cell polarization. *Dis. Model Mech.* **11**, dmm034462 (2018).
22. Chistiakov, D. A., Killingsworth, M. C., Myasoedova, V. A., Orekhov, A. N. & Bobryshev, Y. V. CD68/macrosialin: not just a histochemical marker. *Lab. Invest.* **97**, 4–13 (2017).
23. da Silva, R. P. & Gordon, S. Phagocytosis stimulates alternative glycosylation of macrosialin (mouse CD68), a macrophage-specific endosomal protein. *Biochem J.* **338**, 687–694 (1999).
24. Barros, M. H., Hauck, F., Dreyer, J. H., Kempkes, B. & Niedobitek, G. Macrophage polarisation: an immunohistochemical approach for identifying M1 and M2 macrophages. *PLoS One* **8**, e80908 (2013).
25. Pantano, F. et al. The role of macrophages polarization in predicting prognosis of radically resected gastric cancer patients. *J. Cell Mol. Med.* **17**, 1415–1421 (2013).
26. Zhang, H. et al. Infiltration of diametrically polarized macrophages predicts overall survival of patients with gastric cancer after surgical resection. *Gastric Cancer* **18**, 740–750 (2015).
27. Saylor, J. et al. Spatial mapping of myeloid cells and macrophages by multiplexed tissue staining. *Front Immunol.* **9**, 2925 (2018).
28. Gunthner, R. & Anders, H. J. Interferon-regulatory factors determine macrophage phenotype polarization. *Mediat. Inflamm.* **2013**, 731023 (2013).
29. Gupta, M. et al. IRF8 directs stress-induced autophagy in macrophages and promotes clearance of Listeria monocytogenes. *Nat. Commun.* **6**, 6379 (2015).
30. Qi, C. F. et al. Differential expression of IRF8 in subsets of macrophages and dendritic cells and effects of IRF8 deficiency on splenic B cell and macrophage compartments. *Immunol. Res.* **45**, 62–74 (2009).
31. Hagemeyer, N. et al. Transcriptome-based profiling of yolk sac-derived macrophages reveals a role for Irf8 in macrophage maturation. *EMBO J.* **35**, 1730–1744 (2016).
32. Geller, S. A., Dhall, D. & Alsabeh, R. Application of immunohistochemistry to liver and gastrointestinal neoplasms: liver, stomach, colon, and pancreas. *Arch. Pathol. Lab. Med.* **132**, 490–499 (2008).
33. Stack, E. C., Wang, C., Roman, K. A. & Hoyt, C. C. Multiplexed immunohistochemistry, imaging, and quantitation: a review, with an assessment of Tyramide signal amplification, multispectral imaging and multiplex analysis. *Methods* **70**, 46–58 (2014).
34. Yang, M., McKay, D., Pollard, J. W. & Lewis, C. E. Diverse functions of macrophages in different tumor microenvironments. *Cancer Res.* **78**, 5492–5503 (2018).
35. Norton, S. E., Dunn, E. T., McCall, J. L., Munro, F. & Kemp, R. A. Gut macrophage phenotype is dependent on the tumor microenvironment in colorectal cancer. *Clin. Transl. Immunol.* **5**, e76 (2016).
36. Carstens, J. L. et al. Spatial computation of intratumoral T cells correlates with survival of patients with pancreatic cancer. *Nat. Commun.* **8**, 15095 (2017).
37. Wang, M., Sun, Y. & Huang, Y. K. ISAT: extract cell density and nearest distance based on 'PerkinElmer InForm' software output. https://cran.r-project.org/web/packages/ISAT/index.html (2018).
38. Kratochvill, F. et al. TNF counterbalances the emergence of M2 tumor macrophages. *Cell Rep.* **12**, 1902–1914 (2015).
39. Fabregat, A. et al. The reactome pathway knowledgebase. *Nucleic Acids Res.* **46**, D649–D655 (2018).
40. Fabregat, A. et al. Reactome pathway analysis: a high-performance in-memory approach. *BMC Bioinforma.* **18**, 142 (2017).
41. Szasz, A. M. et al. Cross-validation of survival associated biomarkers in gastric cancer using transcriptomic data of 1,065 patients. *Oncotarget* **7**, 49322–49333 (2016).
42. Dutta, S. et al. The relationship between tumour necrosis, tumour proliferation, local and systemic inflammation, microvessel density and survival in patients undergoing potentially curative resection of oesophageal adenocarcinoma. *Br. J. Cancer* **106**, 702–710 (2012).
43. Roussel, M. et al. Mass cytometry deep phenotyping of human mononuclear phagocytes and myeloid-derived suppressor cells from human blood and bone marrow. *J. Leukoc. Biol.* **102**, 437–447 (2017).
44. Raes, G. et al. Arginase-1 and Ym1 are markers for murine, but not human, alternatively activated myeloid cells. *J. Immunol.* **174**, 6561 (2005).
45. Tsujikawa, T. et al. Quantitative multiplex immunohistochemistry reveals myeloid-inflamed tumor-immune complexity associated with poor prognosis. *Cell Rep.* **19**, 203–217 (2017).
46. Halse, H. et al. Multiplex immunohistochemistry accurately defines the immune context of metastatic melanoma. *Sci. Rep.* **8**, 11158 (2018).
47. Cai, Y. et al. In vivo characterization of alveolar and interstitial lung macrophages in rhesus macaques: implications for understanding lung disease in humans. *J. Immunol.* **192**, 2821–2829 (2014).
48. Van Hove, H. et al. A single-cell atlas of mouse brain macrophages reveals unique transcriptional identities shaped by ontogeny and tissue environment. *Nat. Neurosci.* **22**, 1021–1035 (2019).
49. Biswas, S. K. & Mantovani, A. Macrophage plasticity and interaction with lymphocyte subsets: cancer as a paradigm. *Nat. Immunol.* **11**, 889–896 (2010).
50. Yang, H. et al. Identification of CD163 as an antiinflammatory receptor for HMGB1-haptoglobin complexes. *JCI Insight* **1**, e85375 (2016).
51. Lurier, E. B. et al. Transcriptome analysis of IL-10-stimulated (M2c) macrophages by next-generation sequencing. *Immunobiology* **222**, 847–856 (2017).
52. Borda, J. T. et al. CD163, a marker of perivascular macrophages, is up-regulated by microglia in simian immunodeficiency virus encephalitis after haptoglobin-hemoglobin complex stimulation and is suggestive of breakdown of the blood-brain barrier. *Am. J. Pathol.* **172**, 725–737 (2008).
53. Zizzo, G., Hilliard, B. A., Monestier, M. & Cohen, P. L. Efficient clearance of early apoptotic cells by human macrophages requires M2c polarization and MerTK induction. *J. Immunol.* **189**, 3508–3520 (2012).
54. Movahedi, K. et al. Different tumor microenvironments contain functionally distinct subsets of macrophages derived from Ly6C(high) monocytes. *Cancer Res.* **70**, 5728–5739 (2010).
55. Carmona-Fontaine, C. et al. Metabolic origins of spatial organization in the tumor microenvironment. *Proc. Natl Acad. Sci. USA* **114**, 2934–2939 (2017).
56. Mills, E. L. et al. Succinate dehydrogenase supports metabolic repurposing of mitochondria to drive inflammatory macrophages. *Cell* **167**, 457–470 e413 (2016).
57. Ip, W. K. E., Hoshi, N., Shouval, D. S., Snapper, S. & Medzhitov, R. Anti-inflammatory effect of IL-10 mediated by metabolic reprogramming of macrophages. *Science* **356**, 513–519 (2017).
58. Manzanillo, P., Eidenschenk, C. & Ouyang, W. Deciphering the crosstalk among IL-1 and IL-10 family cytokines in intestinal immunity. *Trends Immunol.* **36**, 471–478 (2015).
59. Moore, K. J., Sheedy, F. J. & Fisher, E. A. Macrophages in atherosclerosis: a dynamic balance. *Nat. Rev. Immunol.* **13**, 709–721 (2013).
60. Bagnall, J. et al. Quantitative analysis of competitive cytokine signaling predicts tissue thresholds for the propagation of macrophage activation. *Sci. Signal.* **11**, eaaf3998 (2018).
61. Thurley, K., Gerecht, D., Friedmann, E. & Hofer, T. Three-dimensional gradients of cytokine signaling between T cells. *PLoS Comput. Biol.* **11**, e1004206 (2015).
62. Rimm, D. L. et al. A prospective, multi-institutional, pathologist-based assessment of 4 immunohistochemistry assays for PD-L1 expression in non-small cell lung cancer. *JAMA Oncol.* **3**, 1051–1058 (2017).
63. Pattison, S. et al. Predictors of outcome after surgery for gastric cancer in a Western cohort. *ANZ J. Surg.* **86**, 469–474 (2016).

Acknowledgements

We thank Dr. Paul Beavis and A/Prof. Paul Neeson for helpful discussions for the study and for reviewing the paper. We also thank Prof. David Bowtell for reviewing the paper, Dr. Sharon Pattison for digitalizing clinical information and conducting patient follow-up, the core facilities at the Peter MacCallum Cancer Centre for supporting data collection and analyses, and all patients and staffs involved in the project. Y.H., M.W. and Y.S. are supported by the Australian Commonwealth Government Research Training Program, the University of Melbourne. Y.H. is supported by the Government Scholarship to Study Abroad (GSSA) issued by Taiwan Ministry of Education. M.W. and Y.S. are supported by the Cancer Therapeutics CRC.

Author contributions

Experimental work: Y.H., N.D., and C.M.; R Script: Y.H., M.W., and Y.S.; Data interpretation: Y.H., A.A., J.A.H., R.A.B., and A.B.; Writing and editing of the paper: Y.H., N.D., J.A.H., R.A.B., and A.B.; Study concept: Y.H., A.A., J.A.H., R.A.B., and A.B.

Appendix 1 Continued

Additional information

Supplementary Information accompanies this paper at https://doi.org/10.1038/s41467-019-11788-4.

Competing interests: The authors declare no competing interests.

Reprints and permission information is available online at http://npg.nature.com/reprintsandpermissions/

Peer review information: *Nature Communications* would like to thank Paul Tumeh and the other, anonymous, reviewers for their contributions to the peer review of this work. Peer review reports are available.

Publisher's note: Springer Nature remains neutral with regard to jurisdictional claims in published maps and institutional affiliations.

Open Access This article is licensed under a Creative Commons Attribution 4.0 International License, which permits use, sharing, adaptation, distribution and reproduction in any medium or format, as long as you give appropriate credit to the original author(s) and the source, provide a link to the Creative Commons license, and indicate if changes were made. The images or other third party material in this article are included in the article's Creative Commons license, unless indicated otherwise in a credit line to the material. If material is not included in the article's Creative Commons license and your intended use is not permitted by statutory regulation or exceeds the permitted use, you will need to obtain permission directly from the copyright holder. To view a copy of this license, visit http://creativecommons.org/licenses/by/4.0/.

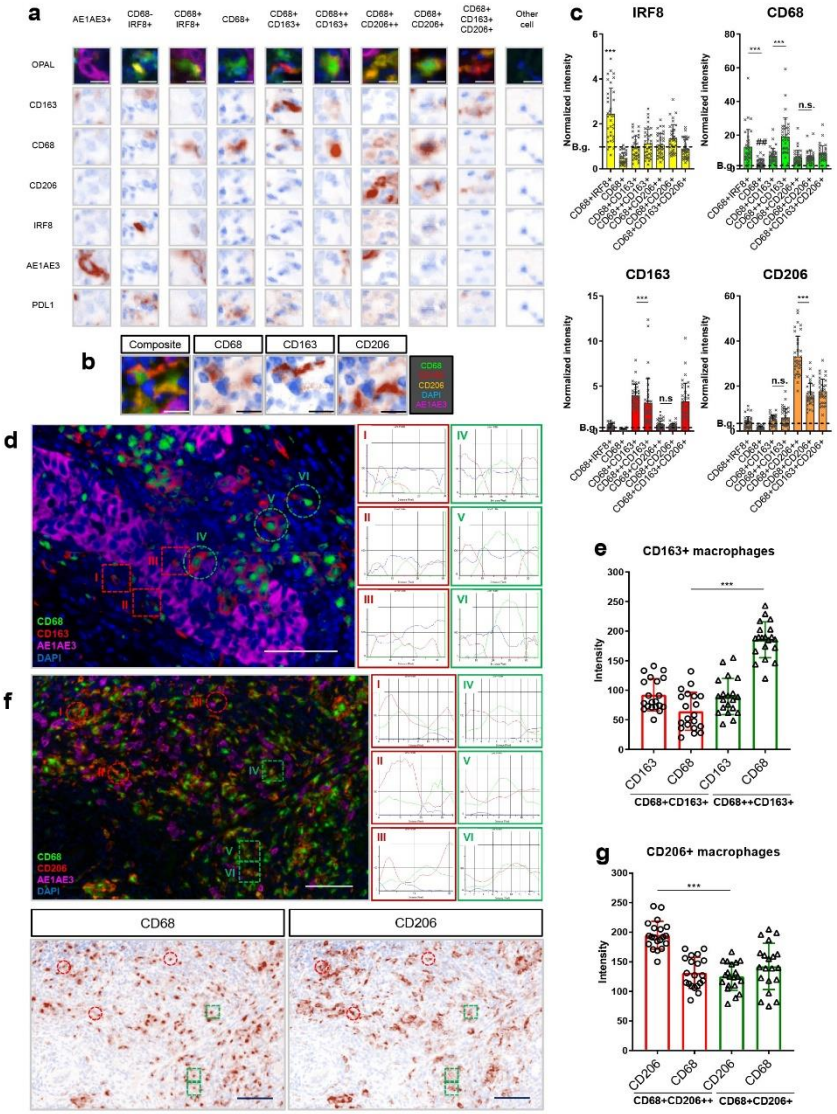
© The Author(s) 2019

Supplementary Table 1. Clinical and pathological characteristics of the MAUGIC study cohort

Groups		Patient number	Percentage in cohort (%)
Age	90-99	1	1.79
	80-89	6	10.71
	70-79	16	28.57
	60-69	12	21.43
	50-59	16	28.57
	40-49	5	8.93
Gender	Female	20	35.71
	Male	36	64.29
Histological classification (Lauren)	Intestinal	37	66.07
	Diffuse	18	32.14
	Mixed	1	1.79
Molecular subtype (TCGA)	EBV	4	7.14
	MSI	9	16.07
	GS	17	30.36
	Others	26	46.43
T stage	T4	1	1.79
	T3	39	69.64
	T2	13	23.21
	T1	3	5.36
N stage	N3	5	8.93
	N2	10	17.86
	N1	18	32.14
	N0	23	41.07
M stage	M1	3	5.36
	M0	53	94.64
AJCC (6^{th})	4+3	27	48.21
	2+1	29	51.79
Recurrence	Yes	30	53.57
	No	24	42.86
	ND	2	3.57

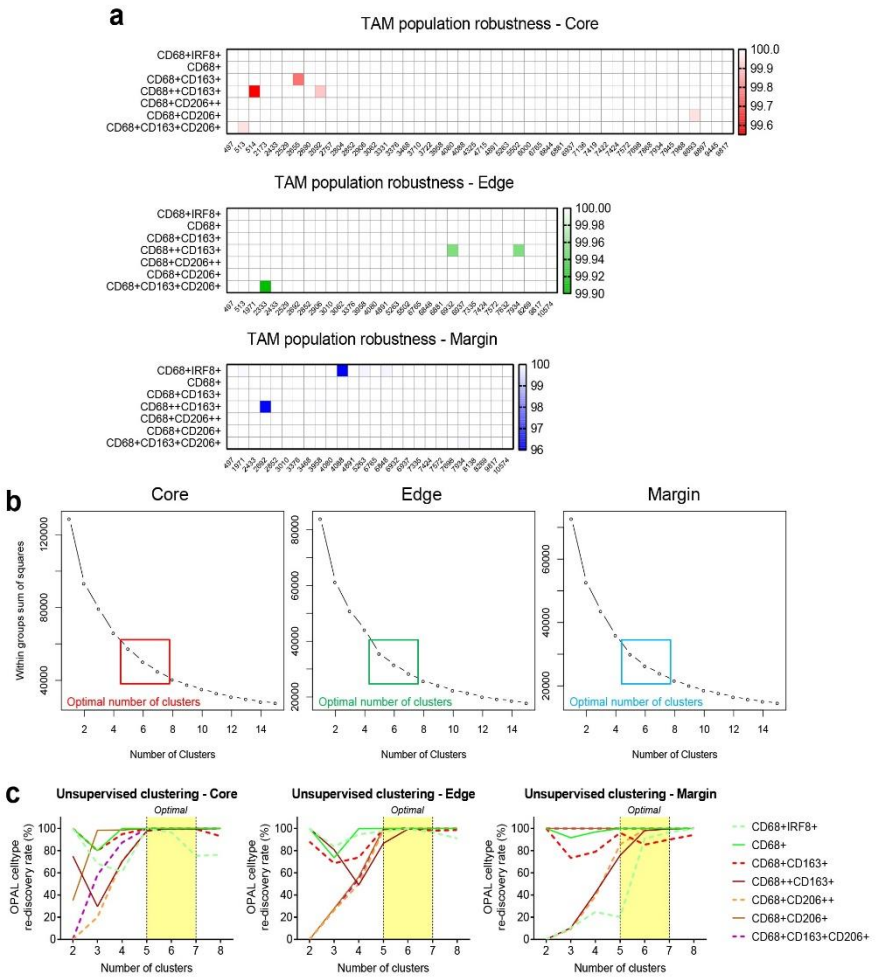
ND: not documented.

Supplementary Figure 1



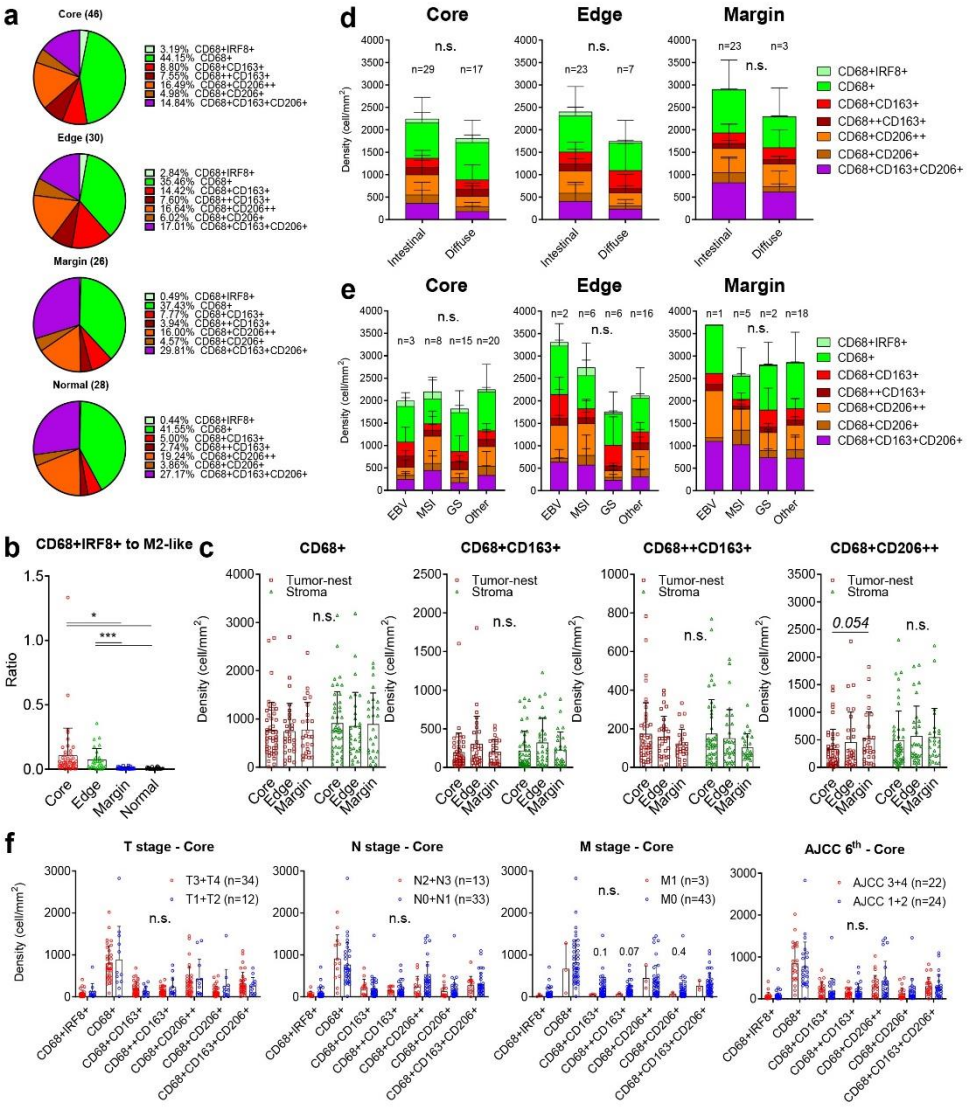
Supplementary Figure 1: Characterization of macrophage populations
a Representative images of the seven major TAM populations. Key: Yellow: IRF8, Green: CD68, Red: CD163, Orange: CD206, Magenta: AE1AE3, Cyan: PDL1, Blue: DAPI. Single-stained IHC color: Blue: DAPI, Brown: Positive staining of markers as indicated (+). Relative intensity between cell types is represented (++). Scale bar: 10 µm. **b** Representative images of adjacent CD163+ (CD206-) and CD206+ (CD163-) macrophages. Scale bar: 10 µm. **c** Marker signatures used for TAM population characterization in patient samples (n=35). Normalized intensity: original intensity of the marker / exposure time. B.g (dash line): background level of staining determined by the mean intensity of tumor (AE1AE3+) and non-macrophage (Other) cells. Error bars represent mean ± SD, ***p<0.001, n.s. not significant. Mann–Whitney's U test. ##p<0.01 comparing to tumor and non-macrophage cells. **d** Intensity of CD68 and CD163 on TAMs analyzed with the ImagePro software. Intensity of markers on each numbered cells were plotted in the matched numbered plots. Red square: CD68+CD163+ TAMs, Green circle: CD68++CD163+ TAMs. X axis: Distance in pixels, Y axis: Intensity of marker. Colors in the plots: CD163 (red), CD68 (green) and DAPI (blue). Scale bar: 100 µm. **e** Quantification of the maximum intensity of CD68 and CD163 expressed on the TAMs (n=20 for each population) in Supplementary Fig. 1d. Error bars represent mean ± SD, ***p<0.001. Mann–Whitney's U test. Each point represents one patient. **f** Intensity of CD68 and CD206 on TAMs analyzed with the ImagePro software. Intensity of markers on each numbered cells were plotted in the matched numbered plots and single-stained IHC image of CD68 and CD206 from the same section. Red circle: CD68+CD206++ TAMs, Green square: CD68+CD206+ TAMs. X axis: Distance in pixels, Y axis: Intensity of marker. Colors in the plots: CD206 (red), CD68 (green) and DAPI (blue). Scale bar: 100 µm. **g** Quantification of the maximum intensity of CD68 and CD206 on the macrophages (n=20 for each population) in Supplementary Fig 1f. Error bars represent mean ± SD, ***p<0.001. Mann–Whitney's U test. Each point represents one patient.

Supplementary Figure 2



Supplementary Figure 2: Validation of TAM population subgrouping/clustering
a Heatmaps represent the accuracy of subsampling of TAMs from each of the TAM population per patient (bottom). Robustness of TAM subgrouping approach for each TAM population per patient in each ROI. 100 cells were randomly subsampled from each of the seven TAM populations per patient within each ROI (Core, Edge, and Margin). The subsampling was repeated for 2000 times. The median marker expression signatures of the subsample cohort (each TAM population in each patient per ROI was compared) to the signature of the overall cohort using the Pearson correlation ($p<0.05$ to test the statistical robustness of the subsampling. The accuracy of the subsampling of each TAM population was at least 96% accurate using the supervised inForm software. Scale: Accuracy (%) **b** Validation of TAM population clusters. The same subsampled cohort (n=500) were used to validate the number of populations using an unsupervised clustering method. The "within group sum of squares (wss)" for different ROIs using the K-means clustering method. Based on the "elbow method", the results suggest that for all ROIs, the optimal number of clusters was around 5 to 7 with our panel. **c** The median marker expression signatures from each clusters with the expression signature of the TAM populations to validate if the TAM populations can be rediscovered in the unsupervised clustering (Pearson, $p<0.01$). The results indicate that within the optimal clustering range (5-7), all TAM populations can be rediscovered, and were much better than other clustering numbers (2-4).

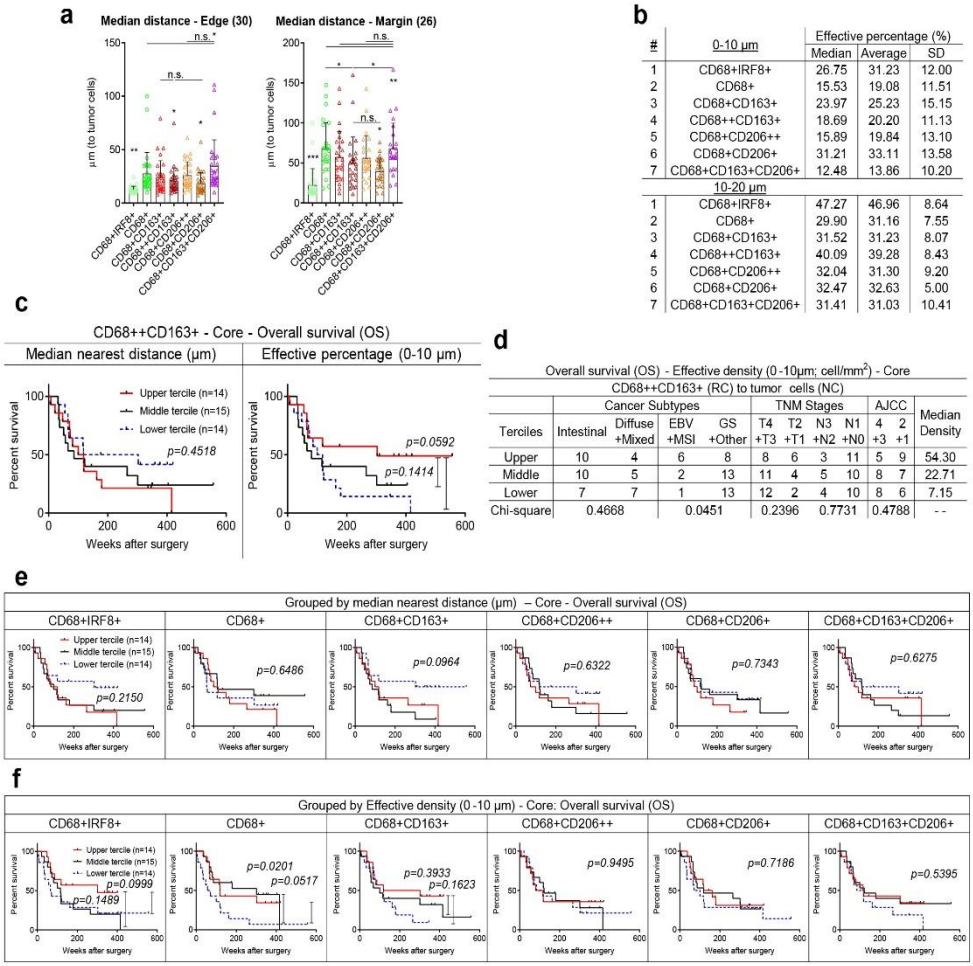
Supplementary Figure 3



Supplementary Figure 3: Density of TAMs varies across regions of interest but not between different cancer subtypes

a TAM population percentage in each ROI. **b** CD68+IRF8+ to M2-like TAMs ratio among the ROIs. Error bars represent mean ± SD. Each dot represents one patient. *p<0.05, ***p<0.001, and not significant (n.s.). Mann–Whitney's U test. **c** Distribution of macrophage populations in the tumor-nest and stoma areas. Mean ± SD. Each dot represents onepatient. Not significant (n.s.). Mann–Whitney's U test. **d-f** Constitution of TAM populations in patient at different ROIs characterized with (**d**) Lauren histological subtype, (**e**) TCGA molecular subtype and (**f**) clinical staging. Error bars represent mean ± SD. Each dot represents one patient. Not significant (n.s.). Mann–Whitney's U test.

Supplementary Figure 4



b

#	0-10 µm	Effective percentage (%)		
		Median	Average	SD
1	CD68+IRF8+	26.75	31.23	12.00
2	CD68+	15.53	19.08	11.51
3	CD68+CD163+	23.97	25.23	15.15
4	CD68++CD163+	18.69	20.20	11.13
5	CD68+CD206++	15.89	19.84	13.10
6	CD68+CD206+	31.21	33.11	13.58
7	CD68+CD163+CD206+	12.48	13.86	10.20
	10-20 µm			
1	CD68+IRF8+	47.27	46.96	8.64
2	CD68+	29.90	31.16	7.55
3	CD68+CD163+	31.52	31.23	8.07
4	CD68++CD163+	40.09	39.28	8.43
5	CD68+CD206++	32.04	31.30	9.20
6	CD68+CD206+	32.47	32.63	5.00
7	CD68+CD163+CD206+	31.41	31.03	10.41

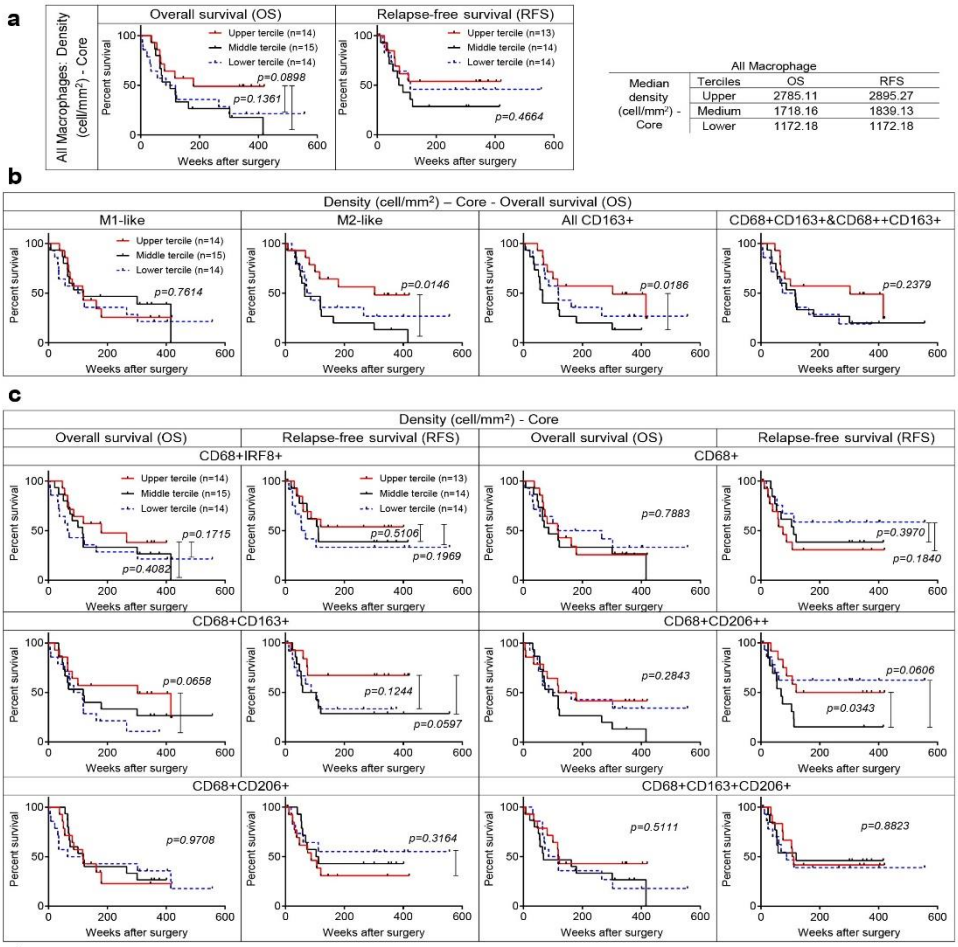
d

Overall survival (OS) - Effective density (0 -10µm; cell/mm^2) - Core

CD68++CD163+ (RC) to tumor cells (NC)											
	Cancer Subtypes				TNM Stages				AJCC		Median Density
Terciles	Intestinal	Diffuse +Mixed	EBV +MSI	GS +Other	T4 +T3	T2 +T1	N3 +N2	N1 +N0	4 +3	2 +1	
Upper	10	4	6	8	8	6	3	11	5	9	54.30
Middle	10	5	2	13	11	4	5	10	8	7	22.71
Lower	7	7	1	13	12	2	4	10	8	6	7.15
Chi-square	0.4668		0.0451		0.2396		0.7731		0.4788		- -

Supplementary Figure 4: TAM-composition change is associated with their proximity to tumor cells
a Median distance of TAM populations (RC) to tumor cell (NC) at the edge and margin. Error bars represent mean ± SD. Each dot represents one patient. *p<0.05, **p<0.01, ***p<0.001 and not significant (n.s.). Mann–Whitney's U test. Light green: CD68+IRF8+, Green: CD68+, Red: CD68+CD163+, Dark red: CD68++CD163+, Orange: CD68+CD206++, Brown: CD68+CD206+, Purple: CD68+CD163+CD206+. Circle: M1-like macrophages. Triangle: M2-like macrophages. **b** Effective percentage of TAM populations within 0-10 and 10-20 µm. **c** Patient OS classified with the median nearest distance and effective percentage (0-10 µm) of CD68++CD163+ TAMs (RC) to tumor cells (NC) in the core. Red: Upper tercile (density >2/3 of the patients in the study cohort), Black: Middle tercile (2/3 ≥ density > 1/3), Blue: Lower tercile (density ≤ 1/3). Log-rank (Mantel-Cox) test. **d** Univariate analyses of clinical parameters to CD68++CD163+ TAM classified OS. Chi-square analysis. **e-f** TAM classified patient OS using the (**e**) median nearest distance and (**f**) effective density (0-10 µm) of each TAM population (RC) to tumor cell (NC) in the core.

Supplementary Figure 5



All Macrophage

Median density (cell/mm²) - Core	Terciles	OS	RFS
	Upper	2785.11	2895.27
	Medium	1718.16	1839.13
	Lower	1172.18	1172.18

d

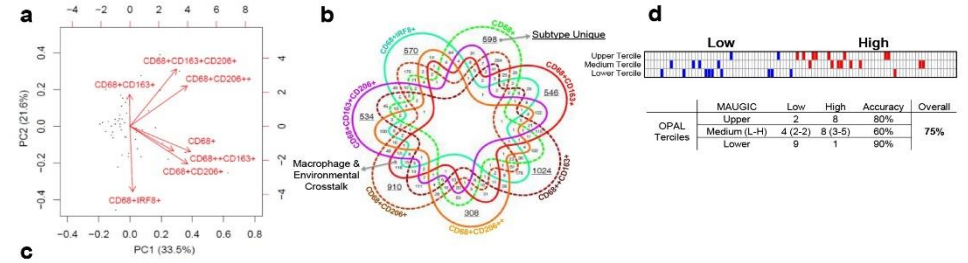
Density (cell/mm²) – Core		Cancer subtypes				TNM stages				AJCC stages		
		Overall Survival (OS)										
	Terciles	Intestinal	Diffuse +Mixed	EBV +MSI	GS +Others	T4+T3	T2+T1	N3+N2	N1+N0	4+3	2+1	Median density
CD68++ CD163+	Upper	9	5	4	10	10	4	4	10	6	8	254.14
	Medium	9	6	3	12	11	4	5	10	8	7	117.80
	Lower	9	5	2	12	10	4	3	11	7	7	60.76
	Chi-square	0.9623		0.6456		0.9912		0.7731		0.8482		- -
		Relapse-free survival (RFS)										
	Terciles	Intestinal	Diffuse+Mixed	EBV+MSI	GS+Others	T4+T3	T2+T1	N3+N2	N1+N0	4+3	2+1	Median density
	Upper	9	4	4	9	9	4	3	10	5	8	254.66
	Medium	8	6	3	11	10	4	6	8	8	6	116.42
	Lower	9	5	2	12	10	4	3	11	7	7	60.76
	Chi-square	0.9623		0.6456		0.9912		0.7731		0.8482		- -

e

	Coefficients	Standard Error	t Stat	P-value
Age	-0.1145	0.0487	-2.3488	0.0246
T.Stage	0.3435	0.1202	2.8582	0.0071
N.Stage	0.3603	0.1460	2.4682	0.0186
M.Stage	0.2669	0.2248	1.1874	0.2431
AJCC^{6th}	-0.2682	0.1471	-1.8236	0.0768
TCGA	-0.5830	0.1275	-4.5720	0.0001
CD68++CD163+ density	-0.0921	0.0684	-1.3456	0.1871

Supplementary Figure 5: Different TAM groupings have minimal effects on patient survival
a-c Patient overall survival (OS) and relapse-free survival (RFS) classified using density of (**a**) all macrophages, (**b**) subgroupings of M1-like and M2-like TAMs and (**c**) the seven distinct TAM population identified in the study. Red: Upper tercile (density >2/3 of the patients in the study cohort), Black: Middle tercile (2/3 ≥ density > 1/3), Blue: Lower tercile (density ≤ 1/3). Log-rank (Mantel-Cox) test. **d** Univariate analysis of clinical parameters to CD68++CD163+ TAM density. Chi-square analysis. **e** Multivariate analysis of clinical parameters and CD68++CD163+ TAM density. Linear regression.

Supplementary Figure 6

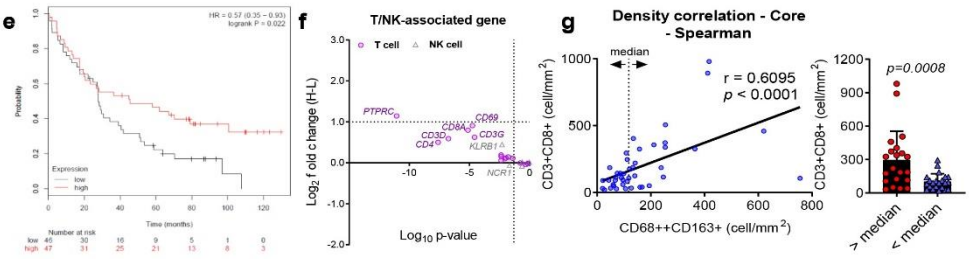


	MAUGIC	Low	High	Accuracy	Overall
OPAL Terciles	Upper	2	8	80%	75%
	Medium (L-H)	4 (2-2)	8 (3-5)	60%	
	Lower	9	1	90%	

c

	Pathway name	FDR	Submitted entities found (*Italic*: gene names)												
Unique POS	CD68+CD163+														
	Nonsense-mediated Decay (NMD) enhanced by the EJC	0.002	*NCBP2*	*RPL15*	*RPL19*	*RPL31*	*RPL34*	*RPL35A*	*RPL9*	*RPS18*	*RPS25*	*RPS27*	*RPS6*	*RPS9*	*UPF3A*
	SRP-dependent Cotranslational Targeting to Membrane	0.006	*RPL15*	*RPL19*	*RPL31*	*RPL34*	*RPL35A*	*RPL9*	*RPS18*	*RPS25*	*RPS27*	*RPS6*	*RPS9*	*SSR1*	
	Cap-dependent Translation Initiation / Completion	0.019	*RPL15*	*RPL19*	*RPL31*	*RPL34*	*RPL35A*	*RPL9*	*RPS18*	*RPS25*	*RPS27*	*RPS6*	*RPS9*		
	SHC-mediated Cascade:FGFR1	0.019	*FGF2*	*FGF9*	*FGFR1*	*SHC1*									
	Transcriptional Activation of p53 Response	0.046	*CDKN1A*												
	CD68++CD163+														
	Extracellular Matrix (ECM) Organization	0.000	*ADAMTS2*	*ADAMTS3*	*ASPN*	*BGN*	*CAPN3*	*CAPN6*	*COL14A1*	*COL1A2*	*COL3A1*	*COL4A1*	*COL5A2*	*COL6A3*	*COL8A1*
			CTSG	*CTSK*	*CTSL*	*CTSO*	*DCN*	*EFEMP1*	*FBLN1*	*FBLN2*	*FBLN5*	*FBN1*	*ITGB2*	*LAMA1*	*LAMA2*
			LAMA4	*LAMB1*	*LOX*	*LOXL3*	*LUM*	*MMP14*	*MMP9*	*NID2*	*PCOLCE*	*TGFB3*	*THBS1*	*TIMP1*	*VCAN*
			VWF												
	Interleukin-10 Signalling	0.026	*CCL4*	*CCL5*	*CCR1*	*CCR5*	*CD86*	*IL10RA*	*TIMP1*						
	MET Activated PTK2 Signaling	0.032	*COL1A2*	*COL3A1*	*COL5A2*	*LAMA1*	*LAMA2*	*LAMA4*	*LAMB1*						
	Nuclear Receptor Transcription Pathway	0.042	*ESR1*	*NR1H3*	*NR3C1*	*PPARD*									
	CD68+CD163+CD206+														
	HSF1-dependent Transactivation	0.021	*COL4A6*	*HSPA1L*	*HSPA2*										
	RUNX1 and FOXP3 Control the Development of Tregs	0.042	*CR1*	*IL2RA*											

	Pathway name	FDR	Submitted entities found (*Italic*: gene names)												
Crosstalk POS	CD68+IRF8+														
	IGF2 mRNA Binding Proteins	0.021	*CD44*												
	CD68+														
	IGF2 mRNA Binding Proteins	0.001	*CD44*	*ZBP1*											
	CD68++CD163+														
	Signalling by Interleukins	0.018	*BCL2*	*CASP1*	*CSF3R*	*FLT3*	*FPR1*	*HGF*	*HMOX1*	*IL17RA*	*IL18BP*	*IL18RAP*	*IL1R1*	*IL23R*	*IL3RA*
			IL6ST	*ITGAX*	*JAK1*	*LCP1*	*NFKB1*	*RORA*	*S1PR1*	*SOCS2*	*STAT2*	*STAT5B*	*VIM*		
	IGF2 mRNA Binding Proteins	0.022	*CD44*												
	CD68+CD206++														
	IGF2 mRNA Binding Proteins	0.000	*CD44*												
	CD68+CD206+														
	Signalling by Interleukins	0.001	*CASP1*	*CSF3R*	*HMOX1*	*HNRNP*	*IGHG1*	*IL18BP*	*IL1R1*	*IL1R2*	*IL1RN*	*IL6R*	*IL6ST*	*IRAK2*	*ITGAX*
			JAK1	*LCP1*	*LYN*	*MAP2K7*	*MAPK8*	*PELI1*	*PSME4*	*PTPR21*	*RORA*	*S1PR1*	*SOCS2*	*STAT2*	*VRK3*
	Interleukin-6 signaling	0.009	*IL6R*	*IL6ST*	*JAK1*										
NEG	CD68+CD163+														
	Polo-like kinase mediated events	0.000	*CCNB1*	*CCNB2*	*CENPF*	*LIN9*									
	Cell Cycle, Mitotic	0.001	*BIRC5*	*CCNB1*	*CCNB2*	*CDT1*	*CENPF*	*CENPN*	*CEP152*	*CEP70*	*CEP78*	*GINS2*	*GINS4*	*H2AFZ*	*HIST1H3A*
			HIST1H3I	*HIST1H4A*	*KIF2C*	*KMT5A*	*LIN9*	*NUP107*	*NUP155*	*NUP37*	*ORC4*	*SPDL1*	*TMPO*	*TOP2A*	
	Mitotic Prophase	0.018	*CCNB1*	*CCNB2*	*H2AFZ*	*KMT5A*	*NUP107*	*NUP155*	*NUP37*	*TMPO*	*HIST1H3A*	*HIST1H3I*	*HIST1H4A*		
	Signaling by FGFR2 IIIa TM	0.020	*FGFR2*												
	M Phase	0.045	*BIRC5*	*CCNB1*	*CCNB2*	*CENPF*	*CENPN*	*CEP152*	*CEP70*	*CEP78*	*H2AFZ*	*HIST1H3A*	*HIST1H3I*	*HIST1H4A*	*KIF2C*
			KMT5A	*NUP107*	*NUP155*	*NUP37*	*SPDL1*	*TMPO*							
	CD68++CD163+														
	TP53 Regulated DNA Repair	0.001	*CCNT1*	*CDK12*	*CHEK1*	*FANCD2*	*FANCI*	*GTF2H1*	*MDC1*	*POLR2L*					

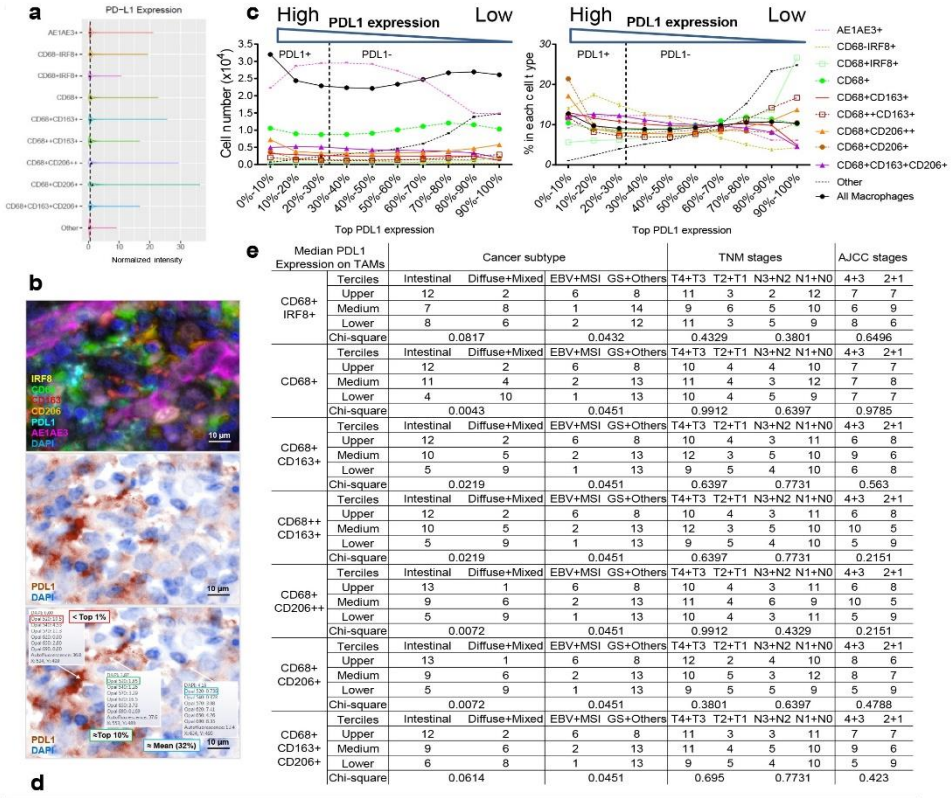


Supplementary Figure 6: Mixture of TAM populations within a same milieu

a Principle component analyses (PCA) of the density of TAM population in the core. **b** Venn diagram of the environmental gene signature for each TAM population, highlighting the population unique and shared crosstalk regions (number of genes).

c Pathways significantly associated with population unique and shared crosstalk genes of each TAM population. Italic: gene names. **d** Method of validation for the correlation between IHC and transcriptomic data. Patients who had both tumor core region for IHC and microarray data available were selected (n=34) for the generation of a CD68++CD163+ TAM associated signature (Fig. 4c). Patients in the MAUGIC cohort (n=99) were characterized into two signature-expressing groups. Patients (n=32 of the 34, the 2 removed from survival analysis were associated with surgical death) who were included in the overall survival analyses for the multiplex IHC study were selected and validated by comparing the relative groupings between the two methods. Patients grouped as the gene signature-high or low group as well as in the Upper or Lower tercile were categorized as accurate grouping, respectively. Patients in the Medium tercile were divided into two groups with the median density of the IHC staining cohort (n=34) and then tested for accuracy. Red/blue: number of patients grouped into the High/Low groups using the IHC derived cell density. **e** Patient OS of the MAUGIC cohort classified using the CD68++CD163+ TAM derived environmental signature. Log-rank (Mantel-Cox) test. **f** Differentially expressed T and NK cell associated genes between groups. **g** Correlation of CD68++CD163+ TAM and CD3+CD8+ T cell density in the Core and comparison between two density groups. Error bars represent mean ± SD. Each dot represents one patient. Mann–Whitney's U test.

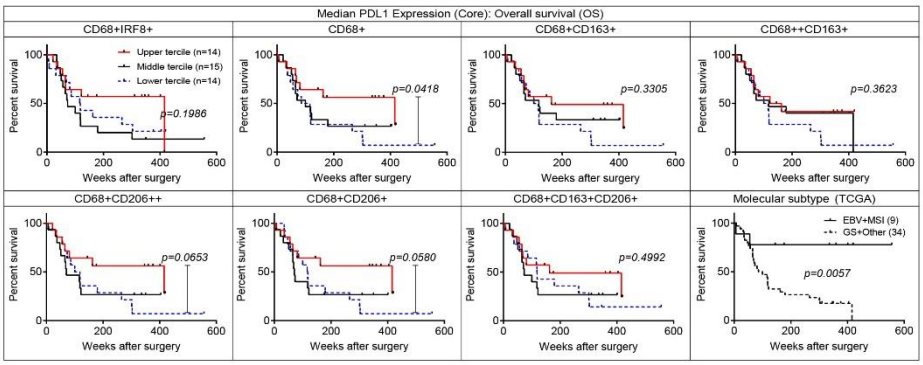
Supplementary Figure 7



e

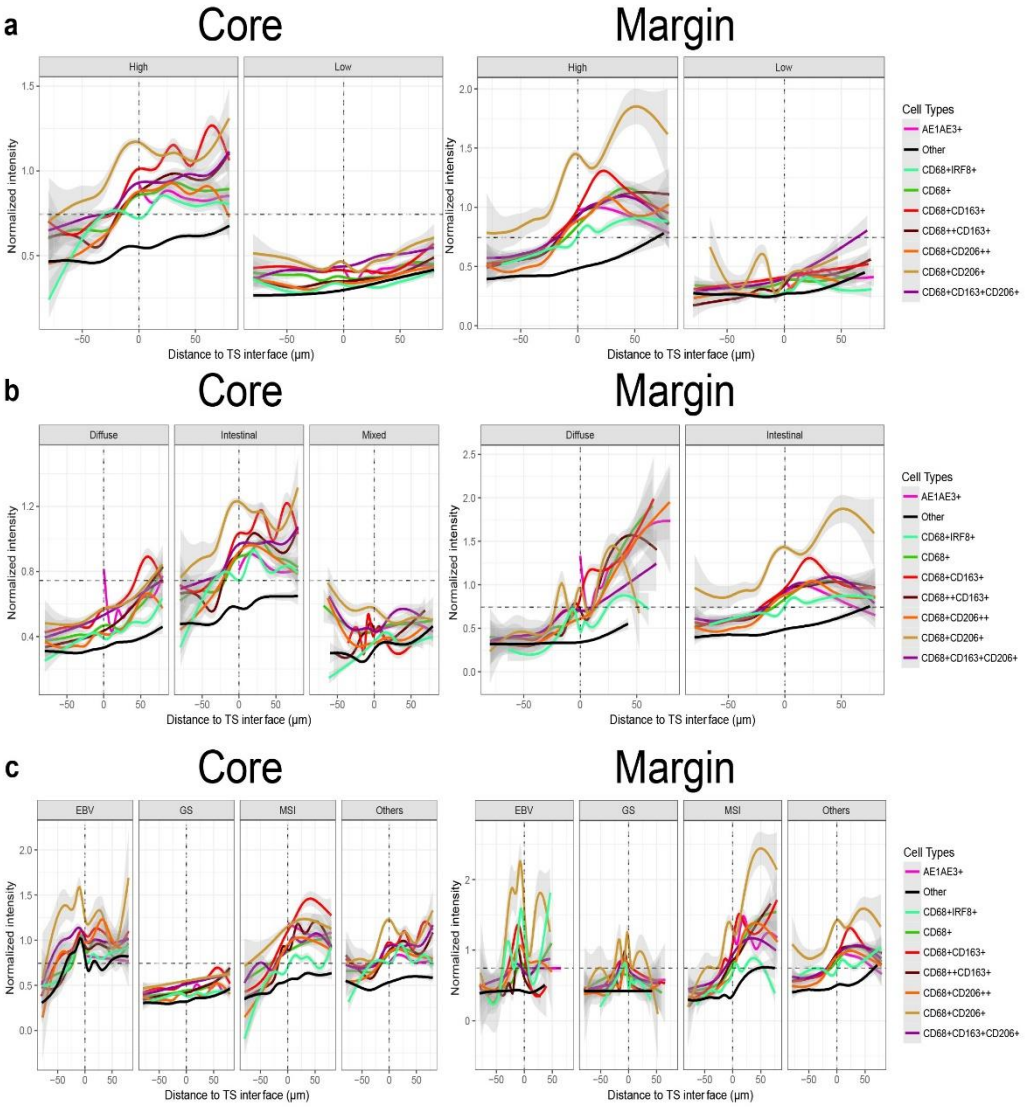
Median PDL1 Expression on TAMs		Cancer subtype				TNM stages				AJCC stages	
	Terciles	Intestinal	Diffuse+Mixed	EBV+MSI	GS+Others	T4+T3	T2+T1	N3+N2	N1+N0	4+3	2+1
CD68+ IRF8+	Upper	12	2	6	8	11	3	2	12	7	7
	Medium	7	8	1	14	9	6	5	10	6	9
	Lower	8	6	2	12	11	3	5	9	8	6
	Chi-square	0.0817		0.0432		0.4329		0.3801		0.6496	
	Terciles	Intestinal	Diffuse+Mixed	EBV+MSI	GS+Others	T4+T3	T2+T1	N3+N2	N1+N0	4+3	2+1
CD68+	Upper	12	2	6	8	10	4	4	10	7	7
	Medium	11	4	2	13	11	4	3	12	7	8
	Lower	4	10	1	13	10	4	5	9	7	7
	Chi-square	0.0043		0.0451		0.9912		0.6397		0.9785	
	Terciles	Intestinal	Diffuse+Mixed	EBV+MSI	GS+Others	T4+T3	T2+T1	N3+N2	N1+N0	4+3	2+1
CD68+ CD163+	Upper	12	2	6	8	10	4	3	11	6	8
	Medium	10	5	2	13	12	3	5	10	9	6
	Lower	5	9	1	13	9	5	4	10	6	8
	Chi-square	0.0219		0.0451		0.6397		0.7731		0.563	
	Terciles	Intestinal	Diffuse+Mixed	EBV+MSI	GS+Others	T4+T3	T2+T1	N3+N2	N1+N0	4+3	2+1
CD68++ CD163+	Upper	12	2	6	8	10	4	3	11	6	8
	Medium	10	5	2	13	12	3	5	10	10	5
	Lower	5	9	1	13	9	5	4	10	5	9
	Chi-square	0.0219		0.0451		0.6397		0.7731		0.2151	
	Terciles	Intestinal	Diffuse+Mixed	EBV+MSI	GS+Others	T4+T3	T2+T1	N3+N2	N1+N0	4+3	2+1
CD68+ CD206++	Upper	13	1	6	8	10	4	3	11	6	8
	Medium	9	6	2	13	11	4	6	9	10	5
	Lower	5	9	1	13	10	4	3	11	5	9
	Chi-square	0.0072		0.0451		0.9912		0.4329		0.2151	
	Terciles	Intestinal	Diffuse+Mixed	EBV+MSI	GS+Others	T4+T3	T2+T1	N3+N2	N1+N0	4+3	2+1
CD68+ CD206+	Upper	13	1	6	8	12	2	4	10	8	6
	Medium	9	6	2	13	10	5	3	12	8	7
	Lower	5	9	1	13	9	5	5	9	5	9
	Chi-square	0.0072		0.0451		0.3801		0.6397		0.4788	
	Terciles	Intestinal	Diffuse+Mixed	EBV+MSI	GS+Others	T4+T3	T2+T1	N3+N2	N1+N0	4+3	2+1
CD68+ CD163+ CD206+	Upper	12	2	6	8	11	3	3	11	7	7
	Medium	9	6	2	13	11	4	5	10	9	6
	Lower	6	8	1	13	9	5	4	10	5	9
	Chi-square	0.0614		0.0451		0.695		0.7731		0.423	

d



Supplementary Figure 7: PDL1 expression is both TAM and gastric cancer subtype associated
a Normalized PDL1 intensity on each cell type. Dashed line: mean intensity of all cell types, black dots: average expressions of the individual cell types. **b** Representative images of PDL1+ cells and intensity of its ranking. **c** Cell number and percentage of PDL1+ cells in each cell type per interval (from high [0%] to low [100%]). Dot and error bar show mean ± SD of five independent randomly selected sampling cohorts (n=5). Dashed line shows the mean PDL1 intensity of the cohort which was used to define the positivity of PDL1. Error bars represent mean ± SD of five independent randomly selected subsampling cohorts. **d** TAM classified patient OS using median PDL1 expression on each TAM population and the survival classified with cancer molecular (TCGA) subtype. Red: Upper tercile (density >2/3 of the patients in the study cohort), Black: Middle tercile (2/3 ≥ density > 1/3), Blue: Lower tercile (density ≤ 1/3). Log-rank (Mantel-Cox) test. **e** Univariate analyses of clinical parameters of TAM population classified OS in Supplementary Fig. 7d. Chi-square analysis.

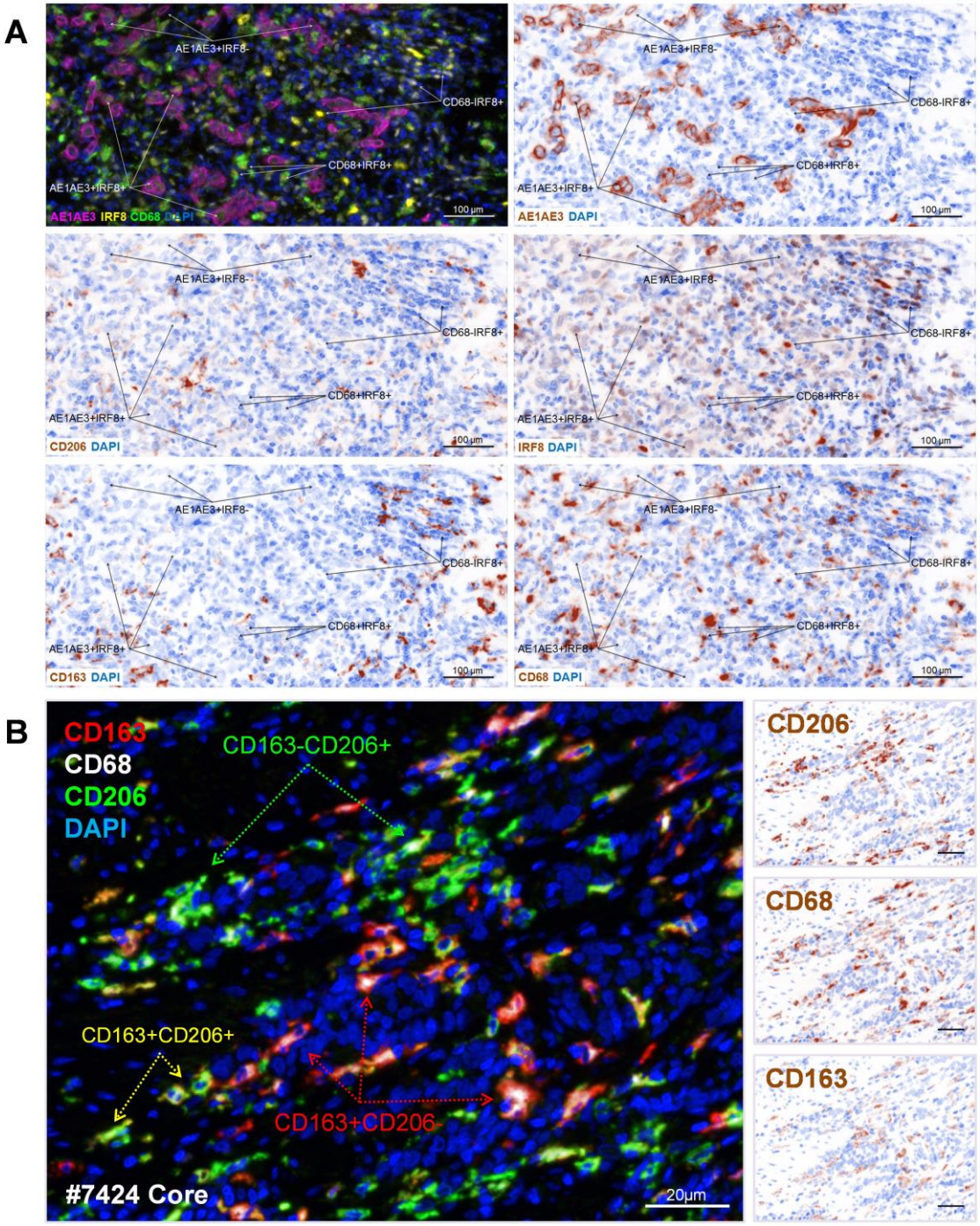
Supplementary Figure 8



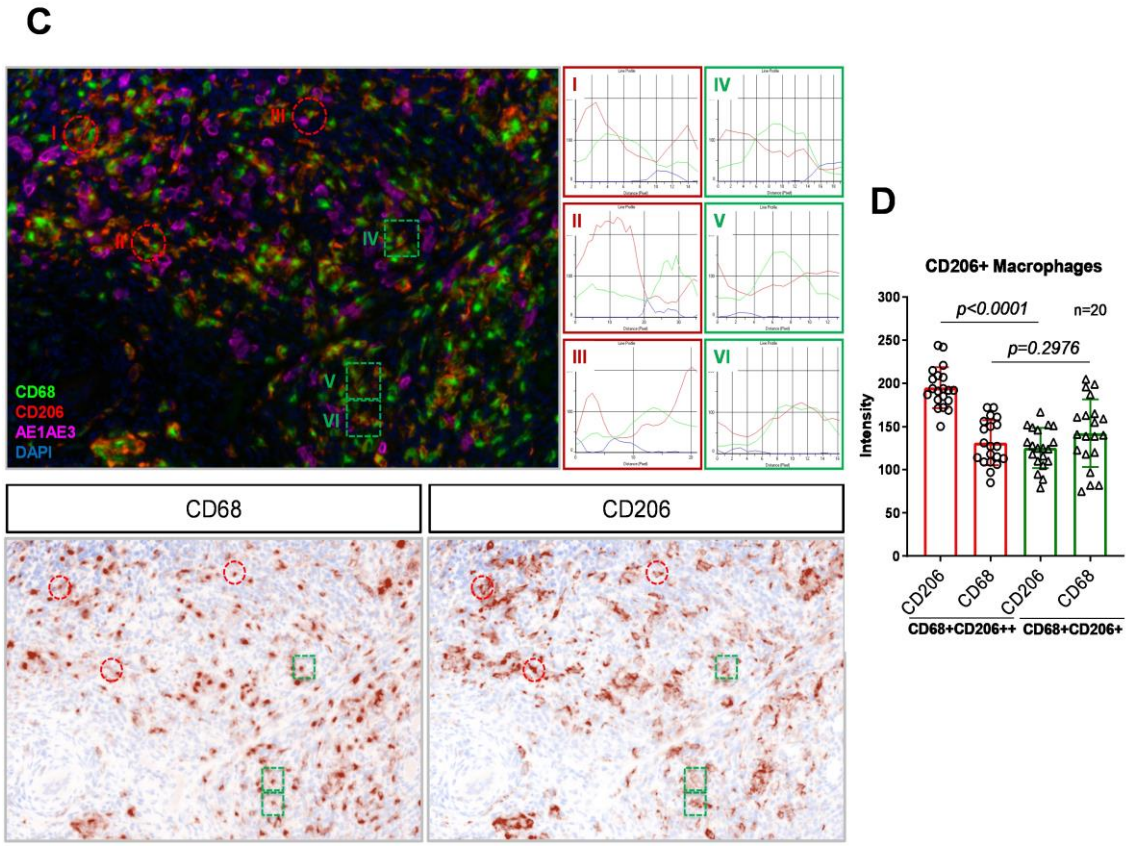
Supplementary Figure 8: High PDL1 TAMs are located in the tumor-nest areas and are gastric cancer subtype associated

a PDL1 expression on each cell population of patient defined as PDL1-high (H) and PDL1-low (L) in the core and at the margin. **b-c** PDL1 expression on each cell population of patient grouped by the cancer (**b**) Histological (Lauren) and (**c**) Molecular (TCGA) classification in the core and at the margin.

Appendix 2 Identification and characterisation of TAM populations



Appendix 2 Continued



(A) M1-like macrophage: CD68+IRF8+ and CD68+. Non-macrophage IRF8+ cells: CD68-IRF8+. AE1AE3+: Tumour cells. (B) Co-localisation of three M2-like macrophage populations: CD163+ (CD206-), CD206+ (CD163-) and CD163+CD206+. Scale bar: 20 µm. (C) Representative image of the CD68+CD206++ and CD68+CD206+ TAMs and marker intensity of CD68 and CD206 on TAMs analysed with the ImagePro software. Intensity of markers on numbered cells were plotted in the matched numbered plots and single-stained IHC image of CD68 and CD206 from the same section. Red circle: CD68+CD206++ TAMs, Green square: CD68+CD206+ TAMs. X axis: Distance in pixels, Y axis: Intensity of marker. Colours in the plots: CD206 (red), CD68 (green) and DAPI (blue). Scale bar: 100 µm. (D) Quantification of the maximum intensity of CD68 and CD206 on the macrophages (n=20 for each population) in (C). Bar and error bars represent mean ± SD, ***p<0.001. Mann-Whitney U test. Figure from[466].

Appendix 3 in vitro-polarised macrophage genes

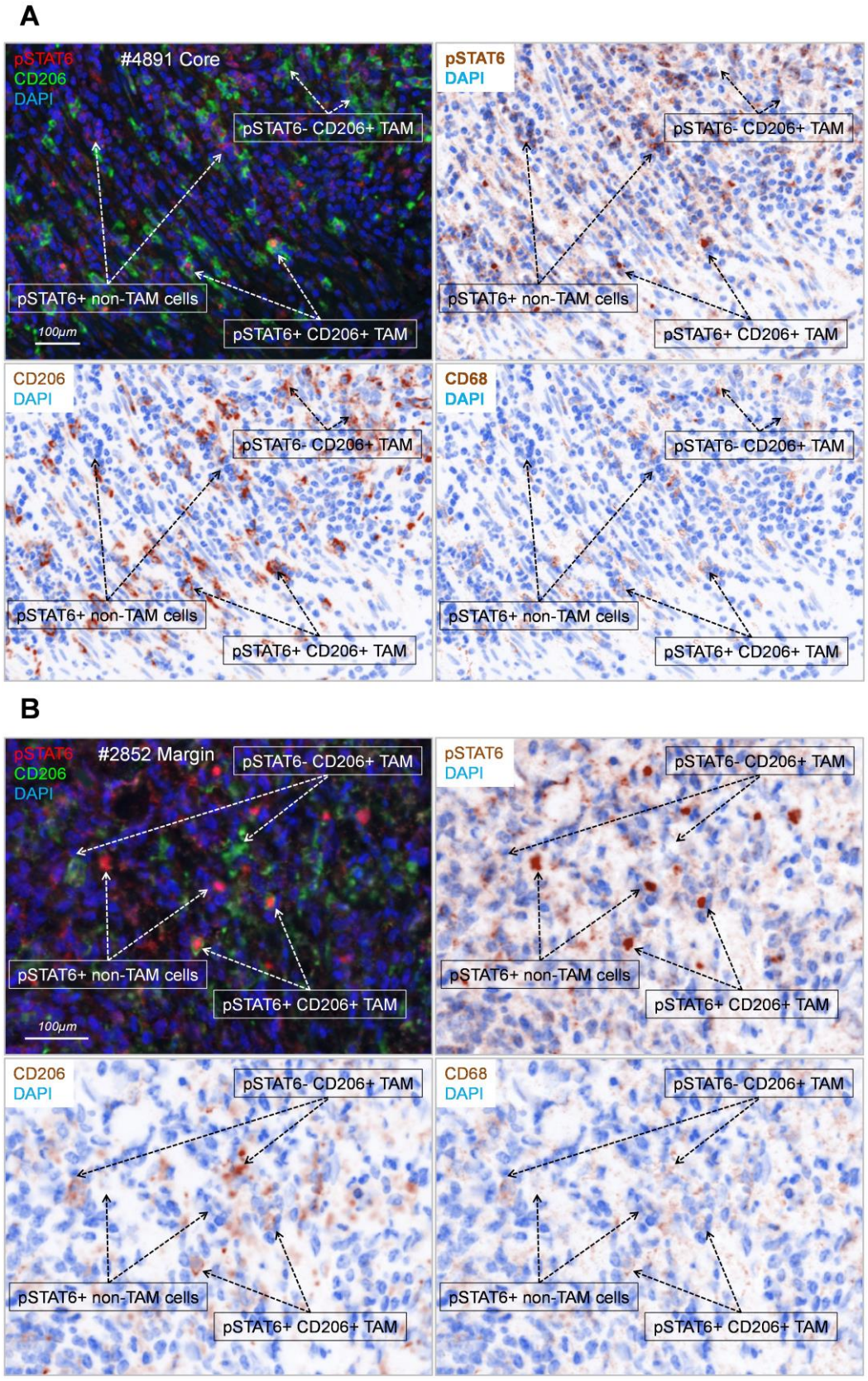
Differentially-expressed genes between the M1/M2 macrophages identified from the literature.

	M1-like (71)				M1/M2-like (19)	
No.	Gene	probe	Gene	probe	Gene	probe
1	AK3	224655_at	INHBA	210511_s_at	ADAMDEC1	206134_at
2	APOL1	209546_s_at	IRF1	202531_at	CCL2	216598_s_at
3	APOL2	221653_x_at	IRF5	205469_s_at	CD68	203507_at
4	APOL3	221087_s_at	IRF7	208436_s_at	CLEC7A	221698_s_at
5	APOL6	241869_at	IRF8	204057_at	HCK	208018_s_at
6	ATF3	202672_s_at	LAMP3	205569_at	HLA-DQA1	213831_at
7	BCL2A1	205681_at	NAMPT	1555167_s_at	HLA-DRB4	209728_at
8	BIRC3	210538_s_at	NOS2	210037_s_at	IL18	206295_at
9	CCL15	210390_s_at	OAS2	204972_at	IL18R	206618_at
10	CCL19	210072_at	OASL	210797_s_at	IL18RAP	207072_at
11	CCL20	205476_at	PDGFA	205463_s_at	IL23	220054_at
12	CCL4	204103_at	PFKFB3	202464_s_at	IL6	205207_at
13	CCL5	1405_i_at	PFKP	201037_at	IL8	202859_x_at
14	CCR7	206337_at	PLA1A	219584_at	TGFB2	220407_s_at
15	CCR8	208059_at	PSMA2	201317_s_at	TGFB3	209747_at
16	CD38	205692_s_at	PSMB9	204279_at	TGFBI	201506_at
17	CD40	205153_s_at	PSME2	201762_s_at	TNFAIP6	206025_s_at
18	CHI3L2	213060_s_at	PTX3	206157_at	TNFalpha	207113_s_at
19	CXCL1	204470_at	RSAD2	242625_at	TNFSF10	202687_s_at
20	CXCL10	204533_at	SLC2A6	220091_at		
21	CXCL11	211122_s_at	SLC31A2	204204_at		
22	CXCL16	223454_at	SLC7A5	201195_s_at		
23	CXCL2	209774_x_at	SLCO5A1	220984_s_at		
24	CXCL3	207850_at	SPHK1	219257_s_at		
25	CXCL9	203915_at	STAT1	209969_s_at		
26	CXCR3	217119_s_at	XAF1	206133_at		
27	CYP27B1	205676_at				
28	EBI3	219424_at				
29	EDN1	218995_s_at				
30	FAS	204780_s_at				
31	GADD45G	204121_at				
32	HESX1	211267_at				
33	HSD11B1	205404_at				
34	IDO1	210029_at				
35	IFNA1	208344_x_at				
36	IFNG	210354_at				
37	IGFBP4	201508_at				
38	IL12A	207160_at				
39	IL12B	207901_at				
40	IL15	205992_s_at				
41	IL15RA	207375_s_at				
42	IL1A	210118_s_at				
43	IL1B	205067_at				
44	IL2RA	211269_s_at				
45	IL7R	205798_at				

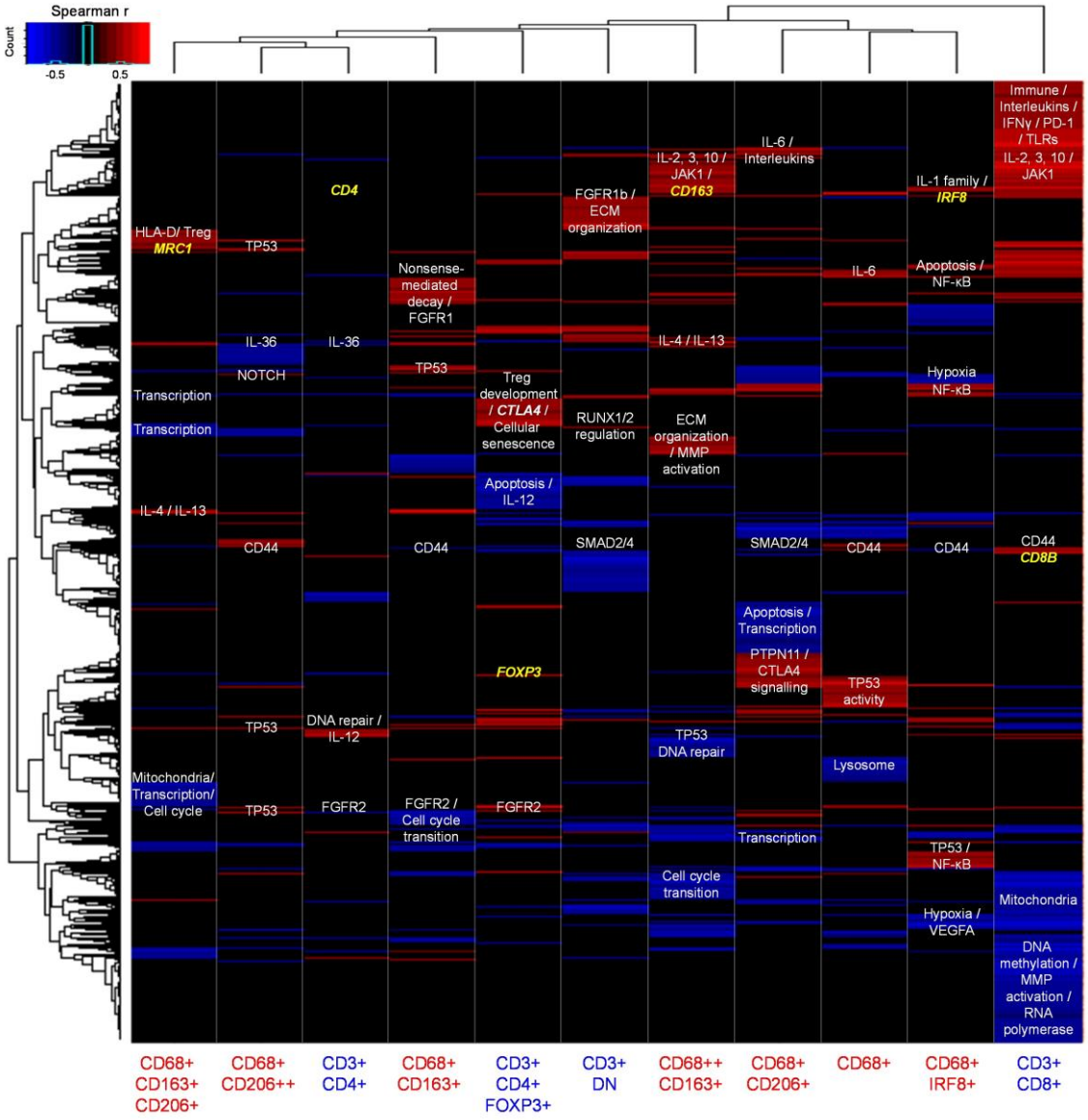
Appendix 3 Continued

	M2-like (82)				Others (45)	
No.	Gene	probe	Gene	probe	Gene	probe
1	ACP5	204638_at	MMP1	204475_at	AKT1	207163_s_at
2	ADK	204119_s_at	MMP2	201069_at	CASP3	202763_at
3	AIF1	215051_x_at	MMP9	203936_s_at	CCL1	207533_at
4	ALOX15	207328_at	MRC1	204438_at	CCL3	205114_s_at
5	ARG1	206177_s_at	MRC2	37408_at	CCR2	207794_at
6	ARG2	203946_s_at	MS4A4A	219607_s_at	CD14	201743_at
7	CA2	209301_at	MS4A6A	223922_x_at	COX-2	1554997_a_at
8	CCL13	206407_s_at	MSR1	208423_s_at	CSF1	211839_s_at
9	CCL17	207900_at	NCF2	209949_at	CSF1R	203104_at
10	CCL18	209924_at	κIA	201502_s_at	CSF2	210229_s_at
11	CCL22	207861_at	NFKBIB	214448_x_at	CXCL12	209687_at
12	CCL23	210549_s_at	NOVA1	205794_s_at	EGF	206254_at
13	CD163	215049_x_at	NPL	223405_at	EGFR	201983_s_at
14	CD180	206206_at	P2RY13	220005_at	ENG	201809_s_at
15	CD200R1	1553395_a_at	P2RY14	206637_at	EPAS1	200878_at
16	CD36	206488_s_at	PDGFB	216061_x_at	FIGF	206742_at
17	CERK	218421_at	PIK3CG	206369_s_at	HGF	210998_s_at
18	CHN2	213385_at	PIK3IP1	221756_at	HIF1A	200989_at
19	CLEC10A	206682_at	PLAU	205479_s_at	HIF3A	233517_s_at
20	CLEC4A	221724_s_at	RNASE6	213566_at	ICAM1	202637_s_at
21	CTSC	201487_at	SEPP1	201427_s_at	IL13	207844_at
22	CTSL1	202087_s_at	SHH	236263_at	IL17A	216876_s_at
23	CXCR4	211919_s_at	SLAMF1	1555626_a_at	IL3RA	206148_at
24	DCSIGN	207277_at	SLC15A3	219593_at	IL-4	207538_at
25	EGR2	205249_at	SLC38A6	214830_at	ITGAM	205786_s_at
26	FCER2	206759_at	SLC4A7	207604_s_at	JAK1	1552611_a_at
27	FGL2	204834_at	SLCO2B1	203472_s_at	JAK2	205842_s_at
28	FN1	216442_x_at	STAT3	208991_at	LDHA	200650_s_at
29	GAS6	1598_g_at	STAT6	201331_s_at	MAPK1	224621_at
30	GAS7	211067_s_at	TAC1	206552_s_at	MAPK14	202530_at
31	HEXB	201944_at	TGFBR2	207334_s_at	MAPK3	212046_x_at
32	HNMT	204112_s_at	TGM2	211003_x_at	MIF	217871_s_at
33	HRH1	205580_s_at	TLR5	210166_at	MKI67IP	224713_at
34	HS3ST1	205465_x_at	TPST2	204079_at	MPG-E8	203686_at
35	HS3ST2	219697_at	TREM2	219725_at	PD1	207634_at
36	IGF1	209540_at	TRPM2	205708_s_at	PDL1	223834_at
37	IL-10	207433_at	VIP	206577_at	PECAM1	208983_s_at
38	IL1RN	212657_s_at			PGE2	206631_at
39	IRF4	216986_s_at			PGF	209652_s_at
40	LIPA	201847_at			PIK3CA	204369_at
41	LPAR6	218589_at			PIK3CB	212688_at
42	LTA4H	208771_s_at			VCAM1	203868_s_at
43	LY86	205859_at			VEGFA	210512_s_at
44	MAF	206363_at			VEGFB	203683_s_at
45	MERTK	206028_s_at			VEGFC	209946_at

Appendix 4 Phosphorylated-STAT6 staining in GC in different ROIs



Appendix 5 Unsupervised clustering of TAM and TIL-associated pathways



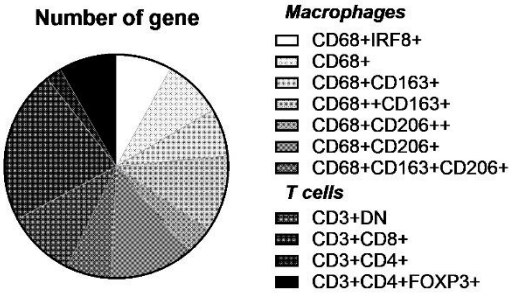
Pathways associated with each of the immune density-derived environmental gene signature using the Reactome online database. *: FDR<0.05. (Benjamini-Hochberg). Red/black/blue: positive/no/negative Spearman correlation. Yellow: gene of the markers used in multiplex IHC panels for cell phenotype characterisation. MRC1: mannose receptor C-type 1, CD206.

Appendix 6 Characterisation of immune gene signatures with pathway categories

A

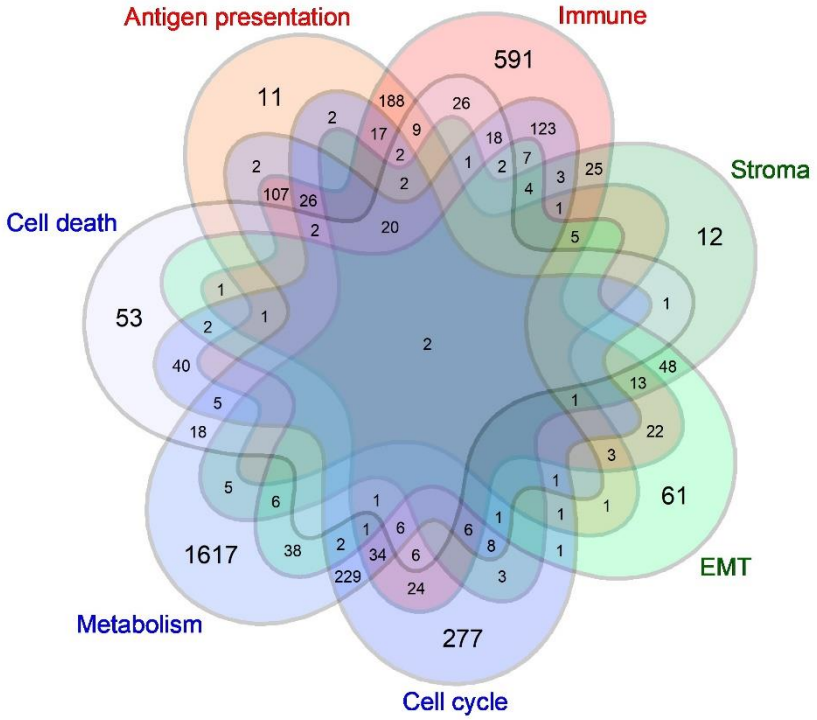
Pathways	Keywords
1. Immune	immune, interleukin, TLR, cytokine, chemokine, IFN, interferon, PD-1, lymphocyte
2. Antigen presentation	antigen, presentation, present, MHC, phagocytosis, reactive, oxidases
3. EMT	matrix, extracellular, EMT, collagen
4. Stroma	collagen, fibrosis, FGF
5. Cell death	apoptosis, caspase, death, necrosis
6. Cell cycle	cycle, mitotic, mitosis
7. Metabolism	metabolism

B



		Macrophage							T cell			
Gene / Cell type		CD68+ IRF8+	CD68+	CD68+ CD163+	CD68++ CD163+	CD68+ CD206++	CD68+ CD206+	CD68+ CD163+ CD206+	CD3+ DN	CD3+ CD8+	CD3+ CD4+	CD3+ CD4+ FOXP3+
Number	10021	1382	1476	1185	1914	725	2059	1120	1710	3815	399	1432
%	100	13.79	14.73	11.83	19.10	7.23	20.55	11.18	17.06	38.07	3.98	14.29

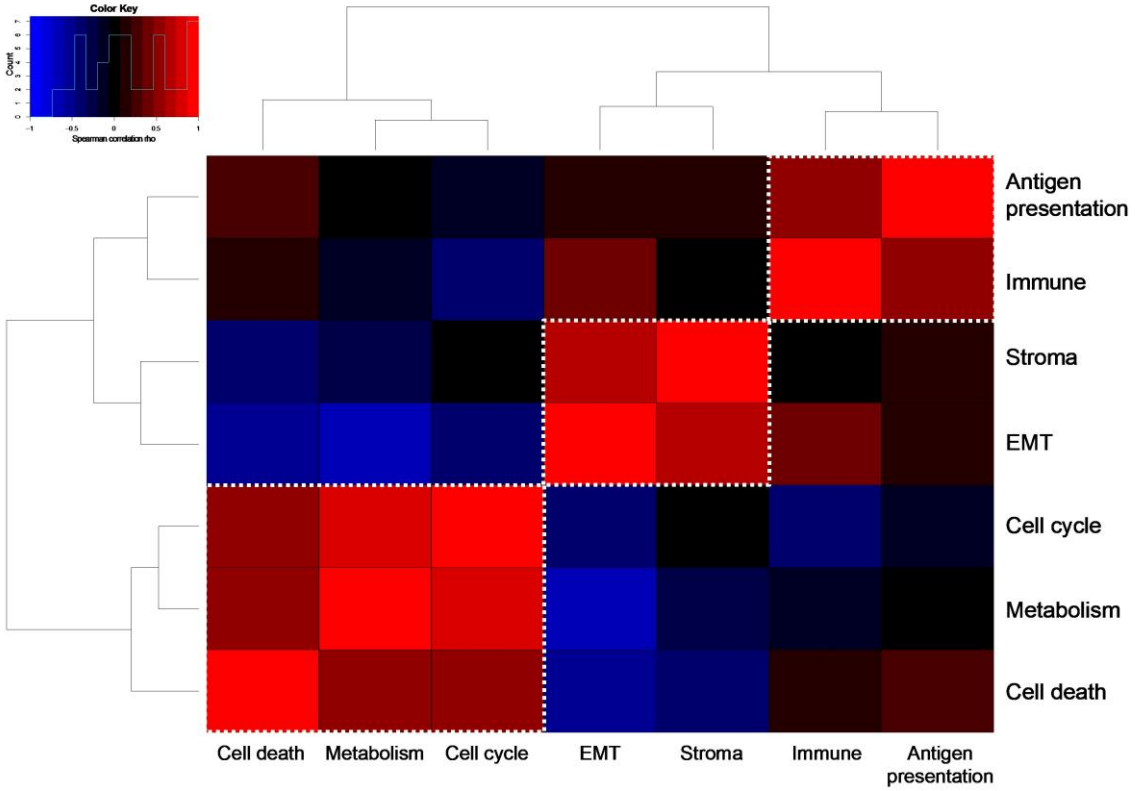
C



Number of gene	Antigen presentation	Immune	Stroma	EMT	Cell cycle	Metabolism	Cell death
	404	1300	167	225	723	2296	218

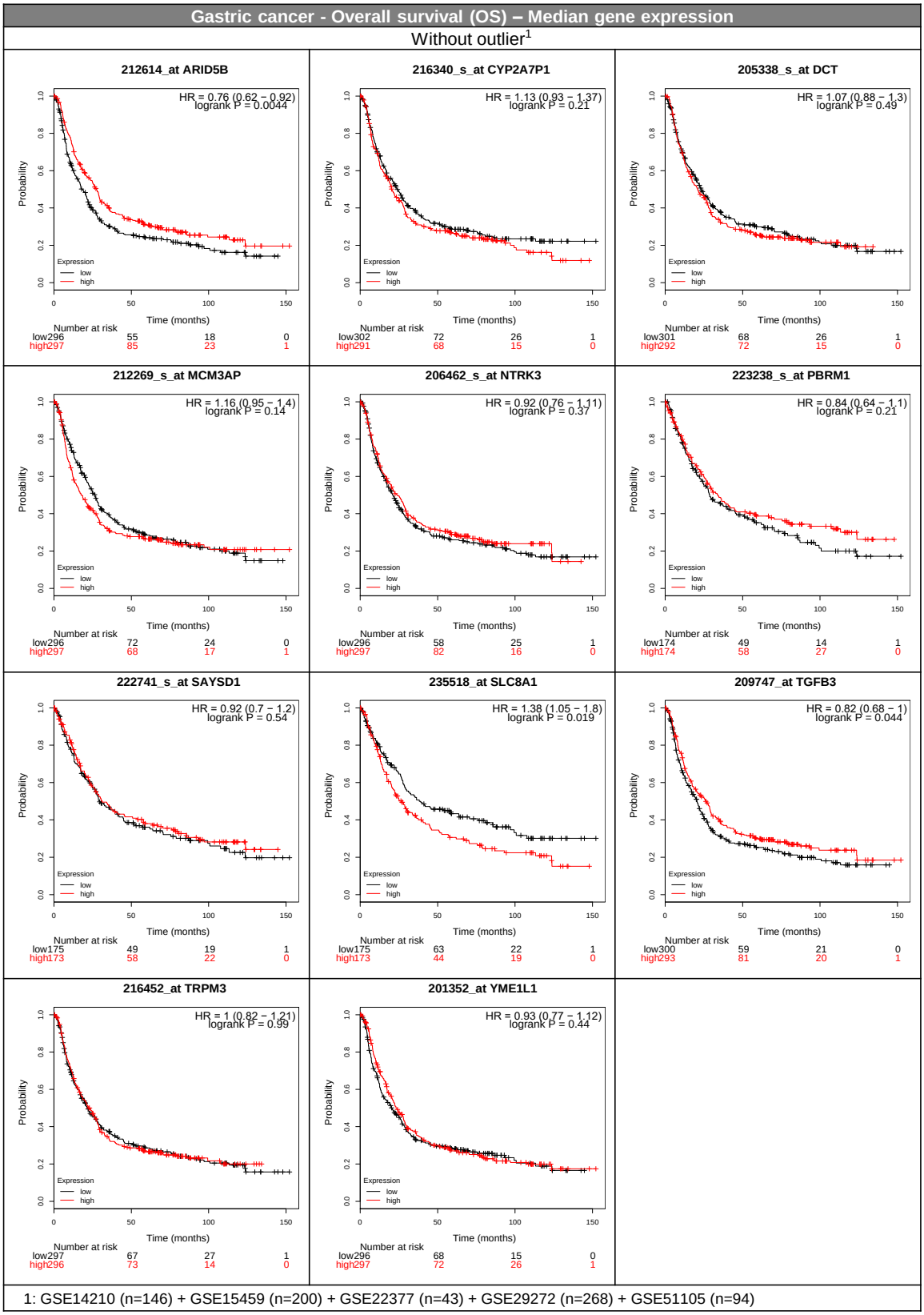
Appendix 6 Continued

D



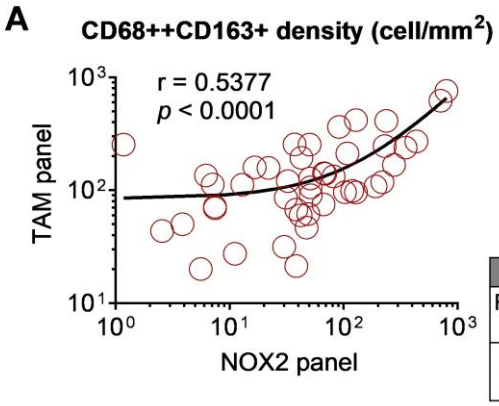
(A) Key words used for TAM-associated pathway identification. (B) Number and percentage of genes between different immune populations. (C) Number and (D) Spearman correlation of genes between identified pathways. Red/black/blue: positive/no/negative correlation.

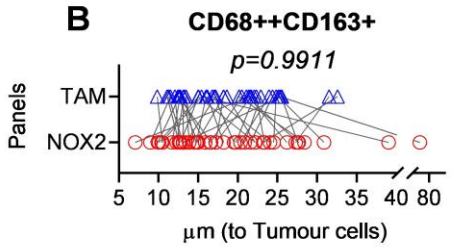
Appendix 7 Overall survival with inversely correlated genes between the CD68++CD163+ and CD68+IRF8+ TAMs



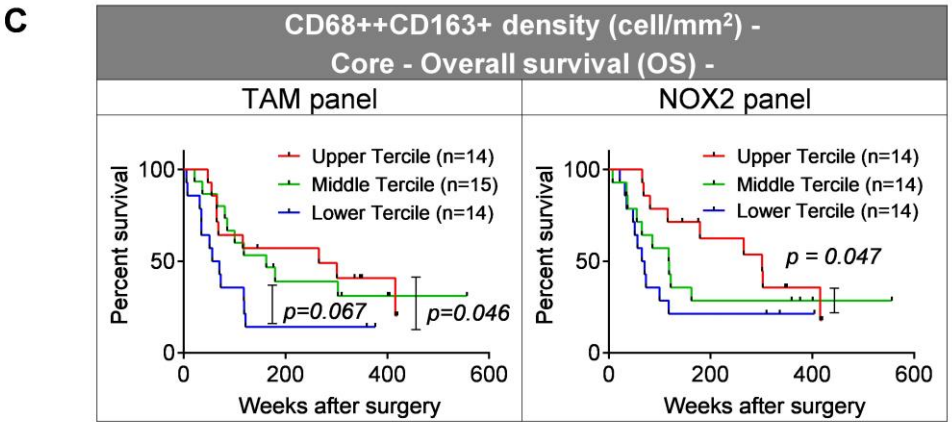
1: GSE14210 (n=146) + GSE15459 (n=200) + GSE22377 (n=43) + GSE29272 (n=268) + GSE51105 (n=94)

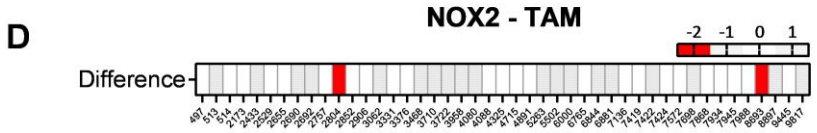
Appendix 8 Validation of cell phenotyping between multiplex IHC panels





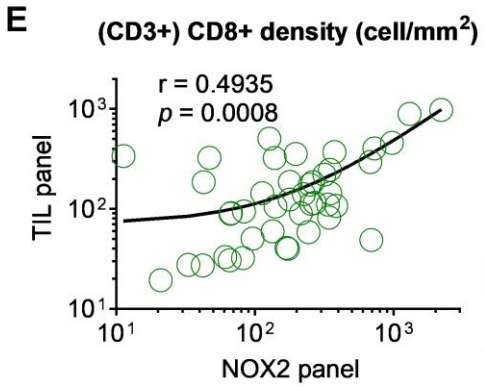
Validation between multiplex IHC panels - Distance						
Reference cell	Nearest cell	Panel	Median	Mean	SD	n
CD68++ CD163+	Tumour	TAM	16.90	18.06	5.59	46
		NOX2	16.62	19.31	10.74	45

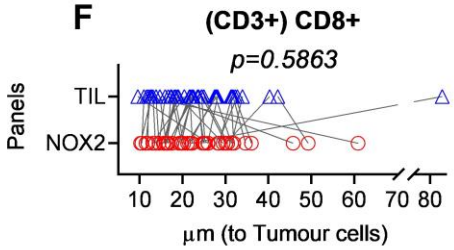




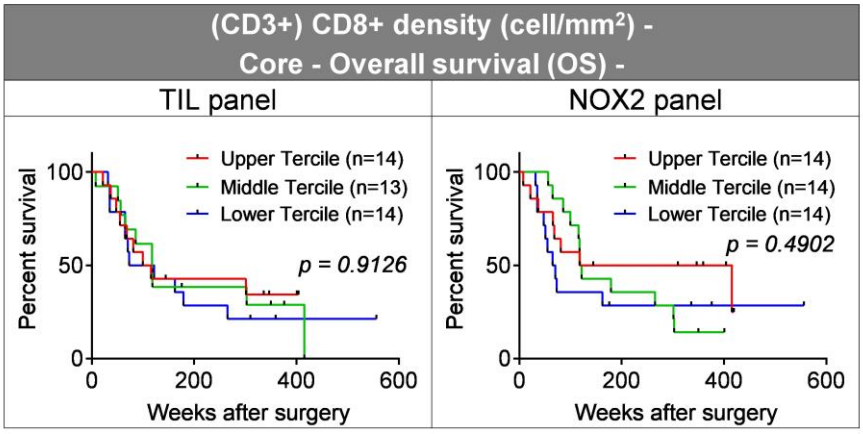
Validation between multiplex IHC panels - OS				
Reference cell	n	Identical	Swapped	Inversed
CD68++CD163+	42	24	16	2
% in cohort	100	57.14	38.10	4.76

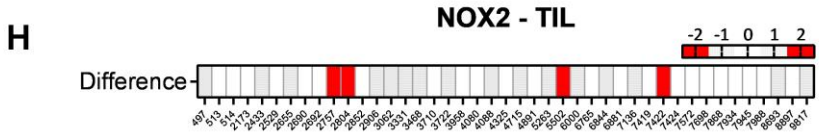
(A-D) Comparing CD68++CD163+ TAM results between multiplex TAM and NOX2 panel: (A) Density Spearman correlation, (B) distance to tumour cells calculated with ISAT, (C) overall survival relevance, (D) and allocation of patients in survival grouping based on their TAM densities within the Core. Identical (white): patient grouping remains the same between panels. Swapped (grey): patient grouping changed between Upper and Middle, and between Middle and Lower terciles in (C). Inversed (red): patient grouping changed between Upper and Lower terciles.





Validation between multiplex IHC panels - Distance						
Reference cell	Nearest cell	Panel	Median	Mean	SD	n
(CD3+) CD8+	Tumour	TIL	22.14	23.73	12.68	43
		NOX2	21.17	23.36	10.56	45

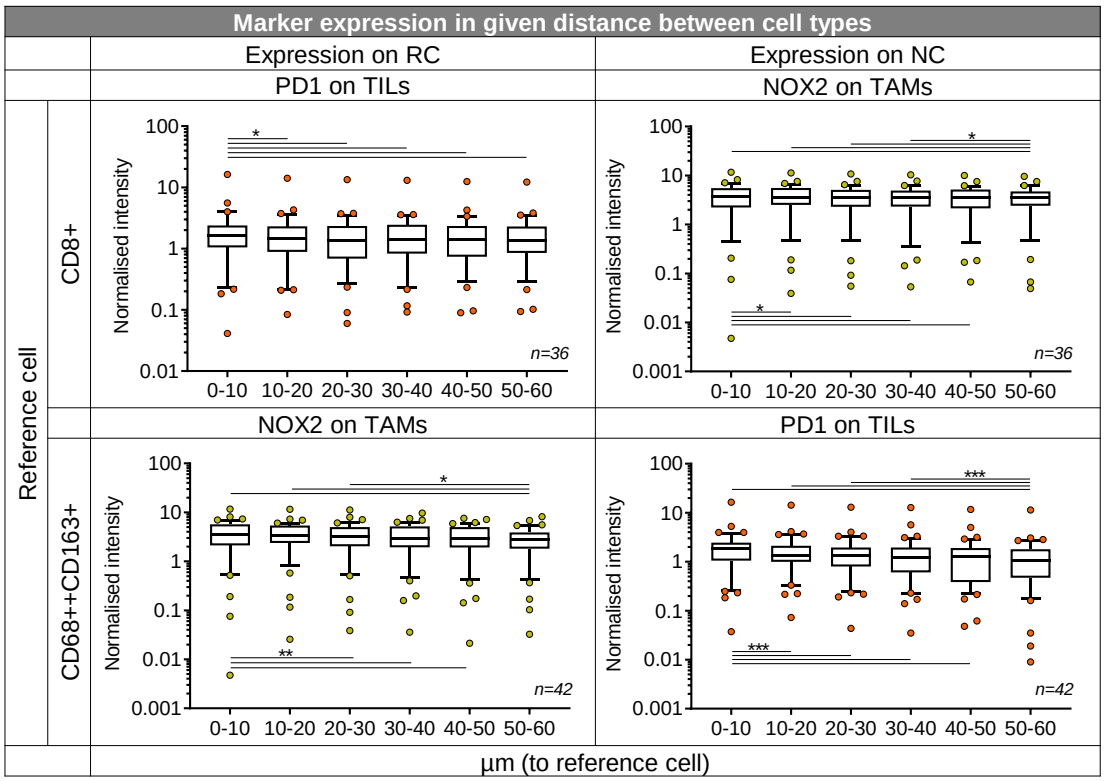




Validation between multiplex IHC panels - OS				
Reference cell	n	Identical	Swapped	Inversed
(CD3+) CD8+	41	23	14	4
% in cohort	100	56.10	34.15	9.76

(E-H) Comparing (CD3+)CD8+ TIL results between multiplex TIL and NOX2 panel: (A) Density Spearman correlation, (B) distance to tumour cells calculated with ISAT, (C) overall survival relevance, (D) and allocation of patients in survival grouping based on their TAM densities within the Core. Identical (white): patient grouping remains the same between panels. Swapped (grey): patient grouping changed between Upper and Middle, and between Middle and Lower terciles in (C). Inversed (red): patient grouping changed between Upper and Lower terciles.

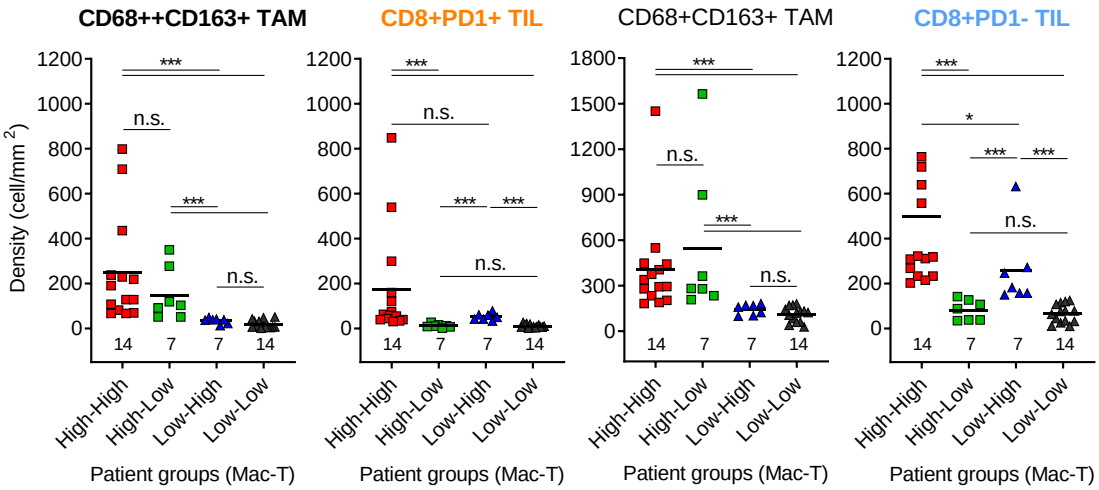
Appendix 9 Functional marker expressions on immune cells in proximity



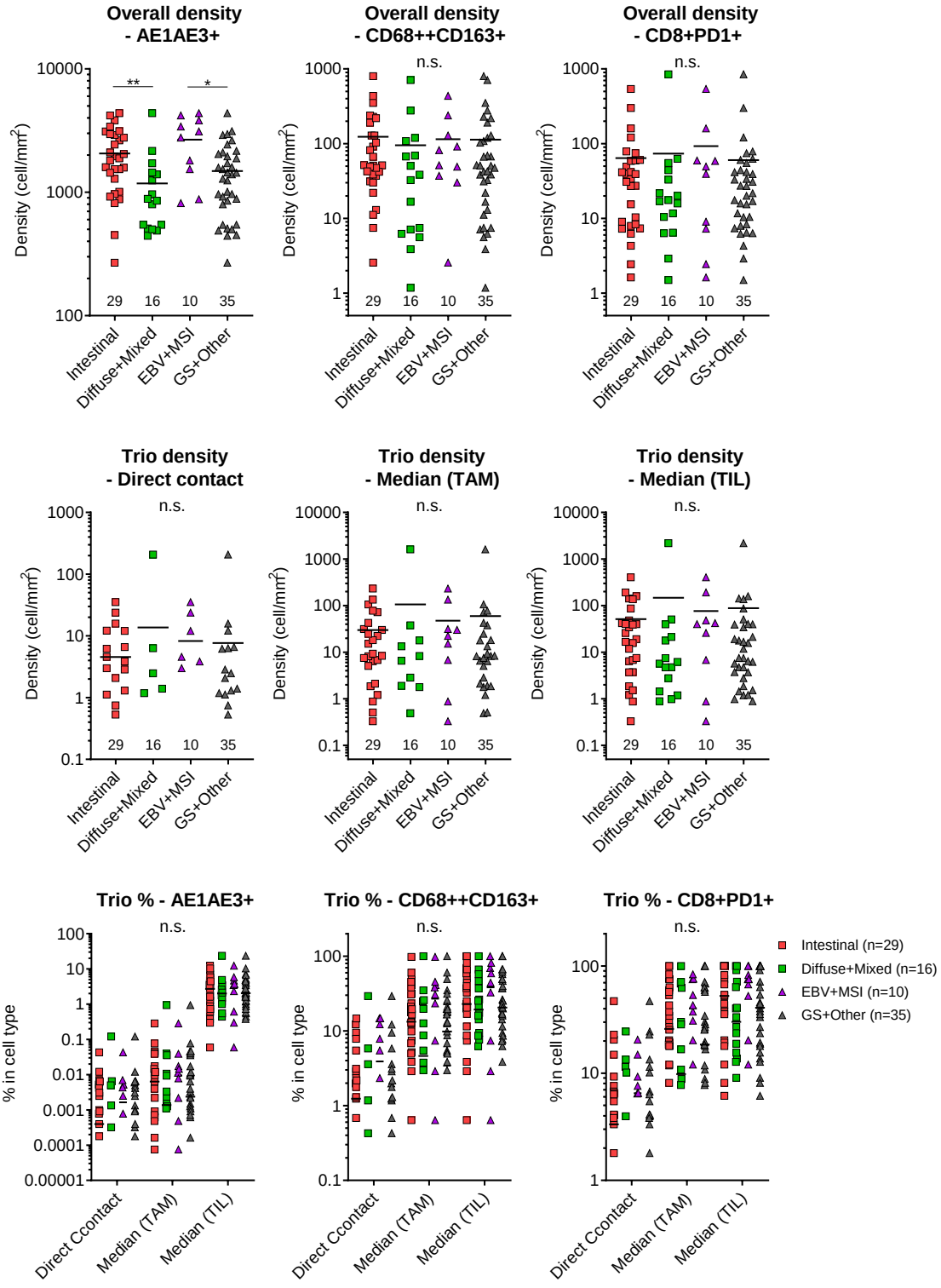
NOX2 and PD1 expression on TAMs and TILs within 60 µm. Lines represent median intensity. n=45 in each distance range. Each point represents the median intensity of the corresponding marker on cells of one patient. *p<0.05 and not significant (n.s.) comparing between marker intensities within each distance range. Wilcoxon matched-pairs signed rank test.

Appendix 10 Density between TAM/TIL stratified patient groups

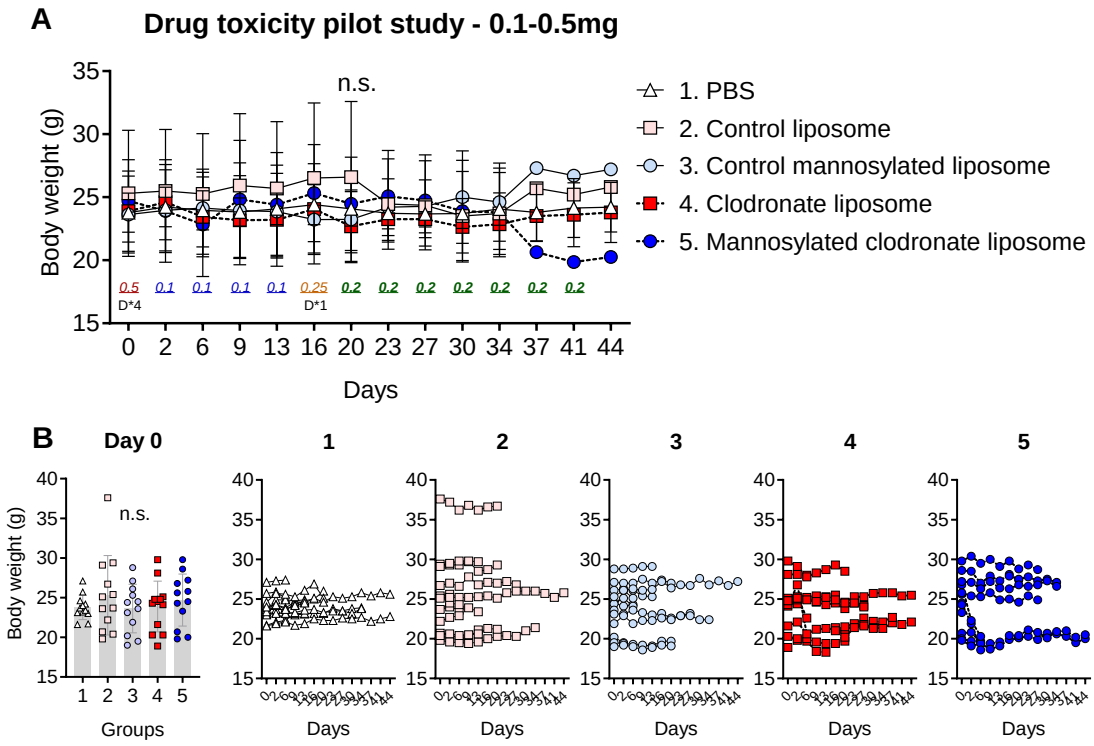
Density of the corresponding cell populations between the four patient groups. Patients overall and relapse-free survival were interrogated between the four groups of patients identified in Figure 7.3.16. Mac-T: grouping related with macrophage and T cell density.



Appendix 11 Immune/Tumour trio density and percentage among GC subtypes

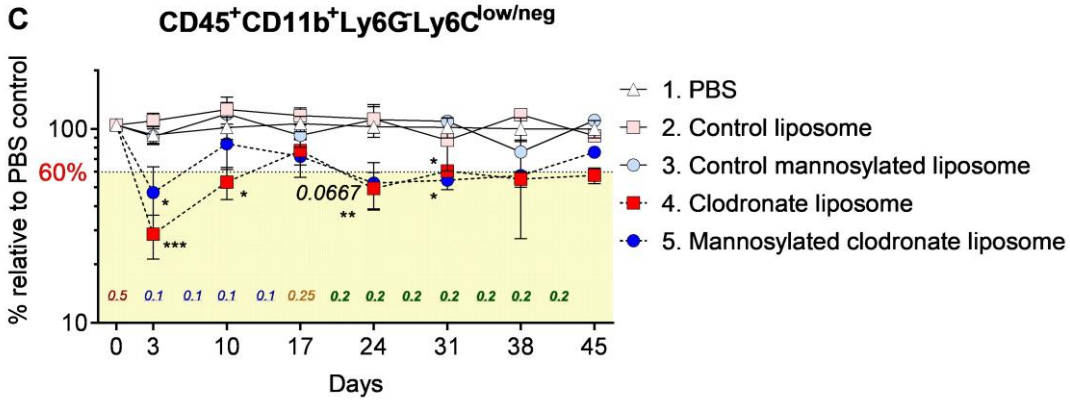


Appendix 12 Full timeline of in vivo macrophage depletion safety study



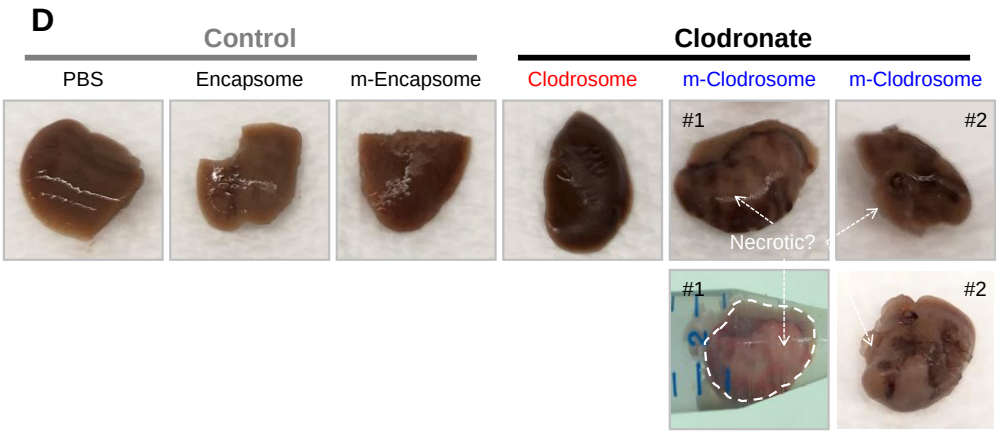
Each coloured symbol represents each data collection time point of each group. (A) Each line (solid and dashed) represents each group. Italic numbers indicate clodronate-liposome dose. D: mouse died. (B) Each line represents individual mice. Bar and error bars represent mean ± SD. Not significant (n.s.) comparing (A) drug injected groups to PBS control and (B) between experimental groups. Mann-Whitney U test.

Appendix 12 Continued



CD45+CD11b+Ly6G-Ly6C$^{low/neg}$ (Median % relative to PBS control)								
Concentration	0.5	0.1		0.25	0.2			
Days post injection	3	3	3	4	3	3	3	4
Duration	3	10	17	21	24	31	38	45
1. PBS	100.00	100.00	100.00	100.00	100.00	100.00	100.00	100.00
2. Control liposome	98.00	145.12	113.18	178.38	106.09	87.37	118.12	92.07
3. Control mannosylated liposome	85.47	120.89	86.84	181.51	103.96	109.38	76.10	110.53
4. Clodronate liposome	25.75	48.46	84.57	158.56	55.12	57.03	55.10	57.58
5. Mannosylated clodronate liposome	21.04	60.78	58.25	168.17	33.56	54.13	57.41	75.88

CD45+CD11b+Ly6G-Ly6C$^{low/neg}$ (Median % relative to PBS control)												
Concentration	0.5	0.1				0.25	0.2					
Days post injection	3	4	3	4	3	4	3	4	3	4	3	4
Duration	3	7	10	14	17	21	24	28	31	35	38	45
1	100.00	100.00	100.00	100.00	100.00	100.00	100.00	100.00	100.00	100.00	100.00	100.00
2	98.00	100.26	145.12	103.70	113.18	178.38	106.09	141.46	87.37	103.21	118.12	92.07
3	85.47	68.32	120.89	92.03	86.84	181.51	103.96	143.21	109.38	93.30	76.10	110.53
4	25.75	25.17	48.46	113.61	84.57	158.56	55.12	43.77	57.03	74.30	55.10	57.58
5	21.04	28.50	60.78	78.16	58.25	168.17	33.56	38.22	54.13	58.21	57.41	75.88



(C) Relative percentage of macrophage-like population of each experimental group normalised to PBS control. Each line represents each experimental group. Each point represents each data collecting time point. *p<0.05, and **p<0.01 comparing clodronate-liposome injected groups to PBS control. Mann-Whitney U test. (D) Representative mouse liver images at Week1 post clodronate-liposome injection with 0.5mg/dose. Abnormal liver morphology observed for the mannosylated clodronate-liposome group.

References

1. Bray, F. *et al.* Global cancer statistics 2018: GLOBOCAN estimates of incidence and mortality worldwide for 36 cancers in 185 countries. *CA Cancer J Clin* **68**, 394-424 (2018).
2. Ferlay, J. *et al.* Estimating the global cancer incidence and mortality in 2018: GLOBOCAN sources and methods. *Int J Cancer* **144**, 1941-1953 (2019).
3. Kim, H. *et al.* Effectiveness of Gastric Cancer Screening on Gastric Cancer Incidence and Mortality in a Community-Based Prospective Cohort. *Cancer Res Treat* **50**, 582-589 (2018).
4. Hamashima, C., Systematic Review, G. & Guideline Development Group for Gastric Cancer Screening, G. Update version of the Japanese Guidelines for Gastric Cancer Screening. *Jpn J Clin Oncol* **48**, 673-683 (2018).
5. Lin, D. *et al.* Gastroesophageal Junction Adenocarcinoma: Is There an Optimal Management? *Am Soc Clin Oncol Educ Book* **39**, e88-e95 (2019).
6. Pinto-De-Sousa, J., David, L., Seixas, M. & Pimenta, A. Clinicopathologic profiles and prognosis of gastric carcinomas from the cardia, fundus/body and antrum. *Dig Surg* **18**, 102-110 (2001).
7. Hu, B. *et al.* Gastric cancer: Classification, histology and application of molecular pathology. *J Gastrointest Oncol* **3**, 251-261 (2012).
8. Dicken, B.J. *et al.* Gastric adenocarcinoma: review and considerations for future directions. *Ann Surg* **241**, 27-39 (2005).
9. Lauren, P. The Two Histological Main Types of Gastric Carcinoma: Diffuse and So-Called Intestinal-Type Carcinoma. An Attempt at a Histo-Clinical Classification. *Acta Pathol Microbiol Scand* **64**, 31-49 (1965).
10. Ma, J., Shen, H., Kapesa, L. & Zeng, S. Lauren classification and individualized chemotherapy in gastric cancer. *Oncol Lett* **11**, 2959-2964 (2016).
11. Cislo, M. *et al.* Distinct molecular subtypes of gastric cancer: from Lauren to molecular pathology. *Oncotarget* **9**, 19427-19442 (2018).
12. Henson, D.E., Dittus, C., Younes, M., Nguyen, H. & Albores-Saavedra, J. Differential trends in the intestinal and diffuse types of gastric carcinoma in the United States, 1973-2000: increase in the signet ring cell type. *Arch Pathol Lab Med* **128**, 765-770 (2004).
13. van der Kaaij, R.T. *et al.* A population-based study on intestinal and diffuse type adenocarcinoma of the oesophagus and stomach in the Netherlands between 1989 and 2015. *Eur J Cancer* **130**, 23-31 (2020).
14. Olafsdottir, H.S. *et al.* [Epidemiology of the two types of gastric adenocarcinoma in Iceland according to the Lauren histological classification 1990-2009]. *Laeknabladid* **102**, 125-130 (2016).
15. Chong, Y. *et al.* DNA methylation status of a distinctively different subset of genes is associated with each histologic Lauren classification subtype in early gastric carcinogenesis. *Oncol Rep* **31**, 2535-2544 (2014).
16. Oliveira, C., Seruca, R. & Carneiro, F. Hereditary gastric cancer. *Best Pract Res Clin Gastroenterol* **23**, 147-157 (2009).

17. Busuttil, R.A. *et al.* Role of p53 in the progression of gastric cancer. *Oncotarget* **5**, 12016-12026 (2014).
18. Zheng, H. *et al.* Pathobiological characteristics of intestinal and diffuse-type gastric carcinoma in Japan: an immunostaining study on the tissue microarray. *J Clin Pathol* **60**, 273-277 (2007).
19. de Martel, C., Forman, D. & Plummer, M. Gastric cancer: epidemiology and risk factors. *Gastroenterol Clin North Am* **42**, 219-240 (2013).
20. Asano, N. *et al.* Cdx2 Expression and Intestinal Metaplasia Induced by H. pylori Infection of Gastric Cells Is Regulated by NOD1-Mediated Innate Immune Responses. *Cancer Res* **76**, 1135-1145 (2016).
21. Pattison, S. *et al.* Early relapses after adjuvant chemotherapy suggests primary chemoresistance in diffuse gastric cancer. *PLoS One* **12**, e0183891 (2017).
22. Hansford, S. *et al.* Hereditary Diffuse Gastric Cancer Syndrome: CDH1 Mutations and Beyond. *JAMA Oncol* **1**, 23-32 (2015).
23. Luo, W., Fedda, F., Lynch, P. & Tan, D. CDH1 Gene and Hereditary Diffuse Gastric Cancer Syndrome: Molecular and Histological Alterations and Implications for Diagnosis And Treatment. *Front Pharmacol* **9**, 1421 (2018).
24. van der Post, R.S. *et al.* Hereditary diffuse gastric cancer: updated clinical guidelines with an emphasis on germline CDH1 mutation carriers. *J Med Genet* **52**, 361-374 (2015).
25. Torabizadeh, Z., Nosrati, A., Sajadi Saravi, S.N., Yazdani Charati, J. & Janbabai, G. Evaluation of E-cadherin Expression in Gastric Cancer and Its Correlation with Clinicopathologic Parameters. *Int J Hematol Oncol Stem Cell Res* **11**, 158-164 (2017).
26. Wu, Z.Y. *et al.* Expression of E-cadherin in gastric carcinoma and its correlation with lymph node micrometastasis. *World J Gastroenterol* **11**, 3139-3143 (2005).
27. Bosman, F.T., Carneiro, F., Hruban, R.H., Theise, N.D. Classification of Tumours of the Digestive System. *Lyon:IARC* (2010).
28. Boussioutas, A. *et al.* Distinctive patterns of gene expression in premalignant gastric mucosa and gastric cancer. *Cancer Res* **63**, 2569-2577 (2003).
29. Kalluri, R. & Weinberg, R.A. The basics of epithelial-mesenchymal transition. *J Clin Invest* **119**, 1420-1428 (2009).
30. Tan, I.B. *et al.* Intrinsic subtypes of gastric cancer, based on gene expression pattern, predict survival and respond differently to chemotherapy. *Gastroenterology* **141**, 476-485, 485 e471-411 (2011).
31. Cancer Genome Atlas Research, N. Comprehensive molecular characterization of gastric adenocarcinoma. *Nature* **513**, 202-209 (2014).
32. Corso, S. & Giordano, S. How Can Gastric Cancer Molecular Profiling Guide Future Therapies? *Trends Mol Med* **22**, 534-544 (2016).
33. Raufi, A.G. & Klempner, S.J. Immunotherapy for advanced gastric and esophageal cancer: preclinical rationale and ongoing clinical investigations. *J Gastrointest Oncol* **6**, 561-569 (2015).
34. Rawla, P. & Barsouk, A. Epidemiology of gastric cancer: global trends, risk factors and prevention. *Prz Gastroenterol* **14**, 26-38 (2019).

35. Plummer, J.M. *et al.* Lynch syndrome in a predominantly Afrocentric population: a clinicopathological and genetic study. *Can J Surg* **55**, 294-300 (2012).
36. Fornasarig, M. *et al.* Molecular and Pathological Features of Gastric Cancer in Lynch Syndrome and Familial Adenomatous Polyposis. *Int J Mol Sci* **19** (2018).
37. Arnold, M. *et al.* The burden of stomach cancer in indigenous populations: a systematic review and global assessment. *Gut* **63**, 64-71 (2014).
38. Gupta, S. *et al.* Race/Ethnicity-, Socioeconomic Status-, and Anatomic Subsite-Specific Risks for Gastric Cancer. *Gastroenterology* **156**, 59-62 e54 (2019).
39. Lui, F.H., Tuan, B., Swenson, S.L. & Wong, R.J. Ethnic disparities in gastric cancer incidence and survival in the USA: an updated analysis of 1992-2009 SEER data. *Dig Dis Sci* **59**, 3027-3034 (2014).
40. Plummer, M. *et al.* Global burden of cancers attributable to infections in 2012: a synthetic analysis. *Lancet Glob Health* **4**, e609-616 (2016).
41. Zamani, M. *et al.* Systematic review with meta-analysis: the worldwide prevalence of Helicobacter pylori infection. *Aliment Pharmacol Ther* **47**, 868-876 (2018).
42. Helicobacter & Cancer Collaborative, G. Gastric cancer and Helicobacter pylori: a combined analysis of 12 case control studies nested within prospective cohorts. *Gut* **49**, 347-353 (2001).
43. de Vries, A.C. & Kuipers, E.J. Epidemiology of premalignant gastric lesions: implications for the development of screening and surveillance strategies. *Helicobacter* **12 Suppl 2**, 22-31 (2007).
44. Ishaq, S. & Nunn, L. Helicobacter pylori and gastric cancer: a state of the art review. *Gastroenterol Hepatol Bed Bench* **8**, S6-S14 (2015).
45. Parsonnet, J., Friedman, G.D., Orentreich, N. & Vogelman, H. Risk for gastric cancer in people with CagA positive or CagA negative Helicobacter pylori infection. *Gut* **40**, 297-301 (1997).
46. Yang, I. *et al.* Different gastric microbiota compositions in two human populations with high and low gastric cancer risk in Colombia. *Sci Rep* **6**, 18594 (2016).
47. Truong, B.X. *et al.* Diverse characteristics of the CagA gene of Helicobacter pylori strains collected from patients from southern vietnam with gastric cancer and peptic ulcer. *J Clin Microbiol* **47**, 4021-4028 (2009).
48. Hayashi, T. *et al.* Differential Mechanisms for SHP2 Binding and Activation Are Exploited by Geographically Distinct Helicobacter pylori CagA Oncoproteins. *Cell Rep* **20**, 2876-2890 (2017).
49. Murphy, G., Pfeiffer, R., Camargo, M.C. & Rabkin, C.S. Meta-analysis shows that prevalence of Epstein-Barr virus-positive gastric cancer differs based on sex and anatomic location. *Gastroenterology* **137**, 824-833 (2009).
50. Cho, J., Kang, M.S. & Kim, K.M. Epstein-Barr Virus-Associated Gastric Carcinoma and Specific Features of the Accompanying Immune Response. *J Gastric Cancer* **16**, 1-7 (2016).
51. Singh, S. & Jha, H.C. Status of Epstein-Barr Virus Coinfection with Helicobacter pylori in Gastric Cancer. *J Oncol* **2017**, 3456264 (2017).

52. Ge, S. *et al.* Association between Habitual Dietary Salt Intake and Risk of Gastric Cancer: A Systematic Review of Observational Studies. *Gastroenterol Res Pract* **2012**, 808120 (2012).
53. Tsugane, S. & Sasazuki, S. Diet and the risk of gastric cancer: review of epidemiological evidence. *Gastric Cancer* **10**, 75-83 (2007).
54. Fox, J.G. *et al.* High-salt diet induces gastric epithelial hyperplasia and parietal cell loss, and enhances Helicobacter pylori colonization in C57BL/6 mice. *Cancer Res* **59**, 4823-4828 (1999).
55. Bertuccio, P. *et al.* Dietary patterns and gastric cancer risk: a systematic review and meta-analysis. *Ann Oncol* **24**, 1450-1458 (2013).
56. Lunet, N. *et al.* Fruit and vegetable consumption and gastric cancer by location and histological type: case-control and meta-analysis. *Eur J Cancer Prev* **16**, 312-327 (2007).
57. Praud, D. *et al.* Cigarette smoking and gastric cancer in the Stomach Cancer Pooling (StoP) Project. *Eur J Cancer Prev* **27**, 124-133 (2018).
58. Wang, P.L., Xiao, F.T., Gong, B.C. & Liu, F.N. Alcohol drinking and gastric cancer risk: a meta-analysis of observational studies. *Oncotarget* **8**, 99013-99023 (2017).
59. Lin, X.J. *et al.* Body mass index and risk of gastric cancer: a meta-analysis. *Jpn J Clin Oncol* **44**, 783-791 (2014).
60. Chen, Y. *et al.* Body mass index and risk of gastric cancer: a meta-analysis of a population with more than ten million from 24 prospective studies. *Cancer Epidemiol Biomarkers Prev* **22**, 1395-1408 (2013).
61. Kamineni, A., Williams, M.A., Schwartz, S.M., Cook, L.S. & Weiss, N.S. The incidence of gastric carcinoma in Asian migrants to the United States and their descendants. *Cancer Causes Control* **10**, 77-83 (1999).
62. Mousavi, S.M., Sundquist, K. & Hemminki, K. Does the risk of stomach cancer remain among second-generation immigrants in Sweden? *Gastric Cancer* **15**, 213-215 (2012).
63. Takahashi, T., Saikawa, Y. & Kitagawa, Y. Gastric cancer: current status of diagnosis and treatment. *Cancers (Basel)* **5**, 48-63 (2013).
64. Mocellin, S. & Pasquali, S. Diagnostic accuracy of endoscopic ultrasonography (EUS) for the preoperative locoregional staging of primary gastric cancer. *Cochrane Database Syst Rev*, CD009944 (2015).
65. Altini, C. *et al.* 18F-FDG PET/CT role in staging of gastric carcinomas: comparison with conventional contrast enhancement computed tomography. *Medicine (Baltimore)* **94**, e864 (2015).
66. Hallinan, J.T. & Venkatesh, S.K. Gastric carcinoma: imaging diagnosis, staging and assessment of treatment response. *Cancer Imaging* **13**, 212-227 (2013).
67. Hsu, P.K., Wu, Y.C., Chou, T.Y., Huang, C.S. & Hsu, W.H. Comparison of the 6th and 7th editions of the American Joint Committee on Cancer tumor-node-metastasis staging system in patients with resected esophageal carcinoma. *Ann Thorac Surg* **89**, 1024-1031 (2010).
68. Pattison, S. *et al.* Predictors of outcome after surgery for gastric cancer in a Western cohort. *ANZ J Surg* **86**, 469-474 (2016).
69. Sano, T. *et al.* Proposal of a new stage grouping of gastric cancer for TNM classification: International Gastric Cancer Association staging project. *Gastric Cancer* **20**, 217-225 (2017).

70. Orditura, M. *et al.* Treatment of gastric cancer. *World J Gastroenterol* **20**, 1635-1649 (2014).
71. Japanese Gastric Cancer, A. Japanese gastric cancer treatment guidelines 2014 (ver. 4). *Gastric Cancer* **20**, 1-19 (2017).
72. Guideline Committee of the Korean Gastric Cancer Association, D.W.G. & Review, P. Korean Practice Guideline for Gastric Cancer 2018: an Evidence-based, Multi-disciplinary Approach. *J Gastric Cancer* **19**, 1-48 (2019).
73. Waye, J.D. Endoscopic Mucosal Resection. *Gastroenterol Hepatol (N Y)* **2**, 156-158 (2006).
74. Bourke, M.J., Neuhaus, H. & Bergman, J.J. Endoscopic Submucosal Dissection: Indications and Application in Western Endoscopy Practice. *Gastroenterology* **154**, 1887-1900 e1885 (2018).
75. Quero, L., Guillerm, S. & Hennequin, C. Neoadjuvant or adjuvant therapy for gastric cancer. *World J Gastrointest Oncol* **7**, 102-110 (2015).
76. Cunningham, D. *et al.* Perioperative chemotherapy versus surgery alone for resectable gastroesophageal cancer. *N Engl J Med* **355**, 11-20 (2006).
77. Schuhmacher, C. *et al.* Neoadjuvant chemotherapy compared with surgery alone for locally advanced cancer of the stomach and cardia: European Organisation for Research and Treatment of Cancer randomized trial 40954. *J Clin Oncol* **28**, 5210-5218 (2010).
78. Zhang, J. *et al.* Efficacy and safety of neoadjuvant chemotherapy with modified FOLFOX7 regimen on the treatment of advanced gastric cancer. *Chin Med J (Engl)* **125**, 2144-2150 (2012).
79. Newton, A.D., Datta, J., Loaiza-Bonilla, A., Karakousis, G.C. & Roses, R.E. Neoadjuvant therapy for gastric cancer: current evidence and future directions. *J Gastrointest Oncol* **6**, 534-543 (2015).
80. Kim, I.H. Current status of adjuvant chemotherapy for gastric cancer. *World J Gastrointest Oncol* **11**, 679-685 (2019).
81. McCloskey, S.A. & Yang, G.Y. Benefits and challenges of radiation therapy in gastric cancer: techniques for improving outcomes. *Gastrointest Cancer Res* **3**, 15-19 (2009).
82. Min, C. *et al.* Chemoradiation therapy versus chemotherapy alone for gastric cancer after R0 surgical resection: a meta-analysis of randomized trials. *Oncology* **86**, 79-85 (2014).
83. Liao, Y., Yang, Z.L., Peng, J.S., Xiang, J. & Wang, J.P. Neoadjuvant chemotherapy for gastric cancer: a meta-analysis of randomized, controlled trials. *J Gastroenterol Hepatol* **28**, 777-782 (2013).
84. Cats, A. *et al.* Chemotherapy versus chemoradiotherapy after surgery and preoperative chemotherapy for resectable gastric cancer (CRITICS): an international, open-label, randomised phase 3 trial. *Lancet Oncol* **19**, 616-628 (2018).
85. Lee, J. *et al.* Phase III trial comparing capecitabine plus cisplatin versus capecitabine plus cisplatin with concurrent capecitabine radiotherapy in completely resected gastric cancer with D2 lymph node dissection: the ARTIST trial. *J Clin Oncol* **30**, 268-273 (2012).
86. Abrahao-Machado, L.F. & Scapulatempo-Neto, C. HER2 testing in gastric cancer: An update. *World J Gastroenterol* **22**, 4619-4625 (2016).
87. Bang, Y.J. *et al.* Trastuzumab in combination with chemotherapy versus chemotherapy alone for treatment of HER2-positive advanced gastric or

gastro-oesophageal junction cancer (ToGA): a phase 3, open-label, randomised controlled trial. *Lancet* **376**, 687-697 (2010).
88. Vidal, O. *et al.* High preoperative serum vascular endothelial growth factor levels predict poor clinical outcome after curative resection of gastric cancer. *Br J Surg* **96**, 1443-1451 (2009).
89. Villarejo-Campos, P. *et al.* Serum VEGF and VEGF-C values before surgery and after postoperative treatment in gastric cancer. *Clin Transl Oncol* **15**, 265-270 (2013).
90. Fuchs, C.S. *et al.* Ramucirumab monotherapy for previously treated advanced gastric or gastro-oesophageal junction adenocarcinoma (REGARD): an international, randomised, multicentre, placebo-controlled, phase 3 trial. *Lancet* **383**, 31-39 (2014).
91. Okines, A.F. *et al.* Epirubicin, oxaliplatin, and capecitabine with or without panitumumab for advanced esophagogastric cancer: dose-finding study for the prospective multicenter, randomized, phase II/III REAL-3 trial. *J Clin Oncol* **28**, 3945-3950 (2010).
92. Ohtsu, A. *et al.* Bevacizumab in combination with chemotherapy as first-line therapy in advanced gastric cancer: a randomized, double-blind, placebo-controlled phase III study. *J Clin Oncol* **29**, 3968-3976 (2011).
93. Van Cutsem, E. *et al.* Bevacizumab in combination with chemotherapy as first-line therapy in advanced gastric cancer: a biomarker evaluation from the AVAGAST randomized phase III trial. *J Clin Oncol* **30**, 2119-2127 (2012).
94. Yuki Kiyozumi, M.I., Kohei Yamashita, Yuki Koga, Naoya Yoshida, Hideo Baba Update on targeted therapy and immune therapy for gastric cancer, 2018. *Journal of Cancer Metastasis and Treatment* **4** (2018).
95. Galon, J. *et al.* Type, density, and location of immune cells within human colorectal tumors predict clinical outcome. *Science* **313**, 1960-1964 (2006).
96. Krummel, M.F. & Allison, J.P. CD28 and CTLA-4 have opposing effects on the response of T cells to stimulation. *J Exp Med* **182**, 459-465 (1995).
97. Ishida, Y., Agata, Y., Shibahara, K. & Honjo, T. Induced expression of PD-1, a novel member of the immunoglobulin gene superfamily, upon programmed cell death. *EMBO J* **11**, 3887-3895 (1992).
98. Lipson, E.J. & Drake, C.G. Ipilimumab: an anti-CTLA-4 antibody for metastatic melanoma. *Clin Cancer Res* **17**, 6958-6962 (2011).
99. Raedler, L.A. Opdivo (Nivolumab): Second PD-1 Inhibitor Receives FDA Approval for Unresectable or Metastatic Melanoma. *Am Health Drug Benefits* **8**, 180-183 (2015).
100. Sharma, P. & Allison, J.P. The future of immune checkpoint therapy. *Science* **348**, 56-61 (2015).
101. Hu, Z. The future of immune checkpoint blockade immunotherapy: towards personalized therapy or towards combination therapy. *J Thorac Dis* **9**, 4226-4229 (2017).
102. Linsley, P.S. *et al.* Human B7-1 (CD80) and B7-2 (CD86) bind with similar avidities but distinct kinetics to CD28 and CTLA-4 receptors. *Immunity* **1**, 793-801 (1994).
103. Peggs, K.S., Quezada, S.A., Chambers, C.A., Korman, A.J. & Allison, J.P. Blockade of CTLA-4 on both effector and regulatory T cell

compartments contributes to the antitumor activity of anti-CTLA-4 antibodies. *J Exp Med* **206**, 1717-1725 (2009).
104. Sage, P.T., Francisco, L.M., Carman, C.V. & Sharpe, A.H. The receptor PD-1 controls follicular regulatory T cells in the lymph nodes and blood. *Nat Immunol* **14**, 152-161 (2013).
105. Thibult, M.L. *et al.* PD-1 is a novel regulator of human B-cell activation. *Int Immunol* **25**, 129-137 (2013).
106. Pena-Cruz, V. *et al.* PD-1 on immature and PD-1 ligands on migratory human Langerhans cells regulate antigen-presenting cell activity. *J Invest Dermatol* **130**, 2222-2230 (2010).
107. Gordon, S.R. *et al.* PD-1 expression by tumour-associated macrophages inhibits phagocytosis and tumour immunity. *Nature* **545**, 495-499 (2017).
108. Lim, T.S. *et al.* PD-1 expression on dendritic cells suppresses CD8(+) T cell function and antitumor immunity. *Oncoimmunology* **5**, e1085146 (2016).
109. Rodrigues, C.P. *et al.* Tolerogenic IDO(+) Dendritic Cells Are Induced by PD-1-Expressing Mast Cells. *Front Immunol* **7**, 9 (2016).
110. Latchman, Y. *et al.* PD-L2 is a second ligand for PD-1 and inhibits T cell activation. *Nat Immunol* **2**, 261-268 (2001).
111. Sharpe, A.H. & Pauken, K.E. The diverse functions of the PD1 inhibitory pathway. *Nat Rev Immunol* **18**, 153-167 (2018).
112. Hui, E. *et al.* T cell costimulatory receptor CD28 is a primary target for PD-1-mediated inhibition. *Science* **355**, 1428-1433 (2017).
113. Riva, A. & Chokshi, S. Immune checkpoint receptors: homeostatic regulators of immunity. *Hepatol Int* **12**, 223-236 (2018).
114. Nielsen, C., Hansen, D., Husby, S., Jacobsen, B.B. & Lillevang, S.T. Association of a putative regulatory polymorphism in the PD-1 gene with susceptibility to type 1 diabetes. *Tissue Antigens* **62**, 492-497 (2003).
115. Velazquez-Cruz, R. *et al.* Association of PDCD1 polymorphisms with childhood-onset systemic lupus erythematosus. *Eur J Hum Genet* **15**, 336-341 (2007).
116. Pardoll, D.M. The blockade of immune checkpoints in cancer immunotherapy. *Nat Rev Cancer* **12**, 252-264 (2012).
117. Seidel, J.A., Otsuka, A. & Kabashima, K. Anti-PD-1 and Anti-CTLA-4 Therapies in Cancer: Mechanisms of Action, Efficacy, and Limitations. *Front Oncol* **8**, 86 (2018).
118. Gong, J., Chehrazi-Raffle, A., Reddi, S. & Salgia, R. Development of PD-1 and PD-L1 inhibitors as a form of cancer immunotherapy: a comprehensive review of registration trials and future considerations. *J Immunother Cancer* **6**, 8 (2018).
119. Darvin, P., Toor, S.M., Sasidharan Nair, V. & Elkord, E. Immune checkpoint inhibitors: recent progress and potential biomarkers. *Exp Mol Med* **50**, 165 (2018).
120. Tumeh, P.C. *et al.* PD-1 blockade induces responses by inhibiting adaptive immune resistance. *Nature* **515**, 568-571 (2014).
121. Rizvi, N.A. *et al.* Cancer immunology. Mutational landscape determines sensitivity to PD-1 blockade in non-small cell lung cancer. *Science* **348**, 124-128 (2015).

122. Alsina, M., Moehler, M., Hierro, C., Guardeno, R. & Tabernero, J. Immunotherapy for Gastric Cancer: A Focus on Immune Checkpoints. *Target Oncol* **11**, 469-477 (2016).
123. Kelly, R.J. Immunotherapy for Esophageal and Gastric Cancer. *Am Soc Clin Oncol Educ Book* **37**, 292-300 (2017).
124. Shaib, W.L., Nammour, J.P., Gill, H., Mody, M. & Saba, N.F. The Future Prospects of Immune Therapy in Gastric and Esophageal Adenocarcinoma. *J Clin Med* **5** (2016).
125. Muro, K. *et al.* Pembrolizumab for patients with PD-L1-positive advanced gastric cancer (KEYNOTE-012): a multicentre, open-label, phase 1b trial. *Lancet Oncol* **17**, 717-726 (2016).
126. Kim, S.T. *et al.* Comprehensive molecular characterization of clinical responses to PD-1 inhibition in metastatic gastric cancer. *Nat Med* **24**, 1449-1458 (2018).
127. Garon, E.B. Cancer Immunotherapy Trials Not Immune from Imprecise Selection of Patients. *N Engl J Med* **376**, 2483-2485 (2017).
128. Lin, S.J. *et al.* Signatures of tumour immunity distinguish Asian and non-Asian gastric adenocarcinomas. *Gut* **64**, 1721-1731 (2015).
129. Rimm, D.L. *et al.* A Prospective, Multi-institutional, Pathologist-Based Assessment of 4 Immunohistochemistry Assays for PD-L1 Expression in Non-Small Cell Lung Cancer. *JAMA Oncol* **3**, 1051-1058 (2017).
130. Kulangara, K. *et al.* Clinical Utility of the Combined Positive Score for Programmed Death Ligand-1 Expression and the Approval of Pembrolizumab for Treatment of Gastric Cancer. *Arch Pathol Lab Med* **143**, 330-337 (2019).
131. Pistillo, M.P. *et al.* IFN-gamma upregulates membranous and soluble PD-L1 in mesothelioma cells: potential implications for the clinical response to PD-1/PD-L1 blockade. *Cell Mol Immunol* (2019).
132. Kowanetz, M. *et al.* Differential regulation of PD-L1 expression by immune and tumor cells in NSCLC and the response to treatment with atezolizumab (anti-PD-L1). *Proc Natl Acad Sci U S A* **115**, E10119-E10126 (2018).
133. Thompson, E.D. *et al.* Patterns of PD-L1 expression and CD8 T cell infiltration in gastric adenocarcinomas and associated immune stroma. *Gut* **66**, 794-801 (2017).
134. Harada, K. *et al.* Tumor-associated macrophage infiltration is highly associated with PD-L1 expression in gastric adenocarcinoma. *Gastric Cancer* **21**, 31-40 (2018).
135. Lee, J., Bass, A.J. & Ajani, J.A. Gastric Adenocarcinoma: An Update on Genomics, Immune System Modulations, and Targeted Therapy. *Am Soc Clin Oncol Educ Book* **35**, 104-111 (2016).
136. Landskron, G., De la Fuente, M., Thuwajit, P., Thuwajit, C. & Hermoso, M.A. Chronic inflammation and cytokines in the tumor microenvironment. *J Immunol Res* **2014**, 149185 (2014).
137. Yang, M., McKay, D., Pollard, J.W. & Lewis, C.E. Diverse Functions of Macrophages in Different Tumor Microenvironments. *Cancer Res* **78**, 5492-5503 (2018).
138. Joyce, J.A. & Pollard, J.W. Microenvironmental regulation of metastasis. *Nat Rev Cancer* **9**, 239-252 (2009).

139. Quail, D.F. & Joyce, J.A. Microenvironmental regulation of tumor progression and metastasis. *Nat Med* **19**, 1423-1437 (2013).
140. Romero-Garcia, S., Moreno-Altamirano, M.M., Prado-Garcia, H. & Sanchez-Garcia, F.J. Lactate Contribution to the Tumor Microenvironment: Mechanisms, Effects on Immune Cells and Therapeutic Relevance. *Front Immunol* **7**, 52 (2016).
141. Joyce, J.A. Therapeutic targeting of the tumor microenvironment. *Cancer Cell* **7**, 513-520 (2005).
142. Looi, C.K. *et al.* Therapeutic challenges and current immunomodulatory strategies in targeting the immunosuppressive pancreatic tumor microenvironment. *J Exp Clin Cancer Res* **38**, 162 (2019).
143. Wang, Z. *et al.* Broad targeting of angiogenesis for cancer prevention and therapy. *Semin Cancer Biol* **35 Suppl**, S224-S243 (2015).
144. Albini, A., Tosetti, F., Li, V.W., Noonan, D.M. & Li, W.W. Cancer prevention by targeting angiogenesis. *Nat Rev Clin Oncol* **9**, 498-509 (2012).
145. Pitt, J.M. *et al.* Targeting the tumor microenvironment: removing obstruction to anticancer immune responses and immunotherapy. *Ann Oncol* **27**, 1482-1492 (2016).
146. Mahajan, U.M. *et al.* Immune Cell and Stromal Signature Associated With Progression-Free Survival of Patients With Resected Pancreatic Ductal Adenocarcinoma. *Gastroenterology* **155**, 1625-1639 e1622 (2018).
147. Zeng, D. *et al.* Tumor Microenvironment Characterization in Gastric Cancer Identifies Prognostic and Immunotherapeutically Relevant Gene Signatures. *Cancer Immunol Res* **7**, 737-750 (2019).
148. Marshall, J.S., Warrington, R., Watson, W. & Kim, H.L. An introduction to immunology and immunopathology. *Allergy Asthma Clin Immunol* **14**, 49 (2018).
149. Turvey, S.E. & Broide, D.H. Innate immunity. *J Allergy Clin Immunol* **125**, S24-32 (2010).
150. Bonilla, F.A. & Oettgen, H.C. Adaptive immunity. *J Allergy Clin Immunol* **125**, S33-40 (2010).
151. Kalish, R.S. Antigen processing: the gateway to the immune response. *J Am Acad Dermatol* **32**, 640-652 (1995).
152. Trinchieri, G., Kubin, M., Bellone, G. & Cassatella, M.A. Cytokine cross-talk between phagocytic cells and lymphocytes: relevance for differentiation/activation of phagocytic cells and regulation of adaptive immunity. *J Cell Biochem* **53**, 301-308 (1993).
153. Pandya, P.H., Murray, M.E., Pollok, K.E. & Renbarger, J.L. The Immune System in Cancer Pathogenesis: Potential Therapeutic Approaches. *J Immunol Res* **2016**, 4273943 (2016).
154. Schreiber, R.D., Old, L.J. & Smyth, M.J. Cancer immunoediting: integrating immunity's roles in cancer suppression and promotion. *Science* **331**, 1565-1570 (2011).
155. Dunn, G.P., Old, L.J. & Schreiber, R.D. The three Es of cancer immunoediting. *Annu Rev Immunol* **22**, 329-360 (2004).
156. Dunn, G.P., Bruce, A.T., Ikeda, H., Old, L.J. & Schreiber, R.D. Cancer immunoediting: from immunosurveillance to tumor escape. *Nat Immunol* **3**, 991-998 (2002).

157. Vicente-Duenas, C., Hauer, J., Cobaleda, C., Borkhardt, A. & Sanchez-Garcia, I. Epigenetic Priming in Cancer Initiation. *Trends Cancer* **4**, 408-417 (2018).
158. Shacter, E. & Weitzman, S.A. Chronic inflammation and cancer. *Oncology (Williston Park)* **16**, 217-226, 229; discussion 230-212 (2002).
159. White, M.K., Pagano, J.S. & Khalili, K. Viruses and human cancers: a long road of discovery of molecular paradigms. *Clin Microbiol Rev* **27**, 463-481 (2014).
160. Diamond, M.S. *et al.* Type I interferon is selectively required by dendritic cells for immune rejection of tumors. *J Exp Med* **208**, 1989-2003 (2011).
161. Vesely, M.D., Kershaw, M.H., Schreiber, R.D. & Smyth, M.J. Natural innate and adaptive immunity to cancer. *Annu Rev Immunol* **29**, 235-271 (2011).
162. Teng, M.W. *et al.* Opposing roles for IL-23 and IL-12 in maintaining occult cancer in an equilibrium state. *Cancer Res* **72**, 3987-3996 (2012).
163. Mittal, D., Gubin, M.M., Schreiber, R.D. & Smyth, M.J. New insights into cancer immunoediting and its three component phases--elimination, equilibrium and escape. *Curr Opin Immunol* **27**, 16-25 (2014).
164. Havel, J.J., Chowell, D. & Chan, T.A. The evolving landscape of biomarkers for checkpoint inhibitor immunotherapy. *Nat Rev Cancer* **19**, 133-150 (2019).
165. Chen, D.S. & Mellman, I. Oncology meets immunology: the cancer-immunity cycle. *Immunity* **39**, 1-10 (2013).
166. Gordon, S. Elie Metchnikoff, the Man and the Myth. *J Innate Immun* **8**, 223-227 (2016).
167. Kain, V. & Halade, G.V. Big eater macrophages dominate inflammation resolution following myocardial infarction. *J Mol Cell Cardiol* **87**, 225-227 (2015).
168. Italiani, P. & Boraschi, D. From Monocytes to M1/M2 Macrophages: Phenotypical vs. Functional Differentiation. *Front Immunol* **5**, 514 (2014).
169. Mills, C.D., Kincaid, K., Alt, J.M., Heilman, M.J. & Hill, A.M. M-1/M-2 macrophages and the Th1/Th2 paradigm. *J Immunol* **164**, 6166-6173 (2000).
170. Mills, C.D. Anatomy of a discovery: m1 and m2 macrophages. *Front Immunol* **6**, 212 (2015).
171. Martinez, F.O. & Gordon, S. The M1 and M2 paradigm of macrophage activation: time for reassessment. *F1000Prime Rep* **6**, 13 (2014).
172. Tokunaga, R. *et al.* CXCL9, CXCL10, CXCL11/CXCR3 axis for immune activation - A target for novel cancer therapy. *Cancer Treat Rev* **63**, 40-47 (2018).
173. Martin-Orozco, N., Isibasi, A. & Ortiz-Navarrete, V. Macrophages present exogenous antigens by class I major histocompatibility complex molecules via a secretory pathway as a consequence of interferon-gamma activation. *Immunology* **103**, 41-48 (2001).
174. Harding, C.V. & Geuze, H.J. Class II MHC molecules are present in macrophage lysosomes and phagolysosomes that function in the phagocytic processing of Listeria monocytogenes for presentation to T cells. *J Cell Biol* **119**, 531-542 (1992).

175. Nolan, A. *et al.* Differential role for CD80 and CD86 in the regulation of the innate immune response in murine polymicrobial sepsis. *PLoS One* **4**, e6600 (2009).
176. Dileepan, K.N., Page, J.C., Li, Y. & Stechschulte, D.J. Direct activation of murine peritoneal macrophages for nitric oxide production and tumor cell killing by interferon-gamma. *J Interferon Cytokine Res* **15**, 387-394 (1995).
177. Stuehr, D.J. & Nathan, C.F. Nitric oxide. A macrophage product responsible for cytostasis and respiratory inhibition in tumor target cells. *J Exp Med* **169**, 1543-1555 (1989).
178. Nathan, C. Specificity of a third kind: reactive oxygen and nitrogen intermediates in cell signaling. *J Clin Invest* **111**, 769-778 (2003).
179. Krausgruber, T. *et al.* IRF5 promotes inflammatory macrophage polarization and TH1-TH17 responses. *Nat Immunol* **12**, 231-238 (2011).
180. Liew, F.Y. *et al.* Resistance to Leishmania major infection correlates with the induction of nitric oxide synthase in murine macrophages. *Eur J Immunol* **21**, 3009-3014 (1991).
181. Oswald, I.P., Afroun, S., Bray, D., Petit, J.F. & Lemaire, G. Low response of BALB/c macrophages to priming and activating signals. *J Leukoc Biol* **52**, 315-322 (1992).
182. Gordon, S. Alternative activation of macrophages. *Nat Rev Immunol* **3**, 23-35 (2003).
183. Roszer, T. Understanding the Mysterious M2 Macrophage through Activation Markers and Effector Mechanisms. *Mediators Inflamm* **2015**, 816460 (2015).
184. Hamilton, J.A. & Achuthan, A. Colony stimulating factors and myeloid cell biology in health and disease. *Trends Immunol* **34**, 81-89 (2013).
185. Mills, C.D. Molecular basis of "suppressor" macrophages. Arginine metabolism via the nitric oxide synthetase pathway. *J Immunol* **146**, 2719-2723 (1991).
186. Yang, Z. & Ming, X.F. Functions of arginase isoforms in macrophage inflammatory responses: impact on cardiovascular diseases and metabolic disorders. *Front Immunol* **5**, 533 (2014).
187. Rath, M., Muller, I., Kropf, P., Closs, E.I. & Munder, M. Metabolism via Arginase or Nitric Oxide Synthase: Two Competing Arginine Pathways in Macrophages. *Front Immunol* **5**, 532 (2014).
188. Geiger, R. *et al.* L-Arginine Modulates T Cell Metabolism and Enhances Survival and Anti-tumor Activity. *Cell* **167**, 829-842 e813 (2016).
189. Murray, P.J. Nonresolving macrophage-mediated inflammation in malignancy. *FEBS J* **285**, 641-653 (2018).
190. Mantovani, A., Sica, A., Allavena, P., Garlanda, C. & Locati, M. Tumor-associated macrophages and the related myeloid-derived suppressor cells as a paradigm of the diversity of macrophage activation. *Hum Immunol* **70**, 325-330 (2009).
191. Ojalvo, L.S., King, W., Cox, D. & Pollard, J.W. High-density gene expression analysis of tumor-associated macrophages from mouse mammary tumors. *Am J Pathol* **174**, 1048-1064 (2009).
192. Wang, S.C., Hong, J.H., Hsueh, C. & Chiang, C.S. Tumor-secreted SDF-1 promotes glioma invasiveness and TAM tropism toward hypoxia in a murine astrocytoma model. *Lab Invest* **92**, 151-162 (2012).

193. Kelly, P.M., Davison, R.S., Bliss, E. & McGee, J.O. Macrophages in human breast disease: a quantitative immunohistochemical study. *Br J Cancer* **57**, 174-177 (1988).
194. Osinsky, S. *et al.* Hypoxia, tumour-associated macrophages, microvessel density, VEGF and matrix metalloproteinases in human gastric cancer: interaction and impact on survival. *Clin Transl Oncol* **13**, 133-138 (2011).
195. Anuja Sathe, S.G., Billy T. Lau, Jiamin Chen, Carlos Suarez, Robert Huang, George Poultsides, Hanlee P. Ji Single cell genomic characterization reveals the cellular reprogramming of the gastric. *bioRxiv* (2019).
196. Sica, A. *et al.* Macrophage polarization in tumour progression. *Semin Cancer Biol* **18**, 349-355 (2008).
197. Qian, B.Z. & Pollard, J.W. Macrophage diversity enhances tumor progression and metastasis. *Cell* **141**, 39-51 (2010).
198. Hanahan, D. & Weinberg, R.A. The hallmarks of cancer. *Cell* **100**, 57-70 (2000).
199. Hanahan, D. & Weinberg, R.A. Hallmarks of cancer: the next generation. *Cell* **144**, 646-674 (2011).
200. Huang, H. *et al.* Specifically targeting angiopoietin-2 inhibits angiogenesis, Tie2-expressing monocyte infiltration, and tumor growth. *Clin Cancer Res* **17**, 1001-1011 (2011).
201. Chiang, C.S. *et al.* Irradiation promotes an m2 macrophage phenotype in tumor hypoxia. *Front Oncol* **2**, 89 (2012).
202. Murdoch, C., Muthana, M., Coffelt, S.B. & Lewis, C.E. The role of myeloid cells in the promotion of tumour angiogenesis. *Nat Rev Cancer* **8**, 618-631 (2008).
203. Chen, P. *et al.* Tumor-associated macrophages promote angiogenesis and melanoma growth via adrenomedullin in a paracrine and autocrine manner. *Clin Cancer Res* **17**, 7230-7239 (2011).
204. Espey, M.G. Tumor macrophage redox and effector mechanisms associated with hypoxia. *Free Radic Biol Med* **41**, 1621-1628 (2006).
205. Ye, L.Y. *et al.* Hypoxia-Induced Epithelial-to-Mesenchymal Transition in Hepatocellular Carcinoma Induces an Immunosuppressive Tumor Microenvironment to Promote Metastasis. *Cancer Res* **76**, 818-830 (2016).
206. Chen, E.P. & Smyth, E.M. COX-2 and PGE2-dependent immunomodulation in breast cancer. *Prostaglandins Other Lipid Mediat* **96**, 14-20 (2011).
207. Jinushi, M. *et al.* Tumor-associated macrophages regulate tumorigenicity and anticancer drug responses of cancer stem/initiating cells. *Proc Natl Acad Sci U S A* **108**, 12425-12430 (2011).
208. Taniguchi, K. & Karin, M. IL-6 and related cytokines as the critical lynchpins between inflammation and cancer. *Semin Immunol* **26**, 54-74 (2014).
209. Yu, H., Lee, H., Herrmann, A., Buettner, R. & Jove, R. Revisiting STAT3 signalling in cancer: new and unexpected biological functions. *Nat Rev Cancer* **14**, 736-746 (2014).
210. Zhao, X. *et al.* Prognostic significance of tumor-associated macrophages in breast cancer: a meta-analysis of the literature. *Oncotarget* **8**, 30576-30586 (2017).

211. Ruffell, B. & Coussens, L.M. Macrophages and therapeutic resistance in cancer. *Cancer Cell* **27**, 462-472 (2015).
212. Raiha, M.R. & Puolakkainen, P.A. Tumor-associated macrophages (TAMs) as biomarkers for gastric cancer: A review. *Chronic Dis Transl Med* **4**, 156-163 (2018).
213. Busuttil, R.A. *et al.* A signature predicting poor prognosis in gastric and ovarian cancer represents a coordinated macrophage and stromal response. *Clin Cancer Res* **20**, 2761-2772 (2014).
214. Wu, M.H., Lee, W.J., Hua, K.T., Kuo, M.L. & Lin, M.T. Macrophage Infiltration Induces Gastric Cancer Invasiveness by Activating the beta-Catenin Pathway. *PLoS One* **10**, e0134122 (2015).
215. Li, J. *et al.* Tumor-infiltrating macrophages express interleukin-25 and predict a favorable prognosis in patients with gastric cancer after radical resection. *Oncotarget* **7**, 11083-11093 (2016).
216. Ohno, S. *et al.* The degree of macrophage infiltration into the cancer cell nest is a significant predictor of survival in gastric cancer patients. *Anticancer Res* **23**, 5015-5022 (2003).
217. Helmink, B.A., Khan, M.A.W., Hermann, A., Gopalakrishnan, V. & Wargo, J.A. The microbiome, cancer, and cancer therapy. *Nat Med* **25**, 377-388 (2019).
218. Wang, F., Meng, W., Wang, B. & Qiao, L. Helicobacter pylori-induced gastric inflammation and gastric cancer. *Cancer Lett* **345**, 196-202 (2014).
219. Fehlings, M. *et al.* Comparative analysis of the interaction of Helicobacter pylori with human dendritic cells, macrophages, and monocytes. *Infect Immun* **80**, 2724-2734 (2012).
220. Thaiss, C.A., Zmora, N., Levy, M. & Elinav, E. The microbiome and innate immunity. *Nature* **535**, 65-74 (2016).
221. Lewis, N.D. *et al.* Immune evasion by Helicobacter pylori is mediated by induction of macrophage arginase II. *J Immunol* **186**, 3632-3641 (2011).
222. Menaker, R.J., Ceponis, P.J. & Jones, N.L. Helicobacter pylori induces apoptosis of macrophages in association with alterations in the mitochondrial pathway. *Infect Immun* **72**, 2889-2898 (2004).
223. Isobe, M. *et al.* The CD300e molecule in mice is an immune-activating receptor. *J Biol Chem* **293**, 3793-3805 (2018).
224. Pagliari, M. *et al.* Helicobacter pylori Affects the Antigen Presentation Activity of Macrophages Modulating the Expression of the Immune Receptor CD300E through miR-4270. *Front Immunol* **8**, 1288 (2017).
225. Yu, G. *et al.* Molecular Characterization of the Human Stomach Microbiota in Gastric Cancer Patients. *Front Cell Infect Microbiol* **7**, 302 (2017).
226. Noy, R. & Pollard, J.W. Tumor-associated macrophages: from mechanisms to therapy. *Immunity* **41**, 49-61 (2014).
227. Lehenkari, P.P. *et al.* Further insight into mechanism of action of clodronate: inhibition of mitochondrial ADP/ATP translocase by a nonhydrolyzable, adenine-containing metabolite. *Mol Pharmacol* **61**, 1255-1262 (2002).
228. Junankar, S. *et al.* Real-time intravital imaging establishes tumor-associated macrophages as the extraskeletal target of bisphosphonate action in cancer. *Cancer Discov* **5**, 35-42 (2015).

229. Zeisberger, S.M. *et al.* Clodronate-liposome-mediated depletion of tumour-associated macrophages: a new and highly effective antiangiogenic therapy approach. *Br J Cancer* **95**, 272-281 (2006).
230. Salvagno, C. *et al.* Therapeutic targeting of macrophages enhances chemotherapy efficacy by unleashing type I interferon response. *Nat Cell Biol* **21**, 511-521 (2019).
231. Arakaki, R. *et al.* CCL2 as a potential therapeutic target for clear cell renal cell carcinoma. *Cancer Med* **5**, 2920-2933 (2016).
232. Teng, K.Y. *et al.* Blocking the CCL2-CCR2 Axis Using CCL2-Neutralizing Antibody Is an Effective Therapy for Hepatocellular Cancer in a Mouse Model. *Mol Cancer Ther* **16**, 312-322 (2017).
233. Bonapace, L. *et al.* Cessation of CCL2 inhibition accelerates breast cancer metastasis by promoting angiogenesis. *Nature* **515**, 130-133 (2014).
234. Germano, G. *et al.* Role of macrophage targeting in the antitumor activity of trabectedin. *Cancer Cell* **23**, 249-262 (2013).
235. Huang, E.H. *et al.* A CXCR4 antagonist CTCE-9908 inhibits primary tumor growth and metastasis of breast cancer. *J Surg Res* **155**, 231-236 (2009).
236. Wong, D., Kandagatla, P., Korz, W. & Chinni, S.R. Targeting CXCR4 with CTCE-9908 inhibits prostate tumor metastasis. *BMC Urol* **14**, 12 (2014).
237. Pantano, F. *et al.* The role of macrophages polarization in predicting prognosis of radically resected gastric cancer patients. *J Cell Mol Med* **17**, 1415-1421 (2013).
238. Geeraerts, X., Bolli, E., Fendt, S.M. & Van Ginderachter, J.A. Macrophage Metabolism As Therapeutic Target for Cancer, Atherosclerosis, and Obesity. *Front Immunol* **8**, 289 (2017).
239. Poh, A.R. & Ernst, M. Targeting Macrophages in Cancer: From Bench to Bedside. *Front Oncol* **8**, 49 (2018).
240. Mantovani, A., Marchesi, F., Malesci, A., Laghi, L. & Allavena, P. Tumour-associated macrophages as treatment targets in oncology. *Nat Rev Clin Oncol* **14**, 399-416 (2017).
241. van Dalen, F.J., van Stevendaal, M., Fennemann, F.L., Verdoes, M. & Ilina, O. Molecular Repolarisation of Tumour-Associated Macrophages. *Molecules* **24** (2018).
242. Honma, K. *et al.* Interferon regulatory factor 4 negatively regulates the production of proinflammatory cytokines by macrophages in response to LPS. *Proc Natl Acad Sci U S A* **102**, 16001-16006 (2005).
243. Satoh, T. *et al.* The Jmjd3-Irf4 axis regulates M2 macrophage polarization and host responses against helminth infection. *Nat Immunol* **11**, 936-944 (2010).
244. Achuthan, A. *et al.* Granulocyte macrophage colony-stimulating factor induces CCL17 production via IRF4 to mediate inflammation. *J Clin Invest* **126**, 3453-3466 (2016).
245. Hsu, A.T. *et al.* Epigenetic and transcriptional regulation of IL4-induced CCL17 production in human monocytes and murine macrophages. *J Biol Chem* **293**, 11415-11423 (2018).

246. Bhattacharjee, A., Pal, S., Feldman, G.M. & Cathcart, M.K. Hck is a key regulator of gene expression in alternatively activated human monocytes. *J Biol Chem* **286**, 36709-36723 (2011).
247. Xiao, W., Hong, H., Kawakami, Y., Lowell, C.A. & Kawakami, T. Regulation of myeloproliferation and M2 macrophage programming in mice by Lyn/Hck, SHIP, and Stat5. *J Clin Invest* **118**, 924-934 (2008).
248. Cougoule, C. *et al.* Three-dimensional migration of macrophages requires Hck for podosome organization and extracellular matrix proteolysis. *Blood* **115**, 1444-1452 (2010).
249. Poh, A.R. *et al.* Inhibition of Hematopoietic Cell Kinase Activity Suppresses Myeloid Cell-Mediated Colon Cancer Progression. *Cancer Cell* **31**, 563-575 e565 (2017).
250. Hussain, S.F. *et al.* A novel small molecule inhibitor of signal transducers and activators of transcription 3 reverses immune tolerance in malignant glioma patients. *Cancer Res* **67**, 9630-9636 (2007).
251. Sinha, P., Clements, V.K. & Ostrand-Rosenberg, S. Reduction of myeloid-derived suppressor cells and induction of M1 macrophages facilitate the rejection of established metastatic disease. *J Immunol* **174**, 636-645 (2005).
252. Kaneda, M.M. *et al.* PI3Kgamma is a molecular switch that controls immune suppression. *Nature* **539**, 437-442 (2016).
253. Schmid, M.C. *et al.* Receptor tyrosine kinases and TLR/IL1Rs unexpectedly activate myeloid cell PI3kgamma, a single convergent point promoting tumor inflammation and progression. *Cancer Cell* **19**, 715-727 (2011).
254. Martini, M., De Santis, M.C., Braccini, L., Gulluni, F. & Hirsch, E. PI3K/AKT signaling pathway and cancer: an updated review. *Ann Med* **46**, 372-383 (2014).
255. Gunderson, A.J. *et al.* Bruton Tyrosine Kinase-Dependent Immune Cell Cross-talk Drives Pancreas Cancer. *Cancer Discov* **6**, 270-285 (2016).
256. Kaneda, M.M. *et al.* Macrophage PI3Kgamma Drives Pancreatic Ductal Adenocarcinoma Progression. *Cancer Discov* **6**, 870-885 (2016).
257. De Vera, A.A. *et al.* Immuno-oncology agent IPI-549 is a modulator of P-glycoprotein (P-gp, MDR1, ABCB1)-mediated multidrug resistance (MDR) in cancer: In vitro and in vivo. *Cancer Lett* **442**, 91-103 (2019).
258. De Henau, O. *et al.* Overcoming resistance to checkpoint blockade therapy by targeting PI3Kgamma in myeloid cells. *Nature* **539**, 443-447 (2016).
259. Ryan J. Sullivan, D.S.H., Anthony W. Tolcher, Amita Patnaik, Geoffrey Shapiro, Bartosz Chmielowski, Antoni Ribas, Les H. Brail, Jennifer Roberts, Lucy Lee, Brenda O'Connell, Jeffrey Lorne Kutok, Suresh Mahabhashyam, Claudio Dansky Ullmann, Michael A. Postow, Jedd D. Wolchok Initial results from first-in-human study of IPI-549, a tumor macrophage-targeting agent, combined with nivolumab in advanced solid tumors. *Journal of Clinical Oncology* (2018).
260. Buhtoiarov, I.N. *et al.* CD40 ligation activates murine macrophages via an IFN-gamma-dependent mechanism resulting in tumor cell destruction in vitro. *J Immunol* **174**, 6013-6022 (2005).

261. Stout, R.D., Suttles, J., Xu, J., Grewal, I.S. & Flavell, R.A. Impaired T cell-mediated macrophage activation in CD40 ligand-deficient mice. *J Immunol* **156**, 8-11 (1996).
262. Hoves, S. *et al.* Rapid activation of tumor-associated macrophages boosts preexisting tumor immunity. *J Exp Med* **215**, 859-876 (2018).
263. Aderem, A. & Underhill, D.M. Mechanisms of phagocytosis in macrophages. *Annu Rev Immunol* **17**, 593-623 (1999).
264. Martinez-Pomares, L. & Gordon, S. Antigen presentation the macrophage way. *Cell* **131**, 641-643 (2007).
265. Hume, D.A. Macrophages as APC and the dendritic cell myth. *J Immunol* **181**, 5829-5835 (2008).
266. Takahashi, S. Molecular functions of SIRPalpha and its role in cancer. *Biomed Rep* **9**, 3-7 (2018).
267. van den Berg, T.K. & van der Schoot, C.E. Innate immune 'self' recognition: a role for CD47-SIRPalpha interactions in hematopoietic stem cell transplantation. *Trends Immunol* **29**, 203-206 (2008).
268. Casey, S.C. *et al.* MYC regulates the antitumor immune response through CD47 and PD-L1. *Science* **352**, 227-231 (2016).
269. Okazawa, H. *et al.* Negative regulation of phagocytosis in macrophages by the CD47-SHPS-1 system. *J Immunol* **174**, 2004-2011 (2005).
270. van Beek, E.M., Cochrane, F., Barclay, A.N. & van den Berg, T.K. Signal regulatory proteins in the immune system. *J Immunol* **175**, 7781-7787 (2005).
271. Jaiswal, S. *et al.* CD47 is upregulated on circulating hematopoietic stem cells and leukemia cells to avoid phagocytosis. *Cell* **138**, 271-285 (2009).
272. Chao, M.P. *et al.* Anti-CD47 antibody synergizes with rituximab to promote phagocytosis and eradicate non-Hodgkin lymphoma. *Cell* **142**, 699-713 (2010).
273. Chan, K.S. *et al.* Identification, molecular characterization, clinical prognosis, and therapeutic targeting of human bladder tumor-initiating cells. *Proc Natl Acad Sci U S A* **106**, 14016-14021 (2009).
274. Manna, P.P. & Frazier, W.A. CD47 mediates killing of breast tumor cells via Gi-dependent inhibition of protein kinase A. *Cancer Res* **64**, 1026-1036 (2004).
275. McCracken, M.N., Cha, A.C. & Weissman, I.L. Molecular Pathways: Activating T Cells after Cancer Cell Phagocytosis from Blockade of CD47 "Don't Eat Me" Signals. *Clin Cancer Res* **21**, 3597-3601 (2015).
276. Weiskopf, K. *et al.* CD47-blocking immunotherapies stimulate macrophage-mediated destruction of small-cell lung cancer. *J Clin Invest* **126**, 2610-2620 (2016).
277. Mohanty, S., Aghighi, M., Yerneni, K., Theruvath, J.L. & Daldrup-Link, H.E. Improving the efficacy of osteosarcoma therapy: combining drugs that turn cancer cell 'don't eat me' signals off and 'eat me' signals on. *Mol Oncol* **13**, 2049-2061 (2019).
278. Lian, S. *et al.* Dual blockage of both PD-L1 and CD47 enhances immunotherapy against circulating tumor cells. *Sci Rep* **9**, 4532 (2019).
279. Yoshida, K. *et al.* CD47 is an adverse prognostic factor and a therapeutic target in gastric cancer. *Cancer Med* **4**, 1322-1333 (2015).
280. Sudo, T. *et al.* Significance of CD47 expression in gastric cancer. *Oncol Lett* **14**, 801-809 (2017).

281. Branimir I. Sikic, N.J.L., Amita Patnaik, Sumit Shah, Sreenivasa R Chandana, Drew W. Rasco, A. Dimitrios Colevas, Timothy J. O'Rourke, Kyriakos P. Papadopoulos, George A. Fisher, Mark Chao, Balaji Agoram, James Y Chen, Jenny Huang, Matthew Axt, Ravindra Majeti, Irving L. Weissman, Chris H.M. Takimoto, Mark D. Pegram, Sukhmani Kaur Padda A first-in-class, first-in-human phase 1 pharmacokinetic (PK) and pharmacodynamic (PD) study of Hu5F9-G4, an anti-CD47 monoclonal antibody (mAb), in patients with advanced solid tumors. *Journal of Clinical Oncology* **36:15_suppl, 3002-3002** (2018).
282. Barkal, A.A. *et al.* CD24 signalling through macrophage Siglec-10 is a target for cancer immunotherapy. *Nature* **572**, 392-396 (2019).
283. Galluzzi, L., Buque, A., Kepp, O., Zitvogel, L. & Kroemer, G. Immunological Effects of Conventional Chemotherapy and Targeted Anticancer Agents. *Cancer Cell* **28**, 690-714 (2015).
284. Klug, F. *et al.* Low-dose irradiation programs macrophage differentiation to an iNOS(+)/M1 phenotype that orchestrates effective T cell immunotherapy. *Cancer Cell* **24**, 589-602 (2013).
285. Dar, T.B., Henson, R.M. & Shiao, S.L. Targeting Innate Immunity to Enhance the Efficacy of Radiation Therapy. *Front Immunol* **9**, 3077 (2018).
286. Tseng, D. *et al.* Anti-CD47 antibody-mediated phagocytosis of cancer by macrophages primes an effective antitumor T-cell response. *Proc Natl Acad Sci U S A* **110**, 11103-11108 (2013).
287. Barker, R.N. *et al.* Antigen presentation by macrophages is enhanced by the uptake of necrotic, but not apoptotic, cells. *Clin Exp Immunol* **127**, 220-225 (2002).
288. Gordon, S. & Pluddemann, A. Macrophage Clearance of Apoptotic Cells: A Critical Assessment. *Front Immunol* **9**, 127 (2018).
289. Gustafson, H.H., Holt-Casper, D., Grainger, D.W. & Ghandehari, H. Nanoparticle Uptake: The Phagocyte Problem. *Nano Today* **10**, 487-510 (2015).
290. Li, S. *et al.* Nanomedicine engulfed by macrophages for targeted tumor therapy. *Int J Nanomedicine* **11**, 4107-4124 (2016).
291. Jiang, P.S. *et al.* Irradiation Enhances the Ability of Monocytes as Nanoparticle Carrier for Cancer Therapy. *PLoS One* **10**, e0139043 (2015).
292. De Palma, M. *et al.* Tumor-targeted interferon-alpha delivery by Tie2-expressing monocytes inhibits tumor growth and metastasis. *Cancer Cell* **14**, 299-311 (2008).
293. Cassetta, L. & Kitamura, T. Macrophage targeting: opening new possibilities for cancer immunotherapy. *Immunology* **155**, 285-293 (2018).
294. DeNardo, D.G. & Ruffell, B. Macrophages as regulators of tumour immunity and immunotherapy. *Nat Rev Immunol* **19**, 369-382 (2019).
295. Hartley, G.P., Chow, L., Ammons, D.T., Wheat, W.H. & Dow, S.W. Programmed Cell Death Ligand 1 (PD-L1) Signaling Regulates Macrophage Proliferation and Activation. *Cancer Immunol Res* **6**, 1260-1273 (2018).
296. Bally, A.P. *et al.* NF-kappaB regulates PD-1 expression in macrophages. *J Immunol* **194**, 4545-4554 (2015).

297. Wang, F. *et al.* Tumor-derived exosomes induce PD1(+) macrophage population in human gastric cancer that promotes disease progression. *Oncogenesis* **7**, 41 (2018).
298. Ma, C.J. *et al.* PD-1 negatively regulates interleukin-12 expression by limiting STAT-1 phosphorylation in monocytes/macrophages during chronic hepatitis C virus infection. *Immunology* **132**, 421-431 (2011).
299. Strauss, L. *et al.* Targeted deletion of PD-1 in myeloid cells induces antitumor immunity. *Sci Immunol* **5** (2020).
300. Mullard, A. Can innate immune system targets turn up the heat on 'cold' tumours? *Nat Rev Drug Discov* **17**, 3-5 (2018).
301. Gubin, M.M. *et al.* High-Dimensional Analysis Delineates Myeloid and Lymphoid Compartment Remodeling during Successful Immune-Checkpoint Cancer Therapy. *Cell* **175**, 1443 (2018).
302. House, I.G. *et al.* Macrophage derived CXCL9 and CXCL10 are required for anti-tumor immune responses following immune checkpoint blockade. *Clin Cancer Res* (2019).
303. Kumar, M.P. *et al.* Analysis of Single-Cell RNA-Seq Identifies Cell-Cell Communication Associated with Tumor Characteristics. *Cell Rep* **25**, 1458-1468 e1454 (2018).
304. Pascual-Garcia, M. *et al.* LIF regulates CXCL9 in tumor-associated macrophages and prevents CD8(+) T cell tumor-infiltration impairing anti-PD1 therapy. *Nat Commun* **10**, 2416 (2019).
305. Gordon, S. & Taylor, P.R. Monocyte and macrophage heterogeneity. *Nat Rev Immunol* **5**, 953-964 (2005).
306. Bassler, K., Schulte-Schrepping, J., Warnat-Herresthal, S., Aschenbrenner, A.C. & Schultze, J.L. The Myeloid Cell Compartment-Cell by Cell. *Annu Rev Immunol* **37**, 269-293 (2019).
307. Mosser, D.M. & Edwards, J.P. Exploring the full spectrum of macrophage activation. *Nat Rev Immunol* **8**, 958-969 (2008).
308. Gordon, S. & Pluddemann, A. Tissue macrophages: heterogeneity and functions. *BMC Biol* **15**, 53 (2017).
309. Hobson-Gutierrez, S.A. & Carmona-Fontaine, C. The metabolic axis of macrophage and immune cell polarization. *Dis Model Mech* **11** (2018).
310. Reynolds, G. & Haniffa, M. Human and Mouse Mononuclear Phagocyte Networks: A Tale of Two Species? *Front Immunol* **6**, 330 (2015).
311. Schneemann, M. & Schoeden, G. Macrophage biology and immunology: man is not a mouse. *J Leukoc Biol* **81**, 579 (2007).
312. Schliefsteiner, C. *et al.* Human Placental Hofbauer Cells Maintain an Anti-inflammatory M2 Phenotype despite the Presence of Gestational Diabetes Mellitus. *Front Immunol* **8**, 888 (2017).
313. Mantovani, A. *et al.* The chemokine system in diverse forms of macrophage activation and polarization. *Trends Immunol* **25**, 677-686 (2004).
314. Porcheray, F. *et al.* Macrophage activation switching: an asset for the resolution of inflammation. *Clin Exp Immunol* **142**, 481-489 (2005).
315. Schulz, D., Severin, Y., Zanotelli, V.R.T. & Bodenmiller, B. In-Depth Characterization of Monocyte-Derived Macrophages using a Mass Cytometry-Based Phagocytosis Assay. *Sci Rep* **9**, 1925 (2019).
316. Sironi, M. *et al.* Differential regulation of chemokine production by Fcgamma receptor engagement in human monocytes: association of

CCL1 with a distinct form of M2 monocyte activation (M2b, Type 2). *J Leukoc Biol* **80**, 342-349 (2006).
317. Edwards, J.P., Zhang, X., Frauwirth, K.A. & Mosser, D.M. Biochemical and functional characterization of three activated macrophage populations. *J Leukoc Biol* **80**, 1298-1307 (2006).
318. Mosser, D.M. & Karp, C.L. Receptor mediated subversion of macrophage cytokine production by intracellular pathogens. *Curr Opin Immunol* **11**, 406-411 (1999).
319. Ferrante, C.J. & Leibovich, S.J. Regulation of Macrophage Polarization and Wound Healing. *Adv Wound Care (New Rochelle)* **1**, 10-16 (2012).
320. Xue, J. *et al.* Transcriptome-based network analysis reveals a spectrum model of human macrophage activation. *Immunity* **40**, 274-288 (2014).
321. Chevrier, S. *et al.* An Immune Atlas of Clear Cell Renal Cell Carcinoma. *Cell* **169**, 736-749 e718 (2017).
322. Lavin, Y. *et al.* Innate Immune Landscape in Early Lung Adenocarcinoma by Paired Single-Cell Analyses. *Cell* **169**, 750-765 e717 (2017).
323. Lin, J.D. *et al.* Single-cell analysis of fate-mapped macrophages reveals heterogeneity, including stem-like properties, during atherosclerosis progression and regression. *JCI Insight* **4** (2019).
324. Muller, S. *et al.* Single-cell profiling of human gliomas reveals macrophage ontogeny as a basis for regional differences in macrophage activation in the tumor microenvironment. *Genome Biol* **18**, 234 (2017).
325. Chung, W. *et al.* Single-cell RNA-seq enables comprehensive tumour and immune cell profiling in primary breast cancer. *Nat Commun* **8**, 15081 (2017).
326. Villani, A.C. *et al.* Single-cell RNA-seq reveals new types of human blood dendritic cells, monocytes, and progenitors. *Science* **356** (2017).
327. Aran, D. *et al.* Reference-based analysis of lung single-cell sequencing reveals a transitional profibrotic macrophage. *Nat Immunol* **20**, 163-172 (2019).
328. Wynn, T.A., Chawla, A. & Pollard, J.W. Macrophage biology in development, homeostasis and disease. *Nature* **496**, 445-455 (2013).
329. Colonna, M. & Butovsky, O. Microglia Function in the Central Nervous System During Health and Neurodegeneration. *Annu Rev Immunol* **35**, 441-468 (2017).
330. Hirayama, D., Iida, T. & Nakase, H. The Phagocytic Function of Macrophage-Enforcing Innate Immunity and Tissue Homeostasis. *Int J Mol Sci* **19** (2017).
331. Bilzer, M., Roggel, F. & Gerbes, A.L. Role of Kupffer cells in host defense and liver disease. *Liver Int* **26**, 1175-1186 (2006).
332. de Back, D.Z., Kostova, E.B., van Kraaij, M., van den Berg, T.K. & van Bruggen, R. Of macrophages and red blood cells; a complex love story. *Front Physiol* **5**, 9 (2014).
333. Hulsmans, M. *et al.* Macrophages Facilitate Electrical Conduction in the Heart. *Cell* **169**, 510-522 e520 (2017).
334. Landsman, L., Varol, C. & Jung, S. Distinct differentiation potential of blood monocyte subsets in the lung. *J Immunol* **178**, 2000-2007 (2007).
335. van Furth, R. & Cohn, Z.A. The origin and kinetics of mononuclear phagocytes. *J Exp Med* **128**, 415-435 (1968).

336. Schulz, C. *et al.* A lineage of myeloid cells independent of Myb and hematopoietic stem cells. *Science* **336**, 86-90 (2012).
337. Hoeffel, G. *et al.* C-Myb(+) erythro-myeloid progenitor-derived fetal monocytes give rise to adult tissue-resident macrophages. *Immunity* **42**, 665-678 (2015).
338. Epelman, S., Lavine, K.J. & Randolph, G.J. Origin and functions of tissue macrophages. *Immunity* **41**, 21-35 (2014).
339. Bain, C.C. *et al.* Constant replenishment from circulating monocytes maintains the macrophage pool in the intestine of adult mice. *Nat Immunol* **15**, 929-937 (2014).
340. Ferrer, I.R. *et al.* A wave of monocytes is recruited to replenish the long-term Langerhans cell network after immune injury. *Sci Immunol* **4** (2019).
341. Gentek, R., Molawi, K. & Sieweke, M.H. Tissue macrophage identity and self-renewal. *Immunol Rev* **262**, 56-73 (2014).
342. Cipriani, G. *et al.* Change in Populations of Macrophages Promotes Development of Delayed Gastric Emptying in Mice. *Gastroenterology* **154**, 2122-2136 e2112 (2018).
343. Cipriani, G., Gibbons, S.J., Kashyap, P.C. & Farrugia, G. Intrinsic Gastrointestinal Macrophages: Their Phenotype and Role in Gastrointestinal Motility. *Cell Mol Gastroenterol Hepatol* **2**, 120-130 e121 (2016).
344. Kielbassa, K., Vegna, S., Ramirez, C. & Akkari, L. Understanding the Origin and Diversity of Macrophages to Tailor Their Targeting in Solid Cancers. *Front Immunol* **10**, 2215 (2019).
345. Soncin, I. *et al.* The tumour microenvironment creates a niche for the self-renewal of tumour-promoting macrophages in colon adenoma. *Nat Commun* **9**, 582 (2018).
346. Zhu, Y. *et al.* Tissue-Resident Macrophages in Pancreatic Ductal Adenocarcinoma Originate from Embryonic Hematopoiesis and Promote Tumor Progression. *Immunity* **47**, 323-338 e326 (2017).
347. Loyher, P.L. *et al.* Macrophages of distinct origins contribute to tumor development in the lung. *J Exp Med* **215**, 2536-2553 (2018).
348. Jappinen, N. *et al.* Fetal-derived macrophages dominate in adult mammary glands. *Nat Commun* **10**, 281 (2019).
349. Wang, S. *et al.* Metabolic reprogramming of macrophages during infections and cancer. *Cancer Lett* **452**, 14-22 (2019).
350. Vats, D. *et al.* Oxidative metabolism and PGC-1beta attenuate macrophage-mediated inflammation. *Cell Metab* **4**, 13-24 (2006).
351. Stunault, M.I., Bories, G., Guinamard, R.R. & Ivanov, S. Metabolism Plays a Key Role during Macrophage Activation. *Mediators Inflamm* **2018**, 2426138 (2018).
352. Colegio, O.R. *et al.* Functional polarization of tumour-associated macrophages by tumour-derived lactic acid. *Nature* **513**, 559-563 (2014).
353. Palmieri, E.M. *et al.* Pharmacologic or Genetic Targeting of Glutamine Synthetase Skews Macrophages toward an M1-like Phenotype and Inhibits Tumor Metastasis. *Cell Rep* **20**, 1654-1666 (2017).
354. Wu, J.Y. *et al.* Cancer-Derived Succinate Promotes Macrophage Polarization and Cancer Metastasis via Succinate Receptor. *Mol Cell* **77**, 213-227 e215 (2020).

355. Tan, Z. *et al.* Pyruvate dehydrogenase kinase 1 participates in macrophage polarization via regulating glucose metabolism. *J Immunol* **194**, 6082-6089 (2015).
356. Palazon, A., Goldrath, A.W., Nizet, V. & Johnson, R.S. HIF transcription factors, inflammation, and immunity. *Immunity* **41**, 518-528 (2014).
357. Sutendra, G. & Michelakis, E.D. Pyruvate dehydrogenase kinase as a novel therapeutic target in oncology. *Front Oncol* **3**, 38 (2013).
358. Kim, J.W., Tchernyshyov, I., Semenza, G.L. & Dang, C.V. HIF-1-mediated expression of pyruvate dehydrogenase kinase: a metabolic switch required for cellular adaptation to hypoxia. *Cell Metab* **3**, 177-185 (2006).
359. Van den Bossche, J. *et al.* Mitochondrial Dysfunction Prevents Repolarization of Inflammatory Macrophages. *Cell Rep* **17**, 684-696 (2016).
360. Zhang, D. *et al.* Metabolic regulation of gene expression by histone lactylation. *Nature* **574**, 575-580 (2019).
361. El-Kenawi, A. *et al.* Acidity promotes tumour progression by altering macrophage phenotype in prostate cancer. *Br J Cancer* **121**, 556-566 (2019).
362. Liberti, M.V. & Locasale, J.W. The Warburg Effect: How Does it Benefit Cancer Cells? *Trends Biochem Sci* **41**, 211-218 (2016).
363. Murdoch, C., Giannoudis, A. & Lewis, C.E. Mechanisms regulating the recruitment of macrophages into hypoxic areas of tumors and other ischemic tissues. *Blood* **104**, 2224-2234 (2004).
364. Henze, A.T. & Mazzone, M. The impact of hypoxia on tumor-associated macrophages. *J Clin Invest* **126**, 3672-3679 (2016).
365. Carmona-Fontaine, C. *et al.* Metabolic origins of spatial organization in the tumor microenvironment. *Proc Natl Acad Sci U S A* **114**, 2934-2939 (2017).
366. Torraca, V., Masud, S., Spaink, H.P. & Meijer, A.H. Macrophage-pathogen interactions in infectious diseases: new therapeutic insights from the zebrafish host model. *Dis Model Mech* **7**, 785-797 (2014).
367. Sica, A. & Mantovani, A. Macrophage plasticity and polarization: in vivo veritas. *J Clin Invest* **122**, 787-795 (2012).
368. Kang, K. *et al.* IFN-gamma selectively suppresses a subset of TLR4-activated genes and enhancers to potentiate macrophage activation. *Nat Commun* **10**, 3320 (2019).
369. Gong, T., Liu, L., Jiang, W. & Zhou, R. DAMP-sensing receptors in sterile inflammation and inflammatory diseases. *Nat Rev Immunol* (2019).
370. Schindler, H., Lutz, M.B., Rollinghoff, M. & Bogdan, C. The production of IFN-gamma by IL-12/IL-18-activated macrophages requires STAT4 signaling and is inhibited by IL-4. *J Immunol* **166**, 3075-3082 (2001).
371. Darwich, L. *et al.* Secretion of interferon-gamma by human macrophages demonstrated at the single-cell level after costimulation with interleukin (IL)-12 plus IL-18. *Immunology* **126**, 386-393 (2009).
372. Langrish, C.L. *et al.* IL-23 drives a pathogenic T cell population that induces autoimmune inflammation. *J Exp Med* **201**, 233-240 (2005).
373. Ciric, B., El-behi, M., Cabrera, R., Zhang, G.X. & Rostami, A. IL-23 drives pathogenic IL-17-producing CD8+ T cells. *J Immunol* **182**, 5296-5305 (2009).

374. Miossec, P. & Kolls, J.K. Targeting IL-17 and TH17 cells in chronic inflammation. *Nat Rev Drug Discov* **11**, 763-776 (2012).
375. Huynh, M.L., Fadok, V.A. & Henson, P.M. Phosphatidylserine-dependent ingestion of apoptotic cells promotes TGF-beta1 secretion and the resolution of inflammation. *J Clin Invest* **109**, 41-50 (2002).
376. Loke, P. *et al.* Alternative activation is an innate response to injury that requires CD4+ T cells to be sustained during chronic infection. *J Immunol* **179**, 3926-3936 (2007).
377. Brandt, E., Woerly, G., Younes, A.B., Loiseau, S. & Capron, M. IL-4 production by human polymorphonuclear neutrophils. *J Leukoc Biol* **68**, 125-130 (2000).
378. Chaudhry, A. *et al.* Interleukin-10 signaling in regulatory T cells is required for suppression of Th17 cell-mediated inflammation. *Immunity* **34**, 566-578 (2011).
379. Hilgenberg, E. *et al.* Interleukin-10-producing B cells and the regulation of immunity. *Curr Top Microbiol Immunol* **380**, 69-92 (2014).
380. Montinaro, A. & Walczak, H. Sterile Inflammation Fuels Gastric Cancer. *Immunity* **48**, 481-483 (2018).
381. O'Reilly, L.A. *et al.* Loss of NF-kappaB1 Causes Gastric Cancer with Aberrant Inflammation and Expression of Immune Checkpoint Regulators in a STAT-1-Dependent Manner. *Immunity* **48**, 570-583 e578 (2018).
382. Varga, T. *et al.* Highly Dynamic Transcriptional Signature of Distinct Macrophage Subsets during Sterile Inflammation, Resolution, and Tissue Repair. *J Immunol* **196**, 4771-4782 (2016).
383. Qualls, J.E. *et al.* Arginine usage in mycobacteria-infected macrophages depends on autocrine-paracrine cytokine signaling. *Sci Signal* **3**, ra62 (2010).
384. Murray, P.J. Macrophage Polarization. *Annu Rev Physiol* **79**, 541-566 (2017).
385. El Kasmi, K.C. *et al.* Toll-like receptor-induced arginase 1 in macrophages thwarts effective immunity against intracellular pathogens. *Nat Immunol* **9**, 1399-1406 (2008).
386. Ip, W.K.E., Hoshi, N., Shouval, D.S., Snapper, S. & Medzhitov, R. Anti-inflammatory effect of IL-10 mediated by metabolic reprogramming of macrophages. *Science* **356**, 513-519 (2017).
387. Manzanillo, P., Eidenschenk, C. & Ouyang, W. Deciphering the crosstalk among IL-1 and IL-10 family cytokines in intestinal immunity. *Trends Immunol* **36**, 471-478 (2015).
388. Baseler, W.A. *et al.* Autocrine IL-10 functions as a rheostat for M1 macrophage glycolytic commitment by tuning nitric oxide production. *Redox Biol* **10**, 12-23 (2016).
389. Xu, M.M. *et al.* Dendritic Cells but Not Macrophages Sense Tumor Mitochondrial DNA for Cross-priming through Signal Regulatory Protein alpha Signaling. *Immunity* **47**, 363-373 e365 (2017).
390. Su, S. *et al.* A positive feedback loop between mesenchymal-like cancer cells and macrophages is essential to breast cancer metastasis. *Cancer Cell* **25**, 605-620 (2014).
391. Zhou, X. *et al.* Circuit Design Features of a Stable Two-Cell System. *Cell* **172**, 744-757 e717 (2018).

392. Link, V.M. *et al.* Analysis of Genetically Diverse Macrophages Reveals Local and Domain-wide Mechanisms that Control Transcription Factor Binding and Function. *Cell* **173**, 1796-1809 e1717 (2018).
393. Bronte, V. *et al.* Recommendations for myeloid-derived suppressor cell nomenclature and characterization standards. *Nat Commun* **7**, 12150 (2016).
394. Zilionis, R. *et al.* Single-Cell Transcriptomics of Human and Mouse Lung Cancers Reveals Conserved Myeloid Populations across Individuals and Species. *Immunity* **50**, 1317-1334 e1310 (2019).
395. Raes, G. *et al.* Arginase-1 and Ym1 are markers for murine, but not human, alternatively activated myeloid cells. *J Immunol* **174**, 6561; author reply 6561-6562 (2005).
396. Scotton, C.J. *et al.* Transcriptional profiling reveals complex regulation of the monocyte IL-1 beta system by IL-13. *J Immunol* **174**, 834-845 (2005).
397. Raes, G. *et al.* Macrophage galactose-type C-type lectins as novel markers for alternatively activated macrophages elicited by parasitic infections and allergic airway inflammation. *J Leukoc Biol* **77**, 321-327 (2005).
398. Hume, D.A., Robinson, A.P., MacPherson, G.G. & Gordon, S. The mononuclear phagocyte system of the mouse defined by immunohistochemical localization of antigen F4/80. Relationship between macrophages, Langerhans cells, reticular cells, and dendritic cells in lymphoid and hematopoietic organs. *J Exp Med* **158**, 1522-1536 (1983).
399. Hamann, J. *et al.* EMR1, the human homolog of F4/80, is an eosinophil-specific receptor. *Eur J Immunol* **37**, 2797-2802 (2007).
400. Vijayan, V. *et al.* Human and murine macrophages exhibit differential metabolic responses to lipopolysaccharide - A divergent role for glycolysis. *Redox Biol* **22**, 101147 (2019).
401. Ariffin, J.K. *et al.* The E3 ubiquitin ligase RNF144B is LPS-inducible in human, but not mouse, macrophages and promotes inducible IL-1beta expression. *J Leukoc Biol* **100**, 155-161 (2016).
402. Szulzewsky, F. *et al.* Human glioblastoma-associated microglia/monocytes express a distinct RNA profile compared to human control and murine samples. *Glia* **64**, 1416-1436 (2016).
403. Murray, P.J. *et al.* Macrophage activation and polarization: nomenclature and experimental guidelines. *Immunity* **41**, 14-20 (2014).
404. Liu, J.Y. *et al.* Distribution pattern of tumor associated macrophages predicts the prognosis of gastric cancer. *Oncotarget* **8**, 92757-92769 (2017).
405. Szasz, A.M. *et al.* Cross-validation of survival associated biomarkers in gastric cancer using transcriptomic data of 1,065 patients. *Oncotarget* **7**, 49322-49333 (2016).
406. Dutta, S. *et al.* The relationship between tumour necrosis, tumour proliferation, local and systemic inflammation, microvessel density and survival in patients undergoing potentially curative resection of oesophageal adenocarcinoma. *Br J Cancer* **106**, 702-710 (2012).
407. Wang, M. Investigating the immune landscape in gastric cancer. *The University of Melbourne* (2019).

408. Busuttil, R.A. *et al.* An orthotopic mouse model of gastric cancer invasion and metastasis. *Sci Rep* **8**, 825 (2018).
409. Stack, E.C., Wang, C., Roman, K.A. & Hoyt, C.C. Multiplexed immunohistochemistry, imaging, and quantitation: a review, with an assessment of Tyramide signal amplification, multispectral imaging and multiplex analysis. *Methods* **70**, 46-58 (2014).
410. Fabregat, A. *et al.* Reactome pathway analysis: a high-performance in-memory approach. *BMC Bioinformatics* **18**, 142 (2017).
411. Fabregat, A. *et al.* The Reactome Pathway Knowledgebase. *Nucleic Acids Res* **46**, D649-D655 (2018).
412. Minyu Wang, Y.S., Yu-Kuan Huang ISAT: Extract Cell Density and Nearest Distance Based on 'PerkinElmer InForm' Software Output https://cran.r-project.org/web/packages/ISAT/index.html. (2018).
413. Ritchie, M.E. *et al.* limma powers differential expression analyses for RNA-sequencing and microarray studies. *Nucleic Acids Res* **43**, e47 (2015).
414. Roussel, M. *et al.* Mass cytometry deep phenotyping of human mononuclear phagocytes and myeloid-derived suppressor cells from human blood and bone marrow. *J Leukoc Biol* **102**, 437-447 (2017).
415. House, I.G. *et al.* Macrophage-Derived CXCL9 and CXCL10 Are Required for Antitumor Immune Responses Following Immune Checkpoint Blockade. *Clin Cancer Res* **26**, 487-504 (2020).
416. Gorris, M.A.J. *et al.* Eight-Color Multiplex Immunohistochemistry for Simultaneous Detection of Multiple Immune Checkpoint Molecules within the Tumor Microenvironment. *J Immunol* **200**, 347-354 (2018).
417. Norton, S.E., Dunn, E.T., McCall, J.L., Munro, F. & Kemp, R.A. Gut macrophage phenotype is dependent on the tumor microenvironment in colorectal cancer. *Clin Transl Immunology* **5**, e76 (2016).
418. Halse, H. *et al.* Multiplex immunohistochemistry accurately defines the immune context of metastatic melanoma. *Sci Rep* **8**, 11158 (2018).
419. Tsujikawa, T. *et al.* Quantitative Multiplex Immunohistochemistry Reveals Myeloid-Inflamed Tumor-Immune Complexity Associated with Poor Prognosis. *Cell Rep* **19**, 203-217 (2017).
420. Saylor, J. *et al.* Spatial Mapping of Myeloid Cells and Macrophages by Multiplexed Tissue Staining. *Front Immunol* **9**, 2925 (2018).
421. Cassetta, L. *et al.* Human Tumor-Associated Macrophage and Monocyte Transcriptional Landscapes Reveal Cancer-Specific Reprogramming, Biomarkers, and Therapeutic Targets. *Cancer Cell* **35**, 588-602 e510 (2019).
422. Carstens, J.L. *et al.* Spatial computation of intratumoral T cells correlates with survival of patients with pancreatic cancer. *Nat Commun* **8**, 15095 (2017).
423. Feng, Z. *et al.* Multiparametric immune profiling in HPV- oral squamous cell cancer. *JCI Insight* **2** (2017).
424. Lizotte, P.H. *et al.* Multiparametric profiling of non-small-cell lung cancers reveals distinct immunophenotypes. *JCI Insight* **1**, e89014 (2016).
425. Chazotte, B. Labeling nuclear DNA using DAPI. *Cold Spring Harb Protoc* **2011**, pdb prot5556 (2011).

426. Geller, S.A., Dhall, D. & Alsabeh, R. Application of immunohistochemistry to liver and gastrointestinal neoplasms: liver, stomach, colon, and pancreas. *Arch Pathol Lab Med* **132**, 490-499 (2008).
427. Gordon, S., Pluddemann, A. & Martinez Estrada, F. Macrophage heterogeneity in tissues: phenotypic diversity and functions. *Immunol Rev* **262**, 36-55 (2014).
428. Baroni, C.D. *et al.* Immunohistochemical heterogeneity of macrophage subpopulations in human lymphoid tissues. *Histopathology* **11**, 1029-1042 (1987).
429. Chistiakov, D.A., Killingsworth, M.C., Myasoedova, V.A., Orekhov, A.N. & Bobryshev, Y.V. CD68/macrosialin: not just a histochemical marker. *Lab Invest* **97**, 4-13 (2017).
430. Rabinowitz, S.S. & Gordon, S. Macrosialin, a macrophage-restricted membrane sialoprotein differentially glycosylated in response to inflammatory stimuli. *J Exp Med* **174**, 827-836 (1991).
431. da Silva, R.P. & Gordon, S. Phagocytosis stimulates alternative glycosylation of macrosialin (mouse CD68), a macrophage-specific endosomal protein. *Biochem J* **338 (Pt 3)**, 687-694 (1999).
432. Holness, C.L. & Simmons, D.L. Molecular cloning of CD68, a human macrophage marker related to lysosomal glycoproteins. *Blood* **81**, 1607-1613 (1993).
433. Ramprasad, M.P., Terpstra, V., Kondratenko, N., Quehenberger, O. & Steinberg, D. Cell surface expression of mouse macrosialin and human CD68 and their role as macrophage receptors for oxidized low density lipoprotein. *Proc Natl Acad Sci U S A* **93**, 14833-14838 (1996).
434. Zeibig, S. *et al.* The Scavenger Receptor CD68 Regulates Platelet Mediated Oxidized Low-Density Lipoprotein (oxLDL) Deposition in Atherosclerotic Vessels at an Early Stage of Atherosclerosis in LDLR(-/-)/ApoBec(-/-) Mice. *Cell Physiol Biochem* **52**, 681-695 (2019).
435. Sambrano, G.R. & Steinberg, D. Recognition of oxidatively damaged and apoptotic cells by an oxidized low density lipoprotein receptor on mouse peritoneal macrophages: role of membrane phosphatidylserine. *Proc Natl Acad Sci U S A* **92**, 1396-1400 (1995).
436. Miki, Y. *et al.* Clearance of oxidatively damaged cells by macrophages: recognition of glycoprotein clusters by macrophage-surface nucleolin as early apoptotic cells. *Biol Pharm Bull* **32**, 564-572 (2009).
437. Barois, N., de Saint-Vis, B., Lebecque, S., Geuze, H.J. & Kleijmeer, M.J. MHC class II compartments in human dendritic cells undergo profound structural changes upon activation. *Traffic* **3**, 894-905 (2002).
438. Song, L., Lee, C. & Schindler, C. Deletion of the murine scavenger receptor CD68. *J Lipid Res* **52**, 1542-1550 (2011).
439. Gunthner, R. & Anders, H.J. Interferon-regulatory factors determine macrophage phenotype polarization. *Mediators Inflamm* **2013**, 731023 (2013).
440. Qi, C.F. *et al.* Differential expression of IRF8 in subsets of macrophages and dendritic cells and effects of IRF8 deficiency on splenic B cell and macrophage compartments. *Immunol Res* **45**, 62-74 (2009).
441. Schneider, A. *et al.* IRF5 Is a Key Regulator of Macrophage Response to Lipopolysaccharide in Newborns. *Front Immunol* **9**, 1597 (2018).

442. Twum, D.Y. *et al.* IFN regulatory factor-8 expression in macrophages governs an antimetastatic program. *JCI Insight* **4** (2019).
443. Li, L., Jin, H., Xu, J., Shi, Y. & Wen, Z. Irf8 regulates macrophage versus neutrophil fate during zebrafish primitive myelopoiesis. *Blood* **117**, 1359-1369 (2011).
444. Hagemeyer, N. *et al.* Transcriptome-based profiling of yolk sac-derived macrophages reveals a role for Irf8 in macrophage maturation. *EMBO J* **35**, 1730-1744 (2016).
445. Langlais, D., Barreiro, L.B. & Gros, P. The macrophage IRF8/IRF1 regulome is required for protection against infections and is associated with chronic inflammation. *J Exp Med* **213**, 585-603 (2016).
446. Marquis, J.F. *et al.* Interferon regulatory factor 8 regulates pathways for antigen presentation in myeloid cells and during tuberculosis. *PLoS Genet* **7**, e1002097 (2011).
447. Muhitch, J.B. *et al.* Tumor-associated macrophage expression of interferon regulatory Factor-8 (IRF8) is a predictor of progression and patient survival in renal cell carcinoma. *J Immunother Cancer* **7**, 155 (2019).
448. Jablonski, K.A. *et al.* Novel Markers to Delineate Murine M1 and M2 Macrophages. *PLoS One* **10**, e0145342 (2015).
449. Suzuki, Y. *et al.* Macrophage mannose receptor, CD206, predict prognosis in patients with pulmonary tuberculosis. *Sci Rep* **8**, 13129 (2018).
450. Zhang, H. *et al.* Infiltration of diametrically polarized macrophages predicts overall survival of patients with gastric cancer after surgical resection. *Gastric Cancer* **18**, 740-750 (2015).
451. Burgdorf, S., Kautz, A., Bohnert, V., Knolle, P.A. & Kurts, C. Distinct pathways of antigen uptake and intracellular routing in CD4 and CD8 T cell activation. *Science* **316**, 612-616 (2007).
452. Zehner, M. & Burgdorf, S. Regulation of antigen transport into the cytosol for cross-presentation by ubiquitination of the mannose receptor. *Mol Immunol* **55**, 146-148 (2013).
453. Martinez-Pomares, L. The mannose receptor. *J Leukoc Biol* **92**, 1177-1186 (2012).
454. Hussell, T. & Bell, T.J. Alveolar macrophages: plasticity in a tissue-specific context. *Nat Rev Immunol* **14**, 81-93 (2014).
455. Hashino, M., Tachibana, M., Shimizu, T. & Watarai, M. Mannose receptor, C type 1 contributes to bacterial uptake by placental trophoblast giant cells. *FEMS Immunol Med Microbiol* **66**, 427-435 (2012).
456. Lee, S.J. *et al.* Mannose receptor-mediated regulation of serum glycoprotein homeostasis. *Science* **295**, 1898-1901 (2002).
457. Lurier, E.B. *et al.* Transcriptome analysis of IL-10-stimulated (M2c) macrophages by next-generation sequencing. *Immunobiology* **222**, 847-856 (2017).
458. Thornton, S. *et al.* A Multiparameter Flow Cytometry Analysis Panel to Assess CD163 mRNA and Protein in Monocyte and Macrophage Populations in Hyperinflammatory Diseases. *J Immunol* **202**, 1635-1643 (2019).
459. Mendoza-Coronel, E. & Ortega, E. Macrophage Polarization Modulates FcgammaR- and CD13-Mediated Phagocytosis and Reactive Oxygen

Species Production, Independently of Receptor Membrane Expression. *Front Immunol* **8**, 303 (2017).
460. Gronbaek, H. *et al.* Soluble CD163, a marker of Kupffer cell activation, is related to portal hypertension in patients with liver cirrhosis. *Aliment Pharmacol Ther* **36**, 173-180 (2012).
461. Borda, J.T. *et al.* CD163, a marker of perivascular macrophages, is up-regulated by microglia in simian immunodeficiency virus encephalitis after haptoglobin-hemoglobin complex stimulation and is suggestive of breakdown of the blood-brain barrier. *Am J Pathol* **172**, 725-737 (2008).
462. Jeong, H., Hwang, I., Kang, S.H., Shin, H.C. & Kwon, S.Y. Tumor-Associated Macrophages as Potential Prognostic Biomarkers of Invasive Breast Cancer. *J Breast Cancer* **22**, 38-51 (2019).
463. Graversen, J.H., Madsen, M. & Moestrup, S.K. CD163: a signal receptor scavenging haptoglobin-hemoglobin complexes from plasma. *Int J Biochem Cell Biol* **34**, 309-314 (2002).
464. Yang, H. *et al.* Identification of CD163 as an antiinflammatory receptor for HMGB1-haptoglobin complexes. *JCI Insight* **1** (2016).
465. Fabriek, B.O. *et al.* The macrophage scavenger receptor CD163 functions as an innate immune sensor for bacteria. *Blood* **113**, 887-892 (2009).
466. Huang, Y.K. *et al.* Macrophage spatial heterogeneity in gastric cancer defined by multiplex immunohistochemistry. *Nat Commun* **10**, 3928 (2019).
467. Kakushadze, Z. & Yu, W. *K-means and cluster models for cancer signatures. *Biomol Detect Quantif* **13**, 7-31 (2017).
468. Singhal, S. *et al.* Human tumor-associated monocytes/macrophages and their regulation of T cell responses in early-stage lung cancer. *Sci Transl Med* **11** (2019).
469. Zaidi, M.R. & Merlino, G. The two faces of interferon-gamma in cancer. *Clin Cancer Res* **17**, 6118-6124 (2011).
470. Castro, F., Cardoso, A.P., Goncalves, R.M., Serre, K. & Oliveira, M.J. Interferon-Gamma at the Crossroads of Tumor Immune Surveillance or Evasion. *Front Immunol* **9**, 847 (2018).
471. Morihiro, T. *et al.* PD-L1 expression combined with microsatellite instability/CD8+ tumor infiltrating lymphocytes as a useful prognostic biomarker in gastric cancer. *Sci Rep* **9**, 4633 (2019).
472. Menyhart, O., Pongor, L.S. & Gyorffy, B. Mutations Defining Patient Cohorts With Elevated PD-L1 Expression in Gastric Cancer. *Front Pharmacol* **9**, 1522 (2018).
473. Cho, J. *et al.* Four distinct immune microenvironment subtypes in gastric adenocarcinoma with special reference to microsatellite instability. *ESMO Open* **3**, e000326 (2018).
474. Angell, H.K. *et al.* PD-L1 and immune infiltrates are differentially expressed in distinct subgroups of gastric cancer. *Oncoimmunology* **8**, e1544442 (2019).
475. Mandai, M. *et al.* Dual Faces of IFNgamma in Cancer Progression: A Role of PD-L1 Induction in the Determination of Pro- and Antitumor Immunity. *Clin Cancer Res* **22**, 2329-2334 (2016).

476. Bagnall, J. *et al.* Quantitative analysis of competitive cytokine signaling predicts tissue thresholds for the propagation of macrophage activation. *Sci Signal* **11** (2018).
477. Thurley, K., Gerecht, D., Friedmann, E. & Hofer, T. Three-Dimensional Gradients of Cytokine Signaling between T Cells. *PLoS Comput Biol* **11**, e1004206 (2015).
478. Oyler-Yaniv, A. *et al.* A Tunable Diffusion-Consumption Mechanism of Cytokine Propagation Enables Plasticity in Cell-to-Cell Communication in the Immune System. *Immunity* **46**, 609-620 (2017).
479. Shen, Z. *et al.* Higher intratumoral infiltrated Foxp3+ Treg numbers and Foxp3+/CD8+ ratio are associated with adverse prognosis in resectable gastric cancer. *J Cancer Res Clin Oncol* **136**, 1585-1595 (2010).
480. Shang, B., Liu, Y., Jiang, S.J. & Liu, Y. Prognostic value of tumor-infiltrating FoxP3+ regulatory T cells in cancers: a systematic review and meta-analysis. *Sci Rep* **5**, 15179 (2015).
481. Ruffell, B. *et al.* Leukocyte composition of human breast cancer. *Proc Natl Acad Sci U S A* **109**, 2796-2801 (2012).
482. Kunisch, E. *et al.* Macrophage specificity of three anti-CD68 monoclonal antibodies (KP1, EBM11, and PGM1) widely used for immunohistochemistry and flow cytometry. *Ann Rheum Dis* **63**, 774-784 (2004).
483. Cai, Y. *et al.* In vivo characterization of alveolar and interstitial lung macrophages in rhesus macaques: implications for understanding lung disease in humans. *J Immunol* **192**, 2821-2829 (2014).
484. Pavelic, K. *et al.* Gastric cancer: the role of insulin-like growth factor 2 (IGF 2) and its receptors (IGF 1R and M6-P/IGF 2R). *J Pathol* **201**, 430-438 (2003).
485. Cianfarani, S. Insulin-like growth factor-II: new roles for an old actor. *Front Endocrinol (Lausanne)* **3**, 118 (2012).
486. Engstrom, A., Erlandsson, A., Delbro, D. & Wijkander, J. Conditioned media from macrophages of M1, but not M2 phenotype, inhibit the proliferation of the colon cancer cell lines HT-29 and CACO-2. *Int J Oncol* **44**, 385-392 (2014).
487. Buhtoiarov, I.N. *et al.* Anti-tumour synergy of cytotoxic chemotherapy and anti-CD40 plus CpG-ODN immunotherapy through repolarization of tumour-associated macrophages. *Immunology* **132**, 226-239 (2011).
488. Pepe, G., Calderazzi, G., De Maglie, M., Villa, A.M. & Vegeto, E. Heterogeneous induction of microglia M2a phenotype by central administration of interleukin-4. *J Neuroinflammation* **11**, 211 (2014).
489. Valleh, M.V., Hyttel, P., Rasmussen, M.A. & Strobech, L. Insulin-like growth factor 2: a modulator of anti-apoptosis related genes (HSP70, BCL2-L1) in bovine preimplantation embryos. *Theriogenology* **82**, 942-950 (2014).
490. Dietrich, D. *et al.* Interleukin-36 potently stimulates human M2 macrophages, Langerhans cells and keratinocytes to produce pro-inflammatory cytokines. *Cytokine* **84**, 88-98 (2016).
491. Sorensen, B.S. *et al.* The usability of a 15-gene hypoxia classifier as a universal hypoxia profile in various cancer cell types. *Radiother Oncol* **116**, 346-351 (2015).

492. Zhang, F. *et al.* VEGF-B is dispensable for blood vessel growth but critical for their survival, and VEGF-B targeting inhibits pathological angiogenesis. *Proc Natl Acad Sci U S A* **106**, 6152-6157 (2009).
493. Vivien, C.J. *et al.* Vegfc/d-dependent regulation of the lymphatic vasculature during cardiac regeneration is influenced by injury context. *NPJ Regen Med* **4**, 18 (2019).
494. Pak, K.H., Park, K.C. & Cheong, J.H. VEGF-C induced by TGF- beta1 signaling in gastric cancer enhances tumor-induced lymphangiogenesis. *BMC Cancer* **19**, 799 (2019).
495. Martinez, F.O. *et al.* Genetic programs expressed in resting and IL-4 alternatively activated mouse and human macrophages: similarities and differences. *Blood* **121**, e57-69 (2013).
496. Duluc, D. *et al.* Tumor-associated leukemia inhibitory factor and IL-6 skew monocyte differentiation into tumor-associated macrophage-like cells. *Blood* **110**, 4319-4330 (2007).
497. Heusinkveld, M. & van der Burg, S.H. Identification and manipulation of tumor associated macrophages in human cancers. *J Transl Med* **9**, 216 (2011).
498. Waqas, S.F.H., Ampem, G. & Roszer, T. Analysis of IL-4/STAT6 Signaling in Macrophages. *Methods Mol Biol* **1966**, 211-224 (2019).
499. Czimmerer, Z. *et al.* The IL-4/STAT6 signaling axis establishes a conserved microRNA signature in human and mouse macrophages regulating cell survival via miR-342-3p. *Genome Med* **8**, 63 (2016).
500. Essandoh, K., Li, Y., Huo, J. & Fan, G.C. MiRNA-Mediated Macrophage Polarization and its Potential Role in the Regulation of Inflammatory Response. *Shock* **46**, 122-131 (2016).
501. Yan, D., Wang, H.W., Bowman, R.L. & Joyce, J.A. STAT3 and STAT6 Signaling Pathways Synergize to Promote Cathepsin Secretion from Macrophages via IRE1alpha Activation. *Cell Rep* **16**, 2914-2927 (2016).
502. Tomita, K. *et al.* STAT6 expression in T cells, alveolar macrophages and bronchial biopsies of normal and asthmatic subjects. *J Inflamm (Lond)* **9**, 5 (2012).
503. Wick, K.R. & Berton, M.T. IL-4 induces serine phosphorylation of the STAT6 transactivation domain in B lymphocytes. *Mol Immunol* **37**, 641-652 (2000).
504. Jiang, X. & Wang, X. Cytochrome C-mediated apoptosis. *Annu Rev Biochem* **73**, 87-106 (2004).
505. Liu, H. *et al.* TNF-alpha-induced apoptosis of macrophages following inhibition of NF-kappa B: a central role for disruption of mitochondria. *J Immunol* **172**, 1907-1915 (2004).
506. Albensi, B.C. What Is Nuclear Factor Kappa B (NF-kappaB) Doing in and to the Mitochondrion? *Front Cell Dev Biol* **7**, 154 (2019).
507. Kawashima, T. *et al.* STAT5 induces macrophage differentiation of M1 leukemia cells through activation of IL-6 production mediated by NF-kappaB p65. *J Immunol* **167**, 3652-3660 (2001).
508. Yamaoka, K. *et al.* Activation of STAT5 by lipopolysaccharide through granulocyte-macrophage colony-stimulating factor production in human monocytes. *J Immunol* **160**, 838-845 (1998).
509. Lehtonen, A., Matikainen, S., Miettinen, M. & Julkunen, I. Granulocyte-macrophage colony-stimulating factor (GM-CSF)-induced STAT5

activation and target-gene expression during human monocyte/macrophage differentiation. *J Leukoc Biol* **71**, 511-519 (2002).
510. Buechler, C. *et al.* Regulation of scavenger receptor CD163 expression in human monocytes and macrophages by pro- and antiinflammatory stimuli. *J Leukoc Biol* **67**, 97-103 (2000).
511. Tippett, E. *et al.* Differential expression of CD163 on monocyte subsets in healthy and HIV-1 infected individuals. *PLoS One* **6**, e19968 (2011).
512. Sander, J. *et al.* Cellular Differentiation of Human Monocytes Is Regulated by Time-Dependent Interleukin-4 Signaling and the Transcriptional Regulator NCOR2. *Immunity* **47**, 1051-1066 e1012 (2017).
513. Lehtonen, A. *et al.* Gene expression profiling during differentiation of human monocytes to macrophages or dendritic cells. *J Leukoc Biol* **82**, 710-720 (2007).
514. Collin, M. & Bigley, V. Human dendritic cell subsets: an update. *Immunology* **154**, 3-20 (2018).
515. Comi, M. *et al.* Coexpression of CD163 and CD141 identifies human circulating IL-10-producing dendritic cells (DC-10). *Cell Mol Immunol* (2019).
516. Maniecki, M.B., Moller, H.J., Moestrup, S.K. & Moller, B.K. CD163 positive subsets of blood dendritic cells: the scavenging macrophage receptors CD163 and CD91 are coexpressed on human dendritic cells and monocytes. *Immunobiology* **211**, 407-417 (2006).
517. Wang, Q. *et al.* Fra-1 protooncogene regulates IL-6 expression in macrophages and promotes the generation of M2d macrophages. *Cell Res* **20**, 701-712 (2010).
518. Ferrante, C.J. *et al.* The adenosine-dependent angiogenic switch of macrophages to an M2-like phenotype is independent of interleukin-4 receptor alpha (IL-4Ralpha) signaling. *Inflammation* **36**, 921-931 (2013).
519. Linnemann, C. *et al.* Adenosine regulates CD8 T-cell priming by inhibition of membrane-proximal T-cell receptor signalling. *Immunology* **128**, e728-737 (2009).
520. Sorrentino, C. *et al.* Adenosine A2A Receptor Stimulation Inhibits TCR-Induced Notch1 Activation in CD8+T-Cells. *Front Immunol* **10**, 162 (2019).
521. Tsukamoto, H. *et al.* Combined Blockade of IL6 and PD-1/PD-L1 Signaling Abrogates Mutual Regulation of Their Immunosuppressive Effects in the Tumor Microenvironment. *Cancer Res* **78**, 5011-5022 (2018).
522. Mace, T.A. *et al.* IL-6 and PD-L1 antibody blockade combination therapy reduces tumour progression in murine models of pancreatic cancer. *Gut* **67**, 320-332 (2018).
523. Barinda, A.J., Ikeda, K., Hirata, K.I. & Emoto, N. Macrophages Highly Express Carbonic Anhydrase 2 and Play a Significant Role in Demineralization of the Ectopic Calcification. *Kobe J Med Sci* **63**, E45-E50 (2017).
524. Kamsteeg, M. *et al.* Increased expression of carbonic anhydrase II (CA II) in lesional skin of atopic dermatitis: regulation by Th2 cytokines. *J Invest Dermatol* **127**, 1786-1789 (2007).

525. Henry, E.K. *et al.* Carbonic anhydrase enzymes regulate mast cell-mediated inflammation. *J Exp Med* **213**, 1663-1673 (2016).
526. McLaughlin, T., Ackerman, S.E., Shen, L. & Engleman, E. Role of innate and adaptive immunity in obesity-associated metabolic disease. *J Clin Invest* **127**, 5-13 (2017).
527. Russo, L. & Lumeng, C.N. Properties and functions of adipose tissue macrophages in obesity. *Immunology* **155**, 407-417 (2018).
528. Michelet, X. *et al.* Metabolic reprogramming of natural killer cells in obesity limits antitumor responses. *Nat Immunol* **19**, 1330-1340 (2018).
529. Springer, N.L. *et al.* Obesity-Associated Extracellular Matrix Remodeling Promotes a Macrophage Phenotype Similar to Tumor-Associated Macrophages. *Am J Pathol* **189**, 2019-2035 (2019).
530. Geha, R.S., Jonsen, M.E., Ault, B.H., Yunis, E. & Broff, M.D. Macrophage T cell interaction in man: binding of antigen-specific human proliferating and helper T cells to antigen-pulsed macrophages. *J Immunol* **126**, 781-786 (1981).
531. Paulnock, D.M. Macrophage activation by T cells. *Curr Opin Immunol* **4**, 344-349 (1992).
532. Roberts, C.A., Dickinson, A.K. & Taams, L.S. The Interplay Between Monocytes/Macrophages and CD4(+) T Cell Subsets in Rheumatoid Arthritis. *Front Immunol* **6**, 571 (2015).
533. Kaufmann, S.H. & Flesch, I.E. The role of T cell--macrophage interactions in tuberculosis. *Springer Semin Immunopathol* **10**, 337-358 (1988).
534. Miyagawa, F. *et al.* Interferon regulatory factor 8 integrates T-cell receptor and cytokine-signaling pathways and drives effector differentiation of CD8 T cells. *Proc Natl Acad Sci U S A* **109**, 12123-12128 (2012).
535. Laidlaw, B.J. *et al.* Production of IL-10 by CD4(+) regulatory T cells during the resolution of infection promotes the maturation of memory CD8(+) T cells. *Nat Immunol* **16**, 871-879 (2015).
536. Saito, T. *et al.* Two FOXP3(+)CD4(+) T cell subpopulations distinctly control the prognosis of colorectal cancers. *Nat Med* **22**, 679-684 (2016).
537. Kather, J.N. *et al.* Topography of cancer-associated immune cells in human solid tumors. *Elife* **7** (2018).
538. Binnewies, M. *et al.* Understanding the tumor immune microenvironment (TIME) for effective therapy. *Nat Med* **24**, 541-550 (2018).
539. Liu, X. *et al.* Regulatory T cells trigger effector T cell DNA damage and senescence caused by metabolic competition. *Nat Commun* **9**, 249 (2018).
540. Arpaia, N. *et al.* A Distinct Function of Regulatory T Cells in Tissue Protection. *Cell* **162**, 1078-1089 (2015).
541. Feng, T., Cao, A.T., Weaver, C.T., Elson, C.O. & Cong, Y. Interleukin-12 converts Foxp3+ regulatory T cells to interferon-gamma-producing Foxp3+ T cells that inhibit colitis. *Gastroenterology* **140**, 2031-2043 (2011).
542. Bal, S.M. & Stadhouders, R. Tregs in fibrosis: To know your enemy, you must become your enemy. *Sci Immunol* **4** (2019).
543. Kalekar, L.A. *et al.* Regulatory T cells in skin are uniquely poised to suppress profibrotic immune responses. *Sci Immunol* **4** (2019).

544. Meng, X. *et al.* Regulatory T cells in cardiovascular diseases. *Nat Rev Cardiol* **13**, 167-179 (2016).
545. Kansy, B.A. *et al.* PD-1 Status in CD8(+) T Cells Associates with Survival and Anti-PD-1 Therapeutic Outcomes in Head and Neck Cancer. *Cancer Res* **77**, 6353-6364 (2017).
546. Thommen, D.S. *et al.* A transcriptionally and functionally distinct PD-1(+) CD8(+) T cell pool with predictive potential in non-small-cell lung cancer treated with PD-1 blockade. *Nat Med* **24**, 994-1004 (2018).
547. Nguyen, G.T., Green, E.R. & Mecsas, J. Neutrophils to the ROScue: Mechanisms of NADPH Oxidase Activation and Bacterial Resistance. *Front Cell Infect Microbiol* **7**, 373 (2017).
548. Kotsias, F., Hoffmann, E., Amigorena, S. & Savina, A. Reactive oxygen species production in the phagosome: impact on antigen presentation in dendritic cells. *Antioxid Redox Signal* **18**, 714-729 (2013).
549. Gardiner, G.J. *et al.* A role for NADPH oxidase in antigen presentation. *Front Immunol* **4**, 295 (2013).
550. Savina, A. *et al.* NOX2 controls phagosomal pH to regulate antigen processing during crosspresentation by dendritic cells. *Cell* **126**, 205-218 (2006).
551. Carneiro, M.B.H. *et al.* NOX2-Derived Reactive Oxygen Species Control Inflammation during Leishmania amazonensis Infection by Mediating Infection-Induced Neutrophil Apoptosis. *J Immunol* **200**, 196-208 (2018).
552. Corzo, C.A. *et al.* Mechanism regulating reactive oxygen species in tumor-induced myeloid-derived suppressor cells. *J Immunol* **182**, 5693-5701 (2009).
553. Mani, N.L. *et al.* Quantitative assessment of the spatial heterogeneity of tumor-infiltrating lymphocytes in breast cancer. *Breast Cancer Res* **18**, 78 (2016).
554. Kamada, T. *et al.* PD-1(+) regulatory T cells amplified by PD-1 blockade promote hyperprogression of cancer. *Proc Natl Acad Sci U S A* **116**, 9999-10008 (2019).
555. Barrett, J.P. *et al.* NOX2 deficiency alters macrophage phenotype through an IL-10/STAT3 dependent mechanism: implications for traumatic brain injury. *J Neuroinflammation* **14**, 65 (2017).
556. Casbon, A.J., Long, M.E., Dunn, K.W., Allen, L.A. & Dinauer, M.C. Effects of IFN-gamma on intracellular trafficking and activity of macrophage NADPH oxidase flavocytochrome b558. *J Leukoc Biol* **92**, 869-882 (2012).
557. Hodny, Z., Reinis, M., Hubackova, S., Vasicova, P. & Bartek, J. Interferon gamma/NADPH oxidase defense system in immunity and cancer. *Oncoimmunology* **5**, e1080416 (2016).
558. Boger, C. *et al.* PD-L1 is an independent prognostic predictor in gastric cancer of Western patients. *Oncotarget* **7**, 24269-24283 (2016).
559. Mantegazza, A.R. *et al.* NADPH oxidase controls phagosomal pH and antigen cross-presentation in human dendritic cells. *Blood* **112**, 4712-4722 (2008).
560. Finbow, M.E. & Harrison, M.A. The vacuolar H+-ATPase: a universal proton pump of eukaryotes. *Biochem J* **324 (Pt 3)**, 697-712 (1997).

561. Hackam, D.J. *et al.* Host resistance to intracellular infection: mutation of natural resistance-associated macrophage protein 1 (Nramp1) impairs phagosomal acidification. *J Exp Med* **188**, 351-364 (1998).
562. Claus, V. *et al.* Lysosomal enzyme trafficking between phagosomes, endosomes, and lysosomes in J774 macrophages. Enrichment of cathepsin H in early endosomes. *J Biol Chem* **273**, 9842-9851 (1998).
563. Delamarre, L., Pack, M., Chang, H., Mellman, I. & Trombetta, E.S. Differential lysosomal proteolysis in antigen-presenting cells determines antigen fate. *Science* **307**, 1630-1634 (2005).
564. Pierre, P. *et al.* Developmental regulation of MHC class II transport in mouse dendritic cells. *Nature* **388**, 787-792 (1997).
565. Pizzolla, A. *et al.* CD68-expressing cells can prime T cells and initiate autoimmune arthritis in the absence of reactive oxygen species. *Eur J Immunol* **41**, 403-412 (2011).
566. Roux, C. *et al.* Reactive oxygen species modulate macrophage immunosuppressive phenotype through the up-regulation of PD-L1. *Proc Natl Acad Sci U S A* **116**, 4326-4335 (2019).
567. Kelkka, T. *et al.* Mice lacking NCF1 exhibit reduced growth of implanted melanoma and carcinoma tumors. *PLoS One* **8**, e84148 (2013).
568. Hintz, K.A. *et al.* Endotoxin induces rapid metalloproteinase-mediated shedding followed by up-regulation of the monocyte hemoglobin scavenger receptor CD163. *J Leukoc Biol* **72**, 711-717 (2002).
569. Timmermann, M. & Hogger, P. Oxidative stress and 8-iso-prostaglandin F(2alpha) induce ectodomain shedding of CD163 and release of tumor necrosis factor-alpha from human monocytes. *Free Radic Biol Med* **39**, 98-107 (2005).
570. Weaver, L.K. *et al.* Pivotal advance: activation of cell surface Toll-like receptors causes shedding of the hemoglobin scavenger receptor CD163. *J Leukoc Biol* **80**, 26-35 (2006).
571. Moller, H.J. Soluble CD163. *Scand J Clin Lab Invest* **72**, 1-13 (2012).
572. Etzerodt, A., Maniecki, M.B., Moller, K., Moller, H.J. & Moestrup, S.K. Tumor necrosis factor alpha-converting enzyme (TACE/ADAM17) mediates ectodomain shedding of the scavenger receptor CD163. *J Leukoc Biol* **88**, 1201-1205 (2010).
573. Etzerodt, A. *et al.* Structural basis for inflammation-driven shedding of CD163 ectodomain and tumor necrosis factor-alpha in macrophages. *J Biol Chem* **289**, 778-788 (2014).
574. Frings, W., Dreier, J. & Sorg, C. Only the soluble form of the scavenger receptor CD163 acts inhibitory on phorbol ester-activated T-lymphocytes, whereas membrane-bound protein has no effect. *FEBS Lett* **526**, 93-96 (2002).
575. Hogger, P. & Sorg, C. Soluble CD163 inhibits phorbol ester-induced lymphocyte proliferation. *Biochem Biophys Res Commun* **288**, 841-843 (2001).
576. Timmermann, M., Buck, F., Sorg, C. & Hogger, P. Interaction of soluble CD163 with activated T lymphocytes involves its association with non-muscle myosin heavy chain type A. *Immunol Cell Biol* **82**, 479-487 (2004).
577. O'Connell, G.C. *et al.* Monocyte-lymphocyte cross-communication via soluble CD163 directly links innate immune system activation and

adaptive immune system suppression following ischemic stroke. *Sci Rep* **7**, 12940 (2017).
578. Piatkowski, A. *et al.* Soluble CD163: A novel biomarker for the susceptibility to sepsis in severe burn injuries. *Indian J Plast Surg* **44**, 118-124 (2011).
579. Nishino, A. *et al.* Usefulness of soluble CD163 as a biomarker for macrophage activation syndrome associated with systemic lupus erythematosus. *Lupus* **28**, 986-994 (2019).
580. Chua, C.L. *et al.* Soluble CD163, a product of monocyte/macrophage activation, is inversely associated with haemoglobin levels in placental malaria. *PLoS One* **8**, e64127 (2013).
581. Kirkegaard-Klitbo, D.M. *et al.* Soluble CD163 predicts incident chronic lung, kidney and liver disease in HIV infection. *AIDS* **31**, 981-988 (2017).
582. Asadullah, K., Sterry, W. & Volk, H.D. Interleukin-10 therapy--review of a new approach. *Pharmacol Rev* **55**, 241-269 (2003).
583. Qiao, J. *et al.* Targeting Tumors with IL-10 Prevents Dendritic Cell-Mediated CD8(+) T Cell Apoptosis. *Cancer Cell* **35**, 901-915 e904 (2019).
584. Wang, Y. *et al.* Autocrine Complement Inhibits IL10-Dependent T-cell-Mediated Antitumor Immunity to Promote Tumor Progression. *Cancer Discov* **6**, 1022-1035 (2016).
585. Emmerich, J. *et al.* IL-10 directly activates and expands tumor-resident CD8(+) T cells without de novo infiltration from secondary lymphoid organs. *Cancer Res* **72**, 3570-3581 (2012).
586. Naing, A. *et al.* PEGylated IL-10 (Pegilodecakin) Induces Systemic Immune Activation, CD8(+) T Cell Invigoration and Polyclonal T Cell Expansion in Cancer Patients. *Cancer Cell* **34**, 775-791 e773 (2018).
587. Henriquez-Olguin, C. *et al.* Cytosolic ROS production by NADPH oxidase 2 regulates muscle glucose uptake during exercise. *Nat Commun* **10**, 4623 (2019).
588. Mantegazza, A.R., Magalhaes, J.G., Amigorena, S. & Marks, M.S. Presentation of phagocytosed antigens by MHC class I and II. *Traffic* **14**, 135-152 (2013).
589. Jansen, C.S. *et al.* An intra-tumoral niche maintains and differentiates stem-like CD8 T cells. *Nature* **576**, 465-470 (2019).
590. Simon, S. & Labarriere, N. PD-1 expression on tumor-specific T cells: Friend or foe for immunotherapy? *Oncoimmunology* **7**, e1364828 (2017).
591. Wherry, E.J. T cell exhaustion. *Nat Immunol* **12**, 492-499 (2011).
592. Jadhav, R.R. *et al.* Epigenetic signature of PD-1+ TCF1+ CD8 T cells that act as resource cells during chronic viral infection and respond to PD-1 blockade. *Proc Natl Acad Sci U S A* **116**, 14113-14118 (2019).
593. Siddiqui, I. *et al.* Intratumoral Tcf1(+)PD-1(+)CD8(+) T Cells with Stem-like Properties Promote Tumor Control in Response to Vaccination and Checkpoint Blockade Immunotherapy. *Immunity* **50**, 195-211 e110 (2019).
594. Chen, Z. *et al.* TCF-1-Centered Transcriptional Network Drives an Effector versus Exhausted CD8 T Cell-Fate Decision. *Immunity* **51**, 840-855 e845 (2019).
595. Simoni, Y. *et al.* Bystander CD8(+) T cells are abundant and phenotypically distinct in human tumour infiltrates. *Nature* **557**, 575-579 (2018).

596. Canale, F.P. *et al.* CD39 Expression Defines Cell Exhaustion in Tumor-Infiltrating CD8(+) T Cells. *Cancer Res* **78**, 115-128 (2018).
597. Duhen, T. *et al.* Co-expression of CD39 and CD103 identifies tumor-reactive CD8 T cells in human solid tumors. *Nat Commun* **9**, 2724 (2018).
598. Dace, D.S., Khan, A.A., Kelly, J. & Apte, R.S. Interleukin-10 promotes pathological angiogenesis by regulating macrophage response to hypoxia during development. *PLoS One* **3**, e3381 (2008).
599. Mazurier, F. *et al.* A novel immunodeficient mouse model--RAG2 x common cytokine receptor gamma chain double mutants--requiring exogenous cytokine administration for human hematopoietic stem cell engraftment. *J Interferon Cytokine Res* **19**, 533-541 (1999).
600. van Rijn, R.S. *et al.* A new xenograft model for graft-versus-host disease by intravenous transfer of human peripheral blood mononuclear cells in RAG2-/- gammac-/- double-mutant mice. *Blood* **102**, 2522-2531 (2003).
601. Ito, T. *et al.* Secreted Ectodomain of SIGLEC-9 and MCP-1 Synergistically Improve Acute Liver Failure in Rats by Altering Macrophage Polarity. *Sci Rep* **7**, 44043 (2017).
602. Miron, V.E. *et al.* M2 microglia and macrophages drive oligodendrocyte differentiation during CNS remyelination. *Nat Neurosci* **16**, 1211-1218 (2013).
603. Kocher, T. *et al.* CD4+ T cells, but not non-classical monocytes, are dispensable for the development of chronic lymphocytic leukemia in the TCL1-tg murine model. *Leukemia* **30**, 1409-1413 (2016).
604. Li, Z., Xu, X., Feng, X. & Murphy, P.M. The Macrophage-depleting Agent Clodronate Promotes Durable Hematopoietic Chimerism and Donor-specific Skin Allograft Tolerance in Mice. *Sci Rep* **6**, 22143 (2016).
605. Misharin, A.V., Morales-Nebreda, L., Mutlu, G.M., Budinger, G.R. & Perlman, H. Flow cytometric analysis of macrophages and dendritic cell subsets in the mouse lung. *Am J Respir Cell Mol Biol* **49**, 503-510 (2013).
606. Kinoshita, M. *et al.* Characterization of two F4/80-positive Kupffer cell subsets by their function and phenotype in mice. *J Hepatol* **53**, 903-910 (2010).
607. Han, Y.H. *et al.* RORalpha Induces KLF4-Mediated M2 Polarization in the Liver Macrophages that Protect against Nonalcoholic Steatohepatitis. *Cell Rep* **20**, 124-135 (2017).
608. Dawson, J.P. *et al.* Epidermal growth factor receptor dimerization and activation require ligand-induced conformational changes in the dimer interface. *Mol Cell Biol* **25**, 7734-7742 (2005).
609. Schyns, J. *et al.* Non-classical tissue monocytes and two functionally distinct populations of interstitial macrophages populate the mouse lung. *Nat Commun* **10**, 3964 (2019).
610. Misharin, A.V. *et al.* Monocyte-derived alveolar macrophages drive lung fibrosis and persist in the lung over the life span. *J Exp Med* **214**, 2387-2404 (2017).
611. Hashimoto, D. *et al.* Tissue-resident macrophages self-maintain locally throughout adult life with minimal contribution from circulating monocytes. *Immunity* **38**, 792-804 (2013).
612. Bain, C.C. *et al.* Resident and pro-inflammatory macrophages in the colon represent alternative context-dependent fates of the same Ly6Chi monocyte precursors. *Mucosal Immunol* **6**, 498-510 (2013).

613. N, A.G. *et al.* Phagocytosis imprints heterogeneity in tissue-resident macrophages. *J Exp Med* **214**, 1281-1296 (2017).
614. Martinez-Pomares, L. *et al.* Fc chimeric protein containing the cysteine-rich domain of the murine mannose receptor binds to macrophages from splenic marginal zone and lymph node subcapsular sinus and to germinal centers. *J Exp Med* **184**, 1927-1937 (1996).
615. Liegeois, M., Legrand, C., Desmet, C.J., Marichal, T. & Bureau, F. The interstitial macrophage: A long-neglected piece in the puzzle of lung immunity. *Cell Immunol* **330**, 91-96 (2018).
616. Gibbings, S.L. *et al.* Three Unique Interstitial Macrophages in the Murine Lung at Steady State. *Am J Respir Cell Mol Biol* **57**, 66-76 (2017).
617. Tan, S.Y. & Krasnow, M.A. Developmental origin of lung macrophage diversity. *Development* **143**, 1318-1327 (2016).
618. Schyns, J., Bureau, F. & Marichal, T. Lung Interstitial Macrophages: Past, Present, and Future. *J Immunol Res* **2018**, 5160794 (2018).
619. Scodeller, P. *et al.* Precision Targeting of Tumor Macrophages with a CD206 Binding Peptide. *Sci Rep* **7**, 14655 (2017).
620. Pang, L. *et al.* Surface Modification of Polymeric Nanoparticles with M2pep Peptide for Drug Delivery to Tumor-Associated Macrophages. *Pharm Res* **36**, 65 (2019).
621. Kratochvill, F. *et al.* TNF Counterbalances the Emergence of M2 Tumor Macrophages. *Cell Rep* **12**, 1902-1914 (2015).
622. Li, C. *et al.* Single cell transcriptomics based-MacSpectrum reveals novel macrophage activation signatures in diseases. *JCI Insight* **5** (2019).
623. Guerriero, J.L. Macrophages: The Road Less Traveled, Changing Anticancer Therapy. *Trends Mol Med* **24**, 472-489 (2018).
624. Nahrendorf, M. & Swirski, F.K. Abandoning M1/M2 for a Network Model of Macrophage Function. *Circ Res* **119**, 414-417 (2016).
625. Ruytinx, P., Proost, P., Van Damme, J. & Struyf, S. Chemokine-Induced Macrophage Polarization in Inflammatory Conditions. *Front Immunol* **9**, 1930 (2018).
626. Heinrich, F. *et al.* Morphologic, phenotypic, and transcriptomic characterization of classically and alternatively activated canine blood-derived macrophages in vitro. *PLoS One* **12**, e0183572 (2017).
627. Otero, K. *et al.* Macrophage colony-stimulating factor induces the proliferation and survival of macrophages via a pathway involving DAP12 and beta-catenin. *Nat Immunol* **10**, 734-743 (2009).
628. Zeyda, M. *et al.* Human adipose tissue macrophages are of an anti-inflammatory phenotype but capable of excessive pro-inflammatory mediator production. *Int J Obes (Lond)* **31**, 1420-1428 (2007).
629. Shen, L. *et al.* M2 tumour-associated macrophages contribute to tumour progression via legumain remodelling the extracellular matrix in diffuse large B cell lymphoma. *Sci Rep* **6**, 30347 (2016).
630. Hagert, C., Sareila, O., Kelkka, T., Jalkanen, S. & Holmdahl, R. The Macrophage Mannose Receptor Regulate Mannan-Induced Psoriasis, Psoriatic Arthritis, and Rheumatoid Arthritis-Like Disease Models. *Front Immunol* **9**, 114 (2018).
631. Luca, M.E. *et al.* Mannosylated PLP(139-151) induces peptide-specific tolerance to experimental autoimmune encephalomyelitis. *J Neuroimmunol* **160**, 178-187 (2005).

632. Kel, J. *et al.* Soluble mannosylated myelin peptide inhibits the encephalitogenicity of autoreactive T cells during experimental autoimmune encephalomyelitis. *Am J Pathol* **170**, 272-280 (2007).
633. Schuette, V. *et al.* Mannose receptor induces T-cell tolerance via inhibition of CD45 and up-regulation of CTLA-4. *Proc Natl Acad Sci U S A* **113**, 10649-10654 (2016).
634. Zizzo, G., Hilliard, B.A., Monestier, M. & Cohen, P.L. Efficient clearance of early apoptotic cells by human macrophages requires M2c polarization and MerTK induction. *J Immunol* **189**, 3508-3520 (2012).
635. Zhou, Y. *et al.* Blockade of the Phagocytic Receptor MerTK on Tumor-Associated Macrophages Enhances P2X7R-Dependent STING Activation by Tumor-Derived cGAMP. *Immunity* **52**, 357-373 e359 (2020).
636. Dvorak, H.F. Leaky tumor vessels: consequences for tumor stroma generation and for solid tumor therapy. *Prog Clin Biol Res* **354A**, 317-330 (1990).
637. Bian, Z. *et al.* Cd47-Sirpalpha interaction and IL-10 constrain inflammation-induced macrophage phagocytosis of healthy self-cells. *Proc Natl Acad Sci U S A* **113**, E5434-5443 (2016).
638. Etzerodt, A. *et al.* Specific targeting of CD163(+) TAMs mobilizes inflammatory monocytes and promotes T cell-mediated tumor regression. *J Exp Med* **216**, 2394-2411 (2019).
639. Weber, L.M. & Robinson, M.D. Comparison of clustering methods for high-dimensional single-cell flow and mass cytometry data. *Cytometry A* **89**, 1084-1096 (2016).
640. Hu, M.W. *et al.* PanoView: An iterative clustering method for single-cell RNA sequencing data. *PLoS Comput Biol* **15**, e1007040 (2019).
641. Matsui, M. *et al.* Targeted delivery of oligomannose-coated liposome to the omental micrometastasis by peritoneal macrophages from patients with gastric cancer. *Cancer Sci* **101**, 1670-1677 (2010).
642. Arlauckas, S.P. *et al.* In vivo imaging reveals a tumor-associated macrophage-mediated resistance pathway in anti-PD-1 therapy. *Sci Transl Med* **9** (2017).
643. Guo, L. *et al.* CD163+ macrophages promote angiogenesis and vascular permeability accompanied by inflammation in atherosclerosis. *J Clin Invest* **128**, 1106-1124 (2018).
644. Dalton, H.J. *et al.* Macrophages Facilitate Resistance to Anti-VEGF Therapy by Altered VEGFR Expression. *Clin Cancer Res* **23**, 7034-7046 (2017).
645. Vitale, I., Manic, G., Coussens, L.M., Kroemer, G. & Galluzzi, L. Macrophages and Metabolism in the Tumor Microenvironment. *Cell Metab* **30**, 36-50 (2019).
646. Mukherjee, S., Sonanini, D., Maurer, A. & Daldrup-Link, H.E. The yin and yang of imaging tumor associated macrophages with PET and MRI. *Theranostics* **9**, 7730-7748 (2019).
647. Blykers, A. *et al.* PET Imaging of Macrophage Mannose Receptor-Expressing Macrophages in Tumor Stroma Using 18F-Radiolabeled Camelid Single-Domain Antibody Fragments. *J Nucl Med* **56**, 1265-1271 (2015).

648. Azad, A.K. *et al.* gamma-Tilmanocept, a New Radiopharmaceutical Tracer for Cancer Sentinel Lymph Nodes, Binds to the Mannose Receptor (CD206). *J Immunol* **195**, 2019-2029 (2015).
649. Eichendorff, S. *et al.* Biodistribution and PET imaging of a novel [68Ga]-anti-CD163-antibody conjugate in rats with collagen-induced arthritis and in controls. *Mol Imaging Biol* **17**, 87-93 (2015).
650. Figueroa-Protti, L., Soto-Molinari, R., Calderon-Osorno, M., Mora, J. & Alpizar-Alpizar, W. Gastric Cancer in the Era of Immune Checkpoint Blockade. *J Oncol* **2019**, 1079710 (2019).
651. Gu, L. *et al.* PD-L1 and gastric cancer prognosis: A systematic review and meta-analysis. *PLoS One* **12**, e0182692 (2017).
652. Goldman, N. *et al.* High macrophage PD-L1 expression not responsible for T cell suppression. *Cell Immunol* **324**, 50-58 (2018).
653. Etzerodt, A. *et al.* Tissue-resident macrophages in omentum promote metastatic spread of ovarian cancer. *J Exp Med* **217** (2020).
654. Movahedi, K. *et al.* Different tumor microenvironments contain functionally distinct subsets of macrophages derived from Ly6C(high) monocytes. *Cancer Res* **70**, 5728-5739 (2010).
655. Mills, E.L. *et al.* Succinate Dehydrogenase Supports Metabolic Repurposing of Mitochondria to Drive Inflammatory Macrophages. *Cell* **167**, 457-470 e413 (2016).
656. Serrat, N. *et al.* The response of secondary genes to lipopolysaccharides in macrophages depends on histone deacetylase and phosphorylation of C/EBPbeta. *J Immunol* **192**, 418-426 (2014).
657. Sandoval, J. *et al.* Epigenetic Regulation of Early- and Late-Response Genes in Acute Pancreatitis. *J Immunol* **197**, 4137-4150 (2016).
658. Moore, K.J., Sheedy, F.J. & Fisher, E.A. Macrophages in atherosclerosis: a dynamic balance. *Nat Rev Immunol* **13**, 709-721 (2013).
659. Altan-Bonnet, G. & Mukherjee, R. Cytokine-mediated communication: a quantitative appraisal of immune complexity. *Nat Rev Immunol* **19**, 205-217 (2019).
660. Toki, M.I. *et al.* High-Plex Predictive Marker Discovery for Melanoma Immunotherapy-Treated Patients Using Digital Spatial Profiling. *Clin Cancer Res* **25**, 5503-5512 (2019).
661. Schwen, L.O. *et al.* Data-Driven Discovery of Immune Contexture Biomarkers. *Front Oncol* **8**, 627 (2018).
662. Jankovic, D., Kugler, D.G. & Sher, A. IL-10 production by CD4+ effector T cells: a mechanism for self-regulation. *Mucosal Immunol* **3**, 239-246 (2010).
663. Barilla, R.M. *et al.* Specialized dendritic cells induce tumor-promoting IL-10(+)IL-17(+) FoxP3(neg) regulatory CD4(+) T cells in pancreatic carcinoma. *Nat Commun* **10**, 1424 (2019).
664. Song, S. *et al.* Tumour-derived IL-10 within tumour microenvironment represses the antitumour immunity of Socs1-silenced and sustained antigen expressing DCs. *Eur J Cancer* **48**, 2252-2259 (2012).
665. Sawant, D.V. *et al.* Adaptive plasticity of IL-10(+) and IL-35(+) Treg cells cooperatively promotes tumor T cell exhaustion. *Nat Immunol* **20**, 724-735 (2019).
666. Proto, J.D. *et al.* Regulatory T Cells Promote Macrophage Efferocytosis during Inflammation Resolution. *Immunity* **49**, 666-677 e666 (2018).

667. Gomez-Roca, C.A. *et al.* Phase I Study of Emactuzumab Single Agent or in Combination with Paclitaxel in Patients with Advanced/Metastatic Solid Tumors Reveals Depletion of Immunosuppressive M2-like Macrophages. *Ann Oncol* (2019).
668. Mardiana, S., Lai, J., House, I.G., Beavis, P.A. & Darcy, P.K. Switching on the green light for chimeric antigen receptor T-cell therapy. *Clin Transl Immunology* **8**, e1046 (2019).
669. Ardura, J.A. *et al.* Targeting Macrophages: Friends or Foes in Disease? *Front Pharmacol* **10**, 1255 (2019).
670. Peranzoni, E. *et al.* Macrophages impede CD8 T cells from reaching tumor cells and limit the efficacy of anti-PD-1 treatment. *Proc Natl Acad Sci U S A* **115**, E4041-E4050 (2018).
671. Chmielewski, M., Kopecky, C., Hombach, A.A. & Abken, H. IL-12 release by engineered T cells expressing chimeric antigen receptors can effectively Muster an antigen-independent macrophage response on tumor cells that have shut down tumor antigen expression. *Cancer Res* **71**, 5697-5706 (2011).
672. Liu, X. *et al.* Dual Targeting of Innate and Adaptive Checkpoints on Tumor Cells Limits Immune Evasion. *Cell Rep* **24**, 2101-2111 (2018).
673. Zhu, Y. *et al.* NADPH oxidase 2 inhibitor diphenyleneiodonium enhances ROS-independent bacterial phagocytosis in murine macrophages via activation of the calcium-mediated p38 MAPK signaling pathway. *Am J Transl Res* **9**, 3422-3432 (2017).
674. Kelkenberg, U., Wagner, A.H., Sarhaddar, J., Hecker, M. & von der Leyen, H.E. CCAAT/enhancer-binding protein decoy oligodeoxynucleotide inhibition of macrophage-rich vascular lesion formation in hypercholesterolemic rabbits. *Arterioscler Thromb Vasc Biol* **22**, 949-954 (2002).
675. Gantke, T. *et al.* Trispecific antibodies for CD16A-directed NK cell engagement and dual-targeting of tumor cells. *Protein Eng Des Sel* **30**, 673-684 (2017).
676. Scott, E.M. *et al.* Bi- and tri-valent T cell engagers deplete tumour-associated macrophages in cancer patient samples. *J Immunother Cancer* **7**, 320 (2019).
677. Ireland, L.V. & Mielgo, A. Macrophages and Fibroblasts, Key Players in Cancer Chemoresistance. *Front Cell Dev Biol* **6**, 131 (2018).
678. Chen, J. *et al.* Single-cell transcriptome analysis identifies distinct cell types and niche signaling in a primary gastric organoid model. *Sci Rep* **9**, 4536 (2019).
679. Zhang, R. *et al.* Cancer-associated fibroblasts enhance tumor-associated macrophages enrichment and suppress NK cells function in colorectal cancer. *Cell Death Dis* **10**, 273 (2019).
680. Cheng, Y. *et al.* Cancer-associated fibroblasts induce PDL1+ neutrophils through the IL6-STAT3 pathway that foster immune suppression in hepatocellular carcinoma. *Cell Death Dis* **9**, 422 (2018).
681. O'Neill, L.A. & Pearce, E.J. Immunometabolism governs dendritic cell and macrophage function. *J Exp Med* **213**, 15-23 (2016).
682. Eissmann, M.F. *et al.* IL-33-mediated mast cell activation promotes gastric cancer through macrophage mobilization. *Nat Commun* **10**, 2735 (2019).

683. Wang, L. *et al.* Increased myeloid-derived suppressor cells in gastric cancer correlate with cancer stage and plasma S100A8/A9 proinflammatory proteins. *J Immunol* **190**, 794-804 (2013).
684. Mattiola, I. *et al.* The macrophage tetraspan MS4A4A enhances dectin-1-dependent NK cell-mediated resistance to metastasis. *Nat Immunol* **20**, 1012-1022 (2019).
685. Davis, M.M., Tato, C.M. & Furman, D. Systems immunology: just getting started. *Nat Immunol* **18**, 725-732 (2017).
686. Carvajal-Hausdorf, D.E. *et al.* Multiplexed (18-Plex) Measurement of Signaling Targets and Cytotoxic T Cells in Trastuzumab-Treated Patients using Imaging Mass Cytometry. *Clin Cancer Res* **25**, 3054-3062 (2019).
687. Bouzekri, A., Esch, A. & Ornatsky, O. Multidimensional profiling of drug-treated cells by Imaging Mass Cytometry. *FEBS Open Bio* **9**, 1652-1669 (2019).
688. Ijsselsteijn, M.E., van der Breggen, R., Farina Sarasqueta, A., Koning, F. & de Miranda, N. A 40-Marker Panel for High Dimensional Characterization of Cancer Immune Microenvironments by Imaging Mass Cytometry. *Front Immunol* **10**, 2534 (2019).
689. Vickovic, S. *et al.* High-definition spatial transcriptomics for in situ tissue profiling. *Nat Methods* **16**, 987-990 (2019).
690. Stahl, P.L. *et al.* Visualization and analysis of gene expression in tissue sections by spatial transcriptomics. *Science* **353**, 78-82 (2016).